Shigeo Kida (Ed.)

IUTAM Symposium on
Elementary Vortices and Coherent Structures: Significance in Turbulence Dynamics

IUTAM

Springer

IUTAM Symposium on Elementary Vortices
and Coherent Structures: Significance in Turbulence Dynamics

FLUID MECHANICS AND ITS APPLICATIONS
Volume 79

Series Editor: R. MOREAU
MADYLAM
Ecole Nationale Supérieure d'Hydraulique de Grenoble
Boîte Postale 95
38402 Saint Martin d'Hères Cedex, France

Aims and Scope of the Series

The purpose of this series is to focus on subjects in which fluid mechanics plays a fundamental role.

As well as the more traditional applications of aeronautics, hydraulics, heat and mass transfer etc., books will be published dealing with topics which are currently in a state of rapid development, such as turbulence, suspensions and multiphase fluids, super and hypersonic flows and numerical modelling techniques.

It is a widely held view that it is the interdisciplinary subjects that will receive intense scientific attention, bringing them to the forefront of technological advancement. Fluids have the ability to transport matter and its properties as well as transmit force, therefore fluid mechanics is a subject that is particulary open to cross fertilisation with other sciences and disciplines of engineering. The subject of fluid mechanics will be highly relevant in domains such as chemical, metallurgical, biological and ecological engineering. This series is particularly open to such new multidisciplinary domains.

The median level of presentation is the first year graduate student. Some texts are monographs defining the current state of a field; others are accessible to final year undergraduates; but essentially the emphasis is on readability and clarity.

IUTAM Symposium on Elementary Vortices and Coherent Structures: Significance in Turbulence Dynamics

Proceedings of the IUTAM Symposium
held at Kyoto International Community House, Kyoto,
Japan, 26-28 October 2004

Edited by

SHIGEO KIDA

Kyoto University,
Department of Mechanical Engineering and Science,
Kyoto, Japan

Springer

Scientific Committee

S. Kida	(Chairman)	Kyoto (Japan)
M.E. Brachet		Paris (France)
M.S. Chong		Melbourne (Australia)
F. Hussain		Houston (USA)
J. Jiménez		Madrid (Spain)
T. Miyauchi		Tokyo (Japan)
H.K. Moffatt		Cambridge (UK)
D. Pullin		Pasadena (USA)

Local Organizing Committee

M. Nagata	(Chairman)	Kyoto (Japan)
M. Funakoshi		Kyoto (Japan)
S. Goto		Kyoto (Japan)
H. Hanazaki		Kyoto (Japan)
G. Kawahara		Kyoto (Japan)
S. Kida		Kyoto (Japan)
S. Komori		Kyoto (Japan)
T. Matsumoto		Kyoto (Japan)
H. Miura		Toki (Japan)
T. Miyazaki		Tokyo (Japan)
K. Ohkitani		Kyoto (Japan)
S. Toh		Kyoto (Japan)
M. Yamada		Kyoto (Japan)
S. Yoden		Kyoto (Japan)

Sponsors of Symposium

This Symposium was held under the auspices of

International Union of Theoretical and Applied Mechanics (IUTAM)

with the support of

Science Council of Japan,
Japan Society of Fluid Mechanics,
The Physical Society of Japan, and
The Japan Society of Mechanical Engineers.

The financial support has been received from

Commemorative Organization for the Japan World Exposition ('70),
Inoue Foundation for Science,
The 21st Century COE Program for Research and Education on Complex Functional Mechanical Systems,
The 21st Century COE Program for Elucidation of the Active Geosphere (KAGI21),
The 21st Century COE Program for Formation and an International Center of Excellence in the Frontiers of Mathematics and Fostering of Researchers in Future Generations, and
The 21st Century COE Program for Center of Diversity and Universality in Physics.

Professor Isao Imai, 7. 10. 1914 – 24. 10. 2004

PROFESSOR ISAO IMAI - 7. 10. 1914 TO 24. 10. 2004

It was on 24 October 2004, two days before the opening of the present IUTAM Symposium, that Professor Isao Imai passed away in Tokyo on cardiac insufficiency at the age of ninety. He was involved in this Symposium as one of the supervisors of its mother project, Special Project Research on *New Developments in Turbulence Study by Means of Turbulent Elementary Vortices* supported by Ministry of Education, Culture, Sports, Science and Technology, and his presence to the Symposium was expected if his health permitted. In the Opening Session of the Symposium, a tribute to his memory has been paid by Professor Keith Moffatt, President of the IUTAM who participated in the Symposium as a member of the Scientific Committee, and a silent prayer to him has been offered by all attendants of the Session. In view of his great achievements in the fields of *Theoretical and Applied Mechanics* and devoted contribution to the IUTAM for many years, it has been decided to dedicate this IUTAM Symposium to the memory of the late Professor Isao Imai.

He was born in 1914 in Tairen of Manchuria, China, and has grown up in Kobe since his family came back to Japan afterward. His outstanding gift was already apparent from his boyhood as he finished his elementary and middle school courses each one year earlier and entered The First High School in Tokyo. Then he proceeded to Tokyo University, Faculty of Science, Department of Physics, and obtained there the degree of B. Sc. in 1936 at the age of 21.

He started his academic career at Osaka University as a research associate to Prof. S. Tomotika, and after two years he came back to Tokyo University as a lecturer, then was promoted to an associate professor and nominated Professor of Physics in 1950. In Tokyo University, he achieved brilliant contributions in science, brought up a number of excellent scientists and extended his scientific influence to general people until his retirement in 1975. Then he continued his academic activity in Osaka University for three years and again came back to Tokyo to teach in Kogakuin University.

His scientific works have mostly been made in the fields of *fluid mechanics* and *mathematical physics*. When he started his research in 1936, fluid mechanics has been in a stage of innovation. The traditional *hydrodynamics*, dealing with the perfect fluid devoid of the compressibility and viscosity of the fluid, had already been in a deadlock and new fields such as *high-speed airflows*, *boundary layers* and *turbulence* have been attracting researchers' interest. The representatives of his early works, that is, *wing theory of arbitrary sections*, *transonic similarity of high-speed airflows* and *theory of slow viscous flows*, are all excellent contributions to these new fields. These subjects concerning the real-fluid effects in fluid flows had already been dealt with by several researchers but not always satisfactorily, and his solutions derived using his unique methods

based on complex analysis are known to be the most general, systematic and complete. He was awarded the Asahi Culture Prize in 1951 and the Prize and Imperial Award of the Japan Academy in 1959. He was elected the Honorary Member of the American Aeronautical Society (now AIAA) in 1962.

The physical generality and the mathematical elegance of his approach have been displayed beyond the realm of *fluid mechanics*. Inspired by the progress in astro-physics and nuclear-fusion research after the War, great interests of researchers have been directed to the new field of *magneto-hydrodynamics* (MHD). He extended his activity to this field and, using a new concept of *virtual fluid*, expressed the MHD flows in terms of ordinary fluid mechanics and reformulated the framework of the MHD. Furthermore, his interest has been directed to *electromagnetism* itself and, defining the electro-magnetic field as a mechanical system satisfying the conservation laws of the momentum and the energy, he reformulated the theory of electromagnetism according to the fluid-mechanical concepts and methodology. As the result, several ambiguities and errors have been removed from the formulas of the electromagnetic forces acting on the solid bodies.

Another important extension of his approach has been made to the theory of *hyper-function*. Taking the reverse view of the conventional concept of fluid mechanics as a branch of applied mathematics, he considered the *hyper-function of Sato* as a *vortex-layer* in fluid mechanics and reformulated the theory of hyper-function. Such a change of the view-point seems to provide us with a clear image of the hyper-function and open a broad way of its application to science and technology.

His ability has also been displayed in administrative posts both domestic and international. He was appointed the president of the Physical Society of Japan, the president of the Japan Society of Fluid Mechanics, the vice-president of the International Union of Pure and Applied Physics (IUPAP), and the bureau member of the International Union of Theoretical and Applied Mechanics (IUTAM). He also held visiting professorship in several universities such as Maryland University, Marseilles University, Cornell University, and Aachen Technical University. In appreciation of his outstanding academic contributions, he was honored as the Person of Distinguished Services in Culture in 1979 and awarded the Order of Cultural Merit in 1988 and the First Order of Merit in 1992.

Looking back his brilliant scientific works for many years, we should recognize his clear line of thought on *fluid physics*. That is to consider the *fluid* as a mechanical system subject to physical conservation principles and to derive the physical laws of *fluid flows* by solving the governing mathematical equations, using new concepts and methods if necessary. Here the *fluid flows* are often expressed as the *singularities* of the equations and their *physical laws* take the form of the *asymptotic similarity* around the singularities. If such an approach

of *fluid physics* may be called *mathematical physics of fluids*, the outstanding feature of his works, the "*clarity and generality*", seems to stem from his stoical adherence to *mathematical physics of fluids*.

Although he himself has not dealt with any particular problem of turbulence, he has always been encouraging the efforts by younger people to upgrade *turbulence research* to the stage of *mathematical physics of fluids*. Actually we may notice several papers in the present Symposium along this line of idea.

Now the subject of *fluid physics* is expanding from the classical Newtonian fluid to electromagnetic fluid, quantum fluid, reacting fluids, atmospheric and oceanic fluids, cosmic and planetary fluids and so on, and all of these new fluids are known to be associated with some kind of turbulent phenomena. It should be our pleasant task to take our steps of *turbulence research* forward to such new fields of *mathematical physics of fluids*.

Tomomasa Tatsumi
Emeritus Professor of Kyoto University

Elementary Vortices and Coherent Structures: Significance in Turbulence Dynamics, Kyoto, Japan, 26 – 28 October 2004

Contents

Part C   Chaotic advection and mixing

Part D   Statistical properties of turbulence

Part E   Rotating and stratified turbulence

Part H   **Finite-time singularity**

Part I   **Superfluid turbulence**

Preface

By the elementary vortices, we mean those tubular swirling vortical structures with concentrated vorticity which are commonly observed in various kinds of turbulent flows as the smallest coherent motion. The elementary vortices play key roles in turbulence dynamics (e.g. enhancement of mixing, diffusion and resistance) and characterizes turbulence statistics (e.g. intermittency). Because of their dynamical importance, manipulation of elementary vortices and coherent structures is expected to be effective and useful in turbulence control as well as in construction of turbulence modeling. Besides its dynamical significance, the vortical structure is convenient in describing and understanding turbulence structure (e.g. skeleton representation with vortex axes), and the topological characterization by knottedness and crossing number. The vorticity equation has rich mathematical structures. The physics and mathematics of vortex reconnection and the finite-time singularity for both Euler and Navier-Stokes equations are related unresolved problems.

For the purpose of deepening our understanding on these subjects and searching new perspectives in theory, prediction, and control of turbulence the IUTAM Symposium entitled *Elementary Vortices and Coherent Structures — Significance in Turbulence Dynamics* was held during 26 – 28 October 2004, at Kyoto International Community House, Kyoto, Japan. There were eighty registered participants, representing eleven countries. The scientific program was composed of 5 sectional lectures of 50 minutes each, 16 regular lectures of 25 minutes each, and 21 posters with oral presentations of 3 minutes each. Most of these presentations are included in this proceedings. All the papers were refereed by all members of Scientific Committee and revised appropriately. They are divided into six groups: (A) Vortex dynamics, (B) Coherent structures, (C) Chaotic advection and mixing, (D) Statistical properties of turbulence, (E) Rotating and stratified turbulence, (F) Instability and transition, (G) Dynamics of thin vortices, (H) Finite-time singularity, and (I) Superfluid turbulence.

It was two days before this Symposium that Professor Isao Imai passed away at the age of ninety. It is really our deep grief that we lost such a distinguished and respectful scientist. He was one of the most influential scientists known worldwide in fluid mechanics and mathematical physics: high-speed flows, viscous flows, magnetohydrodynamics, theory of hyperfunctions, and so on. He was the member of IUTAM bureau in 1984 – 1992. At the opening of the Symposium a memorial address for him was given by Professor H.K. Moffatt, the President of IUTAM, and a silent prayer was offered by all participants. This proceedings is devoted to him with an obituary written by Professor T. Tatsumi, the former member of IUTAM bureau.

This Symposium would not have been performed successfully without devoted cooperation of many people. Professor T. Kambe, the representative of Japan in IUTAM, has encouraged and supported us continuously from the planning stage. The selection of papers for presentation in the Symposium as well as for publication in this proceedings was made based upon strict reviews by the Scientific Committee members. All the practical preparation of the Symposium, including the arrangement of the Symposium venue, the setup of the Symposium homepage, the raising of the financial support, and so on and so forth, was accomplished by the Local Organizing Committee members through their time-consuming efforts. All the miscellaneous tasks, occasionally being unexpected and confusing, were dealt with smoothly by Ms. Y. Shichida, the secretary general, with assistance of Ms. I. Goto. We would like to express our hearty gratitude to all of these people as well as all the participants of the Symposium who activated it.

Generous supports to the Symposium are gratefully acknowledged for IUTAM, the Commemorative Organization for the Japan World Exposition ('70), Inoue Foundation for Science, and the 21st Century COE Programs in Kyoto University for Research and Education on Complex Functional Mechanical Systems, for Elucidation of the Active Geosphere (KAGI21), for Formation and an International Center of Excellence in the Frontiers of Mathematics and Fostering of Researchers in Future Generations, and for Center of Diversity and Universality in Physics.

Shigeo Kida

August 2005

Part A   Vortex dynamics

CLUSTERING OF INTENSE STRUCTURES IN ISOTROPIC TURBULENCE: NUMERICAL AND EXPERIMENTAL EVIDENCE

Frédéric Moisy
Fluides, Automatique et Systèmes Thermiques, Bât. 502, 91405 Orsay Cedex, France
moisy@fast.u-psud.fr

Javier Jiménez
School of Aeronautics, U. Politécnica, 28040 Madrid, Spain
Centre for Turbulence Research, Stanford University, USA
jimenez@torroja.dmt.upm.es

Abstract   The spatial distribution of intense structures in isotropic turbulence is studied from numerical and experimental data. Box-counting of the intense vorticity and strain rate sets gives evidence of a strong clustering at intermediate scales, from which a possible fractal dimension can be defined. Algebraically distributed free intervals between intense velocity derivative from experimental time series confirms this self-similar clustering at larger Reynolds numbers, but without further specifying its dimensionality.

Keywords: Turbulence, clustering, box-counting, fractals, dimension

1.   Introduction

Regions of high levels of dissipation and of vorticity in turbulent flows, such as vortex sheets and tubes, have been observed and characterized for a long time from numerical simulations. They result in highly non-Gaussian statistics of the velocity increments, which may depend both on the geometry of the individual structures, on their size distribution and on their spatial distribution at larger scales. Vortex tubes probably arise from stretched vortex layers formed at earlier time (Passot *et al.* 1995), and it is in those layers, and in the periphery of the vortex tubes, that high levels of energy dissipation are concentrated.

Intense objects are often treated as being randomly distributed in space. With this assumption, Hatakeyama & Kambe (1997) obtained inertial range scaling from an assembly of random Burgers' vortices. However, evidence

(a) $|\omega| > 3\,\omega'$

(b) $|\omega| > 6\,\omega'$

(c) $|s| > 2.8\,s'$
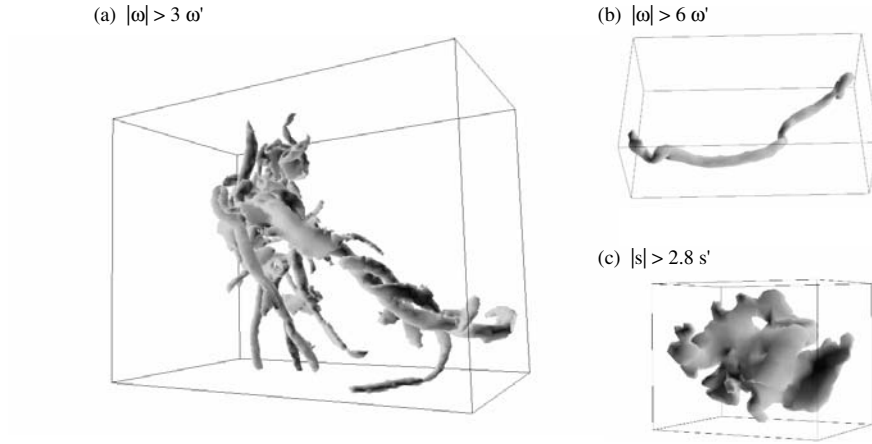
Figure 1. Structures of intense vorticity (a, b) and intense strain rate (c).

from numerics is inconsistent with a fully random distribution. Worms seem to accumulate in the interface between largely empty large-scale eddies (Jiménez *et al.* 1993), leading to an apparent inertial-scale clustering of intense vortices (Porter, Woodward & Pouquet 1997). Box-counting methods have been used by Moisy & Jiménez (2004) to further characterize this clustering.

Experimentally, spatial distributions can be inferred from waiting times between intense events recorded in one-point time series. The results of pressure measurements by Abry *et al.* (1994) showed algebraically-distributed waiting times, for inertial separations, between pressure drops marking large coherent vortices, suggesting self-similar clustering. Belin *et al.* (1996) and Mouri, Hori & Kawashima (2002) gave evidence, from one-point velocity time series, of the clustering of intense velocity gradients, which was shown to be self-similar by Camussi & Guj (1999) and Moisy (2000).

2.   Box-counting of intense sets from numerical data

Examples of structures of intense vorticity and intense strain rates are shown in figure 1 (Moisy & Jiménez 2004). Here, a *structure* simply refers to a connected volume satisfying a thresholding criterion, $|\omega| \geq \tau\omega'$ or $|s| \geq \tau s'$, where the primes denote the rms values, with $\omega'^2 = 2s'^2 = \epsilon/\nu$ (ϵ is the energy dissipation rate and ν the kinematic viscosity). These structures have been extracted from numerical simulations of forced isotropic turbulence at $Re_\lambda = 168$ (Jiménez *et al.* 1993). The resolution is 512^3 collocation points,
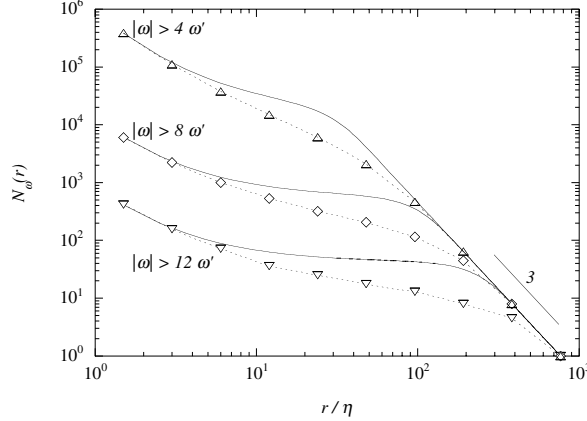
Figure 2. Symbols: Number of boxes of size r covering the vorticity sets, for the thresholds $|\omega| \geq 4$, 8 and 12 ω'. —, Box counts for sets of Poisson-distributed balls of the same total volume (data from the numerical simulation).

with periodic boundary conditions. The box size is 760η and the integral scale L_0 is around 1/4 of the box size, providing a scale separation of $L_0/\eta \simeq 200$.

The vorticity structures essentially show ribbons for moderate thresholds, and long filamentary tubes (figure 1b) for higher ones. The biggest structures associated to a moderate vorticity threshold show patterns resulting from the interaction of an intense vortex tube with surrounding weaker tubes, as in figure 1a. Very large thresholds only show smaller tubes, probably parts of the larger ones observed at lower thresholds, but no sheets or ribbons. The situation is different for the strain rate structures, for which both moderate and large thresholds show essentially sheets or ribbons. For low thresholds, the selected objects show intricate sponge-like patterns (figure 1c), or assemblies of sheets and ribbons. Increasing the threshold results in structures more like isolated sheets or ribbons.

In order to characterize the distribution of these structures in space, we begin by applying the classical method of box-counting to the sets of points of intense vorticity and strain rate magnitude. The computational domain is divided into cubical boxes of side r, and the number $N(r)$ of boxes containing some point of the set is counted. In the case of a pure fractal set of dimension D, the number of boxes would follow a power law $N(r) \sim r^{-D}$. In real systems this relation only holds in a restricted range of scales between a large- and a small-scale cutoff.

Figure 2 shows box counts for the sets of points of high vorticity, $N_\omega(r)$, for different values of the threshold. Similar results are obtained for the box count of the strain rate sets. The curves approach $N_\omega(r) \sim r^{-3}$ as $r \rightarrow L$, in which
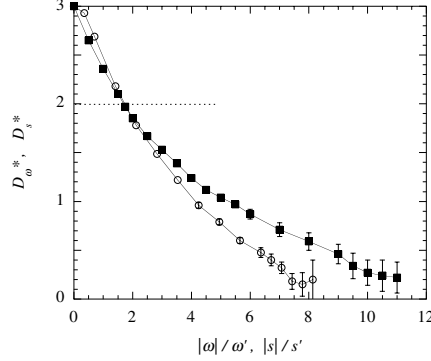
Figure 3. Minimum of the local slope of box counts as a function of the threshold, for the vorticity (■) and the strain rate (○) fields. The intersections of these curves with $D = 2$ (horizontal dashed line) indicate the thresholds above which sets of negative dimension are expected from experimental one-point measurements (see § 3).

case both the high-dissipation and the high-enstrophy sets look as a single solid object. At the small-scale end, $r \approx \eta$, the slopes also increase, reflecting the compactness of the objects at scales which are small enough for viscous effects to be important. For $r \ll \eta$ both sets should look as collections of small solid volumes, and one should expect the box counts to behave as $N(r) \simeq r^{-3}$. For intermediate scales, $\eta \ll r \ll L$, the box counts show a continuous evolution with the threshold, and none of the curves displays a real power-law range.

In order to interpret these box counts, it is of interest to compare them with box counts of sets with no clustering. If we consider a set of Poisson-distributed balls of radius δ, the expected number of covering boxes is

$$N_0(r) = \left(\frac{L}{r}\right)^3 \left(1 - \exp[-(r + \delta)^3/r_0^3]\right), \tag{1}$$

where r_0 is the mean distance between the balls. Together with the box-counts of figure 1 are plotted the best fits given by equation (1), using the constraint that the actual sets and the Poisson sets have the same volume, i.e. $N_0(r) \simeq N_\omega(r)$ for $r \to \eta$. Clearly the actual box counts are not described well by the assumption of Poisson-distributed balls. The actual number of covering boxes $N_\omega(r)$ is found to be significantly smaller than $N_0(r)$ for the central range $10\eta < r < 200\eta$, implying that the regions of high vorticity are concentrated on a smaller fraction of space than the random balls.

The clustering of the intense vorticity and strain rate sets for intermediate scales can be further characterized by introducing a local scaling exponent, defined as the logarithmic slope $D(r) = -\ln N(r)/dr$. Since one must recover the trivial exponent $D = 3$ at both large and small scales, one may expect the
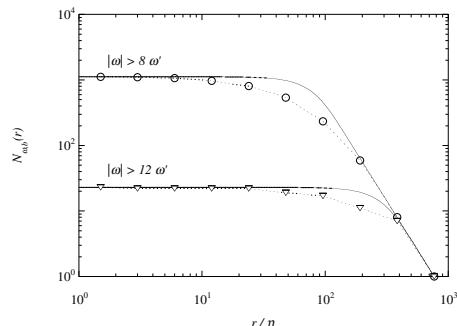
Figure 4. Symbols: Number of boxes of size r covering the set of baricenters of the vorticity structures, for the thresholds $|\omega| \geq 6$ and $12\ \omega'$. —, Box counts for sets of Poisson-distributed points.

minimum slope, D^*, to provide a useful measure of the dimensionality of the clustering. In the ideal case of objects distributed in space with a fractal dimension D, we should expect $D^* \to D$ in the limit of very large scale separation $\eta \ll r \ll L$. For finite scale separation, both the large- and the small-scale contamination tend to increase the observed minimum D^*, which therefore only represents an upper bound for the possible fractal dimension.

This minimum slope D^* is plotted in figure 3 as a function of the threshold for the vorticity and the strain rate sets. Both D^*_ω and D^*_s decrease as the threshold increases, and none of them shows a plateau on which to define a threshold-independent dimension. The sets associated to typical fluctuations, $|\omega| \simeq \omega'$ and $|s| \simeq s'$, have dimensions of about 2.5, suggesting that regions of typical dissipation and enstrophy levels are wrinkled sheets, in qualitative agreement with other indirect estimates (Sreenivasan 1991; Sreenivasan & Antonia 1997).

Since the vorticity and strain rate sets considered here are a collection of structures as those shown in figure 1, two contributions are expected for the box counts. For scales smaller or of the order of the structures size, the box counts essentially describe the geometry and the size distribution of the structures, while for larger scales the box counts is more sensitive to their spatial distribution. Since we are interested in the clustering of the intense structures, one may separate the latter contribution from the global box-counting, by replacing each structure by a single point located at its baricenter, and applying the box-counting method to the resulting point sets. This procedure is only valid in the limit of very large threshold, for which the mean distance between structures is expected to be much larger than the structure size.

Figure 4 shows the box counts $N_b(r)$ for the set of baricentres of the intense vorticity structures for two values of the threshold. As before, the scaling $N_b(r) \sim r^{-3}$ for large scales indicates the homogenous covering at large scales.

At small scales, $N_b(r)$ saturates at the total number of structures, as expected for a set of points. The cross-over between the small-scale plateau and the large-scale decrease occurs at the typical distance r_0 between structures, which depends on the threshold.

These box-counts may be compared to that of Poisson-distributed points, by taking $\delta = 0$ in equation (1). As for the global box-counting, the actual curves are well below the Poisson law, indicating that the points are concentrated in a smaller fraction of space than for the random set. This clustering fraction is maximum for scales in the inertial range, and takes values around 0.5. Similar results are obtained for the clustering of intense strain rate structures. One may conclude that the clustering effect shown in figure 2 is not only an effect of the intense vorticity field being concentrated into structures, but also that the structures themselves are concentrated into clusters.

3.   Clustering of intense events from experimental data

An issue raised by the previous observations in the low Reynolds number numerical simulations is whether the clustering of intense regions is still present at higher Reynolds number, and whether a range of scales exists for which this clustering is self-similar.

The decrease of the dimension D_α^* as the threshold is increased in figure 3 has important consequences for experiments for which only one-point measurements are available. From those measurements, the clustering of intense regions may be characterized from the distribution of the free intervals between successive intense events (Belin *et al.* 1996; Moisy 2000; Mouri, Hori & Kawashima 2002). For a fractal set of points of dimension $0 < d < 1$ with self-similar clustering, the distribution of the free intervals Δx decays as Δx^{-1-d} (Feder 1988). However, for large enough thresholds, figure 3 shows that both the vorticity and the dissipation fields concentrate into sets of dimension $D < 2$. As a consequence, the corresponding sets defined from one-dimensional cuts, as obtained from one-point time series with the use of the Taylor's hypothesis, should have a dimension $d = D - 2 < 0$, and are therefore almost surely empty. Only the presence of a small-scale cutoff, imposed by the Kolmogorov length scale or by the probe resolution, ensures that the one-dimensional sections are not empty.

Distributions of the free intervals Δx between successive intense velocity derivatives have been computed from experimental time series. The data are from a low temperature helium experiment, in which a large range of microscale Reynolds numbers can be spanned in very controlled conditions, Re_λ from 150 up to 2000 (Zocchi *et al.* 1994; Moisy, Tabeling & Willaime 1999). The flow takes place in a cylinder and is driven by two rotating disks equipped with blades, 20 cm in diameter and spaced 13 cm apart. Velocity measurements
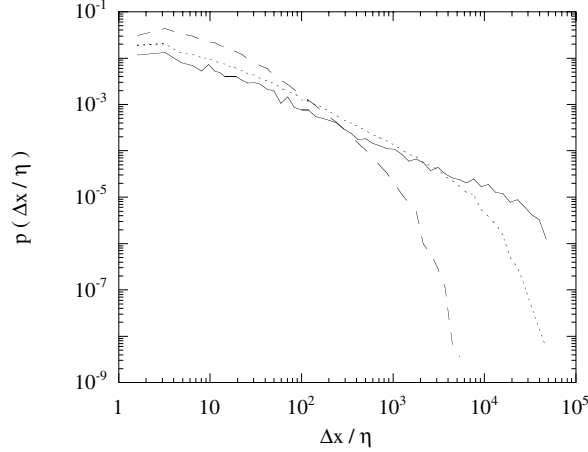
Figure 5. Probability density functions of the free intervals between intense velocity derivative $|\partial_x u|$ from the experimental time series, for $Re_\lambda = 1300$. They have been computed using logarithmic bins to ensure an acceptable number of events in the bins corresponding to the highest intervals. Thresholds: $--, 2(\partial_x u)'; \ldots, 5(\partial_x u)'; —, 8(\partial_x u)'$.

were carried out using a hot wire anemometer, and the Taylor hypothesis has been used to convert temporal fluctuations into spatial ones.

Figure 5 shows the probability density function $p(\Delta x/\eta)$ of the free intervals between intense longitudinal velocity derivative, $|\partial_x u| \geq \tau(\partial_x u)'$, for 3 different values of the threshold τ, for $Re_\lambda = 1300$. As before, the prime denotes the rms value, which is related to the mean energy dissipation rate using the assumption of isotropy, $(\partial_x u)'^2 = 2s'^2/15 = \epsilon/15\nu$. Note that, since only the longitudinal component of the velocity can be measured in the experiment, the intense longitudinal velocity derivatives are expected to trace essentially the intense strain rate regions rather than the intense vorticity regions. With this approximation, the quantity $(\partial_x u)^2$ has been extensively used as a one-dimensional surrogate for the local energy dissipation rate $\epsilon(\mathbf{x})$ (Sreenivasan 1991).

For sufficiently large threshold, the pdfs show a clear power law decay over a significant range of scales, starting from the dissipative range, $\Delta x \simeq 3\eta$, up to a large scale cutoff, of order of $10^3 - 10^4\eta$, that depends on the threshold. This algebraic decay confirms that the intense events do not appear randomly in space, but tend to form self-similar clusters with no characteristic scale. Beyond the large scale cutoff, the pdfs decay approximately exponentially, indicating statistically uncorrelated events at large scales. The poorly defined scaling law for moderate threshold probably originates from the increasing contribution from the exponential decay, that may contaminate intermediate scales.
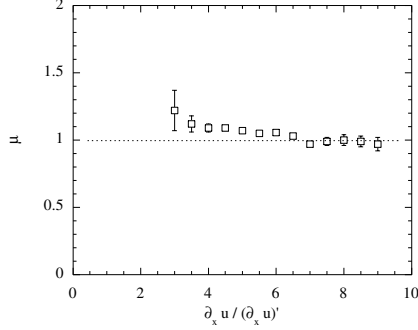
Figure 6a. Exponent μ of the power law from the distribution of free intervals between intense velocity derivative, $p(\Delta x) \sim \Delta x^{-\mu}$, as a function the threshold (data from the figure 5).
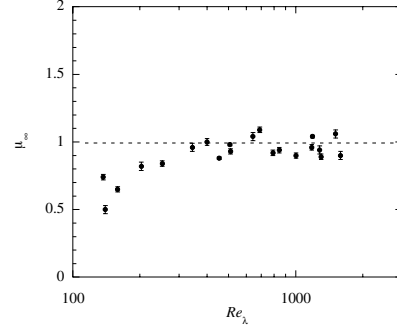
Figure 6b. Exponent μ in the limit of large threshold, $\tau \gg 1$, as a function of Re_λ.

The exponent μ of the power law decay, $p(\Delta x) \sim \Delta x^{-\mu}$, is plotted as a function of the threshold τ in figure 6a. It is found to slightly decrease from values larger than 1, and saturates toward approximately 1 for large threshold. This trend is consistent with the fractal dimension D^* determined from the numerical simulations, that takes values less than 2 for large enough threshold (see figure 3). As a consequence, the law $p(\Delta x) \sim x^{-1-d}$ with $d = D - 2$ does not hold any more for $d < 0$, and the distributions collapse towards the single curve $p(\Delta x) \sim \Delta x^{-1}$ for sufficiently large threshold. Similar observations have been reported for the free intervals between intense scalar fronts in turbulent mixing (Moisy *et al.* 2000).

In figure 6b is plotted the exponent μ_∞, obtained in the limit $\tau \gg 1$, as a function of Re_λ, indicating that the power law $p(\Delta x) \sim \Delta x^{-1}$ is robust for sufficiently large Reynolds numbers, $Re_\lambda > 400$. This asymptotic exponent μ_∞ is found to increase from 0.5 to approximately 1 for $Re_\lambda < 400$. It must be noted that values of μ less than 1 for low Reynolds numbers can not be interpreted in the frame of the law $p(\Delta x) \sim x^{-1-d}$ for an exact fractal set of points of dimension d, and probably results from finite scaling effects.

These experimental distributions confirm that the intense events appear within self-similar clusters, and cannot be considered as randomly distributed. This is consistent with the clustering of the intense dissipation events observed in the low Reynolds numbers simulations, but the one-dimensional cut in the experiment does not allow to further characterize the dimensionality of this clustering.

4. Discussion and conclusion

Three-dimensional box-counting from numerical simulations, and pdf of free intervals from experiments, gave evidence that the intense regions in isotropic turbulence, in the form of vortex sheets or tubes, tend to form clusters of inertial range extent. The dynamics of formation of the small scale structures from the instability of stretched shear layers at larger scales is probably the reason for this phenomenon. One may speculate that, for large Reynolds numbers, this process may repeat at different scales, leading to the observed self-similar clustering.

It is important to note that algebraic distributions for free intervals are not a trivial consequence of the self-similarity of the velocity field itself. Orey (1970) rigorously established that level sets from a Gaussian process with a power-law spectrum, $E(k) \sim k^{-n}$ with $1 < n < 3$, lead to fractal set of point of dimension $d = (3-n)/2$. In the case of the Kolmogorov spectrum, $n = 5/3$, this relation yields $d = 2/3$, and pdf of free intervals between iso-values of the velocity should decay as $p(\Delta x) \sim \Delta x^{-d-1} \sim \Delta x^{-5/3}$. Although turbulent velocity fluctuations are not Gaussian, the experimental results of Praskovsky *et al.* (1993) and Scotti, Meneveau & Saddoughi (1995) were in good agreement with Orey's theorem. However, it is clear that a fractal velocity field does not imply that the derivative fields are also fractal, and thus provides no insight into the spatial distribution of intense structures. Orey's theorem does not hold for the vorticity or dissipation fields, which have a spectrum $k^2 E(k) \sim k^{1/3}$. For instance, a Gaussian process with power-law spectrum and random phase has sets of iso-derivatives that are randomly distributed. One may conclude that the clustering of intense structures with a distribution of free intervals as $p(\Delta x) \sim \Delta x^{-1}$ is not a trivial consequence of the Kolmogorov spectrum, but is a true intermittency effect, that reveals the hierarchical organization of the small scale structures in turbulence.

References

ABRY, P., FAUVE, S., FLANDRIN, P. & LAROCHE, C. 1994 Analysis of pressure fluctuations in swirling turbulent flows. *J. Phys. II France* **4**, 725–733.

BELIN, F., MAURER, J., TABELING, T. & WILLAIME, H. 1996 Observation of intense filaments in fully developed turbulence. *J. Phys. II France* **6**, 573–583.

CAMUSSI, R. & GUJ, G. 1999 Experimental analysis of intermittent coherent structures in the near field of a high Re turbulent jet flow. *Phys. Fluids* **11**, 423–431.

FEDER, J. 1988 *Fractals*, Plenum, New York.

HATAKEYAMA, N. & KAMBE, T. 1997 Statistical laws of random strained vortices in turbulence. *Phys. Rev. Lett.* **79**, 1257–1260.

JIMÉNEZ, J., WRAY, A.A., SAFFMAN, P.G. & ROGALLO, R.S. 1993 The structure of intense vorticity in isotropic turbulence. *J. Fluid. Mech.* **255**, 4, 65–90.

12

MOISY, F., TABELING, P. & WILLAIME, H. 1999 Kolmogorov Equation in a fully developed turbulence experiment, *Phys. Rev. Lett.* **82** (20), 3994–3997.

MOISY, F. 2000 Etude expérimentale des fluctuations de vitesse, de température et de pression en turbulence développée. *Thesis* Univ. Paris 6.

MOISY, F., ANDERSEN, J.S., WILLAIME, H. & TABELING, P. 2000 Passive scalar intermittency: Statistics of the cliffs, in *Advances in Turbulence VIII* (ed. C. Dopazo) CIMNE Barcelona, 835–838.

MOISY, F. & JIMÉNEZ, J. 2004 Geometry and clustering of intense structures in isotropic turbulence., *J. Fluid. Mech.* **513**, 111–133.

MOURI, H., HORI, A. & KAWASHIMA, Y. 2002 Vortex tubes in velocity fields of laboratory isotropic turbulence: dependence on the Reynolds number. *Phys. Rev. E* **67**, 06305.

OREY, S. 1970 Gaussian sample functions and the Hausdorf dimension of level crossings. *Z. Wahrscheinlichkeitheorie verw. Geb.* **15**, 249–256.

PASSOT, T., POLITANO, H., SULEM, P.L., ANGILELLA, J.R & MENEGUZZI, M. 1995 Instability of strained vortex layers and vortex tube formation in homogeneous turbulence. *J. Fluid. Mech.* **282**, 313–338.

PORTER, D.H., WOODWARD, P.R. & POUQUET, A. 1997 Inertial range structures in decaying compressible turbulent flows, *Phys. Fluids* **10**, 237–245.

PRASKOVSKY, A.A., FOSS, J.F., KLEIS, S.J. & KARYAKIN, M.Y. 1993 Fractal properties of isovelocity surfaces in high Reynolds number laboratory shear flows. *Phys. Fluids A* **5**, 2038–2042.

SCOTTI, A., MENEVEAU, C. & SADDOUGHI, S.G. 1995 Fractal dimension of velocity signals in high-Reynolds-number hydrodynamic turbulence. *Phys. Rev. E* **51** 5594–5608.

SREENIVASAN, K.R. 1991 Fractals and multifractals in fluid turbulence. *Annu. Rev. Fluid Mech.* **23**, 539–600.

SREENIVASAN, K.R. & ANTONIA, R.A. 1997 The phenomenology of small-scale turbulence. *Annu. Rev. Fluid Mech.* **29**, 435–472.

ZOCCHI, G., TABELING, P., MAURER, J., & WILLAIME, H. 1994 Measurement of the scaling of the dissipation at high Reynolds numbers *Phys. Rev. E* **50** (5), 3693–3700.

MULTI MODES FOR THE VORTEX SHEET-TUBE TRANSFORMATION PROCESS AND VISCOELASTIC EFFECT

Kiyosi Horiuti, Yohei Takagi, Syouji Abe
Department of Mechano-Aerospace Engineering, Tokyo Institute of Technology
2-12-1 O-okayama, Meguro-ku, Tokyo 152-8552 Japan
khoriuti@mes.titech.ac.jp

Abstract   A process for formation of the stretched spiral vortex was investigated using the DNS data of homogeneous turbulence. It was shown that vortex tube was generated not by a rolling up of single vortex sheet but through an interaction of dual sheets. Depending on the alignment of vorticity vectors on vortex tube and vortex sheets which emanate from vortex tube, three modes of configuration were shown to exist. Frequency of appearance of three modes and its implication for turbulence generation was discussed in isotropic and sheared flows.

Keywords: Stretched spiral vortex, vortex sheet, isotropic turbulence, sheared turbulence

1.   Introduction

Primary elements which constitute the turbulent flow field are vortex sheets and vortex tubes (e.g., Horiuti 2001). These two structures are not distinctively separable because vortex tube is generally formed along vortex sheet during the rolling up of the sheet. One of the notable models which induces energy cascade and subsequent energy dissipation is the stretched spiral vortex model (Lundgren 1982). This model comprises of the vortex tube and the sheets which wraps around the tube, and yields the energy spectrum obeying the $-5/3$ law. The aim of the present study is to reveal a process for formation of the stretched spiral vortex, and show the role of the occurrence of this formation process on turbulence generation.

2.   A formation process of spiral vortex in isotropic turbulence

We utilized the DNS data for incompressible decaying/forced homogeneous isotropic turbulence, which were generated with 256^3 and 512^3 grid points.

In this section, we show the results obtained using the data in the decaying case with the 256^3 grid points and at an instant when the Reynolds number based on the Taylor microscale, $R_\lambda \approx 88$. In the present study, vortex tube and vortex sheet were identified using the second-order invariant of the velocity gradient tensor, Q, and the eigenvalue of the $-(S_{ik}\Omega_{kj} + S_{jk}\Omega_{ki})$ term, $[-(S_{ik}\Omega_{kj} + S_{jk}\Omega_{ki})]_+$, respectively. S_{ij} and Ω_{ij} denote the strain-rate and vorticity tensors, respectively. The eigenvalues were ordered so that the eigenvalue, the eigenvector of which is maximally aligned with the vorticity vector, is chosen as the z component, the largest remaining eigenvalue as the $+$ component, the smallest one as the $-$ component (Horiuti 2001). The eigenvalues of S_{ij} tensor are denoted as σ_z and $\sigma_\pm$.

Figure 1. Isosurfaces of the $[-(S_{ik}\Omega_{kj} + S_{jk}\Omega_{ki})]_+$ eigenvalue (plotted using the white color), and Q (black), obtained from DNS.

Figure 2. Front view of isosurfaces of $[-(S_{ik}\Omega_{kj}+S_{jk}\Omega_{ki})]_+$ (white), Q (black), and the dissipation term (dark gray).

In an early stage, several flat sheets, the lateral extents of which were several times the integral scale, emerged in the flow field. With lapse of time, the formation of tube occurred along these extensive sheets. Figure 1 shows the side view of the isosurfaces of the Q term, and the $[-(S_{ik}\Omega_{kj} + S_{jk}\Omega_{ki})]_+$ eigenvalue. It is seen in Fig. 1 that the vortex tube, which can be identified as a concentrated region of Q and drawn using the black color in the figure, was formed and the vortex sheets, which were drawn using the white color, were stretched and entrained by the vortex tube, and spiraling around the tube. These tube and sheets formed a structure similar to that of the stretched spiral vortex model (Lundgren 1982). Figure 2 shows the front view of the distribution of the dissipation term superposed on the isosurfaces of the vortex sheet and tube. It can be seen that the dissipation takes large values along this stretched spiral

vortex, indicating that intense energy cascade and subsequent dissipation take place along the sheet with the stretching and differential rotation of the sheets.

Figure 3a shows the schematic sketch of the distributions of the vorticity vectors along the vortex tube and sheets shown in Fig. 1. It was found that the distributions of the vorticity vectors on the two sheets shown in Fig. 1 were asymmetric, i.e., the vorticity vectors on upper sheet were perpendicular to those along the vortex tube, while the vorticity vectors on lower sheet were parallel to those along the tube. Arrangement of these vorticity vector alignment is different from that obtained using a conventional theory for the formation of vortex tube along vortex sheet, i.e., the rolling up of single vortex sheet due to the Kelvin-Helmholz instability (e.g., Neu 1994). This theory yields an arrangement of the vorticity vectors shown in Fig. 3b. In the following, the configurations shown in figures 3b and 3a are referred to as Mode 1 and Mode 2, respectively. The configuration with Mode 1 was considered in Lundgren (1982).
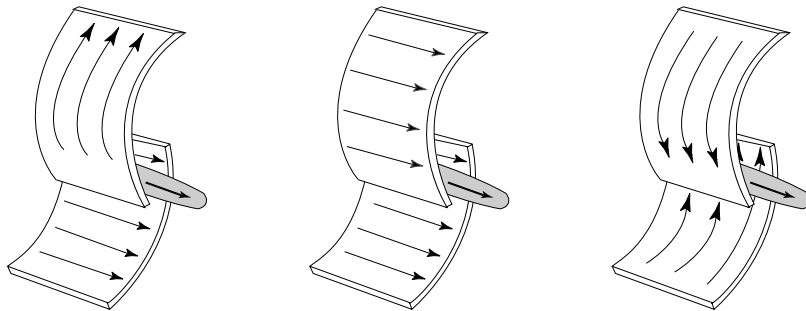
Figure 3a. Sketch of the vorticity vector arrangement along the dual sheets and the tube in Mode 2

Figure 3b. Sketch for Mode 1

Figure 3c. Sketch for Mode 3

Appearance of the configuration in Mode 2 is inconsistent with the stability analysis for the stagnation-point flow (Kerr and Dold 1994), in which it was shown that the vorticity component perpendicular to the direction of the diverging flow decays, and that the parallel component can grow. To educe the formation process of the configuration shown in Fig. 1, we traced the time development of the structures back in time. It was revealed that the vortex sheets shown in Fig. 1 actually consists of two different sheets, and the tube shown in Fig. 1 was not formed by a rolling-up of a single sheet, but formed through an interaction of the dual sheets. At an earlier time, these dual sheets formed a τ-shaped configuration, and one of the dual sheets was perpendicular to another sheet, and generated the stagnation point flow on another sheet. In

the region surrounded by the dual sheets, weak circulation associated with low pressure was generated. A schematic sketch of the basic configuration of the vorticity and velocity vectors along the dual sheets is shown in Fig. 4. The filled and dashed lines denote the velocity and vorticity vectors, respectively. The dual sheets were stretched by the recirculating flow, and the low-pressure region concentrated to form the vortex tube with lapse of time. Because these vortex sheets were similar to Burgers' vortex layer, the vorticity vectors on the two sheets are parallel to the velocity vectors on the sheets. Therefore, the direction of the vorticity vectors in the recirculating region is perpendicular to the direction of the vorticity vectors on the dual sheets. Thus, to adjust this non-aligned and incompatible arrangement of the vorticity directions, the direction of the vorticity vectors on the stretched sheets were altered by the recirculating flow. This alteration was characterized by the appearance of the region with $\sigma_z < 0$ on the sheets. Due to the continuity constraint, the transverse component, σ_+, became positive in turn, and this led to reduction of the vorticity in the stretching ($z-$)direction, ω_z, and increase of the transverse vorticity, ω_+. The vorticity direction on the sheet was converted to the transverse direction, which is parallel to the vorticity direction in the recirculating region. When the vorticity directions on both stretched sheets were altered, the configuration with Mode 1 was formed, while the vorticity direction only on one of the stretched sheets was altered, the configuration with Mode 2 was formed.
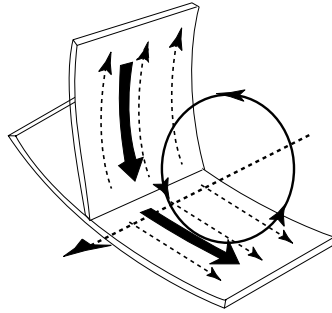
Figure 4. Sketch of the vorticity and velocity vector arrangement on the dual sheets and the recirculating region
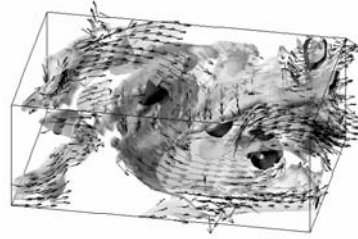
Figure 5. Front view of isosurfaces of $[-(S_{ik}\Omega_{kj}+S_{jk}\Omega_{ki})]_+$ (white), Q (black). Arrows denote the vorticity vectors.

The circulation around the tube with Mode 1 was generally large, and the tube with Mode 1 persisted for a rather long period of time, but most of the spiral vortices identified in the DNS data were in Mode 2. It should be noted that the direct wrapping up of the dual sheets shown in Fig. 4 by the recirculating flow leads to the configuration shown in Fig. 3c, in which the vorticity vectors

along both sheets are perpendicular to those along the vortex tube (Mode 3). The Mode 3 configuration was considered in Pullin and Lundgren (2001) and Kawahara *et al.* (1997). Mode 3, however, was rarely identified in the DNS data, because when the circulation of the vortex tube was sufficiently large, the vorticity direction on the stretched sheets were altered. Mode 3 may be realizable only in the recirculating flow with very weak circulation. Analysis of inter-component energy transfer in Mode 2 showed that on the upper branch of the two sheets in Fig. 1, the turbulent energy of $z-$component tended to be transferred to the energy of the transverse (+) component which is in the direction parallel to the tube, indicating that the upper branch of Mode 2 may not be energetic and even the configuration with Mode 2 may tend to be converted into the configuration with Mode 1. Indeed, it was shown in Pullin *et al.* (2001) that Mode 3 yields the energy spectrum with a slope of $-7/3$ which is steeper than that of the Kolmogorov law.

As the frequency of occurrence of this spiral vortex formation increased, intense energy cascade took place, and the energy spectrum showed a profile with a slope of the $-5/3$ law. As the Reynolds number was increased in the 512^3 case, a cluster of the spiral vortices was formed due to an abundant occurrence of formation of the spiral vortices along the vortex sheets. Similar results were obtained in the forced case.

3. Appearance of Mode 3 configuration in sheared turbulence

To examine the effect of the mean shear on the spiral vortex formation, we utilized the DNS data for a nearly homogeneous sheared turbulence, which is in a statistically stationary state by an volume forcing (Schumacher 2001). The isosurfaces of the vortex sheets and the vortex tube (rib vortices) and the distribution of the vorticity vectors along the sheets are shown in Fig. 5. Due to the imposition of the mean shear, the shear layer with spanwise vorticity was formed, and this shear layer was entrained by the streamwise vortex tube and wrapped around the tube. The vortex vector configuration shown in Fig. 5 is in Mode 3. In this flow, the vorticity direction on the sheets were not altered because the spanwise vorticity of the sheets was intense. It is interesting to note that the energy spectrum obtained in this flow consisted of the two components. The energy spectrum showed a slope of $-5/3$, while the co-spectrum exhibited a slope of $-7/3$. These results were consistent with those in Ishihara *et al.* (2002). We speculate that an appearance of Mode 3 may be responsible for generation of $-7/3$ co-spectrum.

We note that by terminating an occurrence of the spiral vortex formation with an incorporation of viscoelasticity, the turbulence generation may be annihilated (Horiuti *et al.* 2005).

References

HORIUTI, K. 2001 A classification method for vortex sheet and tube structures in turbulent flows. *Phys. Fluids* **13**, 3756–3774.

HORIUTI, K. 2003 Roles of nonaligned eigenvectors of strain-rate and subgrid-scale stress tensors in turbulence generation. *J. Fluid Mech.* **491**, 65–100.

HORIUTI, K., ABE, S., AND TAKAGI, Y. 2005 Effect of non-affine voscoelasticity on turbulence generation. *in Proc. Int. Symp. on Engineering Turbulence Modelling and Measurements 6.*

ISHIHARA T., YOSHIDA K., AND KANEDA Y. 2002 Anisotropic velocity correlation spectrum at small scales in a homogeneous turbulent shear flow. *Phys. Rev. Lett.* **88**, No. 154501.

KAWAHARA, G., KIDA, S., TANAKA, M., & YANASE, S. 1997 Wrap, tilt and stretch of vorticity lines around a strong thin straight vortex tube in a simple shear flow. *J. Fluid Mech.* **353**, 115–162.

KERR, O.S., AND DOLD, J.W. 1994 Periodic steady vortices in a stagnation-point flow. *J. Fluid Mech.* **276**, 307–325.

LUNDGREN, T.S. 1982 Strained spiral vortex model for turbulent structures. *Phys. Fluids* **25**, 2193–2203.

NEU, J.C. 1984 The dynamics of stretched vortices. *J. Fluid Mech.* **143**, 253–276.

PULLIN, D.I., AND LUNDGREN, T.S. 2001 Axial motion and scalar transport in stretched spiral vortices. *Phys. Fluids* **13**, 2553–2563.

SCHUMACHER, J. 2001 Derivative moments in stationary homogeneous shear turbulence. *J. Fluid Mech.* **441**, 109–118.

DYNAMICS OF SMALL-SCALE VORTICITY AND STRAIN-RATE STRUCTURES IN THE TRANSITION FROM ISOTROPIC TO SHEAR TURBULENCE

James G. Brasseur
Department of Mechanical Engineering, The Pennsylvania State University
University Park, PA 16802, U.S.A.
brasseur@psu.edu

Winston Lin
Honeywell Transportation and Power Systems
3201 W. Lomita Blvd., Torrance, CA 9050, U.S.A.
winston.lin@honeywell.com

Abstract   Local topological and statistical measures of enstrophy and strain-rate structures are compared with global statistics to determine the effects of mean shear on the interactions between fluctuating vorticity and strain rate in DNS of transitioning isotropic to shear turbulence. "Structures" are extracted as concentrations of turbulence fluctuations, allowing quantitative with visual analysis. We find that mean shear adjusts the alignment of fluctuating vorticity and strain rate so as to (1) enhance global and local alignments between vorticity and the second eigenvector of fluctuating strain rate, (2) two-dimensionalize fluctuating strain rate, and (3) align the compressional components of fluctuating and mean strain rate. Shear causes amalgamation of structures and suppresses strain-rate structures between enstrophy structures. Shear enhances "passive" strain-rate fluctuations—strain rate kinematically induced by local vorticity concentrations with negligible enstrophy production—relative to "active," or vorticity-generating, strain-rate fluctuations. Enstrophy structures separate into "active" and "passive" based on the second eigenvalue of fluctuating strain rate. The time evolution of a shear-induced hairpin enstrophy structure was analyzed. The structure originated in the initial isotropic state as a vortex sheet, evolved into a vortex tube during a transitional period, and developed into a well-defined horseshoe vortex in the shear-dominated state.

Keywords: Turbulence, turbulence structure, vorticity, strain rate, shear flow

19

1.   Introduction

In fully developed turbulence, the small scales evolve from dynamical inter-actions between vorticity and strain-rate fluctuations ubiquitous over the flow. Local concentrations of strain-rate fluctuations are kinematically induced by distributions of concentrated vorticity that change locally at a rate determined by the magnitudes and alignments of vorticity and strain rate in regions of overlap. The alignments are modulated by mean gradients depending on the relative strengths of mean-to-fluctuating velocity gradients and Reynolds number. Here we study the effects of mean shear on the structure and evolution of fluctuating vorticity and strain rate in fully developed homogeneous turbulence at Reynolds numbers and normalized mean shear rates comparable to the lower inertial layer of wall-bounded shear flows. To isolate the direct effects of mean shear on the fluctuating vorticity and strain-rate fields we analyze direct numer-ical simulation (DNS) data during transition from isotropic to shear-dominated fully developed homogenous turbulence, focusing on local and global dynam-ical evolution of vorticity and strain-rate production and alignments between the vorticity and strain rate induced by shear.

Using the Rogallo (1981) pseudo-spectral algorithm, we carried out well-resolved DNS of the transition from isotropic to shear-dominated homoge-nous turbulence with normalized shear-rate $S^* = Sq^2/\epsilon \sim 6 - 10$, where $S = dU/dy$, $q^2 = \langle u_i u_i \rangle$ and ϵ is dissipation-rate. Initial isotropic decaying turbulence was generated on a $256 \times 128 \times 128$ grid in a box with aspect ratio $2 : 1 : 1$ in $x : y : z$ to maintain isotropy. At the initiation of isotropic power-law decay, the data were interpolated onto a 128^3 grid with cell aspect ratio 2, and shear was switched on. To separate the effects of mean shear from the transition from Gaussian initial conditions, S was switched on only after the isotropic de-caying turbulence was produced (in contrast with Rogers and Moin 1987, Kida and Tanaka 1994, Nomura and Diamessis 2000). During the simulation period ($St = 0$ to 4), S^* increased from 2.6 to 10, $Re_\lambda = q_{11,1}\lambda/\nu$ increased from 22 to 65, and production-to-dissipation-rate reached an asymptote of 1.6.

2.   Turbulence "structures" as concentrations of turbulence fluctuations

"Structures" are defined as local three-dimensional (3-D) volumes in which a turbulence variable was concentrated, surrounding a peak in the fluctuating variable, at fixed time. Subjective empirical evidence suggests that all well-resolved structures, as defined, are temporally coherent.

We developed an algorithm that identifies the surfaces of individual structures during a process of extraction that orders structures in order of peak fluctuation level, for subsequent visual and statistical analysis. To conceptualize the ap-proach, imagine 3-D concentrations of turbulence fluctuations as analogous to
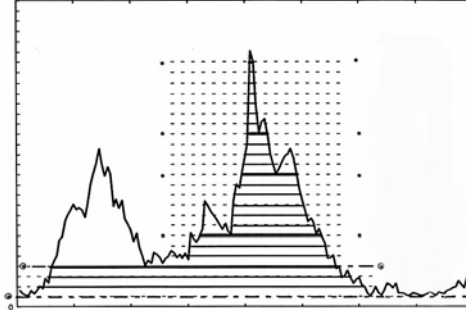
Figure 1. A simplified 1-D illustration of the process by which volumetric concentrations of a fluctuating variable are extracted and defined as "structures" for subsequent analysis.

two-dimensional "mountains" of varying height, expanse and connectivity rising from a rough planar "terrain" of lower level crags and crevices as illustrated in Fig. 1. The "mountains" represent concentrations of the variable surrounded by interstitial spaces of lower-level fluctuations. Whereas a "structure" visualized with 3-D isosurfaces generally isolates and displays only the tails of the corresponding pdf (the peaks of the highest "mountains" of Fig. 1), we extract from the dataset the complete 3-D mountains of Fig. 1, each of which includes both its peak and lower level topography surrounding its peak defining the full mountain. Applied to a DNS dataset, a "structure" is the entire concentration of a fluctuating variable surrounding a peak in 3-D space, distinct from other structures, and separated by a boundary that surrounds both high- and low-level fluctuations. Thus, an extracted vortex contains not only the highest levels of vorticity within the vortex core (Jiménez *et al.*, 1993), but also the contiguous low-level vorticity fluctuations within the complete structure.

Details of the extraction algorithm with automated determination of structure boundaries are given by Lin (1993). In Fig. 2 we contrast traditional isosurface visualization of enstrophy (ω^2) with extracted enstrophy structures. Fig. 2(a) shows an isosurface of enstrophy at a relatively high threshold of 3 SD in a 64^3 subdomain of a 128^3 DNS of homogeneous shear turbulence at $R_\lambda = 74$ and $S^* = 9$. Compare this traditional visualization of vortical structure with the first 30-40 most intense enstrophy structures in the same subdomain of the dataset (Fig. 2(b)) obtained using the extraction algorithm described above. Note that isosurfaces display only part of individual vortical structures. Whereas tube-like streamwise vortices are apparent in the isosurface image, when the entire structure surrounding the more intense regions is extracted, well-defined horseshoe vortices appeared—structure commonly observed in wall-bounded shear turbulence (vid. Robinson, 1991). Once extracted, it is straightforward to interrogate internal structure in a variety of useful ways.
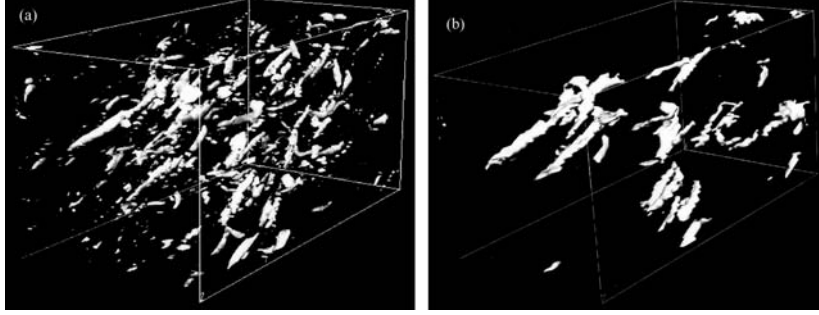
Figure 2. Comparison of (a) a single isosurface of fluctuating enstrophy (ω^2) at 3 SD with (b) 30-40 primary enstrophy structures from the same 64^3 subdomain of a 128^3 DNS of homogeneous turbulent shear flow; $R_\lambda = 74, S^* = 9$.

3. Global enstrophy and strain-rate balances

The dynamic equations for fluctuating vorticity (ω_i) and strain-rate (s_{ij}) variance in homogeneous shear turbulence contain the following terms:

$$\frac{\mathrm{d}\langle\omega^2\rangle}{\mathrm{d}t} = \langle\mathbf{P}_{\omega^2}\rangle + \langle\overline{\mathbf{P}}_{\omega^2}\rangle + \langle\mathbf{D}_{\omega^2}\rangle,$$

$$\frac{\mathrm{d}\langle s^2\rangle}{\mathrm{d}t} = \langle\mathbf{P}_{s^2}\rangle + \langle\overline{\mathbf{P}}_{s^2}\rangle + \langle\mathbf{PR}_{s^2}\rangle + \langle\mathbf{D}_{s^2}\rangle. \tag{1}$$

Here $\langle\mathbf{P}_{\omega^2}\rangle$ and $\langle\overline{\mathbf{P}}_{\omega^2}\rangle$ are production rates of vorticity variance by vortex stretching from turbulence fluctuations and mean velocity gradients, respectively. Similar production terms, $\langle\mathbf{P}_{s^2}\rangle$ and $\langle\overline{\mathbf{P}}_{s^2}\rangle$, exist in the evolution of strain-rate variance, Eq. (2). $\langle\mathbf{D}_{\omega^2}\rangle$ and $\langle\mathbf{D}_{s^2}\rangle$ are the rates of viscous dissipation of vorticity and strain-rate variance. Strain-rate variance is also influenced by correlations between fluctuating pressure force gradient and fluctuating velocity gradient, $\langle\mathbf{PR}_{s^2}\rangle$. In homogeneous turbulence, $\langle\omega^2\rangle = 2\langle s^2\rangle$ and

$$\langle\mathbf{P}_{\omega^2}\rangle = 2\langle\omega_i s_{ij}\omega_j\rangle = -\frac{3}{2}\langle s_{ij}s_{jk}s_{ki}\rangle,$$

$$\langle\mathbf{P}_{s^2}\rangle = -\langle s_{ij}s_{jk}s_{ki}\rangle - \frac{1}{4}\langle\omega_i s_{ij}\omega_j\rangle = \frac{24}{13}\langle\mathbf{P}_{\omega^2}\rangle. \tag{2}$$

Thus, on average, the rates of strain-rate and vorticity production are proportional. Whereas the proportionalities between $\langle\omega^2\rangle$ and $\langle s^2\rangle$, and between $\langle\mathbf{P}_{\omega^2}\rangle$ and $\langle\mathbf{P}_{s^2}\rangle$, are only true after the ensemble average, the productions of enstrophy and strain-rate variance are given also locally by the middle expressions in (3). Thus, there is dynamic significance to conditional averages of these quantities *within* structures.

4. Active vs. passive strain rate

In local principal axes, the three principal strain rates (eigenvalues) are α, β and γ, where $\alpha > 0$ is elongational, $\gamma < 0$ is compressional, and β may be either; the corresponding eigenvectors are $\mathbf{e}_\alpha, \mathbf{e}_\beta, \mathbf{e}_\gamma$. In principal axes, $\mathbf{P}_{\omega^2} = 2(\alpha\omega_\alpha^2 + \beta\omega_\beta^2 - |\gamma|\omega_\gamma^2)$ locally, so the relative orientations between the vorticity vector and strain-rate tensor are of considerable dynamical interest. Ashurst *et al.* (1987) with DNS data and Tsinober *et al.* (1992) with experiment (and subsequently others) found that in isotropic turbulence vorticity fluctuations tend to align with the second principal eigenvector of the strain-rate tensor, and that this eigenvalue tends to be positive with a ratio $\alpha : \beta : \gamma$ of roughly $2 : 1 : -3$. Figure 3a shows the pdf of $\beta_n \equiv \beta/(s^2/6)^{1/2}$ in the isotropic state and under shear when $S^* = 10$, where β_n is bounded between +1 and -1. In the isotropic state the most frequent value of β_n is 0.6 implying $\alpha : \beta : \gamma \approx 2.2 : 1 : -3.2$ is most common. Under the influence of mean shear β_n continually decreases until, at $S^* = 10$, the most probable value of $\beta_n \approx 0.28$, implying $\alpha : \beta : \gamma \approx 5.6 : 1 : -6.6$. Thus, shear has a strong tendency to move the local fluctuating strain-rate field asymptotically towards local two-dimensionality with second eigenvalue reduced relative to the extensional and compressional eigenvalues.
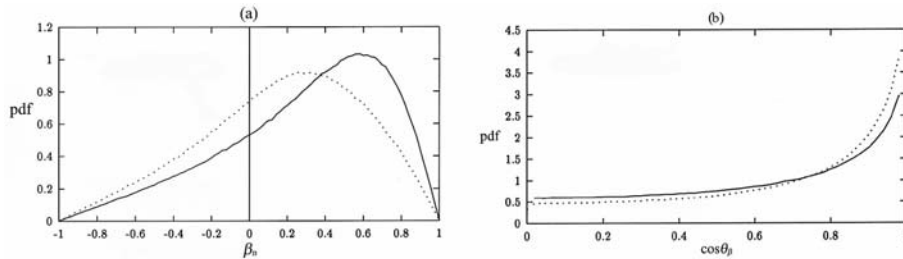
Figure 3. Pdfs of (a) normalized second eigenvalue of fluctuating strain rate; (b) cosine of the angle between second principal direction of fluctuating strain-rate tensor and vorticity. Solid curves: isotropic; dotted curves: $St = 4$. Solid curves: isotropic. Dotted curves: shear ($S^* = 10$).

Figure 3b shows that the tendency for fluctuating vorticity to align with the second eigenvector of s_{ij} is enhanced by shear. However, whereas we find that the average magnitude of the second eigenvalue is roughly independent of ω^2, the alignment between the second eigenvector and vorticity fluctuations is stronger at high vorticity intensity levels (not shown). However, whereas β_n decreases globally with shear over all vorticity and strain rate intensity levels, when the second eigenvalue is conditioned on the level of enstrophy

production, we find that in regions of higher enstrophy production the average level of β_n remains near 0.6 (the most probable value of β_n in isotropic turbulence) *independent of the influence of shear* (not shown). The shift in β_n to lower values with shear, the corresponding two-dimensionalization of s_{ij}, and the increased alignment of the second strain rate eigenvector, are therefore associated with strain-rate fluctuations that do not contribute to the production of enstrophy (and strain-rate variance).

We conclude that strain-rate fluctuations must be of two types: *"active"* fluctuations that contribute to vortex stretching, and *"passive"* strain-rate fluctuations that do not. The dynamical interactions between mean shear and turbulence appears to enhance passive strain-rate fluctuations–those fluctuations characterized by local two dimensionalization of s_{ij} (decreasing β_n), improved alignment between $\mathbf{e}_\beta$ and ω, and no vortex stretching-in contrast with active strain-rate fluctuations involving higher levels of β_n and alignment between the second eigenvector of s_{ij} and fluctuating vorticity. Furthermore, shear encourages the elongational eigenvector $\mathbf{e}_\alpha$ to align at $90°$ to fluctuating vorticity (not shown), as $\mathbf{e}_\beta$ tends to align more strongly with ω, and β_n tends to decrease, consistent with an increase in passive s_{ij} fluctuations.

In Fig. 4 we plot the joint pdf of the directions of the third principal eigenvector of fluctuating strain rate (compressional) of the highest intensity s^2 structures (§2) over spherical angles (θ, ϕ), where θ is defined from the $+y$ axis and ϕ is positive from the $+x$ axis towards $-z$. The joint pdf of $\mathbf{e}_\gamma$ is concentrated at $(+45°, \pm180°)$, the direction of compressional mean strain. The same tendency is observed within lower intensity s^2 structures, implying that the compressional direction of fluctuating strain rate is strongly aligned with the compressive component of mean strain rate. Furthermore, fluctuating vorticity tends to align with the principal elongational component of mean strain rate (not shown). We conclude that the tube-like vortical structures aligning at $45°$ and rotating by mean shear (Fig. 2) are continuously flattened by the combination of fluctuating and mean strain rate acting together at $90°$ to the axis of the vortex (Brasseur & Wang, 1995; Lin, 1993).

To summarize, we find that: (1) mean shear tends to stretch fluctuating vorticity at $45°$ then rotate it slowly towards the mean flow direction, (2) mean strain rate tends to align fluctuating compressional strain rate in the same direction as the compressional component of mean strain, enhancing the tendency to flatten aligned vortex tubes, (3) whereas the second eigenvector of fluctuating strain rate tends to align with vorticity in the isotropic state (with the first eigenvector showing slight tendency of alignment), the application of mean shear destroys the alignment with the first eigenvector and generates an even stronger alignment with the second eigenvector; (4) mean shear tends to two-dimensionalize the structure of fluctuating strain rate with enhanced alignment between ω and $\mathbf{e}_\beta$ but with no change in enstrophy production rate, implying that enstrophy
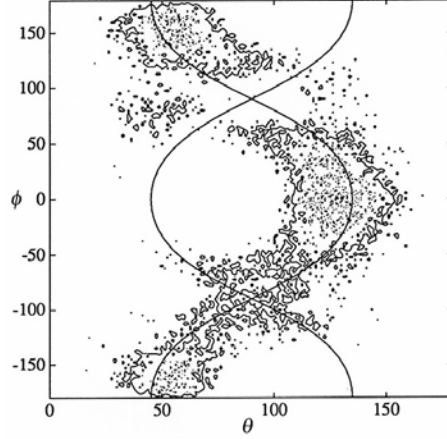
Figure 4. Joint pdf of the directions of the compressional eigenvector of fluctuating strain rate within the highest intensity s^2 structures.

production follows primarily from the interaction between fluctuating vorticity and the second eigenvalue of the fluctuating strain-rate tensor both in isotropic and shear turbulence, and therefore (5) the primary effect of shear is to enhance passive (non enstrophy producing) strain-rate fluctuations, s_{ij} fluctuations with strong alignment between vorticity and the second eigenvector, but with low second eigenvalue, of s_{ij}. We propose that passive strain-rate fluctuations are those *kinematically* induced by local concentrations of enstrophy with coherent vorticity defining localized vortex tubes and shear-layers. Shear aligns concentrated vorticity, generating coherent tube and sheet-like vortices that are aligned, stretched and flattened by mean shear, also increasing the alignment between ω and $\mathbf{e}_\beta$, decreasing β_n, and forcing the generation of passive strain-rate fluctuations.

5. Local dynamics within vorticity and strain-rate structures

Using the algorithm described in §3, we extracted hundreds of primary ω^2 and s^2 structures in the isotopic state and after application of mean shear at $St = 4$ ($S^* = 10$). Although the extracted structures are ordered by peak intensity, to confirm the robustness of our analytical method we repeated the statistics using peak, mean and standard deviation as intensity measures, and obtained the same results (Brasseur & Lin 1991). 1800 ω^2 structures and 1920 s^2 structures were extracted from the initial isotropic state and ordered by intensity. The structures contribute 39% and 28%, respectively, to the global variance of vorticity and strain rate while only occupying 13% and 10% of

global volume, reflecting the concentrated nature of the fluctuations within. In the sheared state $800\,\omega^2$ and $810\,s^2$ structures were extracted contributing 50% and 38%, respectively to global variance, and 16% and 13% to the volume. The variance-to-volume-ratio is 3 to 1 in both isotropic and sheared states, the average volume of ω^2 and s^2 structures increases by 300%, indicating major amalgamation and growth of structures by shear. Whereas the contribution to global variance $\langle\omega^2\rangle$ and $\langle s^2\rangle$ increases for typical structures, the variance per structure volume changed little after application of shear. The variance-per-volume in these structures changed by only $3-4\%$ under the influence of shear, yet their relative contributions to vorticity and strain-rate production increased by $12-65\%$. Interestingly, the contribution of vorticity structures to strain-rate production $s_{ij}s_{jk}s_{ki}$, and of strain-rate structures to vorticity production $\omega_i\omega_j s_{ij}$, is much larger than strain-rate structures to strain-rate production and vorticity structures to vorticity production. We conclude that shear creates overlaps between regions of concentrated strain rate and vorticity by reducing the relative number of strain-rate structures outside vorticity structures in the low-vorticity interstitial regions.

Figure 5(a) shows average enstrophy production-rate in each enstrophy structure in the shear-dominated state ordered by the intensity of enstrophy within each structure, relative to global average production-rate. The highest intensity structures (100-200 structures) have distinguishingly higher rates of vorticity production than do lower-intensity structures. In the isotropic state one finds a similar, but more gradual, decrease in $\langle\mathbf{P}_{\omega^2}\rangle_{\omega^2}$ with decreasing structure intensity. In both isotropic and shear turbulence nearly all extracted enstrophy structures (which contain $40-50\%$ of global enstrophy) are enstrophy producing, on average. Any compression of vortex lines apparently must occur in the low-magnitude fluctuations between the vortical structures. Whereas the highest intensity structures are distinguished by higher levels of enstrophy production, Figure 5(b) shows no clear trend in the magnitude of the second eigenvalue of fluctuating strain rate except for an increased variability with lower-intensity structures. The same is true of $\langle\cos\theta_\beta\rangle_{\omega^2}$ (not shown). Interestingly, Fig. 5(b) indicates that $\langle\beta_n\rangle_{\omega^2}\approx 0.3$, the most probable value of β_n with shear state shown by the pdf of Fig. 3(a). We conclude that the shear-induced two-dimensionalization of strain-rate fluctuations described for most probable fluctuations in §4 is associated with vortical structures as extracted here.

It appears that the changes in structure of strain rate and vorticity caused by shear for most probable strain-rate fluctuations (§4) are associated with the extracted vortical structures. In particular, two-dimensionalization of s_{ij}, increases in passive strain rate, and increased role of the second eigenvalue in active vortex stretching, are all within the vortical structures extracted as concentrations of enstrophy. When we again plot the average second eigenvalue
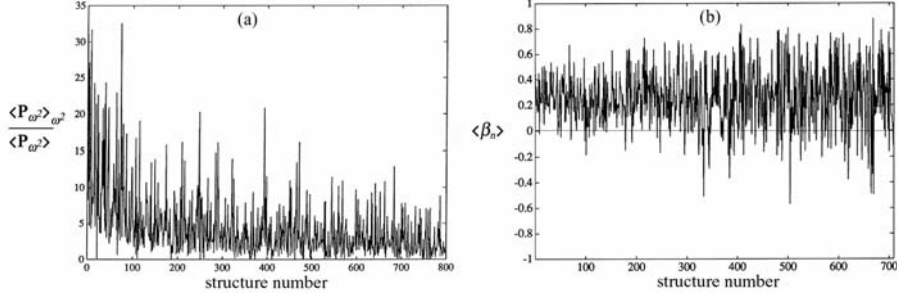
Figure 5. Average of fluctuating variables within each enstrophy structure plotted against structure number in the shear-dominated state ($St = 4$), ordered by structure intensity. (a) Structure average of enstrophy production-rate, nondimensionalized by global production-rate. (b) Structure average of normalized second eigenvalue of the fluctuating strain-rate tensor.

within enstrophy structures, but with the structures reordered according to average enstrophy production-rate in each structure, the structures with enstrophy production are found to be those with higher $\langle \beta_n \rangle_{\omega^2}$ (not shown). Thus we observe a distinction between "active" and "passive" enstrophy structures in sheared turbulence distinguished by the degree of two-dimensionalization of the strain rate within each structure, but not by the alignment between vorticity and second principal axis of strain rate (enhanced by shear in all structures). "Active" vortices resist two-dimensionalization by mean shear and contain "active" strain rate with $\langle \beta_n \rangle_{\omega^2} \sim 0.3 - 0.6$ and enstrophy production. "Passive" vortices are two-dimensionalized by shear and contain "passive" strain-rate fluctuations with low values of $\langle \beta_n \rangle_{\omega^2}$, kinematically tied to the local vorticity field and with negligible enstrophy production.

6. Local dynamics within vorticity and strain-rate structures

We applied an interactive approach (Moquin & Brasseur 1992) in which (1) a structure of interest was identified in the shear-dominated period, (2) the same structure was identified in datasets a short time earlier and later by searching the same local region and interactively extracting structures within the localized sub-volume using the algorithm in $S2$, (3) repeating the interactive extraction process at each $St = 0.2$ and storing the structure nodes and sub-volume coordinates at each time increment from $St = 0 - 4$. Using this approach, we analyze visually and quantitatively the evolution of a single well-defined hairpin vortex in the asymptotic shear state from its origin in the isotropic state. We begin with a well-formed hairpin vortex at $St \approx 2$. The change in topology of

extracted structure is shown at every $St = 0.2$ from the isotropic state ($St = 0$) to time $St = 2.2$ in Fig. 6 (each in its extracted subvolume). It is fascinating to discover that the horseshoe vortex at $St = 2.2$ originates from a vortical structure with sheet-like topology in the isotropic state (Fig. 6(a)). The initial structure is, in fact, a localized vortex sheet and its evolution occurs in three phases: (1) transition from a vortex sheet to a short vortex tube, (2) transition from vortex tube into a sheet-like hairpin vortex, and (3) evolution into squashed vortex tubes with hairpin topology.

The transition from a sheet to a tube is demonstrated by Figs. 6 (a)-(c). When the strain-rate and enstrophy structures are displayed separately with vorticity vectors (Lin 1993), the isotropic enstrophy and strain-rate fields overlap, consistent with vortex sheet topology. However, in the transition period after shear is switched on, the local shear layer undergoes a rapid change in topology from sheet-like to tube-like with unidirectional vorticity. In a classical vortex tube, the locally induced strain-rate field is asymmetrically distributed around the tube core. The vortex tube after transition (Fig. 6(c)), however, has elliptical cross section with local strain rate concentrated on two sides of the vortex core. This process takes place during the transition in global statistics from isotropic to equilibrium evolution under shear.
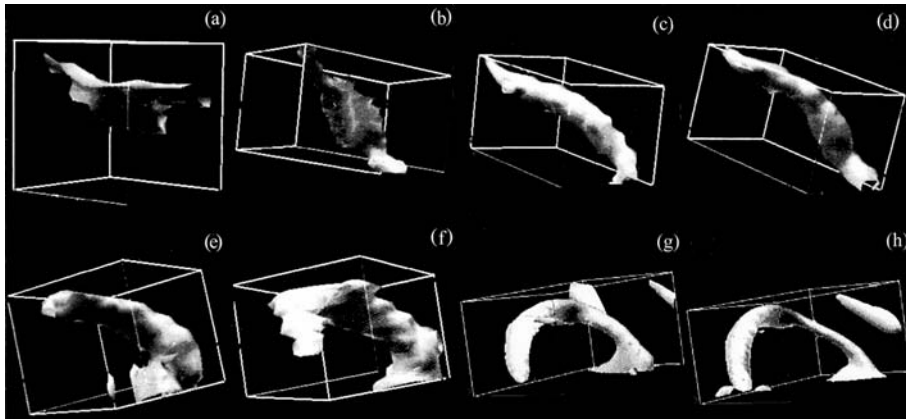
Figure 6. Time evolution of an enstrophy structure over the period $St = 0$ to 2.8 in increments of 0.4. The extracted subvolume at each time is shown by the box.

The aspect ratios (AR) of the enstrophy structure decreases rapidly from 12 in the isotropic initial state to 2 at $St = 0.6$, then to AR ≈ 1 at $St = 1$, shortly after which the tube begins a transition to a hairpin vortex. As shown in Figs. 6(c)-(f), the process involves the elongating and flattening of the vortex tube and the bending over and formation of a rather flattened head that is distinct

from a single tube-like leg. As the vortex elongates and bends, the leg of the hairpin remains tube-like with little overlap with the more concentrated strain-rate fluctuations. The elongation process does not appear to be associated with stretching of vortex lines by fluctuating strain rate, and its extension likely reflects continuous stretching by mean strain rate. As the head of the hairpin formed, however, it flattens and evolves into a structure akin to a local shear layer. This flattening is a consequence of the orientation of the compressional eigenvector of mean strain rate and, in a statistical sense, fluctuating strain rate (§4). At $St \approx 1.6$, the long and short axes of the vortex head were about 6 and 3 Kolmogorov scales, respectively. Although there appears to be some feeble attempt to roll up, this local shear layer remains relatively stable. Afterwards, the enstrophy structure continues to evolve into a fully formed hairpin vortex head and limbs alternating between sheet-like to tube like, and back again.

The three topological phases of evolution are mirrored by the dynamical relationships associated with enstrophy and strain-rate production. For example, we compare the correlations between the square of fluctuating vorticity and strain rate with the cosine of the angle between vorticity ω and second principle strain-rate direction $\mathbf{e}_\beta$ averaged within the evolving enstrophy structure and plotted over time. These correlations show well-defined changes that mirrored the three periods of topological changes in vortex structure.

7.   Conclusions

Shear alters vorticity dynamics through the restructuring of the local vorticity and strain-rate fields in relationship to the mean strain rate, and consequently in relationship to each other. In this study normalized mean shear is comparable to mixing layers jets, wakes, and boundary layers. We find that both linear and nonlinear interactions generate a tendency for two-dimensionalization of fluctuating strain rate so as to encourage the generation of aligned flattened vortex tubes and horseshoe vortices. Passive and active strain rate fluctuations are enhanced by shear within the more intense enstrophy structures. Enhanced passive strain rate is associated with increased kinematic association between axial vorticity and two-dimensionalized strain rate as vorticity is progressively aligned. Enhanced active strain rate is confined to those high-intensity vortical structures with significant enstrophy production arising from enhanced second eigenvalue of fluctuating strain rate, but not from enhanced alignment. Interestingly, it is possible for horseshoe vortices to evolve from vortex sheets, rather than vortex tubes, with a structure that changes locally between sheet-like and tube-like, with "squashed" tube being the preferred topology. Local correlations and alignments between vorticity and strain-rate fluctuations mirror temporal changes in topology during formation and evolution of the horseshoe vortex structure.

30

References

ASHURST, T., KERSTEIN, A., KERR, R. & GIBSON, C. 1997 Alignment of vorticity and scalar gradient with strain rate in simulated Navier-Stokes turbulence. *Phys. Fluids A.* **A30**, 2343–2353.

BRASSEUR, J.G. & LIN, W.-Q. 1991 Structure and statistics of intermittency in homogeneous turbulent shear flow. *Advances in Turbulence,.* **3**, 3–12.

BRASSEUR, J.G. & WANG, Q. 1992 Structural evolution of homogeneous turbulence at different scales analyzed using 3D wavelet transforms. *Phys. Fluids A.* **4**, 2538–2554.

JIMÉNEZ, J. WRAY, A.A., SAFFMAN, P.G. & ROGALLO, R.S. 1993 The structure of intense vorticity in homogeneous isotropic turbulence. *J. Fluid Mech.* **255**, 65–90.

KIDA, S. & TANAKA, M. 1994 Alignment of vorticity and scalar gradient with strain rate in simulated Navier-Stokes turbulence. *Phys. Fluids A.* **339**, 121–142.

LIN, W.-Q. 1993 *Structural and Dynamical Characteristics of Intermittent Structures in Homogeneous Turbulent Shear Flow.* Ph.D. Thesis, Department of Mechanical Engineering, The Pennsylvania State University, University Park, PA.

MOQUIN, B. & BRASSEUR, J.G. 1992 Application of a new fully object-oriented programming methodology to the analysis of multidimensional turbulence data (abstract). *Bull Amer. Phys. Soc.* **37**, 1781.

NOMURA, K.K. & DIAMESSIS, P.J. 2000 The interaction of vorticity and rate-of-strain in homogeneous sheared turbulence. *Phys. Fluids* **12**, 846–864.

ROBINSON, S.K. 1991 Coherent motions in the turbulent boundary layer. *Ann. Rev. Fluid Mech.* **23**, 601–639.

ROGALLO, R.S. 1981 Numerical experiments in homogeneous turbulence. *NASA Tech. Memo* 81315.

ROGERS, M.M. & MOIN, P. 1987 The structure of the vorticity field in homogeneous turbulent shear flow. *J. Fluid Mech.* **176**, 33–66.

TSINOBER, A., KIT, E. & DRACOS, T. 1992 Experimental investigation of the field of velocity gradients in turbulent flows. *J. Fluid Mech.* **242**, 169–192.

INTERACTION BETWEEN A COLUMNAR VORTEX AND EXTERNAL TURBULENCE

Naoya Takahashi, Takeshi Miyazaki
Department of Mechanical Engineering and Intelligent Systems,
University of Electro-Communications, 182-8585, Japan
naoya@mce.uec.ac.jp, miyazaki@mce.uec.ac.jp

Abstract   The interaction between a columnar vortex and external turbulence is investigated numerically. As columnar vortices, the Lamb-Oseen vortex and the q-vortex are used. The columnar vortex is immersed in an initially isotropic homogeneous turbulence field, which itself is produced by a direct numerical simulation of decaying turbulence. Using visualization techniques, we investigate the formation of inhomogeneous fine turbulent eddies around the columnar vortex, vortex-core deformations and the dynamical evolution in the passive scalar field.

Keywords: Columnar vortex, direct numerical simulation, turbulence

1.   Introduction

Interactions between intense columnar vortices and surrounding turbulent motions occur often in engineering and environmental flows, and they occur naturally in most sheared turbulent flows, such as circular jets, plane jets, and mixing layer. These interactions are thought to play an important role in the three-dimensionalization of the flow fields. It is also of practical interest to estimate the lifetime of trailing vortices under the influence of atmospheric turbulence.

We investigate the dynamical evolution of the vortex structure and the passive scalar structure, which appears in the isotropic homogeneous turbulence interacting with the columnar vortex. The characteristics of the flow field are analyzed by using several flow-visualization techniques. The statistics of the turbulence around the columnar vortex are investigated by computing the two-point energy spectrum tensors, and they are compared with the results of rapid distortion theory (RDT, Miyazaki & Hunt 2000).
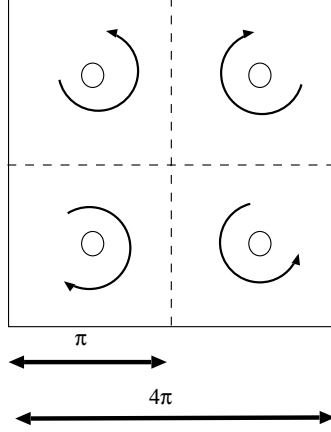
Figure 1. Arrangement of the columnar vortices in the cubic box with periodic boundary conditions.

2. Numerical method

We solve the Navier-Stokes equation for incompressible fluids

$$\frac{\partial \mathbf{u}}{\partial t} + \mathbf{u} \cdot \nabla \mathbf{u} = -\frac{1}{\rho}\nabla p + \nu\nabla^2\mathbf{u}, \qquad (1)$$

$$\nabla \cdot \mathbf{u} = 0 \qquad (2)$$

and the transport equation for the passive scalar (such as a passive temperature field or a dye)

$$\frac{\partial s}{\partial t} + \mathbf{u} \cdot \nabla s = \kappa\nabla^2 s \qquad (3)$$

under periodic boundary conditions with period 4π. A spectral method is used to solve the equations. The time integration is performed using the Runge-Kutta-Gill method with spatial resolutions of 256^3 and 512^3. The columnar vortex is immersed in an initially isotropic homogeneous turbulence field, which itself is produced numerically by a direct numerical simulation of decaying turbulence. It is well known that under a strain field of a vortex pair the Widnall-Bliss-Tsai instability and the Crow instability occur. To suppress these instabilities, we embed four columnar vortices with alternating directions to eliminate a strain field with azimuthal wavenumber $m = 2$ (shown in Fig. 1). To verify that the instabilities are not excited, we carry out direct numerical simulations with four columnar vortices embedded in the field with very small noise: No instabilities are excited. As the columnar vortex, we use the q-vortex, which is a model for

trailing vortices. The q-vortex is defined by

$$(U_r, U_\theta, U_z) = \left(0, \frac{\Gamma_0}{2\pi r}\left\{1 - \exp\left(-\frac{r^2}{r_0^2}\right)\right\}, \frac{\Gamma_0}{2\pi r_0 q}\exp\left\{-\frac{r^2}{r_0^2}\right\}\right), \quad (4)$$

where U_r, U_θ and U_z are the radial, azimuthal and axial components of the velocity field, $r_0 \ (= 0.5)$ is the radius of the columnar vortex, and q is the swirling parameter. The initial circulation Γ_0 is an arbitrary parameter, so we set the circulation strong enough to dominate the vortex dynamics of the flow field as

$$\Gamma_0 = 40r_0^2\omega_{rms}, \quad (5)$$

where ω_{rms} is the root-mean-square of the vorticity of the initial turbulence. The Reynolds number Γ_0/ν of the columnar vortex takes values between $20,000$ and $80,000$. We consider three values of q, namely $-\infty$ (the Lamb-Oseen vortex), -0.45 (unstable case) and -1.5 (marginally stable case).

We analyse the calculated field statistically using the function

$$\langle\langle u_i(r_1, \theta_1, z_1, t)u_j(r_2, \theta_2, z_2, t)\rangle\rangle =$$

$$\sum_{m=-\infty}^{\infty}\int_{-\infty}^{\infty}dk_z\Phi_{ij}(r_1, r_2, t; k_z, m)\exp[ik_z(z_1 - z_2) + im(\theta_1 - \theta_2)], \quad (6)$$

where k_z is the axial wavenumber, m is the azimuthal wavenumber, and $\langle\langle\cdot\rangle\rangle$ is the ensemble average over twenty realizations. This statistical function was introduced as two-point energy spectrum tensor for RDT by Miyazaki & Hunt 2000. We use it for analyzing the nonlinearity of the field. The kernel Φ_{ij} of the correlation function enables us to investigate the dynamics of the vortices in detail, such as scale dependence, nonlinear interaction, and the comparison with RDT.

3. Lamb-oseen vortex ($q = -\infty$)

3.1 Flow field

In the case of the Lamb-Oseen vortex (Takahashi *et al.* 2005), the columnar vortex undergoes a deformation due to the interaction, and the vortex wraps worms around its surface in a spiral structure (Fig. 2). In larger scales, we can see that a vortex has a columnar structure at the center of the region, and that it is curved. In finer scales, we observe the characteristic structure of thin, tube- and ring-like shapes, which implies that the vortex rings have developed from the fine-scale structure, which was input as worms in the initial turbulence. Figure 3 shows the time evolution of the maxima of the axisymmetric axial and radial components of the two-point energy spectrum tensor (Eq. (6)) summed over k_z, which has peaks at $r \geq r_0$. The axial component $|\Phi_{zz}|$ grows proportional to
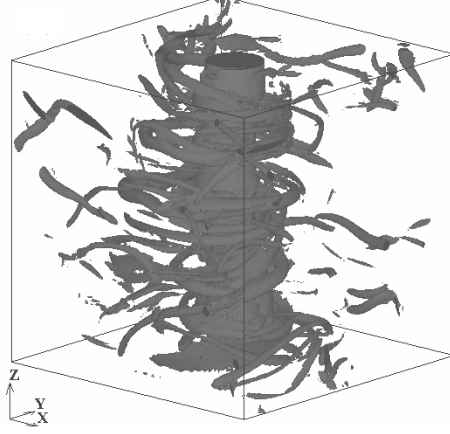
Figure 2. Isosurface of vorticity of the Lamb-Oseen vortex case at $t/T = 6$.
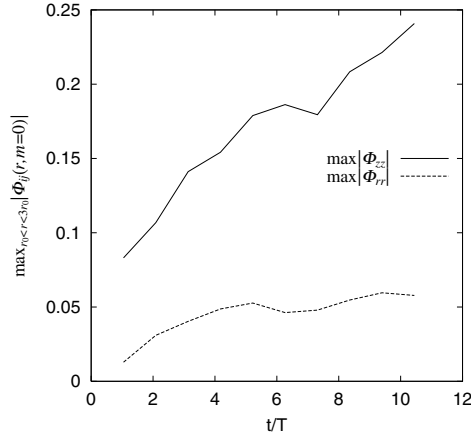
Figure 3. Peak values at $r_0(t) \leq r \leq 3r_0(t)$ of the axisymmetric axial and radial two-point energy spectrum tensor $|\Phi_{ij}(r, r, t; m)|$ summed over k_z which has peaks at $r \geq r_0(t)$: axial component ($|\Phi_{zz}|$, solid line) and radial component ($|\Phi_{rr}|$, dotted line).

$t^{0.9}$, whereas the radial component $|\Phi_{rr}|$ hardly grows. This shows the excitation of axial disturbances around the surface of the vortex core that corresponds to the blocking effect. The modes with higher azimuthal wavenumbers also grow, but their amplitudes are negligible compared to that of the axisymmetric and bending modes. This result is consistent with RDT. On the other hand, the azimuthal disturbances increase proportional to t, which is different from RDT ($\propto t^2$). At present, we do not understand the reason for this.
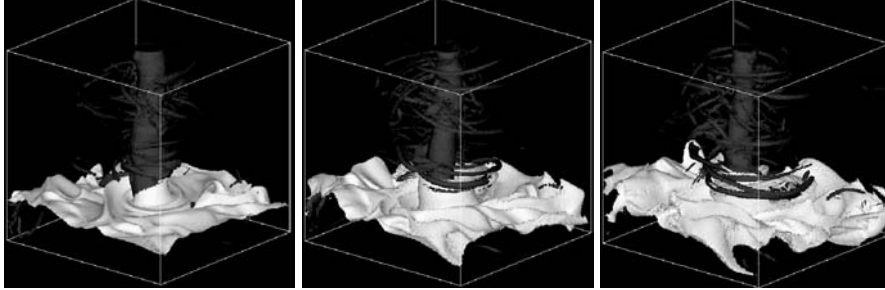
Figure 4.   Time evolution of isosurfaces of enstrophy (dark gray) and passive scalar (light gray).

To show the discrepancy between the linear theory and the numerical results, we change the intensity of the turbulent flow. We introduce a damping parameter A_D of the initial turbulence $\boldsymbol{u}_i = A_D \boldsymbol{u}$, and perform simulation for $A_D = 10^{-2}$, 10^{-1} and $10^{-0.5}$. We immerse the columnar vortex, and perform the time integration of Eqs. (1) and (2). For small A_D ($\leq 10^{-1}$), we cannot find the excitation of the vortex wave via visualization techniques. For large A_D ($\geq 10^{-0.5}$), we find humps on the surface of the vortex core. Next, we focus on the small-scale structures, which depend on A_D in the initial turbulent field. For small A_D($\leq 10^{-1}$), we observe that they deform to spirals and surround the vortex core. On the other hand, for large A_D ($\geq 10^{-0.5}$), the circumference of the spirals become short, and they cannot surround the vortex core. The deformation of the vortical structures under various values of A_D is analysed using the two-point energy spectrum tensors Φ_{ij}. For $A_D \leq 10^{-1}$, the time dependence of Φ_{zz} is proportional to t^2, consistent with RDT. For $A_D \geq 10^{-0.5}$, the time dependence of Φ_{zz} deviates from the graph for t^2. This result suggests that mainly the nonlinear interaction between the columnar vortex and turbulence affects the properties of the velocity field.

3.2   Passive scalar field

The scalar field is initialized with the profile $s_0(z)$, which depends only on the axial component of z and has a Gaussian profile. The instantaneous snapshot of the scalar field shows noticeable advection of the passive scalar field around the surface of the vortex core (Fig. 4). This phenomenon may be due to the fact that the blocking effect of the velocity field is excited where the mean axial gradient of the scalar field is large. Another characteristic advection is observed separately from the vortex core. The fine-scale structure (worm) wraps the passive scalar; i.e., the swirling motion of the fine structure becomes important in the scalar advection.

4.   *q*-vortex

4.1   Unstable case ($q = -0.45$)

The q vortex with $q = -0.45$ is the case most unstable against the bending disturbance $m = 1$ (Mayer & Powell 1992). Fig. 5 shows the time evolution of the vortical structure using enstrophy visualization. At the early stage, we observe the excitation of the linear instability, which causes the deformation of the structure of the columnar vortex. As shown in Fig. 5a, the structure around the columnar vortex has two helices. At the next stage (Fig. 5b), the deformation of the columnar vortex is large, and the helices separate from each other. Simultaneously, we observe that the surfaces of the helices are uneven, namely that secondary structures occur on the surface of each helix. These deformations are amplified at the last stage(Fig. 5c), and the vortical structure becomes complex (like a rib). After a while, the columnar vortex breaks down abruptly.
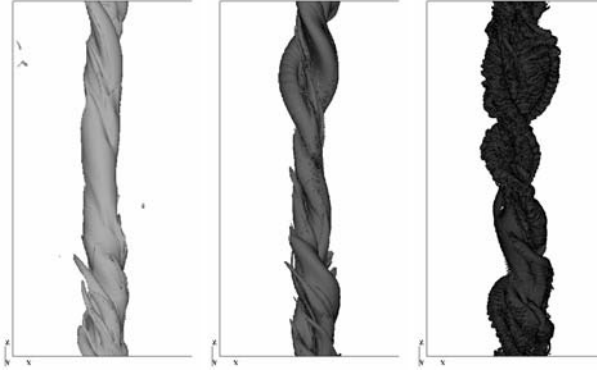
Figure 5.   Isosurfaces of vorticity (q-vortex, $q = -0.45$). From left to right: (a) $t/T = 0.84$, (b) 1.3 and (c) 1.7.

A way to illustrate the energy transfer process across scales is through the two-point energy spectrum tensor $\Phi_{ij}(r, r, t; k_z, m)$ (Eq. (6)) at various values of k_z and m. Figs. 6a and b are contour plots for the maximum values of $\Phi_{ij}(r, r, t; k_z, m)$ at $t/T = 0.47$ and 1.7, respectively. At an early stage ($t/T = 0.47$), Fig. 6a shows that $\max |\Phi_{zz}(r, r, t; k_z, m)|$ at low wavenumbers is larger than at high wavenumbers. This implies the energy transfer from larger to smaller scales, i.e. the normal energy cascade. This tendency of energy cascade changes at a later stage ($t/T = 1.7$) when the characteristic deformation of the columnar vortex is observed. Fig. 6b shows that $\max |\Phi_{zz}(r, r, t; k_z, m)|$ at low wavenumbers $(k_z r_0, m) = (10, 0)$ has almost the same amplitude as that
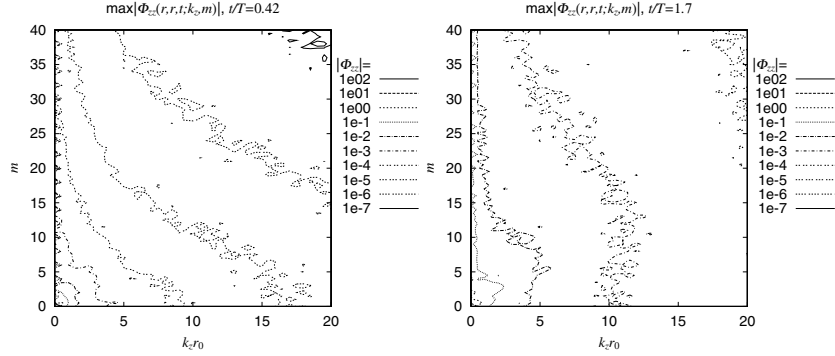
Figure 6. Contour map of the maximum value of $|\Phi_{zz}(r, r, t; k_z, m)|$ in (k_z, m) plane: (a)$t/T = 0.47$, (b) 1.7. The contour lines are plotted in logarithmic scale.

of higher wavenumbers $(10, 15)$. This implies that the energy of the columnar vortex is transferred to larger and smaller scales simultaneously.

4.2   Stable case ($q = -1.5$)

We investigate the marginally stable case in which the q-vortex has the swirl parameter $q = -1.5$. This parameter is selected so that the q-vortex is almost neutrally stable, because the q-vortex of $|q| > \sqrt{2}$ is stabilized against shortest wavenumber disturbances (WKB modes, Leibovich & Stewartson 1983).

Fig. 7 shows vortical structures of the q-vortex of swirl parameter $q = -1.5$ with isosurface of vorticity at $t/T \simeq 1.67$. Inside the vortex core, an emergence of thin and strong spiral structures, which are different from worms, are observed. This indicates that the nonlinear interaction is concentrated inside the core. These structures generated around the surface of the core are wound up by the columnar vortex, which stretches and thins the structure. The thin and strong filaments around the vortex core have swirling motion. After long times ($t/T > 5$), these filaments are thinned and elongated enough to be dissipated by viscosity.

5.   Summary

We investigated the interaction between a columnar vortex and external turbulence using direct numerical simulations.

We observed that the Lamb-Oseen vortex ($q = -\infty$) wraps worms around itself which form spirals. Inside the vortex core, axisymmetric, and bending vortex waves are excited. The velocity disturbance corresponding to the worms become statistically axisymmetric, whereas the corresponding vorticity disturbance increases not only in the axisymmetric mode but also in other modes.
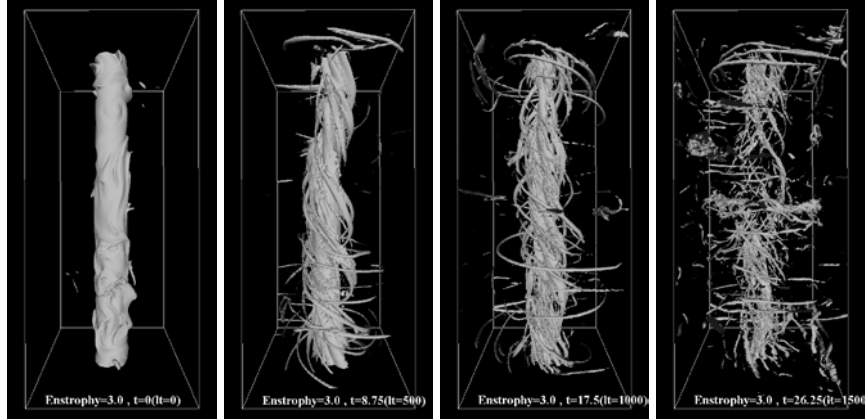
Figure 7.   Time evolution of isosurfaces of the q-vortex with $q = -1.5$.

These results are consistent with RDT. The initial turbulence affects the growth of the velocity and vorticity disturbance. In the case with damping initial turbulence, the growth is proportional to t^2, which coincides with the RDT results. In the normal initial turbulence, the growth is proportional to $t^{0.9}$ and t^1 respectively. The interaction promotes scalar advection on the surface of the vortex core: the blocking effect of the velocity field on the surface of the vortex core, and the fine scale structure (worm) around the vortex core.

We observed the q-vortex for two values of swirl parameter q. In the case of the unstable columnar vortex (q-vortex, $q = -0.45$), helical structures occur due to the linear instability. At the saturation of the linear instability, the secondary instability sets in and the columnar vortex breaks down. We showed that the energy at fine scales increases abruptly when the vortex breakdown occurs. In the case of the marginally stable columnar vortex (q-vortex, $q = -1.5$), thin and strong spirals form inside the vortex core. These structures are stretched by the differential rotation around the columnar vortex, and they are dissipated gradually.

References

MIYAZAKI, T. & HUNT, J. C. R. 2000 Linear and nonlinear interactions between a columnar vortex and external turbulence. *J. Fluid Mech.* **402**, 349.

MAYER, E. W. AND POWELL, K. G. 1992 Viscous and inviscid instabilities of a trailing vortex. *J. Fluid Mech.* **245**, 91.

TAKAHASHI, N., ISHII, H. AND MIYAZAKI, T. 2005 The Influence of Turbulence on a Columnar Vortex. *Phys. Fluids* (in print).

LEIBOVICH, S. AND STEWARTSON, K. 1983 A sufficient condition for the instability of columnar vortices, *J. Fluid Mech.* **126**, 335.

VORTEX STRUCTURES IN A ROUGH-WALL CHANNEL FLOW AND THEIR INFLUENCE ON PASSIVE SCALAR

Paolo Orlandi, Stefano Leonardi
Dip. Mecc. e Aer., Università "La Sapienza", Rome, Italy
orlandi@kolmogorov.ing.uniroma1.it

Robert Anthony Antonia
Discipline of Mech. Eng., University of Newcastle, NSW, 2308, Australia

Abstract   DNSs of turbulent channel flows with one rough wall and one smooth wall are presented to show how the vorticity field depends on the shape and orientation of the roughness elements. The passive scalar is also evaluated. The high correlation coefficients between vorticity and scalar gradients, in the wall layer, emphasize that in all cases flow visualizations can be used in a laboratory to have a qualitative picture of the modifications of the high- and low-speed streaks. Joint probability density function between vorticity and scalar gradients show how the bursting events affect the scalar distribution.

Keywords: Turbulence, roughness, vorticity, heat transfer

1.   Introduction

The heat transfer in turbulent wall-bounded flows depends on the near-wall vortical structures. It follows that an increase or reduction of the heat transfer can be achieved through the modification of these structures. Flows with different types of vortical structures, such as flows over rough surfaces, may be useful to understand the correlation between heat transfer and vorticity. Experimental investigations are rather difficult due to the complexity in carrying out reliable vorticity and temperature measurements near the roughness elements. Numerical simulations are limited to low Reynolds numbers. Nonetheless, assuming that the flow physics in the near-wall region is less dependent on the Reynolds number than the outer region, much can be learned from low-Re simulations.

There have been many previous experimental and numerical studies of rough surfaces with different roughness element shapes. These elements produce dif-

ferent effects on the incoming flow depending on the orientation of the structures and on the separation of the solid elements. Leonardi *et al.* (2003) performed numerical simulations to explain why the maximum drag for square bars orthogonal to the flow occurred at $w/k = 7$ (w indicates the separation between elements and k the height). By comparison with circular rods it was observed that the resistance, for $w/k > 3$, is weakly dependent on the shape of the elements. Orlandi *et al.* (2004) investigated the modifications of the statistics for square, circular and triangular elements both aligned and orthogonal to the flow for $w/k = 1$, in which case the shape and orientation plays a large effect. Near the plane of the crests flow isotropization was observed. Under these conditions there is an increase of disorder of the near-wall vortical structures compared with those for a smooth wall. On the other hand, for elements aligned with the flow, the organization may be increased. Due to these drastic changes to the vorticity field we should expect large modifications to the statistics of a passive scalar injected at the solid walls. The present paper focuses on the modifications to the vorticity and passive scalar statistics in the region close to the plane of the crests where the effect on the fluid motion between the elements is strong. The same geometries of Orlandi *et al.* (2004) are considered. Throughout the paper the geometries are denoted by capital letters, C for the smooth wall channel, S for square bars, R for circular rods and T for triangular elements. The orientation of the elements is indicated by the subscript N for transverse, and P for longitudinal elements. The first number in the subscript relates to k (2 for $k/h = 0.2$ and 1 for $k/h = 0.1$) and the last to w/k. Statistics for C, S_{2N1}, R_{2N1}, T_{2N1}, T_{2N0}, S_{2P1}, R_{2P1}, T_{2P1}, T_{2P0} are discussed.

Different geometries are considered, each simulation starts from the flow and thermal fields of a smooth channel, with symmetric mean velocity and antisymmetric temperature profile. Thus, the heat entering at one wall is equal to that exiting from the other. In the simulations, one wall is rough and the other smooth. The time necessary to reach for the velocity field a statistical steady state, is not sufficient for the thermal field and an imbalance occurs between the heat entering from the rough wall and that exiting from the smooth wall. This imbalance depends on the shape of the disturbances. The profiles of the passive scalar statistics near the two walls do not vary, time variations being localised to the central part of the channel. Since our interest is in the region close to the walls, we think that this condition is tolerable.

2.   Numerical procedure

The Navier-Stokes equations are discretized in an orthogonal coordinate system using a staggered second-order finite-difference approximation. More details of the numerical method can be found in Orlandi (2000). To deal with different types of geometrical elements, an accurate method consists in main-

taining the equations in orthogonal coordinates and approximate the complex geometry by the immersed boundary technique. Here, as described in Orlandi *et al.* (2004), at the first point outside the roughness element, the second-order derivatives are discretized as is usually done at the first point close to a smooth wall; but here the geometrical coefficients vary along the solid wall. Near the boundaries, the scheme is first-order accurate without an effect on the flow since the flow physics implies that near a solid boundary the velocity tends to zero linearly. The non-linear terms are evaluated without any correction to account for the changes of the metric near the solid boundary. The accuracy of the method was validated by Orlandi *et al.* (2004) where the pressure distribution around circular bars was compared with that measured by Furuya *et al.* (1976). Minor discrepancies between the numerical and experimental results could be ascribed to the different types of flows and the Reynolds number. In the laboratory, the Reynolds number was higher and a boundary layer was considered. The temperature field is treated as the velocity field and for isothermal walls it is preferable to locate θ (temperature) at the same location as u_2 (wall-normal velocity).

Two different computational boxes are considered. The first one for orthogonal disturbances has physical dimensions $L_1 = 8h$, $L_2 = 2.2h$ and $L_3 = \pi h$ respectively in the streamwise x_1, normal x_2 and spanwise x_3 directions. The grid used was $400 \times 158 \times 128$. For the disturbances aligned with x_1 the dimensions were $L_1 = 8h$, $L_2 = 2.2h$ and $L_3 = 4h$ and the grid was $256 \times 158 \times 200$. With these dimensions, it was possible for disturbances of height $k = 0.2h$ and $w/k = 1$ to have respectively 20 and 10 elements. Each element was described by a 10×30 grid. For both configurations the basic smooth channel flow was at $Re = U_P h/\nu = 4200$ (U_P is the laminar Poiseuille velocity at the center of the channel), corresponding to a $R_\tau \approx 180$. The reduced resolution in x_1 for the second configuration reflects the expectation of more ordered turbulent structures.

No heat sources are added in the temperature transport equation. This choice differs from that in previous DNS of heated turbulent channels (e.g. Kim & Moin 1989) where a heat source is added, so that the scalar is created at the interior and removed on the walls. In these simulations, as for the total shear stress, the sum of the turbulent and molecular heat fluxes normal to the wall, normalized by the wall heat flux, decreases linearly from 1 at the wall to 0 at the channel centerline. Without the heat source, the total heat flux remains constant across the channel, when a statistical steady state is reached. This case was considered by Johansson & Wikstrom (1999) that performed simulations at $R_\tau = 180$ and 265. Orlandi & Leonardi (2004) have shown that finite differences produced results in good agreement with those by Johansson & Wikstrom (1999) obtained by a pseudospectral code. To avoid the use of very

fine grids for resolving temperature scales smaller than those of the velocity, Pr has been taken equal to 1.

For smooth walls, for symmetry reasons, the thermal equilibrium is reached in a reasonable time. In channels with one rough wall and one smooth wall, the transient needed to reach thermal equilibrium can be long and hence a large amount of CPU is necessary. The flow, was analyzed in an interval of time when $\partial\Theta/\partial t$ is constant (Θ is the bulk temperature). For flows with orthogonal disturbances $\partial\Theta/\partial t$ is greater than that for longitudinal disturbances. This is a first indication that with normal disturbances the heat transfer is greater than for longitudinal disturbances. Orlandi *et al.* (2004) observed that only for triangular geometries aligned with the flow and with $w/k = 0$, a drag reduction was achieved. For this case $\partial\Theta/\partial t$ is negative implying that the heat transfer is reduced.

3. Results

3.1 Vorticity correlations

The results for the statistics of the velocity field were presented and discussed by Orlandi *et al.* (2004) and are not repeated here. Instead we focus on the one-point correlations of the vorticity field. Since the latter is related to the small scales, the distribution in the y direction of the rms vorticity should indicate the effect the shape of the roughness has on the vortical structures. From previous DNS of smooth-wall channels, it was observed that ω_2 is strictly linked to the high- and low-speed streaks, that are located in a vertical layer of the order of 20 wall units. At the present Reynolds number, this layer is approximately equal to $y = 0.1h$ where the maximum of $\widetilde{\omega_2}$ is located (Fig. 1a). The tilde denotes rms value and averages are taken with respect to time and both spanwise and streamwise directions. Fig. 1a shows that near a smooth wall, the vorticity components differ substantially from each other whereas in the rest of the channel they coincide. It can be deduced that over a large part of the channel ($0.3 < |y| < 1.0$) the small scales of the velocity field are approximately isotropic. On the other hand, the large scales (rms velocity) are isotropic only at the center of the channel.

Fig. 1b-d show that, for orthogonal elements, there is a large increase of ω_3 due, in particular, to the modifications to the flow near the leading edge of the cavities. As expected, the sharp vertex of the triangle produces stronger and thinner layers and as a consequence $\widetilde{\omega_2}$ decays faster. The strong vertical ejections into the outer region produce higher levels of $\widetilde{\omega_1}$ compared with the other two components and, in addition, all components increase in the region far from the plane of the crests. With regard to the near-wall region the profile of $\widetilde{\omega_1}$ shows that the streamwise vortices loose their coherence. In Fig. 1 a well defined minimum at $y = 0.03$ is appreciable; by increasing the amount of
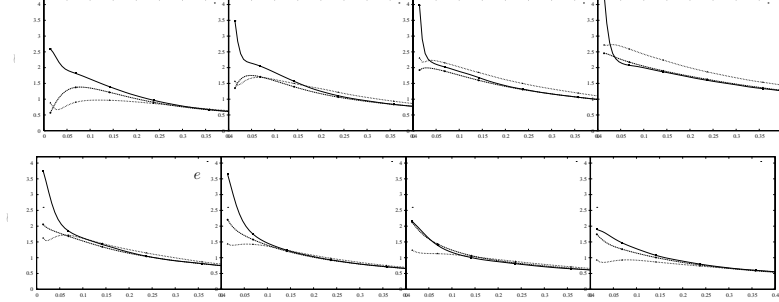
Figure 1. RMS vorticity distributions ——— □ ω_3, - - - - ● ω_2, ········ △ ω_1 a) smooth wall, b) S_{2N1}, c) R_{2N1}, d) T_{2N1}, e) S_{2P1}, f) R_{2P1}, g) T_{2P1}, h) T_{2P0}).
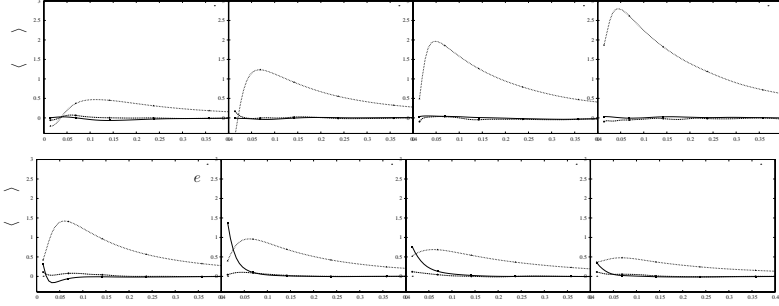
Figure 2. Vorticity correlations ——— □ $\langle \omega_2 \omega_3 \rangle$, - - - - ● $\langle \omega_1 \omega_3 \rangle$, ········ △ $\langle \omega_1 \omega_2 \rangle$; a) smooth wall, b) S_{2N1}, c) R_{2N1}, d) T_{2N1}, e) S_{2P1}, f) R_{2P1}, g) T_{2P1}, h) T_{2P0}).

the disturbance, rather small for square bars (Fig. 1b), the minimum reduces and gets closer to the plane of crests. For triangles (Fig. 1d), the disturbance becomes quite strong and the minimum almost disappears. On the plane of the crests, the amount of solid boundary reduces with the consequence that $\widetilde{\omega_2}$ is no longer zero. This is the component that is most affected by the roughness and the distribution change drastically.

The amount of non-solid surface at the plane of the crest for the aligned elements plays a more important role, as can be observed by the profiles of $\widetilde{\omega_2}$ in Fig. 1e-h. In some of the configurations, the profiles of $\widetilde{\omega_2}$ coincide with those of $\widetilde{\omega_3}$ (triangular riblet with $w/k = 0$). In "riblets" of triangular shape, for any w/k, these two vorticity components are greater than $\widetilde{\omega_1}$ and for the drag reducing shape ($w/k = 0$, Fig. 1h) the difference extends for a greater distance than for the geometry with a slight drag increase (Fig. 1g). To summarise, the tendency to have the same level of rms vorticity for the spanwise and normal components indicates that the structures are more ordered than on a smooth wall.

Fig. 2a shows that only one component of the symmetric vorticity tensor is large and the other two are close to zero. The small oscillations in the near wall region are related to the lack of fields saved to evaluate the statistics; usually, the components of the off diagonal terms converge more slowly than the diagonal elements. Fig. 2b-d show that for orthogonal disturbances $\langle \omega_1 \omega_2 \rangle$ is increased significantly while $\langle \omega_2 \omega_3 \rangle$ and $\langle \omega_1 \omega_3 \rangle$ remain small. The effect of the disturbance is to increase the peak value by leaving unchanged the shape of the profile. On the other hand, for parallel elements, depending on the shape of the grooves, the symmetry is broken in a narrow layer close to the plane of the crests, and this is more pronounced for $\langle \omega_3 \omega_2 \rangle$ than $\langle \omega_1 \omega_3 \rangle$. This corroborates the previous statement about more ordered structures. The increase and decrease in organization are important for understanding the interaction between vorticity and the passive scalar. The modifications of the Joint Probability Density Function (JPDF) help to explain how the most relevant events are modified.

From the plots in Fig. 2, three configurations can be selected to understand the differences between parallel and normal elements; in particular the triangular elements with $w/k = 1$ (T_{2N1}, T_{2P1}) whose results are compared with those for a smooth wall. The JPDF underlines the contribution from different events to the correlation coefficient $R_{q_i q_j} = \langle q_i' q_i' \rangle / \sqrt{\langle q_i'^2 \rangle \langle q_j'^2 \rangle}$. Here, a prime indicates a fluctuation and angular brackets averages in time and both spanwise and streamwise directions. The profiles of $R_{q_i q_j}$ can be quite different from those of $\langle q_i' q_i' \rangle$ and indeed Fig. 3a-c corroborate this. Whereas $\langle \omega_1' \omega_2' \rangle$ decreases far from the wall (Fig. 2), $R_{\omega_1 \omega_2}$ remains constant. In addition, while $\langle \omega_3' \omega_2' \rangle$ for the aligned elements is large, the correlation coefficient is rather small. The JPDF is evaluated at $y = 0.07$ where the differences between the correlation coefficients are quite large. Hereafter q_i stands for $q_i' / \sqrt{\langle q_i'^2 \rangle}$.

The JPDFs in Fig. 4bdf explain that $R_{\omega_3 \omega_2}$ are small because the contributions from quadrants I and II as well as those from III and IV are equal. The quadrant analysis shows that quadrants III and IV contribute slightly more than I and II. Flow visualizations in horizontal planes emphasize that ω_2 and ω_3 are organised according to structures of different shapes; elongated structures for ω_2 and in patches for ω_3. These two types are not correlated. This is a very interesting result because one could expect that the bursting events, detected by ω_3, are those which create the streaks. The JPDF between ω_1 and ω_3, not reported for lack of space, has a greater symmetry and this corroborates what is shown in Fig. 3, that $R_{\omega_3 \omega_1}$ is smaller than $R_{\omega_3 \omega_2}$. Also ω_1 is located in patches and is correlated with ω_2 in the sense that there is a large probability that the two vorticity components have the same sign. In the case of ordered structures (smooth wall and T_{2P1}) Fig. 4 shows that strong positive and negative ω_1 occur where ω_2 is low. For T_{2P1} (Fig. 4e) the contribution from quadrants I and III is greater than for a smooth wall (Fig. 4a). For structures with less organiza-
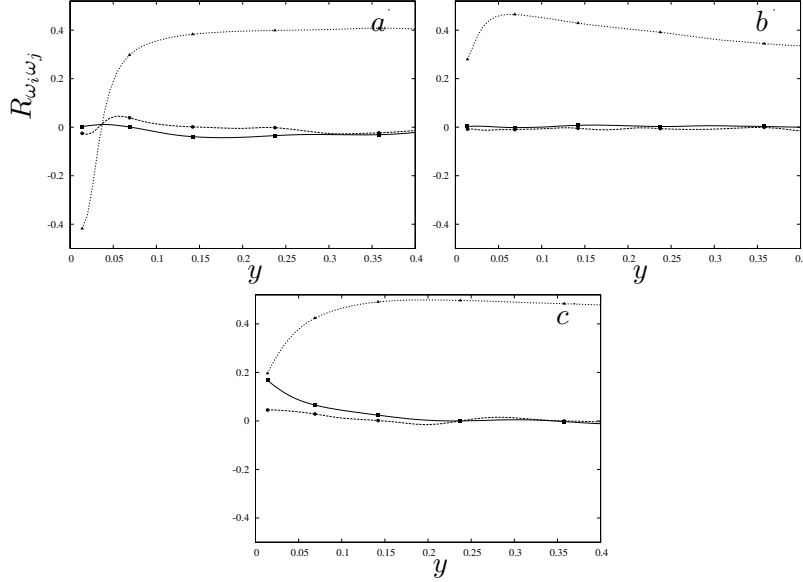
Figure 3. Normalised vorticity correlations ——□$R_{\omega_2\omega_3}$, - - - - ●$R_{\omega_1\omega_3}$, ⋯⋯⋯ △$R_{\omega_1\omega_2}$; a) smooth wall, b) T_{2N1}, c) T_{2P1}.

tion the correlation coefficient increases (Fig. 3b) and this reflects the larger probability of finding large values of ω_1 and ω_2 of the same sign.

3.2   Vorticity scalar-gradient correlations

The distribution of temperature and its correlation with the velocity field is of interest for deciding whether flow visualizations can provide a qualitative picture how streaks are modified by the roughness elements. The scalar gradients are important in combustion. To our knowledge, the correlation between scalar gradients ($g_i = \partial\theta/\partial x_i$) and vorticity has not been evaluated or discussed even for a smooth wall. The correlation tensor, $\gamma_{ij} = \langle g_i'\omega_j'\rangle$, for a smooth wall has four relatively large components, γ_{32}, γ_{23}, γ_{31}, γ_{13}.

To obtain a better comprehension of the correlation between g_i' and ω_j', the correlation coefficient $R_{g_i\omega_j} = \gamma_{ij}/\sqrt{\langle g_i'^2\rangle\langle\omega_j'^2\rangle}$ can be evaluated. Fig. 5a shows that, for a smooth wall, $R_{g_3\omega_2}$ and $R_{g_2\omega_3}$ have the same magnitude but opposite signs; near the wall, these correlations are rather high. For $R_{g_3\omega_2}$ this should be expected since $R_{u_1\theta}$ is very high. In fact, a high g_3' indicates the alternation of positive and negative θ', while a high ω_2' indicates the alternation of low- and high-speed streaks. The high $R_{g_2\omega_3}$ implies that large contributions to g_2' arise from bursting events, in the near-wall region, which are connected to high values of ω_3'. Also the correlation between g_1' and ω_3' is related to sweeps
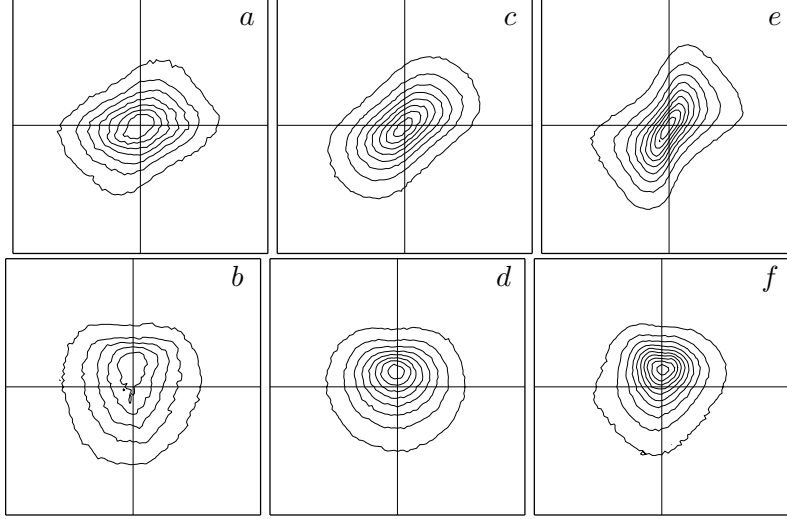
Figure 4. Contours of the JPDF between ω_2 (abscissa) and ω_3 (ordinate) on the top and ω_2 (abscissa)and ω_1 (ordinate) on the bottom. a), b) smooth wall; c) d) T_{2N1}; e) f) T_{2P1}.
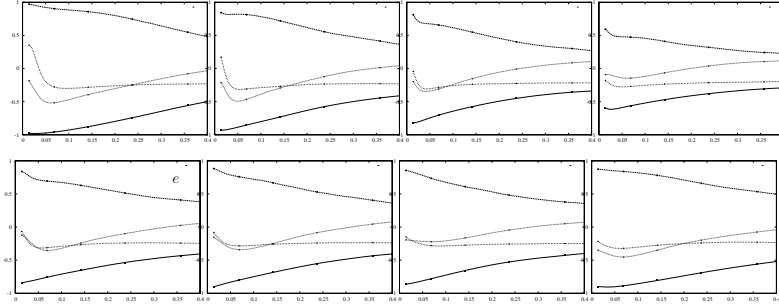
Figure 5. Correlations coefficients $R_{g_i\omega_j}$ ——— □ $R_{g_3\omega_2}$, ‒ ‒ ‒ ‒ ● $R_{g_2\omega_3}$, ········· △ $R_{g_1\omega_3}$ —·— ▽ $R_{g_3\omega_1}$ a) ——— smooth wall, b) S_{2N1}, c) R_{2N1}, d) T_{2N1}, e) S_{2P1}, f) R_{2P1}, g) T_{2P1}, h) T_{2P0}).

and ejections; the substantial difference between $R_{g_2\omega_3}$ and $R_{g_1\omega_3}$ implies that the bursting events play a bigger role in forming streaks more than in determining their lengths. Through visualization in a (x_2, x_3) plane of contours of ω_1 and θ (not given here), it can be appreciated that spikes of θ are located where high values of ω_1 occur. There is a difference in the very near-wall region between regions with ω_1 concentrated in thin layers and regions with ω_1 concentrated in circular patches. This explains the change of sign for $R_{g_3\omega_1}$ near the wall.

The physics associated with the correlation coefficients $R_{g_i\omega_j}$ in the smooth channel (Fig. 5a) is more interesting in the near-wall layer. It would be therefore

useful to understand in how these correlations are affected by the roughness elements. Fig. 5 shows that, for the orthogonal disturbances, there is a decrease of $R_{g_3\omega_2}$ which becomes substantial for T_{2N1}. As shown in Leonardi *et al.* (2003), the roughness, through u_2' disturbances emanating from the grooves, reduces the coherence of the streaks (ω_2') and hence that of g_3'. For the triangular elements, the disturbances are the strongest and the reduction of $R_{g_3\omega_2}$ the smallest. This reduction occurs also for the aligned grooves but in this case the shape of the elements is irrelevant. This can be understood through the JPDF in Fig. 6; the effect on $R_{g_3\omega_2}$ is stronger than for aligned elements. In the former case, the probability of having high values of ω_2 increases and consequently the probability of high values of g_3 is also increased. These two quantities can be considered as those which emphasize the formation of streaks near the wall. From the JPDF, however, it is not possible to infer whether a modification in the length occurred. Flow visualizations show that indeed the length is reduced in the presence of the geometrical disturbances; in particular, for aligned triangles, the structures maintain the coherence but are shorter. The greater contribution of quadrants II and IV indicates that low and high speed streaks can be detected by flow visualizations and this holds also for the normal disturbances. These plots show that ω_2 and g_3 have zero skewness.

It is well known that the bursting events are skewed with more events ($\omega_3' < 0$ sweeps) contributing to high-speed than low-speed streaks. As a consequence, g_2 is also negatively skewed; this is reproduced by the JPDF between ω_3 and g_2 (Fig. 6 subscript 2). With aligned elements the distribution of sweeps is essentially unchanged but probability of strong ejections increases. For the normal elements, the probability of the sweeps changes and Fig. 6 shows that the greater changes occur for $g_2 > 0$.

The JPDFs permit also to understand the reduction of $R_{g_3\omega_1}$ and $R_{g_1\omega_3}$ in the presence of roughness. For the former coefficient, Fig. 6 (subscript 3) shows that the differences between the quadrants are reduced and that these do not depend on the shape and orientation of the elements; this was shown in Fig. 5, where, for all cases, $R_{g_3\omega_1} = -0.25$. In accord to Fig. 5, where only for the smooth wall there is a change of sign in the wall region, it has been observed that near the wall, the first and third quadrants contribute more than the other two. Very near the wall, locations with large g_3 coincide with those where ω_1 is maximum. Fig. 5 shows that at a certain distance from the wall, this coincidence is lost, and this holds also in presence of geometrical disturbances.

Fig. 6 (subscript 4) explains why at $y = 0.07$ in Fig. 5 there is a large reduction of $R_{g_1\omega_3}$ from -0.517 for the smooth wall, to -0.145 for T_{2N1} and -0.220 for T_{2P1}. From the PDF of g_1 it appears that this quantity has a positive skewness with a large probability for strong positive gradients. Strong positive and negative gradients are located in localised patches, the positive being correlated with sweeps and the negative with ejections. The correlation
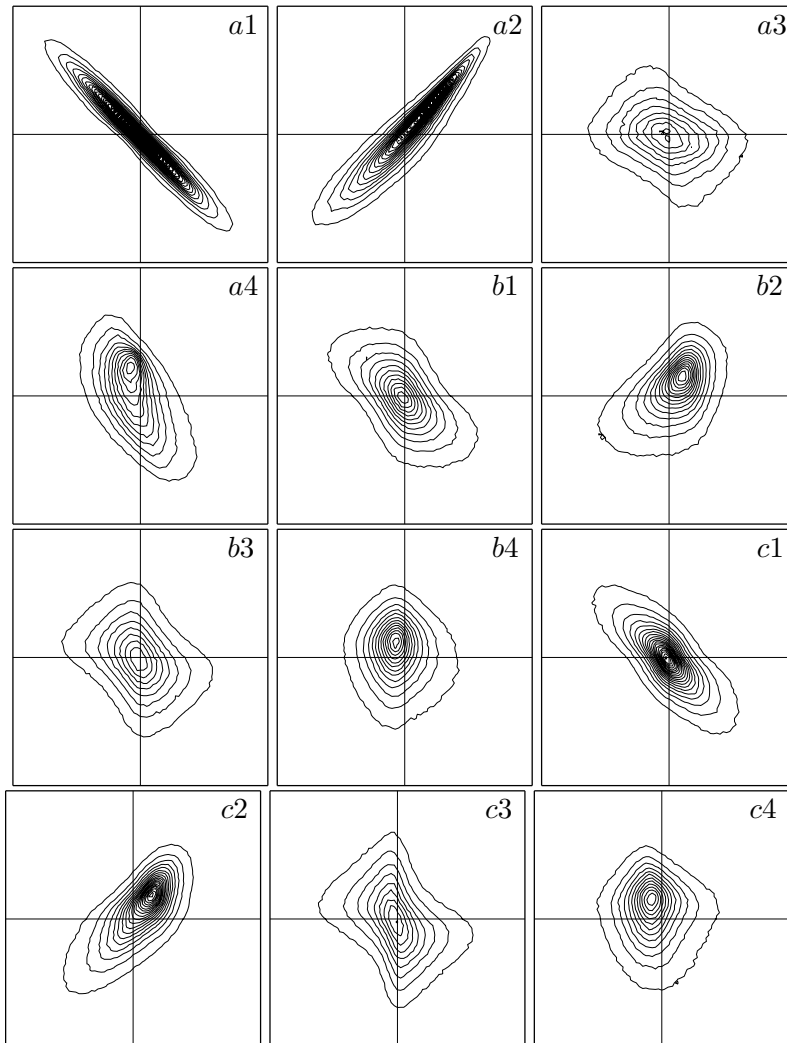
Figure 6. Contours of the JPDF between (1) g_3 and ω_2, (2) g_2 and ω_3, (3) g_3 and ω_1, (4) g_1 and ω_3; a) smooth wall, b) T_{2N1}, c) T_{2P1}.

coefficients decrease in the T_{2N1} configuration because these strong positive gradients are uncorrelated with the sweeps. Contour plots in horizontal planes show that g_1 are more equally distributed but in regions where ω_3 is rather small. An intermediate behavior between these two cases occurs when the elements are aligned with the flow.

4.   Conclusions

DNSs of flows in channels with rough walls of different shapes are used to understand the interaction between the vorticity field and a passive scalar field. Although the Reynolds number is small we believe that, for rough wall flows, the Reynolds number dependence is less important than for a smooth wall. By changing the shape and the orientation of the roughness elements, it is possible to change the vorticity field. In all cases, there is a good correlation between streamwise velocity and passive scalar; this implies that the correlation coefficient between ω_2 and g_3 is rather high. This result is of large interest to the experimentalist because laboratory flow visualizations can provide a qualitative picture of the variations of the shape of high- and low-speed streaks.

We have also understood through the JPDF between vorticity and temperature gradients why, in certain cases, the correlation coefficients are reduced appreciably compared with the smooth wall. This is important in applications where combustion occurs in the presence of solid walls. Although we were not able to develop this theme here due to shortage of space, the present results can be useful in designing combustion chambers given that the passive scalar gradients are modified by the shape of the roughness.

References

FURUYA, Y., MIYATA, M. & FUJITA, H. 1976. Turbulent boundary layer and flow resistance on plates roughened by wires. *J. Fluids Eng.* **98**, 635-644.

JOHANSON A.V. & WIKSTROM P.M. 1999. DNS and modeling of passive scalar transport in turbulent channel flow with focus on scalar dissipation modeling. *Flow Turbulence and Combustion* **63**, 223-245.

KIM, J., MOIN, P. 1989. Transport of passive scalars in a turbulent channel flow. In Andre, J.C. *et al* (Eds) *Turbulent Shear Flows vol. 6 Springer, Berlin*, 85-96.

LEONARDI, S., ORLANDI, P., SMALLEY R.J., DJENIDI, L. & ANTONIA, R. A. 2003. Direct numerical simulations of turbulent channel flow with transverse square bars on the wall. *J.Fluid Mech.* **491**, 229-238.

ORLANDI, P. 2000. *Fluid Flow Phenomena : A Numerical Toolkit*, Dordrecht, Kluwer.

ORLANDI, P., & LEONARDI, S. 2004. Passive scalar in a turbulent channel flow with wall velocity disturbances. To appear in *Flow Turbulence and Combustion* .

ORLANDI, P., LEONARDI, S., & ANTONIA, R.A. 2004. Turbulent channels flow with wall roughness. Submitted to *J. Fluid Mech.*

Part B   Coherent structures

THE NEAR-WALL STRUCTURES OF TURBULENT WALL FLOWS

Javier Jiménez
School of Aeronautics, Universidad Politécnica, 28040 Madrid, Spain
jimenez@torroja.dmt.upm.es

Genta Kawahara
Dept. of Aeronautics and Astronautics, Kyoto University, Kyoto 606-8501, Japan
gkawahara@kuaero.kyoto-u.ac.jp

Mark P. Simens, Juan C. del Álamo
School of Aeronautics, Universidad Politécnica, 28040 Madrid, Spain

Abstract   Models for the viscous and buffer layers over smooth walls are reviewed. It is shown that there is a family of numerically-exact nonlinear structures which account for about half of the energy production and dissipation in the wall layer. The other half can be modelled by the unsteady bursting of those structures. Many of the best-known characteristics of the wall layer, such as the lateral spacing among the streaks, are well predicted by these models. The limitations of minimal models are then discussed, and it is noted that a better approximation is to represent the velocity streaks as 'semi-infinite' wakes of the wall-normal velocity structures, both in the buffer and in the logarithmic layer. The consequences of this characterization on the causal relation between bursting structures are also briefly discussed.

Keywords: Turbulence, boundary layers, nonlinear systems.

1.   Introduction

This paper reviews current theories about the flow in the immediate vicinity of smooth walls. We will see that, although this part of the flow is geometrically very thin in the high-Reynolds number limit, it is the seat of a large fraction of the total velocity difference across the turbulent boundary layer. The same is true for the total energy production and dissipation, and for many of the features that distinguish wall-bounded turbulent shear flows from those away

from walls. The study of this region of the flow is simpler than that of turbulence in general, in part because the characteristic Reynolds numbers associated with its wall-normal coordinates are small, but also because of the local importance of the mean shear. It is for that reason that we will be able to offer relatively closed models for its behaviour.

In the same way that the near-wall region dominates a large fraction of the flow at intermediate Reynolds numbers, the logarithmic layer does the same at higher ones. As the Reynolds number tends to infinity, the fraction of the total velocity difference which is confined to the logarithmic layer tends to unity. Working in large part by analogy with the near-wall region we will also be able to say something about the lower part of the logarithmic layer, and thus about most of the energy-relevant aspects of the turbulent boundary layer.

The modern study of this part of the flow began experimentally in the 1970's (Kim *et al.* 1971; Morrison 1971), and got a strong impulse with the advent of direct numerical simulations in the late 1980's and 1990's (Kim *et al.* 1987). We will mostly use here evidence from numerical simulations. That emphasis is partly a personal bias of the authors, but it is not altogether arbitrary. The thinness of the near-wall region makes it well-suited to simulation and difficult to explore experimentally, and much of the available information is numerical. In §2 we outline the models that have been proposed for this part of the flow, including how recent work on equilibrium solutions is related to turbulence. In §3 and §4 we discuss the time-dependent bursting and the characterization of the streamwise-velocity streaks as wakes. The conclusions are summarized in §5.

2. The structure of near-wall turbulence

Wall-bounded turbulence over smooth walls can be described in terms of two sets of scaling parameters (Tennekes & Lumley 1972). Viscosity is important near the wall, and the length and velocity scales in that region are constructed with the kinematic viscosity ν and with the friction velocity u_τ. Magnitudes expressed in these 'wall units' are denoted by $^+$ superscripts. The near-wall layer extends at most to $y^+ = 150$ (Österlund *et al.* 2000) and, since y^+ can be interpreted as a Reynolds number, its relatively-low values make near-wall turbulence a good candidate for simple models.

Far from the wall the velocity also scales with u_τ, but the length scale is the flow thickness h. Between those two regions there is an intermediate layer with no fixed length scale, where the mean velocity is given approximately by

$$U^+ = \kappa^{-1} \log y^+ + A. \tag{1}$$

The Kármán constant, $\kappa \approx 0.4$, is an essentially universal property of turbulence in the logarithmic layer, but the intercept, $A \approx 5$ for smooth walls, is a boundary condition that depends on the viscous inner region.
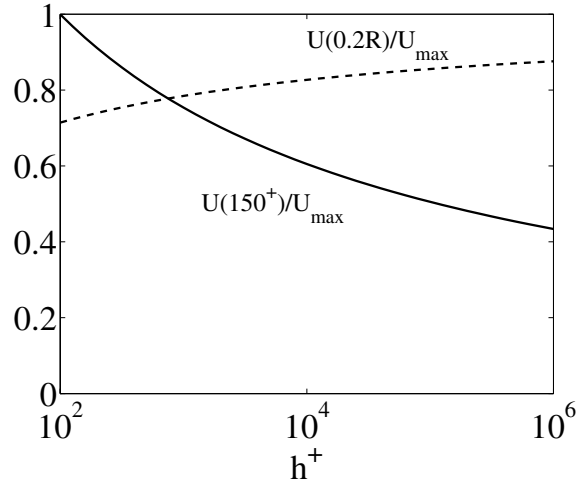
Figure 1. Fraction of the velocity difference across the different layers of wall-bounded turbulent flows, according to equation (1). ——— , across the near-wall region, $y^+ < 150$; −−−− , across the logarithmic layer, $y < 0.2h$.

That inner layer is extremely important for the flow as a whole. The ratio between the inner and outer length scales is the friction Reynolds number, h^+, which may range up to $h^+ = 5 \times 10^5$ for large water pipes. In that limit the near-wall layer is only about 3×10^{-4} times the pipe radius, but it follows from (1) that even in that case 40% of the velocity drop takes place below $y^+ = 150$.

Most of the remaining drop of the mean velocity happens within the logarithmic layer, that can be defined as the inner 20% of the flow (Österlund *et al.* 2000). Figure 1 shows the fractions of the velocity within the near-wall and the logarithmic layers. Because of (1), they only depend logarithmically on h^+ and, while the near-wall fraction decays with h^+, the logarithmic layer eventually accounts for the whole velocity drop. Turbulence is characterized by the expulsion of the energy dissipation away from the large energy-containing eddies. In wall-bounded flows that separation occurs not only in scale space, but also in the shape of the mean velocity profile. The singularities are expelled both from the large scales and from the centre of the flow towards the wall. Because of this singular nature, the near-wall layer is not only important for the rest of the flow, but it is also largely independent from it (Jiménez & Pinelli 1999).

2.1   Classical models for the sublayer

Because of this global influence, the region below $y^+ \approx 150$ has been intensively studied. It is dominated by coherent streaks of the streamwise

velocity and by quasi-streamwise vortices. The former are an irregular array of long ($\lambda_x^+ \approx 1000$) sinuous alternating streamwise jets superimposed on the mean shear, with an average spanwise separation of the order of $\lambda_z^+ \approx 50 - 200$ (Smith & Metzler 1983). The vortices are slightly tilted away from the wall (Jeong *et al.* 1997), and stay in the near-wall region for $x^+ \approx 200$. Several vortices are associated with each streak, with a longitudinal spacing of the order of $\lambda_x^+ \approx 400$ (Jiménez & Moin 1991). Most of them merge into disorganized vorticity after leaving the wall neighbourhood (Robinson 1991).

It was proposed very early that streaks and vortices form a regeneration cycle in which the vortices are the results of an instability of the streaks (Swearingen & Blackwelder 1987), and the streaks are caused by the advection of the mean velocity gradient by the vortices (Bakewell & Lumley 1967; Kim *et al.* 1971). It is for example known that disturbing the streaks inhibits the formation of the vortices (Jiménez & Pinelli 1999). The manipulation is only effective if the flow is perturbed between $y^+ \approx 10$ and $y^+ \approx 60$, suggesting that it is between those levels that the streaks are involved in the vortex-generation process. There is a substantial body of numerical (Hamilton *et al.* 1995; Waleffe 1997; Schoppa & Hussain 2002) and analytic (Reddy *et al.* 1998; Kawahara *et al.* 2003) work on the linear instability of model streaks. It shows that they are unstable to sinuous perturbations associated with inflection points of the perturbed velocity profile, whose eigenfunctions correspond approximately with the shape and location of the observed vortices. This type of models imply a time-dependent cycle in which streaks and vortices are created, grow, generate each other, and eventually decay. Additional references can be found in Jiménez & Pinelli (1999).

A slightly different point of view is that the regeneration cycle is organized around a nonlinear travelling wave, a fixed point in some phase space, which represents a nonuniform streak. This is not too different from the previous model, which essentially assumes that the undisturbed streak is a fixed point, and that the cycle is an approximation to an orbit lying near its unstable manifold. The new models however consider fixed points which are nontrivially perturbed streaks, and therefore separates the dynamics of turbulence from those of transition.

Nonlinear equilibrium solutions of the three-dimensional Navier–Stokes equations, with the right characteristics, have been obtained numerically in the past few years for plane Couette flow (Nagata & Busse 1983; Nagata 1990; Waleffe 2003), plane Poiseuille flow (Toh & Itano 2001; Waleffe 2001; Waleffe 2003), and autonomous wall flows (Jiménez & Simens 2001). Several of those solutions contain a wavy low-velocity streak flanked by a pair of staggered quasi-streamwise vortices of alternating signs (Waleffe 1998; Kawahara *et al.* 2003), closely resembling the spatially-coherent objects educed from the near-wall region of true turbulence. Their mean and fluctuation intensity profiles are

reminiscent of the experimental ones (Jiménez & Simens 2001; Waleffe 2003), and the same is true of other properties.

In those cases in which the stability of these solutions has been investigated, they have been found to be unstable saddles in phase space at the Reynolds numbers at which turbulence is observed. They are not therefore expected to exist as such in real turbulence, but the flow could spend a substantial fraction of its lifetime in their neighbourhood. Exact limit cycles and heteroclinic orbits based on these fixed points have been found numerically (Kawahara & Kida 2001; Toh & Itano 2003), and reduced dynamical models of the near-wall region have been formulated in terms of low-dimensional projections of such solutions (Aubry 1988; Sirovich & Zhou 1994; Waleffe 1997).

Two questions remain open: whether all the exact solutions that have been published for wall-bounded flows are related to each other and to near-wall turbulence, and whether real turbulence is best described in terms of steady structures or in terms of unsteady events.

The first question is addressed in figure 2. The earliest and best-known nontrivial steady solutions of a wall-bounded Navier-Stokes shear flow are those in (Nagata 1990), which were recently extended by Jiménez *et al.* (2005) to a wider range of parameters. A representative solution family is shown in figure 2(*a*), where the friction coefficient is given in terms of the spanwise wavelength and of the friction Reynolds number. The solutions can be classified into 'upper' and 'lower' branches in terms of their mean wall shears. The gray patch in the lower coordinate plane in figure 2(*a*) is the region in which solutions exist, and it is significant that it coincides very approximately with the range in which streaks spacing is found experimentally (Smith & Metzler 1983). It is shown in Jiménez *et al.* (2005) that most of the known wall-bounded solutions by other authors can also be classified into one or the other branch. The 'lower' solutions have strong and essentially straight streaks, and weak vortices in the form of vorticity sheets. Those solutions are essentially weakly nonlinear versions of the eigenfunctions of the linear instability of the velocity streaks (Kawahara *et al.* 2003). 'Upper' solutions have weaker sinuous streaks flanked by stronger vortices, which are nonlinear enough to have collapsed into roughly circular cores. They consequently have weaker root-mean-square streamwise-velocity fluctuations u', and stronger wall-normal ones v' than those in the lower branch. Their velocity fluctuation profiles agree well with those of real turbulence.

The relative strength of both types of fluctuations for a particular solution can be characterized by the maximum values of its profiles of r.m.s. u' and v'. Different solutions can then be compared among themselves, and with fully-turbulent flows, by means of those two numbers. The r.m.s. profiles of the exact solutions, which are computed over periodic domains of size $L_x^+ \times L_z^+ \approx 400 \times 100$ parallel to the wall, cannot however be compared directly with the
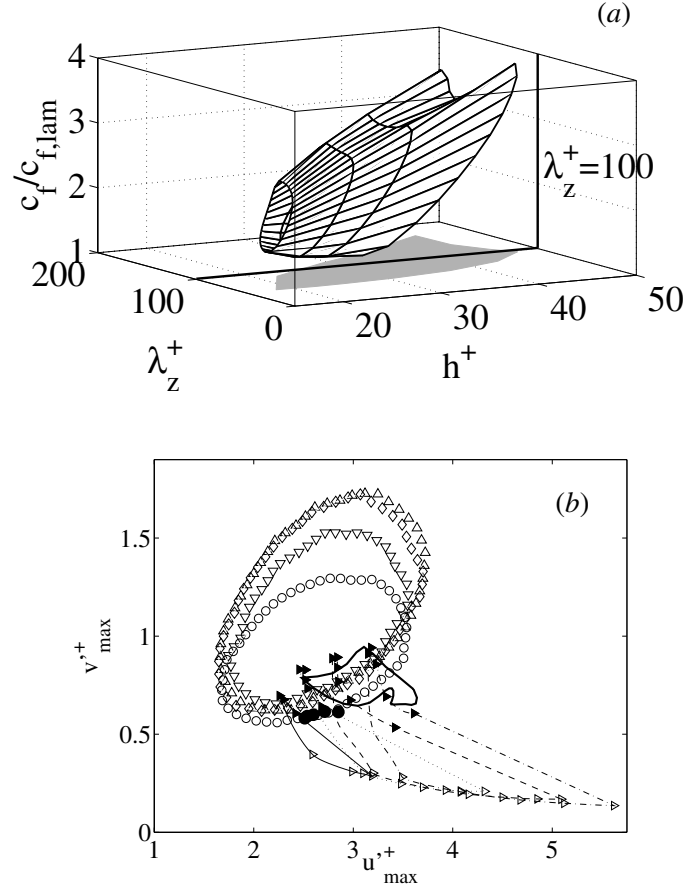
Figure 2. (*a*) Solution surface for Nagata's steady solutions in Couette flow, in terms of the spanwise wavelength, and of the friction Reynolds number. $\lambda_x/h = 2\pi$ (Jiménez *et al.* 2005). (*b*) Comparison of some exact solutions with the near-wall turbulent structures, in terms of the maxima of the u' and v' r.m.s. profiles taken over boxes of size $b_x^+ \times b_z^+ \times y^+ = 380 \times 110 \times 50$. $\triangleright$, Nagata's solutions for Couette flow (Jiménez *et al.* 2005). Solid symbols are 'upper branch' solutions, and open ones are 'lower branch'. $\bullet$, autonomous permanent waves (Jiménez & Simens 2001). The solid loop is an exact limit cycle in plane Couette flow (Kawahara & Kida 2001). Other open symbols are probability isocontours from large-box Poiseuille flows (del Álamo *et al.* 2004): $\triangle$, $h^+ = 1880$; $\diamondsuit$, 950; $\triangledown$, 550; $\circ$, 180. They contain 90% of the p.d.f.

fluctuation profiles compiled from experiments or from full-scale simulations, which typically have domains of the order of $L_x^+ \times L_z^+ \approx 10{,}000 \times 5{,}000$.

To allow the comparison in figure 2(*b*), each wall of the large computational boxes was divided into 'minimal' sub-boxes with the same wall-parallel dimensions as the computational boxes of the exact solutions, $b_x^+ \times b_z^+ \approx 380 \times 110$, and the statistics were compiled over them. Each sub-box was characterized

by its maximum r.m.s. intensities below $y^+ = 50$, and the values for different sub-boxes were summarized as a joint probability density function of the two quantities, compiled over the different sub-boxes and over time. Each flow was not therefore characterized by a single point, but by the probability distribution of the possible states of the sub-boxes.

The results in figure 2(b) suggest that only the 'upper-branch' exact solutions are representative of real turbulence. They also show that the correspondence is reasonably good, but that there are fluctuations in the near-wall region of real turbulent flows which are substantially stronger than those of the exact solutions.

3.   Bursting versus steady solutions

The next question is whether those stronger fluctuations can best be described by a different kind of steady solutions or by unsteady ones. The unsteady models discussed at the beginning of section 2 follow the original interpretation of the visualizations of the sublayer by Kim *et al.* (1971), which was that the streaks regenerate through intermittent 'bursting'. That interpretation has sometimes been dismissed as a visualization artifact, and even the original authors acknowledged that their visualizations could be consistent with advecting permanent objects (Offen & Kline 1975). Bursting became associated with the ejections observed by stationary velocity probes, specially after numerical simulations showed that the velocity streaks were long-lived. The events identified in the analysis of single-point data were associated to the passing of quasi-streamwise vortices, intermittent in space but not necessarily in time (Robinson 1991). This explanation bypassed the question of whether the observed temporally-intermittent sublayer events were artifacts or really existed.

The difficulty of following for long times individual structures in fully turbulent flows complicates the distinction between permanent structures and time-dependent processes with a long period, but intermittent breakdown of near-wall turbulence is observed in minimal-flow numerical simulations (Jiménez & Moin 1991) in which spatial intermittency is not an issue. In these simulations the wall-parallel periodic dimensions of the computational box are small enough to produce a periodic array of identical essentially-single structures, and the analysis is simplified because those structures can easily be followed in time. An example is given in figure 3, where the evolution of the flow near the wall in a minimal channel is represented in terms of the production P and of the dissipation D, integrated below $\delta^+ = 50$. Each instantaneous state of the minimal flow is represented by a point in the (P, D) plane, and the joint p.d.f. in figure 3 is compiled as the system evolves in time. The arrows in the figure represent the mean evolution velocity in parameter space.
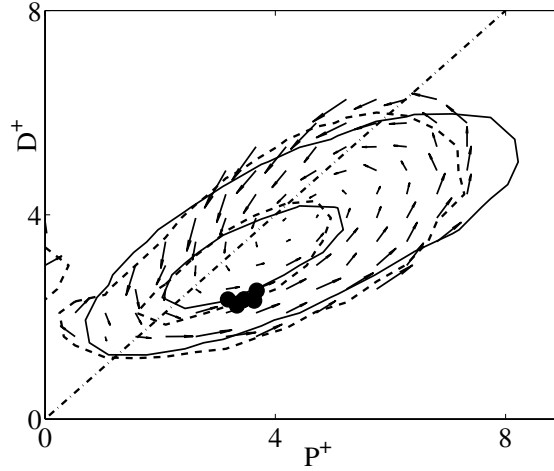
Figure 3. Joint probability density functions of the turbulent energy production and dissipation below $y^+ = 35$. $h^+ \approx 180$. The diagonal line is energy equilibrium, $P = D$. The arrows are explained in the text. ---- , minimal Poiseuille flow, $L_x^+ \times L_z^+ = 450 \times 125$; ——— , full channel, analysed over similar sub-boxes. The isolines contain 40% and 90% of the data. ● , equilibrium solutions from Jiménez & Simens (2001).

The flow describes a cycle in the $(P, \, D)$ plane, during which the fluctuations accumulate energy when $P > D$, grow, cross into the dissipative part of the plane where $D > P$, and finally decay. The period of the cycle is of the order of $T^+ \approx 400$ in the high-Reynolds number limit (Jiménez *et al.* 2005), during which the structures advect about $x^+ = 5000$. The steady upper-branch equilibrium waves described above are in this representation production-dominated in the near-wall layer and relatively quiescent. The Couette limit cycle which was included in figure 2, but which is not plotted here for clarity, is a miniature version of the energy cycle in figure 3, with whom it shares many characteristics (Jiménez *et al.* 2005).

Figure 3 shows that the minimal flow 'bursts' in the sense of the original unsteady descriptions of Kim *et al.* (1971). The same temporal information is not accessible for full flows, because of the problem of identifying individual structures, but a joint p.d.f. of P and D can be compiled for them over minimal sub-boxes. Such a p.d.f. is included in figure 3, and it is similar enough to that of the minimal case to strongly suggest that the full flow is also bursting.

Note that these bursts are not ejections associated with the passing of quiescent vortices. The sub-boxes that we have used to analyse the flow are large enough to always contain a full vortex pair, and in particular they are large enough for their mean wall-normal velocity to be always very close to zero. The scatter in figure 3 is due to differences between quiescent and excited full
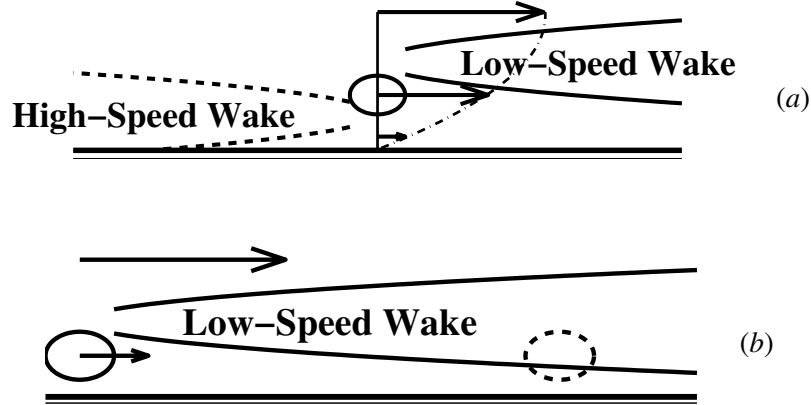
Figure 4. (*a*) Sketch of the wakes left in the mean velocity profile by a compact v-structure moving with an advection velocity intermediate between the flow below and above it. The wakes below the structure contain higher velocities than the local mean, but they are in slower-moving fluid and are left behind. Those above the structure contain lower velocities, and ride ahead of the v-structure. (*b*) Because the low-speed streaks created by the vortices are only semi-infinite, the new vortices created by their instability form downstream of the original ones. Models using a minimal flow unit wrap the original and the new vortical structures into a single one.

sets of structures. The mean profiles of most quantities change according to their position in the bursting cycle (Jiménez *et al.* 2005). The general effect of bursting is to move the active structures away from the wall.

4. Longer structures as wakes

4.1 Wakes in the buffer region

The model in the previous section is suggestive, and we have seen that it accounts for many of the characteristics of the viscous and buffer layers. In essence it assumes that the near-wall region is populated with compact nonlinear structures, formed by a segment of an infinitely-long streamwise-velocity streak, and by its associated quasi-streamwise vortices. They stay in the neighbourhood of some steady equilibrium solution, and move along the wall with an advection velocity of the order of $U_c^+ = 10$ (Kim & Hussain 1993). However it is clear that this cannot be the whole story.

Consider the situation in figure 4(*a*), in which the compact vortical structure advects along the wall with a velocity intermediate between the mean velocities close to the wall and far away from it. The vertical advection induced by the vortices creates a high-speed streak near the wall, and a low-speed one farther up but, because of the relative velocities of the mean flow and of the perturbation, the former is left behind, while the former rides ahead of the vortices. These relative positions of the v and u structures in the buffer layer were documented

(a)   (b)
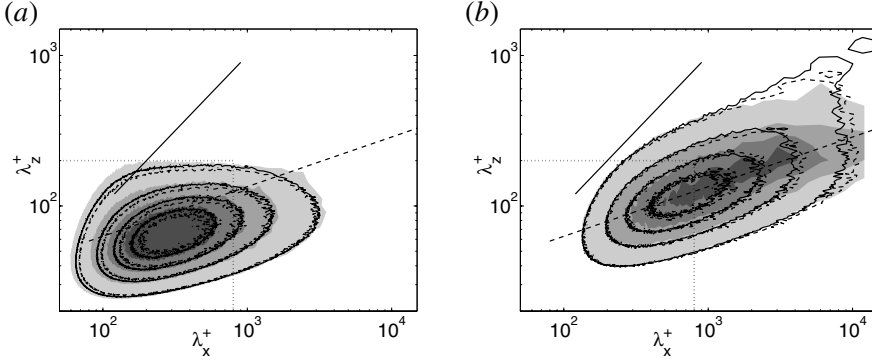
Figure 5.   Two-dimensional spectral energy density $k_x k_z E/u_\tau^2$ in the buffer layer, $y^+ = 16$. Shaded, autonomous flow masked above $\delta^+ = 60$ (Jiménez *et al.* 2004); ———— , channel. $h^+ = 550$; ---- , channel. $h^+ = 950$ (del Álamo *et al.* 2004). The solid diagonal is $\lambda_z = \lambda_x$, and the dashed one is $\lambda_z \sim \lambda_x^{1/3}$. The dotted rectangle is the Fourier transform of the minimal box $\lambda_x^+ \times \lambda_z^+ = 400 \times 100$. (*a*) Wall-normal velocity. (*b*) Streamwise velocity.

in Jiménez *et al.* (2004). The high-speed streaks formed in this way are close to the wall, and they are quickly dissipated by viscosity. The low-speed streaks diffuse away from the wall and last longer (Jiménez *et al.* 2004), but they are nevertheless only semi-infinite, instead of truly infinite as in the model of the previous section. The result is that they can only close the regeneration cycle by forming new vortices somewhere downstream of the original ones, as in figure 4(*b*). The minimal-flow box wraps both the new and the old vortices into a single structure, and makes the semi-infinite streak appear fully infinite. We have seen that the resulting minimal model accounts for many of the statistical aspects of the buffer region, but the true model should be closer to the one just described.

The difference between the lengths of the compact v structures and the longer u streaks is seen in the spectral energy densities in figure 5. The wall-normal velocity is roughly contained within the minimal box, and scales in wall units for the three Reynolds numbers represented. The spectrum of streamwise velocity in figure 5(*b*) is more complex. Within the minimal box the u-spectra of the three Reynolds numbers scale well in wall units, and more or less coincide with those of v. This part of the spectrum is the one described by the minimal models in the previous section. In the upper-left corner there is a component which depends on the Reynolds number. Those structures scale in outer units, and correspond to global modes spanning the whole boundary layer (del Álamo & Jiménez 2003). Between both extremes there is a spectral ridge which scales well in this representation, although probably with a Reynolds-dependent length. It follows the power law $\lambda_z \sim \lambda_x^{1/3}$, which is consistent with diffusion in a shear. It can be shown that it is formed by structures which are essentially linear, in
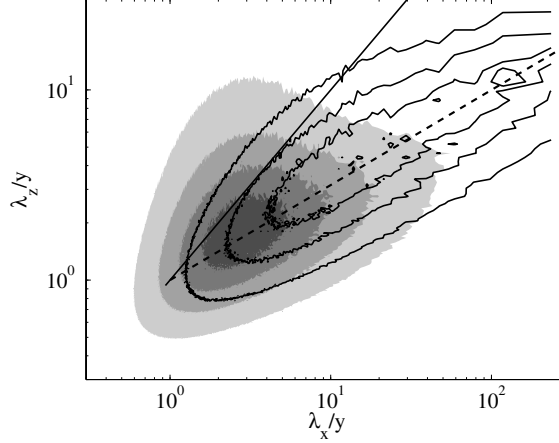
Figure 6. Two-dimensional spectral energy density $k_x k_z E / u_\tau^2$ in the logarithmic layer layer, $y/h = 0.11$, $h^+ = 950$. The shaded contours are the wall-normal velocity; the lines are the streamwise velocity. The solid diagonal is $\lambda_z = \lambda_x$, and the dashed one is $\lambda_z = (y\lambda_x)^{1/2}$.

the sense that the wall-normal velocity generates the streamwise fluctuations, but the latter do not influence the former (Jiménez *et al.* 2004). Confirmation of this interpretation of the u-structures as wakes generated by v will be given below using similar relations in the logarithmic layer.

4.2 Wakes in the logarithmic region

As we move away from the wall, the form of the energy spectrum changes (del Álamo & Jiménez 2003; del Álamo *et al.* 2004). The spectra of u and v at one station in the lower logarithmic region are shown in figure 6. The wall-normal velocity is concentrated in scales which are roughly isotropic and or the order of the wall distance y, but u has in addition a long ridge of 'wakes'. It follows in this case

$$\lambda_z \approx (y\lambda_x)^{1/2}, \tag{2}$$

rather than a cube-root law found in the viscous layer. This is also consistent with the model of a wake left by compact structures, because in the logarithmic and outer layers the velocity is almost constant, and the diffusion of the wake is due to an eddy viscosity which, on dimensional grounds, is $\nu_T \approx u_\tau y$. The similarity solution is then (del Álamo *et al.* 2004)

$$u \sim u[y/x, \; z/(yx)^{1/2}]. \tag{3}$$

It was shown by del Álamo & Jiménez (2003) and by del Álamo *et al.* (2004) that the short structures of the wall-normal velocity are effectively detached from the wall, in the sense that the correlation of individual Fourier modes
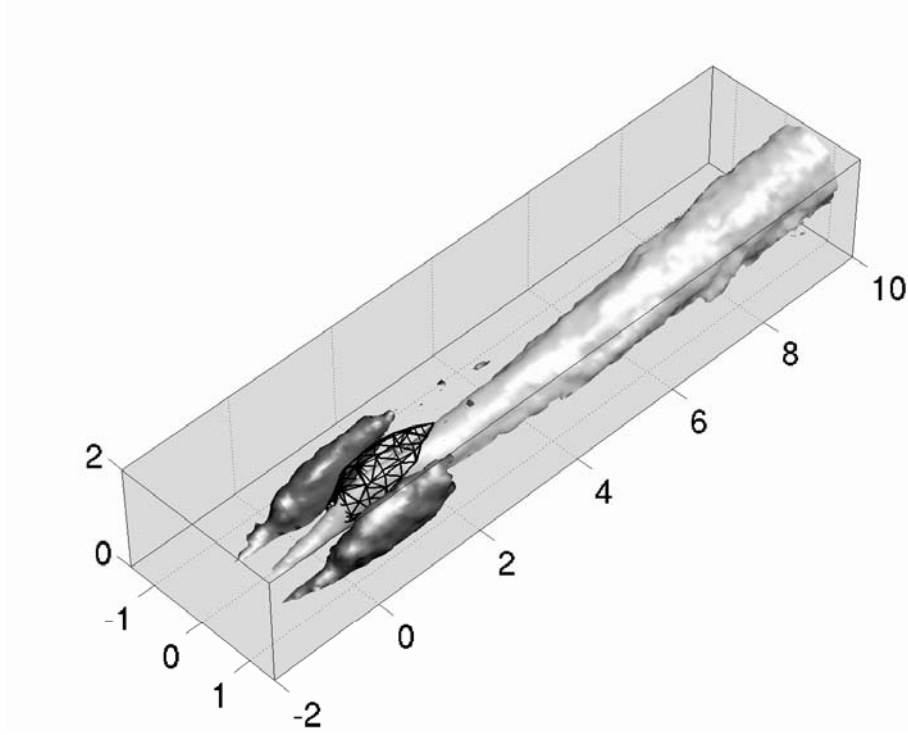
Figure 7. Perturbation velocity field conditioned on the presence of a vortex cluster, whose mean position is given by the meshed object. The flow is from bottom-left to top-right. $h^+ = 950$. Only clusters with $y_{max}^+ > 100$ are used. The lighter central object downstream of the cluster is the isosurface $u^+ = U^+(y) - 0.15$. The two darker objects to the sides and upstream of the cluster are $u^+ = U^+(y) + 0.35$.

between the logarithmic and the buffer layer is very small. The height over which those correlations are large increases as the structures become longer. The eddies touch the wall when λ_x is some low multiple of y, and the attached eddies beyond that limit are the ones that populate the wake ridge.

The nature of the v structures generating the wakes is discussed in del Álamo *et al.* (2005), which studies the vorticity structures in the buffer and logarithmic layers using simulations in full numerical boxes with $h^+ \leq 1900$ (del Álamo *et al.* 2004). Vortices are defined as being formed by points in which the discriminant D of the velocity gradient tensor is larger than a properly-defined threshold (Chong *et al.* 1990). Connected sets of such points are collected into individual vortex clusters, which break naturally into two distinct groups according to whether their lowest points are above or below a critical level around $y^+ \approx 20$. We will call the latter group attached and the former detached. The most interesting clusters are those attached to the wall and reaching above

$y^+ = 100$ into the logarithmic layer. When each of them is inscribed into a parallelepipedal box aligned to the coordinate directions, the boxes are self-similar, with dimensions $\Delta_z \approx 1.5\Delta_y$ and $\Delta_x \approx 3\Delta_y$. For attached clusters it makes sense to associate Δ_y with the height y, because their minimum distance to the wall is small. When this is done, and when Δ_x and Δ_z are also equated to the streamwise and spanwise wavelengths, the dimensions of the bounding boxes roughly coincide with the location of the spectral peak for the wall-normal velocity v. The vortices themselves appear to be arranged as surfaces or shells within the boxes because, while the volume of the bounding box increases as Δ_y^3, the volume contained in points classified as vortices increases only as Δ_y^2.

A conditionally-averaged flow field, based on the centres of the vortex boxes, and scaled with their vertical dimensions, shows a strong v ejection surrounded by two counter-rotating vortices, as in a classical hairpin. The antisymmetry is only statistical and, as in the case of the buffer-layer vortices (Robinson 1991), there is little evidence for symmetry in individual vortex clusters.

When the conditionally-averaged flow field is extended down- and up-stream from the location of the vortex box, the result is that in figure 7. The central object extending downstream from the vortex cluster is the low velocity streak, while the two lower objects on the sides and upstream are high-velocity features. The location of both features is consistent with the wake model in figure 4(*a*). The spanwise symmetry of figure 7 is again only statistical. Individual structures are typically irregular. When the transverse velocities are plotted in planes normal to the stream, the averaged vortical structure of the wakes contains two weak counter-rotating vortices which are much larger than the size of the original vortex packet, and which are reminiscent of the downstream structure of the wake of a transverse jet in a boundary layer (Fric & Roshko 1994).

Similar ramp-vortex structures have been observed by previous investigators (Adrian *et al.* 2000; Christensen & Adrian 2001), with geometric characteristics similar to those found here, but the present interpretation of their relation with the vortex packets is, to our knowledge, new. The results in del Álamo *et al.* (2005) suggest that the detached vortex clusters are associated with the interior of the low-velocity ramps (Tanahashi *et al.* 2004), and that they may be responsible for the maintenance of the shear layers which define the ramp tops. The attached clusters are only found at the ramp origins. Note for example the absence of any coherent low-velocity structure upstream of the vortex box in figure 7(*a*), except near the wall. When the conditioned flow field is computed for the detached vortex clusters, the low-speed region extends upstream and downstream of the box.

The velocity perturbations due to the ramps are of the order of u_τ, and the total projected surface of the boxes bounding the wakes is enough to cover the whole wall with some overlap. The perturbation due to the wakes is therefore

a substantial fraction of the total perturbation energy in the channel, as could be expected from the u spectrum in figure 6.

The spectra at different wall distances show that the wakes widen along the ridge (2) until $\lambda_z \approx 2h$ (del Álamo *et al.* 2004). This effectively determines the longest wavelength in the spectrum, which is

$$\lambda_{x,max}/h \approx 4h/y. \tag{4}$$

This limit is longest at the bottom of the logarithmic layer, where $y^+ \approx 100$ and $\lambda_{x,max}/h \approx h^+/20$. These are very long structures that, even taking into account possible numerical factors, point to hundreds of boundary-layer thicknesses at high Reynolds numbers. Spectral peaks of the order of $20h$ have been documented in experiments (Jiménez 1998; Kim & Adrian 1999), where they are probably limited by the length of the experimental records. The full simulations being used here only reach to $\lambda_x \approx 25h$ and, although longer to our knowledge than any other available simulation, they are not long enough to settle the matter. The premultiplied spectra of u at the bottom of their logarithmic layers are still essentially flat at their longest wavelengths, as seen in figure 6. On the other hand, numerical experiments with shorter simulation boxes show very little difference in the part of the spectrum that is resolved by the simulations (del Álamo *et al.* 2004), suggesting that those very long structures are essentially passive and do not feed into the shorter ones. This brings to mind the similar property of the buffer-layer streaks mentioned in the previous section. We have already noted that short simulation boxes model the long scales as if they were infinitely long, and the previous results suggest that structures longer than about $5h$ behave as if they were dynamically infinite.

The shortening of the spectra above the lower logarithmic layer predicted by (4) had been previous noted experimentally, although without explanation (Lawn 1971; Jiménez 1998; Kim & Adrian 1999).

An interesting question is whether the vortex clusters and the ramps discussed here are features of the whole logarithmic layer, or just of its lower edge. The probability density function $p(\Delta_y)$ for the dimensions of the attached vortex clusters collapses well in wall units for different Reynolds numbers, with a maximum around $\Delta_y^+ = 50$ (del Álamo *et al.* 2005). This suggests that the clusters are buffer-layer phenomena which should become negligible for most of the logarithmic layer when h^+ is large enough, but this is not necessarily so, and depends on the behaviour of $p(\Delta_y)$. The projected area of each vortex cluster on the plane of the wall is $\Delta_x \Delta_z \approx 5\Delta_y^2$, and for any p.d.f. decaying slower than Δ_y^{-2} the largest clusters would be the ones covering most area. This would for example be the case for the distribution $p(\Delta_y) \sim \Delta_y^{-1}$, which was suggested in (Perry *et al.* 1986) on similarity grounds. In our simulations the decay of $p(\Delta_y)$ depends on the threshold used to define the vortices, with ill-

defined decay slopes which are always steeper than Δ_y^{-3}, although the Reynolds numbers are too low to draw definite conclusions.

5. Conclusions

We have reviewed the present understanding of the dynamics of turbulent flows near smooth walls. This is a subject that, like most others in turbulence, is not completely closed, but which has evolved in the last decades from empirical observations to relatively coherent theoretical models. It is also one of the first cases in turbulence, perhaps together with the structure of small-scale vorticity in isotropic flow, in which the key technique responsible for cracking the problem has been numerical simulation. The reason is that the Reynolds numbers of the important structures are low, and therefore accessible to computation, while experiments are difficult. For example the spanwise Reynolds number of the streaks is only of the order of $z^+ = 100$, which is less than a millimetre in most experiments, but we have seen that it is well predicted by the range of parameters in which the associated equilibrium solutions exist.

We have seen that, to a good approximation, the dynamics of the near-wall regions are described by these equilibrium solutions, and that much of what is not explained by them can be accounted for by their unsteady bursting. We have however argued that this description is not complete, and that the bursting does not probably refer to the periodic temporal behaviour of a single structure, but to the generation of new structures by the instability of the wakes left by the original ones. The presence of the wakes has been explicitly demonstrated in the lower logarithmic layer, where the the quasi-streamwise vortices of the buffer layer are substituted by self-similar vortex tangles, and the ramp-like wakes take the place of the streaks. Note that, in this case, the downstream regeneration of the vortex tangles in the wakes generalizes the formation of hairpin trains studied by previous researchers in the absence of background fluctuations (Zhou *et al.* 1999).

The description of the buffer layer in term of minimal equilibrium or periodic solution should then be seen as a first approximation which folds the actual flow structure into the spatially periodic minimal box. Although we have seen that this folding has very little influence in the overall statistics, the causal relations are different and, for example, control strategies developed from minimal flows might not necessarily be optimal for the real case.

68

References

ADRIAN, R.J., MEINHART, C.D. & TOMKINS, C.D. 2000 Vortex organization in the outer region of the turbulent boundary layer, *J. Fluid Mech.* **422**, 1–54.

DEL ÁLAMO, J.C. & JIMÉNEZ, J. 2003 Spectra of very large anisotropic scales in turbulent channels, *Phys. Fluids* **15** L41–L44.

DEL ÁLAMO, J.C., JIMÉNEZ, J., ZANDONADE, P. & MOSER, R.D. 2004 Scaling of the energy spectra of turbulent channels, *J. Fluid Mech.* **500**, 135–144.

DEL ÁLAMO, J.C., JIMÉNEZ, J., ZANDONADE, P. & MOSER, R.D. 2005 Attached and detached vortex clusters in the logarithmic region, submitted *J. Fluid Mech.*

AUBRY, N., HOLMES, P., LUMLEY, J.L. & STONE, E. 1988 The dynamics of coherent structures in the wall region of a turbulent boundary layer, *J. Fluid Mech.* **192**, 115–173.

BAKEWELL, H. P. & LUMLEY, J. L. 1967 Viscous sublayer and adjacent wall region in turbulent pipe flow. *Phys. Fluids* **10**, 1880–1889.

CHONG, M.S., PERRY, A.E. & CANTWELL, B.J. 1990 A general classification of three-dimensional flow fields, *Phys. Fluids* A **2**, 765–777.

CHRISTENSEN, K.T. & ADRIAN, R.J. 2001 Statistical evidence of hairpin vortex packets in wall turbulence, *J. Fluid Mech.* **431**, 433–443.

FRIC, T.F. & ROSHKO, A. 1994 Vortical structure in the wake of a transverse jet, *J. Fluid Mech.* **279**, 1–47.

HAMILTON, J. M., KIM, J. & WALEFFE, F. 1995 Regeneration mechanisms of near-wall turbulence structures. *J. Fluid Mech.* **287**, 317–348.

JEONG, J., HUSSAIN, F., SCHOPPA, W. & KIM, J. 1997 Coherent structures near the wall in a turbulent channel flow. *J. Fluid Mech.* **332**, 185–214.

JIMÉNEZ, J. 1998 The largest structures in turbulent wall flows. In *CTR Annual Research Briefs*, 943–945. Stanford University.

JIMÉNEZ, J. 2004 Turbulent flows over rough walls, *Ann. Rev. Fluid Mech.* **36**, 173–196.

JIMÉNEZ, J., DEL ÁLAMO, J.C. & FLORES, O. 2004 The large-scale dynamics of near-wall turbulence, *J. Fluid Mech.* **505**, 179–199.

JIMÉNEZ, J., KAWAHARA, G., SIMENS, M.P., NAGATA, M. & SHIBA, M. 2004 Characterization of near-wall turbulence in terms of equilibrium and 'bursting' solutions, *Phys. Fluids* **17**, 015105.1–16.

JIMÉNEZ, J. & MOIN, P. 1991 The minimal flow unit in near wall turbulence. *J. Fluid Mech.* **225**, 221–240.

JIMÉNEZ, J. & PINELLI, A. 1999 The autonomous cycle of near wall turbulence, *J. Fluid Mech.* **389**, 335–359.

JIMÉNEZ, J. & SIMENS, M.P. 2001 Low-dimensional dynamics in a turbulent wall flow, *J. Fluid Mech.* **435**, 81–91.

KAWAHARA, G., JIMÉNEZ, J., UHLMANN, M. & PINELLI, A. 2003 Linear instability of a corrugated vortex sheet – a model for streak instability, *J. Fluid Mech.* **483** 315–342.

KAWAHARA, G. & KIDA, S. 2001 Periodic motion embedded in plane Couette turbulence: regeneration cycle and burst, *J. Fluid Mech.* **449**, 291–300.

KIM, K. C. & ADRIAN, R. J. 1999 Very large-scale motion in the outer layer. *Phys. Fluids* A **11**, 417–422.

KIM, J. & HUSSAIN, F. 1993 Propagation velocity of perturbations in channel flow. *Phys. Fluids* A **5**, 695–706.

KIM, H.T., KLINE, S.J. & REYNOLDS, W.C. 1971 The production of turbulence near a smooth wall in a turbulent boundary layers, *J. Fluid Mech.* **50**, 133–160.

KIM, J., MOIN, P. & MOSER, R. 1987 Turbulence statistics in fully developed channel flow at low Reynolds number. *J. Fluid Mech.* **177**, 133–166.

LAWN, C.J. 1971 The determination of the rate of dissipation in turbulent pipe flow, *J. Fluid Mech* **48**, 477-505.

MORRISON, W.R.B., BULLOCK, K.J. & KRONAUER, R.E. 1971 Experimental evidence of waves in the sublayer. *J. Fluid Mech.* **47**, 639–656.

NAGATA, M. & BUSSE, F.H. 1983 Three-dimensional tertiary motions in a plane shear flow, *J. Fluid Mech.* **135**, 1–26.

NAGATA, M. 1990 Three-dimensional finite-amplitude solutions in plane Couette flow: bifurcation from infinity, *J. Fluid Mech.* **217**, 519–527.

OFFEN, G.R. & KLINE, S.J. 1975 A proposed model for the bursting process in turbulent boundary layers, *J. Fluid Mech.* **70**, 209–228.

ÖSTERLUND, J.M., JOHANSSON, A.V., NAGIB, H.M. & HITES 2000 A note on the overlap region in turbulent boundary layers, *Phys. Fluids* **12**, 1–4.

PERRY, A.E., HENBEST, S. & CHONG, M.S. 1986 A theoretical and experimental study of wall turbulence. *J. Fluid Mech* **165**, 163–199.

REDDY, S.C., SCHMID, P.J., BAGGETT, J.S. & HENNINGSON, D.S. 1998 On stability of streamwise streaks and transition thresholds in plane channel flows. *J. Fluid Mech.* **365**, 269–303.

ROBINSON, S.K. 1991 Coherent motions in the turbulent boundary layer. *Ann. Rev. Fluid Mech.* **23**, 601–639.

SCHOPPA, W. & HUSSAIN, F. 2002 Coherent structure generation in near-wall turbulence. *J. Fluid Mech.* **453**, 57–108.

SIROVICH, L. & ZHOU, X. 1994 Dynamical model of wall-bounded turbulence. *Phys. Rev. Lett.* **72**, 340–343.

SMITH, C.R. & METZLER, S.P. 1983 The characteristics of low speed streaks in the near wall region of a turbulent boundary layer. *J. Fluid Mech.* **129**, 27–54.

SWEARINGEN, J.D. & BLACKWELDER, R.F. 1987 The growth and breakdown of streamwise vortices in the presence of a wall. *J. Fluid Mech.* **182**, 255–290.

TANAHASHI, M., KANG, S.-J., MIYAMOTO, T., SHIOKAWA, S. & MIYAUCHI, T. 2004 Scaling law of fine scale eddies in turbulent channel flows up to $Re_\tau = 800$. *Int. J. Heat and Fluid Flow* **25**, 331–340.

TENNEKES, H. & LUMLEY, J.L. 1972 *A first course in turbulence*, chapter 8. MIT Press.

TOH, S. & ITANO, T. 2001 On the regeneration mechanism of turbulence in the channel flow, *Proc. Iutam Symp. on Geometry and Statistics of Turbulence*. (eds. T. Kambe, T. Nakano and T. Muiyauchi), Kluwer. 305–310.

TOH, S. & ITANO, T. 2003 A periodic-like solution in channel flow, *J. Fluid Mech.* **481**, 67–76.

WALEFFE, F. 1997 On a self-sustaining process in shear flows, *Phys. Fluids* **9**, 883–900.

WALEFFE, F. 1998 Three-dimensional coherent states in plane shear flows. *Phys. Rev. Letters* **81**, 4140–4143.

WALEFFE, F. 2001 Exact coherent structures in channel flow, *J. Fluid Mech.* **435**, 93-102.

70

WALEFFE, F. 2003 Homotopy of exact coherent structures in plane shear flows, *Phys. Fluids* **15**, 1517–1534.

ZHOU, J., ADRIAN, R.J., BALACHANDER, S. & KENDALL, T.M. 1999 Mechanisms for generating coherent packets of hairpin vortices in channel flow, *J. Fluid Mech.* **397**, 353–396.

COHERENT FINE SCALE EDDIES IN THE LOGARITHMIC REGION OF TURBULENT CHANNEL FLOWS

Toshio Miyauchi, Shin-Jeong Kang, Mamoru Tanahashi
Department of Mechanical and Aerospace Engineering,
Tokyo Institute of Technology,
2-12-1 Ookayama, Meguro-ku, Tokyo 152-8550, Japan

Abstract   Coherent fine scale eddies (CFSEs) play an important role in generating streak structures and Reynolds shear stress not only in the near-wall region but also in the logarithmic region. The diameter and maximum azimuthal velocity of the CFSEs in the near-wall, logarithmic and wake regions can be scaled by Kolmogorov length η and velocity u_k. The most expected diameter and maximum azimuthal velocity of the CFSEs are about $10\,\eta$ and $2.0\,u_k$ in the near-wall region $(y^+ < 40)$. In the logarithmic region $(40 < y^+ < 200 \sim 300)$, they become about $8.5\,\eta$ and $1.7u_k$, respectively. These features are independent of Reynolds number up to $Re_\tau = 1270$. Large-scale structure in turbulent channel flows is organized by the CFSEs in the logarithmic region, which contribute to the streamwise velocity deficit (i.e. low-momentum region). By visualizing spatial distributions of the CFSE axes, it is made clear that the probability that the CFSEs exist in low-momentum regions is higher than that existing in high-momentum regions. The low-momentum regions of the logarithmic layer are composed of the CFSEs which have narrower diameter and stronger azimuthal velocity.

1.   Introduction

It has been shown that turbulence is composed of universal fine scale eddies (i.e. coherent fine scale eddies, hereafter CFSEs) from the results of direct numerical simulations (DNSs) (Jiménez *et al.* 1993, Jiménez & Wray 1998, Tanahashi *et al.* 1999a, 1999b, 2001, 2004). In the near-wall region $(y^+ < 60)$, quasi-streamwise vortices are elongated in the edge of the low-speed streak and kinked above it away from the wall (Jeong *et al.* 1997). These streamwise eddies possess the same feature as the CFSEs which have been observed in homogeneous turbulence and turbulent free-shear flows (Tanahashi *et al.* 1999a, 2001). The characteristics of the CFSEs can be scaled by the Kolmogorov

71

length (η) and r. m. s. of velocity fluctuation (u_{rms}) in turbulent flows of low Reynolds number, and the most expected diameter and maximum azimuthal velocity are about 8η and $0.5 \sim 1.0u_{rms}$ (Jiménez $et\ al.$ 1993, Tanahashi $et\ al.$ 1999a). Recent study in homogeneous isotropic turbulence up to $Re_\lambda \approx 220$ has revealed the exact scaling of the CFSEs (Miyauchi $et\ al.$ 2002). Similar to the results obtained in low Re_λ cases, the most expected diameter is 8η even for highest Re_λ. On the other hand, the maximum azimuthal velocity can be exactly scaled by u_k in place of u_{rms} and the maximum azimuthal velocity shows a peak at $1.2u_k$ for all Re_λ. Note that relatively strong CFSEs can be well scaled by u_{rms} even for higher Re_λ cases. Jiménez & Wray (1998) have reported that the azimuthal velocity can be scaled by u_{rms} for relatively high Reynolds number cases up to $Re_\lambda \approx 170$. The difference between Miyauchi $et\ al.$ (2002) and Jiménez & Wray (1998) is mainly caused by the detection method of the fine scale eddy. Since Jiménez & Wray (1998) use enstrophy magnitude to identify the eddy, stronger eddies may be detected preferentially. The detailed discussion about the detection scheme has been reported in Tanahashi $et\ al.$ (1999a). In turbulent channel flows, directional dependence or alignment of the rotating axis can be observed near the wall. Tanahashi $et\ al.$ (1999b, 2004) have suggested that the aligned CFSEs correspond to the streamwise vortices. The streamwise vortices are frequently observed near the wall, and are inclined at 9 degrees in the vertical plane and tilted alternately at $+4$ and -4 degrees in the horizontal plane (Jeong $et\ al.$ 1997).

From the PIV measurements, Adrian $et\ al.$ (2000) have observed that ejection patterns on streamwise-wall normal planes near the wall ($y^+ < 50 \sim 100$) are consistent with the vortex legs bending and becoming quasi-streamwise vortices, and the inclination angles of the neck and head vary from 15 to 75 degrees (45 degrees is typical). The spanwise wavelengths of the maxima in pre-multiplied energy spectrum of streamwise fluctuating velocity are linearly increased in the logarithmic region (Jiménez 1998, Tomkins & Adrian 2003, Kawamura $et\ al.$ 2003, Álamo & Jiménez 2003). The increase of these spanwise wavelengths is caused by the low-speed region existing in logarithmic region, and results in the large-scale motion in wall turbulence. The large-scale motions are important in wall turbulence because their lifetime is long. Tomkins & Adrian (2003) have suggested that the dominant large-scale motions at elevated Reynolds numbers are low u-momentum regions elongated in the streamwise direction from PIV measurements on streamwise-spanwise planes in turbulent boundary layers. They have also argued that the low-momentum regions are consistently associated with vortical motions at each height. In the present study, DNSs of turbulent channel flows up to $Re_\tau = 1270$ are conducted. The characteristics of the CFSEs in the near-wall and logarithmic regions are discussed by analyzing these DNS data. We also investigate structure of the

CFSE cluster and features of the CFSEs embedded in the low-momentum parts of the logarithmic regions.

2. DNS database

DNSs of turbulent channel flows are carried out by solving incompressible Navier-Sokes equations and continuity equation. Reynolds number based on the friction velocity (u_τ) and channel half width (δ) is 400, 800 and 1270. Spectral methods are used in the streamwise (x) and spanwise (z) directions and 4th-order central finite difference scheme is used in the wall-normal (y) direction. Periodic boundary conditions for the velocity and pressure fields are used in the x and z directions. No-slip conditions for the velocity are used at the walls. Table 1 shows the computational domain size (L_x, L_y, L_z), the number of grid points (N_x, N_y, N_z) and spatial resolution ($\Delta_x^+, \Delta_y^+, \Delta_z^+$) in the x, y and z directions. For more details about the numerical method, see Tanahashi *et al.* (1999c).

3. Coherent fine scale eddies in the near-wall and logarithmic regions

Figure 1 shows iso-surfaces of the second invariant (Q) of the velocity gradient tensor for $Re_\tau = 400$, where Q is normalized by δ and the mean streamwise velocity U_c at the channel center. The domain size visualized is lower half of the computational domain. The second invariant of the velocity gradient tensor is defined by $Q = (\Omega_{ij}\Omega_{ij} - S_{ij}S_{ij})/2$, where S_{ij} and Ω_{ij} are the symmetric and antisymmetric parts of the velocity gradient tensor $A_{ij}(= \partial u_i/\partial x_j = S_{ij} + \Omega_{ij})$. Streamwise vortices near the wall and hairpin-type vortices can be visualized by the positive Q region, which coincides with the results by λ_2 (Jeong *et al.* 1997) and Δ-definition (Blackburn *et al.* 1996). However, all of the visualizations including Fig. 1 depend on the threshold of the variables. To educe CFSEs without any threshold from the flow fields, a new identification scheme (Tanahashi *et al.* 1999a) based on local flow pattern is employed. The educed section includes a local maximum of Q along with the axis of a fine scale eddy, and a central point of swirling motion is identified. The diameter and maximum azimuthal velocity of the detected CFSEs can be scaled by η and u_k (Tanahashi *et al.* 2004).

The probability density functions (pdfs) of the diameter and maximum azimuthal velocity of the CFSEs in the near-wall region ($y^+ < 40$), the logarithmic region ($40 < y^+ < 200 \sim 300$) and the wake region near the center of the channel are shown in Fig. 2 for all Reynolds number case simulated. The diameter and maximum azimuthal velocity are normalized by η and u_k at y^+ where the CFSE exists. The η and u_k are calculated from the mean dissipation rate ($\bar{\epsilon}(y^+)$) of turbulent kinetic energy at y^+. The most expected

Table 1. Numerical parameters for DNS of turbulent channel flows.

Re_τ	Re	$L_x \times L_y \times L_z$	$N_x \times N_y \times N_z$	Δx^+	Δy^+	Δz^+
400	8200	$3\pi\delta \times 2\delta \times \pi\delta$	$384 \times 385 \times 192$	9.817	0.479~5.183	6.544
800	17760	$2\pi\delta \times 2\delta \times \pi\delta$	$512 \times 769 \times 384$	9.817	0.479~5.183	6.544
1270	30320	$2\pi\delta \times 2\delta \times \pi\delta$	$864 \times 1239 \times 648$	9.236	0.450~5.183	6.157
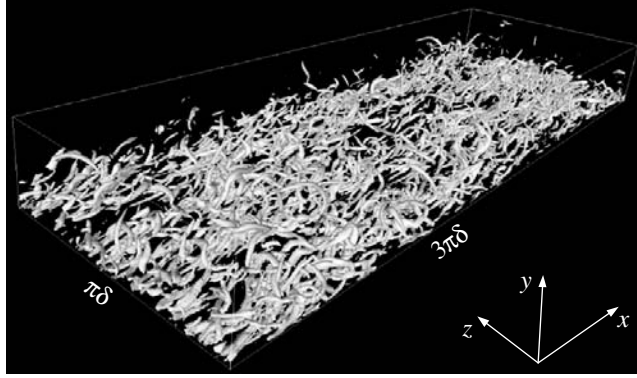
Figure 1. Contour surfaces of second invariant Q of the velocity gradient tensor for $Re_\tau = 400$ ($Q = 4$, domain size: $l_x \times l_y \times l_z = 3\pi\delta \times \delta \times \pi\delta$). Perspective view from above and upstream.

diameter and maximum azimuthal velocity in the near-wall region are about $10\,\eta$ and $2.0u_k$ for all Reynolds numbers. In the logarithmic region they are about $8.5\,\eta$ and $1.7u_k$, which are slightly wider and stronger than those in homogeneous isotropic turbulence (Miyauchi *et al.* 2002) and turbulent mixing layers (Tanahashi *et al.* 2001). However, the most expected diameter and maximum azimuthal velocity in the wake region become about 8η and $1.2u_k$, respectively, which coincide with the features of the CFSEs in homogeneous turbulence and turbulent mixing layers. It should be noted that the CFSEs with diameter wider than about $40\,\eta$ hardly exist in the near-wall region. Both pdfs for all regions are independent of the Reynolds number. Figure 3 shows joint pdfs of the diameter and the maximum azimuthal velocity of the CFSEs in the near-wall and logarithmic regions for $Re_\tau = 800$. Since the intervals of contour lines are selected to be $\log_2 p$, probability densities on neighboring two contour lines are different by 2 times. The most expected diameter and maximum azimuthal velocity are the same as shown in Fig. 2. The joint pdfs show peaks at the same position (D=10 (near-wall) $\sim 8\eta$ (wake region), $v_{\theta,max}$=2.0 (near-wall)$\sim 1.2u_k$ (wake region)) which is independent of Re_τ, whereas the shapes of joint pdfs show weak y^+-dependence. The joint pdf in the near-wall region is more compact than those away from the wall, and the probability of the CFSEs with diameters
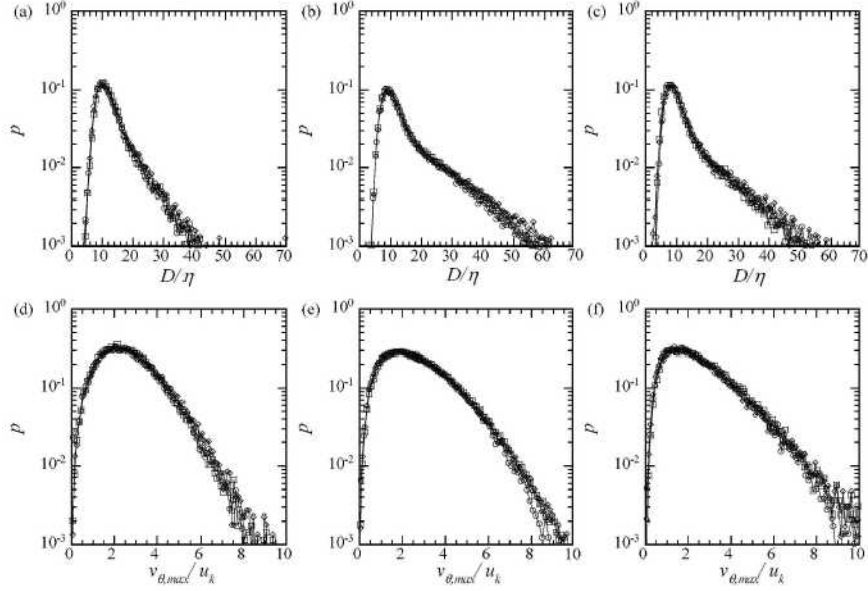
Figure 2. Probability density functions of the diameter (a)~(c) and maximum azimuthal velocity (d)~(f) of the CFSEs for all Reynolds numbers. (a) and (d): near-wall regions, (b) and (e): logarithmic regions, (c) and (f): wake regions near the channel center. $\circ$: $Re_\tau = 400$, $\square$: $Re_\tau = 800$ and $\diamond$: $Re_\tau = 1270$.
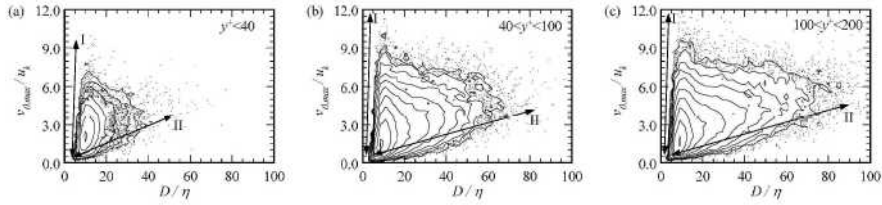
Figure 3. Joint probability density functions of the diameter and maximum azimuthal velocity of the CFSEs for $Re_\tau = 800$. (a) : near-wall region, (b) and (c): logarithmic region.

and maximum azimuthal velocities greater than 40η and $8u_k$ is very low as shown in Fig. 2. There are two regions in the joint pdfs where probabilities of the CFSEs are nearly zero. One is in the region of very small diameter (I). Diameters corresponding to the boundary of zero-probability increase linearly with the increase of the maximum azimuthal velocity. Another is in the region of small maximum azimuthal velocity (II). In this region, the maximum azimuthal velocity at the zero-boundary increases linearly with the increase of diameter. The former corresponds to the CFSEs with very high speed of rotation and deeply related to intermittency of turbulence, and the latter cor-
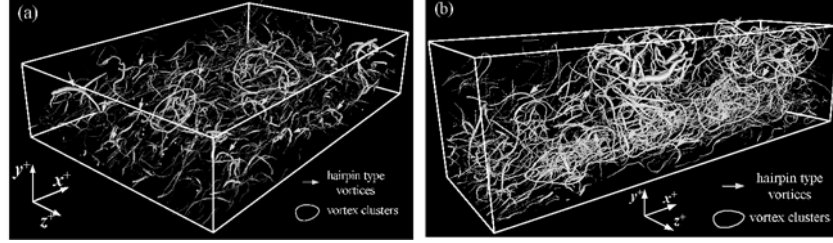
Figure 4. Spatial distributions of the CFSE axes. The diameters of the CFSE axes are drawn to be proportional to the square root of Q_c^*. (a) $Re_\tau = 400$, domain size is $l_x^+ \times l_y^+ \times l_z^+ = 1884 \times 400 \times 1256$, (b) $Re_\tau = 800$, domain size is $l_x^+ \times l_y^+ \times l_z^+ = 2513 \times 800 \times 713$.

responds to the large tube-like structure with relatively weak swirling motion. This tendency becomes stronger in the upper region of the logarithmic layer ($100 < y^+ < 200 \sim 300$). From distributions of the inclination angles and the tilting angles of axes of these CFSEs, Tanahashi *et al.* (2004) have shown that these two angles show strong directional dependence with the decrease of y^+. This directional dependence of the axes at $Re_\tau = 800$ has been observed even for $y^+ \approx 600$. The strong anisotropy in the near-wall region can be attributed to the smallest CFSEs, since the variance of the diameters becomes relatively small near the wall as shown in Fig. 2 (a) and Fig. 3 (a).

4.   Structure of the CFSE cluster

Figure 4 shows spatial distributions of the CFSE axes for $Re_\tau = 400$ and 800. Their diameters have been drawn to be proportional to the square root of Q_c^* on the axes, where the superscript $*$ indicates a non-dimensional quantity scaled by η and u_k. Since the CFSEs in turbulent channel flows are scaled by η and u_k, the vortical structures could be visualized very well even in the regions far from the wall. These visualizations provide evidence for the existence of hairpin type vortices (see marked arrow) and groups of the CFSEs throughout the logarithmic region (see marked circles). In the case of $Re_\tau = 800$, the clusters of the CFSEs are clearly observed because the logarithmic region is wider than that in case of $Re_\tau = 400$. From the PIV measurements on $x - z$ planes in turbulent boundary layer, Tomkins & Adrian (2003) and Ganapathisubramani *et al.* (2003) have shown that the low u-momentums region enveloped by positive and negative vortex cores representing the packets of hairpin vortex are the dominant large-scale motions in the logarithmic region. Figure 5 (a) shows spatial distributions of the CFSE axes with the iso-surface of streamwise fluctuating velocity in a typical region for $Re_\tau = 800$. The threshold value of the iso-surface in Fig. 5 (a) is selected to be $u'^+ = -1.8$, which is equal to about $-u'^+_{rms}$ at $y \approx 0.5\delta$.
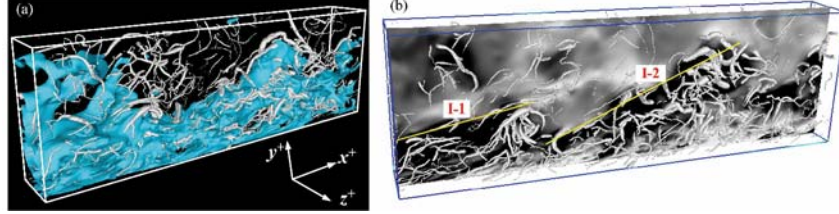
Figure 5.   Spatial distributions of the CFSE axes with (a) the iso-surface of u'^{+} and with (b) the contour of u'^{+} on $x - y$ plane at $z^{+} \approx 200$. Domain size is $l_x^{+} \times l_y^{+} \times l_z^{+} = 2513 \times 800 \times 328$, threshold of the iso-surface is $u'^{+} = -1.8$.

The large-scale low-momentum region is composed of the CFSE clusters in the outer region. This visualization also reveals that the scale growth of the low-momentum region from the bottom of logarithmic region is related with the CFSE clusters. Figure 5 (b) shows spatial distributions of the CFSE axes and the contour of streamwise fluctuating velocity on $x - y$ plane at $z^{+} \approx 200$. In this figure, the light-gray and dark-gray regions indicate high- and low-speed regions, respectively. It is clearly observed that the CFSE clusters are embedded in the low-momentum region ($u'^{+} < -1.8$; black color) of the logarithmic layer. The CFSE cluster in the bottom of the logarithmic layer lies within a low-momentum region (I-1 zone) which has a slope of about 7 degrees. Another CFSE cluster in I-2 zone forms a low-momentum region which includes the CFSE cluster in the bottom of logarithmic layer. This low-momentum region along with the CFSE cluster grows at a 17 degrees to the wake region in vertical plane. From the PIV measurement in the $x - y$ plane of the turbulent boundary layer, Adrian *et al.* (2000) have shown that zones of relatively uniform streamwise momentum ($0.79U_{\infty}$) exist within the packets of hairpin vortex and the nesting of one packet within another leads to the creation of multiple zones of different uniform momentum.

From the y^{+} dependence of distributions of the CFSE axes, Tanahashi *et al.* (2004) have shown that the distributions of the CFSE axes with weaker swirling motions are not so much related to low-speed streaks in the logarithmic region. To estimate a relation between the streak structure and the CFSEs in the logarithmic region, conditional pdfs of streamwise fluctuating velocity $u_c'^{+}$ ($= u_c^{+} - \overline{u^{+}}(y^{+})$, where $\overline{u^{+}}(y^{+})$ is the mean streamwise velocity profile) at the CFSE centers are plotted in Fig. 6. Here, pdfs are conditioned by the values of Q_c^{*} which is less than or greater than $\overline{Q_c^{*}}(y^{+})$, where $\overline{Q_c^{*}}(y^{+})$ indicates the average values of Q_c^{*} for $x - y$ plane per $\Delta y^{+} = 20$ from the wall. There are a lot of the CFSEs in the low-momentum regions ($u_c'^{+} < -1.0 \sim -1.5$) compared with those in the high-momentum regions in the outer layer, especially in the logarithmic layer. This tendency is clearly observed for $Q_c^{*} > \overline{Q_c^{*}}(y^{+})$ in the logarithmic layer, and is independent of Reynolds numbers (up to $Re_{\tau} = 1270$).
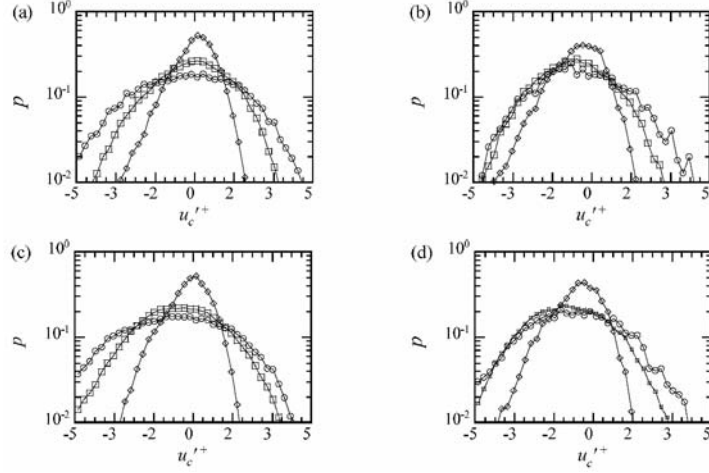
Figure 6. Conditional pdfs of $u_c'^+$ at the CFSE centers for $Re_\tau = 400$ (a),(b) and 800 (c),(d). (a) and (c): $Q_c^* < \overline{Q_c}^*(y^+)$, (b) and (d): $Q_c^* > \overline{Q_c}^*(y^+)$. $\circ$: near-wall region, $\square$: logarithmic region and $\diamond$: wake region.
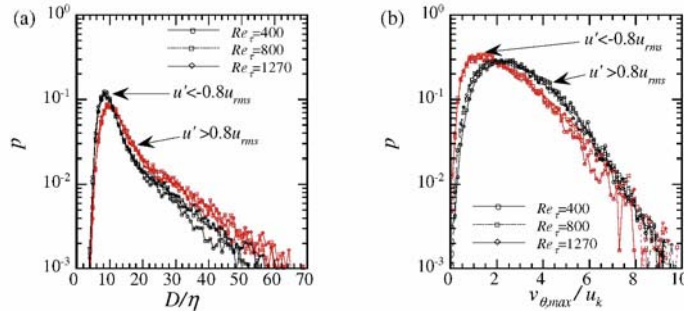
Figure 7. Conditional pdfs of the diameter (a) and maximum azimuthal velocity (b) of the CFSEs in the high-momentum ($u' > 0.8u_{rms}$) and low-momentum ($u' < -0.8u_{rms}$) regions of the logarithmic layer.

This result shows that the low-momentum regions of the logarithmic layer consist of the CFSE clusters with relatively strong rotation rate. The characteristics of the CFSEs in the high- and low-momentum regions of the logarithmic layer have been investigated by using pdfs of the diameter and maximum azimuthal velocity of the CFSEs conditioned with streamwise fluctuating velocity at the CFSE center for all Reynolds numbers. Figure 7 (a) and (b) show the pdfs of the diameter and maximum azimuthal velocity of the CFSEs in the high- and low-momentum regions of the logarithmic layer ($45 < y^+ < 200 \sim 300$). The most

expected diameter and maximum azimuthal velocity in the high-momentum regions are about 10η and $1.3u_k$, respectively. In the high-momentum region of the logarithmic layer, the diameter and maximum azimuthal velocity tend to become wider and weaker compared with those of the CFSEs without conditioning by u' (i.e. the expected values in the whole flow field). However, the probabilities of the diameter and maximum azimuthal velocity in the low-momentum regions show peaks at 8η and $2.4u_k$, respectively. In the low-momentum regions of the logarithmic layer, the most expected diameter and maximum azimuthal velocity of the CFSEs are slightly narrower and $30 \sim 50\%$ stronger than the most expected values of CFSEs in the whole flow field. Especially, the most expected maximum azimuthal velocity of the CFSE in the low-momentum regions is about 2 times of that in the high-momentum regions.

5.   Conclusions

In the present study, direct numerical simulations of turbulent channel flows were conducted up to $Re_\tau = 1270$ to investigate the characteristics of the CFSE and the CFSE cluster in the near-wall, logarithmic and wake regions. The CFSEs in turbulent channel flows can be scaled by the Kolmogorov length and velocity in each region. In the near-wall region, the most expected diameter and maximum azimuthal velocity are about $10\ \eta$ and $2.0\ u_k$, but they become about $8.5\ \eta$ and $1.7\ u_k$ in the logarithmic region. These results are independent of Reynolds number up to $Re_\tau = 1270$. The joint pdfs of the diameter and maximum azimuthal velocity of the CFSEs are also independent of Reynolds numbers, but they have weak y^+-dependence. The probability of the CFSEs with the diameter and maximum azimuthal velocity greater than 40η and $8u_k$ is very low in the near-wall region. To investigate the low-momentum region and the CFSE clusters in the logarithmic region, the CFSE axes were educed by using an axis tracing method (Tanahashi *et al.* 1999a, Tanahashi *et al.* 2004). There are many clusters of the CFSEs in the logarithmic region of turbulent channel flows. In the logarithmic region, the probability of the CFSEs existing in low-momentum regions ($u'^+ < -1.0 \sim -1.5$) is much higher than that of the CFSEs existing in high-momentum regions ($u'^+ > 1.0 \sim 1.5$), which is emphasized for the relatively strong CFSEs. The CFSE clusters form low-momentum regions in the bottom of the logarithmic layer, and this low-momentum region stands up with a small angle (about $10 \sim 20$ degrees) in vertical plane to the wake region. These clusters are composed of the CFSEs which have a slightly narrower diameter and much stronger swirling motion compared with those in the high-momentum region.

References

Adrian, R.J., Meinhart, C.D. and Tomkins, C.D. (2000) Vortex organization in the outer region of the turbulent boundary layer, *J. Fluid Mech.*, **422**, 1–54.

Álamo, J.C. and Jiménez (2003) Spectra of very large anisotropic scales in turbulent channels, *Phys. Fluids*, **15**, L41–L44.

Blackburn, H.M., Manasour, N.N. and Cantwell, B.J. (1996) Topology of fine-scale motions in turbulent channel flow, *J. Fluid Mech.*, **310**, 269–292.

Ganapathisubramani, B. Longmire, E. K. and Marusic, I. (2003) Characteristics of vortex packets in turbulent boundary layers, *J. Fluid Mech.*, **478**, 35–46.

Kawamura, H., Abe, H., Matsuo, Y. and Choi, H. (2003) Large-scale structures of velocity and scalar fields in turbulent channel flows, *Proc. Int. Symp. Dynamics and Statistics of Coherent Structures in Turbulence: Roles of Elementary Vortices*, 49–64.

Jeong, J., Hussain, F., Schoppa, W. and Kim, J. (1997) Coherent structures near the wall in a turbulent channel flow, *J. Fluid Mech.*, **332**, 185–214.

Jiménez, J., Wray, A. A., Saffman, P. G. and Rogallo, R. S. (1993) The structure of intense vorticity in isotropic turbulence, *J. Fluid Mech.*, **255**, 65–90.

Jiménez, J. (1998) The largest scales of turbulent wall flows, *Center for Turbulence Research Annual Research Briefs*, Stanford Univ./NASA Ames Research, 137–154.

Jiménez, J. and Wray, A. A. (1998) The structure of intense vorticity in isotropic turbulence, *J. Fluid Mech.*, **373**, 255–285

Miyauchi, T., Tanahashi, M. and Iwase, S. (2002) Coherent fine scale eddies and energy dissipation rate in homogeneous isotropic turbulence up to $Re_\lambda \approx 220$, *presented at IUTAM symposium on Reynolds number scaling in turbulent flow*.

Tanahashi, M., Miyauchi, T. and Ikeda, J. (1999a) Identification of coherent fine scale structure in turbulence, *Simulation and Identification of Organized Structures in Flow*, 131–140.

Tanahashi, M., Shiokawa, S., Das, S. K. and Miyauchi, T. (1999b) Scaling of fine scale eddies in near-wall turbulence, *J. Jpn. Soc. Fluid Mech.*, **18**, 256–261.

Tanahashi, T., Shoji, K., Das, S.K. and Miyauchi, T. (1999c) Coherent fine scale structures in turbulent channel flows, *Trans. JSME*, **65**, 3244-3251.

Tanahashi, M., Iwase, S. and Miyauchi, T. (2001) Appearance and alignment with strain rate of coherent fine scale eddies in turbulent mixing layer, *J. Turbulence*, **2 (6)**, 1–18.

Tanahashi, M., Kang, S.-J., Miyamoto, T., Shiokawa, S. and Miyauchi, T. (2004) Scaling law of fine scale eddies in turbulent channel flows up to Re_τ=800, *Int. J. Heat and Fluid Flow*, **25**, 331–340.

Tomkins, C.D. and Adrian, R.J. (2003) Spanwise structure and scale growth in turbulent boundary layers, *J. Fluid Mech.*, **490**, 37–74

ON THE POSSIBLE EXISTENCE OF A CO-SUPPORTING CYCLE OF LARGE-SCALE AND NEAR-WALL STRUCTURES IN WALL TURBULENCE

Tomoaki Itano
Department of Aeronautics and Astronautics, Graduate School of Engineering, Kyoto University, Yoshida-Honmachi, Sakyo-ku, Kyoto 606-8501, Japan
itano@kuaero.kyoto-u.ac.jp

Sadayoshi Toh
Department of Physics and Astronomy, Graduate School of Science, Kyoto University, Kitashirakawa, Sakyo-ku, Kyoto 606-8502, Japan
toh@scphys.kyoto-u.ac.jp

Abstract   Direct numerical simulation of a turbulent channel flow in a periodic domain of relatively wide spanwise extent, but minimal streamwise length, is carried out at Reynolds number $Re_\tau = 349$. The large-scale structures previously observed in studies of turbulent channel flow using huge computational domains are also shown to exist even in the streamwise-minimal channel of the present work. In the system, it is also clearly observed how the large-scale structures and the near-wall structures affect each other. While the collective behaviour of near-wall structures enhances a large-scale structure, the resulting large-scale structure in turn activates the generation and drift of the latter. Hence near-wall and large-scale structures interact in a co-supporting cycle.

1.   Introduction

In the vicinity of the wall, including the viscous and buffer layers which together constitute the near-wall region, a pair of streamwise vortices induces a low-speed streaky region, "wall streak", the instability of which makes the near-wall region energetic, and regenerates the streamwise vortices. This cyclic process, which was first recognized as self-sustaining process in plane Couette

81

flow by Hamilton *et al.* (1995) and Waleffe (1997) is thought to be common in many types of wall-bounded turbulent flows. It has been recently explained by exact solutions (*cf.* Waleffe (1998); Kawahara & Kida (2001)) (*cf.* Waleffe 1998, Kawahara & Kida 2001) for the minimal flow unit proposed by Jiménez & Moin (1991). Although the process may largely account for turbulent fluctuations in the near-wall region, the minimal flow unit is a small subspace of the huge computational domain which is required to simulate "real" turbulence. In the real turbulence therefore, large-scale structures in the outer region and a huge number of these near-wall structures in the near-wall region, interacting and developing spatially, participate in the production and transfer of turbulent fluctuation toward the outer region (Miyake *et al.* 1987, Lee & Kim 1991, Komminaho *et al.* 1996) .

In the present work, our main interest is in understanding the collective behaviour of the near-wall structures, and investigating how the behaviour could be associated with the large-scale structures from a physical point of view. As a first step of the challenge, we prevent the near-wall and large-scale structures from evolving spatially in the streamwise direction and thus restrict the streamwise length of the computational box to the minimal length in direct numerical simulations of channel flow. Because this channel still has large spanwise extent comparable to the extent of huge computational domains used previously, we will call this box a "streamwise-minimal" channel. In the present approach, we will show that large-scale structures can exist even in the streamwise-minimal channel, and propose a mechanism for the sustenance of large-scale structures based on the observation of the dynamical behaviors of a large-scale structure and near-wall structures.

2.   Streamwise-minimal flow

The numerical scheme we use to simulate channel flow is the same as used in Toh & Itano (2003), which is based on that developed by Kim *et al.* (1987). The origin of coordinate system is taken on the mid-plane of the channel with the x,y,z axes in the streamwise, wall-normal and spanwise directions, respectively. The no-slip boundary condition is imposed at the top ($y = +h$) and bottom ($y = -h$) walls, where h is half the channel width. Flow is driven by constant streamwise volume flux Q per unit spanwise length. We define the characteristic velocity U_c as $3Q/4h$; for laminar Poiseuille flow U_c is just the centerline velocity. In the present work, we fix the Reynolds number based on U_c, h and the kinematic viscosity ν at 9000. In order to guarantee the total computational time T is long enough for the statistical convergence of turbulent flow in our domain, we confirm that the relative error of the time average of wall friction defined as $|\langle f \rangle_t - \langle f \rangle_T|/\langle f \rangle_T$ is less than 1% for any $t > T/2$, where $\langle f \rangle_t = \frac{1}{t} \int_0^t \nu \frac{\partial U}{\partial y}(t', y = \pm h) \mathrm{d}t'$. The Reynolds number based on the

Table 1. Parameters used in several past studies.

		Re	Re_τ	L_x^+	L_z^+
minimal flow	Jiménez & Moin (1991)	2000		(300)	(100)
		3000		(250)	(110)
		5000		(400)	(80)
	Jiménez & Pinelli (1999)	4500	201	360	105
		9000	428	448	128
		18000	633	397	113
large-scale structure	Moser, Kim & Mansour (1999)		180	2270	756
			395	2560	1250
			590	3720	1840
	Del Álamo & Jiménez (2001)		185	6974	2320
			550	13800	6910
	Abe, Kawamura & Matsuo (2001)		640	4020	12100
present work	(streamwise-minimal)	9000	349	384	833
	(minimal)	9000	320	352	139

friction velocity, $Re_\tau = U_\tau h/\nu$, is 349 and 320 for our streamwise-minimal and minimal channels respectively, where $U_\tau = \sqrt{\langle f \rangle_T}$.

Table 1 summarizes the Reynolds numbers and dimensions of computational domains which were used in several earlier studies. In the present work, the streamwise length of our streamwise-minimal channel is set to be approximately minimal by reference to the domain sizes of the minimal flow units used by Jiménez & Pinelli (1999). Thus, it is obvious that the streamwise length L_x of our domain is much shorter than that used in the earlier studies which suggested the existence of large-scale structures in the turbulent channel flow. On the other hand, the spanwise extent of the domain is relatively wide; since it is more than 800 in wall units, about six to eight wall streaks could survive in the near-wall region in our domain. The spanwise extent L_z of the domain is $2.39h$ for the streamwise-minimal channel. Therefore, L_z exceeds just the critical value, $2h$, necessary for large-scale structure to exist in the outer region, as described by Jiménez (1998).

As seen in figure 1a, the empirical law of the wall and log-law velocity profile whose description has been obtained by many researchers (for example, see Schlichting 1979), appears to offer a good approximation. Figure 1b shows the turbulent intensity obtained for our channels. Note that the peak value of the turbulent intensity of streamwise velocity fluctuation is somewhat larger than that obtained from direct numerical simulations with not only minimal flow unit but also huge domains; for example Moser *et al.* (1999) found turbulent intensity to vary between 2.6 to 2.8 for $180 < Re_\tau < 590$. This difference also exists in comparison with the minimal flow as described by Jiménez & Pinelli (1999). Thus, the large peak value is probably due to our domain size;
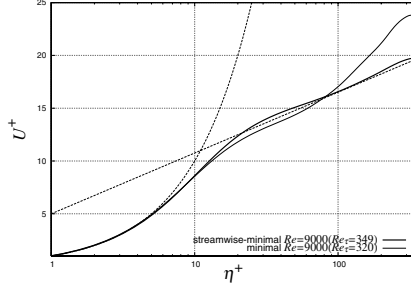
Figure 1a. Mean streamwise velocity of the present channels in wall units. Thick and thin curves correspond to those of streamwise-minimal ($Re_\tau = 349$) and standard-minimal flow ($Re_\tau = 320$). Dashed lines are $U^+ = 2.5 \log \eta^+ + 5$ and $U^+ = \eta^+$, where η is distance from the wall, $\eta = h - |y|$.
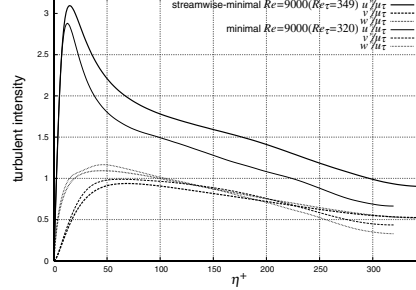
Figure 1b. Turbulent intensity profiles. Thick curves correspond to streamwise (solid), wall-normal (dashed), and spanwise (dotted) velocity profiles of streamwise-minimal channel at $Re = 9000$ ($Re_\tau = 349$). Thin curves correspond to those in the standard minimal flow at $Re = 9000$ ($Re_\tau = 320$).

the large spanwise extent of our domain allows large-scale structures to exist in the outer region, while the short streamwise length of our domain may encourage increased interaction between near-wall structures and large-scale structures. In fact, turbulent intensity in the centre region of our domain lies between those obtained for the minimal flow unit and huge domains, especially regarding the intensity of the spanwise velocity. This suggests that our channel contains not only near-wall structure but also large-scale structure, although it cannot completely reproduce turbulent flow in huge domains.

3. Large-scale structure

The pre-multiplied power spectra have been often used to suggest the existence of large-scale structures in channel flow, *e.g.*, Jiménez (1998) and Abe *et al.* (2001). Specifically, we define the pre-multiplied power spectra as

$$\phi_{ff}(k_z)|_\eta = k_z E_{ff}(k_z, y) \bigg/ \sum_{k_z = 2\pi/L_z}^{max(k_z)} E_{ff}(k_z, y), \tag{1}$$

$$E_{ff}(k_z, y) = \frac{1}{TL_x} \int_0^T \int_0^{L_x} (|f_{k_z}(x, y, t)|^2 + |f_{-k_z}(x, y, t)|^2) \mathrm{d}x\mathrm{d}t, \tag{2}$$

where $f_{k_z}(x, y, t)$ is the Fourier coefficient for a spanwise wavenumber k_z of velocity component $f(x, y, z, t)$, $f = u, v, w$ and distance from the wall $\eta = h - |y|$. We use pre-multiplied spectra $\phi(k_z) \equiv k_z E(k_z)$ so that areas under the curve in log-lin plots correspond to the actual energy content, *i.e.* $E(k_z)\mathrm{d}k_z = \phi(k_z)\mathrm{d}(\ln k_z)$. Figures 2a-c show pre-multiplied power spectra
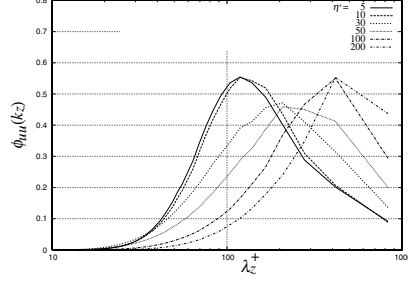
Figure 2a.
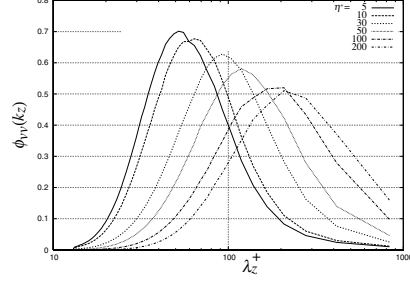
Figure 2b.
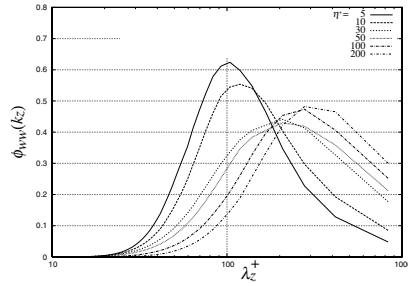
Figure 2c.

Figure 2. Pre-multiplied power spectrum, $\phi(k_z)$, as a function of $\lambda_z = 2\pi/k_z$. (a) ϕ_{uu}, (b) ϕ_{vv}, (c) ϕ_{ww} in the case of the streamwise-minimal channel at $Re = 9000$ ($Re_\tau = 349$). Increasing distance from the wall, $\eta = h - |y|$, corresponds to a rightward shift towards the long-wavelength end of the spectrum. All the spectra are normalized to unit area under the curve in the log-lin plots, to emphasize their frequency content.

obtained for the present streamwise-minimal channel. The characteristic length giving the spectrum peak is dependent on distance from the wall and is thought to correspond to the spanwise scale of a relatively dominant structure at each distance in the flow. In the case of the streamwise-minimal channel, ϕ_{uu} and ϕ_{ww} at $\eta^+ = 5$ peak approximately at $\lambda_z^+ = 100$, which corresponds to the accepted mean spacing of the wall streaks in the near-wall region. With increasing η in both cases, the peaks move to a longer wavelength corresponding to the outer length.

Compared with the spectra of u and w, the spanwise wavelength of the peak of ϕ_{vv} is a half of the other two in the near-wall region. This fact was originally considered by Kim *et al.* (1987). They investigated the spanwise two-point autocorrelations of velocity components and found that the minimum of the spanwise autocorrelation $R_{vv}(z)$ of wall-normal velocity v is at $\Delta z^+ \simeq 25$. They claimed that this spanwise characteristic separation of $R_{vv}(z)$ is consistent with the mean diameter of the streamwise vortical structures. Thus, it is not surprising that the spanwise length of the peak of ϕ_{vv} differs from that of the near-wall structure. Still, the difference between the peak of ϕ_{vv} and the other two has remained open. We argue that this is a direct consequence of no-slip and incompressibility in the following. Suppose that the flow near the wall is

independent of the streamwise direction and can be described as

$$v(\eta, z) \sim (v_1 e^{i\kappa z} + v_2 e^{i2\kappa z})\eta^2 \quad \text{and} \quad w(\eta, z) \sim (w_1 e^{i\kappa z} + w_2 e^{i2\kappa z})\eta, \quad (3)$$

where $\lambda_z = 2\pi/\kappa$ is taken as the most energetic spanwise wavelength in the near-wall region, $\lambda_z^+ = 100$ in wall units ($\lambda_z^+ = \lambda_z U_\tau/\nu$). From the definition of pre-multiplied spectrum, $\phi_{vv}(\kappa)/\phi_{vv}(2\kappa) \sim \kappa|v_1|^2/(2\kappa|v_2|^2) = |v_1/v_2|^2/2$ and $\phi_{ww}(\kappa)/\phi_{ww}(2\kappa) \sim |w_1/w_2|^2/2$. Exploiting the incompressibility, we obtain $2v_1 = \kappa w_1$ and $2v_2 = 2\kappa w_2$, thus in the near-wall region

$$\frac{\phi_{vv}(\kappa)}{\phi_{vv}(2\kappa)} \sim \frac{1}{4}\frac{\phi_{ww}(\kappa)}{\phi_{ww}(2\kappa)}. \quad (4)$$

Actually, $\phi_{ww}(k_z)$ peaks at $\lambda_z^+ = 100$ but $\phi_{vv}(k_z)$ instead peaks at 50, since $\phi_{ww}(\kappa)/\phi_{ww}(2\kappa) \approx 3$ is obtained from figure 2a and thus $\phi_{vv}(2\kappa) > \phi_{vv}(\kappa)$. (In fact, comparing results with the full numerical solution we were able to see that the two-mode approximations (3) appear to adequately capture the leading-order behaviour of the solutions.)

In this section, it is shown that the pre-multiplied power spectra of streamwise and spanwise velocities have two specified peaks corresponding to the mean intervals of near-wall structure in the near-wall region and large-scale structure in the outer region. These characteristics have been also reported in many studies using direct numerical simulation with more realistic huge channel, for example Jiménez (1998). The similarities between the streamwise-minimal channel and a huge channel suggest that the former contains a large-scale structure quite close to that in the latter. If this is so, we will then be interested in what makes a large-scale structure and, how the large-scale structure contributes to turbulence, in the streamwise-minimal channel.

4. Co-supporting cycle

The streamwise-minimal channel allows for only one near-wall and one large-scale structure with respect to the streamwise direction. This artificial restriction inhibits some of the rich spatio-temporal properties observed in huge domains, for example, the spatial growth of structures and the interaction between structures aligned in the streamwise direction (Adrian *et al.* 2000). Still, this simplified system appears to include fundamental dynamics of both the large-scale structure and near-wall structures.

The structures interact with each other while moving around in a streamwise cross-section and repeating their own dynamical processes. In order to understand the dynamics of the structures as a whole, we below represent the location of a near-wall structure or a large-scale structure simply as the low-speed zone at $\eta^+ = 5$ (near-wall region) or 200 (outer region) respectively. The low-speed zone is defined as z satisfying $u^{2D}(t, y, z) < U(t, y)$ at time t and the distance

0 200 400 ˜ 600
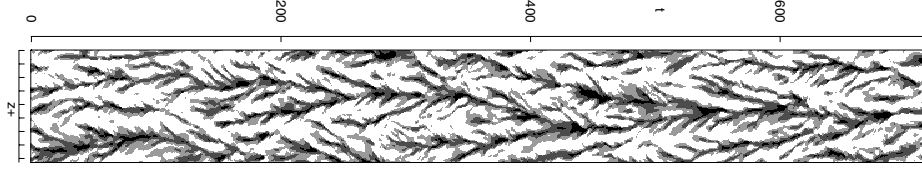
Figure 3a. Shaded regions represent the low-speed zone, $u^{2D}(t, y, z) < U(t, y)$ at $\eta^+ = 5$ (near-wall region) in the lower half domain ($-h < y < 0$) in the interval $0 < t < 720$. The vertical axis z^+ is scaled by 100 wall units.
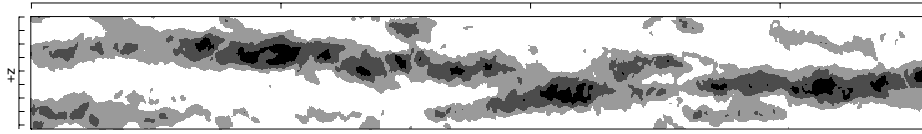
Figure 3b. Same as in (a) but at $\eta^+ = 200$ in the outer region.

from the lower wall $\eta = h - |y|$, where

$$u^{2D}(t, y, z) = \frac{1}{L_x} \int_0^{L_x} u(t, x, y, z)\mathrm{d}x \quad \text{and}$$

$$U(t, y) = \frac{1}{L_z} \int_0^{L_z} u^{2D}(t, y, z)\mathrm{d}z.$$

(5)

Time-development of low-speed zones in both regions are shown in figures 3a and b, which allow us to trace the spanwise movement and generation processes of near-wall and large-scale structures. In fact, the characteristic spanwise wavelength λ_z^+ at the peak of ϕ_{uu} mentioned in the previous section finds reasonable agreement with the mean spanwise interval between two adjacent minima; as may be seen from the figure, $\Delta z^+ \approx 100$ and 400 for $\eta^+ = 5$ and 200, respectively.

Moreover, from figure 3a we can see that the branches may be classified into two types: dominant branches, which survive for a relatively long time, and weak branches. As time elapses, weak branches are successively merged into a few dominant branches in almost all of the merging events in the near-wall region, while some weak branches emerge from structure-free areas. The branches in figure 3a are reminiscent of rivers in a map of a mountainy area and thus we call the regions where branches gather "valley" and the structure-free regions where branches emerge "watershed". It is also significant to note that large-scale structures in figure 3b appear to be located always above a valley, that is, a long-lived dominant branch in figure 3a, while a watershed in figure 3a separates two adjacent large-scale structures in figure 3b.

The dynamics of the large-scale structures and near-wall structures in the streamwise-minimal channel is described as follows (see figure 5): Immature
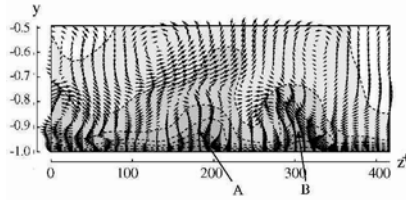
Figure 4a. Snapshots of flow in the $Re = 9000$ ($Re_\tau = 349$) case in a (z, y) cross-section at $t = 120$. Vector field indicates (w^{2D}, v^{2D}). Shaded region indicates $u^{2D} < 0.7U_c$ and contour levels are $0.6U_c, 0.5U_c, ..., 0.1U_c$.
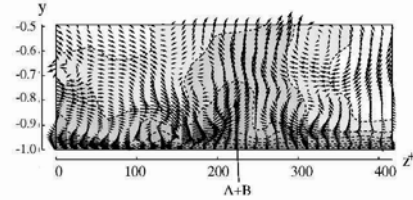
Figure 4b. Same as in (a) but $t = 140$. A concentrated eruption follows a merging event of near-wall structures A and B in the panel (a).
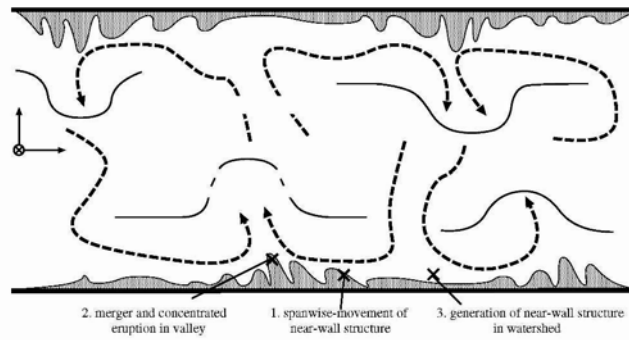
Figure 5. Schematic view of a snapshot in our channel in a (z, y) cross-section, where three elementary processes of the co-supporting cycle are described. Thin solid curves indicate contours of u^{2D} in the outer region, each bulge of which corresponds to the low-speed region of a large-scale structure. The circulation of a large-scale structure is represented by thick dashed curve. Shaded regions near the walls denote wall streaks.

near-wall structures are continually generated through a local instability near a watershed between two adjacent large-scale circulations and slowly move toward either of the two. Moreover, a dominant near-wall structure continually attracts and merges weaker structures into itself, beneath the low-speed region of a large-scale structure. We considered that the introduction of a tight coupling between a large-scale structure and near-wall structures makes it possible to explain these facts. The coupling consists of three elementary processes described below (see figure 5).

1 One of the two circulations of a large-scale structure induces the near-wall structures to move in the spanwise direction toward the area under the low-speed region of the large-scale structure.

2 Generally, when two near-wall structures merge, a concentrated eruption* occurs which causes an influx of fluid from the near-wall region into the outer region. Such a merging event is seen in figures 4a and 4b. In our simulations, a concentrated eruption appears to be slightly stronger than a burst* which occurs as part of the self-sustaining process of a near-wall structure. The concentrated eruption also brings about strong suction from both sides which acts to maintain the large-scale circulation, moreover, through drawing in fluid with lower streamwise speed from the near-wall region also acts to maintain the low-speed region of the large-scale structure.

3 There is a watershed, a separation region close to the wall formed by the part of one of the circulations of the large-scale structure, in which fluid is directed towards the channel wall. In these regions, new wall streaks are created continually through some instability.

* The term "eruption" is used for blowup occurring through merging process of near-wall structures and "burst" for blowup as a part of SSP of a single near-wall structure. The eruption often occurs and thus is robust. This fact may be confirmed in some animations at the web: http://www-kyoryu.scphys.kyoto-u.ac.jp/movies/ .

The coupling with the near-wall structures through the three processes above probably enables the large-scale structure to survive. However, in the cycle the large-scale structure is not just passive, but active enough to contribute to the generation, spanwise-movement and merger of near-wall structures, which re-activate the large-scale structure itself. Therefore, we denote the whole cycle as "co-supporting cycle" of a large-scale structure and near-wall structures, to distinguish this from the self-sustaining process of a single near-wall structure.

5. Concluding remarks

In this paper, we have shown that large-scale structures exist even in a streamwise-minimal box whose streamwise dimension is confined to the minimal length required for the sustenance of turbulence. In the present study, a large-scale structure involves two counter-rotating large-scale circulations and a streak-like low-speed region. The large-scale structures are likely to be coupled with near-wall structures and sustained by their direct interaction. We have therefore proposed a sustaining cycle of a large-scale structure in the streamwise-minimal flow and called this a co-supporting cycle.

The minimal channel has been originally defined as the computational domain restricted in both the streamwise and spanwise directions. It is expected that, in the minimal flow, large-scale structures are fallen apart so that the co-supporting cycle is disrupted. In order to examine the effect upon the near-

wall region of large-scale structures, we moreover perform the minimal flow turbulent channel. This minimal channel is set at the same bulk Reynolds number, $Re = 9000$, and with the same streamwise length but with the one-sixth spanwise extent of the streamwise-minimal channel investigated (see table 1). To briefly summarize the result, it is observed that the generation and merger processes of near-wall structures was suppressed in the minimal channel. It follows that the wall friction is reduced by about 15%. In addition, in the outer region, the turbulent intensity of u is obviously decreased by about 0.2 in the minimal channel (see figure 1b). In contrast, there is a little difference of the turbulent intensity of v between the minimal and streamwise-minimal channels in the outer region. This fact suggests that the inflow towards the outer region in bursts in the self-sustaining process is comparable to that of the eruption in co-supporting cycle, but that the resulting bulge of low-speed zone in the outer region dissipates in the former more quickly than in the latter because of the difference of spanwise extent of the inflows, *i.e.*, $\partial_t u \sim \nu \partial_z^2 u$.

Finally, it remains to make it convincing that the co-supporting cycle can be realized even in the huge computational box. Del Álamo & Jiménez (2001) and Del Álamo & Jiménez (2003) reported that the pre-multiplied power spectrum of the streamwise velocity, which characterizes the large-scale structure, decomposes into two components: quasi-isotropic modes of relatively short streamwise length scales and (maybe infinitely) long modes deeply penetrated into the near-wall region. They suggested that the latter modes interact with the near-wall region. In this work, we have seen that our large-scale structures are dominated by modes with $k_x = 0$, i.e., with infinitely long streamwise length. We conclude, therefore, that our large-scale structure corresponds to their long, deep modes and thus reflect some properties of the large-scale structure observed in real turbulence. Thus, since streamwise-minimal channel may accommodate large-scale structure, the collective motion of wall streaks and their interactions as well as the self-sustaining processes of individual near-wall structures, the present study will contribute significantly to the elucidation of real wall-bounded turbulence.

References

ABE, H., KAWAMURA, H. & MATSUO, Y. 2001 Direct numerical simulation of a fully developed turbulent channel flow with respect to Reynolds number dependence. *Trans. ASME J. Fluids Eng.* **123**, 382–393.

ADRIAN, R.J., MEINHART, C.D. & TOMKINS, C.D. 2000 Organization of vortical structure in the outer region of the turbulent boundary layer. *J. Fluid Mech.* **422**, 1–51.

DEL ÁLAMO, J.C. & JIMÉNEZ, J. 2001 Direct numerical simulation of the very large anisotropic scales in a turbulent channel. *Center for turbulence Research Annual Research Briefs* 329–341.

DEL ÁLAMO, J.C. & JIMÉNEZ, J. 2003 Spectra of the very large anisotropic scales in turbulent channels. *Phys. Fluids* **15**, L41–44.

HAMILTON, J.M., KIM, J. & WALEFFE, F. 1995 Regeneration mechanisms of near-wall turbulence structures. *J. Fluid Mech.* **287**, 317–348.

JIMÉNEZ, J. & MOIN, P. 1991 The minimal flow unit in near-wall turbulence. *J. Fluid Mech.* **225**, 213–240.

JIMÉNEZ, J. & PINELLI A. 1999 The autonomous cycle of near wall turbulence. *J. Fluid Mech.* **389**, 335–359.

JIMÉNEZ, J. 1998 The largest scales in the turbulent wall flows . *Center for Turbulence Research Annual Research Briefs* 137–154.

KOMMINAHO, J., LUNDBLADH, A. & JOHANSSON, A.V. 1996 Very large structures in plane turbulent Couette flow. *J. Fluid Mech.* **320**, 259–285.

KAWAHARA, G. & KIDA, S. 2001 Periodic motion embedded in plane Couette turbulence: regeneration cycle and burst . *J. Fluid Mech.* **449**, 291–300.

KIM, J., MOIN, P. & MOSER, R. 1987 Turbulence statistics in fully developed channel flow at low Reynolds number. *J. Fluid Mech.* **177**, 133–166.

LEE, M.J. & KIM, J. 1991 The structure of turbulence in a simulated plane Couette flow . *Proc. 8th Symposium on turbulent shear flows* paper 5-3.

MIYAKE, Y., KAJISHIMA, T. & OBANA,S. 1987 Direct numerical simulation of plane Couette flow at transitional Reynolds number. *JSME Int. J.* **30**, 57-65.

MOSER, R.D., KIM, J. & MANSOUR N.N. 1999 Direct numerical simulation of turbulent channel flow up to $Re_\tau = 590$. *Phys. Fluids* **11**, 943–945.

SHLICHTINGH. 1979 Boundary-Layer Theory 7th edition. *McGRAW-HILL.*

TOH, S. & ITANO, T. 2003 A periodic-like solution in channel flow. *J. Fluid Mech.* **481**, 67–76.

TOH, S. & ITANO, T. 2004 Interaction between a large-scale structure and near-wall structures in channel flow *J. Fluid Mech.* to appear.

WALEFFE, F. 1997 On a self-sustaining process in shear flows . *Phys. Fluids* **9**, 883–900.

WALEFFE, F. 1998 Three-dimensional coherent states in plane shear flows. *Phys. Rev. Lett.* **81**, 4140–4143.

PERIODIC MOTION IN HIGH-SYMMETRIC FLOW

Lennaert van Veen, Shigeo Kida
Department of Mechanical Engineering, Graduate School of Engineering, Kyoto University, Yoshida-Honmachi, Sakyo-ku, Kyoto 606-8501 Japan
veen@mech.kyoto-u.ac.jp, kida@mech.kyoto-u.ac.jp

Genta Kawahara
Department of Aeronautics and Astronautics, Graduate School of Engineering, Kyoto University, Yoshida-Honmachi, Sakyo-ku, Kyoto 606-8501 Japan
gkawahara@kuaero.kyoto-u.ac.jp

Abstract   We investigate unstable periodic motion embedded in isotropic turbulence with high symmetry. Several orbits of different period are continued from the regime of weak turbulence into developed turbulence. The orbits of short period diverge from the turbulent state as the Reynolds number increases but the orbit of longest period we analysed, about two to three eddy-turnover times, represents several average values of the turbulence well. In particular we measure the energy dissipation rate and the largest Lyapunov exponent as a function of the viscosity. At the largest micro-scale Reynolds number attained in the continuation we compare the energy spectra of periodic and turbulent motion. The results suggest that periodic motion of a sufficiently long period can represent turbulence in a statistical sense.

Keywords: Isotropic turbulence, unstable periodic motion, high-symmetric flow.

1.   Introduction

In the paradigm of dynamical systems theory, turbulence is a manifestation of high dimensional chaos. It is represented in phase space by fractal attractors which consist of countably infinitely many unstable periodic orbits. From this point of view, unstable periodic orbits are natural objects to consider when investigating turbulence. However, in turbulence research this paradigm is not widely adhered to. Turbulence research is rather concentrated on sophisticated statistical analysis and simulation of flows at high resolution. We feel, however, that the direct and constructive application of the tools of dynamical systems

theory will be a valuable contribution to the understanding of the nature of turbulence.

The main obstacle in applying the ideas of dynamical systems theory to developed turbulence is the large number of degrees of freedom. More specifically the main problem is the computation and manipulation of the matrix of derivatives of the vector field or the associated Poincaré map. The computation time and memory requirements have until recently restricted the continuation and bifurcation analysis of equilibria and periodic motion to regular or weakly turbulent flow. In the case of Taylor-Couette flow, for instance, bifurcation analysis was carried out and compared successfully to experiments at low Reynolds number (see Cliffe *et al.* (2000)).

Recently, plane Couette flow has been the subject of bifurcation analysis beyond the onset of developed turbulence. Moehlis *et al.* (2002) exploited the spatial symmetries and used empirical orthogonal basis functions computed at a Reynolds number of about 400, where turbulence is sustained. Their model is then reduced to only $O(10)$ degrees of freedom and standard software can be used for the analysis of equilibria and periodic orbits. A result of this analysis was the identification of attracting heteroclinic cycles connecting unstable streaky structures. A disadvantage of this approach is the coupling between elementary structures such as streaks and streamwise vortices in the basis functions that limits the description of their interaction. Kawahara & Kida (2001) used a more general approach, handling about $15,000$ degrees of freedom at the same Reynolds number. They found two kinds of unstable periodic motion. One represents turbulent and the other laminar flow. In a turbulent integration the state point of the flow wanders back and forth between these motions, highlighting the phenomenon of bursting.

Inspired by that success we study unstable periodic motion in isotropic turbulence. In order to reduce the number of degrees of freedom the *high symmetry*, introduced by Kida (1985), is imposed on the solutions. Under this symmetry condition a resolution of 128^3 gives us about $10,000$ degrees of freedom. We identify several unstable periodic orbits in the weakly turbulent regime, at a micro-scale Reynolds number of $R_\lambda = 50$ and continue them up to $R_\lambda = 67$, where turbulence is developed. The continuation algorithm requires the computation of the matrix of derivatives of the Poincaré map, which is done by finite differencing on a parallel computer. We compare the energy dissipation rate, the largest Lyapunov exponent and the energy spectrum of the periodic motion to those of the turbulent state. A recent result in shell model turbulence by Kato & Yamada (2003) suggests that an unstable periodic solution can represent the turbulent energy cascade process. Indeed, we find periodic motion, with a period of about two to three eddy-turnover times, which reproduces the turbulent averages well. The motion with shorter period, however, diverges from the turbulent state as the micro-scale Reynolds number increases.

Increasing computing power and advances in numerical algorithms are making way for the application of continuation and bifurcation analysis to turbulence. The current work on unstable periodic motion is only a first step. To go to a higher resolution or relax the symmetry condition might require the application of new ideas from numerical linear algebra. Methods which circumvent the computation of the matrix of derivatives have recently been applied successfully to Navier-Stokes flow for finding equilibria and periodic motion (see Nore *et al.* (2003); Sánchez *et al.* (2004)). If such analysis can be applied to general high Reynolds number flow much insight can be gained into the nature of turbulence.

2.   High-symmetric flow

We consider the motion of an incompressible viscous fluid in a periodic box given by $0 < x_1, x_2, x_3 \leq 2\pi$. In terms of the Fourier representation of velocity and vorticity,

$$\boldsymbol{v} = \mathrm{i} \sum_{\boldsymbol{k}} \widetilde{\boldsymbol{v}}(\boldsymbol{k}) \mathrm{e}^{\mathrm{i}\boldsymbol{k}\cdot\boldsymbol{x}}, \qquad \boldsymbol{\omega} = \sum_{\boldsymbol{k}} \widetilde{\boldsymbol{\omega}}(\boldsymbol{k}) \mathrm{e}^{\mathrm{i}\boldsymbol{k}\cdot\boldsymbol{x}}, \tag{1}$$

the Navier-Stokes equation and the continuity equation are written as

$$\frac{\mathrm{d}}{\mathrm{d}t}\widetilde{\omega}_i(\boldsymbol{k}) = \epsilon_{ijk}k_j k_l \widetilde{v_k v_l} - \nu k^2 \widetilde{\omega}_i(\boldsymbol{k}), \tag{2}$$

$$k_i \widetilde{u}_i = 0, \tag{3}$$

where ν is the kinematic viscosity, ϵ_{ijk} is the permutation symbol and the tilde denotes the Fourier transform. By definition we have

$$\widetilde{\omega}_i(\boldsymbol{k}) = -\epsilon_{ijk}k_j \widetilde{v}_k(\boldsymbol{k}). \tag{4}$$

In terms of the standard norm, energy and enstrophy are given by

$$E = \frac{1}{2}\|\boldsymbol{v}\|^2, \qquad Q = \frac{1}{2}\|\boldsymbol{\omega}\|^2, \tag{5}$$

respectively. We will also monitor the energy dissipation rate, the Taylor microscale Reynolds number and the largest Lyapunov exponent, defined respectively by

$$\epsilon = 2\nu Q, \qquad R_\lambda = \sqrt{\frac{10}{3}} \frac{1}{\nu} \frac{E}{\sqrt{Q}}, \qquad \Lambda = \lim_{t\to\infty} \frac{1}{t} \int_0^t \lambda(t')\mathrm{d}t', \tag{6}$$

where $\lambda(t)$ is the largest local Lyapunov exponent as computed from the linearised Navier-Stokes equation. Energy is supplied by fixing the smallest wavenumber components of velocity to a constant value. The smallest wavenumber corresponding to a nonzero velocity component is $k_f = |\boldsymbol{k}_f| = \sqrt{11}$ and the energy of these fixed components is $E_f = 3/8$.
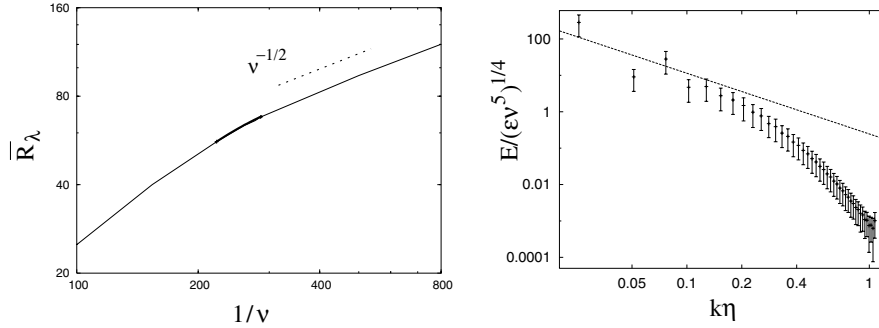
Figure 1. Left: time averaged micro-scale Reynolds number as a function of viscosity. Continuation of periodic orbits is done at the onset of the $1/\sqrt{\nu}$ scaling, as indicated by the bold line. Right: one-dimensional longitudinal energy spectrum at $\bar{R}_\lambda = 67$. The error bars denote standard deviation and the straight line the Kolmogorov scaling.

In our simulations we use a cubic truncation given by $|k_x|, |k_y|, |k_z| < N/2$ with $N = 128$ and set the maximal wavenumber to $k_{max} = [N/3]$ to eliminate aliasing interactions. Under the high-symmetry condition we have about $n = 10,000$ degrees of freedom. For time stepping we use the fourth-order Runge-Kutta-Gill scheme with step size $\Delta t = 0.005$. In the following, time averaged quantities are denoted by an over bar. In the energy spectra, the wavenumber is normalised by the Kolmogorov dissipation scale $\eta = \sqrt[4]{\nu^2/(2Q)}$.

Kida *et al.* (1989) studied the transition to turbulence in high-symmetric flow and found that at $\nu \approx 0.005$ ($\bar{R}_\lambda \approx 50$) the Ruelle-Takens route to chaos is followed. The chaotic motion corresponds to weak turbulence in the sense that the spatial structure of the flow remains simple. Around $\nu = 0.004$ ($\bar{R}_\lambda = 60$) developed turbulence sets in, which is reflected by the scaling of $\bar{R}_\lambda$ as $1/\sqrt{\nu}$, as shown in figure 1 (left). The energy dissipation rate $\bar{\epsilon}$ becomes approximately constant as a function of ν. The longest intrinsic time scale of isotropic turbulence is the large eddy-turnover time. It can be estimated from the frequency power spectra of enstrophy and energy and takes the value $T_T = 4.4$.

Below we describe the continuation of periodic orbits at the onset of developed turbulence. In figure 1 (right) the energy spectrum is shown at the maximal micro-scale Reynolds number that can be attained with our resolution, $\bar{R}_\lambda = 67$. In order to see a developed inertial range we would need to increase the resolution. For the time being, this is not feasible for reasons that will become apparent in the next section.

3. Continuation of unstable periodic orbits

We look for time periodic solutions of Eqs. (2)–(4), i.e. vorticity fields that satisfy $\widetilde{\boldsymbol{\omega}}(\boldsymbol{k}, t) = \widetilde{\boldsymbol{\omega}}(\boldsymbol{k}, t + T)$ for all wave vectors $\boldsymbol{k}$, all time t and some period T. Consider the n-dimensional phase space of Eqs. (2)–(4). A point in this space corresponds to a vorticity field $\boldsymbol{\omega}$. We specify a hyperplane S in this space by fixing one of the large wave vector components of vorticity to a constant. Periodic orbits are then fixed points of the iterated Poincaré map $\mathcal{P}_\nu$ on S:

$$\mathcal{P}_\nu^{(p)}(\boldsymbol{X}) - \boldsymbol{X} = \boldsymbol{0}, \tag{7}$$

where $\boldsymbol{X} \in \mathbb{R}^{n-1}$. Equation (7) is highly nonlinear and can be solved by Newton-Raphson iteration. However, for large n the initial guess should be rather close to the fixed point to guarantee convergence. In order to find initial points we perform very long time integrations with $\nu = 0.0045$, in the weakly turbulent regime. We compute the intersection points with the plane S and if a point is mapped close to itself after p iterations of the Poincaré map, i.e.

$$\|\mathcal{P}_\nu^{(p)}(\boldsymbol{X}) - \boldsymbol{X}\|_Q < \delta, \tag{8}$$

it is marked as an initial point. Here, $\|.\|_Q$ denotes the enstrophy norm, i.e. the enstrophy of the vorticity field corresponding to a given point in phase space. A suitable threshold for the distance is given by $\delta = 0.2$, about 10 % of the standard deviation of enstrophy in time. Thus we find a collection of periodic orbits with p ranging from 1 to 5.

For continuation of the periodic orbits down to $\nu = 0.0035$ we use the pseudo-arclength method, which requires solving an equation similar to Eq. (7) at each step. The most time consuming part of this algorithm is the computation of the derivatives of the Poincaré map $D_{\boldsymbol{X}, \nu} \mathcal{P}_\nu$. We use finite differencing for the derivatives, which means that for each Newton-Raphson iteration we have to run $(n + 1)$ integrations, which can be conveniently done in parallel. We use 128 processors simultaneously on a Fujitsu GP7000F900 parallel computer. The computation of one iteration of the Poincaré map and its derivatives takes about 25 minutes of CPU time on each processor. The average step size in the parameter is $\Delta\nu \approx 4 \cdot 10^{-5}$ and about three Newton-Raphson iterations are taken at each step before the residue is smaller than 10^{-9} in the enstrophy norm. This brings the total computation time for continuation of a period one orbit ($p = 1$) down to $\nu = 0.0035$ to about 31 hours.

We computed the distribution of the return time of the Poincaré map in a long time integration. It takes the average value $T_{\mathrm{R}} = 2.2$ and is sharply peaked. Consequently, the periodic orbits identified as fixed points of $\mathcal{P}_\nu^{(p)}$ have a period $T \approx pT_{\mathrm{R}}$. This holds true in the whole range $0.0035 < \nu < 0.0045$. In the following we refer to them as period-p orbits.

The results of the continuations are shown in figure 2. At each point of the continuation curve we compute the energy dissipation rate and the largest

Lyapunov exponent of the periodic motion for comparison to the turbulent state. The largest Lyapunov exponent for the periodic motion is computed directly from the eigenvalues of $D_X \mathcal{P}_\nu$. Computation of the curves of the period-3 and period-4 motion is still in progress, but it seems that only the period-5 motion reproduces the turbulent averages well. The motion of shorter period displays a monotonically decreasing energy dissipation rate. The largest Lyapunov exponent gives a less clear-cut picture, but again the value found for the period-5 motion is close to that of turbulence, especially at higher $\overline{R}_\lambda$. At $\nu \approx 0.00367$ the first and the second Lyapunov exponents cross, which shows up as a cusp in the curve. In the next section we will further investigate the period-5 motion and its relation to turbulence at $\overline{R}_\lambda = 67$.

4. Periodic motion representing turbulence

Figure 3 shows the probability density function (PDF) of the turbulent state, projected on energy input rate e and energy dissipation rate ϵ, along with a projection of the period-5 motion. The PDF is skewed due to bursting events in which relatively large amounts of kinetic energy are absorbed and dissipated. The periodic motion makes a large excursion to high energy dissipation rate corresponding to such a burst. Dots are drawn on the periodic motion at equal time intervals so that we can see that most time is spent near the time averaged energy dissipation rate and in one slow excursion to relatively low values.

Next we compare the energy spectrum averaged along the periodic motion to that of turbulent motion, as shown in figure 4 (left). The two are in good agreement all the way down to the Kolmogorov dissipation scale. As explained below, the error bars denote the expected difference if we compare the turbulent
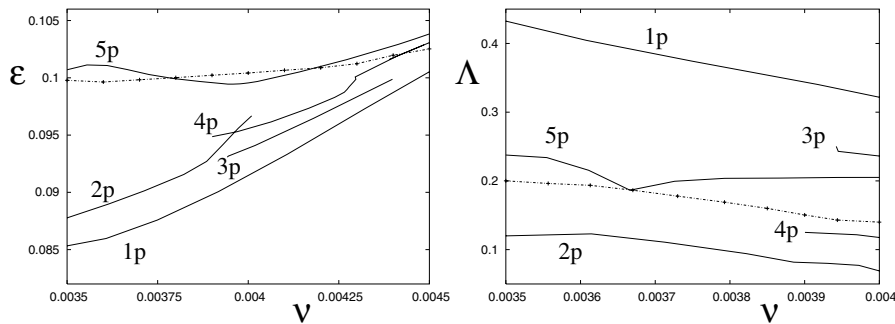
Figure 2. Left: the average energy dissipation rate in the periodic motion (solid lines) compared to turbulent motion (dashed line). Right: the largest Lyapunov exponent of the periodic motion (solid lines) compared to turbulent motion (dashed line).

spectrum to randomly chosen, non periodic time segments of the same length. Figure 4 (right) shows a comparison of our results to laboratory measurements of shear flow at $\overline{R}_\lambda = 130$ done by Champagne *et al.* (1970). There is good agreement beyond the energy containing range, which demonstrates that our results are not an artifact of the imposed spatial symmetries.
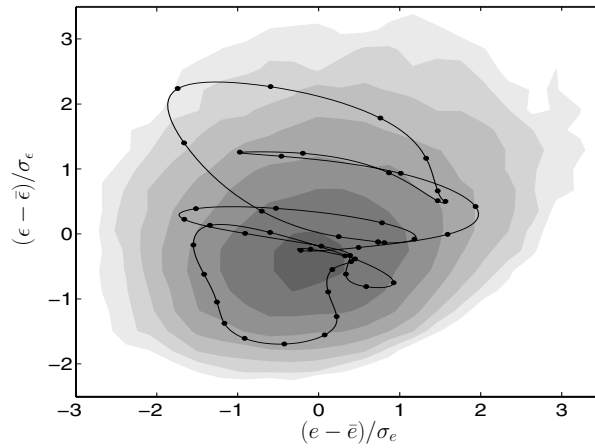
Figure 3. Contours of the PDF of turbulence projected on energy input rate and energy dissipation rate. Contours are drawn at 80% of the peak value and successive factors of 0.5, with on the axes departure from time average normalised by standard deviation. The period-5 motion is shown by the solid line with dots at equal time intervals.
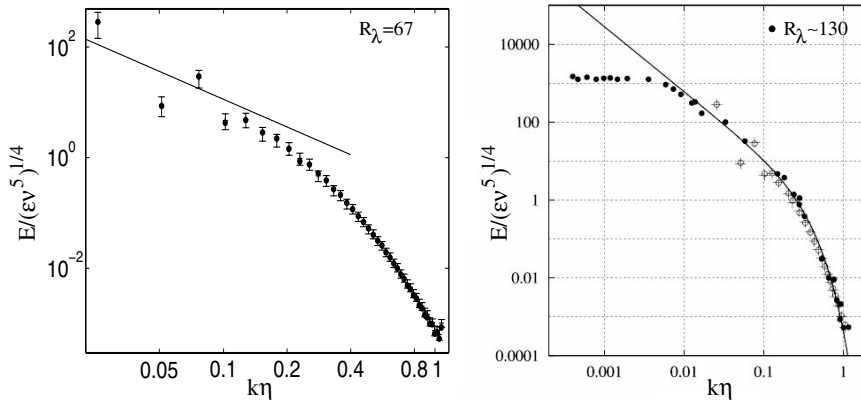
Figure 4. One-dimensional longitudinal energy spectrum. Left: period-5 motion (dots) and turbulence (bars). For an explanation of the error bars see text. Right: turbulence (circles), period-5 motion (pluses) and laboratory measurements (dots).

In order to quantify the difference between the periodic motion and the turbulence we compare it to the standard deviation of an ensemble of randomly selected, non periodic time segments. If quantity a is measured as a function of time, the running mean over interval τ is defined by

$$a_\tau(t) = \frac{1}{\tau} \int_t^{t+\tau} a(t') \mathrm{d}t'. \tag{9}$$

Obviously, a has expectation value $\overline{a}$. If a behaves like a random variable, its standard deviation is given by $\sigma_{a_\tau} = \sigma_a \sqrt{T_a/\tau}$, where σ_a is the standard deviation and T_a the typical time scale of variation of a. For the quantities under consideration here, namely the energy dissipation rate ϵ, the largest local Lyapunov exponent λ and the energy spectrum $E_\parallel$, this assumption is readily verified numerically. Let $\overline{a}_{per}$ be the average of a in the periodic motion. Then the normalised difference,

$$d_a(\tau) = \frac{|\overline{a}_{per} - \overline{a}|}{\sigma_{a_\tau}}, \tag{10}$$

indicates how well the periodic motion reproduces the turbulent average of a.

The typical time scales of variation of ϵ and λ are $T_\epsilon \approx T_\mathrm{T}/2$ and $T_\lambda \approx T_\mathrm{T}/4$, respectively, and their standard deviations are given by $\sigma_\epsilon \approx 0.016$ and $\sigma_\lambda \approx 0.4$. For the period-5 motion we set $\tau = 5T_\mathrm{R}$ and find that $d_\epsilon(5T_\mathrm{R}) < 0.25$ and $d_\lambda(5T_\mathrm{R}) < 0.4$ for viscosity in the range $0.0035 \leq \nu \leq 0.004$, which shows that the period-5 motion does indeed reproduce the turbulent averages remarkably well. When considering the energy spectrum we have to take it into account that the typical time scale of variation of $E_\parallel(k)$ depends on the spatial scale $l = 2\pi/k$. On dimensional grounds we assume that the typical time scale is given by $(l^2/\overline{\epsilon})^{1/3}$. If we denote by $\Sigma(k)$ the standard deviation of $E_\parallel(k)$, as plotted in figure 1 (right), and by $\Sigma_\tau(k)$ the standard deviation in an ensemble of averages over time segments of length τ, we have

$$\Sigma_\tau(k) = \Sigma(k) \left(\frac{4\pi^2}{k^2 \overline{\epsilon} \tau^3} \right)^{\frac{1}{6}}. \tag{11}$$

In figure 4 (left), $\Sigma_\tau(k)$ is drawn with error bars for $\tau = 5T_\mathrm{R}$. The spectrum measured in the periodic motion falls within these error bars for all wavenumbers.

Finally, we examine the time dependence of the energy spectrum. Figure 5 shows the departure from time mean of the band averaged energy spectrum as a function of time (a) along the periodic orbit and (b) in turbulent motion. The time axis has been normalised by T_R. The horizontal scale is logarithmic to illuminate the cascade process, thought to be a series of decompositions of coherent structures into parts about half their size. This process is visible as
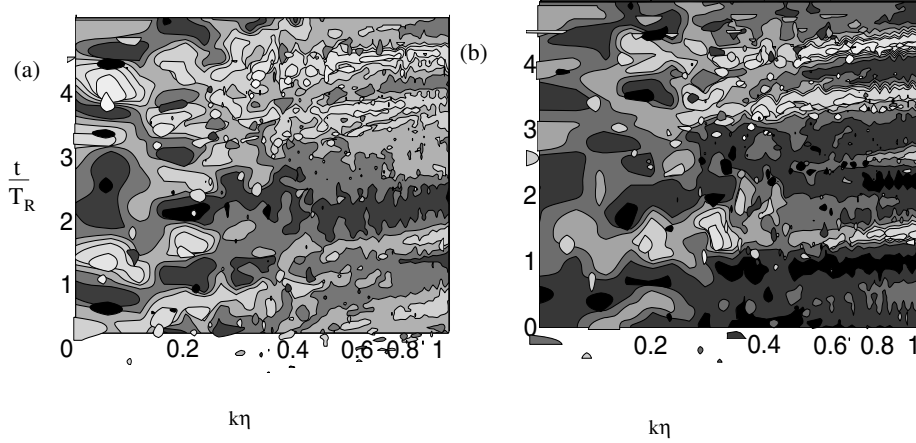
Figure 5. Three-dimensional energy spectrum as a function of time. The departure from time mean, normalised by standard deviation, is drawn with contours at regular intervals from $+1.5$ (lightest) to -0.62 (darkest). The scales are normalised by T_R and η. The horizontal scale is logarithmic to illuminate the energy cascade process. (a) Embedded periodic orbit. (b) Fragment from a turbulent time series.

streaks with constant inclination. The time interval between these streaks is about one eddy-turnover time $T_T/2$ and agrees well between the periodic and turbulent motion. Also, we see a quiescent phase during the first half of the period, and a bursting phase during the second half of the period, both in the periodic and in the turbulent motion. The turbulent time segment was selected from a long time series by looking at the energy input rate and energy dissipation rate and comparing them to the periodic behaviour, as in the projection shown in figure 3. In a turbulent integration time segments as close to the periodic motion as the one shown in figure 5(b) typically occur every ten eddy-turnover times or so.

5. Conclusion

We have analysed several unstable periodic orbits in isotropic turbulence with high symmetry. These orbits, with periods up to three large eddy-turnover times, were distilled from long time integrations in the weakly turbulent regime and continued into developed turbulence. We computed the energy dissipation rate and the largest Lyapunov exponent in the periodic motion as a function of viscosity, and compared them to the values found in the turbulent state. It turns out that the orbits with a period up to two large eddy-turnover times diverge from the turbulent state as the micro-scale Reynolds number increases. However, the orbit with a period of about $2.5 T_T$ reproduces the turbulent averages well.

We have investigated the period-5 motion in some detail at the maximal micro-scale Reynolds number, $R_\lambda = 67$. The one-dimensional longitudinal energy spectrum, measured in the periodic motion, almost coincides with the spectrum found in turbulent motion. It also compares well to laboratory measurements, which goes to show that the similarity between the periodic and the turbulent motion is not an artifact of the imposed symmetries. Looking at the time dependent energy spectrum, we see that turbulent time intervals very similar to the periodic motion frequently recur in a turbulent time series.

A measure for the difference between the periodic and turbulent motion is given by the standard deviation of an ensemble of averages over the same period. We have shown that for the energy dissipation rate, the largest Lyapunov exponent and the energy spectrum the averages produced by the periodic motion are significantly closer to the turbulent averages than expected for randomly selected, non periodic time intervals.

The current work raises several questions. For instance, what is the minimal period of periodic motion that represents turbulence? The longest intrinsic time scale in isotropic turbulence is the large eddy-turnover time. Arguing that the period of the periodic motion should be significantly longer than the longest intrinsic time scale, this might explain the minimal period of two to three eddy-turnover times that we observe. However, due to the complexity of the system under consideration we could only analyse five orbits in full and only at the onset of developed turbulence, thus our understanding is incomplete. A more detailed account of the current results can be found in van Veen *et al.* (2006).

In future work we aim to investigate the spatial structure of the periodic motion in detail. We can learn about the structure of isotropic turbulence by analysing periodic motion, which is inherently simpler than analysing turbulence itself. Also, by application of new algorithms, such as the matrix free methods recently used by Nore *et al.* (2003) and Sánchez *et al.* (2004), we hope to increase the resolution and study periodic motion in turbulence with a developed inertial range.

This paper is dedicated to the late Professor Isao Imai.

References

CHAMPAGNE, F.H., HARRIS, V.G. & CORRSIN, S. 1970 Experiments on nearly homogeneous turbulent shear flow. *J. Fluid. Mech.* **41**, 81–139.

CLIFFE, K.A., SPENCE, A. & TAVENER, S.J. 2000 The numerical analysis of bifurcation problems with applications to fluid dynamics. *Acta Numer.* **9**, 39–131.

KATO, S. & YAMADA, M. 2003 Unstable periodic solutions embedded in a shell model turbulence. *Phys. Rev. E* **68**, 025302.

KAWAHARA, G. & KIDA, S. 2001 Periodic motion embedded in plane Couette turbulence: regeneration cycle and burst. *J. Fluid Mech.* **449**, 291–300.

KIDA, S. 1985 Three-dimensional periodic flow with high-symmetry. *J. Phys. Soc. Jap.* **54**, 2132–2136.

KIDA, S., YAMADA, M. & OHKITANI, K. 1989 A route to chaos and turbulence. *Phys. D* **37**, 116–125.

MOEHLIS, J., SMITH, T.R., HOLMES, P. & FAISST, H. 2002 Models for turbulent plane Couette flow using the proper orthogonal decomposition. *Phys. Fluids* **14**, 2493–2507.

NORE, C., TUCKERMAN, L.S., DAUBE, O. & XIN, S. 2003 Survey of instability thresholds of flow between exactly counter-rotating disks. *J. Fluid Mech.* **477**, 51–88.

SÁNCHEZ, J., NET, M., GARCÍA-ARCHILLA, B. & SIMÓ, C. 2004 Newton-Krylov continuation of periodic orbits for Navier-Stokes flow. *J. Comput. Phys.* **201**, 13–33.

VAN VEEN, L., KIDA, S. & KAWAHARA 2006 Periodic motion representing isotropic turbulence. *Fluid Dyn. Res.* **38**, 19–46.

VORTEX TUBES IN VELOCITY FIELDS OF LABORATORY TURBULENCE AT HIGH REYNOLDS NUMBERS

Hideaki Mouri
Meteorological Research Institute, Nagamine, Tsukuba 305-0052, Japan
hmouri@mri-jma.go.jp

Akihiro Hori, Yoshihide Kawashima
Meteorological and Environmental Service, Inc., Tama, Tokyo 206-0012, Japan

Abstract   The most elementary structures of turbulence, i.e., vortex tubes, are studied using laboratory velocity data for boundary layers with Reynolds numbers $Re_\lambda = 295$–1258. We conduct conditional averaging for enhancements of a small-scale velocity increment and obtain the typical velocity profile for vortex tubes. Their radii are of the order of the Kolmogorov length. Their circulation velocities are of the order of the root-mean-square velocity fluctuation. These properties are independent of the Reynolds number and are hence expected to be universal.

Keywords: Vortex tubes, small-scale intermittency, laboratory experiment

1.   Introduction

Turbulence contains vortex tubes as the most elementary spatial structures. Regions of strong vorticity are organized into tubes. They occupy a small fraction of the volume and are embedded in the random background flow.

The basic parameters of vortex tubes at microscale Reynolds numbers $Re_\lambda \leq 200$ have been derived with direct numerical simulations (e.g., Jiménez *et al.* 1993; Makihara *et al.* 2002). The radii are of the order of the Kolmogorov length η. The total lengths are of the order of the integral length. The circulation velocities are of the order of the Kolmogorov velocity u_K or the root-mean-square velocity fluctuation $\langle u^2 \rangle^{1/2}$.

However, the universality of these tube parameters has not been established since it is difficult to conduct a direct numerical simulation at $Re_\lambda > 200$. We accordingly study velocity fields of laboratory turbulence at $Re_\lambda = 295$–1258 and estimate some parameters of vortex tubes from their circulation flows (for

details, see Mouri *et al.* 2004). The velocity field is intermittent at small scales. A small-scale velocity variation is enhanced at the positions of circulation flows associated with vortex tubes.

2.   Experiment

The experiment was done in a wind tunnel of the Meteorological Research Institute. We use the coordinates x, y, and z in the streamwise, spanwise, and floor-normal directions. The origin $x = y = z = 0$ m is taken on the tunnel floor at the entrance to the test section. Its size was $\delta x = 18$ m, $\delta y = 3$ m, and $\delta z = 2$ m. Over the entire floor of the test section, we placed blocks as roughness elements. Their size was $\delta x = 0.06$ m, $\delta y = 0.21$ m, and $\delta z = 0.11$ m. The spacing of adjacent blocks was $\delta x = \delta y = 0.5$ m. We set the incoming-wind velocity at $x = 0$ m to be $U_i = 2$–20 m s^{-1}.

Using a hot-wire anemometer, we measured the streamwise (u) and spanwise (v) velocities. The measurement positions were at $x = 12.5$ m, where the boundary layer was well developed. The 99% thickness was about 0.8 m. The displacement thickness was about 0.2 m. They were almost independent of the incoming-wind velocity. The measurement height was $z \simeq 0.3$ m in the log-law sublayer.

The signal was linearized, low-pass filtered at 2–20 kHz, and then sampled digitally at 4–40 kHz. The data length was $(2$–$8) \times 10^7$ points. We obtained $Re_\lambda = 295$, 430, 655, 861, 1054, and 1258 for $U_i = 2$, 4, 8, 12, 16, and 20 m s^{-1}. The energy spectra are shown in figure 1a.

3.   Velocity profile of vortex tubes

The typical profiles for circulation flows of vortex tubes in the streamwise (u) and spanwise (v) velocities are extracted as the typical profiles for small-scale intermittency. We average signals centered at the position where the absolute value of the spanwise-velocity increment $|v(x+\delta x) - v(x)|$ is enhanced above a certain threshold (e.g., Mouri *et al.* 2003). The scale δx is set to be the sampling interval. The threshold is set to be the highest percentile for the absolute values of the velocity increments. Thus 1% of them are used for the averaging. When the velocity increment is negative, we invert the sign of the v signal before the averaging. The results are shown in figure 2a (solid lines).

The threshold value for the enhancement of the velocity increment has been determined with a compromise. If the threshold is higher, the statistics are less significant. If the threshold is lower, the contamination with the background flow is more significant. We have nevertheless ascertained that our following results are qualitatively independent of the threshold if the fraction of the velocity increments used for the averaging is 0.1–1%. These velocity increments comprise the tail of the probability density distribution that is well above the
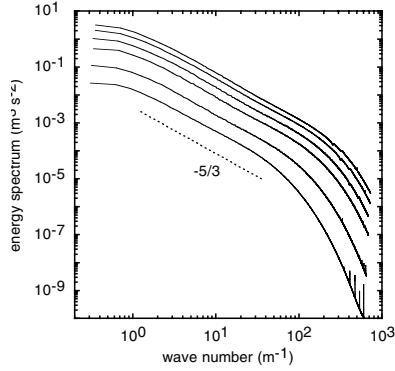
Figure 1a. Energy spectrum of the spanwise velocity at $Re_\lambda = 295, 430, 655, 861, 1054$, and 1258 (from bottom to top). The wave number is in units of m^{-1} instead of the usual radian m^{-1}. The other flow parameters are as follows. The Kolmogorov length η is $0.0554, 0.0331, 0.0197, 0.0154, 0.0123$, and 0.0106 cm. The Kolmogorov velocity u_K is $0.0260, 0.0438, 0.0737, 0.0955, 0.122$, and 0.141 m s^{-1}. The root-mean-square fluctuation of the spanwise velocity $\langle v^2 \rangle$ is $0.227, 0.462, 0.958, 1.42, 2.01$, and 2.53 m s^{-1}.
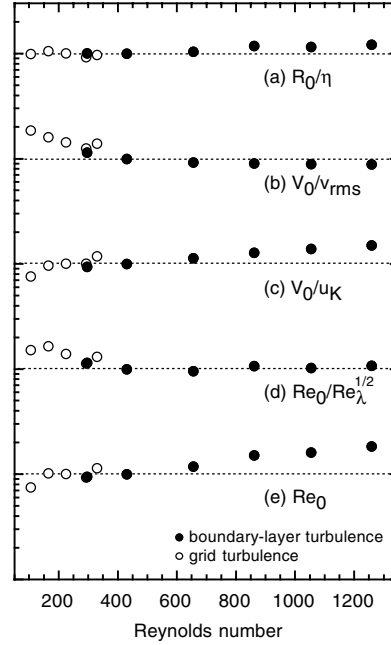
Figure 1b. Dependence of tube parameters on Re_λ. (a) R_0/η. (b) $V_0/\langle v^2 \rangle^{1/2}$. (c) V_0/u_K. (d) $Re_0/Re_\lambda^{1/2}$. (e) Re_0. These quantities are normalized by their values at $Re_\lambda = 430$, i.e., $R_0/\eta = 6.04$, $V_0/\langle v^2 \rangle^{1/2} = 0.526$, $V_0/u_K = 5.55$, $Re_0/Re_\lambda^{1/2} = 1.62$, and $Re_0 = 33.5$.

Gaussian distribution with the same standard deviation as shown in figure 2b. The only deficit is that the threshold is too high for some weak vortex tubes. They are not considered here.

For reference, in figure 2a (dotted lines), we show the circulation flow of a Burgers vortex as a model for vortex tubes:

$$u_\Theta(R) \propto \frac{\nu}{aR} \left[1 - \exp\left(-\frac{aR^2}{4\nu} \right) \right] \qquad (a > 0). \qquad (1)$$

Here ν is the kinematic viscosity. The circulation is maximal at the tube radius $R = R_0 = 2.24(\nu/a)^{1/2}$. We have determined the radius R_0 and the maximum circulation velocity V_0 so as to fit the observed v profile around its peaks.

Since the observed v profile is close to the profile of a Burgers vortex, we confirm the existence of vortex tubes at high Reynolds numbers. Their circulation

flows are responsible for small-scale intermittency. The radius R_0 is several times the Kolmogorov length η, while the maximum circulation velocity V_0 is about a half of the root-mean-square velocity fluctuation $\langle v^2 \rangle$ or several times the Kolmogorov velocity u_K (e.g., Jiménez *et al.* 1993; Makihara *et al.* 2002).

The u profiles in figure 2a are separated for $u(x + \delta x) - u(x) > 0$ and $u(x + \delta x) - u(x) \leq 0$ at $x = 0$ (designated as u^+ and u^-). They are dominated by the circulation flow u_Θ of vortex tubes passing the probe at some distances or with some incident angles.
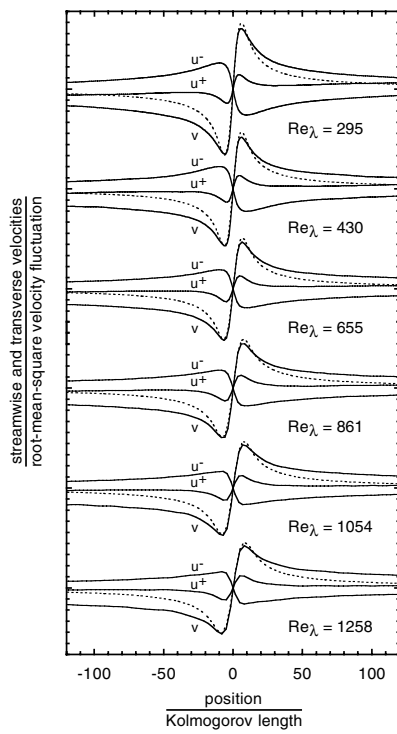
Figure 2a. Typical profiles for vortex tubes in the streamwise (u) and spanwise (v) velocities. The unit scale on the ordinate corresponds to one-tenth of the root-mean-square velocity fluctuation $\langle v^2 \rangle^{1/2}$. The dotted lines denote the profiles of Burgers vortices.
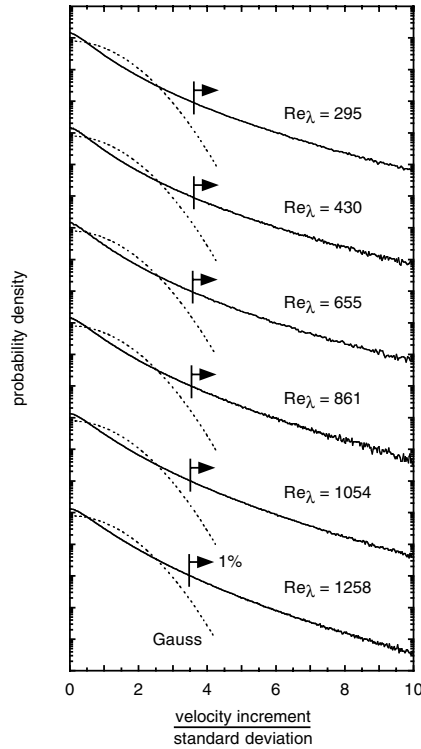
Figure 2b. Probability density distribution of the absolute velocity increment $|v(x + \delta x - v(x)|$. The arrows indicate the range of the enhanced velocity increments used in our analyses. The dotted lines denote a Gaussian distribution.

4. Dependence on the Reynolds number

The dependences of the tube parameters on the microscale Reynolds number Re_λ are studied here. To extend the Re_λ range, we also use velocity data from our previous experiment of grid turbulence at $Re_\lambda = 105$–329 (Mouri *et al.* 2003). These data are reanalyzed in the same manner as for our present data. The results are summarized in figure 1b, where quantities are normalized by their values at $Re_\lambda = 430$.

The tube radius R_0 scales with the Kolmogorov length η as $R_0 \propto \eta$ over the entire range of the Reynolds number [figure 1b(a)].

The maximum circulation velocity V_0 scales with the root-mean-square velocity fluctuation $\langle v^2 \rangle^{1/2}$ as $V_0 \propto \langle v^2 \rangle^{1/2}$ at $Re_\lambda > 400$ [figure 1b(b)]. Since this is not the case at $Re_\lambda \leq 400$, the scaling is achieved at high Reynolds numbers. The maximum circulation velocity V_0 also scales with the Kolmogorov velocity u_K as $V_0 \propto u_K$ [figure 1b(c)]. However, at $Re_\lambda > 400$, this scaling is less significant than the scaling with the velocity fluctuation $\langle v^2 \rangle^{1/2}$.

The scaling laws for the radius R_0 and the maximum circulation velocity V_0 lead to the scaling law for the Reynolds number $Re_0 = R_0 V_0 / \nu$ that characterizes the circulation flows of vortex tubes:

$$
\begin{aligned}
Re_0 &\propto Re_\lambda^{1/2} && \text{if} \quad R_0 \propto \eta \quad \text{and} \quad V_0 \propto \langle v^2 \rangle^{1/2}, \quad \text{or} \\
Re_0 &= \text{constant} && \text{if} \quad R_0 \propto \eta \quad \text{and} \quad V_0 \propto u_K.
\end{aligned}
\tag{2}
$$

The present result favors the former scaling [figure 1b(d)] rather than the latter [figure 1b(e)] at least for $Re_\lambda > 400$.

For general vortex tubes, we do not necessarily expect the scaling laws $V_0 \propto \langle v^2 \rangle^{1/2}$ and $Re_0 \propto Re_\lambda^{1/2}$. Weak vortex tubes are not considered here because our velocity profiles were obtained for enhancements of a velocity increment. Actually in direct numerical simulations, the scaling law $V_0 \propto u_K$ was obtained when vortex tubes were identified as local minima of the pressure (e.g., Makihara *et al.* 2002). The scaling law $V_0 \propto \langle v^2 \rangle^{1/2}$ was obtained when vortex tubes were identified as enhancements of the vorticity above a threshold (e.g., Jiménez *et al.* 1993).

5. Conclusion and future prospects

For the first time at high Reynolds numbers, we have obtained the scaling laws $R_0 \propto \eta$, $V_0 \propto \langle v^2 \rangle^{1/2}$, and $Re_0 = V_0 R_0 / \nu \propto Re_\lambda^{1/2}$. They are expected to be universal among vortex tubes in turbulence at high Reynolds numbers. To confirm this expectation, experiments at the higher Reynolds numbers are desirable. Those at similar Reynolds numbers but under different experimental configurations are also desirable.

110

The vortex tubes have been identified using enhancements of a velocity increment above a threshold. Thus our results are biased against weak tubes. The development of a method to identify vortex tubes with various strengths is desirable. We nevertheless believe that our results are useful because strong vortex tubes play an important role in small-scale intermittency. Their role in energy dissipation is also expected to be important.

References

JIMÉNEZ, J., WRAY, A. A., SAFFMAN, P. G. & ROGALLO, R. S. 1993 The structure of intense vorticity in isotropic turbulence. *J. Fluid Mech.* **255**, 65–90.

MAKIHARA, T., KIDA, S. & MIURA, H. 2002 Automatic tracking of low-pressure vortex. *J. Phys. Soc. Jpn.* **71**, 1622–1625.

MOURI. H., HORI, A. & KAWASHIMA, Y. 2003 Vortex tubes in velocity fields of laboratory isotropic turbulence: dependence on the Reynolds number. *Phys. Rev. E* **67**, 016305.

MOURI. H., HORI, A. & KAWASHIMA, Y. 2004 Vortex tubes in turbulence velocity fields at Reynolds numbers $Re_\lambda \simeq 300$–1300. *Phys. Rev. E* **70**, 066305.

LOCAL VORTEX IDENTIFICATION CRITERIA: INTER-RELATIONSHIPS AND A UNIFIED OUTLOOK

Pinaki Chakraborty, S. Balachandar, Ronald J. Adrian
Department of Theoretical and Applied Mechanics,
University of Illinois at Urbana-Champaign,
Urbana, Illinois 61801, USA

Abstract   We consider local vortex identification in turbulent flows using the two kinematic parameter framework of Chakraborty, Balachandar & Adrian (2005) (hereafter referred to as CBA05). The inter-relationships between the various local criteria are summarized and the notion of 'equivalent thresholds' is applied to two canonical turbulent flows: sphere wake and channel flow. Remarkably similar vortex structures are extracted using the 'equivalent thresholds'.

Keywords: Vortex identification, turbulence

1.   Introduction

The characteristic shape of vortical structures in turbulent flows forms the basis of the structural approach of understanding turbulence. Owing to the lack of a universally accepted definition of a vortex, many different vortex identification schemes have been proposed for identifying vortical regions in complex flows. Here, we restrict attention to local or point-wise schemes to identify vortex filaments (as opposed to vortex sheets or vortex blobs). Vortex filaments allows for simple understanding of a large part of the entire flow using the Biot-Savart law. Also, since the filaments occupy a rather small volume, the Biot-Savart law effects a type of data compression, making the entire flow understandable in terms of the vortex induced flow and the dynamics of the filament.

We consider various commonly used local vortex identification criteria, namely: Q, λ_2, Δ, and λ_{ci} (for references see CBA05). They are based on local point-wise analysis of the velocity gradient tensor ($\boldsymbol{\nabla v}$) and the essential difference between them comes from the defining characteristic each criterion ascribes to a vortex filament. CBA05 proposed a two kinematic parameter framework to inter-relate the different criteria and explain the similarity and

differences in the vortex structure educed by the application of the different schemes. Hence, the two parameters provide a new way of interpreting the different criteria and thus serves to formulate a unified interpretation of the different schemes. For many turbulent flows, owing to the local two-dimensionality of the intensely swirling structures, CBA05 proposed the idea of 'equivalent thresholds' that result in remarkably similar looking vortex structures. The next section summarizes the two-parameter system and the inter-relationships between the different criteria. Thereafter the proposal of 'equivalent thresholds' is applied to two canonical turbulent flow examples: sphere wake and channel flow.

2.   Enhanced swirling strength and inter-relationships

The proposal of enhanced swirling strength criterion of CBA05 uses the reference frame of a critical point. In the regions where the eigenvalues of ∇v are complex, two kinematic parameters are identified: the imaginary part of the complex eigenvalue (λ_{ci}) and the ratio of the real to imaginary part of the complex eigenvalue ($\lambda_{cr}/\lambda_{ci}$). The plane of swirling is identified to be the plane spanned by the complex eigenvectors. In this plane, for the instantaneous streamlines, $2\pi/\lambda_{ci}$ is the time for one complete revolution and $\exp(2\pi\lambda_{cr}/\lambda_{ci})$ is the ratio of the final to initial radial positions. Hence, these two parameters have unambiguous interpretation in terms of the local flow kinematics. Although this two-parameter formulation is valid for both incompressible and compressible flows, here we restrict attention to incompressible flows.

CBA05 explored the inter-relationships between the different criteria using these two parameters. In the region of complex eigenvalues of ∇v, Q and Δ can be explicitly related with these parameters in closed form relations:

$$Q \;\; = \lambda_{ci}^2 \left(1 - 3 \left(\tfrac{\lambda_{cr}}{\lambda_{ci}} \right)^2 \right), \tag{1a}$$

$$\Delta \;\; = \tfrac{\lambda_{ci}^6}{27} \left[1 + 9 \left(\tfrac{\lambda_{cr}}{\lambda_{ci}} \right)^2 \right]^2 . \tag{1b}$$

In general, the λ_2 criterion cannot be expressed in terms of the eigenvalues of ∇v. CBA05 established that in an approximate sense $\lambda_2 < 0$ region corresponds to the region of $|\lambda_{cr}/\lambda_{ci}|$ values being $O(1)$. CBA05 defined a parameter $\tilde{\lambda}_2$ as a proxy for λ_2 and obtained an exact relation for $\tilde{\lambda}_2$ as

$$\tilde{\lambda}_2 = \lambda_{ci}^2 \left(\left(\frac{\lambda_{cr}}{\lambda_{ci}} \right)^2 - 1 \right) . \tag{2}$$

For the special case, when the eigen-basis vectors of ∇v are orthonormal, λ_2 and $\tilde{\lambda}_2$ are equivalent.

(a) λ_{ci}

(b) Q

(c) λ_2

(d) $\tilde{\lambda}_2$

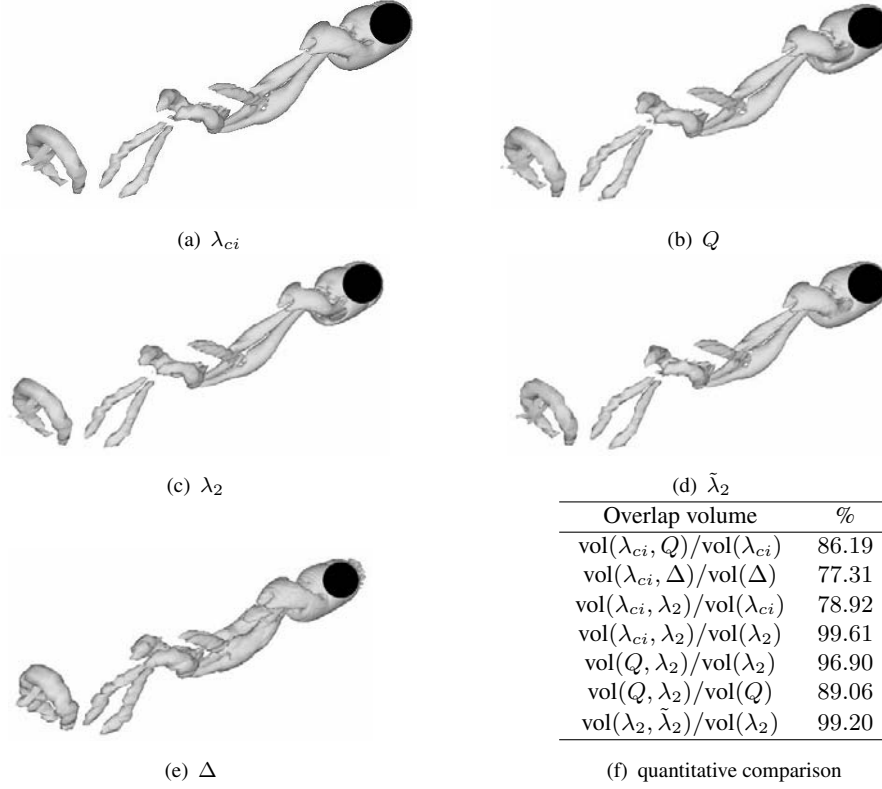| Overlap volume	%
$\mathrm{vol}(\lambda_{ci}, Q)/\mathrm{vol}(\lambda_{ci})$	86.19
$\mathrm{vol}(\lambda_{ci}, \Delta)/\mathrm{vol}(\Delta)$	77.31
$\mathrm{vol}(\lambda_{ci}, \lambda_2)/\mathrm{vol}(\lambda_{ci})$	78.92
$\mathrm{vol}(\lambda_{ci}, \lambda_2)/\mathrm{vol}(\lambda_2)$	99.61
$\mathrm{vol}(Q, \lambda_2)/\mathrm{vol}(\lambda_2)$	96.90
$\mathrm{vol}(Q, \lambda_2)/\mathrm{vol}(Q)$	89.06
$\mathrm{vol}(\lambda_2, \tilde{\lambda}_2)/\mathrm{vol}(\lambda_2)$	99.20

(e) Δ

(f) quantitative comparison

Figure 1. Vortex structure in the wake of uniform flow past a rigid sphere for $(\lambda_{ci})_{th} R/U = 0.25$, where R and U are the radius of the sphere and the ambient flow velocity respectively. The sphere is represented by solid black color and the incident flow is from the right. Frame (f) depicts quantitative comparison of overlapping vortex volumes, where $\mathrm{vol}(\alpha, \beta)$ represents overlapping vortex volumes identified by the parameters α and β.

3. 'Equivalent thresholds' and turbulent flows

CBA05 considered the following problem: given the threshold conditions

$$\lambda_{ci} \geq (\lambda_{ci})_{th} = \epsilon \qquad \text{and} \qquad (\lambda_{cr}/\lambda_{ci}) \leq (\lambda_{cr}/\lambda_{ci})_{th} = \delta, \qquad (3)$$

what are the corresponding 'equivalent thresholds' for Q, Δ, and λ_2? This equivalence is in the sense of extracting similar vortex regions. This problem, in general, has no unique solution. CBA05 made a simple proposal for the 'equivalent thresholds' which is based on the following observation: inside the intense vortical structures of most turbulent flows, the swirling motion dominates and the ratio $|\lambda_{cr}/\lambda_{ci}|$ takes small values. For incompressible flows the
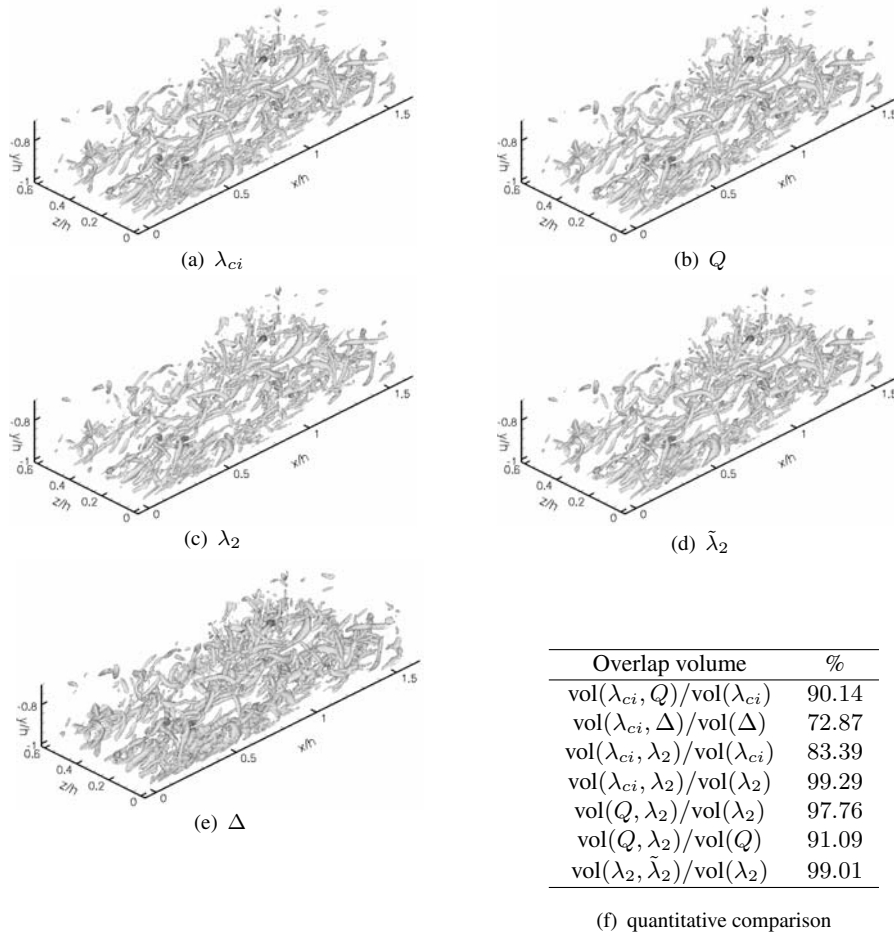
(a) λ_{ci}

(b) Q

(c) λ_2

(d) $\tilde{\lambda}_2$

(e) Δ

Overlap volume	%
$\mathrm{vol}(\lambda_{ci}, Q)/\mathrm{vol}(\lambda_{ci})$	90.14
$\mathrm{vol}(\lambda_{ci}, \Delta)/\mathrm{vol}(\Delta)$	72.87
$\mathrm{vol}(\lambda_{ci}, \lambda_2)/\mathrm{vol}(\lambda_{ci})$	83.39
$\mathrm{vol}(\lambda_{ci}, \lambda_2)/\mathrm{vol}(\lambda_2)$	99.29
$\mathrm{vol}(Q, \lambda_2)/\mathrm{vol}(\lambda_2)$	97.76
$\mathrm{vol}(Q, \lambda_2)/\mathrm{vol}(Q)$	91.09
$\mathrm{vol}(\lambda_2, \tilde{\lambda}_2)/\mathrm{vol}(\lambda_2)$	99.01

(f) quantitative comparison

Figure 2. Vortex structure in channel flow for $(\lambda_{ci})_{th} h/(Re_\tau u_\tau) = 0.14$, where h and u_τ are the half channel height and the friction velocity respectively. For the sake of clarity $1/16 \times 1/4 \times 1/16$ of the simulation box is shown. The coordinates (x, y, z) represent the streamwise, wall-normal, and spanwise directions respectively. Frame (f) depicts quantitative comparison of overlapping vortex volumes, where $\mathrm{vol}(\alpha, \beta)$ represents overlapping vortex volumes identified by the parameters α and β.

limit $\lambda_{cr}/\lambda_{ci} \to 0$ corresponds to two-dimensional motion in the vortex plane, thereby indicating that the local motion in the intense structures is essentially planar with limited radial motion. Based on the above observation, CBA05 proposed the following 'equivalent thresholds':

$$Q \geq Q_{th} = \epsilon^2, \qquad (4)$$

$$\Delta \geq \Delta_{th} = \frac{1}{27}\epsilon^6, \qquad (5)$$

$$\lambda_2 \quad \leq \quad (\lambda_2)_{th} = (\tilde{\lambda}_2)_{th} = -\epsilon^2. \tag{6}$$

The above thresholds become exact in the limit $\lambda_{cr}/\lambda_{ci} = 0$. Note that λ_2 and $\tilde{\lambda}_2$ are equal as well in this limit. Now we apply the above 'equivalent thresholds' to two canonical turbulent flow examples.

4.   Results

Vortex structure in the wake region of uniform flow past a rigid sphere is computed using DNS data at Reynolds number (based on the diameter of sphere) $Re = 610$ (Bagchi & Balachandar 2004). We use equations 4 - 6 to get the thresholds for the different vortex identification criteria and the resulting wake structure is shown in figure 1.

Vortex structure in a channel flow is computed using DNS data at friction Reynolds number $Re_\tau = 940$ (del Álamo *et al.* 2004). We use equations 4 - 6 to get the thresholds for the different vortex identification criteria and the resulting wake structure is shown in figure 2.

We observe that the usage of 'equivalent thresholds' for the two canonical turbulent flow examples considered results in nearly identical vortex structures extracted by the various criteria. This observation is similar to the isotropic turbulence example studied in CBA05. The values of $|\lambda_{cr}/\lambda_{ci}|$ were observed to be small inside the intense vortices, which explains the similarity in the vortex structures. Also, as remarked in CBA05, the Δ criterion is seen to educe a comparatively denser vortex structure.

References

DEL ÁLAMO, J.C., JIMÉNEZ, J., ZANDONADE, P. & MOSER, R.D. 2004 Scaling of the energy spectra of turbulent channels *J. Fluid Mech.* **500**, 135–144.

BAGCHI, P. & BALACHANDAR, S. 2004 Response of the wake of an isolated particle to an isotropic turbulent flow. *J. Fluid Mech.* **518**, 95–123.

CHAKRABORTY, P., BALACHANDAR, S. & ADRIAN, R.J. 2005 On the relationships between local vortex identification schemes. *J. Fluid Mech.* **535**, 189–214.

Part C Chaotic advection and mixing

PERSISTENT MULTIPLE-SCALE STAGNATION POINT STRUCTURE

J.C. Vassilicos[1], J. Davila[2], S. Goto[3], E. Hascoet[1], D. Osborne[1], L. Rossi[1]

[1] *Department of Aeronautics, Imperial College London, SW7 2AZ, UK*

[2] *E. Superior de Ingenieros, Camino de los Descubrimientos s/n, 41092-Sevilla, Spain*

[3] *Department of Mechanical Engineering, Kyoto University, 606-8501, Japan*

j.c.vassilicos@imperial.ac.uk

Abstract
In isotropic turbulence, stagnation points form a fractal multiple-scale network in space such that their number density $n_s = C_s \, L^{-d} \, (L/\eta)^{D_s}$ where C_s is a dimensionless constant, L/η is the inner to outer length-scale ratio and the fractal dimension D_s is given by $p + 2D_s/d = 3$; d is the dimensionality of the flow and p is the exponent of the energy spectrum. On the other hand, the statistical persistence of stagnation points is defined in terms of the statistics of stagnation point velocities, and we show that, on average, stagnation points stop moving as the Reynolds number tends to infinity in the frame where the mean flow is zero. In that same limit, stagnation points tend to become zero-acceleration points on average, and to be persistent. Turbulent-like velocity fields obtained by Kinematic Simulations (KS) can be made to reproduce some persistence properties of the multiple-scale stagnation point network by appropriately choosing the KS time-dependence. Studies of turbulent pair diffusion in such KS lead to $\langle \Delta^2 \rangle \approx G_\Delta L^2 (u't/L)^\gamma$ (where Δ is the pair separation at time t, u' is the r.m.s. turbulent velocity and G_Δ is the Richardson dimensionless constant) with $\gamma = 2d/D_s$. A simple argument based on the time between successive encounters of particle-pairs with stagnation points and on a re-interpretation of the locality-in-scale hypothesis in terms of a multiplicative pair-separation process confirms this relation between the Lagrangian exponent γ and the Eulerian exponent D_s. This model also leads to $G_\Delta \sim C_s^{\,2/D_s}$ thus suggesting that the Richardson constant might not be universal. Simulations confirm that G_Δ is an increasing function of C_s. Finally, we seek to corroborate these ideas and results with a low Reynolds number *laboratory* simulation of high Reynolds number two-dimensional turbulence. We complement this laboratory simulation with DNS of the same and similar flows. In this laboratory simulation we reproduce the cat's eyes within cat's eyes topological streamline structure of two-dimensional turbulence by appropriate multiple-scale electromagnetic forcing of a quasi-two-dimensional brine flow. In particular, we are able to impose the value of D_s. PIV measurements of the energy spectrum corroborate the formula $p + 2D_s/d = 3$.

Keywords: Turbulence, pair diffusion, flow topology, stagnation points, electromagnetic forcing, fractal geometry

1. Multiple-scale persistent flow topology

In this paper, the word "coherent" in "coherent structure" is interpreted to mean persistent in time, and the word "structure" refers to the multiple-scale topological structure of stagnation points. One reason amongst others why we focus attention on stagnation points is their impact on turbulent diffusion by virtue of the strong curvature of streamlines in their vicinity. Indeed, Fung *et al.* (1992) conjectured that straining stagnation points (hyperbolic points in two-dimensional flows and stagnation points with a non-zero real eigenvalue of the velocity gradient matrix in three-dimensional flows; see Davila & Vassilicos 2003) are responsible for sudden pair separation events and that pairs travel together for a long time and do not separate significantly till they meet such points. In laboratory experiments of two-dimensional turbulence electromagnetically forced at the small scales so as to generate an approximate $-5/3$ power-law energy spectrum, Jullien *et al.* (1999) confirmed that fluid element pairs travel together for long stretches of time and then separate suddenly, but they did not attempt to identify the events responsible for these sudden separations.

1.1 Multiple-scale network of stagnation points

Fung & Vassilicos (1998) attempted to reconcile the locality-in-scale hypothesis (Richardson 1926, Obukhov 1941, Batchelor 1950) with the straining stagnation points and found, numerically using Kinematic Simulations (KS) with energy spectra $E(k) \sim k^{-p}$ where $1 < p < 3$, that in two-dimensional turbulence the multiple-scale instantaneous streamline structure consists of cats' eyes within cats' eyes, or equivalently figures of eight within figures of eight (see figure 1). This provides a suggestive schematic picture of the multiple-scale topological structure of straining stagnation points which was confirmed in Direct Numerical Simulations (DNS) of inverse cascading two-dimensional turbulence with $E(k) \sim k^{-5/3}$ (Goto & Vassilicos 2004).
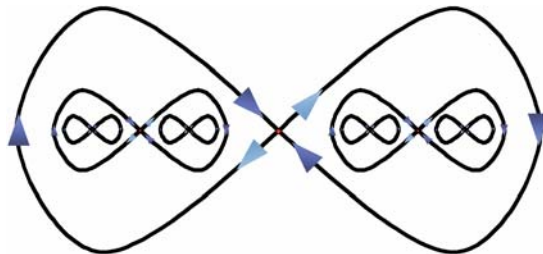

Figure 1.   Schematic of a fractal (multi-scale) flow based on an 8 in 8 topology.

The concept of "structure" in "coherent structure" does not need to be localised. In statistically isotropic and homogeneous two-dimensional ($d = 2$) turbulence stagnation points are distributed on a fractal set in space in the manner just described. In three-dimensions the schematic topology is yet unknown, but it is possible to quantify this topological structure of stagnation points in terms of the number density n_s per unit area ($d = 2$) or per unit volume ($d = 3$) which is an increasing power-law function of the ratio of the inner to the outer length-scales L/η. Specifically,

$$n_s(L/\eta) = C_s L^{-d}(L/\eta)^{D_s} ,\tag{1}$$

where C_s is a dimensionless constant which we refer to as the "Avogadro number of turbulence" ("how many stagnation points per litre of turbulence?") and where the fractal dimension D_s of the stagnation point structure of turbulence is found to be equal to 2 when $d = 3$ (Davila & Vassilicos 2003) and $4/3$ when $d = 2$ (Goto & Vassilicos 2004) by means of DNS (three-dimensional and two-dimensional in the inverse energy cascade regime) and also laboratory measurements (on the basis of some assumptions required to interpret one-dimensional hot wire data, see Davila & Vassilicos 2003 for more details). Stagnation points are therefore distributed on a fractal set both in two-dimensional and three-dimensional homogeneous isotropic turbulence.

KS of statistically isotropic and homogeneous turbulence, which are Gaussian turbulent-like flows with prescribed incompressibility, energy spectrum $E(k) \sim k^{-p}$ and time dependence, reproduce the multiple-scale stagnation point structure of the turbulence with

$$p + 2D_s/d = 3\tag{2}$$

(Davila & Vassilicos 2003). In fact, this formula can be derived kinematically on the assumption of sufficient phase scrambling in Fourier space. Surprisingly perhaps, when $p = 5/3$, this formula implies $D_s = 2$ for $d = 3$ and $D_s = 4/3$ for $d = 2$ in agreement with DNS isotropic and homogeneous turbulence.

We now sketch this heuristic kinematic derivation. (Formula (2) can, however, be obtained rigorously for fractional Brownian motions in conjunction with a rule for estimating fractal dimensions of intersections of surfaces; see Orey 1970 and Davila & Vassilicos 2003.) Assume that one component, say u_1, of the velocity field $\boldsymbol{u}(\boldsymbol{x}, t)$ has an instantaneous zero-crossing surface of fractal dimension D larger or equal to $d - 1$. Any rectilinear cut through this surface will have fractal dimension $D - d + 1$ and on account of the statistical isotropy of the turbulence considered here, the statistics of the fluctuations of u_1 along this cut (measured with coordinate x, say) will be the same as the statistics of $\boldsymbol{u}(\boldsymbol{x}, t)$ in the entire flow. Therefore the dimension of the graph of $u_1(x)$ is $D - d + 2$. A characteristic length of the graph $u_1(x)$ for a length-resolution r along the axis x can be estimated to be proportional to

$r^{-1}\sqrt{\langle[u_1(x+r)-u_1(x)]^2\rangle + r^2}$ if there is sufficient Fourier phase scrambling for the signal to be "homogeneous" enough that the structure function $\langle[u_1(x+r)-u_1(x)]^2\rangle$ may be used in this way. Another way to estimate this same length at that same resolution is the fractal estimate $r^{1-(D-d+2)}$. Hence, for r sufficiently small, $\langle[u_1(x+r)-u_1(x)]^2\rangle \sim r^{2(d-D)}$ which implies $E(k) \sim k^{-p}$ with $p - 1 = 2(d - D)$. Stagnation points of $\boldsymbol{u}(\boldsymbol{x},t)$ are intersections of the zero-crossing surfaces of each component of $\boldsymbol{u}(\boldsymbol{x},t)$, and the fractal dimension D_s of the set of these intersections is $D_s = d(D - d + 1)$ (see Davila & Vassilicos 2003) which leads to (2).

1.2   Statistical persistence of stagnation points

Having established and characterised in terms of the fractal dimension D_s the multiple-scale topological structure of stagnation points, we now attempt to establish its persistence. We measure the statistical persistence of stagnation points in terms of the statistics of stagnation point velocities $\boldsymbol{V}_s$ (velocities with which stagnation points move, *not* fluid velocities). Given an arbitrary frame of reference, the fluid velocity $\boldsymbol{u}$ at a stagnation point $\boldsymbol{s}(t)$ at time t vanishes, i.e. $\boldsymbol{u}(\boldsymbol{s},t) = \boldsymbol{0}$, and remains so for as long as this stagnation point exists. Hence, during the stagnation point's life-time, $\boldsymbol{0} = (\mathrm{d}/\mathrm{d}t)\boldsymbol{u}(\boldsymbol{s},t) = \partial\boldsymbol{u}/\partial t + \boldsymbol{V}_s\cdot\nabla\boldsymbol{u}$ at position $\boldsymbol{s}$ and time t, and $\boldsymbol{V}_s \equiv \mathrm{d}\boldsymbol{s}/\mathrm{d}t$. The fluid acceleration is defined as $\boldsymbol{a} \equiv \partial\boldsymbol{u}/\partial t + \boldsymbol{u}\cdot\nabla\boldsymbol{u}$ at all positions $\boldsymbol{x}$ and times t. Setting $\boldsymbol{x} = \boldsymbol{s}$, we obtain

$$\boldsymbol{a} = -\boldsymbol{V}_s \cdot \nabla\boldsymbol{u} \tag{3}$$

at any time t and any stagnation point $\boldsymbol{s}(t)$ of the flow. Note that this relation holds in any frame of reference. What changes with frame is the number and positions of stagnation points (where these relations hold). It follows that the acceleration r.m.s. a' is related to the r.m.s. V_s' of $\boldsymbol{V}_s$ in any frame by

$$V_s' \sim a'\tau_\eta \,, \tag{4}$$

where τ_η is the Kolmogorov time micro-scale. Strictly, a' is the acceleration r.m.s. over all stagnation points, but it is also equal to the acceleration r.m.s. over the entire field because Galilean transformations leave a' unchanged even though they cause the r.m.s. statistics to be calculated over different ensembles of points. Our DNS and KS calculations of a' and V_s' support this view.

Kolmogorov scaling applied to a' (laboratory experiments by La Porta *et al.* (2001) support Kolmogorov scaling of a') implies that the r.m.s. ratio V_s'/u' (where u' is the turbulence velocity fluctuation r.m.s.) scales as $(L/\eta)^{-1/3} \sim Re_\lambda^{-1/2}$ (where Re_λ is the Taylor-length-based Reynolds number). Furthermore, due to correlations between accelerations and velocities, which we capture by three-dimensional statistically isotropic and homogeneous DNS turbu-

lence, $\langle \boldsymbol{V}_s \rangle = 0$ in the frame where the mean flow is zero but not in other frames, and persistence of stagnation points is therefore maximised in that privileged frame where the mean flow is zero (see Goto *et al.* 2005). In fact, in that frame, stagnation points stop moving relative to Lagrangian trajectories as the Reynolds number tends to infinity as a consequence of $V_s'/u' \sim (L/\eta)^{-1/3} \sim Re_\lambda^{-1/2}$. Of course, large-scale stagnation points cannot be expected to be so persistent as they strongly depend on boundary conditions and the large eddies of the flow. But, in view of (1), there are so many more small-scale stagnation points than large-scale ones that the large-scale unsteadiness does not contribute much to the statistical quantity V_s'.

We also estimate the mean life-time of stagnation points to be of the order of the integral time scale. This estimate relies on the following argument constructed around the notion that stagnation points disappear and reappear when they meet, and uses the number density of stagnation points (1). This number density implies that the average distance between stagnation points is the Taylor microscale $\lambda = L(\eta/L)^{2/3}$. Hence, the time that two stagnation points will take to meet if they move head on is $\lambda/[u'(\eta/L)^{1/3}]$, where $u'(\eta/L)^{1/3}$ is the velocity of these stagnation points. Stagnation points can only be expected to disappear as a result of stagnation point "collisions". However, most of the time they will miss each other, so the estimate of the average life-time of stagnation points must also involve the probability that stagnation points may collide. We think of stagnation points as being surrounded by an influence sphere the size of which relates to the "size" of the stagnation point (i.e. the size of the streamlines emanating from it). Because there are stagnation points of varying size, we define the time $t(\delta)$ for stagnation points of size δ to meet as being $L(\delta/L)^{2/3}/[u'(\delta/L)^{1/3}]$ (compare with the time $\lambda/[u'(\eta/L)^{1/3}]$ given above). The probability $p(\delta/L)$ for such points to meet (or rather for their spheres of influence to meet) is proportional to $(\delta/L)^d (L/\delta)^{D_s}$. The average life-time of stagnation points is therefore given by

$$\int_\eta^L t(\delta)\, p(\delta/L)\, \mathrm{d}(\delta/L) , \tag{5}$$

which integrates to L/u'. Hence, stagnation points are on average long-lived.

2.   The impact of the persistent multiple-scale flow topology on turbulent pair diffusion

KS turbulent-like velocity fields can be made to reproduce persistence properties of stagnation points, and in particular small values of V_s'/u', by carefully choosing the KS time-dependence even though they do not physically reproduce the exact sweeping effect of smaller eddies by larger ones (Osborne 2004). Studies of two-particle turbulent diffusion in such KS lead to

$\langle \Delta^2 \rangle \approx G_\Delta L^2 (u't/L)^\gamma$ (where Δ is the pair separation at time t, G_Δ is the Richardson dimensionless constant and $\langle \, \cdot \, \rangle$ represents an average over many pairs and/or realisations) with

$$\gamma = 2d/D_s \qquad (6)$$

(D_s can be changed in KS by changing p). These KS results (see Fung & Vassilicos 1998, Davila & Vassilicos 2003) indicate a correlation between γ and D_s but not necessarily a causal relation. Such a causal relation can, however, be obtained in the context of a simple mechanical model of turbulent pair diffusion which is based on the time between successive encounters of particle-pairs with stagnation points and on a re-interpretation of the locality-in-scale hypothesis in terms of a multiplicative pair-separation process (see Goto & Vassilicos 2004 for more details).

The fundamental assumption underpinning this model is that, in the frame of reference where $\langle \boldsymbol{V}_s \rangle = 0$, particle pairs travel with velocity u' whereas straining stagnation points remain persistent by not moving much and as a consequence, pairs and stagnation points move relative to each other with characteristic velocity u' and with enough persistence for their encounters to result, on average, in sudden pair-separation bursts. The time between successive bursts is interpreted to be proportional to the doubling time $T_\rho(\Delta)$ (see Boffetta *et al.* 1999): a pair which, after a given burst, has separation Δ, takes a time $T_\rho(\Delta)$ to meet another straining stagnation point and then suddenly increase its separation by a factor $\rho > 1$ to $\rho\Delta$. This doubling time can be estimated from the number density of stagnation points n_s: it is proportional to the characteristic distance between straining stagnation points of size Δ or larger. This characteristic distance is $[n_s(L/\Delta)]^{-1/d}$, and therefore $T_\rho(\Delta) \sim [n_s(L/\Delta)]^{-1/d}/u' = (C_\rho L/u')(L/\Delta)^{-D_s/d}$ where $C_\rho \sim C_s^{-1/d}$. The time t required for pair separations to evolve from Δ_0 to $\Delta(t) = \rho^n \Delta_0$ is, on average, $t = \sum_{j=0}^{n-1} T_\rho(\rho^j \Delta_0)$ which implies, for long enough times, that $\langle \Delta^2 \rangle \approx G_\Delta L^2 (u't/L)^\gamma$ with γ given by the KS result (6) and $G_\Delta \sim C_\rho^{-2d/D_s} \sim C_s^{2/D_s}$. This model stresses the importance, for pair diffusion, of straining stagnation points and persistent streamline structure of the turbulence rather than just high strain rate regions. (How these regions may relate to straining stagnation points is currently a central issue in our research.) This model also leads to $G_\Delta \sim C_s^{2/D_s}$ thus suggesting that the Richardson constant might not be universal because C_s is expected to be determined by the large scales of motion. DNS and KS confirm that G_Δ is an increasing function of C_s (Davila & Vassilicos 2003, Goto & Vassilicos 2004).

3. Low Reynolds number laboratory simulation of high Reynolds number turbulence

Finally, we seek to corroborate these ideas and results with a low Reynolds number *laboratory* simulation of high Reynolds number two-dimensional turbulence. We complement this laboratory simulation with DNS of the same and similar flows which can be analysed in more detail. In this laboratory simulation we reproduce the cat's eyes within cat's eyes topological streamline structure of two-dimensional turbulence by appropriate multiple-scale electromagnetic forcing of a shallow layer quasi-two-dimensional (Q2D) brine flow (see figure 2 and Rossi *et al.* 2004).

Electromagnetic forcing of Q2D brine flow has been used in previous works to generate Q2D chaotic advection (e.g. Rothstein *et al.* 1999) and Q2D turbulent flows (e.g. Jullien *et al.* 1999 and references therein). In these experiments as well as here, electromagnetic body forcing is produced with magnetic fields generated by permanent magnets (placed under the horizontal bottom wall supporting the thin layer of brine) and an electrical current generated by electrodes placed on opposite sides of the square tank. The difference here compared to previous works is that the electromagnetic forcing acts over many (here three) length-scales on a fractal-like set because we are using three different magnet sizes organised as in figure 2b,c,d (one pair of largest North/South magnets; four pairs of medium-sized North/South magnets; and eight pairs of smallest North/South magnets). This choice of fractal-like structure has been made so as to reproduce the multiple-scale streamline topology which consists of cat's eyes within cat's eyes. This particular fractal-like set-up of magnets gives $D_s \approx 0.6$ if one considers the stagnation points generated by each pair of magnet and their sizes.

The thickness of the layer of brine is chosen at 5 mm in order to achieve the best compromise between quasi-two-dimensionality (Satijn *et al.* 2001) and reduced bottom friction (Clercx *et al.* 2003) so that the flow can be driven by the magnets and not halted by the bottom wall. The magnets' distances to the bottom wall are chosen so as to create electromagnetic forces that are roughly the same in the flow above each magnet, whatever the magnet's size. (We computed these forces by the method described in Rossi (2001) and they are shown in figure 2c). The size of our tank (1700^2 mm^2) is large compared to the size of our magnets (160 mm; 40 mm; 10 mm) and the electromagnetic forcing area represents only 2.8 % of the total area of the bottom wall which is small compared to all previous such laboratory set-ups. Hence, the flow region of interest is far away from the boundaries of the tank, and we find that the flow does acquire the desired topology shown in figures 1 and 2. Dye visualisation of the flow reported in figure 3 shows how the flow develops and acquires its fractal topology. Velocities are of the order of ten millimetres per
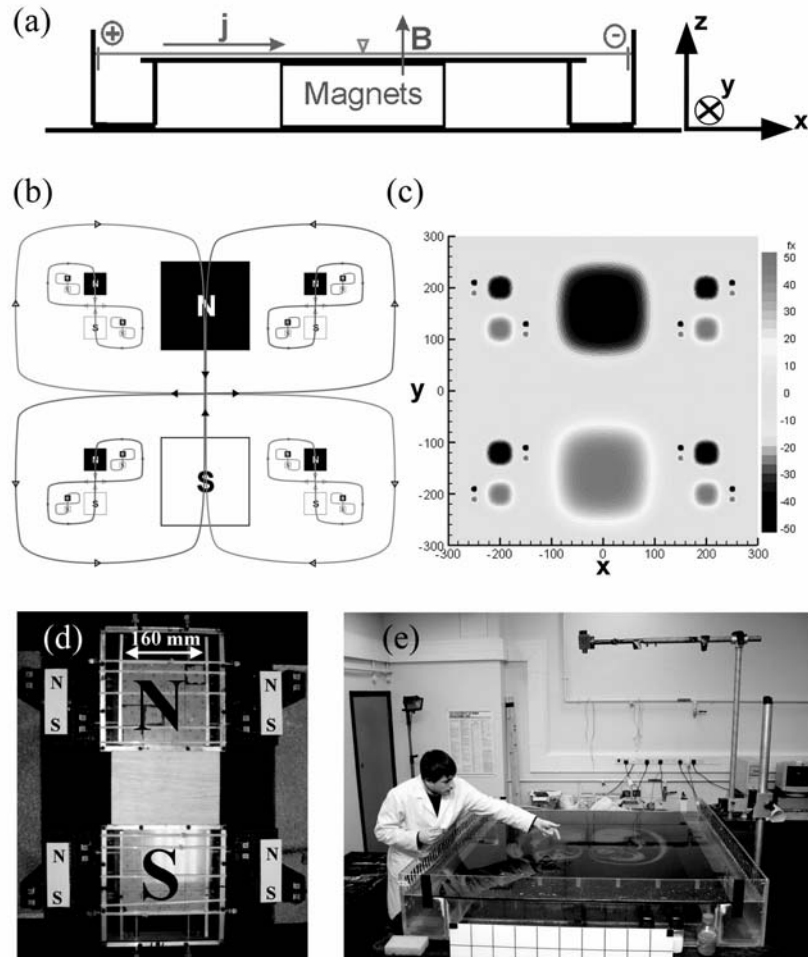
Figure 2. (a) Rig's schematic for electromagnetic forcing of a shallow brine layer. (b) Schematic of a fractal flow and associated permanent magnets. (c) Electromagnetic forcing distribution, $I = 1$A, $B_{\text{ref}} = 1$T, f_x in N/m^2. (d) Under-wall distribution of permanent magnets used in experiments. (e) Photograph of the rig.

second and are measured with Particle Image Velocimetry (PIV) (see figure 4). We control the magnitudes of these velocities by tuning the current between the electrodes on either side of the tank and we find that we can change the intensity of the flow without significantly changing the fractal-like streamline topology over more than one decade of velocity magnitude. The flow is laminar but electromagnetically forced to have many scales of motion, which is why we refer to it as a low Reynolds number laboratory simulation of high Reynolds
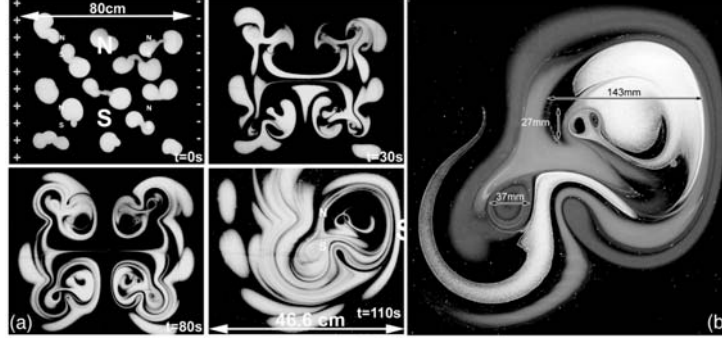
Figure 3. Dye visualisations for $I = 0.3$A. (a) Entire flow, magnets (M160 and M40) are indicated by N and S, while the electrical potential is indicated by $+$ and $-$. The power is switch on at $t = 0$. (b) Quarter flow, picture taken about 75s after switch on.
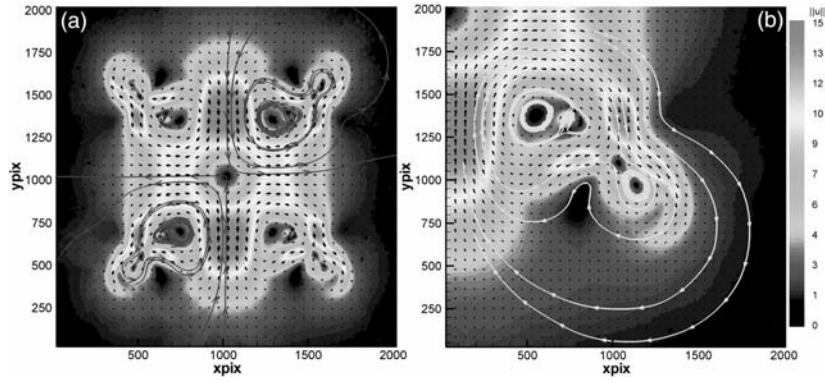

Figure 4. PIV measurements for $I = 0.3$A. (a) Entire flow, physical frame about 80cm; 1pixel≈0.397mm. (b) Quarter of the flow, physical frame about 40cm; 1pixel≈0.202mm. 1 vector velocity every 8 measurement point, $|\boldsymbol{u}|$ in mm/s.

number turbulence. The Reynolds number is low in the sense that the flow is too slow and too controlled by the Lorentz forces to allow flow instabilities to set in.

In parallel with this laboratory experiment, we are running DNS of two-dimensional Navier-Stokes flow under similar fractal-like electromagnetic forcing and periodic boundary conditions. Our integrations are carried out with a pseudo-spectral code on a 1024^2 grid and the domain size ($2\pi \times 2\pi$) is large compared to the size of the square magnets ($2\pi/5 \times 2\pi/5$; $2\pi/20 \times 2\pi/20$; $2\pi/80 \times 2\pi/80$). Referring to the Lorentz force as $f_0\boldsymbol{f}(\boldsymbol{x})$, f_0 being the amplitude and $\boldsymbol{f}(\boldsymbol{x})$ accounting for the spatial distribution of the magnets; modelling the wall's friction force by a Rayleigh $-\alpha\boldsymbol{u}$ term; and rescaling all quantities with the length-scale f_0/α^2 and the time-scale α^{-1}, the equations of motions
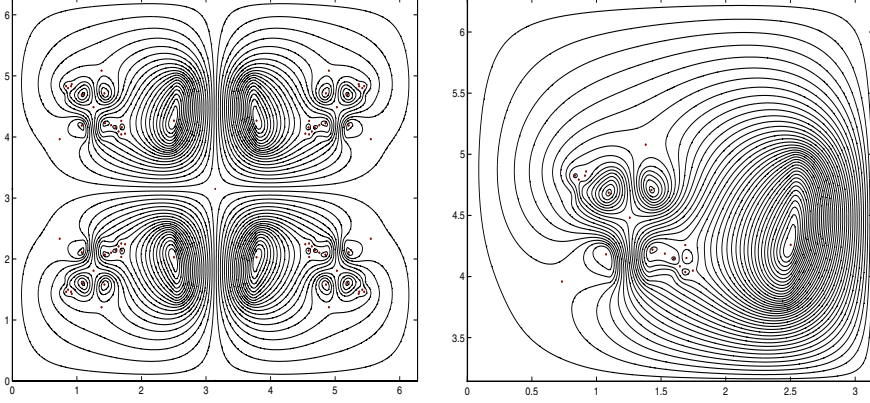
Figure 5. DNS streamlines pattern and stagnation points locations; full flow (left hand side) and top left quarter (right hand side).

are

$$\frac{\partial \boldsymbol{u}}{\partial t} + \boldsymbol{u} \cdot \boldsymbol{\nabla} \boldsymbol{u} = -\boldsymbol{\nabla} p - \boldsymbol{u} + \frac{1}{H_a{}^2}\nabla^2\boldsymbol{u} + \boldsymbol{f} \,, \tag{7}$$

where H_a stands for Hartmann number and $H_a{}^2 = f_0^2/\nu\alpha^3$, and

$$\boldsymbol{\nabla} \cdot \boldsymbol{u} = 0 \,. \tag{8}$$

Our PIV measurements show that the energy spectrum $E(k)$ of the flow has an approximate power-law shape k^{-p} with $p \approx 2.4$ over a significant range of scales which includes the magnet sizes (see figure 6). This exponent p lies between the $5/3$ value which would result from forcing a two-dimensional turbulence at the small scales and the value 3 which characterises a two-dimensional turbulence forced at the large scales. Indeed, the present forcing extends over various scales, and it is important to note that the obtained value $p = 2.4$ agrees with equation (2) as $d = 2$ and $D_s \approx 0.6$ in the present case. This result suggests that we might be able to control the energy spectrum's power-law exponent p by suitably designing the fractal-like electromagnetic force field. Such control of the energy spectrum should allow to test relation (6) between the Lagrangian exponent γ and the Eulerian fractal dimension D_s.

The numerical simulations demonstrate that, when $\alpha t \gg 1$, the total kinetic energy of the flow remains constant in time and equal to $C f_0^2/\alpha^2$ where $C = C(H_a)$ is a dimensionless number which increases with H_a but eventually appears to tend towards a constant. The DNS also show very good agreement with the laboratory experiment both in the energy spectrum and the detailed streamline pattern (see figures 5 and 6). The small differences in streamline shapes are due to the fact that the ratio of the size of the box (or tank) over the size of the largest magnets is twice smaller in the DNS than in the rig.
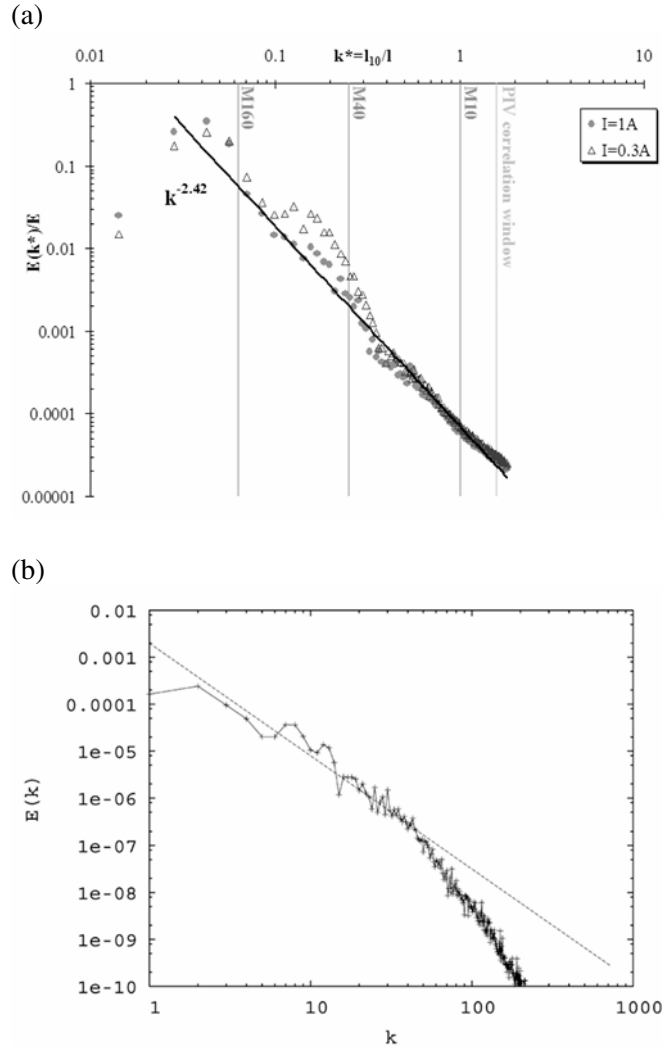
(a)

(b)

Figure 6. Energy spectrum, (a) experiments and (b) DNS with $H_a = 8 \times 10^4$, the straight line gives $E(k) \propto k^{-2.4}$.

Currently the flow is stationary in time, but various modes of time dependence are envisaged for the near future. Studies of turbulent diffusion are to follow to test the relation between flow topology and turbulent stirring, in particular Eulerian-Lagrangian relations such as $\gamma = 2d/D_s$ and such as $G_\Delta \sim C_s^{2/D_s}$.

References

BATCHELOR, G. K. 1950 The application of the similarity theory of turbulence to atmospheric diffusion. *Q. J. R. Meteorol. Soc.* **76**, 133–146.

BOFFETTA, G., CELANI, A., CRISANTI, A. & VULPIANI, A. 1999 Relative dispersion in fully developed turbulence: Lagrangian statistics in synthetic flows. *Europhys. Lett.* **46**, 177–182.

CLERCX, H.J.H., VAN HEIJST, G.J.F. & ZOETEWEIJ, M.L. 2003 Quasi-two-dimensional turbulence in shallow fluid layers: The role of bottom friction and fluid layer depth. *Phys. Rev. E* **67**, 066303.

DAVILA, J & VASSILICOS, J.C. 2003 Richardson's pair diffusion and the stagnation point structure of turbulence. *Phys. Rev. Lett.* **91**, 144501.

FUNG, J.C.H., HUNT, J.C.R., MALIK, N.A. & PERKINS, R.J. 1992 Kinematic simulation of homogeneous turbulent flows generated by unsteady random Fourier modes. *J. Fluid Mech.* **236**, 281–318.

FUNG, J.C.H. & VASSILICOS, J.C. 1998 Two-particle dispersion in turbulent-like flows. *Phys. Rev. E* **57**, 1677–1690.

GOTO, S. & VASSILICOS, J.C. 2004 Particle pair diffusion and persistent streamline topology in two-dimensional turbulence. *New J. Phys.* **6**, 65.

GOTO, S., OSBORNE, D.R., VASSILICOS, J.C. & HAIGH, J.D. 2005 Acceleration statistics as measures of statistical persistence of streamlines in isotropic turbulence. *Phys. Rev. E* **71**, 015301.

JULLIEN, M.C., PARET, J. & TABELING, P. 1999 Richardson pair dispersion in two-dimensional turbulence. *Phys. Rev. Lett.* **82**, 2872-2875.

LA PORTA, A., VOTH, G.A., CRAWFORD, A.M., ALEXANDER, J. & BODENSCHATZ, E. 2001 Fluid particle accelerations in fully developed turbulence. *Nature* **409**, 1017–1019.

OBUKHOV, A. 1941 Spectral energy distribution in turbulent flow. *Acad. Sci. U.S.S.R., Geog. & Geophys., Moscow* **5**, 453–566.

OREY, S. 1970 Gaussian sample functions and the Hausdorff dimension of level crossing, *Z. Wahrscheinlichkeitstheorie verw. Geb.* **15**, 249–256.

OSBORNE, D.R. 2004 Ph.D. thesis, Imperial College London, London UK.

RICHARDSON, L.F. 1926 Atmospheric diffusion shown on a distance-neighbour graph. *Proc. R. Soc. Lond. A* **110**, 709–737.

ROSSI, L. 2001 Ph.D. thesis, Universite Joseph Fourier, Grenoble, France.

ROSSI, L., VASSILICOS, J.C. & HARDALUPAS, Y. 2004 2D fractal flow controlled by electromagnetic forcing in the laboratory. In *Advances in Turbulence X* (Eds. H. I. Andersson & P.-A. Krogstad), CIMNE, Barcelona.

ROTHSTEIN, D., HENRY, E. & GOLLUB, J.P. 1999 Persistent patterns in transient chaotic fluid mixing. *Nature* **401**, 770–772.

SATIJN, M.P., CENSE, A.W., VERZICCO, R., CLERCX, H.J.H. & VAN HEIJST, G.J.F. 2001 Three-dimensional structure and decay properties of vortices in shallow fluid layers. *Phys. Fluids* **13**, 1932–1945.

STREAMLINES, COHERENT VORTICES AND PAIR DIFFUSION IN TWO-DIMENSIONAL TURBULENCE

Susumu Goto
Department of Mechanical Engineering,
Kyoto University,
Yoshida-Honmachi, Sakyo, Kyoto, 606-8501, Japan
susumu-goto@mail-box.jp

J.C. Vassilicos
Department of Aeronautics,
Imperial College, London,
SW7 2AZ, UK
j.c.vassilicos@imperial.ac.uk

Abstract   A new approach to particle pair diffusion in self-similar turbulence is developed in terms of coherent structures, i.e. coherent vortices and streamlines associated with them. The well-known Richardson equation can be re-derived by a simple model proposed by this approach. The model and its implications are verified by the use of direct-numerical simulation of pair diffusion in the inverse energy cascade regime of two-dimensional turbulence.

Keywords: Turbulent diffusion, coherent vortex, stagnation point, the Richardson law

1.   Introduction

The pair diffusion of fluid particles in statistically homogeneous isotropic self-similar turbulence was first investigated by Richardson (1926). In the paper, based on his intuition and the measurements of atmospheric turbulence, he proposed the following governing equation for the probability density function (PDF) $P(\Delta, t)$ of the separation $\Delta(t)$ between particle pairs

$$\frac{\partial P}{\partial t} = \frac{\partial}{\partial \Delta} \left(F \, \Delta^{d-1} \frac{\partial}{\partial \Delta} \left(\frac{P}{\Delta^{d-1}} \right) \right) . \tag{1}$$

Here, d is the spatial dimension, and $F(\Delta)$ ($\sim \Delta^{\frac{4}{3}}$) is a scale-dependent diffusivity. Interestingly, some recent experiments (see Ott & Mann 2000) support
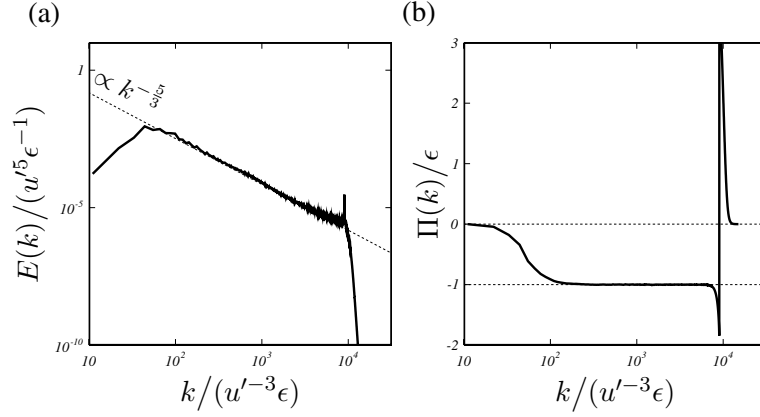
131

Figure 1. (a) Energy spectrum $E(k)$ and (b) energy flux function $\Pi(k)$ in the inverse energy cascade regime of two-dimensional turbulence. Here, u' is the root-mean square velocity.

the solution of the Richardson equation (1) (although it is not conclusive due to limited Reynolds numbers). Since (1) was an ansatz, the first purpose of the present article is to understand the physics behind this equation.

On the other hand, Fung *et al.* (1992) and Fung & Vassilicos (1998) emphasised the importance of streamlines and stagnation points in pair diffusion. They claimed that particle pairs separate only when they encounter straining stagnation points. Later, Dávila & Vassilicos (2003) suggested based on numerical results of kinematic simulations that the exponent γ of the mean square separation, $\langle \Delta^2 \rangle \sim t^\gamma$, can be related to the fractal dimension D_s of spatial distribution of straining stagnation points as follows

$$\gamma = 2d/D_s \,. \tag{2}$$

However, it seems strange that pair diffusion which is Galilean invariant can be explained by a theory based on straining stagnation points which are *not* Galilean invariant. Hence, the second purpose of the present article is to resolve this superficial inconsistency, and to reformulate how the statistics of pair diffusion can be described in terms of the spatial distribution of stagnation points. We shall show that we must choose a specific frame to relate the statistics of pair diffusion with those of spatial distribution of straining stagnation points.

2. Pair diffusion in terms of coherent vortices

2.1 Self-similar structure of coherent vortices

In what follows, we investigate pair diffusion using observations from direct numerical simulation (DNS) of self-similar turbulence, i.e. turbulence with a
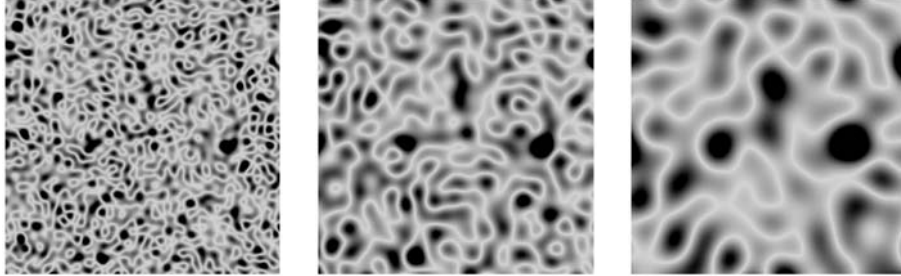
Figure 2. Contour of coarse-grained vorticity obtained by low-pass filtering with a sharp cutoff wavenumber k_c. Left, $k_c = k_f/4$; middle, $k_f/8$; right, $k_f/16$. Here, k_f is the peak wavenumber of the forcing spectrum.

sufficiently wide inertial range. As it remains difficult to simulate directly such self-similar turbulence in three-dimensional space, we restrict ourselves to the case of two-dimensional turbulence with a small-scale force. Employing an energy sink at large scales, the energy cascades from small to large scales, and a statistically stationary state can be achieved (figure1). By using 4096^2 grid points in a periodic box, the inertial range, where the energy spectrum $E(k)$ is proportional to $\epsilon^{\frac{2}{3}} k^{-\frac{5}{3}}$ and the energy flux $\Pi(k)$ is equal to $-\epsilon$, extends over two decades (see Goto & Vassilicos 2004 for details of the simulation). We consider pair diffusion in this inertial range.

The coherent vortices in this velocity field reveal a simple self-similar structure. Figure 2 shows the coarse-grained vorticity fields obtained by low-pass filtering of the energy spectrum with a sharp cut-off wavenumber k_c within the inertial range. Since the enstrophy spectrum is proportional to $k^2 E(k) \sim k^{\frac{1}{3}}$ in the inertial range, coherent vortices of cut-off scale can be seen. The temporal movements of these vortices show that a cluster of smaller-scale vortices corresponds to a larger-scale vortex. In other words, smaller-scale coherent vortices are auto-rotating (by the definition of vorticity), and at the same time they are swept by larger-scale coherent vortices. Since the velocity field is self-similar in the inertial range, it is reasonable that the coherent vortices also have this self-similar structure. Although it is hard to state what kind of self-similarity of coherent vortices can be observed in three-dimensional isotropic turbulence (because the coherent structures are observed as vortex tubes or sheets, and their length scales are not unique), coherent vortices in the inverse energy cascade regime of two-dimensional isotropic turbulence seem to possess this simple self-similar structure. Note, in passing, that the coherent vortical structure in decaying two-dimensional turbulence (see Dritschel 1993, e.g.) must be very different from that in the present system.
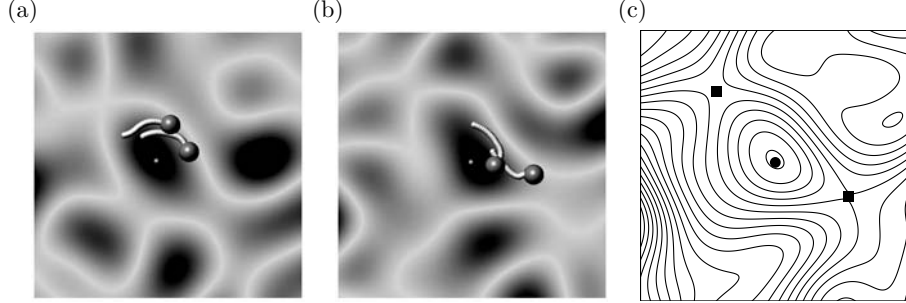
(a) (b) (c)

Figure 3. (a)(b) Particle pair's trajectories together with the intensity of vorticity. (c) Stream-lines in the Lagrangian frame moving with the central vortex in (b). At the same time with (b).

2.2 Trapping and release of particles by coherent vortices

Bearing the picture of the self-similar coherent vortical structure in mind, it is easy to describe particle motions and pair diffusion, since DNS observations show that particle motions at each scale of the inertial range are well described in terms of flow induced by coherent vortices at that scale. The characteristic motion of a single particle is as follows: it is trapped by a vortex at each scale for the duration of one eddy turnover time of the vortex, and leaves occasionally (see §3) the vortex to be trapped by another adjoining vortex at that scale. Then, the typical motion of a particle pair can be described as follows: a pair with separation Δ is likely to be trapped by a same coherent vortex of size Δ. As long as the two particles are trapped by the vortex, the separation remains $O(\Delta)$. However, when one of the particles leaves the vortex, the separation suddenly increases from Δ to $\xi\Delta$ (see DNS visualisation in figure 3(a)(b) and a schematic picture in figure 5(a)). Here, we assume $\xi(> 1)$ to be a constant. Because the particles remain trapped by a vortex of larger scale $\xi\Delta$, their relative motions are now determined by the flow induced by vortices at that scale $\xi\Delta$. This scale-by-scale separation picture allows us to propose a model of the temporal evolution of particle pair separation Δ in a self-similar manner as

$$\Delta_0 \xrightarrow{T(\Delta_0)} \xi\Delta_0 \xrightarrow{T(\xi\Delta_0)} \xi^2\Delta_0 \xrightarrow{T(\xi^2\Delta_0)} \cdots . \tag{3}$$

This model has two physical parameters: the scale ratio ξ and the time-scale $T(\Delta)$ for a particle pair to be trapped by a single vortex of size Δ. Here, we assume, based on the above observation from DNS, that the time $T(\Delta)$ is proportional to the eddy turnover time of vortices of size Δ, i.e.

$$T(\Delta) \sim \frac{\Delta}{\sqrt{E(1/\Delta)/\Delta}} \sim \epsilon^{-\frac{1}{3}}\Delta^{\frac{2}{3}} . \tag{4}$$

Then, the probability $Q_n(t)$ for a particle pair separation to be between $\xi^n \Delta_0$ and $\xi^{n+1}\Delta_0$ may be governed by

$$\frac{\mathrm{d}}{\mathrm{d}t}\, Q_n = b_{n-1}\, Q_{n-1} - b_n\, Q_n \quad \left(\text{with } b_n \propto T(\xi^n \Delta_0)^{-1} \propto (\xi^n \Delta_0)^{-\frac{2}{3}} \right). \quad (5)$$

A Taylor expansion of the above equation up to the second order leads to the governing equation for the PDF $P(\Delta, t)$ of particle pair separations,

$$\frac{\partial P}{\partial t} = -B\,\alpha\, \frac{\partial}{\partial \Delta} \left(\Delta^{\frac{1}{3}} P \right) + \frac{B\,\alpha^2}{2} \frac{\partial}{\partial \Delta} \left(\Delta \frac{\partial}{\partial \Delta} \left(\Delta^{\frac{1}{3}} P \right) \right), \quad (6)$$

where $\alpha \equiv \log \xi$. Notice that the derived equation is a generalisation of the Richardson equation (1), which is recovered by the specific choice $\alpha = 6/(3d - 2)$; $\alpha = \frac{3}{2}$ for $d = 2$, and $\alpha = \frac{6}{7}$ for $d = 3$. It is interesting that the solution (see (7), below) of (6) leads to the well-known t^3 law (Richardson 1926) of mean square separations, $\langle \Delta^2 \rangle$, irrespective of the value of α. This may be seen also by the invariance of (6) under the scale-transformation $\Delta \to \lambda \Delta$ and $t \to \lambda^{\frac{2}{3}} t$.

It is straightforward to show that the solution of (6) with initial condition $P(\Delta, 0) \propto \delta(\Delta)$ has the similarity form as

$$\widetilde{P}(\widetilde{\Delta}) = A\, \widetilde{\Delta}^{-\frac{1}{3}+\frac{2}{\alpha}}\, \exp \left(-G_0^{\frac{1}{3}}\, \widetilde{\Delta}^{\frac{2}{3}} \right), \quad (7)$$

where

$$\widetilde{\Delta} \equiv \Delta / \langle \Delta^2 \rangle^{\frac{1}{2}}, \quad (8)$$

A is a normalise factor, and $G_0 \equiv (3 + 3/\alpha)\,(2 + 3/\alpha)\,(1 + 3/\alpha)$. Note that the functional form of $\widetilde{P}$ given by (7) is uniquely determined when we choose an α. Now we compare (7) with DNS estimation in figure 4. The numerical estimation of $P(\Delta, t)$ is well fitted with the value of $\alpha = 1.3$ ($\xi \approx 4$). This is nearly equal to $\alpha = \frac{3}{2}$ corresponding to the Richardson equation (1) for $d = 2$.

In summary, based on the schematic picture (3) of particle pair separation in terms of scale-by-scale trapping and release by the self-similar structure of coherent vortices we have re-derived the Richardson equation (1). Thus, one may depict the physics behind the equation. Indeed, the model described in this section seems not far from the original picture that Richardson seemed to have in mind when he proposed (1); Richardson 1926 reads *"Suppose that we were to let loose a sphere* 0.01 *cm. in diameter of acetylene... after a few seconds, part may get caught in one of the gusts..., while another part remain in a lull,... Next squalls of several minutes' duration separate it more rapidly... Then one part gets into a cyclone and another remains behind in an anticyclone..."* A weak point of the schematic picture, however, is that it cannot specify when or where one of two particles changes the vortex to be trapped (and the particle pair separates suddenly). We deal with this problem in the next section.
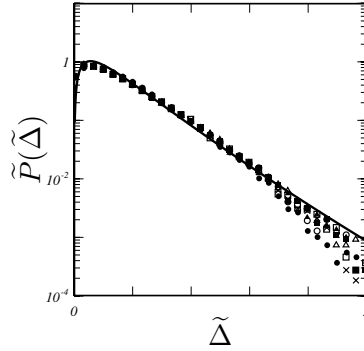
Figure 4. PDF of normalised pair separation Δ by its root-mean square. Symbols, DNS estimations for different times; solid curve, the solution (7) of the derived equation (6) for $\alpha = 1.3$.

3.   Pair diffusion in terms of persistent streamlines

3.1   Streamlines and trajectories

A question to be addressed here is when and where a particle leaves the coherent vortex trapping it. To answer this question we first note the fact that *if the velocity field is frozen in time, the trajectories of particles coincide with streamlines, and the motion of particles can be described in terms of streamline topology.* Of course turbulence is never stationary, but one may choose a frame where the local velocity field is approximately stationary within some time-scale. Indeed, this frame is the Lagrangian (local) frame moving with a coherent vortex with a relatively long lifetime.

In order to define unambiguously the velocity of the Lagrangian frame moving with a coherent vortex, we introduce zero-acceleration points, i.e. the points where $\boldsymbol{a} \equiv \partial \boldsymbol{u}/\partial t + \boldsymbol{u} \cdot \nabla \boldsymbol{u} = \boldsymbol{0}$. There are two (elliptic and hyperbolic) types of zero-acceleration points with different streamline topologies around them. These two types are classified by the sign of $\nabla \cdot \boldsymbol{a}$. Our present DNS shows that many elliptic points are located at the centres of coherent vortices, and many hyperbolic points reside in zero-vorticity strips between the vortices. Hence, we define the velocity of the Lagrangian frame as the fluid velocity at the elliptic zero-acceleration point at the centre of a vortex. Note that in the Lagrangian frame moving with a zero-acceleration point, the point is a stagnation point and the streamlines around it may be persistent in time because $\partial \boldsymbol{u}/\partial t$ vanishes at that point in this frame. It is worth mentioning, in passing, that our identification of vortex centres in two-dimensional turbulence is closely related to the low-pressure vortex identification of Miura & Kida (1997) in three-dimensional
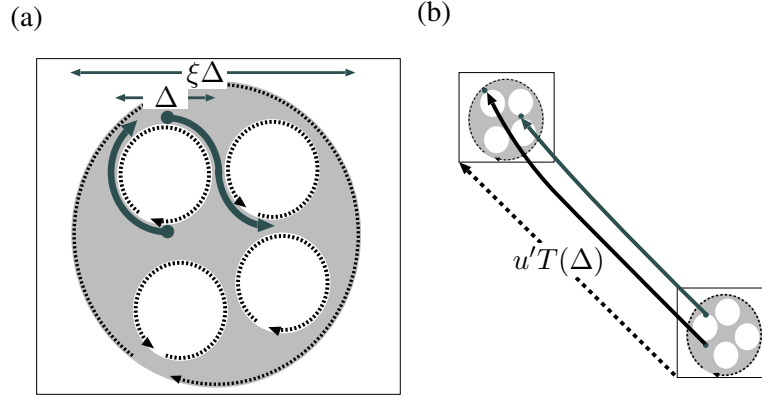
(a)　　　　　　　　　　　　　　(b)

Figure 5. Schematic picture of particle pair motion (a) in the Lagrangian frame, and (b) in the Eulerian frame.

turbulence, since the pressure gradient is the dominant contribution to the acceleration.

In figure 3(c), we plot the streamlines in the Lagrangian frame moving with the central vortex in the figure at the same time as (b). By comparing the particle trajectories plotted in (b) with the streamlines plotted in (c), it is clearly seen that the trajectories approximately coincide with persistent streamlines in the Lagrangian frame moving with the coherent vortex. Particles change through the action of hyperbolic streamlines, and therefore particle pairs separate suddenly around *a hyperbolic stagnation point in the Lagrangian frame* in which streamlines are approximately stationary.

3.2   Ballistic motion of particle pairs

As seen in the previous section, particle trajectories approximately coincide with streamlines in the Lagrangian frame moving with a coherent vortex. Let us observe the motion of the same particle pair in an Eulerian frame (see figure 5(b)). Note that coherent vortices move with a speed of the order of the root-mean square velocity u', on average, *in the frame where the mean velocity vanishes*. While trapped by the vortex, the particle pair moves with this speed, which is much faster than the relative swirling motion around the centre of the vortex when the Reynolds number is large. Hence, this motion becomes ballistic in the Eulerian frame. Indeed, such ballistic motions of particle pairs have been observed in laboratory experiments (Jullien *et al.* 1999; Ott & Mann 2000).

The mean distance $\ell_b(\Delta)$ of ballistic motions at the scale Δ can be written, by the use of (4), as

$$\ell_b(\Delta) \sim u' \, T(\Delta) \sim \mathcal{L}^{\frac{1}{3}} \, \Delta^{\frac{2}{3}} \,, \tag{9}$$

where we have used the Taylor relation, $\epsilon \sim u'^3/\mathcal{L}$. Here, $\mathcal{L}$ denotes the integral scale. It might be interesting to notice that ℓ_b is proportional to the Taylor scale when Δ is the Kolmogorov scale. Since $\ell_b(\Delta)$ gets larger (and more conspicuous) with Δ, the ballistic motion observed in the experiments may be $\ell_b(\mathcal{L}) \sim \mathcal{L}$.

3.3   Impact of stagnation points on the pair diffusion

In §3.1 we have observed that the sudden separations of particle pairs take place around hyperbolic stagnation points in the Lagrangian frame moving with coherent vortices. It is interesting, based on this observation, to restate the hypothesis employed in previous papers (Fung *et al.* 1992; Fung & Vassilicos 1998; Dávila & Vassilicos 2003; Goto & Vassilicos 2004):

> (hypothesis) the *mean* length $\ell_b(\Delta)$ of the ballistic motion of a particle pair with separation Δ is proportional to the *mean* distance $\ell_s(\Delta)$ between straining (hyperbolic) stagnation (zero-velocity) points of the coarse-grained velocity field obtained by low-pass filtering with a sharp cut-off Δ in the Eulerian frame, i.e.

$$\ell_b(\Delta) \sim \ell_s(\Delta) \,. \tag{10}$$

Here we refer to the choice of frame. It is obvious that neither the mean length of ballistic motions nor the mean distance between stagnation (zero-velocity) points are Galilean invariant. It is therefore reasonable to choose one specific frame to formulate the above hypothesis. Recall that the derivation of (9) requires the mean velocity of the flow (and therefore the mean velocity of coherent vortices) to vanish. Hence, the above hypothesis may be formulated most naturally in the frame where the mean velocity vanishes.

Let N_s be the number of straining stagnation points in the Eulerian velocity field induced by vortices larger than Δ. In general, N_s depends on Δ, $\mathcal{L}$ and the system size L_0, and is related to ℓ_s by

$$\ell_s \sim L_0/N_s^{\frac{1}{d}} \,. \tag{11}$$

Hence, (9) and the hypothesis (10) lead to the estimation of N_s as

$$N_s \sim \left(\frac{L_0}{\mathcal{L}}\right)^d \left(\frac{\mathcal{L}}{\Delta}\right)^{D_s} \qquad \left(\text{with} \quad D_s = \frac{2d}{3}\right) \,. \tag{12}$$
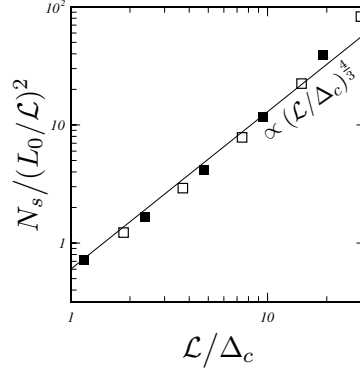
Figure 6. The number N_s of stagnation points in the coarse-grained velocity field obtained by low-pass filtering with a sharp cut-off Δ_c for two-different Reynolds numbers; open squares, $\mathcal{L}/(2\pi/k_f) = 19$; solid squares, 30.

We plot DNS-estimated $N_s(\mathcal{L}, \Delta)$ in figure 6 in the two-dimensional ($d = 2$) turbulence for different Δ and $\mathcal{L}$, where L_0 is fixed at 2π. This figure clearly supports (12).

It is worth mentioning that the fractal dimension D_s of the spatial distribution of stagnation points can be related to the exponent p of the energy spectrum $E(k) \sim k^{-p}$ in the self-similar range by

$$D_s = \frac{d(3 - p)}{2} \tag{13}$$

(see Dávila & Vassilicos 2003 for a rigorous derivation by the use of a theorem on the Hausdorff dimension of the graph of Gaussian fractal signal, or Vassilicos *et al.* 2005 for a physical derivation). Equation (13) is consistent with (12), because we are considering the case of the Kolmogorov spectrum ($p = \frac{5}{3}$). Thus, it has been shown that the implication (12) of the hypothesis (10) is supported by both the present DNS (figure 6) and the mathematical formula (13).

Finally, we reconstruct the simple model developed in §2.2 in terms of the fractal dimension D_s under the hypothesis (10). By using (12), (11), (10) and (9) in this order, we can estimate the time-scale $T(\Delta)$ for a particle pair separation to remain Δ as

$$T(\Delta) \sim u'^{-1} \mathcal{L}^{1-\frac{D_s}{d}} \Delta^{\frac{D_s}{d}} . \tag{14}$$

Then, it can be shown by the same procedure as in §2.2 that the governing equation for $P(\Delta, t)$ is the same as (6) provided that $\Delta^{\frac{1}{3}} P$ is replaced by

$\Delta^{1-\frac{D_s}{d}} P$ on the right-hand side. The scale-similarity, $\Delta \to \lambda\Delta$ and $t \to \lambda^{\frac{D_s}{d}} t$, of the derived equation (see Goto & Vassilicos 2004 for the explicit derivation) implies that the mean square separation $\langle \Delta^2 \rangle$ evolves in time as

$$\langle \Delta^2 \rangle \sim t^{\frac{2d}{D_s}} , \tag{15}$$

which leads to the relationship (2) suggested by kinematic simulations (Dávila & Vassilicos 2003).

4.   Concluding remarks

We reviewed our recent efforts to understand the background physics of particle pair diffusion in self-similar turbulence in terms of coherent structures. Here, the word "coherent" is used to express persistence in time, and the word "structure" does not necessarily indicate a vortex. It is shown that a simple description of the pair diffusion in terms of coherent vortices does lead to the Richardson PDF equation (§2); the proposed model is schematically described in terms of stepwise self-similar separations (3). It is also shown that persistent streamlines in the Lagrangian frame moving with coherent vortices are useful for the description of particle trajectories. Finally, we have restated the hypothesis (10) on the importance of stagnation points for pair diffusion in §3. Although the hypothesis does require further investigation, its implication (12) for the number of stagnation points is supported by the present DNS (figure 6) and the kinematic formula (13). The hypothesis may be of great use if it is valid, because it directly leads to nontrivial relations such as (2) between an Eulerian variable (the fractal dimension D_s) and Lagrangian statistics (the exponent of mean square separation of pair diffusion). It has been shown (see Vassilicos *et al.* 2005) by the use of Kolmogorov theory on the one hand and DNS data of three-dimensional isotropic turbulence on the other that the characteristic velocity V_s of stagnation points (in the frame where the mean flow velocity vanishes) becomes much slower than u' at very high Reynolds number, and that stagnation points in that frame become zero-acceleration points at large Reynold numbers. Hence, in high Reynolds number turbulence, stagnation points and streamlines around them are persistent even in the Eulerian frame in the sense that $\ell_b(\Delta) \gg V_s T(\Delta)$. Here, $V_s T(\Delta)$ is the typical distance of stagnation point movements for the duration that a particle pair separates from Δ to $\xi\Delta$. This seems to be the reason why hypothesis (10) appears to be valid in the present system.

References

DÁVILA, J. & VASSILICOS, J.C. 2003 Richardson's pair diffusion and the stagnation point structure of turbulence, *Phys. Rev. Lett.* **91**, 144501.

DRITSCHEL, D.G. 1993 Vortex properties of two-dimensional turbulence, *Phys. Fluids A* **5**, 984–997.

FUNG, J.C.H., HUNT, J.C.R., MALIK, N.A. & PERKINS, R.J. 1992 Kinematic simulation of homogeneous turbulent flows generated by unsteady random Fourier modes, *J. Fluid Mech.* **236**, 281–318.

FUNG, J.C.H. & VASSILICOS, J.C. 1998 Two-particle dispersion in turbulent-like flows, *Phys. Rev. E* **57**, 1677–1690.

GOTO, S. & VASSILICOS, J.C. 2004 Particle pair diffusion and persistent streamline topology in two-dimensional turbulence, *New J. Phys.* **6**, 65.

JULLIEN, M.-C., PARET, J. & TABELING, P. 1999 Richardson pair dispersion in two-dimensional turbulence, *Phys. Rev. Lett.* **82**, 2872–2875.

MIURA, H. & KIDA, S. 1997 Identification of tubular vortices in turbulence, *J. Phys. Soc. Jpn.* **66**, 1331–1334.

OTT, S. & MANN, J. 2000 An experimental investigation of relative diffusion of particle pairs in three-dimensional turbulent flow, *J. Fluid Mech.* **422**, 207–223.

RICHARDSON, L.F. 1926 Atmospheric diffusion shown on a distance-neighbour graph, *Proc. Roy. Soc. London* A **110**, 709–737.

VASSILICOS, J.C., DÁVILA, J., GOTO, S., HASCOET, E., OSBORNE, D. & ROSSI, L. 2005 Persistent multiple-scale stagnation point structure, In *Proc. IUTAM symposium on Elementary Vortices and Coherent Structures* .

SELF-SIMILARITY OF BALLISTICALLY SEPARATING MOTIONS IN TURBULENT RELATIVE DISPERSION

Takeshi Ogasawara, Sadayoshi Toh
Department of Physics, Graduate School of Science, Kyoto University,
Kitashirakawa Oiwakecho, Sakyo-ku, Kyoto 606-8502 Japan
ogasawara@kyoryu.scphys.kyoto-u.ac.jp, toh@scphys.kyoto-u.ac.jp

Abstract   Dynamical properties of passive particle pairs are investigated in two-dimensional free convection turbulence by direct numerical simulation. In terms of the exit-time statistics, it is confirmed that the growth of relative separations $r(t)$ is consistent with the prediction of the Bolgiano-Obukhov scaling in the inertial range, $\langle r^2(t) \rangle \propto t^5$. Furthermore, by looking into the probability density function (PDF) of exit-time, motions of relative separations of particle pairs are classified into two types: ballistic and diffusive motions, both of which satisfy the Bolgiano-Obukhov scaling. The probability density function of exit-time of diffusively separating motions is described by Richardson's diffusion equation, and that of ballistically separating motions corresponds to the PDF of the Lagrangian velocity increment. Our results also indicate that the PDF of the Lagrangian velocity increment relates to that of the stretching rate of a relative separation in the dissipation range.

1.   Introduction

Recently, researches on the relative dispersion in fully-developed turbulence have been stimulated by the progress of particle-tracking techniques both in experiments and numerical simulations (Jullien *et al.* 1999, Boffetta & Sokolov 2002). Through these researches, ballistically separating motions of particle pairs have been clarified to be relevant even in the inertial range, which are probably caused by some coherence such as fine coherent vortical structures or straining stagnation points embedded in turbulent fluctuations (Boffetta & Sokolov 2002, Goto & Vassilicos 2004). However, we have not yet understood their nature and role in pair dispersion processes well.

In this paper we will show that we can extract, in terms of exit-time statistics, ballistically separating motions of particle pairs from separation processes. Besides, we will show that the probability density function (PDF) of their exit-time relates to the PDF of the Lagrangian velocity increment, and show that some of our results suggest that it also relates to the PDF of the stretching rate of relative separation in the dissipation range.

We carry out DNS of 2-D free convection (2D-FC) turbulence instead of that of 3-D Navier-Stokes (3D-NS) turbulence. This is because the 2D-FC turbulence has both statistical and dynamical characteristics similar to those of 3D-NS turbulence (Toh & Matsumoto 2003), and because DNS of 2D-FC turbulence requires much less computer resources than that of 3D-NS turbulence.

2. 2-D free convection turbulence

The basic equations of the 2D-FC system are

$$\partial_t \boldsymbol{u} + (\boldsymbol{u} \cdot \nabla)\boldsymbol{u} = -\rho_0^{-1}\nabla p + \nu \triangle \boldsymbol{u} - \alpha g T \boldsymbol{e}_g, \tag{1}$$

$$\partial_t T + (\boldsymbol{u} \cdot \nabla)T = \kappa \triangle T, \tag{2}$$

where $\boldsymbol{u}$, T and p represent the solenoidal velocity, temperature and pressure fields, respectively. $\boldsymbol{e}_g$ is the unit vector in the direction of the gravity. In our DNS, a large-scale forcing and friction are added to the temperature and velocity fields respectively in order to keep the system statistically stationary.

The entropy $S \equiv \frac{1}{2}\int T^2 d\boldsymbol{x}$ is a conserved quantity of 2D-FC system in the inviscid limit, and S cascades from larger to smaller scales similar to the energy cascade in 3D-NS turbulence (Toh & Suzuki 1994). This entropy cascade leads Bolgiano-Obukhov (BO) scaling of the energy and entropy spectra in the inertial range, $E(k) \propto k^{-11/5}$ and $S(k) \propto k^{-7/5}$. The scaling law of velocity increment $\delta \boldsymbol{v}(r)$ is also predicted that $\delta \boldsymbol{v}(r) \propto r^{3/5}$. According to the BO scaling, the growth of pair separation $r(t)$ is expected as $\langle r^2(t) \rangle \propto t^5$, where $\langle \cdot \rangle$ denotes an ensemble average.

We carry out DNS of 2D-FC system by using the 4th-order Runge-Kutta (RK4) and pseudo-spectral method with resolution of 2048^2.

3. Exit-time statistics

The exit-time $T_{\mathrm{E}}(\delta; \rho)$ is defined by $T_{\mathrm{E}}(\delta; \rho) \equiv T_{\mathrm{F}}(\rho\delta) - T_{\mathrm{F}}(\delta)$, where $T_{\mathrm{F}}(\delta)$ is the time when $r(t)$ reach the threshold δ for the first time (first-passage time). According to the BO scaling, spatial scale dependence of exit-time is expected that $\langle T_E(\delta; \rho) \rangle \propto \delta^{2/5}$.

We use exit-time statistics (Boffetta & Sokolov 2002) to investigate dynamics of particle pairs for the following reasons: (i) Exit-time statistics can specify a spatial scale by choosing a threshold δ. (ii) The interval between thresholds
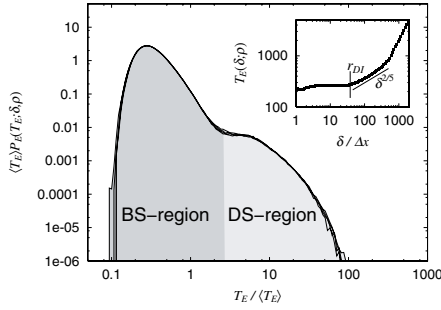
Figure 1. The PDF of exit-time ($\rho = 1.1$) obtained by our DNS at four different scales in the inertial range. Each of them is rescaled with its mean. The inset plot is the spatial scale dependence of the mean exit-time.
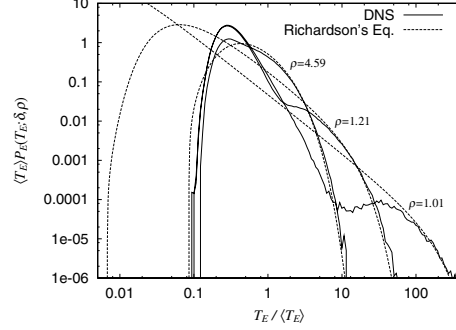
Figure 2. The PDF of exit-time obtained by our DNS and that of calculated from Richardson's diffusion equation at $\rho = 1.01$, 1.21 and 4.59. Each of them is rescaled with its mean.

(the width for averaging) can be controlled by ρ; This means that we can control the degree of coarse graining of dispersion process.

In our simulation, particle pairs are distributed homogeneously with relative separations of the grid scale Δx at initial time, and tracked by the advection equation with the RK4 method. We prepare spatial thresholds δ_n as $\delta_n = \rho^{n-1}\Delta x$ and calculate exit-time $T_E(\delta_n; \rho) = T_F(\delta_{n+1}) - T_F(\delta_n)$ for all particle pairs.

The inset of figure 1 shows the spatial scale dependence of the mean exit-time, in which we can confirm the BO scaling in the inertial range. Figure 1 shows that rescaled PDFs of different scales in the inertial range collapse onto a single curve. This means that pair dispersion process is self similar in the inertial range. Besides, it is clear that the PDF of exit-time is divided into two regions: a sharp peak and a long tail. We call them the BS- and DS-regions, respectively. Figure 2 shows the PDF in the DS-region fits with the PDF of exit-time calculated from Richardson's diffusion equation. This indicate that particle pairs in the DS-region separate diffusively and are described by Richardson's diffusion equation.

4. Ballistically separating motions

If particle pairs separate ballistically, it is expected that a relative separation r is governed by $\mathrm{d}r/\mathrm{d}t = A_I r^{3/5}$, according to the BO scaling, in the inertial range, and $\mathrm{d}r/\mathrm{d}t = A_D r$ in the dissipation range. In fact, the relative separations of particle pairs in the dissipation range grow exponentially on average as shown in the inset of figure 1, that is, the constancy of the mean exit-time corresponds to the exponential growth. The relative velocity of a particle pair is
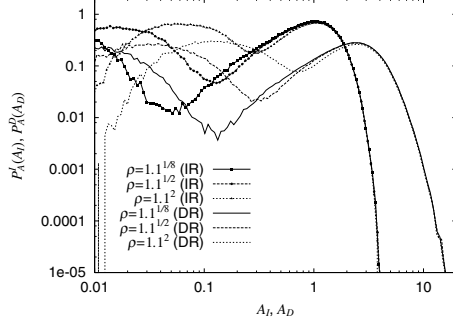
Figure 3. The PDFs of A_I and A_D calculated from the PDF of exit-time. (IR) and (DR) refer to the PDF of A_I at $\delta = 118\Delta x$ in the inertial range and that of A_D at $\delta = 4.2\Delta x$ in the dissipation range, respectively.
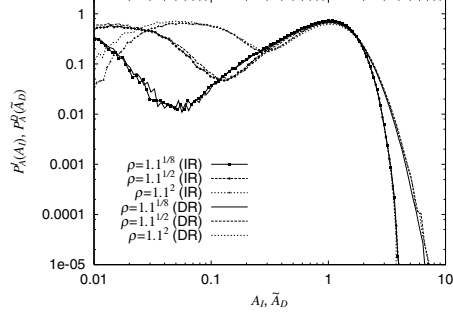
Figure 4. The PDFs of A_I and $\tilde{A}_D$. (IR) and (DR) represent the same meanings as figure 3.

the Lagrangian velocity increment of the scale of the relative separation, hence A_I is the coefficient of the scaling law of the Lagrangian velocity increment[1], $A_I = C_I \epsilon_\theta^{1/5}(\alpha g)^{-2/5}$. Besides, A_D is regarded as the stretching rate of relative separation in the dissipation range.

Suppose that a relative separation r grows ballistically from δ to $\rho\delta$ on a time interval T_E'. This means that the exit-time of the particle pair at δ is T_E'. Thereby, with the above two equations, the coefficients A_I and A_D are calculated as

$$A_I = \frac{5}{2}\frac{(\rho^{2/5} - 1)\delta^{2/5}}{T_E'}, \tag{3}$$

$$A_D = \frac{\log \rho}{T_E'}. \tag{4}$$

We can transform the PDF of exit-time into those of A_I and A_D as shown in figure 3 by Eqs. (3) and (4). The PDFs of A_I (A_D) of different values of ρ collapse onto a single curve for large values of A_I (A_D). The collapse regions of the PDF of A_I and A_D correspond to the BS-regions of the PDF of exit-time. These collapses indicate that PDFs of A_I and A_D are nearly independent not only from δ but also from ρ, and that particle pairs having the exit-time T_E' separate with a constant A_I (A_D) on average in the inertial (dissipation) range. This result indicates that there exists some long-range coherence which is consistent with the BO scaling.

Since the PDFs of A_I and A_D for the collapse regions look similar in shape, we expect these two PDFs are related with each other. At a matching scale r_{DI},

if exists, Eqs. (3) and (4) should give the same exit-time T'_E as

$$\frac{5}{2}\frac{(\rho^{2/5}-1)r_{DI}^{2/5}}{A_I} = \frac{\log\rho}{A_D}. \tag{5}$$

Furthermore, suppose that the crossover region in δ is narrow and thus ρ is close to unity as $\rho = 1 + \alpha$ with $\alpha \ll 1$, Eq. (5) yields the following relation between A_I and A_D:

$$A_I = r_{DI}^{2/5} A_D. \tag{6}$$

Figure 4 shows the PDF of A_I and that of $\tilde{A}_D \equiv r_{DI}^{2/5} A_D$ with $r_{DI} = 38\Delta x$. Here r_{DI} is estimated as shown in the inset of figure 1. We can see that the PDF of A_I agrees with that of $\tilde{A}_D$ for the same ρ except high values for $A_I > 2$. This result suggests that there are some relations between the dynamics of particle pairs in the inertial range and that in the dissipation range.

5.   Concluding remarks

We confirmed the relative dispersion in 2D-FC turbulence obeys the BO scaling in terms of exit-time statistics. The separation of particle pairs consists of ballistic (fast) and diffusive (slow) motions both in the dissipative and inertial ranges. Diffusively separating motion in the inertial range is governed by Richardson's diffusion equation on average. The ballistically separating motions from δ to $\rho\delta$ on an exit-time T are almost deterministic and governed by $\mathrm{d}r/\mathrm{d}t = A_I r^{3/5}$ in the inertial range and by $\mathrm{d}r/\mathrm{d}t = A_D r$ in the dissipation range where A_I and A_D are really almost constant for each motion. This constancy of A_I and A_D suggests that the ballistic separation is occurred along some coherence which might result from a T-vortical structure (Toh & Matsumoto 2003). By the relations (Eqs.(3) and (4)) we can obtain the PDFs of A_I and A_D which correspond to the PDF of Lagrangian velocity increment in the limit of $\rho \to 1$. The coincidence of the PDFs of A_I and A_D for intermediate values of them indicates a tight link between the separation processes of particle pairs in the inertial and dissipation ranges via some coherence.

Notes

1. $\langle \delta \boldsymbol{v}(r) \rangle = C_I \epsilon_\theta^{1/5}(\alpha g)^{2/5} r^{3/5}$ according to the BO scaling, where ϵ_θ is the entropy- dissipation rate and C_I is considered to be a universal constant.

References

BOFFETTA, G. & SOKOLOV, I. M. 2002 Statistics of two-particle dispersion in two-dimensional turbulence. *Phys. Fluids* **14**, 3224-3232.

Goto, S. & Vassilicos, J. C. 2004 Particle Pair Diffusion and Persistent Streamline Topology in Two-Dimensional Turbulence. *New J. Phys.* **6**, 65.

148

JULLIEN, M. C. , PARET, J. & TABELING, P. 1999 Richardson Pair Dispersion in Two Dimensional Turbulence. *Phys. Rev. Lett.* **82**, 2872–2875.

TOH, S. & SUZUKI, E. 1994 Entropy Cascade and Energy Inverse Transfer in Two-Dimensional Convective Turbulence. *Phys. Rev. Lett.* **73**, 1501–1505.

TOH, S. & MATSUMOTO, T. 2003 A class of steady solutions to two-dimensional free convection. *Phys. Fluids* **15**, 3385–3396.

TWO-PARTICLE DIFFUSION AND FINE-SCALE STRUCTURES OF TURBULENCE

Yasuhiko Sakai, Haruka Kuwahara
Department of Mechanical Science and Engineering, Nagoya University,
Furo-cho, Chikusa-ku, Nagoya 464-8603, Japan

ysakai@mech.nagoya-u.ac.jp, haruka@sps.mech.nagya-u.ac.jp

Kazuki Maeyama
Honda Motor Co., Ltd.,
Minamiaoyama, Minato-ku, Tokyo 107-0062, Japan

maeyama@grape.plala.or.jp

Hiroyuki Tsunoda
Department of Research Interdisciplinary Graduate School of Medicine and Engineering Science, Yamanashi University,
Koufu, Yamanashi 400-8510, Japan

tsunoda@yamanashi.ac.jp

Abstract   The purpose of this study is to elucidate the relation between a growth of two-particle distance and the fine-scale structures of turbulence by the three-dimensional direct numerical simulation. It is shown that the Lagrangian bursts of particle-pair occur in the straining stagnation region, where $\Delta < 0$ (here, $\Delta = (Q/3)^3 + (R/2)^2$ with Q and R being the 2nd and 3rd invariance of the velocity gradient tensor). The scaling law of $\langle(\Delta l)^2\rangle \sim \tau^\gamma$ (Δl and τ are the increment of separation distance and the diffusion time, respectively) has been investigated. It is found that the relation $\gamma = 6/D_s$ is useful, where D_s is the power exponent of $n_s \approx C_s L^{-3} (L/\eta)^{D_s}$ (L and η are the integral length scale and Kolmogorov microscale, respectively; n_s is the number density of straining stagnation points; C_s is a dimensionless number). It is also shown that the trajectories of particle-pairs in the (Q, R) space are useful to recognize the fine-scale structure bearing the Lagrangian burst of particle-pair.

Keywords: DNS, turbulence, two-particle diffusion, fine-scale structure, Lagrangian burst

1.   Introduction

Two-particle relative diffusion is a fundamental phenomenon in turbulence. To begin with, we consider a pair of fluid particles which leave the given neighboring points at time t_0, and reach the coordinates $\boldsymbol{x_1} = \boldsymbol{x_1}(t)$ and $\boldsymbol{x_2} = \boldsymbol{x_2}(t)$ at a single time $t > t_0$. For the stationary homogeneous turbulence, it is convenient to take t_0 as the origin of time and replace t by $\tau = t - t_0$. In this paper τ is called the diffusion time. The general problem is to determine the statistical characteristics of two-particle separation $l(\tau) = |\boldsymbol{l}(\tau)| = |\boldsymbol{x_2}(t_0+\tau) - \boldsymbol{x_1}(t_0+\tau)|$. It is known that the two-particle diffusion is classified according to the diffusion time τ (Monin & Yaglom 1975). At small diffusion time, the increment of two-particle separation is proportional to τ, while at large diffusion time, it is proportional to $\sqrt{\tau}$. Here, the special attention is given to the transitional period between the small and large diffusion time. At this transitional period, in case of the small initial separation between two particles, the rapid growth of separation distance can be observed (Yeung 1994, Malik & Vassilicos 1999), and it occurs suddenly and intermittently in the space (Fung & Vassilicos 1998). The purpose of this study is to elucidate the relation between a rapid growth of two-particle distance and the fine-scale structures of turbulence by the three-dimensional direct numerical simulation (DNS).

2.   Fine-scale structures of turbulence

The topology of fine-scale motions in turbulence may be classified conveniently by the critical theory (Chong *et al.* 1990). The velocity gradient tensor $W_{ij} = \partial u_i/\partial x_j$ can be decomposed into the symmetric tensor of rate of strain $S_{ij} = (W_{ij} + W_{ji})/2$ and the skew-symmetric tensor of rate of rotation $\Omega_{ij} = (W_{ij} - W_{ji})/2 = -(1/2)\varepsilon_{ijk}\omega_k$ (ω_i being the vorticity and ε_{ijk} the Eddington alternating tensor). For an incompressible flow, the eigenvalues λ of W_{ij} are solutions of the characteristic equation $\lambda^3 + Q\lambda + R = 0$, where $Q = -(1/2)W_{ij}W_{ji} = -(1/2)(S_{ij}S_{ji} + \Omega_{ij}\Omega_{ji}) = (1/2)\{(1/2)\omega_k\omega_k - S_{ij}S_{ji}\} = (1/2)\nabla^2 p$ and $R = -(1/3)W_{ij}W_{jk}W_{ki}$. The discriminant Δ is given by $\Delta = (Q/3)^3 + (R/2)^2$. The local geometry of the flow is characterized by Q and R (or Δ)(see Chong *et al.* 1990 for details). If $\Delta < 0$, the streamlines form stagnation (saddle) points, and if $\Delta > 0$ they show the spiral curves like vortex. Note that in the region of $\Delta < 0$ a sphere is deformed into a "pancake" or a "cigar" according as $R > 0$ or $R < 0$. In the following, the region of $\Delta < 0$ is referred to the "straining stagnation region".

3.   Simulation method and conditions

We perform the DNS of nondecaying homogeneous isotropic incompressible turbulence using a standard pseudospectral code with grids of 128^3. In the velocity fields of Taylor microscale Reynolds numbers Re_λ ranging from 40 to 120, 4096 particle-pairs are released and tracked by the fourth-order-accurate cubic-spline method. In all runs, the initial separation of particle-pairs is set at $l_0/\eta = 1$, where η is the Kolmogorov length.

4.   Results and discussions

First, we investigate what structures cause the rapid growth of the particle-pair separation. When a violent pair separation (here called "Lagrangian burst" of particle-pair) occurs, it is expected that its separation velocity is larger in comparison with other non-bursting particle-pairs. Therefore, we pick up the particle-pair with the largest separation velocity among all the sample particle-pairs in case of $Re_\lambda = 120$, then investigate the Lagrangian time evolutions of Q, R and Δ for that specific bursting particle-pair. In Figs.1a and 1b, we plot the time evolutions of $R(\tau)$ and $\Delta(\tau)$ of each component particle in the particle-pair and the separation distance $l(\tau)$. Here, τ_η is the Kolmogorov time scale, and the superscript $'$ denotes the r.m.s. value. It is found in this figure that the Lagrangian burst of particle-pair is provoked in the region of $R > 0$ and $\Delta < 0$ (note that $Q < 0$ in this case since $\Delta = (Q/3)^3 + (R/2)^2$). This means that this particle-pair meets the pancake type of straining stagnation region, then separates in sudden burst.

Next, we examine the relation between the power law for the mean square separation increment $\langle (\Delta l)^2 \rangle \sim \tau^\gamma$ ($\Delta l = (\Delta l_i \Delta l_i)^{1/2}$, γ is the power exponent) and the spatial distribution of the straining stagnation regions. Dávila & Vassilicos (2003) showed by the kinematic simulations (KS), DNS and laboratory
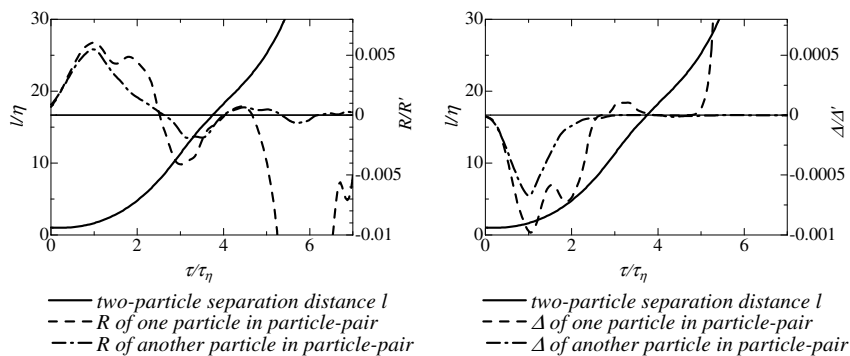

Figure 1a.   Time evolutions of R and l *Figure 1b.*   Time evolutions of Δ and l

experiments of homogeneous isotropic turbulence that the number of straining stagnation points per unit volume is given by

$$n_s \approx C_s L^{-3} \left(\frac{L}{\eta} \right)^{D_s}, \tag{1}$$

where $D_s = 2$, C_s is a dimensionless number and L is the integral length scale. The exponent D_s can be interpreted as a fractal dimension. By KS, they also found that γ and D_s are related by

$$\gamma = \frac{6}{D_s}. \tag{2}$$

When $D_s = 2$, we obtain $\gamma = 3$ which is consistent with Richardson's law. In the present simulations of $40 < Re_\lambda < 120$, the Richardson's law can not be observed because of small Reynolds number, but instead our data showed a τ^4 behavior over $10 < \tau/\tau_\eta < 10^2$. Equation (2) then gives $D_s = 1.5$. In order to check this value of D_s, we estimate the volume V_{ss} of the straining stagnation regions in the space of L^3, and examine the scaling law,

$$V_{ss} \sim \left(\frac{L}{\eta} \right)^{D_{ss}}. \tag{3}$$

The result of this estimation is shown in Fig.2. It is found that $D_{ss} = 1.5$ fits with the data very well. This suggests that the relation (2) holds even if Re_λ is so small that the "locality assumption" for the particle-pair diffusion (see Fung & Vassilicos 1998, Goto & Vassilicos 2004) may not be applicable.

Further, in order to make the role of the straining stagnation regions clearer, we calculated PDF of the square separation increment $(\Delta l)^2 = |\Delta \mathbf{l}|^2 = \Delta l_i \Delta l_i$ under the following three conditions, i.e., [1] both of, [2] at least one of, or [3] neither of two particles are contained in the straining region. The results at $\tau/\tau_\eta = 4$ in case of $Re_\lambda = 120$ are presented in Fig.3. It is found that the PDF in Conditions 1 and 2 is smaller in the range of small separation increment $\Delta l/\eta \leq 17$ ($\Delta l_i \Delta l_i/\eta^2 \leq 300$), and larger around $\Delta l/\eta = 20$ ($\Delta l_i \Delta l_i/\eta^2 = 400$) in comparison with the one in no condition. On the contrary, the PDF in Condition 3 is larger in $\Delta l/\eta \leq 17$, and smaller around $\Delta l/\eta = 20$. This implies that the straining stagnation regions have the effect of increasing the separation distance of particle-pair. Thus, it is expected that the Lagrangian bursts of particle-pair occur in the straining stagnation regions.

Next we investigate the trajectories of particle-pairs in the (Q, R) space. Figure 4 presents the trajectories of a particle-pair undergoing the Lagrangian burst in case of $Re_\lambda = 120$. Particles 1 and 2 are initially at point A and B, respectively and move closely together until particle 1 suddenly starts to go away at point C, presumably because of being trapped by another fine structure. It is
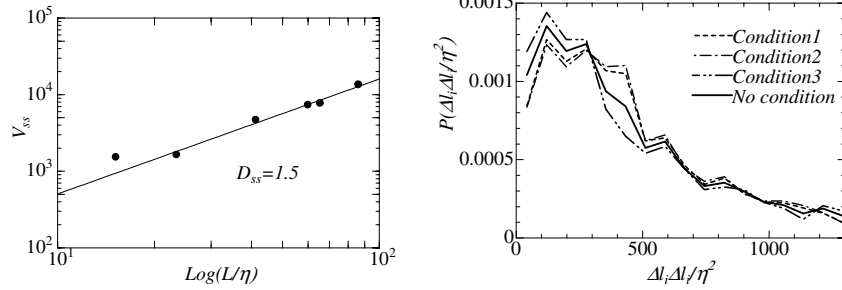
Figure 2. The scaling law $V_{ss} \sim (L/\eta)^{D_{ss}}$

Figure 3. PDF of square separation increment $(\Delta l)^2 = \Delta l_i \Delta l_i$ at $\tau/\tau_\eta = 4.0$ in case of $Re_\lambda = 120$.

also confirmed that the time until the two-particle distance increases rapidly in the (Q, R) space coincides with the time until the Lagrangian burst of particle-pair occurs in the physical space. This result suggests that the trajectories of particle-pairs in the (Q, R) space are useful to recognize the fine-scale structure bearing the Lagrangian burst of particle-pair.
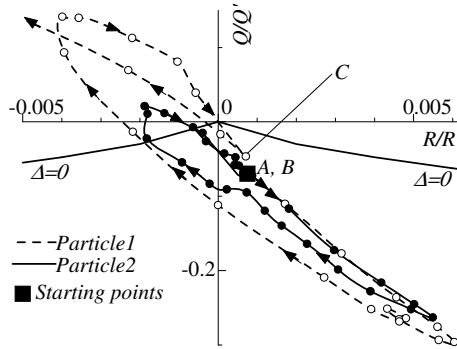
Figure 4. Trajectories of a particle-pair undergoing the Lagrangian burst in the (Q, R) space ; the open and solid circles are plotted at constant time intervals. The parameters with superscript $'$ denote $Q' = u_{r.m.s}^2/\eta^2$, $R' = u_{r.m.s}^3/\eta^3$, where $u_{r.m.s}$ is the r.m.s. value of velocity fluctuation.

5. Conclusions

The results presented in this article show that the most violent particle-pair separation occurs when it meets the pancake type of stagnation region, and the relation $\gamma = 6/D_s$ (equation (2)) is useful even if Re_λ is so small that the "locality assumption" for the particle-pair diffusion (Dávila & Vassilicos 2003, Goto & Vassilicos 2004) is not applicable. It is also shown that the Lagrangian

burst of particle-pair can be recognized well by the trajectories of particle-pair in the (Q, R) space.

Acknowledgments

References

CHONG, M. S., PERRY, A. E. & CANTWELL, B. J. 1990 A general classification of three-dimensional flow fields. *Phys. Fluids* **A2**, 765-777.

DÁVILA, J. & VASSILICOS, J. C. 2003 Richardson's pair diffusion and the stagnation point structure of turbulence. *Phys. Rev. Lett.* **91**, 144501.1-144501.4.

FUNG, J. C. H. & VASSILICOS, J. C. 1998 Two-particle dispersion in turbulentlike flows. *Phys. Rev.* **E57**, 1677-1690.

GOTO, S. & VASSILICOS, J. C. 2004 Particle pair diffusion and persistent streamline topology in two-dimensional turbulence. *New J. Phys.* **6**, 65 (http://www.njp.org/).

MALIK, N. A. & VASSILICOS, J. C. 1999 A Lagrangian model for turbulent dispersion with turbulent-like flow structure: comparison with direct numerical simulation for two-particle statistics. *Phys. Fluids* **11**, 1572-1580.

MONIN, A. S. & YAGLOM, A. M. 1975 *Statistical Fluid Mechanics: Mechanics of Turbulence*, Vol.2, edited by Lumley, J. L., The MIT Press, 536-567.

YEUNG, P. K. 1994 Direct numerical simulation of two-particle relative diffusion in isotropic turbulence. *Phys. Fluids* **6**, 3416-3428.

FLOW DUE TO A POINT VORTEX IN AN OSCILLATING AND ROTATING STRAINING FLOW

Konrad Bajer
Institute of Geophysics, Warsaw University,
ul. Pasteura 7, 02-093 Warszawa, Poland
kbajer@fuw.edu.pl

Michal Branicki
DAMTP, Centre for Mathematical Sciences, University of Cambridge,
Wilberforce Road, Cambridge CB3 0WA, U.K.
M.Branicki@damtp.cam.ac.uk

Abstract   We consider a simple model of transport of a passive scalar around a coherent vortex at distances much larger than its size but much smaller than the distance to its nearest neighbours. The vortex is approximated by a point vortex with circulation Γ, the strain rate has harmonic time-dependence, and the principal axes rotate with constant angular velocity.

Keywords: Chaotic advection, point vortex, time-dependent straining flow, coherent structures in turbulence.

1.   Introduction

The flow in the late stages of the decaying two-dimensional turbulence is dominated by a small number of strong coherent vortices (McWilliams 1984). Except for their brief and relatively infrequent interactions these *coherent structures* move like interacting point vortices, i.e., the motion of their centres can be reasonably described in terms of point vortex dynamics by a finite set of ODEs. The motion of more than three point vortices usually exhibits deterministic chaos while that of three vortices is integrable, unless we take into account their internal structure (Bajer & Matloch 2004). However, even when the motion of vortices is regular, as long as it is unsteady, the trajectories of fluid particles may be chaotic.

155

At close range coherent structures resemble vortex patches of roughly elliptical shape that can be approximated by Kida vortices (Kida 1981). The chaotic pathlines in their vicinity had been studied previously (Polvani & Wisdom 1990). Here we investigate the kinematics of the flow at a distance sufficient to make the point-vortex approximation. We focus on one vortex and approximate the combined effect of distant companions as time-dependent linear strain (Jimenez *et al.* 1996).

The system exhibits rich behaviour with different characteristics in different regions. Close to the vortex the straining flow can be regarded as small perturbation of the vortex flow while far away we have the opposite situation. Both regimes allow analytical treatment (Branicki 2001) the details of which will be described elsewhere.

2. Dynamical system

The time-dependence of the the ambient strain at the location of a given vortex is caused by the change of positions of its neighbours. That change of positions can be, broadly speaking, decomposed into rotation and deformation. The rotation of the system of neighbours results in the rotation of the principal axes of strain while deformation results in the change of the strain rate. In the following we assume that the principal axes of strain rotate with *constant* angular velocity λ and the strain rate $\beta(t)$ has harmonic time variation

$$\beta(t) = B \frac{\Delta + \cos(\omega t)}{\Delta + 1} = Bb(t), \qquad B, \, \Delta, \, \omega \text{ — arbitrary constants.} \quad (1)$$

When written in a frame of reference co-rotating with strain the flow can be described by a two-dimensional, non-autonomous dynamical system

$$\begin{bmatrix} \dot{x} \\ \dot{y} \end{bmatrix} = \frac{\Gamma}{2\pi \left(x^2 + y^2\right)} \begin{bmatrix} -y \\ x \end{bmatrix} + \begin{bmatrix} -Bb(t) & \lambda \\ -\lambda & Bb(t) \end{bmatrix} \begin{bmatrix} x \\ y \end{bmatrix}. \quad (2)$$

Using natural units of length and time, $L = (\Gamma/2\pi B)^{1/2}$, $T = B^{-1}$, we rewrite the (non-dimensionalised) equations in polar coordinates (ϱ, φ) obtaining

$$\dot{\varrho} = -\varrho \cos 2\varphi \frac{\Delta + \cos \Omega\tau}{\Delta + 1},$$

$$\dot{\varphi} = \sin 2\varphi \frac{\Delta + \cos \Omega\tau}{\Delta + 1} + \frac{1}{\varrho^2} - \Lambda, \quad (3)$$

where $\Omega = \omega/B$, $\Lambda = \lambda/B$ and $\tau = Bt$. As we can see, the problem is determined by three dimensionless parameters: the rotation rate of the principal axes of strain Λ; the frequency of the variations of the strain amplitude Ω and the amplitude (bias parameter) of those variations Δ.

The exploration of the three-dimensional parameter space of this problem reveals a rich and diverse behaviour of the system.
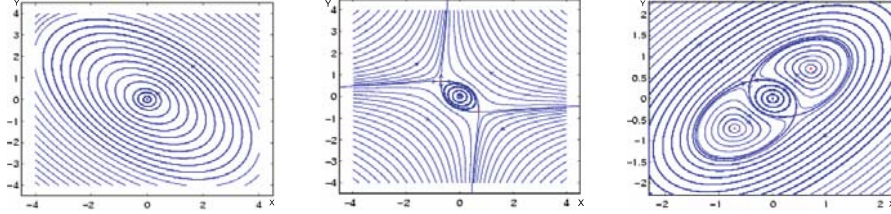
Figure 1. Streamlines of the steady ($\Omega = 0$) flow (3) with $\Lambda = -2$ (left), $\Lambda = 0$ (middle) and $\Lambda = 2$ (right).

3. Steady state

When $\Omega = 0$ the system (3) is two-dimensional, time-independent and therefore integrable. Its phase portrait depends only on Λ.

For $\Lambda = 0$ we have a typical cat's eye pattern with two hyperbolic stagnation points at the distance where the strain and the vortex flow are comparable. Then the asymptotic angle of the separatrices is $90°$. In co-rotating strain ($\Lambda < 0$, the same sense of rotation as the vortex), as Λ decreases there is a bifurcation at $\Lambda = -1$ upon which the two hyperbolic stagnation points disappear at infinity and for $\Lambda < -1$ we have a simple recirculating flow with closed streamlines. In the counter-rotating strain ($\Lambda > 0$) there is a bifurcation at $\Lambda = 1$ when two new elliptical stagnation points are born at infinity and approach the vortex as Λ increases (figure 1). When the strain rate becomes time-dependent ($\Omega \neq 0$) the flows shown in figure 1 are perturbed. The exact stroboscopic maps of the pathlines may, in general, be obtained only numerically except in some special parameter regimes when they can be approximately calculated analytically. One example is the highly symmetric situation with non-rotating ($\Lambda = 0$) and sign-reversing ($\Delta = 0$) strain.

4. Far field in the highly symmetric case $\Lambda = \Delta = 0$

In the far field the vortex is a small perturbation of strain. When we rescale the radial coordinate, $\varrho \to \epsilon^{-1/2}\varrho$ and put $\Lambda = \Delta = 0$, the system (3) becomes

$$\dot{\varrho} = -\varrho \cos 2\varphi \cos \Omega\tau, \qquad \dot{\varphi} = \sin 2\varphi \cos \Omega\tau + \epsilon\varrho^{-2}, \qquad \epsilon \ll 1. \quad (4)$$

The unperturbed system, $\epsilon = 0$, has two invariants,

$$I = \tfrac{1}{2}\varrho^2 \sin 2\varphi, \qquad C = e^{\Omega^{-1}\sin\Omega\tau}\left(\varrho\sin\varphi\right)^{-1}, \quad (5)$$

that change slowly upon perturbation thus defining an *adiabatic invariant* that can be computed. Figure 2 shows that the Poincaré sections of the perturbed system indeed lie on the surfaces of this adiabatic invariant.
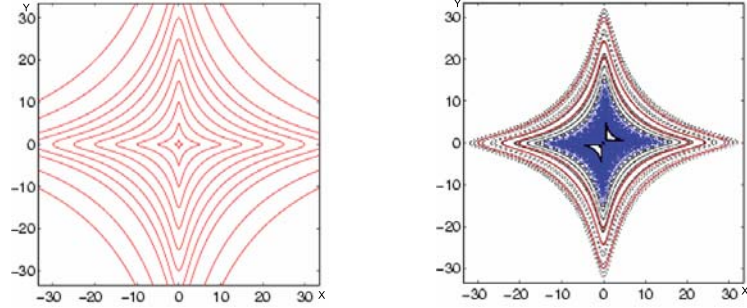
Figure 2. The highly symmetric case, $\Lambda = \Delta = 0$. The surfaces of constant adiabatic invariant (left) and computed Poincaré sections of the sytem (4). The sections are the stroboscopic maps with common period of all unperturbed orbits, i.e. $T = 2\pi\Omega^{-1}$.

5. Near field and intermediate field

The system (3) can be cast in a (non-autonomous) Hamiltonian form. In the near field, $\varrho \ll 1$, we use the rescaling $\varrho \to \epsilon^{1/2}\varrho$. The Hamiltonian expressed in terms of the action-angle variables becomes

$$H = -\tfrac{1}{2}\ln J + \epsilon J\Lambda + \epsilon J\sin 2\theta\frac{\Delta + \cos\Omega\tau}{\Delta + 1}, \qquad J = \tfrac{1}{2}\varrho^2, \quad \theta = -\varphi, \qquad \epsilon \ll 1,$$

(6)

which is a sum of two Hamiltonians: the Hamiltonian corresponding to pure point vortex flow and the perturbing Hamiltonian due to strain. The action variable is, clearly, an invariant of the unperturbed system (pure vortex). For $\epsilon > 0$, a new invariant can be calculated by means of the canonical perturbation theory. In figure 3 we compare the results of such calculations with the computed stroboscopic sections of the perturbed system for one particular choice of parameters. The dashed line in the left panel of figure 3 is the outline of the rational torus whose breakup gave rise to two primary islands (Tabor 1989).
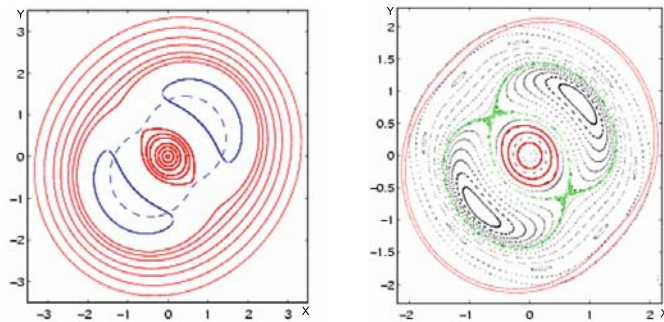

Figure 3. The near field. The isosurfaces of the invariant derived from the canonical perturbation theory (left) and the computed Poincaré sections of the sytem (right).

Finally in figure 4 we show the computed Poincaré sections for three different sets of parameters chosen to illustrate the complexity of the phase-space structure for this apparently simple system. The time-dependent, Hamiltonian perturbation creates localised regions of strong chaos. It may also mimic diffusion when a prticle 'leaks' across the cat's eye boundary and is carried away by the straining flow. Further details will be presented in a forthcoming article.
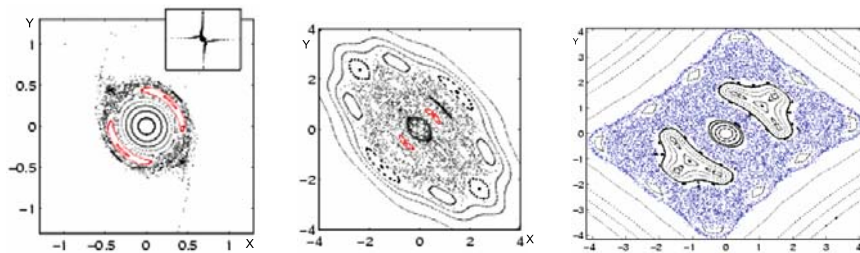

Figure 4. Poincaré sections of the system (3) for such values of the parameters for which various chaotic domains are particularly prominent: $\Omega = 10.1, \Lambda = 0, \Delta = 1.5$ (left); $\Omega = 2.1, \Lambda = 0.5, \Delta = 0$ (middle); $\Omega = 1.1, \Lambda = 0, \Delta = 0$ (right).

Two-dimensional turbulence is ruled by the motion of a relatively small number of coherent vortices that may spontanaeously emerge from a sea of small-scale vorticity. Each vortex feels the presence of other vortices whose combined influence is, in the first approximation, that of an irrotational ambient straining flow with variable rate of strain. The model presented in this paper reveals the complexity of advection between coherent structures. This advection, when combined with viscous diffusion, influences the level of weak background vorticity in two-dimensional turbulence.

References

BAJER, K. & MATLOCH, Ł. 2004 Dynamics of asymmetric point vortices. In *Advances in Turbulence X* (Proceedings of the Tenth European Turbulence Conference, 29 June – 2 July 2004, Trondheim, Norway, eds. H. I. Andersson & P.-Å. Krogstad), p. 824. CIMNE.

BRANICKI, M. 2001 Flow kinematics near a point-vortex in a time-dependent straining flow. M. Sc. thesis. Warsaw University.

JIMÉNEZ, J., MOFFATT, H. K. & VASCO, C. 1996 The structure of the vortices in freely decaying two-dimensional turbulence. *J. Fluid Mech.* **313**, 209–222.

160

KIDA, S. 1981 Motion of an elliptic vortex in a uniform shear flow. *J. Phys. Soc. Japan*, **50**, 35-17–3520.

MCWILLIAMS, J. 1984 The emergence of isolated coherent vortices in turbulent flow. *J. Fluid Mech.* **146**, 21–43.

POLVANI, L. M. & WISDOM, J. 1990 On chaotic flow around the Kida vortex. In *Topological Fluid Mechanics* (Proceedings of the IUTAM Symposium, Cambridge, 13–August 1989, ed. H.K. Moffatt & A. Tsinober), pp. 34–44. Cambridge University Press.

TABOR, M. 1989 *Chaos and Integrability in Nonlinear Dynamics: An Introduction*. Wiley 1989.

Part D Statistical properties of turbulence

STATISTICAL PROPERTY OF PRESSURE FLUCTUATION IN FULLY DEVELOPED TURBULENCE

Yoshiyuki Tsuji

Department of Energy Engineering and Science, Graduate School of Engineering, Nagoya University,

Furocho, Chikusa-ku, Nagoya 464-8603, Japan

c42406a@nucc.cc.nagoya-u.ac.jp

Takashi Ishihara

Department of Computational Science and Engineering, Graduate School of Engineering, Nagoya University,

Furocho, Chikusa-ku, Nagoya 464-8603, Japan

Abstract   Pressure fluctuation is measured by using a condenser microphone and piezoresistive transducer. In order to confirm the experimental accuracy, measured data are compared with direct numerical simulation. This basic test encourages us to study small-scale statistics from the standpoint of Kolmogorov universal scaling. The power-law exponent and proportional constant of normalized pressure spectrum are discussed. The clear power law with scaling exponent $-7/3$ is confirmed in the range of $R_\lambda \geq 600$. These Reynolds numbers are much larger than those in velocity fluctuation for achieving the Kolmogorov scaling. The spectral constant K_p is not universal but depends on Reynolds number.

Keywords: Turbulence, pressure statistics, universal spectral scaling

1.   Introduction

Pressure is a fundamental quantity contained in the dynamical equation of fluid motion. In a usual notation, pressure relates to the acceleration vector, $\mathbf{a} = D\mathbf{u}/Dt = -\nabla(p/\rho) + \nu\nabla^2\mathbf{u}$. This means that acceleration is decomposed into the contributions from the pressure gradient and viscous force, while the fluid density ρ is constant (Monin & Yaglom 1975). Taking the divergence of the acceleration equation together with the incompressibility condition, we obtain the Poisson equation, $\nabla^2(p/\rho) = -\partial u_i/\partial x_j \partial u_j/\partial x_i$ $(i, j = 1, 2, 3)$. Only the velocity derivative terms appear on the right-hand side, so small-scale velocity

fluctuations dominate the pressure gradient. It is known that large negative pressure indicates large vorticity or small dissipation region. Pressure is the key physical quantity to identify the small-scale structures and plays an important role in acceleration (Nelkin 1994, Sreenivasan & Antonia 1997). However, it is the least understood quantity due to the difficulty inherent in measuring this term by conventional equipment. In this paper, we measure the static pressure fluctuation in a fully developed turbulence, and study its statistical property from the standpoint of Kolmogorov scaling (Tsuji & Ishihara 2003).

2. Experimental condition

The data are measured on the centerline in a free jet. A small wind tunnel with a 40×40 mm^2 nozzle size and a large wind tunnel with a 400×700 mm^2 nozzle is operated in the velocity range of $5 \leq U_J \leq 15$. U_J m/s is the average velocity at the nozzle exit. The Reynolds numbers are in the range of $200 \leq R_\lambda \leq 1200$, here R_λ is the Taylor micro-scale Reynolds number. Velocity and pressure fluctuations are measured at the same time. Velocity fluctuation is measured by a hot-wire made of tungsten wire with a diameter of $\phi = 5$ μm and a sensitive length of $\ell_s = 0.7$ mm. The probe is operated by a constant-temperature anemometer and it is set at a distance of 2 mm from the pressure probe. The measurement of pressure fluctuation in the flow field is accomplished with a small piezoresistive transducer, and a standard quarter-inch condenser microphone developed by Kobashi (1957), Toyoda *et al.* (1993). The detailed conditions are mentioned in Tsuji & Ishihara (2003).

The transducer has a frequency response from DC up to 150 kHz with a dynamic range of 3.5×10^3 Pa. The maximum errors contained in linearity and hysteresis are 0.25%. A microphone is available for measuring the frequency of $20 \sim 70 \times 10^3$Hz. The lower frequency is restricted owing to its mechanical system. The dynamic range is $2 \times 10^{-2} \sim 3.2 \times 10^3$ Pa, so a very small amplitude can be measured. The probe is a standard Pitot-static tube measuring 1.0 mm in outside diameter and 0.1 mm in thickness. Four static-pressure holes (0.4 mm in diameter) are spaced $90°$ apart and located at a distance of 22 tube diameters from the tip of the probe to minimize sensitivity to cross-flow error. The leeward end is terminated by the microphone or transducer. The sensor diameters are $d_T = 1.6$ mm and $d_M = 7.0$ mm for the transducer and microphone, respectively.

The transducer can detect the low-frequency pressure, but its amplitude cannot be small. The measurable amplitude is put at more than 10 Pa. The microphone can detect a very small amplitude, but low-frequency data cannot be obtained. This ability is the reverse to a transducer. Thus, a microphone is preferred for use with a low Reynolds-number flow, because of its small amplitude but moderate-scale motions with a frequency of more than 20 Hz. The

static pressure increases with the Reynolds number, and large-scale motions are generated accordingly. In this condition, a transducer is used instead of a microphone for measurement. We suppose that a microphone is available up to $R_\lambda \simeq 350$, but a transducer may be used beyond this Reynolds number. The sensors are fitted with tubing as a pressure duct, as shown in Fig. 1, and are inserted into the flow domain in such a way that the axis of the microphone (or the transducer) itself is aligned with the mean stream. We have preliminarily checked the angle between the pressure probe and the flow direction for its effect on the measured data. The error was less than 2.5% for $-15 \le \theta \le +15$. Statistical quantities such as spectrum and pdf does not change significantly while θ is not so large. The frequency response of the system is limited by the Helmholtz-resonator response of the tube and sensor cavity (Kobashi 1957, Toyoda et al.1993) Toyoda et al.1993).

DNS of incompressible homogeneous turbulence is performed using periodic boundary conditions of periods of 2π in each of the three Cartesian coordinate directions. There are three different runs in which $R_\lambda = 94\,(N = 256^3)$, $164\,(N = 512^3)$, and $283\,(N = 1024^3)$. Here N is the number of grid points. An almost statistically stationary state is achieved with an energy flux nearly equal to the energy dissipation rate $\langle \varepsilon \rangle$ in the case of $R_\lambda = 283$. Detailed explanations on DNS are given in Ishihara *et al.* (2003).

3. Results and discussion

3.1 Quantitative evaluation of measured data

Observing the measured pressure fluctuation, as shown in Fig. 2, it is noted that its fluctuation takes occasionally large negative values. This might correspond to the small vortex filaments visualized by Douady *et al.* (1991). The probability density function (PDF) of pressure is plotted in Fig. 3, which is negatively skewed. In order to check the quantitative accuracy, measured PDF
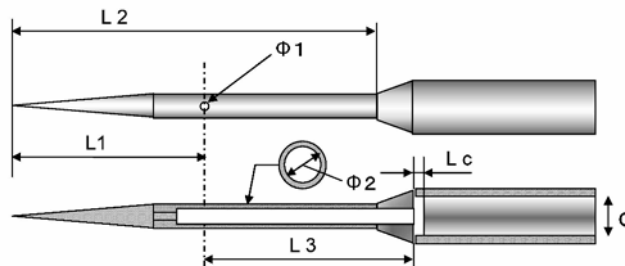

Figure 1. Schematic view of static pressure probe. $\phi_1 = 0.4$ mm, $\phi_2 = 1.0$ mm, $L_1 = 22.5$ mm, $L_2 = 47.5$ mm, $L_3 = 30.0$ mm.
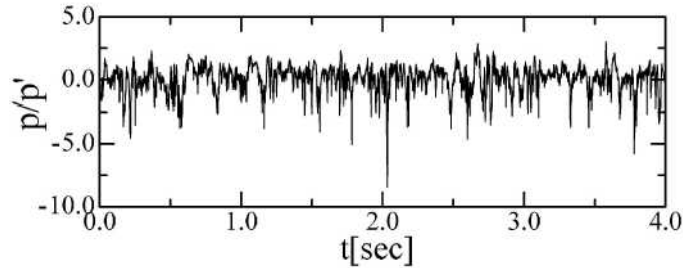
Figure 2. Typical example of pressure fluctuation at $R_\lambda = 1150$. Vertical axis is normalized by its standard deviation.

is compared with that of DNS for almost the same Reynolds number. PDF shifts to the positive side and its maximum peak locates slightly away from $p = 0$. There is a small qualitative difference between DNS and the experiment around $|p/p'| \leq 1$, where p' is a standard deviation of p. On the positive side, experimental values are slightly larger than DNS. They are closer to the Gaussian profile. On the negative side, $-6 \leq p/p' \leq 0$, PDFs agree with one another sufficiently.
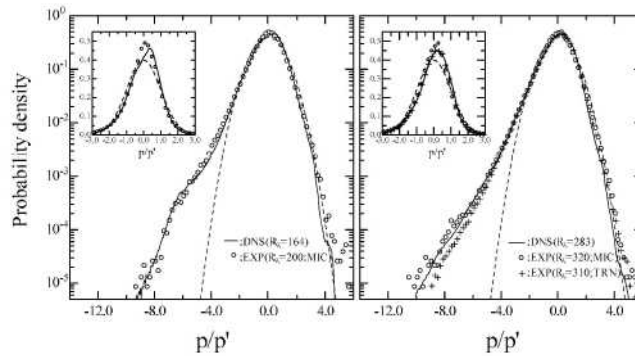
Figure 3. PDF of measured pressure (symbols) are compared with DNS (solid lines). p' is a standard deviation of p. Insets show the core region $|p/p'| \leq 3.0$. Dotted line is Gaussian profile.

Two-point pressure correlations can be expressed in terms of fourth-order structure functions of velocity. In homogeneous isotropic flow, the longitudinal velocity correlation coefficient $f(r)$ is used for evaluating the right-hand side of the Poisson equation subject to the quasi-normal assumption. It means that fourth-order velocity structure functions are represented by products of factored second-order quantities (Monin & Yaglom 1975). Using this assumption, the
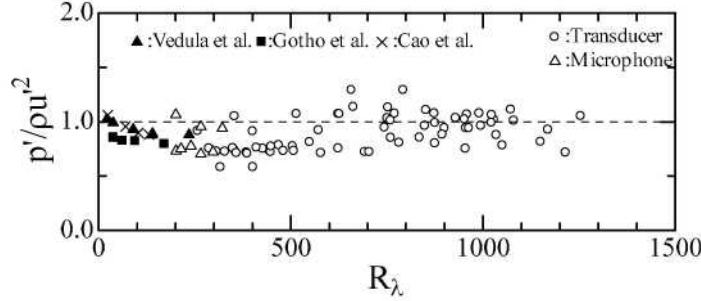
Figure 4.   Root-mean-square of pressure fluctuation is normalized by $\rho u'^2$, where u' is standard deviation of streamwise velocity fluctuation.

root-mean-square of pressure is scaled by $\rho u'^2$ like $p'/(\rho u'^2) = C_1$, where u' is a standard deviation of velocity fluctuation. In the case of an empirical relation, $f(r) \simeq \exp(-r^2)$, C_1 is about 0.7 (Hinze 1975). Batchelor evaluated $C_1 = 0.58$ by using $f(r)$ obtained in a high Reynolds number experiment (Monin & Yaglom 1975). Recent DNS data suggest $0.8 \leq C_1 \leq 1.0$ for $R_\lambda < 300$ but a weak dependence of Reynolds number is confirmed (Gotoh & Fukayama 2001, Vedula & Yeung 1999, Cao, Chen & Doolen 1999). In the course of this study, C_1 is found to be slightly dependent on R_λ. C_1 is about 0.7 in the low-Reynolds-number range, but increases gradually up to 1.0 until R_λ reaches 700. In larger Reynolds numbers, $700 \leq R_\lambda \leq 1200$, the ratio is almost constant; $C_1 \simeq 1.0$. As plotted in Fig. 4, these experimental results indicate quantitative agreement with the present DNS results.

3.2   Scaling of pressure spectrum

Kolmogorov presented hypotheses for small-scale statistics based on the idea of local isotropy, which is restated by the relation,

$$E_{pp}(k_1) = \rho^2 \langle \varepsilon \rangle^{3/4} \nu^{7/4} \phi_p(k_1 \eta) , \tag{1}$$

for the case of pressure fluctuation, where ν is kinetic viscosity, $\langle \varepsilon \rangle$ is energy dissipation rate per unit mass on average, and η is a typical length scale defined by $\eta \equiv (\nu^3 / \langle \varepsilon \rangle)^{1/4}$. The wavenumber is defined by $k_1 \equiv 2\pi f/U$, where f is the time frequency and U the local mean velocity. ϕ_p is a non-dimensional function. When the Reynolds number becomes large, according to Kolmogorov's idea, the spectrum exhibits a simpler form independent of kinetic viscosity as

$$E_{pp}(k_1) = K_p \rho^2 \langle \varepsilon \rangle^{4/3} k_1^{-7/3} . \tag{2}$$

The $-7/3$ power-law scaling was supported theoretically with various assumptions in 1950's by Batchelor (1951), Inoue (1951), and Obukhoff & Yaglom
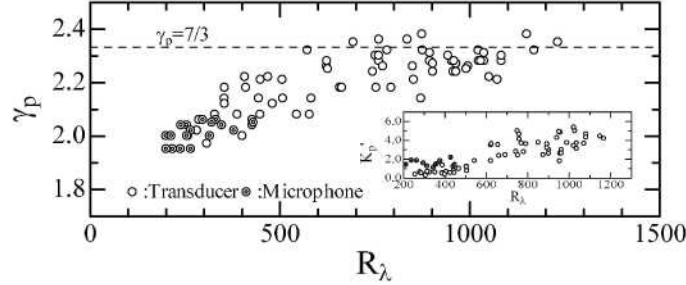
Figure 5.   Scaling exponent γ_p and constant K_p' defined by Eq. (3) are plotted as a function of Reynolds number.

(1951). George *et al.* (1984) and Jones *et al.* (1979) measured the pressure spectrum in the mixing layer of a round jet, and Elliott (1972) and Albertson *et al.* (1998) measured the pressure in the atmospheric boundary layer. But all these experiments were not enough to ascertain the power-law scaling exponent and the scaling form of Eq. (1). The relation was also investigated by analyzing the data of direct numerical simulation of homogeneous isotropic turbulence (Pumir 1994; Gotoh & Fukayama 2001; Vedula & Yeung 1999; Cao *et al.* 1999). However, the Reynolds number was too low to confirm the validity of the scaling form. At this stage, there is no consensus on the scaling exponent of the pressure spectrum and on the Kolmogorov similarity scaling.

We study here how the spectral form varies depending on the Reynolds number. Especially, the spectral exponent and constant K_p are studied from the standpoint of Kolmogorov scaling. A power-law exponent of pressure spectrum is systematically obtained by fitting the relation

$$E_{pp}(k_1) = K_p{'}\rho^2 \langle \varepsilon \rangle^{3/4} \nu^{7/4}(k_1\eta)^{-\gamma_p} , \qquad (3)$$

against the measured spectrum, while the normalized spectrum $E_{pp}/(k_1\eta)^{-\gamma_p}$ shows the broadest flat region. $K_p{'}$ is a non-dimensional quantity. If the scaling exponents γ_p are plotted as a function of R_λ, they indeed depart from $7/3$ in low Reynolds numbers. This trend is similar to the results of DNS. But the exponents certainly approach $7/3$ as the Reynolds number increases. In this experiment, the $-7/3$ power-law scaling is confirmed for $600 \ll R_\lambda$. Small-scale intermittency effect is not discussed here.

There has been little discussion as to the value of a spectral constant. We had systematically obtained K_p' by way of Eq. (3). K_p' is a increasing function of R_λ, and it is 5.0 ± 1.0 at $R_\lambda \simeq 1000$. By fitting $E_{pp}(k_1) = K_p\rho^2 \langle \varepsilon \rangle^{4/3} k_1^{-7/3}$ against the measured spectrum, we found that K_p is about 6.5 at $R_\lambda = 1030$. Therefore, we conclude that the Reynolds number dependence of K_p is not neg-
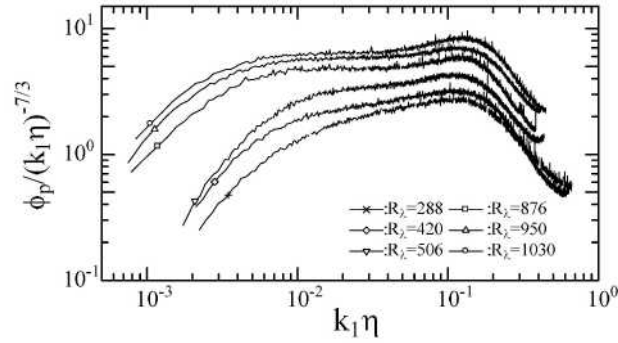
Figure 6. Pressure spectra are normalized by Kolmogorov scaling defined by Eq. (3) with $\gamma_p = 7/3$.

ligible. The exponent γ_p approaches $7/3$ when R_λ is larger than 600. This is a significantly higher Reynolds number than needed for inertial scaling in velocity statistics. The pressure spectrum has a noticeably narrower scaling region than the velocity. This is consistent with the result that the higher Reynolds number is needed to realize a clear $-7/3$ power-law scaling (Ishihara *et al.* 2003).

In Fig. 6 the pressure spectra are normalized in Kolmogorov scaling defined by Eq. (3) with $\gamma_p = 7/3$. As the Reynolds number increases, a flat region appears where we expect the inertial range. In the dissipation region, there is a small bump for $0.03 \leq k_1\eta$. It takes a maximum around $k_1\eta = 0.14$. However, in low Reynolds numbers it is difficult to distinguish between the inertial range and the bump region. Thus, the power low exponent γ_p inevitably represents the slope of the beginning part of the bump. Gotoh & Fukayama (2001) reported that the $-5/3$ slope observed in DNS is due to the spectral bump around $k\eta \simeq 0.2$. Comparing the spectral bump in the experiment with that of DNS, we see that the bump exists at almost the same location ($0.03 \leq k\eta$), but the DNS bump steeply increases and takes its maximum at $k\eta \simeq 0.2$. The maximum value, depending on the Reynolds number, is clearly larger than that in the experiment.

References

ALBERTSON, J. D., KATUL, G. G., PARLANGE, M. B., AND EICHINGER, W. E. 1998, Spectral Scaling of Static Pressure Fluctuations in the Atmospheric Surface Layer: The Interaction between Large and Small Scales, *Physics of Fluids*, **10**, 1725–1731.

BATCHELOR, G. K. 1951, Pressure Fluctuations in Isotropic Turbulence, *Proc. Camb. Phil. Soc.*, **47**, 359–374.

CAO, N., CHEN, S. & DOOLEN, G. D. 1999, Statistics and Structures of Pressure in Isotropic Turbulence, *Phys. of Fluids*, **11**, 2235–2250.

170

DOUADY, S., COUDER, Y. & BRACHET, M. E. 1991, Direct Observation of the Intermittency of Intense Vorticity Filaments in Turbulence, *Physical Rev. Lett.*, **67** 983–986.

ELLIOTT, J. A. 1972, Microscale Pressure Fluctuations Measured within the Lower Atmospheric Boundary Layer, *J. Fluid Mech.*, **53**, 351–383.

GOTOH, T. & FUKAYAMA, D. 2001, Pressure Spectrum in Homogeneous Turbulence, *Phys. Rev. Lett.*, **86** 3775–3778.

GEORGE, W. K., BEUTHER, P. D. AND ARNDT, R. E. A. 1984, Pressure Spectra in Turbulent Free Shear Flows, *J. Fluid Mech.*, **148**, 155–191.

HINZE, O. 1975, *Turbulence*. McGraw-Hill, New York.

INOUE, E. 1951, The Application of the Turbulence Theory to the Large-scale Atmospheric Phenomena, *Geophys. Mag.*, **23**, 1–14.

ISHIHARA, T., KANEDA, Y., YOKOKAWA, M., ITAKURA, K. & UNO, A. 2003, Spectra of Energy Dissipation, Enstrophy and Pressure by High-Resolution Direct Numerical Simulations of Turbulence in a Periodic Box, *J. Phys. Soc. Jpn.*, **72**, 983–986.

JONES, B. G., ADRIAN, R. J., NITHIANANDAN, C. K., PLANCHON JR., H. P., 1979, Spectra of Turbulent Static Pressure Fluctuations in Jet Mixing Layers, *AIAA Journal*, **17**, 449–457.

KOBASHI, Y. 1957, Measurements of Pressure Fluctuation in the Wake of Cylinder, *J. Physical Soc. Japan*, **12** 533–543.

MONIN, A. S. & YAGLOM, A. M. 1975, *Statistical Fluid Mechanics*. MIT, Cambridge, MA, Vol. 2.

NELKIN, M. 1994, Universality and Scaling in Fully Developed Turbulence, *Advances in Physics*, **43** 143–181.

OBUKHOFF, A. M. AND YAGLOM, A. M. 1951, The Microstructure of Turbulent Flow, *NACA TM 1350*.

PUMIR, A. 1994, A Numerical Study of Pressure Fluctuations in Three-dimensional, Incompressible, Homogeneous, Isotropic Turbulence, *Phys. Fluids*, **6**, 2071–2083.

SREENIVASAN, K. R. & ANTONIA, R. A. 1997, The Phenomenology of Small-scale Turbulence, *Annu. Rev. Fluid Mech.*, **29** 435–472.

TOYODA, K., OKAMOTO, T, & SHIRAHAMA, Y 1993, Eduction of Vortical Structures by Pressure Measurements in Noncircular Jet, *Fluid Mech. and Its Applications*, **21** 125–136.

TSUJI, Y. & ISHIHARA, T. 2003, Similarity Scaling of Pressure Fluctuation in Turbulence, *Physical Rev. E*, **68** 026309.

VEDULA, P. & YEUNG, P. K. 1999, Similarity Scaling of Acceleration and Pressure Statistics in Numerical Simulation of Isotropic Turbulence, *Phys. of Fluids*, **11**, 1208–1220.

INTERMITTENCY, FIELD STRUCTURES AND ACCURACY OF DNS IN A PASSIVE SCALAR TURBULENCE

Takeshi Watanabe, Toshiyuki Gotoh
Department of Mechanical Engineering, Applied Physics Program, Nagoya Institute of Technology,
Gokiso, Showa-ku, Nagoya 466-8555 Japan
watanabe@nitech.ac.jp, gotoh.toshiyuki@nitech.ac.jp

Abstract   Resolution requirements of direct numerical simulation (DNS) for passive scalar advected by homogeneous turbulence are numerically investigated. We examine the effects of dissipation intermittency on the small-scale statistics by performing DNSs with various spatial resolutions at the fixed Reynolds number $R_\lambda \simeq 180$. It is found that the statistics of intermittent fluctuations for the energy and scalar dissipations strongly depend on the value of cutoff wavenumber K_{max}. However the behavior of spectra and high-order structure functions at the scales much larger than the Kolmogorov scale $\bar\eta$ are found to be insensitive to the variation of $K_{max}\bar\eta$.

Keywords: Passive scalar, intermittency, direct numerical simulation

1.   Introduction

It is well-known from the direct numerical simulations (DNSs) and experiments for the homogeneous turbulence that the energy dissipation field $\epsilon(\mathbf{x}) = \nu(\partial_i u_j + \partial_j u_i)^2/2$ shows strong intermittency of fluctuations (Frisch 1995). It is thought that such a dissipation intermittency poses the stringent resolution requirements of DNS (Sreenivasan 2004), which is given by

$$K_{max}\eta_{min} \geq 1, \tag{1}$$

instead of the usual requirement by $K_{max}\bar\eta \geq 1$, where K_{max} is a cutoff wavenumber due to the truncation of Fourier series expansion, $\bar\eta = (\nu^3/\bar\epsilon)^{1/4}$ is the Kolmogorov scale. The smallest dissipation scale η_{min} is defined by $\eta_{min} \equiv (\nu^3/\epsilon_{max})^{1/4} = (\bar\epsilon/\epsilon_{max})^{1/4}\bar\eta$, where ϵ_{max} is the largest value of $\epsilon(\mathbf{x})$ in space. A multifractal theory of turbulence (Frisch 1995) evaluates $\epsilon_{max}/\bar\epsilon \sim R_\lambda^2$ (Sreenivasan 2004), where R_λ is the Taylor microscale Reynolds number. The existence of strong intermittency means $\epsilon_{max}/\bar\epsilon \gg 1$. In this case,

the resolution requirement based on $\bar{\eta}$, i.e. $K_{max}\bar{\eta} = 1 \sim 2$ as used in the recent DNSs (Wang *et al.* 1999, Yeung *et al.* 2002, Gotoh *et al.* 2002), yields the failure of (1); $K_{max}\eta_{min} \ll 1$. Thus the statistical nature at sub-Kolmogorov scale must be affected by the contaminations around K_{max}.

The effects of dissipation intermittency on the resolution requirement of DNS become to be more significant in the case for the passive scalar in turbulence (Sreenivasan 2004). This is originated from the empirical fact that the dissipation field of the scalar variance $\chi(\mathbf{x}) = \kappa(\partial_i\theta)^2$ exhibits stronger intermittency of fluctuation than that in $\epsilon(\mathbf{x})$ (Warhaft 2000), where κ is diffusivity. The dissipation scale of scalar variance, namely the Batchelor scale $\bar{\eta}_B = (\kappa^2\nu/\bar{\epsilon})^{1/4}$, varies with the Schmidt number $S_C = \nu/\kappa$ as

$$\bar{\eta}_B = S_C^{-1/2}\bar{\eta}. \tag{2}$$

This relation means that the spatial resolution finer than that only in the velocity field is required for the passive scalar DNS with $S_C \gg 1$ in order to resolve the small-scale natures in the scalar field.

Above suggestions bring us a very important problem when we aim to realize as high-R_λ turbulence as possible by DNS in the limited computational resource. Is the resolution requirement $K_{max}\bar{\eta} = 1$ adequate for the DNS of high-R_λ turbulence with passive scalar transport even when $S_C = 1$? The purpose of the present study is to examine this point by investigating the effect of the contamination around K_{max} on the behavior of several important statistical quantities like the spectra and structure functions.

2. Direct numerical simulations and results

The fundamental equations of motion for the incompressible velocity field $u_i(\mathbf{x}, t)$ $(i = 1, 2, 3)$ and the scalar field $\theta(\mathbf{x}, t)$ are given by the Navier-Stokes equation and the advection diffusion equation, respectively. We consider only a case of $S_C = 1$. Several settings of DNS and the definitions of statistical quantities are the same ways as those in our previous paper (Watanabe & Gotoh 2004). All the parameters included in a series of DNS are fixed except the spatial resolution N^3 (or K_{max}). We performed three cases of DNS, which are named as Run A ($N = 256^3$, $K_{max}\bar{\eta} = 1.0$), Run B ($N = 512^3$, $K_{max}\bar{\eta} = 2.0$) and Run C ($N = 1024^3$, $K_{max}\bar{\eta} = 3.7$). In these cases, we obtained the turbulent states with $R_\lambda \simeq 180$, and the values of fundamental statistics like the normalized mean dissipations $(\hat{\epsilon}, \hat{\chi}) = (0.48, 0.32)$, the integral scales $(L, L_\theta) = (1.20, 0.78)$ and the Taylor microscales $(\lambda, \lambda_\theta) = (0.21, 0.12)$ were almost independent of N. Moreover, we refer to our previous result of the high-R_λ DNS with the passive scalar transport (Run 2 in Watanabe & Gotoh 2004); the case for $R_\lambda = 427$, $N = 1024^3$ and $K_{max}\bar{\eta} = 1.06$ is named as WG04.
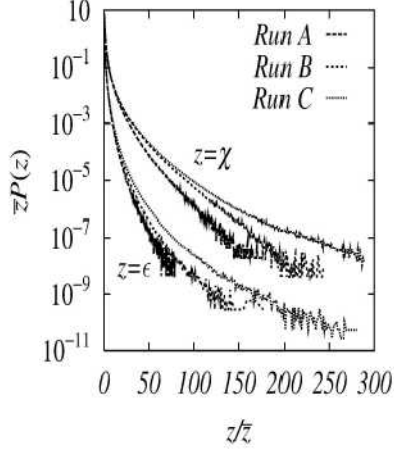
Figure 1a. $K_{max}\bar{\eta}$-dependences of PDFs for $\epsilon/\bar{\epsilon}$ and $\chi/\bar{\chi}$. Curves for χ are shifted by 10 for clarity.
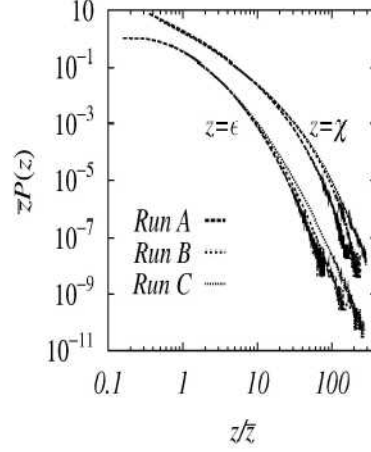
Figure 1b. Log-log plot of figure1a.

Figure 1 shows the behavior of probability density functions (PDFs) for $\epsilon/\bar{\epsilon}$ and $\chi/\bar{\chi}$ obtained by Runs A, B and C. The PDFs for $\chi/\bar{\chi}$ have larger probabilities of rare fluctuations than those for $\epsilon/\bar{\epsilon}$. Thus $\chi/\bar{\chi}$ is more intermittent than $\epsilon/\bar{\epsilon}$. The probabilities in the tail part for both cases increase as $K_{max}\bar{\eta}$ increases. In the case for Run C, we can approximately evaluate as $\epsilon_{max}/\bar{\epsilon} \sim 300$. This means $\eta_{min} \sim \bar{\eta}/4$, i.e. $K_{max}\eta_{min} \simeq 1$. Thus the condition for Run C satisfies the resolution requirement of DNS given by (1) (Sreenivasan 2004). As shown in figure1b, in contrast, each PDF is on the same curve in the ranges $\epsilon/\bar{\epsilon} < 10$ and $\chi/\bar{\chi} < 10$. Quantitative examination yields that the moments evaluated by Run A are underestimated, in which $\langle(\epsilon/\bar{\epsilon})^3\rangle$ and $\langle(\chi/\bar{\chi})^3\rangle$ are about 55 and 43 percents for those by Run C, respectively. The above results suggest that the high-order derivative statistics are sensitive to the variation of $K_{max}\bar{\eta}$, but for the low-order statistics, the effect of resolution is negligible as far as $K_{max}\bar{\eta} \geq 1$ as mentioned in the previous paragraph.

Next we examine the effects of resolution on the behavior for spectra and structure functions. The classical scaling theory of turbulence with passive scalar transport (Kolmogorov 1941, Obukhov 1949, Corrsin 1951, named as KOC) yields the scaling laws in the inertial-convective range (ICR); the energy spectrum $E(k)$ and the scalar variance spectrum $E_\theta(k)$ are given by

$$E(k) = \bar{\epsilon}^{2/3}k^{-5/3}f(k\bar{\eta}), \quad E_\theta(k) = \bar{\chi}\bar{\epsilon}^{-1/3}k^{-5/3}f_\theta(k\bar{\eta}_B, \bar{\eta}/\bar{\eta}_B), \quad (3)$$

respectively, where $f(x)$ and $f_\theta(x,y)$ are universal scaling functions being free from the details of large-scale natures. In the case for $S_C = 1$, the statistical properties in the range $k\bar{\eta} \ll 1$ are independent of ν and κ, i.e. $f(x) = K$
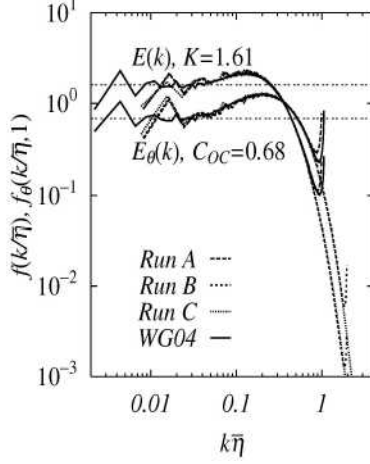
Figure 2. $K_{max}\bar{\eta}$-dependences of compensated spectra $f(x)$, $f_{\theta}(x,1)$ for Runs A, B, C and WG04.
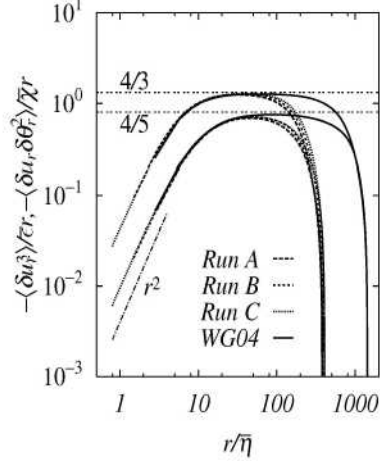
Figure 3. Approach of the curves to the 4/5 and 4/3 laws for Runs A, B, C and WG04.

and $f_{\theta}(x,1) = C_{OC}$ with $x \ll 1$, where K and C_{OC} is the Kolmogorov and Obukhov-Corrsin constants, respectively. Figure 2 shows the behavior of $f(k\bar{\eta})$ and $f_{\theta}(k\bar{\eta},1)$ obtained by Runs A, B, C and WG04. It is clearly recognized that the results for Runs A, B and C are on the same curve irrespective of $K_{max}\bar{\eta}$ except the range $k \sim K_{max}$. Moreover the bodies of spectra are satisfactorily in good agreement with that evaluated by WG04. This result strongly suggests that we can accurately obtain the behavior of spectra from ICR to viscous-convective range even in the case for $K_{max}\bar{\eta} \simeq 1$ as used in WG04.

The effects of resolution on the third-order structure functions for the longitudinal velocity increment δu_r and the scalar increment $\delta \theta_r$ are also examined. There are asymptotically exact statistical laws in $\bar{\eta}, \bar{\eta}_B \ll r \ll L$, the so-called 4/5 and 4/3 laws, derived from the fundamental equations of motion under the hypoteses of isotropy and homogeneity (Monin & Yaglom 1975) as

$$-\langle(\delta u_r)^3\rangle/\bar{\epsilon}r = 4/5, \quad -\langle \delta u_r (\delta \theta_r)^2 \rangle/\bar{\chi}r = 4/3. \quad (4)$$

Figure 3 shows the results by DNS. The plateaus of the compensated 4/5 and 4/3 laws for Runs A, B and C are narrower than those by WG04 because of low-R_{λ}. The curves for Runs A, B and C are almost independent of $K_{max}\bar{\eta}$ except the range $r \sim L$. This comes from the non-stationary effects at the large scales due to the shorter averaging times of Runs B and C than that of Run A.

The intermittency problem in the high-R_{λ} turbulence is highlighted in the scaling of the high-order structure functions. The $K_{max}\bar{\eta}$-dependences of the q-th order structure functions, $S_q^L(r) = \langle|\delta u_r|^q\rangle$, $S_q^{\theta}(r) = \langle|\delta \theta_r|^q\rangle$ and $S_q^{\theta L}(r) = \langle|\delta u_r \delta \theta_r^2|^{q/3}\rangle$ are examined for this purpose. The DNS results are shown in

figure 4, in which the structure functions with order q ($q = 3, 4, 6$ and 8) are compensated by the KOC scaling. In the range $r/\bar{\eta} < 10$, each structure function is sensitive to the variation of $K_{max}\bar{\eta}$ as q increases, while in $r/\bar{\eta} > 10$ the curves are almost independent of $K_{max}\bar{\eta}$. These features are also confirmed more clearly by examining their local slopes (figures are not shown).
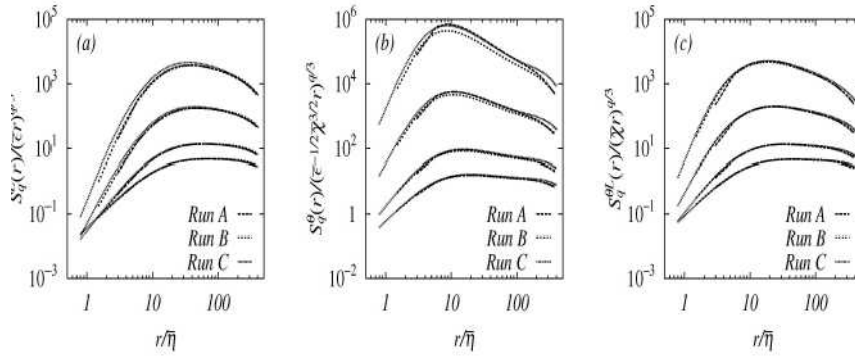

Figure 4. $K_{max}\bar{\eta}$-dependences of (a) $S_q^L(r)$, (b) $S_q^\theta(r)$ and (c) $S_q^{\theta L}(r)$ compensated by KOC scaling. Curves are for $q = 3, 4, 6$ and 8 from the lowermost curve.

3. Summary

We have examined the resolution requirement of passive scalar DNS by investigating the $K_{max}\bar{\eta}$-dependences of the several statistics in the velocity and scalar fields. It was clarified that the high-order derivative statistics are sensitive to the variation of $K_{max}\bar{\eta}$. In contrast, it was shown that the statistics like the spectra and the third-order structure functions are insensitive to the variation of $K_{max}\bar{\eta}$. It is quite an encouraging result that the scalar variance spectra at wavenumbers $k\bar{\eta} < 0.7$ are accurately computed even when $K_{max}\bar{\eta} = 1$, although the previous DNSs have computed the spectra with the condition $K_{max}\bar{\eta} \simeq 1.5$ stronger than $K_{max}\bar{\eta} = 1$ (Wang *et al.* 1999, Yeung *et al.* 2002). Moreover it was shown that the high-order structure functions significantly depend on $K_{max}\bar{\eta}$ in the range $r/\bar{\eta} < 10$, but their $K_{max}\bar{\eta}$-dependences are negligible in $r/\bar{\eta} > 10$ when $q \leq 8$. Our previous study showed that the ICR exists in $r/\bar{\eta} > 200$ (Watanabe & Gotoh 2004). This fact suggests that the condition $K_{max}\bar{\eta} = 1$ is satisfactory to assure the accuracy of the passive scalar DNS with $S_C = O(1)$ for studying the scaling structures associated with the intermittency problems in ICR scale.

176

References

CORRSIN, S. 1951 On the spectrum of isotropic temperature fluctuations in isotropic turbulence. *J. Appl. Phys.* **22**, 469–473.

FRISCH, U. 1995 *Turbulence: the Legacy of A. N. Kolmogorov*. Cambridge University Press.

GOTOH, T., FUKAYAMA, D. & NAKANO, T. 2002 Velocity field statistics in homogeneous steady turbulence obtained using a high–resolution direct numerical simulation. *Phys. Fluids* **14**, 1065–1081.

KOLMOGOROV, A. N. 1941 The local structure of turbulence in incompressible viscous fluid for very large Reynolds number. *Dokl. Akad. Nauk SSSR* **30** 9–13.

MONIN, A. S. & YAGLOM, A. M. 1975 *Statistical Fluid Mechanics, Mechanics of Turbulence*, Vol 2. MIT press.

OBUKHOV, A. M. 1949 Structure of the temperature field in turbulent flows. *Izv. Akad. Nauk. SSSR. Geophr. Geofiz* **13**, 58–69.

SREENIVASAN, K. R. 2004 Possible effects of small-scale intermittency in turbulent reacting flows. In *Turbulence, Flow and Combustion*, Kluwer.

WANG, L. P., CHEN, S. & BRASSEUR, J. G. 1999 Examination of hypotheses in the Kolmogorov refined turbulence theory through high–resolution simulations. Part 2. Passive scalar field. *J. Fluid Mech.* **400**, 163–197.

WARHAFT, Z. 2000 Passive scalars in turbulent flows. *Annu. Rev. Fluid Mech.* **32**, 203–240.

WATANABE, T. & GOTOH, T. 2004 Statistics of a passive scalar in homogeneous turbulence. *New J. Phys.* **6**, 40.

YEUNG, P. K., XU, S. & SREENIVASAN, K. R. 2002 Schmidt number effects on turbulent transport with uniform mean scalar gradient. *Phys. Fluids* **14**, 4178–4191.

SELF-SIMILARITY OF VORTICITY DYNAMICS IN DECAYING TWO-DIMENSIONAL TURBULENCE

Takahiro Iwayama
Graduate School of Science and Technology, Kobe University,
Rokkoudai-Machi, Nada-ku, Kobe 657-8501 Japan
iwayama@kobe-u.ac.jp

Theodore G. Shepherd
Department of Physics, University of Toronto
60 St. George Street, Toronto, Ontario, M5S 1A7, Canada
tgs@atmosp.physics.utoronto.ca

Abstract   A new similarity theory is proposed for decaying two-dimensional Navier–Stokes turbulence, including the viscous range, which encompasses all Reynolds numbers and various degrees of hyperviscosity. In the high Reynolds number limit where the energy $\mathcal{E}$ is invariant, the theory predicts the enstrophy decay law $\mathcal{Q} \sim t^{-1/p}$, where t is time and p is the degree of hyperviscosity ($p = 1$ is the usual Laplacian viscosity). This is at variance with the vortex scaling theory of Carnevale *et al*. (1991). However it is consistent with previously published numerical simulations using the usual viscosity. That enstrophy decay in the high Reynolds number limit may depend on the degree of hyperviscosity suggests that the inviscid limit is singular. Indeed, our similarity theory based on the inviscid equations predicts an upscale energy flux for all wavenumbers, in violation of basic physical constraints. This may be part of the reason for the failure of Batchelor's (1969) decay law $\mathcal{E} \sim t^0$, $\mathcal{Q} \sim t^{-2}$.

Keywords: Decaying two-dimensional turbulence, self-similarity, Batchelor's similarity hypothesis

1.   Introduction

Self-similarity has been one of the most attractive approaches to the study of decaying turbulence. Batchelor (1969) proposed a self-similar energy spectrum for decaying two-dimensional Navier–Stokes (2-D NS) turbulence in the limit of high Reynolds number and predicted the energy and enstrophy decay laws as $\mathcal{E} \sim t^0$ and $\mathcal{Q} \sim t^{-2}$, respectively. However, his theory has not been supported

by direct numerical simulations. It is well known that the existence of coherent vortices is responsible for the failure of Batchelor's theory (Bartello & Warn 1996). Recently, self-similar evolution of the energy spectrum for decaying 2-D NS turbulence with the usual viscosity has been found numerically at various Reynolds numbers (Bartello & Warn 1996, Chasnov 1997, Das *et al.* 2001). At a particular low Reynolds number, $Re = 15.73$, the energy and enstrophy decay as $\mathcal{E} \sim t^{-1}$ and $\mathcal{Q} \sim t^{-2}$, respectively (Chasnov 1997). For high but finite Re, the energy and enstrophy decay laws are approximated well by $\mathcal{E} \sim t^0$ and $\mathcal{Q} \sim t^{-1}$ (Bartello & Warn 1996, Chasnov 1997, Das *et al.* 2001). Although Chasnov & Herring (1998) proposed a self-similarity theory to explain these decay laws, their theory only treats the NS equation with the usual viscosity. Here we propose a theory for decaying 2-D NS turbulence that is applicable to the case of hyperviscosity. We also discuss the failure of Batchelor's similarity hypothesis within our framework.

2. Theory

We consider decaying evolution of the 2-D NS equation with hyperviscosity of degree p. The starting point of the present analysis is the evolution equation for the energy spectrum,

$$\frac{\partial}{\partial t} E(k) = T(k) - 2\nu_p k^{2p} E(k). \tag{1}$$

Here k is the horizontal wavenumber (the system is assumed to be isotropic), $T(k)$ is the nonlinear energy transfer function between wavenumbers, and ν_p is the hyperviscosity coefficient.

We suppose that the energy spectrum has the self-similar form,

$$E(k) = c\Lambda^{\sigma} t^{\delta} G(x), \quad x \equiv k\,\Lambda, \tag{2}$$

where σ and δ are constants, c is also a constant with the dimension of $(\text{length})^{3-\sigma}/(\text{time})^{\delta+2}$, G is a positive definite function of universal form, and Λ is a length scale. That is, the energy spectrum is supposed to be scaled in terms of length Λ and time t. We do not explicitly define the length scale Λ. If the self-similarity is satisfied over all wavenumbers, then all length scales must grow at the same rate. Therefore, it is possible to take Λ to be either the energy containing scale or the dissipation scale. When $\sigma = 3$ and $\delta = -2$, the dimension of $\Lambda^{\sigma} t^{\delta}$ coincides with that of $E(k)$ and c is non-dimensional. However, for other choice of σ and δ, the dimension of $\Lambda^{\sigma} t^{\delta}$ does not coincide with that of $E(k)$ and c is dimensional. Therefore, we refer to self-similarity (2) with $\sigma = 3$ and $\delta = -2$ as *normal self-similarity*, and to other cases as *anomalous self-similarity*.

The self-similar forms of the energy transfer function $T(k)$ and the energy flux $\Pi(k)$, which is defined by $\Pi(k) = -\int_0^k T(k')\,\mathrm{d}k'$, are then obtained as

$$T(k) = c\Lambda^\sigma t^{\delta-1} G_1(x) \tag{3}$$

and

$$\Pi(k) = c\Lambda^{\sigma-1} t^{\delta-1} G_2(x), \tag{4}$$

respectively. Here, G_1 and G_2 are also functions of universal form. From the definition of $\Pi(k)$, the relation between G_1 and G_2 is given by

$$G_2(x) = -\int_0^x G_1(x')\,\mathrm{d}x'. \tag{5}$$

In addition, conservation of energy in the nonlinear interactions ensures

$$\int_0^\infty G_1(x)\,\mathrm{d}x = 0. \tag{6}$$

Using (2) and (3), (1) reduces to

$$G_1(x) = \gamma \frac{\mathrm{d}}{\mathrm{d}x}\{xG(x)\} + \{(\sigma-1)\gamma + \delta\}G(x) + 2\nu_p \Lambda^{-2p} t x^{2p} G(x),$$
$$\gamma \equiv \frac{\mathrm{d}\ln\Lambda}{\mathrm{d}\ln t}. \tag{7}$$

In order to ensure the existence of the functions of universal form, (7) must be explicitly independent of time t. This constrains γ and $\Lambda^{-2p}t$ to be constant, which requires

$$\gamma = \frac{1}{2p}. \tag{8}$$

Leaving γ arbitrary for now, integrating (7) with respect to x from 0 to ∞, and using (6) and assumptions $xG(x) \to 0$ as $x \to 0$ and $x \to \infty$, we obtain

$$\{(1-\sigma)\gamma - \delta\}\int_0^\infty G(x)\,\mathrm{d}x = 2\nu_p \Lambda^{-2p} t \int_0^\infty x^{2p} G(x)\,\mathrm{d}x. \tag{9}$$

Since the energy evolution equation is given by $\mathrm{d}\mathcal{E}/\mathrm{d}t = -2\nu_p \int_0^\infty k^{2p} E(k)\,\mathrm{d}k$, (9) is equivalently written as

$$\frac{\mathrm{d}\mathcal{E}}{\mathrm{d}t} = -\{(1-\sigma)\gamma - \delta\}\frac{\mathcal{E}}{t}. \tag{10}$$

Equation (10) is the closed energy equation and leads to the energy decay law,

$$\mathcal{E} \sim t^{-\theta}, \quad \theta = (1-\sigma)\gamma - \delta. \tag{11}$$

The energy dissipation must be non-negative, which leads to the inequality $(1 - \sigma)\gamma \geq \delta$. A similar analysis to the enstrophy spectral evolution equation leads to the enstrophy decay law,

$$\mathcal{Q} \sim t^{-\theta - 2\gamma}. \tag{12}$$

In the case of normal self-similarity with the usual viscosity ($p = 1$), *i.e.*, inserting $\gamma = 1/2$, $\sigma = 3$ and $\delta = -2$ into (11) and (12), the latter equations reduce to $\mathcal{E} \sim t^{-1}$ and $\mathcal{Q} \sim t^{-2}$, respectively. That is, this case recovers the critical Reynolds number decay law numerically found by Chasnov (1997). Moreover, the above analysis shows that normal self-similarity cannot exist in the high Reynolds number limit, for which $\theta = 0$.

Study of decaying two-dimensional turbulence has been performed not only by numerical simulations but also by laboratory experiments (*e.g.*, Hansen *et al.* 1998). A major difference between numerical simulations and laboratory experiments is that the effect of bottom friction of the container on the evolution of the system cannot be ignored in laboratory experiments. The effect of bottom friction can be modelled by an additional linear damping term of the vorticity equation as follows:

$$\frac{\partial \omega}{\partial t} + J\left(\varphi,\, \omega\right) = -\alpha\omega + (-1)^{p-1}\nu_p\nabla^{2p}\omega, \tag{13}$$

where α is the friction coefficient and is regarded as a constant. When the additional linear damping term exists in the vorticity equation of the two-dimensional Navier-Stokes system, the former equation of (7) is replaced by

$$G_1(x) = \gamma\frac{\mathrm{d}}{\mathrm{d}x}\left\{xG(x)\right\} + \left\{(\sigma - 1)\gamma + \delta\right\}G(x) + 2\nu_p\Lambda^{-2p}tx^{2p}G(x) + \alpha tG(x). \tag{14}$$

In order to ensure the existence of the functions of universal form, the above equation must be explicitly independent of time t. Then, the friction coefficient must depend on time as $\alpha \sim t^{-1}$. Therefore, our analysis suggests that in the presence of a bottom friction modelled by a linear damping of the vorticity equation, with a constant friction coefficient, self-similar evolution of the energy spectrum over all wavenumbers cannot be realized.

3. Dynamical interpretation of failure of Batchelor's similarity hypothesis

Next, we consider the inviscid case of normal self-similarity. Neglecting the viscosity term (setting $\nu_p = 0$) and setting $\sigma = 3$ and $\delta = -2$, (7) reduces to

$$G_1(x) = \gamma\frac{\mathrm{d}}{\mathrm{d}x}\left\{xG(x)\right\} + 2(\gamma - 1)G(x). \tag{15}$$

As before, γ must be constant in order to allow the existence of the universal functions G and G_1, but now γ is not yet determined. However, for $\sigma = 3$ and $\delta = -2$, (11) and (12) reduce to $\mathcal{E} \sim t^{-2(1-\gamma)}$ and $\mathcal{Q} \sim t^{-2}$, respectively. Therefore, one obtains $\gamma = 1$ as the condition to ensure energy conservation in the inviscid limit. The above decay law is nothing but Batchelor's prediction. Therefore, in the case of inviscid and normal self-similarity, our general theory recovers Batchelor's similarity hypothesis (Batchelor (1969)).

The above discussion sheds light on the reasons for the failure of Batchelor's similarity hypothesis. Using (5) and setting $\gamma = 1$, (15) reduces to

$$G_2(x) = -xG(x), \tag{16}$$

where we assume $xG(x) \to 0$ as $x \to 0$, again. Since the function $G(x)$ is positive definite, (16) implies that $G_2(x)$ is negative definite, *i.e.* the energy flux is upscale for all wavenumbers. Thus, the relation (16) cannot possibly represent downscale transfers of energy. However, it is well known from Fjørtoft (1953) and Merilees & Warn (1975) that decaying 2-D turbulence must involve a spread of energy both to larger and to smaller scales. The relation (16) is in contradiction with this basic dynamical fact. This is a dynamical interpretation for the failure of Batchelor's similarity hypothesis.

4.   Summary

In this paper, we have proposed a new self-similarity hypothesis for decaying 2-D NS turbulence, including viscous effects. The self-similarity hypothesis proposed in this study allows for dimensionally anomalous scaling, and is therefore called anomalous self-similarity, in contrast to normal self-similarity which has a dimensionless multiplicative factor. Our analysis shows that the self-similar spectra observed by Chasnov (1997) at a critical Reynolds number correspond to normal self-similarity, while those observed at high Reynolds number by Chasnov (1997) and Das *et al.* (2001), as well as by Bartello & Warn (1996) using the usual viscosity, correspond to anomalous self-similarity. In the inviscid case, our analysis leads to Batchelor's (1969) similarity hypothesis, which is not observed in numerical simulations. However, our analysis provides an explanation for the failure of Batchelor's similarity hypothesis from the viewpoint of energy transfer in wavenumber space.

182

References

BARTELLO, P. & WARN, T. 1996 Self-similarity of decaying two-dimensional turbulence. *J. Fluid Mech.* **326**, 357–372.

BATCHELOR, G. K. 1969 Computation of the energy spectrum in homogeneous two-dimensional turbulence. *Phys. Fluids Suppl.* **12**, II-233–II-239.

CARNEVALE, G. F., MCWILLIAMS, J. C., POMEAU, Y., WEISS, J. B. & YOUNG, W. R. 1991 Evolution of vortex statistics in two-dimensional turbulence. *Phys. Rev. Lett.* **66**, 2735–2737.

CHASNOV, J. R. 1997 On the decay of two-dimensional homogeneous turbulence. *Phys. Fluids* **9**, 171–180.

CHASNOV, J. R. & HERRING, J. R. 1998 Self-similar decay of two-dimensional turbulence. In *Advances in Turbulence VII*, Kluwer, 415–418.

DAS, C., KIDA, S. & GOTO, S. 2001 Overall self-similar decay of two-dimensional turbulence. *J. Phys. Soc. Japan.* **70**, 966–976.

FJØRTOFT, R. 1953 On the changes in the spectral distribution of kinetic energy for two-dimensional non-divergent flow. *Tellus* **5**, 225–230.

HANSEN, A. E., MARTEAU, D. & TABELING, P. 1998 Two-dimensional turbulence and dispersion in a freely decaying system. *Phys. Rev.E* **58**, 7261–7271.

MERILEES, P. E. & WARN, H. 1975 On energy and enstrophy exchanges in two-dimensional non-divergent flow. *J. Fluid Mech.* **69**, 625–630.

A GRID-FREE REDISTRIBUTION MODEL FOR A VORTEX METHOD AND TURBULENT FLOW ANALYSIS

Kota Fukuda, Kyoji Kamemoto
Department of Mechanical Engineering, Graduate School of Engineering, Yokohama National University,
79-5, Tokiwadai, Hodogaya-ku, Yokohama-city, 240-8501 Japan
fukuda@ynu.ac.jp, kamemoto@ynu.ac.jp

Abstract   This paper presents a new grid-free type of redistribution model for turbulent flow analysis, in which each vortex particle is redistributed into some elements in accordance with its stretching rate. The model is applied to an inclined collision of two vortex rings. Energy spectra are analyzed and compared with existing DNS data and results of experiments by Saddoughi & Veeravalli (1994). The energy cascade and dissipation process are reasonably simulated. In addition, the LES model proposed by Kiya & Izawa (1999) is applied to the proposed redistribution model. The results show that the analyzed energy spectra are in close agreement with the existing DNS data up to high wave number region.

Keywords: Vortex methods, 3-D core spreading method, redistribution model, turbulence analysis, stretching effect

1.   Introduction

In vortex methods, vorticity distribution in the flow field is represented by discrete vortex elements. When compared to other computational schemes, vortex methods have the advantage that the nonlinear distortion or stretching of the vorticity region is directly calculated. Numerical resolution is dependent on the scale of the discrete vortex elements. When their size approaches the Kolmogorov dissipation scale, the calculation becomes the Direct Numerical Simulation (DNS) of turbulence. The Kolmogorov dissipation scale is dependent on the local strain rate. Therefore, particle redistribution schemes are necessary for high strain regions. Usually, vortex methods are divided into two methods. The first is the vortex-in-cell (VIC) method, in which the stream function is calculated on the fixed grid, and the velocity is computed by finite differences on the grid. The second is the Biot-Savart law method, in which the

velocity is calculated by the Biot-Savart law, without using the grid. Cottet *et al.* (2002) calculated two examples of fundamental turbulent flow using the VIC method and a grid-based redistribution model. The results indicated that the energy spectra were close to those analyzed by DNS. Nakanishi & Kamemoto (1992) proposed 3-D core spreading method which is based on the Biot-Savart law method. In this method, each vortex element is replaced by one vortex blob element at each time step. The great advantage of this scheme is that it can be easily applied to flows with complex geometry because of its grid-free characteristic (see, for example, Ojima & Kamemoto 2000). In high strain regions, however, the spatial resolution becomes worse because the distance of each vortex element becomes larger than its core radius.

In our previous study (Fukuda & Kamemoto 2001), the unsteady deformation of sub-core scale eddies of vortex blob elements was numerically investigated by discretizing one vortex blob with smaller-scale vortex particles and calculating their evolution. The results showed that the deformation of the sub-core scale structure of a vortex blob is dependent on its stretching rate. Recently, Fukuda & Kamemoto (2004) proposed a new grid-free type of redistribution model based on 3-D core spreading method, in which the deformation of each vortex particle is estimated by its stretching rate and each vortex element is redistributed into a number of vortex blobs in accordance with the estimated scale. The model was applied to an inclined collision of two vortex rings. The analyzed energy spectra were in close agreement with the existing DNS data and results of experiments by Saddoughi & Veeravalli (1994).

For high Reynolds number flows, turbulence models are necessary to simulate them in reasonable computational time. In this study, the LES model proposed by Kiya & Izawa (1999) was applied to the redistribution model. In the calculation using the proposed redistribution model, the vortical structure in the high strain region is represented by small-scale vortex elements. Therefore, by applying the LES model to the proposed redistribution model, it may be possible to simulate the effects of sub-core scale vortices more accurately than the calculation using the conventional 3-D core spreading method and the LES model. In this study, the energy spectra were analyzed and compared to the existing DNS data and results of experiments.

2. Mathematical basis

2.1 Basic equation

The governing equations of viscous and incompressible flows are described by the vorticity transport equation,

$$\frac{\partial \boldsymbol{\omega}}{\partial t} + (\boldsymbol{u} \cdot \bigtriangledown)\boldsymbol{\omega} = (\boldsymbol{\omega} \cdot \bigtriangledown)\boldsymbol{u} + \nu \nabla^2 \boldsymbol{\omega}. \tag{1}$$

where $\boldsymbol{u}$ is the velocity vector and the vorticity $\boldsymbol{\omega}$ is defined as $\boldsymbol{\omega}=\bigtriangledown\times\boldsymbol{u}$.

2.2   3D vortex blob model and 3D core spreading method

Vorticity distribution in the flow field is represented by the vortex blob element which is the spherical model with a radially symmetric distribution of vorticity. The velocity induced by vortex blobs is calculated by the Biot-Savart law and the trajectory of the vortex particle over the time step dt is calculated by the second order Adams-Bashforth method. On the other hand, the time evolution of vorticity is calculated using the 3-D core spreading method modified by Nakanishi & Kamemoto (1992). In this method, the stretch term and diffusion term are separately considered and the viscous term is expressed by the core spreading method proposed by Leonard (1980).

2.3   Redistribution model

When the stretching effect is larger than the diffusion effect, the time evolution of the length becomes larger than the one of the core radius. In this redistribution model, each discrete element is replaced by some vortex blobs according to its deformed length and radius estimated by the 3-D core spreading method and therefore the spatial resolution is maintained or improved. The number of the redistributed vortex blobs for one deformed element is decided using

$$n = floor\left(l_{t+\Delta t}/(C \cdot 2\sigma_{t+\Delta t})\right). \tag{2}$$

Here, the function $floor(x)$ gives the largest integer less than or equal to x. C is the key factor used to select the resolution of the redistribution model. When C is low, the spatial resolution becomes high. In this study, the value of C=1.0 is selected. Each redistributed element has the equivalent volume and the total volume of the redistributed elements is the same as the volume of the deformed element. The length of the deformed element is divided into n parts, and new elements are redistributed on their center points. The vortex strength is conserved through the redistribution procedure.

2.4   Subgrid-scale model

Kiya & Izawa (1999) proposed the nonlinear core spreading algorithm, in which the subgrid-scale viscosity ν_{SGS} is estimated using the local vorticity stretching rate $(1/\omega)\,(d\omega/dt)$. In this study, the model is applied to the proposed redistribution model. For the constant C', the value of 0.17 is employed.

3.   Calculation conditions

The inclined collision of two vortex rings is analyzed. The initial set-up of the vortex rings is as Table 1. Each vortex ring is inclined by angle θ. The

Table 1. Vortex rings parameter in the initial state.

Ring circulation	Γ_0	2.0
Cut-off radius of a ring	δ_0/R_0	0.275
Inclined angle	θ	30°
Distance of two rings	D/R_0	3.0
Reynolds number	$Re_{\Gamma_0} = \Gamma_0/\nu$	2200

initial vorticity distribution on the cross section of the single vortex ring is

$$\omega(r) = 1/(aR_0{}^2)\cdot\exp\left(-r^3/R_0{}^3\right) \qquad (a = 1.414), \qquad (3)$$

where r and R_0 are the position on the cross section and the core radius of the vortex ring respectively. This condition is consistent with one of the study by Knio & Ghoniem (1990). The initial circulation on the cross section is $\Gamma_0 = 2.0$. The selected time step is $\Delta t = 0.02R_0{}^2/\Gamma_0$. On vortex blob scale in the initial state, the number of blobs is N_0=15288 and the initial cut-off radius is σ_0/R_0=0.085.

4. Calculation results

Figures 1 (a) and (b) show the instantaneous flow patterns at $t\Gamma_0/R_0{}^2$=12.0 calculated by the proposed redistribution model and both the redistribution model and LES model proposed by Kiya & Izawa (1999) respectively. The results show that the spatial resolution in the high strain region is maintained by the redistribution model. There are not significant effects of the LES model on the flow patterns. Figures 2 (a) and (b) show the analyzed one-dimensional longitudinal power energy spectra based on Kolmogorov's universal scale using the proposed redistribution model and both the proposed redistribution model and LES model respectively. The energy dissipation rate ϵ is obtained from

$$\epsilon = 2\nu \int_0^{1/(2\sigma_{min})} k_x{}^2 E(k_x)\mathrm{d}K_x. \qquad (4)$$

Here, σ_{min} is the core radius of the smallest discrete vortex element. According to the results, the energy spectra decrease close to the existing DNS data; the energy cascade mechanism is reasonably simulated. In the present calculations, the energy spectra are elongated to the high wave number region as the progress of time, which means that smaller elements are introduced and the energy is appropriately redistributed to each vortex element. Especially, by applying the LES model, the analyzed energy spectra are in close agreement with the existing DNS data up to higher wave number region.
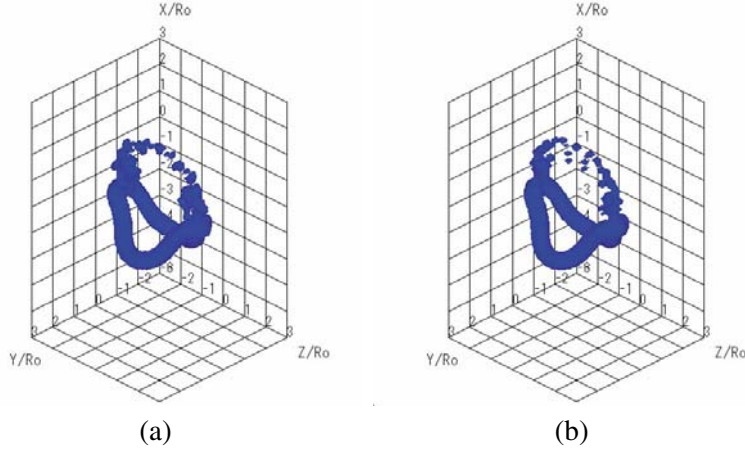
Figure 1. Isosurfaces of vorticity $|\boldsymbol{\omega}|$=2 at $t\Gamma_0/R_0{}^2$=12. (a) redistibution model, (b) redistibution model and LES model.
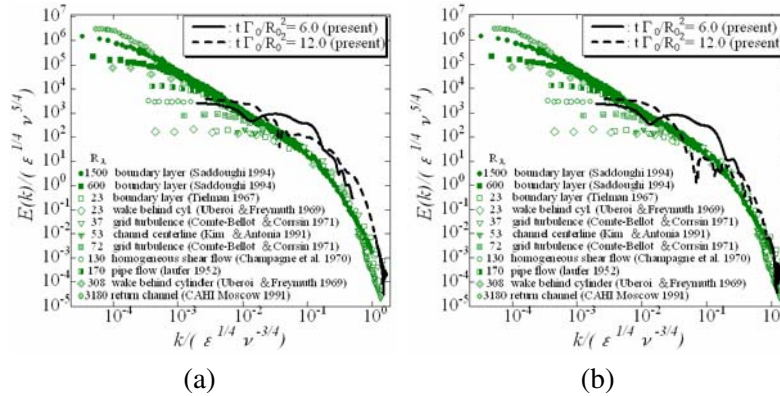

Figure 2. Time evolution of energy spectra compared with other DNS data and results of experiments (Saddoughi et al. 1994) (a) redistibution model, (b) redistibution model and LES model.

5.   Conclusions

In this paper, an inclined collision of two vortex rings was simulated using a new grid-free type of redistribution model and the LES model proposed by Kiya & Izawa (1999). The results showed that the redistribution model is useful to maintain the spatial resolution in high strain regions. Furthermore, the analyzed energy spectra were in close agreement with the existing DNS data up to high wave number region.

188

References

C OTTET G.H, M ICHAUX B., O SSIA S. AND V ANDER L INDEN G. 2002 A Comparison of Spetral and Vortex Methods in Three-Dimensional Incompressible Flows. *J. Comp. Phys.* **175**, 702–712.

F UKUDA , K. & K AMEMOTO , K. 2001 Numerical Investigation of Unsteady Deformation of Eddy Structure by Vortex Methods. *Proc. of the 2nd ICVM.*, 63–70.

F UKUDA , K. & K AMEMOTO , K. 2004 A Lagrangian Redistribution Model toward the Construction of a Turbulence Model for Vortex Methods. *Trans. Jpn. Soc. Mech. Eng.* **70-697 B**, 2311–2318. (in Japanese)

K IYA , M. & I ZAWA , S. 1999 Vortex Method Simulation of Forced, Impulsively Started Round Jet. *Proc. of 1999 ASME FEDSM.* **99-6813**.

K NIO O. M. & G HONIEM , A. F. 1990 Numerical study of a three dimensional vortex method. *J. Comput. Phys.* **86**, 75–106.

L EONARD , A. 1980 Vortex methods for flow simulation. *J. Comput. Phys.* **37**, 289.

N AKANISHI , Y. & K AMEMOTO , K. 1992 Numerical Simulation of Flow around a Sphere with Vortex Blobs. *J. Wind Engng. and Ind. Aero.* **46&47**, 363–369.

O JIMA , A. & K AMEMOTO , K. 2000 Numerical Simulation of Unsteady Flow around Three Dimensional Bluff Bodies by an Advanced Vortex Method. *Jpn. Soc. Mech. Eng. Int. J.* **43B**. 127–135.

S ADDOUGHI S. G. & V EERAVALLI S. V. 1994 Local Isotropy in Turbulent Boundary Layers at High Reynolds Number. *J. Fluid Mech.* **268**, 333–372.

Part E   Rotating and stratified turbulence

A NEW TWIST TO ROTATING STRATIFIED TURBULENCE

David G. Dritschel, William J. McKiver
Mathematical Institute, University of St Andrews
St Andrews KY16 9SS Scotland

dgd@mcs.st-and.ac.uk, william@mcs.st-and.ac.uk

Abstract   The turbulent motion of the Earth's atmosphere and oceans is hugely influenced by the effects of rotation and stratification. These effects alter the nature of turbulence profoundly from that of a homogeneous fluid. In particular, motions are dominantly horizontal, with vertical motions some three to four orders of magnitude smaller than horizontal motions. Moreover, coherent structures — vortices — are highly anisotropic, with vertical scales one to two orders of magnitude smaller than horizontal scales. And, fluid particle motions are doubly constrained: they must remain on (nearly flat) density surfaces and must retain their scalar value of 'potential vorticity'. These constraints are shown to be powerful, even in flow regimes for which rotation and stratification are not dominant effects.

1.   Introduction

A fundamental problem in fluid dynamics that remains a mystery, even after half a century of dedicated research, is turbulence. It is a central feature of atmospheric and oceanic dynamics, within which the effects of rotation and stratification are paramount. These effects, however, have not been properly accounted for in previous research. In particular, it is well known in meteorology and oceanography that the distribution of 'potential vorticity' (representing the 'balanced motions') has the greatest influence on the observed fluid motion, whereas higher-frequency 'inertia-gravity waves' (representing the 'imbalanced motions') are of secondary importance (see Ford *et al.* 2000, Dritschel & Viúdez 2003 & refs.). Many previous studies and numerical simulations have considered these two types of motion to be of comparable importance (cf. Smith & Waleffe 2002) — this is not the regime relevant to atmospheric and oceanic turbulence. Here, we address this regime in detail, using arguably the most advanced numerical method available, the contour-advective semi-Lagrangian

(CASL) algorithm (Dritschel & Ambaum 1997, Dritschel & Viúdez 2003). This approach is novel because it directly addresses the dominantly balanced regime of turbulence. Numerical results indicate that this regime extends far beyond the confines of fast rotation and strong stratification (small Rossby and Froude numbers, R and F). Moreover, they indicate that there is no qualitative difference between turbulence at small R and F, and turbulence at $\mathcal{O}(1)$ R and F, over a moderate number of characteristic eddy rotation periods.

2. Problem formulation

2.1 Mathematical system

We consider an incompressible rotating stratified fluid of negligible viscosity, a situation appropriate to oceanic turbulence in particular (the atmospheric case is complicated by the exponential dependence of density with height). We make the usual Boussinesq approximation, valid for density profiles which vary little from a background constant (in the ocean, this variation is around 0.3%, see Gill 1982). Although this variation is weak, the increase of density with depth is sufficient to render the motion layerwise-two-dimensional over most of the ocean; i.e. the stratification is important. The mean gradient of stratification defines the buoyancy frequency through $N = \sqrt{-g\rho_0^{-1}\mathrm{d}\bar{\rho}/\mathrm{d}z}$, where g is the acceleration due to gravity, $\bar{\rho}(z)$ is the mean density as a function of height over the region of interest (typically a few hundred kilometres in each horizontal direction), and ρ_0 is the mean density (mean of $\bar{\rho}(z)$ over z). Rotation is also important for oceanic scales of interest, and it gives rise to a Coriolis acceleration $f\boldsymbol{k} \times \boldsymbol{u}$ in the momentum equations, where f is the local vertical component of the planetary vorticity $2\boldsymbol{\Omega}_E$, $\boldsymbol{k}$ is the local vertical unit vector, and $\boldsymbol{u}$ is the velocity field.

In what follows, we consider only constant values of f, N and $\boldsymbol{k}$, appropriate to sufficiently small regions of the ocean away from the Equator. This allows one to study rotating stratified turbulence in the simplest context. Even so, the problem is not at all simple. Turbulence depends fundamentally on three basic parameters. The first is the ratio of frequencies f/N (this tends to range from about 10^{-2} to 10^{-1} in the oceans, and about an order of magnitude smaller in the atmosphere, see Gill 1982). To date, most studies have considered $f/N = \mathcal{O}(1)$, which is inappropriate but numerically less demanding (the time step is predicated by the buoyancy frequency N). The relevant regime of small f/N has been given much less attention, as regards turbulence, though this regime is what concerns weather forecasting and ocean modelling. Here, following previous related studies of simpler flows (Viúdez & Dritschel 2003, Dritschel & Viúdez 2003), we consider small f/N, specifically $f/N = 10^{-1}$. The principle effect of reducing f/N is to weaken the vertical motion and flatten isopycnals (constant density surfaces). Further work is required to determine

if smaller f/N has any qualitative effect on turbulence. The second basic parameter which shapes turbulence is the Rossby number R, defined as $||\zeta||/f$, where ζ is the relative vertical vorticity (with respect to a frame rotating at the rate $f/2$), in some norm $||.||$. Small Rossby number means that rotation is important. Without stratification, vortex lines would tend to become vertical, leading to 2D motion (with ζ conserved following fluid particles, see Gill 1982). Rotation enhances vertical correlations. The third basic parameter is the Froude number F, defined as $||\boldsymbol{\omega}_h/N_{\text{tot}}||$, where $\boldsymbol{\omega} = \boldsymbol{\nabla} \times \boldsymbol{u}$ is the vorticity, $\boldsymbol{\omega}_h$ is the horizontal part of it, and N_{tot} is the total buoyancy frequency, corrected for local variations in density, i.e. $N_{\text{tot}} = \sqrt{-g\rho_0^{-1}\partial\rho(\boldsymbol{x},t)/\partial z}$. Small Froude number means that stratification is important. Without rotation, stratification tends to generate layering, decoupled motions over vertical length scales exceeding $||\boldsymbol{u}||/N$ (corresponding to $\mathsf{F} = \mathcal{O}(1)$). Stratification thus breaks down vertical coherence for scales larger than this. The joint effect of rotation and stratification leads to three-dimensional structures — coherent vortices (see below for definition) — whose characteristic *scale ratio* H/L is $\mathcal{O}(f/N)$ (Charney 1971, Dritschel *et al.* 1997, Reinaud *et al.* 2003 & refs.). This implies $\mathsf{F} \sim \mathsf{R}$. In the atmosphere and oceans, the Rossby number is $\mathcal{O}(10^{-1})$, but values of $\mathcal{O}(1)$ do occur, e.g. near the Gulf Stream, which generates many strong vortices through meandering instabilities.

Details of the governing mathematical equations and their numerical treatment may be found in published works (Dritschel & Viúdez 2003 & refs.). The most significant novel aspect of the numerical approach is to make explicit use of the material conservation of 'potential vorticity' Π, i.e. $\mathrm{D}\Pi/\mathrm{D}t = 0$, where we use the dimensionless form

$$\Pi \equiv (\boldsymbol{k} + \boldsymbol{\omega}/f)\boldsymbol{\cdot}(\boldsymbol{k} + \boldsymbol{\nabla}b/N^2)\,, \tag{1}$$

where $b = -g(\rho - \bar{\rho})/\rho_0$ is the buoyancy. Note, Π is proportional to the total (absolute) vorticity dotted into the gradient of the density.

This is accomplished by tracking material *contours* of potential vorticity (PV) on isopycnal surfaces (which are also material). This proves to be a very efficient and accurate approach, and is crucial for the accurate modelling of these flows.

Having chosen PV as a 'prognostic' variable, we are faced with what to choose for the other two (altogether, there are three independent time derivatives in the equations). One could use any other independent set of variables (two components of velocity for example), but there is an advantage to choosing a pair of variables that represents, as far as is practically possible, what the PV cannot: namely the inertia–gravity waves. This motivates choosing a pair of variables which measure the departure from the leading-order (in R and F) 'geostrophic' and 'hydrostatic' balances (obtained by striking out the acceleration in the momentum equations, and equating the horizontal and ver-

tical parts respectively). This leads to taking the components of the horizontal ageostrophic vorticity $\boldsymbol{\omega}_h^{\mathrm{ag}} = \boldsymbol{\omega}_h + \boldsymbol{\nabla}_h b/f$ to be the other two prognostic variables. (Advantages of this choice are discussed in Dritschel & Viúdez 2003.)

2.2 Quasi-geostrophic balance

In the small Rossby number limit, with $\mathsf{F} \sim \mathsf{R}$, the full equations simplify to the *quasi-geostrophic* (QG) balance equations (Pedlosky 1987, Dritschel & Viúdez 2003). These equations are obtained by truncating the full equations, written in the prognostic variables Π and $\boldsymbol{\omega}_h^{\mathrm{ag}}$, at $\mathcal{O}(\mathsf{R})$. Then, the prognostic equations for $\boldsymbol{\omega}_h^{\mathrm{ag}}$ can be dropped ($\boldsymbol{\omega}_h^{\mathrm{ag}} = \mathcal{O}(\mathsf{R}^2)$), and the PV in Eq.(1) can be simplified to its linear part:

$$q = \zeta + fN^{-2}\partial b/\partial z \,. \tag{2}$$

The quantity q is known as the QG PV. Like Π, q is materially conserved, $\mathrm{D}q/\mathrm{D}t = 0$, but it is advected by a 2D non-divergent velocity field of the form $\boldsymbol{u} = (-\partial\psi/\partial y, \partial\psi/\partial x, 0)$ where the streamfunction $\psi(x, y, z, t)$ is recovered by inverting a 3D *linear* operator:

$$\frac{\partial^2\psi}{\partial x^2} + \frac{\partial^2\psi}{\partial y^2} + \frac{f^2}{N^2}\frac{\partial^2\psi}{\partial z^2} = q \,. \tag{3}$$

Note, the buoyancy is $b = f\partial\psi/\partial z$ at this order. By stretching z by N/f, the operator becomes Laplace's operator, and the inversion problem is isotropic in x, y, and Nz/f. The explicit dependence on f/N then disappears, and moreover there is no explicit dependence on R. It is convenient then to scale the equations by R and work in terms of the stretched vertical coordinate, hereafter simply denoted z. The QG system is not isotropic, however, because the advecting velocity field is layerwise-2D.

Nevertheless, it is appropriate to stretch coordinates in this way, even in the full system, and not treat the turbulence problem as a simple variation on homogeneous turbulence. Rotation and stratification are here the leading-order effects, and it is essential to account for them, e.g. by using much finer resolution in the original height coordinate than in the horizontal coordinates. Many phenomena in the atmosphere and oceans appear roughly isotropic after stretching the vertical coordinate by N/f (e.g. ocean vortices are roughly 10–100 km wide and 1–10 km deep), and this is consistent with Charney's theory of geostrophic turbulence (Charney 1971) as well as recent high-resolution QG turbulence studies (Reinaud *et al.* 2003 & refs.).

2.3 Parameter settings and initialisation

Several simulations were carried out to compare the behaviour of turbulence at finite R with QG turbulence. To this end, first a QG simulation was carried

out (see Reinaud *et al.* 2003 for related simulations), starting with an isotropic PV field (after the customary vertical stretching) consisting of spheres of QG PV $q = \pm 4\pi \Rightarrow T_{\mathrm{eddy}} = 1$, where T_{eddy} is a characteristic vortex rotation period. An equal number and volume of cyclonic and anti-cyclonic vortices were placed randomly (without overlap) in the domain initially. Their sizes were picked from a frequently-observed power-law number density distribution (Reinaud *et al.* 2003), and approximately a tenth of the domain was covered by the vortices. The domain is a triply-periodic cube (in stretched coordinates), with a basic grid resolution of 128 in each direction. Four times as many layers were used to represent the PV on isopycnal surfaces, and a grid 4 times finer in each horizontal direction was used in converting PV contours into gridded PV values, needed in the rest of the numerical algorithm. Contour surgery, which limits the growth in complexity of the contours, was applied at a twentieth of the horizontal grid resolution (see Dritschel & Viúdez 2003 for further details of these standard parameter settings).

The QG simulation was then run for 60 time units, well into the decaying stage (peak contour complexity occurs around $t = 40$). The QG PV field at $t = 55$ was extracted and used to initialise three other simulations now using the full equations at finite R. We set the true PV anomaly $\varpi = \Pi - 1 = \varepsilon q/4\pi$, where ε can be thought of as an approximate Rossby number. In the full model, the initial values of $\boldsymbol{\omega}_h^{\mathrm{ag}}$ must also be set. Taking zero values results in an unrealistically strong generation of inertia–gravity waves. Instead, we make use of a time-ramping procedure (Viúdez & Dritschel 2003, Dritschel & Viúdez 2003) in which we artificially grow ϖ from 0 to its final amplitude (keeping it fixed in space) over a period $\Delta\tau_I \gg T_{\mathrm{iner}}$, where $T_{\mathrm{iner}} = 2\pi/f$ is the inertial period. Meanwhile we evolve $\boldsymbol{\omega}_h^{\mathrm{ag}}$ from zero initial values (a state of rest). At the end of the initialisation period, the fields are found to contain only weak inertia–gravity waves, a state consistent with atmospheric and oceanic observations. Here we take $\Delta\tau_I = 10T_{\mathrm{iner}}$.

The full model was then integrated forwards, over the equivalent of 5 QG time units, in three cases: $\varepsilon = 0.25$, 0.5 and 0.75. An explicit third-order time stepping procedure was used, with a time step $\Delta t = 0.1T_{\mathrm{buoy}}$, where $T_{\mathrm{buoy}} = 2\pi/N$ is the buoyancy period. This ensures that the inertia–gravity waves, with frequencies lying between f and N, are well resolved in time. A larger time step could have been used for the PV advection, which tends to be much slower.

3.   Results

3.1   Potential vorticity evolution

A comparison of the three full model solutions with the QG solution, at the equivalent of QG $t = 60$, is presented in Fig.1. Note, in the case $\epsilon = 0.25$,
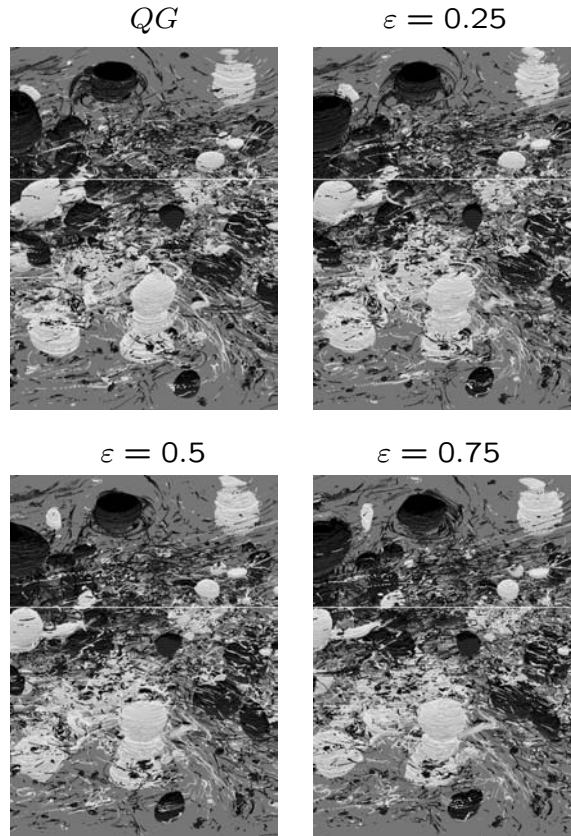
Figure 1.   Comparison of the PV anomaly fields ϖ for various Rossby numbers ε, as labelled, at 60 QG time units. The QG case corresponds to $\varepsilon \to 0$. The view is orthographic, $60°$ from the vertical, and from a point in the y-z plane. Cyclonic vortices with $\varpi > 0$ are lightly shaded, while anti-cyclonic vortices are darkly shaded. Only the inner eighth of the domain is shown.

this corresponds to 400 buoyancy periods or 40 inertial periods, plenty of time for exciting inertia–gravity waves (see below). Most remarkable is the close agreement in the PV fields at this time, despite the fact that $R_{max} = 0.98$ and $F_{max} = 0.60$ in the case $\epsilon = 0.75$. One would not expect the QG model to do so well, at least according to popular belief. Part of this surprising agreement may be due to the nearly balanced initialisation used in setting up the initial fields: poor initialisation can rapidly deteriorate forecast accuracy. This is well known in weather forecasting.

Note that the vortices have remained roughly isotropic; that is, they retain an f/N aspect ratio in the original coordinates. This demonstrates the need to ensure that the vertical grid spacing is f/N finer than the horizontal grid

spacing. Otherwise, one would not correctly represent the dominantly balanced vortical motions, and as a consequence misrepresent the imbalanced inertia–gravity wave motions as well. Once again, approaching this problem from homogeneous turbulence is misleading.

3.2   Vertical velocity and isopycnal displacement
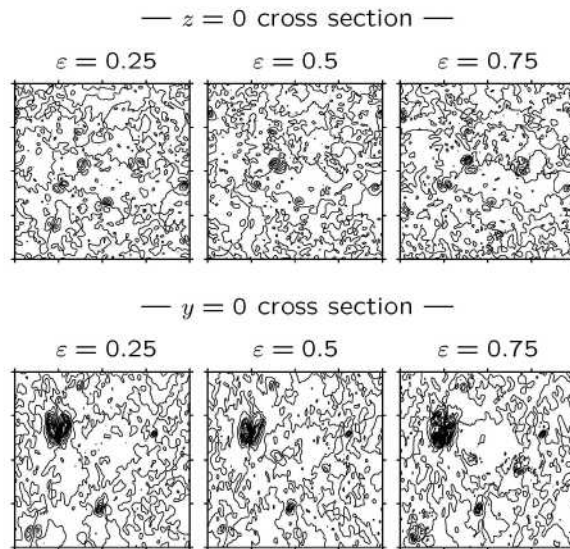
Figure 2.   Comparison of the vertical velocity fields w for various Rossby numbers ε, as labelled, at 60 QG time units. Contour intervals are 0.00004, 0.0001 and 0.004 for $\varepsilon = 0.25$, 0.5 and 0.75, respectively.

The vertical velocity field w is extraordinarily weak in most atmospheric and oceanic motions, and is often taken to be a measure of inertia–gravity wave activity. However, there can be a significant balanced component (i.e. arising from the PV), particularly for small R and F, and when starting close to a state with minimal wave activity.

A comparison of w in the three full model solutions, at QG $t = 60$, is presented in Fig.2. Both horizontal and vertical cross sections are shown. Again, there is close agreement for the largest magnitude structures, indicating that they are balanced motions linked with the PV (see below and Viúdez & Dritschel 2003). The maximum amplitudes are some two to three orders of magnitude smaller than those for the horizontal velocity components (not shown). The smaller, more random parts of the field are likely to be inertia–gravity waves (Viúdez & Dritschel 2003, Viúdez & Dritschel 2004).
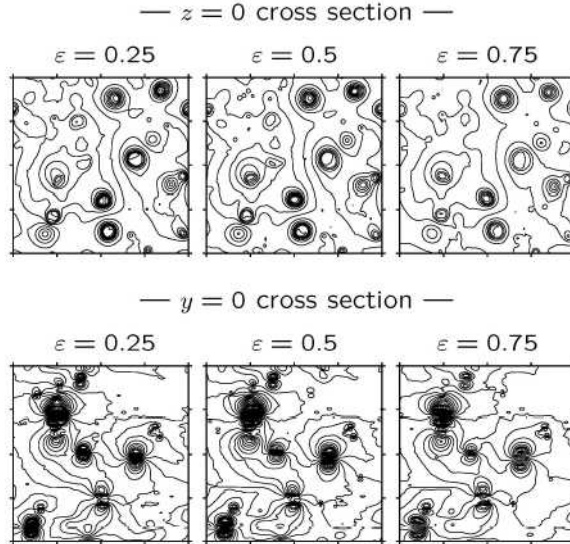
Figure 3. Comparison of the isopycnal displacement fields D for various Rossby numbers ε, as labelled, at 60 QG time units. Contour intervals are 0.002, 0.004 and 0.008 for $\varepsilon = 0.25$, 0.5 and 0.75, respectively.

The vertical displacement of isopycnals $D = -b/fN$ (stretched by N/f) is compared in the same format in Fig.3. Note that this field is substantially smoother that w and is virtually free of inertia–gravity waves. This is true also of the horizontal velocity field (not shown). Evidently, D is closely linked to the PV field (see below). The monopolar structures seen in the $z = 0$ cross section occur where the cross section cuts a vortex, either above or below its mid-plane (cf. Viúdez & Dritschel 2003, Dritschel & Viúdez 2003). The displacement is toward the vortex centre for cyclones, and away for anti-cyclones. $D \approx 0$ passing through the vortex centre. Mainly dipolar structures are seen in the $y = 0$ cross section, consistent with the above. Again, the agreement between the fields at this time is surprisingly close.

3.3   Field intercomparison

To establish the link between the PV and the flow variables, a comparison of w, ζ/f, D and ϖ is presented in Fig.4. First, the PV field is clearly the most compact, with only a small fraction of the domain occupied by nonzero anomalies. Some of these anomalies are directly correlated with ζ/f, which is less compact (note the strong gradients in ζ/f at the locations of the PV contours). Others are not. In some places, there are strong values of ζ/f with no evident PV anomaly. In these places, ζ/f is induced by PV anomalies in

layers just above or below the central layer shown — the vorticity extends over a wider range than does ϖ. In turn, there are close links between D and ζ/f, except where as noted before the cross section cuts close to the centre of a vortex. Finally, strongest w values occur along the flanks of the most deformed vortices: these are associated with the rise and fall of the isopycnal surfaces as the vortex rotates (Viúdez & Dritschel 2003). All of this demonstrates that the flows simulated, even at $\mathcal{O}(1)$ Rossby numbers, remain largely driven by the PV — remain nearly balanced — with only a small amount of inertia–gravity wave activity. The latter appears to play virtually no role in the dynamics of turbulence in this regime.
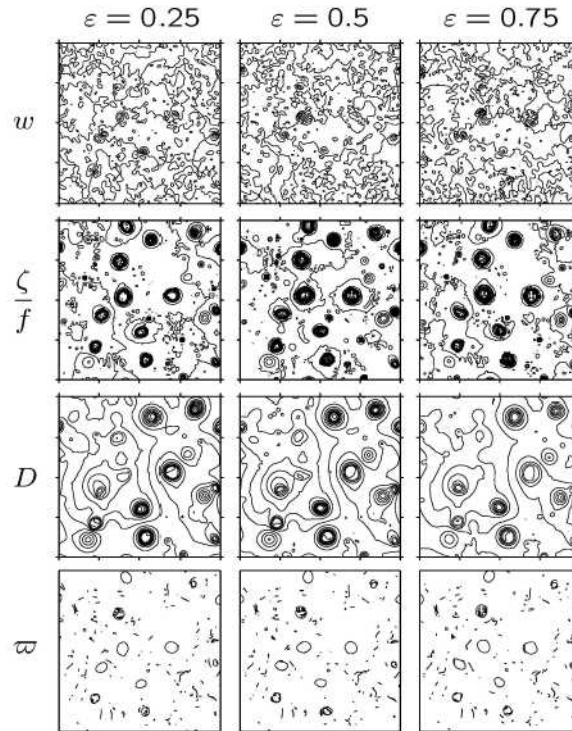
Figure 4. Comparison of the vertical velocity w, local Rossby number ζ/f, isopycnal displacement D and PV anomaly ϖ, for various Rossby numbers ε, at $z = 0$ and at 60 QG time units. Contour intervals are the same as before for w and for D, while for ζ/f they are 0.02, 0.03 and 0.06 for $\varepsilon = 0.25$, 0.5 and 0.75, respectively. The PV contour interval is ε.

4.   Conclusions

This paper has demonstrated that rotating stratified turbulence, starting from a near balanced state with minimal inertia–gravity waves, remains close to bal-

ance for times $t \lesssim 10T_{\text{eddy}} \sim 20T_{\text{iner}}/\mathsf{R}$. The turbulence evolution over this period is *quantitatively* similar to quasi-geostrophic turbulence, which strictly applies only for $\mathsf{R} \ll 1$. This is interesting theoretically, but also important practically. Since the potential vorticity field is responsible for much of the observed fluid motion, it must be simulated with great care. Numerical accuracy depends *crucially* upon the treatment of potential vorticity.

Acknowledgments

References

CHARNEY, J. G. 1971 Geostrophic turbulence. *J. Atmos. Sci.* **28**, 1087–1095.

DRITSCHEL, D. G. & AMBAUM, M. H. P. 1997 A contour-advective semi-Lagrangian algorithm for the simulation of fine-scale conservative fields. *Quart. J. Roy. Meteor. Soc.* **123**, 1097–1130.

DRITSCHEL, D. G., DE LA TORRE JUÁREZ, M. & AMBAUM, M. H. P. 1999 On the three-dimensional vortical nature of atmospheric and oceanic flows. *Phys. Fluids* **11(6)**, 1512–1520.

DRITSCHEL, D. G. & VIÚDEZ, A. 2003 A balanced approach to modelling rotating stably-stratified geophysical flows. *J. Fluid Mech.* **488**, 123–150.

FORD, R., MCINTYRE, M. E. & NORTON, W. A. 2000 Balance and the slow quasimanifold: some explicit results. *J. Atmos. Sci.* **57**, 1236–1254.

GILL, A. E. 1982 *Atmosphere-Ocean Dynamics*. Academic Press.

PEDLOSKY, J. 1997 *Geophysical Fluid Dynamics*. Springer-Verlag.

REINAUD, J., DRITSCHEL, D. G. & KOUDELLA, C. R. 2003 The shape of vortices in quasi-geostrophic turbulence. *J. Fluid Mech.* **474**, 175–191.

SMITH, L. M. & WALEFFE, F. 2002 Generation of slow large scales in forced rotating stratified turbulence. *J. Fluid Mech.*, **451**, 145–168.

VIÚDEZ, A., AND DRITSCHEL, D. G. 2003 Vertical velocity in mesoscale geophysical flows. *J. Fluid Mech.* **483**, 199–223.

VIÚDEZ, A., AND DRITSCHEL, D. G. 2004 Optimal potential vorticity balance of geophysical flows. *J. Fluid Mech.* **521**, 343–352.

ENERGY CASCADE PROCESSES IN STRATIFIED TURBULENCE

Yuji Kitamura
Division of Earth and Planetary Sciences, Graduate School of Science, Kyoto University,
Oiwake-cho, Kitashirakawa, Sakyo-ku, Kyoto 606-8501 Japan
kitamura@kugi.kyoto-u.ac.jp

Yoshihisa Matsuda
Department of Astronomy and Earth Science, Tokyo Gakugei University,
4-1-1 NukuiKitamachi, Koganei-city, Tokyo 184-8501 Japan
ymatsuda@u-gakugei.ac.jp

Abstract   In order to investigate the formation process of the $k_H^{-5/3}$ energy spectrum observed in the atmospheric mesoscales, we perform numerical experiments on forced turbulence in a rotating stratified fluid and examine the energy cascade processes. When the energy injection by the dynamical forcing is concentrated in small scales, upscale energy cascade is expected to form a $k_H^{-5/3}$ spectrum. However, our result shows that the upscale cascade is not enough to form this spectrum for the terrestrial parameter range. On the other hand, the spectral slope generated by downscale energy cascade from energy injection in larger scales is close to -2 and is not sensitive to static stability when the Coriolis parameter is greater than the terrestrial angular velocity.

Keywords: Stratified turbulence, energy cascade, numerical experiment

1.   Introduction

The atmospheric energy spectrum as a function of horizontal wavenumber k_H over the range from a few kilometers to synoptic scales was obtained by Nastrom *et al.* (1984) and Nastrom and Gage (1985). They found that the spectra follow the -3 power law in the range from 1000 to 3000 km and the $-5/3$ power law in the horizontal scales less than a few hundred km (about 400–500 km). More recent observations also support the $-5/3$ power law in the mesoscales (Cho *et al.* 1999). Numerical simulations using the GFDL-SKYHI GCM reproduced these spectral slopes (Koshyk *et al.* 1999, Koshyk and Hamilton 2001). While the formation mechanism of the k_H^{-3} spectrum can

be interpreted as enstrophy downscale cascade in quasi-geostrophic turbulence (Charney 1971), an interpretation of the $k_H^{-5/3}$ spectrum in the mesoscales is more complicated. It can be speculated as it is created by energy cascades like 3D turbulence or inverse energy cascades like 2D turbulence. Lilly (1983) attempted to understand the energy spectrum in the mesoscales from inverse energy cascades in stratified turbulence. However, numerical simulations of stratified turbulence indicate that inverse energy cascades does not occur unless Rossby number is less than unity (Métais *et al.* 1994).

In this study, numerical experiments on stratified turbulence are conducted with a simple dynamical model. We investigate downscale energy cascades from energy injection at large scales as well as inverse energy cascades from small scales. We examine whether or not an inverse energy cascade process makes a $-5/3$ spectral slope in smaller wavenumber. Further, energy spectra formed by the energy cascade are also discussed.

2. Model description

We assume a nonhydrostatic, incompressible Boussinesq fluid on an f-plane. The domain is set to 400×400 km^2 in a horizontal plane and 10 km vertically. The number of the computational grids is $200 \times 200 \times 40$, which corresponds to 2 km resolution in the horizontal direction and 250 m in the vertical one. The boundary conditions are assumed to be cyclic in the horizontal direction and rigid at the top and bottom. Time-integration is carried out for 15 days with a time interval of 50 seconds. We analyze the results for the last five days where turbulence is speculated to be in quasi-equilibrium in our calculations.

The dependence of the forcing amplitude on the total horizontal wavenumber k_H is given by the following formulation:

$$|F(k_H)|^2 = F_0^2 \frac{k_H^{\gamma/2}}{(k_0 + k_H)^\gamma}. \tag{1}$$

Here, k_0 and γ characterize a spectral peak wavenumber and a spectral band width, respectively. F_0 determines a forcing amplitude. We examine two types of the forcing distribution: $(k_0, \gamma) = (20, 100)$ (referred as Type I hereafter) and $(k_0, \gamma) = (1, 20)$ (Type II). In experiments with the Type I forcing, we expect upscale energy cascades from the peak wavenumber of the forcing and intend to examine energy spectrum in the wavenumbers smaller than it. On the other hand, the Type II forcing distribution has a peak at the domain size in order to examine energy cascade processes to smaller scales. The vertical distribution of the forcing is assumed to have the first baroclinic structure. Following the traditional studies in forced turbulence (*e.g.* Lilly, 1969), a random Markovian formulation is used for time evolution of the forcing function.
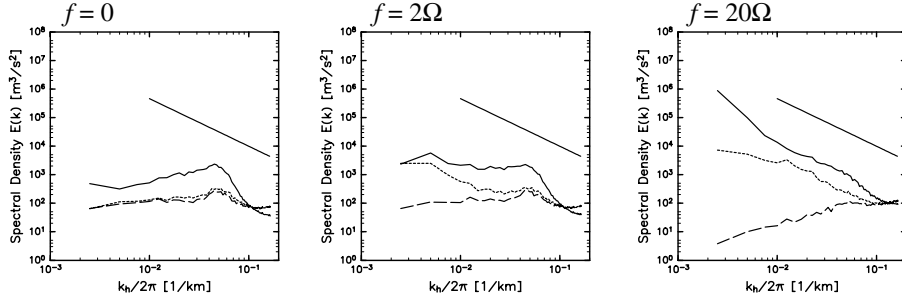
Figure 1. Energy spectra as a function of horizontal wavenumber for the Type I forcing cases. Each panel represents $f = 0$, 2Ω and 20Ω from the left. Solid, dashed and dotted lines indicate rotational part and divergent part of kinetic energy and potential energy, respectively. The reference straight line represents a $-5/3$ power law.

The eddy viscosity and diffusivity forms are assumed for the dissipation terms. In order to determine the eddy viscosity and thermal diffusion coefficients, we adopt the formulation based on the Smagorinsky-Lilly parameterization (Smagorinsky 1963, Lilly 1962), which is well known as a parameterization of LES. Namely,

$$\nu_{(h,v)} = (C_S \Delta_{(h,v)})^2 \sqrt{\frac{1}{2} \left(\frac{\partial u_i}{\partial x_j} + \frac{\partial u_j}{\partial x_i} \right)^2} f_\nu(\text{Ri}),$$

$$\kappa_{(h,v)} = \nu_{(h,v)} \frac{f_\kappa(\text{Ri})}{f_\nu(\text{Ri})}, \tag{2}$$

where $\Delta_{(h,v)}$ is the horizontal and vertical grid intervals and C_S is called the Smagorinsky constant, which is set to 0.21. In this formulation, effects of stratification are explicitly expressed as functions of Richardson number Ri. In our numerical experiments, the following empirical formulae based on laboratory experiments and the measurements in atmospheric boundary layer by Ueda *et al.* (1981) are adopted:

$$f_\nu(\text{Ri}) = \begin{cases} (1 + 2.5\text{Ri})^{-1} & (\text{Ri} > 0), \\ \min((1 - 25\text{Ri})^{1/3}, 6) & (\text{Ri} < 0), \end{cases} \tag{3}$$

$$f_\kappa(\text{Ri}) = \begin{cases} (1 + 5.625\text{Ri})^{-2} & (\text{Ri} > 0), \\ 1 + 5(1 - \exp(12\text{Ri}))^2 & (\text{Ri} < 0). \end{cases} \tag{4}$$

3. Results

Figure 1 indicates energy spectra obtained for Type I forcing and atmospheric stratification with 20 minutes of Brunt-Väisälä period. Amplitude of the vortical
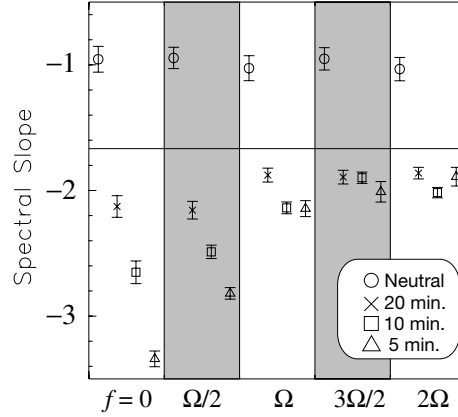
Figure 2. The spectral slopes estimated by the least-squares method in the range from 10 to 100 km. The horizontal reference line denotes $-5/3$. Error bars are taken as two times a standard deviation.

mode (solid line) is dominant especially in the lower wavenumbers. However, a $-5/3$ slope in the lower wavenumbers cannot be seen in the range $0 \leq f \leq 2\Omega$ (Ω is the terrestrial angular velocity) due to too small amplitude of the energy in the large scales. This energy distribution shows that upscale energy cascades is not sufficient to form the $-5/3$ slope. It is suggested that the inverse cascade process like 2D turbulence cannot be appropriate for the formation mechanism of the spectrum in the atmospheric mesoscales. On the other hand, the distribution close to $-5/3$ spectral slope is obtained in the lower wavenumbers than the forcing scale in the high rotation cases, $f = 20\Omega$. In this case, Rossby and Froude numbers averaged over the domain are about 0.3 and these values are consistent with the criterion for predominance of inverse energy cascade shown by Métais *et al.* (1994).

In the experiments using Type II forcing, the spectral slope largely depends on rotation and stratification. In order to summarize this dependency, we estimate the slopes by the least-squares method in the range from 10 to 100 km and illustrate the results in Figure 2. In all the cases, error bars are small enough to discuss the dependency. In the cases without stratification, the slope is about -1 and the dependence on rotation is weak, while the classical theory of 3D isotropic turbulence predicts that the energy spectrum can be expressed by a $k_H^{-5/3}$ (k_H: *horizontal* wavenumber) (Lilly 1983). This discrepancy would be attributed to the aspect ratio of the computational domain in our experiments. In the experiments including stratification, the slope becomes steeper as Brunt-Väisälä period is shorter, but its dependence is not so sensitive in the $f = 2\Omega$
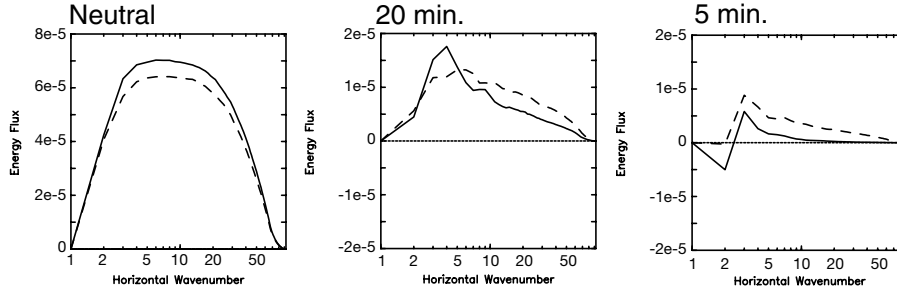
Figure 3. Energy flux averaged over the last five days for the Type II forcing cases. Results for same stratification are drawn in a same panel. Solid and dashed lines indicate $f = 0$ and 2Ω, respectively.

cases. For the rotation rate more than Ω, the slope of the total energy is within the range from -1.9 to -2.1.

We calculate total energy flux for Type II forcing cases (Figure 3). In neutral stratification cases, the total energy flux has a positive constant value in the horizontal scale of 20–100 km. This fact indicates that an inertial subrange appears in the range of this scale. The value of the flux is 7×10^{-5} $(\mathrm{m}^2/\mathrm{s}^3)$ for $f = 0$ and 6×10^{-5} $(\mathrm{m}^2/\mathrm{s}^3)$ for $f = 2\Omega$. The flux in the case with stratification has a positive peak in the horizontal wavenumber 3–5 and decreases in the higher wavenumber. The flux is smaller for larger static stability and the smaller flux corresponds to the steeper slope of the energy spectrum (Figure 2). Effects of rotation appear in high wavenumbers; the increase of the rotation rate contributes to energy transfer to the high wavenumbers.

4.   Summary

In the small-scale forcing cases, energy transfer to lower wavenumbers increases with static stability, but this upscale energy cascade is too small to form the $k^{-5/3}$ spectrum in the terrestrial parameter range of rotation and stratification. On the other hand, upscale energy cascade by the vortical mode is dominant in the case with an extremely rapid rotation rate. The spectral slope generated by downscale energy cascade is within the range from -1.9 to -2.1 for $f \geq \Omega$ and in the case close to the one observed in the mid- and high latitudes. However, it is sensitive to static stability without rotation, while the observed spectral slope is universal throughout all latitudes (Cho *et al.* 1999).

References

CHARNEY, J. G. 1971 Geostrophic turbulence. *J. Atmos. Sci.* **28**, 1087–1095.

CHO, J. Y. N., ZHU, Y., NEWELL, R. E., ANDARSON, B. E., BARRICK, J. D., GREGORY, G. L., SACHSE, G. W., CARROLL, M. A., ALBERCOOK, G. M. 1999 Horizontal wavenumber spectra of winds, temperature, and trace gases during the Pacific Exploratory Missions, 1. Climatology. *J. Geophys. Res.* **104**, 5697–5716.

KOSHYK, J. D., HAMILTON, K., MAHLMAN, J. D. 1999 Simulation of the $k^{-5/3}$ mesoscale spectral regime in the GFDL SKYHI general circulation models. *Geophys. Res. Lett.* **26**, 843–846.

KOSHYK, J. D. & HAMILTON, K. 2001 The horizontal kinetic energy spectrum and spectral budget simulated by a high-resolution troposphere-stratosphere-mesosphere GCM. *J. Atmos. Sci.* **58**, 329–348.

LILLY, D. K. 1962 On the numerical simulation of buoyant convection. *Tellus* **14**, 148–172.

LILLY, D. K. 1969 Numerical simulation of two-dimensional turbulence. *Phys. Fluids* **12**(Suppl. II), 240–249.

LILLY, D. K. 1983 Stratified turbulence and the mesoscale variability of the atmosphere. *J. Atmos. Sci.* **40**, 749–761.

METAIS, O., RILEY, J. J., LESIEUR, M. 1994 Numerical simulations of stably stratified rotating turbulence. pp. 139–151 in *Stably-stratified flows — flow and dispersion over topography*. Eds. I. P. Castro and N. J. Rockliff. Clarendon Press, Oxford.

NASTROM, G. D., GAGE, K. S., JASPERSON, W. H. 1984 The atmospheric kinetic energy spectrum, $10^0 - 10^4$ km. *Nature* **310**, 36–38.

NASTROM, G. D. & GAGE, K. S. 1985 A climatology of atmospheric wavenumber spectra of wind and temperature observed by commercial aircraft. *J. Atmos. Sci.* **42**, 950–960.

SMAGORINSKY, J. 1963 General circulation experiments with the primitive equations I. The basic experiment. *Mon. Wea. Rev.* **91**, 99–164.

UEDA, H., MITSUMOTO, S., KOMORI., S. 1981 Buoyancy effect on the turbulent transport processes in the lower atmosphere. *Q. J. R. Meteorol. Soc.* **107**, 561–578.

ASYMMETRIZATION OF JET PROFILES IN β-PLANE TURBULENCE

Jitsuko Hasegawa
Japan Meteorological Agency, Japan
j-hasegawa@naps.kishou.go.jp

Keiichi Ishioka, Shigeo Yoden
Division of Earth and Planetary Sciences, Graduate School of Science, Kyoto University, Japan
ishioka@gfd-dennou.org, yoden@kugi.kyoto-u.ac.jp

Abstract   An asymmetry of jet profiles is found between eastward and westward jets which appear spontaneously in two-dimensional β-plane decaying turbulence. Westward jets are narrower and more intense than eastward jets. A theory for this asymmetrization is developed using Rossby wave propagation theory. The theoretical explanation also makes clear the maintenance mechanism of the zonal jets.

Keywords: β-plane turbulence, jet formation, Rossby wave propagation theory

1.   Introduction

Spontaneous zonal jet formation is a well-known significant feature in two-dimensional β-plane turbulence (Rhines 1975, Vallis & Maltrud 1993). The formation itself is considered due to the energy upward cascade which is in favor of zonal structure by the existence of the β term. Why the formed zonal jets are maintained in the turbulence, however, has been an open question. Vallis & Maltrud (1993) found an asymmetry between eastward and westward jet profiles which emerged from turbulent states in forced-dissipative experiments. That is, eastward jets are narrower and more intense than westward jets. This asymmetry is thought to be related to the Rayleigh-Kuo criterion of barotropic instability. Whether such an asymmetry exists or not in decaying experiments, however, has not been explored. Therefore, we study the maintenance mechanism and symmetric properties of the zonal jets in two-dimensional β-plane decaying turbulence numerically, by conducting a number of ensemble exper-

iments. Furthermore, we propose a theoretical scenario to explain the found asymmetry using the Rossby wave propagation theory.

2.   Model

The system under consideration is a non-divergent two-dimensional flow with a hyper-viscosity on a β-plane. The flow is governed by the vorticity equation,

$$\frac{\partial \zeta}{\partial t} + \frac{\partial \psi}{\partial x}\frac{\partial \zeta}{\partial y} - \frac{\partial \psi}{\partial y}\frac{\partial \zeta}{\partial x} + \beta\frac{\partial \psi}{\partial x} = (-1)^{p+1}\nu_{2p}(\nabla^2)^p\zeta. \tag{1}$$

Here, $\zeta \equiv \nabla^2\psi$ is the vorticity, ψ is the streamfunction, x is the longitude, y is the latitude, t is the time, ∇^2 is Laplacian, ν_{2p} is the hyper-viscosity coefficient, p is the order of the hyper-viscosity. We fix p and ν_p as $p = 2$ and $\nu_p = 1.0 \times 10^{-10}$. We assume the periodic boundary condition in both x and y directions as

$$\zeta(x, y + 2\pi, t) = \zeta(x, y, t) = \zeta(x + 2\pi, y, t).$$

To integrate (1) numerically, we adopt Fourier spectral method with the truncation wavenumber of 1024 for the spatial discretization. The time integration scheme is the classical 4th-order Runge-Kutta scheme.

The initial condition is given by a random vorticity field which has a peak in the energy spectrum at wavenumber $K = 226$. The phase of each component is set randomly. The total energy of the initial state is set at $1/2$. This means that the root-mean-square velocity (u_0) for the initial state is 1. We sweep the value of β as an experimental parameter as $\beta = 100, 200, 400, 800, 1600, 3200, 6400, 12800, 25600, 51200$. The results for $\beta = 6400$ are presented mainly below.

3.   Results

Figure 1 shows the zonal-mean zonal flow profiles at the final stage ($t = 12$) for the 10 different values of β. The width of each jet is roughly estimated by Rhines scale $L = \sqrt{u_0/\beta}$. Checking the jet profiles in detail, we can find an asymmetry between westward and eastward jet profiles. Figure 2 shows composites of intense jet profiles at the final stage for $\beta = 6400$. It is clear that there is an asymmetry between Figs. 2(b) and (d), that is, westward jets are narrower and more intense than eastward jets. This asymmetry can be also seen in the time-evolution of the peak flow speeds of westward jets and eastward jets (Fig. 3). Although there is no difference initially, the peak speed of westward jets becomes larger than that of eastward jets. We confirmed the existence of asymmetry for other values of β and checked its statistical validity by using other random initial conditions.
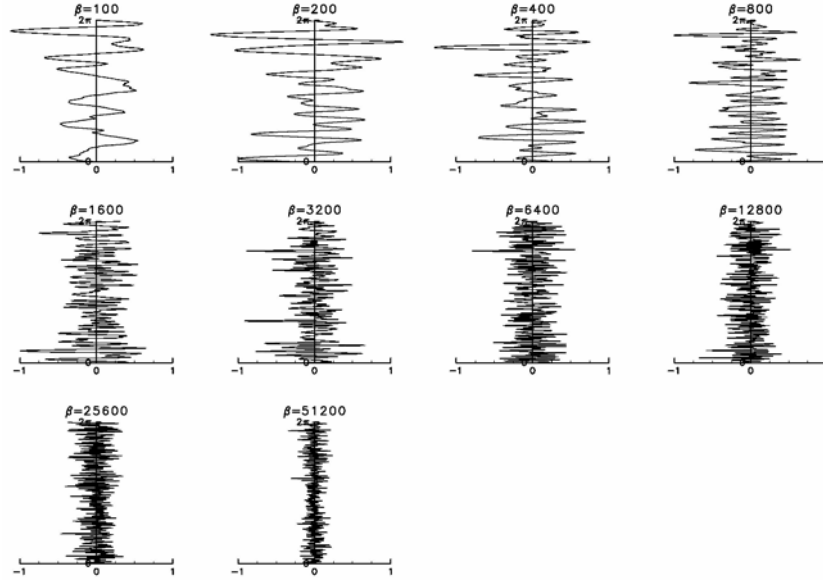
Figure 1. Zonal-mean zonal flow profiles at $t = 12$ for various values of β. The vertical axis indicates y.
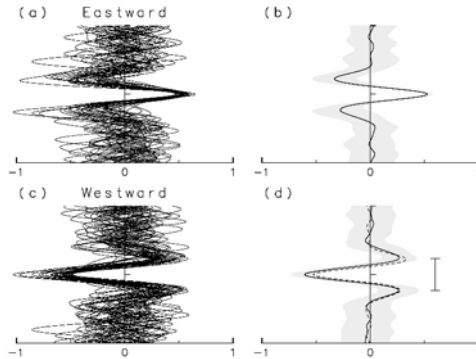

Figure 2. Composite of intense jet profiles at $t = 12$ for $\beta = 6400$. (a): composite of 36 intense eastward jet profiles. (b): the mean profile and the standard deviation of (a) (gray area). (c): composite of 42 intense westward jet profiles. (d): the mean profile and the standard deviation of (c) (gray area). the dashed line is the mirror image of the profile in (b)
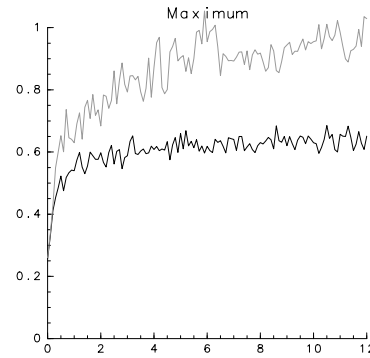

Figure 3. Time evolutions of the peak flow speeds of westward jets (gray) and eastward jets (black) for $\beta = 6400$. The horizontal axis indicates time t.

4. Theory

In order to explain the asymmetry described in the previous section, we propose a following scenario for the asymmetry formation.

(i) At the early stage, weak zonal jets are formed through the upward energy cascade in the β-plane turbulence.

(ii) According to the Rossby wave propagation theory, l^2 (l being the latitudinal wavenumber) of Rossby waves becomes so large in westward jet regions that Rossby waves are dissipated more easily than in eastward jet regions due to the hyper-viscosity.

(iii) When Rossby waves are dissipated, they leave their westward pseudo-momentum to zonal jets. Therefore, westward jets are intensified sharply.

We check the validity of this scenario, using the linearized equation of (1),

$$\frac{\partial \zeta'}{\partial t} + U(y)\frac{\partial \zeta'}{\partial x} + \left(\beta - \frac{\mathrm{d}^2 U}{\mathrm{d}y^2}\right)\frac{\partial \psi'}{\partial x} = (-1)^{p+1}\nu_{2p}(\nabla^2)^p \zeta'.$$

Here, $U(y)$ is a prescribed basic zonal flow, and $\zeta' = \nabla^2 \psi'$. The acceleration is evaluated by

$$\Delta U = -\int_0^t \frac{\mathrm{d}}{\mathrm{d}y}(\overline{u'v'})\mathrm{d}t',$$

where $u' = -\partial \psi'/\partial y$ and $v' = \partial \psi'/\partial x$.

First, we consider an idealized situation. The prescribed basic zonal flow profile is set as

$$U(y) = -A\sin(my).$$

The initial disturbance is set to be a monochromatic wave,

$$\psi'(x, y, t = 0) = \sin(kx + ly)$$

with $k = l = m = 64$ and $A = 0.14$. This choice is based on the mean values of the wavenumbers for both zonal components and wavy disturbances, and of the speed of zonal jets in the nonlinear time-evolution at $t = 0.2$ when zonal jets start growing but the asymmetry has not yet developed. Figure 4 shows the total acceleration (ΔU) for this idealized situation. As is expected in the proposed scenario, the westward acceleration is sharper and more intense in the westward jet region than the eastward acceleration in the eastward jet region.

The situation above is a little too idealized to confirm the scenario because the initial disturbance is set to be a monochromatic wave. Therefore, we adopt a more relevant initial condition. We set the initial ψ' to be the same field as that of the turbulent field in the time-evolution of (1) at $t = 0.2$ excluding zonal components. Figure 5 shows the total acceleration for this situation. Even in this case, the westward acceleration is sharper and more intense in the westward jet region, which confirm our scenario for the asymmetry formation.
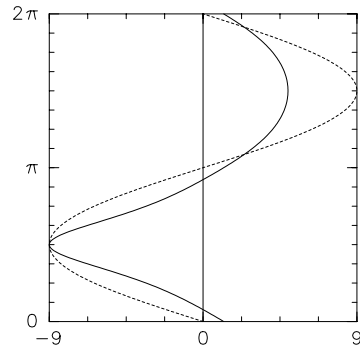
Figure 4. Total acceleration by an initially monochromatic Rossby wave in the linearized model. Solid line: the total acceleration. Dotted line: the prescribed zonal flow profile. Only one cycle of the zonal jet is shown.
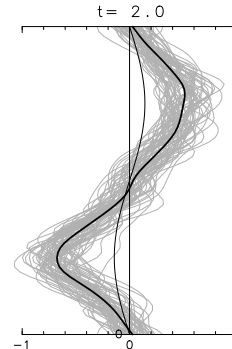
Figure 5. Composite of total accelerations by Rossby waves in the linearized model. Thin gray lines: the acceleration profiles. Thick line: the mean profile of the total accelerations. Thin line: the prescribed zonal flow profile. Every cycle of the zonal jet is put together.

5. Conclusions

We found an asymmetry in zonal jet profiles in β-plane decaying turbulence — westward jets are narrower and more intense than eastward jets. We made clear that the asymmetry is due to the change of l^2 of Rossby waves by the basic zonal flow using Rossby wave propagation theory. This mechanism also contributes to the maintenance of zonal jets.

References

RHINES, P. B. 1975 Waves and turbulence on a beta-plane. *J. Fluid Mech.* **69**, 417 – 443.

VALLIS, G. K. & MALTRUD M. E. 1993 Generation of mean flows and jets on a beta plane and over topography. *J. Phys. Oceanogr.* **23**, 1346 – 1362.

DYNAMICS OF VELOCITY FIELD
IN DEVELOPED THERMAL TURBULENCE

Takashi Mashiko
Department of Physics, Graduate School of Science, University of Tokyo,
7-3-1 Hongo, Bunkyo-ku, Tokyo 113-0033 Japan
mash@daisy.phys.s.u-tokyo.ac.jp

Yoshiyuki Tsuji
Department of Energy Science and Engineering, Graduate School of Engineering,
Nagoya University
Furocho, Chikusa-ku, Nagoya 464-8603 Japan
c42406a@nucc.cc.nagoya-u.ac.jp

Masaki Sano
Department of Physics, Graduate School of Science, University of Tokyo,
7-3-1 Hongo, Bunkyo-ku, Tokyo 113-0033 Japan
sano@phys.s.u-tokyo.ac.jp

Abstract   We have measured instantaneous velocity profiles in mercury thermal turbulence in a cylindrical cell of 1/2-aspect-ratio. In our previous work, we obtained some intriguing results from the measurement of the vertical velocity profile $w(z)$ along the central axis of the cell. To investigate the velocity field in more detail, we have recently improved the apparatus so that horizontal velocity profiles $u(x)$ and $v(y)$ just below the top plate can be measured as well as $w(z)$. In this paper, some preliminary results from the measurements of the horizontal profiles are introduced together with the speculation of the shape of the mean flow, and future prospects are presented.

Keywords: Thermal turbulence, mercury, ultrasonic velocimetry

1.   Introduction

Thermal turbulence is a ubiquitous phenomenon and has been studied for a long time as a prototype of complex physical systems. Nevertheless, many problems still remain open: How is the ultimate state of thermal turbulence at very high Rayleigh number (Ra)? Are there some statistical laws of fluctuations

peculiar to thermal turbulence? How does the mean flow emerge and behave in well-developed thermal turbulence? To attack most of the open problems, it is highly desired to understand the structure of the velocity field in terms of both time and space. However, such a requirement has not been achieved to a satisfactory extent so far, due to the difficulty of the measurement of instantaneous velocity profiles.

We applied the ultrasonic velocimetry in thermal turbulence for the first time and measured instantaneous velocity profiles in a 1/2-aspect-ratio cylinder filled with mercury. The main reason for the use of mercury is its low Prandtl number ($Pr \sim 0.025$ at room temperature). In low-Pr fluids, the boundary layers get destabilized and hence a new state beyond the hard turbulence is likely to be induced, at relatively low Ra. Therefore, the use of a low-Pr fluid is adequate to study well-developed thermal turbulence and seek the ultimate state. The Rayleigh number ($Ra \equiv \alpha g \Delta T h^3 / \kappa \nu$, where α, κ, ν, g, and h are the expansion coefficient, thermal diffusivity, kinematic viscosity of the fluid, gravitational acceleration, and the cell height, respectively) is a nondimensional expression of the temperature difference ΔT between the top and bottom boundaries, and can be increased to very high values in this apparatus of $h = 612$ mm height; $2 \times 10^9 \leq Ra \leq 6 \times 10^{10}$, which is the world record for low-Pr fluids. In the previous work, we measured the vertical velocity profile $w(z)$ along the central axis of the cell, which brought about some intriguing results (Mashiko *et al.* 2004a; Mashiko *et al.* 2004b): The energy spectrum $E(k)$ was calculated from $w(z)$ without employing Taylor's frozen-flow hypothesis for the first time, which agreed well with the prediction of $E(k) \propto k^{-11/5}$ in the Bolgiano theory (Bolgiano 1959). Also, possible shapes and sloshing motion of the mean flow were proposed through the principal component analysis and other analyses. Furthermore, the reversal of the mean profile near the boundary plate was discovered. However, measurements in the previous work were just for the one-dimensional profile $w(z)$. To further examine the velocity field, we have recently started new measurements.

2.   Experiment

2.1   Improvement of the apparatus

We improved the apparatus so that the horizontal velocity profiles $u(x)$ and $v(y)$ near the boundary plate can be measured as well as $w(z)$ (Fig. 1). Ultrasound transducers X and Y are installed for the measurements of $u(x)$ and $v(y)$, respectively, in addition to Z for $w(z)$. Each of X and Y is located so that its cylindrical axis should lie 4.5 mm below the bottom surface of the top plate, where the diameter of each transducer is 8 mm (the beam diameter is 5 mm). The transducer emits ultrasound pulses of frequency $f_0 = 4$ MHz and receives the echoes scattered in the fluid. One-dimensional profile of the veloc-

ity component along the beam axis is obtained by detecting the Doppler-shift frequencies.
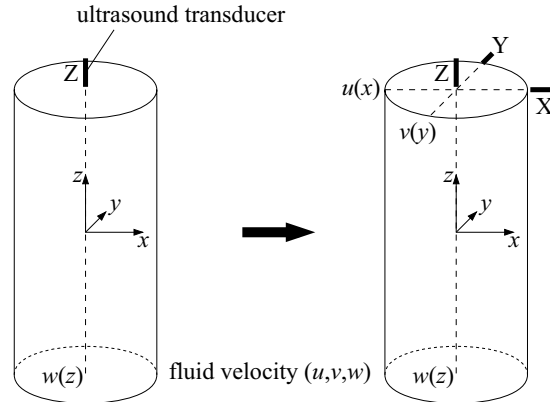

Figure 1. Improvement of the experimental system. Horizontal velocity profiles $u(x)$ and $v(y)$ are measured in addition to $w(z)$.

2.2 Results

We show in Fig. 2 typical results of the measurements of $u(t, x)$ and $v(t, y)$ in the form of the spatiotemporal plots (left), together with the corresponding mean profiles $\langle u(x) \rangle$ and $\langle v(y) \rangle$ (right). Both u and v were measured at $Ra = 2.69 \times 10^{10}$ (but separately) with the sampling time of $\Delta t = 64.8$ ms and the spatial resolutions of $\Delta x = \Delta y = 2.18$ mm. The span of each spatiotemporal plot is $0 \leq t \leq 32.3$ s in time and $-128.8 \leq x, y \leq 148.1$ mm in space which covers most of the plate diameter ($-153 \leq x, y \leq 153$ mm). In these plots, slanted straight patterns are characteristic, as indicated by white arrows. By flow visualization in water thermal turbulence, Zocchi *et al.* (1990) observed traveling waves along the boundary plate. They suggested that the waves are produced when plumes (mushroom-shaped thermal structures) hit the plate. We presume that the slanted straight patterns in Fig. 2 are the sign of such traveling of thermal structures, whereas the thermal structures are possibly rather vague without clear perimeters like the plumes, in the low-Pr fluid, mercury. We are going to elucidate the identity and detailed behavior of the thermal structures in further measurements.

We notice that the spatiotemporal plots are mostly covered by white-colored regions. This means that the horizontal flow just below the top plate is unidirectional in most part of the plate, while the opposite flow is observed just in a little portion of the plate. This tendency is also confirmed by the mean profiles, each of which was calculated from 10000 successive instantaneous profiles: Both

$\langle u(x) \rangle$ and $\langle v(y) \rangle$ are asymmetric in that the zero-crossing points (x_{zero} and y_{zero}) are far from the z axis ($x = y = 0$). While the mean profiles shown in the figure were calculated from data over 648 s, the asymmetry was generally observed even in measurements for more than 4.5 hours. On the other hand, we found that the vertical mean profile $\langle w(z) \rangle$ was symmetric in that the zero-crossing point nearly corresponds with $z = 0$, *i.e.* the cell center (Mashiko *et al.* 2004a), where data of nearly the same length were used for the calculation of the horizontal and vertical mean profiles. Also, it was found that $|u_{\mathrm{max}}|$ and $|v_{\mathrm{max}}|$, $|x_{\mathrm{zero}}|$ and $|y_{\mathrm{zero}}|$ generally increase as Ra increases.
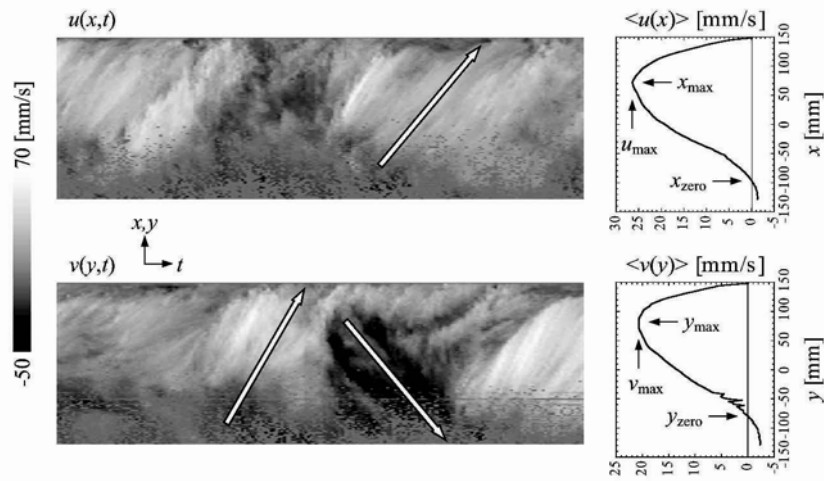
Figure 2. Spatiotemporal plots of the velocity field (left) and the mean profiles (right). The top plots are of u and the bottom are of v.

3.   Discussion

By the present measurement of the horizontal velocity profiles, we can advance in the speculation of the mean flow. In the previous measurement of $w(z)$, we found that the flow is upward in the upper half of the cell and downward in the lower half on average and proposed two simple patterns as the shape of the mean flow as shown in Fig. 3 (Mashiko *et al.* 2004a). In this figure, probable mean profiles are schematically shown by gray arrows. The left pattern would be accompanied by asymmetric horizontal profiles, while the right pattern seems to be accompanied by symmetric profiles. Actually, the horizontal mean profiles were asymmetric, as was shown in Fig. 2. Therefore, we suggest that the left pattern is preferable for the mean-flow shape in a cylinder of 1/2-aspect-ratio. Then we can interpret the above-mentioned properties qualitatively. For example, the increase of $|x_{\mathrm{zero}}|$ and $|y_{\mathrm{zero}}|$ with the increase

of Ra is explained by that the main elliptic roll of the mean flow comes to run closer to the cell perimeter when Ra is increased (Xia *et al.* 1997). Also, the increase of $|u_{\max}|$ and $|v_{\max}|$ can be explained by the increase of the mean-flow velocity. By the way, assuming the symmetry of the experimental setup, the mean profiles should be symmetric in long-enough time scales. Symmetric horizontal mean profiles might be obtained in much longer measurements.
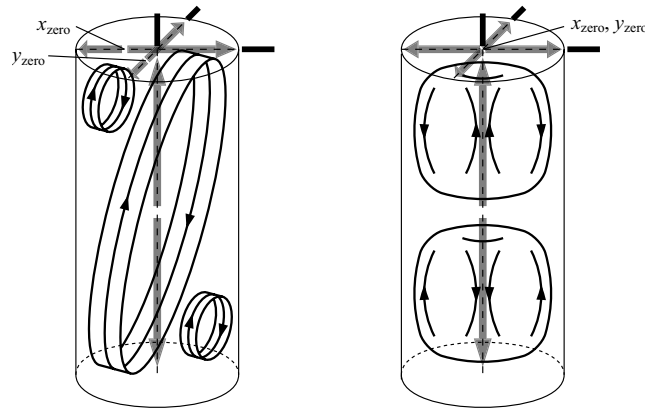

Figure 3. Speculation of the mean flow. We proposed two simple shapes of the mean flow from the result of $\langle w(z) \rangle$ in the previous work. Horizontal profiles $\langle u(x) \rangle$ and $\langle v(y) \rangle$ in the present work imply that the left one is likely.

4. Summary

We introduced preliminary results of the measurements of the horizontal velocity profiles $u(x)$ and $v(y)$ in the boundary region. In particular, the mean-flow behavior was discussed. We are going to start the simultaneous measurements of $u(x)$, $v(y)$, and $w(z)$ soon. The above-mentioned behaviors of the mean flow (in terms of $|u_{\max}|$ and $|v_{\max}|$, $|x_{\mathrm{zero}}|$ and $|y_{\mathrm{zero}}|$) and the sloshing motion speculated in the previous work will be clearly confirmed in such a trial. Also, the reversal of $w(z)$ near the boundary plate (Mashiko *et al.* 2004b) will be investigated in detail. Additionally, we aim to establish statistical laws of fluctuations in thermal turbulence. For example, we will observe the variance of the energy spectrum $E(k)$ with varying Ra, and compare the results with theories.

218

References

BOLGIANO, JR., R. 1959 Turbulent spectra in a stably stratified atmosphere *J. Geophys. Res.* **64**, 2226–2229.

MASHIKO, T., TSUJI, Y., MIZUNO, T. & SANO, M. 2004a Instantaneous measurement of velocity fields in developed thermal turbulence in mercury *Phys. Rev. E* **69**, 036306.

MASHIKO, T., TSUJI, Y., MIZUNO, T. & SANO, M. 2004b Measurement of velocity field in thermal turbulence in mercury by ultrasonic Doppler method *Theor. Appl. Mech. Jpn.* **53**, 207–214.

XIA, K.-Q., SUN, C., & ZHOU, S.-Q. 1997 Particle image velocimetry measurement of the velocity field in turbulent thermal convection *Phys. Rev. E* **68**, 066303.

ZOCCHI, G., MOSES, E., & LIBCHABER, A. 1990 Coherent structures in turbulent convection, an experimental study *Physica A* **166**, 387–407.

INSTABILITY OF CO-ROTATING VERTICAL VORTICES IN A STRATIFIED FLUID

Pantxika Otheguy, Paul Billant, Jean-Marc Chomaz
LadHyX, CNRS - Ecole Polytechnique,
Ecole Polytechnique, 91128 Palaiseau, FRANCE

pantxika.otheguy@ladhyx.polytechnique.fr

Paul.Billant@ladhyx.polytechnique.fr

Jean-Marc.Chomaz@ladhyx.polytechnique.fr

Abstract   We show numerically, theoretically and experimentally that two co-rotating vertical vortices in a stably stratified fluid are subjected to a new three-dimensional similar to the zigzag instability observed on counter-rotating vortices (Billant & Chomaz, 2000). This zigzag instability induces the formation of thin horizontal layers with a thickness inversely proportional to the Brunt-Väisälä frequency. This three-dimensional instability is believed to make stratified turbulence depart from two-dimensional turbulence since it alters the merging of vortices.

Keywords: Vortex, stratification, three-dimensional instability, layers, merging

1.   Introduction

The atmosphere — especially the stratosphere — and the ocean are characterized by a stable stratification that limits vertical motions and makes the flow mainly horizontal. Riley *et al.* (1981) have shown that if both the horizontal and the vertical scales of the flow are large compared to the buoyancy length scale, the leading order dynamics are then two-dimensional. Building upon this conjecture, Lilly (1983) has proposed that the kinetic energy spectra observed in the atmosphere at mesoscale are a manifestation of a two-dimensional dynamics with a transfer of energy from small ($\sim$ 1 km) to large ($\sim$ 500 km) scales. Recently, Lindborg (1999) invalidated this interpretation by deducing from high order statistical moments that the energy cascade is in the opposite direction: from large to small scales. Billant & Chomaz (2001) proposed that the dynamic is not two-dimensional because the vertical scale selected by the flow is the local buoyancy length scale $L_B = U/N$ (where U is the horizontal velocity scale and N the Brunt-Väisälä frequency), invalidating the hypothesis of Riley *et al.* (1981). Billant & Chomaz (2000) have also shown that

the vertical scale selection is due to an instability, named zigzag instability, in the specific case of a counter-rotating vortex pair. In the present paper, we extend the work of Billant & Chomaz (2000) and study the stability of a pair of co-rotating vortices in a stratified fluid. We show that the zigzag instability also affects such basic state and decorrelates the flow on the buoyancy length scale. This suggests that the zigzag instability is a general instability affecting stratified flows with at least two vortices.

2. Three-dimensional linear stability analysis

2.1 Numerical analysis

The three-dimensional stability of a pair of co-rotating vertical vortices has been investigated numerically using a pseudo-spectral solver of the linearized Navier-Stokes equations. The basic state has been obtained numerically from a two-dimensional numerical simulation initialized by two co-rotating axisymmetric gaussian vortices. The two vortices adapt to each other and evolve quickly toward a quasi-steady state. The three-dimensional stability of this basic flow is then investigated as a function of the Froude number in the case where the ratio of the vortex radius a and the separating distance b is $a/b = 0.15$. We have observed that the elliptic instability is the most unstable instability when the horizontal Froude number $F_h = \Gamma/\pi a^2 N$, where Γ is the vortex circulation, is large: $F_h > 10$. In contrast, we have found that the zigzag instability is the most unstable instability for strong stratification: $F_h < 2.85$.

As seen on the vertical vorticity of the eigenmode (figure 1a), the zigzag instability translates the two vortices with almost no deformation along opposite directions. This motion amounts to a small rotation of the vortex pair as a whole together with a slight variation of the separating distance. The instability will consequently bring the vortices closer or farther, alternatively along the vertical.

Figure 1b shows further that the growth rate of the zigzag instability is a function of the wavenumber times the Froude number: $k_z F_h$ for small F_h. This self-similarity means that the most unstable wavenumber is inversely proportional to the Froude number implying that the wavelength decreases as the stratification increases. The instability will therefore generate horizontal layers with a thickness scaling as the buoyancy length in agreement with the scaling law of Billant & Chomaz (2000) in the case of counter-rotating vortices. The fact that co-rotating and counter-rotating vortex pairs are both affected by the zigzag instability suggests that this instability is a generic three-dimensional instability of stratified flows.

In addition, by varying the parameter a/b for a given Froude number, we have been able to show that the growth rate of the zigzag instability scales like the strain $\epsilon = \Gamma/2\pi b^2$ while its most amplified wavelength scales on the separating distance b, not on the vortex radius a.
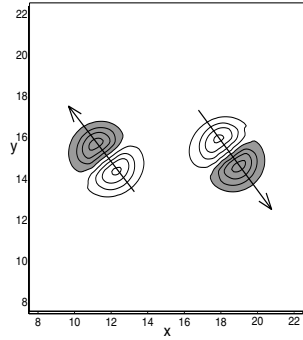
Figure 1a. Vertical vorticity of the eigen-mode of the zigzag instability for $F_h = 1$, $Re = 1000$, $a/b = 0.15$ and $k_z = 1.5$. The arrows indicate the direction of translation of the two vortices due to the zigzag instability.
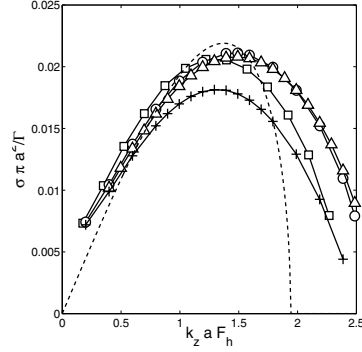
Figure 1b. Growth rate as a function of $k_z F_h$ for $Re = 15000$, $F_h = 1.7\,(\square)$, $F_h = 1\,(\circ)$, $F_h = 0.5\,(\triangle)$ and $F_h = 0.2\,(+)$. The dotted line represents the asymptotic growth rate (1).

The additional effect of a planetary rotation has been also investigated in order to draw a link between the zigzag instability observed in strongly stratified fluids and the tall-column instability observed in strongly stratified and rapidly rotating fluids (quasi-geostrophic fluids) (Dritschel & de la Torre Juárez, 1996). The maximum growth rate of the zigzag instability is approximately independent of the Rossby number ($Ro = \Gamma/\pi a^2 f$, where f is the Coriolis parameter equal to twice the planetary rotation rate). In contrast, the most unstable wavenumber k_{zm} varies continuously and scales as the Rossby number for small Ro for a given F_h. This result together with the dependence: $k_{zm} \propto 1/F_h$ shows that the most unstable wavenumber scales as $k_{zm} \propto Ro/F_h$ i.e. $k_{zm} \propto N/f$ for small F_h and Ro in agreement with the quasi-geostrophic theory (Dritschel *et al.*, 1999).

2.2 Theoretical analysis of the zigzag instability

The numerical results have been confirmed by an asymptotic stability analysis for well-separated vortices and for small horizontal and vertical Froude numbers. We first consider bending perturbations on a single axisymmetric Lamb-Oseen vortex, and then the coupling between these bending perturbations on each vortex and the strain due to the companion vortex. This leads to the growth rate of the zigzag instability for small F_h, $F_h k_z$ and a/b as

$$\sigma_a^2 = -\frac{2\Gamma^2}{\pi^2 b^2} D_0 (F_h k_z)^2 - D_0^2 \frac{\Gamma^2}{\pi^2} (F_h k_z)^4, \tag{1}$$

where D_0 is a negative constant. As seen in figure 1b, the asymptotic growth rate of the zigzag instability is in excellent agreement with the numerical linear stability analysis. Furthermore, the formula shows that $\sigma_{max} = \Gamma/\pi b^2$ and $k_{zm} = 1/F_h b\sqrt{-1/D_0}$, i.e. the growth rate scales like the strain and the most amplified wavelength scales like $F_h b$ in agreement with the scaling laws found numerically.

3. Experiment and direct numerical simulation

3.1 Experimental observations

The existence of the zigzag instability on the co-rotating vortex pair has been confirmed experimentally. The experiments have been performed in a 100cm wide, 100cm long and 70cm deep glass tank filled with a linear stratified salt solution. Two co-rotating columnar vortices are created by quickly rotating two flaps with an apparatus similar to the one used by Meunier & Leweke (2001). The flow is visualized by UV light and fluoresceine dye.

For strong stratification, we have observed the zigzag instability (figure 2). Just after their formation (time t_1), the two vortices rotate one around the other and are straight along the vertical. At time t_2, the zigzag instability which distorts symmetrically the two vortices can be clearly seen. The distance between the vortices varies sinusoidally along the vertical generating layers where merging is accelerated or delayed (time t_3) resulting in a complex twisting of the vortices (time t_4).

$t_1 = 0s$ $\qquad$ $t_2 = 81s$ $\qquad$ $t_3 = 87s$ $\qquad$ $t_4 = 135s$
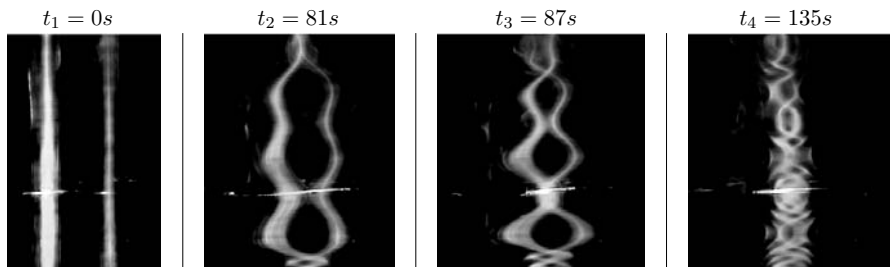
Figure 2. Side view visualizations of the zigzag instability of two co-rotating vortices in a strongly stratified fluid at different times.

3.2 Direct Numerical Simulations

In addition, we have performed direct numerical simulations of the zigzag instability (this work is done in collaboration with Y. Kimura of Nagoya University). A pseudo-spectral code simulating the Navier-Stokes equation under the Boussinesq approximation has been initialized by two Lamb-Oseen vortices.

As seen in figure 3, the pairing between the two co-rotating vortices is alternatively enhanced and delayed along the vertical generating a layered structure as observed in the experiments. Ultimately, the two vortices merge all along the vertical. The wavelength observed is in good agreement with both experiment and linear theory.
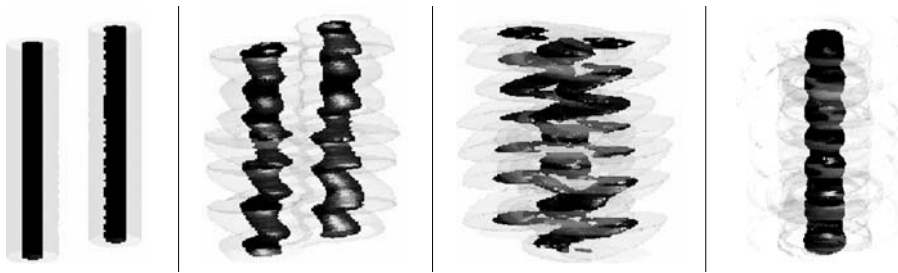

Figure 3. Direct numerical simulations of the zigzag instability: two contours (5% and 60% of the maximum vertical mean) of vertical vorticity are shown in light grey and dark grey at different times. The resolution used is 128^3, and the parameters are $F_h = 1.3$, $Re = 2000$ and $a/b = 0.15$.

4. Summary

A new zigzag instability has been discovered in the case of two co-rotating vertical vortices in a stably stratified flow. The numerical stability analysis has shown that the instability consists in displacement of the vortices and selects a vertical wavelength proportional to the buoyancy length ($L_B=U/N$) with a growth rate proportional to the strain rate. The coupling between the bending modes of each vortex with the strain field is the origin of the instability. Experimental observations and DNS show that the instability does not saturate and leads to the vertical decorrelation of the flow on a scale proportional to L_B. As vortex merging plays a crucial role in two-dimensional turbulence, this new three-dimensional instability is believed to alter the energy transfer and therefore makes three-dimensional stratified turbulence depart from two-dimensional turbulence.

Acknowledgments

References

MEUNIER, P. & LEWEKE, T. 2001 Three-dimensional instability during vortex merging. *Phys. Fluids* **13**, 2747–2750.

224

BILLANT, P. & CHOMAZ, J.-M. 2000 Theoretical analysis of the zigzag instability of a vertical columnar vortex pair in a strongly stratified fluid. *J. Fluid Mech.* **419**, 29–63.

BILLANT, P. & CHOMAZ, J.-M. 2001 Self-similarity of strongly stratified inviscid flows. *Phys. Fluids* **13**, 1645–1651.

LILLY D. K. 1983 Stratified turbulence and the mesoscale variability of the atmosphere. *J. Atmos. Sci.* **40**, 749–761.

LINDBORG E. 1999 Can the atmospheric kinetic energy spectrum be explained by two-dimensional turbulence ? *J. Fluid Mech* **388**, 59–288.

RILEY J. J., METCALFE R. W. & WEISSMAN M. A. 1981 Direct numerical simulations of homogeneous turbulence in density stratified fluids. *Proc. AIP Conf. Nonlinear properties of internal waves (ed. B.J. West)*, 79–112.

DRITSCHEL D. G. AND DE LA TORRE JUÁREZ M. & AMBAUM M. H. P. 1999 The three-dimensional vortical nature of atmospheric and oceanic turbulent flows. *Phys. Fluids* **11**, 1512–1520.

DRITSCHEL D. G. AND DE LA TORRE JUÁREZ M. 1996 The instability and breakdown of tall columnar vortices in a quasi-geostrophic fluid. *J. Fluid Mech.* **328**, 129–160.

ACTION OF COHERENT VORTICES IN ROTATING DUCT FLOWS

Yoshito Kaga
Graduate School of Natural Science and Technology, Okayama University,
3-1-1, Tsushima-Naka, Okayama-city, Okayama 700-8530, Japan[*]
kaga@fcs.coe.nagoya-u.ac.jp

Shinichiro Yanase
Department of Mechanical Engineering, Faculty of Engineering and Information Technolgy Center, Okayama University,
3-1-1, Tsushima-Naka, Okayama-city, Okayama 700-8530, Japan
yanase@mech.okayama-u.ac.jp

Abstract   In rotating duct flows, coherent longitudinal vortical structures develop even for very low Reynolds numbers due to the shear-Coriolis instability, where the mean absolute vorticity is close to zero. We investigate the creation mechanism of zero-mean-absolute-vorticity region focusing on the role of the longitudinal vortical structures for the plane-Poiseuille- and plane-Couette-type flows with the system rotation. It is found that the way of the vortex tubes to create zero-mean-absolute-vorticity state is different between the two cases. For the rotating plane-Poiseuille-type flow, the generated longitudinal vortex tubes develop the spanwise vorticity around them, whereas for the rotating plane-Couette-type flow, they enhance the spanwise vorticity inside them. However, it is common for the two cases that zero-mean-absolute-vorticity state is created by the action of the coherent longitudinal vortices in the anticyclonic region.

1.   Introduction

Rotating shear flows have been attracting interest of many researchers because of their ample applications in meteorology, turbo-machinery, and so on. In the rotating shear flow, if the direction of the system rotation is opposite to

---

[*]present address
Energy Conversion Research Center, Doshisha University, 1-3 Tatara-Miyakodani, Kyotanabe 610-0394, Japan

that of the vorticity of the basic shear, the shear-Coriolis instability (inertia instability) occurs and coherent vortical structures are generated in the anticyclonic region (Bradshaw 1969, Yanase *et al.* 1993). The vortical structures due to the shear-Coriolis instability tend to make the mean absolute vorticity close to zero. This zero-mean-absolute-vorticity state is observed numerically for the rotating free shear flow (Métais *et al.* 1995), the rotating plane-Couette-type flow (Bech & Andersson 1997) and the rotating plane-Poiseuille-type flow (Kristoffersen & Andersson 1993, Lamballais *et al.* 1998) and experimentally for the rotating plane-Poiseuille-type flow (Johnston *et al.* 1972, Kitoh 1999). The physical mechanism of this phenomenon is, however, not well understood so far.

In the present study, we elucidate it by use of numerical simulations. For this purpose, we examine the plane-Poiseuille- and plane-Couette-type flows with the system rotation, and find the difference of the creation mechanism of zero-mean-absolute-vorticity regions between these two typical flows with special consideration on the role of coherent vortical structures.

2. Numerical methods

We consider an incompressible viscous fluid flowing between two parallel plates perpendicular to the y-axis located at $y = \pm h$. The basic flow is directed along the x-axis and the whole system rotates around the z-axis with the angular velocity $\widetilde{\Omega}$ (see Fig. 1). All variables are nondimensionalized by use of h, the kinetic viscosity ν and the maximum velocity U_0 of the basic flow. The Reynolds number is defined by $Re = hU_0/\nu$. The basic flows are $U(y) = 1 - y^2$ for the rotating plane-Poiseuille-type flow and $U(y) = y$ for the rotating plane-Couette-type flow. We assume that the flow is periodic in the x- and z-directions and the computational domain is $(L_x, L_y, L_z) = (2\pi/\alpha, 2, 2\pi/\beta)$, where α and β are the basic wavenumbers in the x- and z-directions, respectively. We take $\alpha = 1$ and $\beta = 2$, which are chosen by aretaking into consideration of the linear instability to wavy disturbances performed by Finlay (1997).

The nondimensionalized Navier-Stokes and continuity equations in the rotating coordinate system are written as

$$\frac{\partial \boldsymbol{u}}{\partial t} + (\boldsymbol{u} \cdot \nabla)\boldsymbol{u} = -\nabla P + \frac{1}{Re}\triangle \boldsymbol{u} + 2\Omega \boldsymbol{u} \times \boldsymbol{k}, \tag{1}$$

$$\nabla \cdot \boldsymbol{u} = 0, \tag{2}$$

where $\boldsymbol{k}$ is the unit vector in the z-direction, $P = p - (\Omega \boldsymbol{k} \times \boldsymbol{x})^2/2$ the modified pressure and $\Omega = \widetilde{\Omega}h/U_0$ the rotating angular velocity. The velocity $\boldsymbol{u}$ and vorticity $\boldsymbol{\omega}$ are decomposed into the basic ($^-$) and perturbed ($\hat{}$) terms as $\boldsymbol{u} = (\bar{u}_x, \bar{u}_y, \bar{u}_z) + (\hat{u}_x, \hat{u}_y, \hat{u}_z)$, $\boldsymbol{\omega} = (\bar{\omega}_x, \bar{\omega}_y, \bar{\omega}_z) + (\hat{\omega}_x, \hat{\omega}_y, \hat{\omega}_z)$. The Fourier
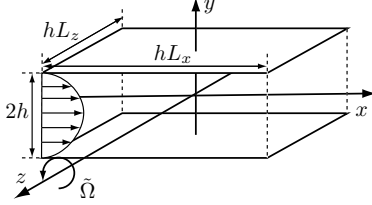
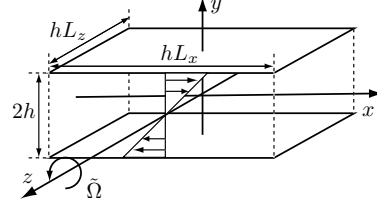*Figure 1a.* Rotating plane-Poiseuille-type flow.

Figure 1b. Rotating plane-Couette-type flow.

series expansion is employed to the x- and z-directions and the Chebyshev polynomial expansion to the y-direction.

3.   Results

3.1   Rotating plane-Poiseuille-type flow

For the rotating plane-Poiseuille-type flow, we performed time-evolution calculations for $Re \leq 550$ and $0 \leq \Omega \leq 1$. We obtained many characteristic solutions exhibiting typical vortical structures, such as steady, traveling-wave, time-periodic and chaotic solutions. We also obtained exact traveling-wave solutions by use of the Newton-Raphson iteration method (see Yanase & Kaga 2004).

We show the vortical structures of the chaotic solution at $Re = 400$ and $\Omega = 0.25$ in Fig. 2, where tubular vortical structures of the chaotic solution are visualized with iso-surfaces of a positive value of the second invariant of velocity gradient $Q = -\frac{1}{2}\frac{\partial u_i}{\partial x_j}\frac{\partial u_j}{\partial x_i}$ (see Jeong & Hussain 1995). We display these vortex tubes by black and gray for positive and negative ω_x, respectively. As seen in this figure, the tubular vortical structures appear in the anticyclonic region ($y < 0$), and the upflow region ($u_y > 0$) occupies narrower space than the downflow region ($u_y < 0$), because the negative Coriolis force $-2\Omega u_x$ in the whole flow region enhances the downflow. Figure 3 shows the distribution of three mean values of the chaotic solution of Fig. 2, $\langle \omega_z + 2\Omega \rangle$, $\langle \omega_z \rangle$ and $\langle \hat{\omega}_z \rangle$, where the symbol $\langle \ \rangle$ denotes double averaging which includes a spatial average over a plane perpendicular to the y-axis and a temporal average over some given time period. It is found that $\hat{\omega}_z$ develops in the anticyclonic region ($y < 0$) and the mean absolute vorticity $\langle \omega_z + 2\Omega \rangle$ approaches zero there. Figure 4 shows a (y, z) cross section of the chaotic solution. In this figure, the position of zero-local-absolute-vorticity in the (y, z) plane is denoted by the thick line and positive- and negative-local-absolute-vorticity regions distribute respectively above and below the line. It should be noted here that zero-local-absolute-vorticity locates at $y = -\Omega$ for the undisturbed basic flow. Downflow and upflow induced by the Coriolis force increase and decrease the spanwise
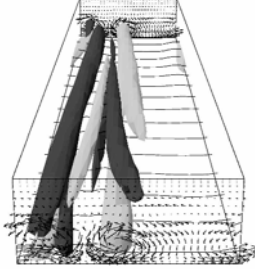
Figure 2. Tubular vortical structures of the chaotic solution at $Re = 400$ and $\Omega = 0.25$.
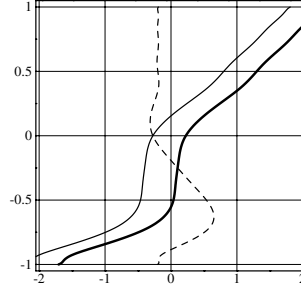

Figure 3. Mean values of the chaotic solution at $Re = 400$ and $\Omega = 0.25$. Thick line: $\langle \omega_z + 2\Omega \rangle$, thin line: $\langle \omega_z \rangle$, thin dashed line: $\langle \hat{\omega}_z \rangle$.
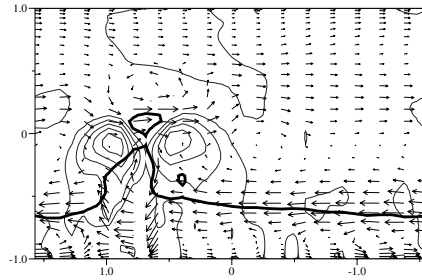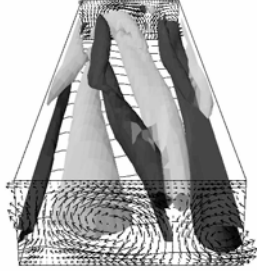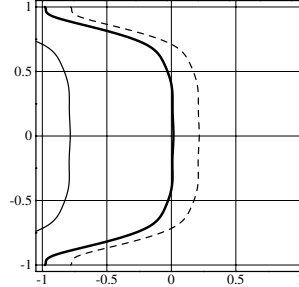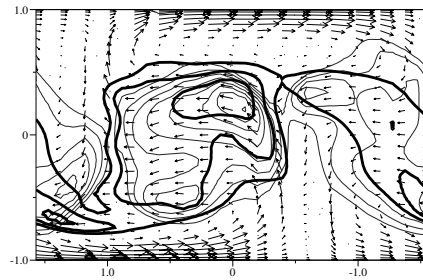

Figure 4. (y, z) cross section of the chaotic solution at $Re = 400$ and $\Omega = 0.25$. Thick line: $\omega_z + 2\Omega = 0$, thin lines: contours of positive Q, arrows: vorticity vectors of $(\hat{\omega}_y, \hat{\omega}_z)$.

vorticity ω_z around the position of zero-local-absolute-vorticity respectively, because u_x are accelerated in the opposite directions above and below the position of zero-local-absolute-vorticity by the term $u_y(-\partial u_x/\partial y + 2\Omega)$ in Eq. (1), and simultaneously the streamwise vortex tubes are formed there (see Fig. 8a below). Then, the positive- and negative-local-absolute-vorticity regions distribute by turns in the region where vortical structures exist, and the mean absolute vorticity is close to zero there.

3.2   Rotating plane-Couette-type flow

For the rotating plane-Couette-type flow, we performed time-evolution calculations for $Re \leq 400$ with the anticyclonic system rotation $0 \leq \Omega \leq 0.5$. In this case, we also obtained many characteristic solutions exhibiting typical vortical structures as in the preceding section.

Figure 5. Tubular vortical structures of the chaotic solution at $Re = 250$ and $\Omega = 0.40$.

Figure 6. Mean values of the chaotic solution at $Re = 250$ and $\Omega = 0.40$. Thick line: $\langle \omega_z + 2\Omega \rangle$, thin line: $\langle \omega_z \rangle$, thin dashed line: $\langle \hat{\omega}_z \rangle$.

Figure 7. (y, z) cross section of the chaotic solution at $Re = 250$ and $\Omega = 0.40$. Thick lines: contours of $\omega_z + 2\Omega \geq 0$, thin lines: contours of positive Q, arrows: vorticity vectors of $(\hat{\omega}_y, \hat{\omega}_z)$.

Swirling vortex tubes are generated in the central region between two plates by the Coriolis force $-2\Omega u_x$ in the y-direction, therefore swirling motion becomes active if Ω is increased. We show the results of the chaotic solution obtained at $Re = 250$ and $\Omega = 0.40$ in Figs. 5–7, which correspond to Figs. 2–4 for the rotating plane-Poiseuille-type flow. As shown in Fig. 5, the tubular vortical structures appear in the central region between two parallel plates, which contrasts with the rotating plane-Poiseuille-type flow in which they appear in the anticyclonic region for $-1 < y < 0$. The zero-mean-absolute-vorticity region is created more prominently than that of the rotating plane-Poiseuille-type flow (see Fig. 6), because the swirling motion of the longitudinal vortex tubes spreads out in a dominant part of the flow region. Figure 7 shows the flow in a (y, z) cross section of the chaotic solution. For the plane-Couette-type flow with the anticyclonic system rotation, the local-absolute-vorticity for the undisturbed basic shear is negative in a whole flow region. If the longitudinal

vortex tubes are generated, however, the local-absolute-vorticity becomes positive inside the vortex tubes (Fig. 7). Accordingly, zero-mean-absolute-vorticity region is created in the central region by the development of the $\hat{\omega}_z$ inside the vortex tubes, while, for the rotating plane-Poiseuille-type flow, it is created by the development of the $\hat{\omega}_z$ around the position of zero-local-absolute-vorticity (see Fig. 8).
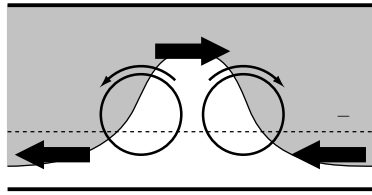

Figure 8a. Sketch of the generation mechanism of zero-mean-absolute-vorticity region for rotating plane-Poiseuille-type flow. Gray and white regions are positive and negative local-absolute-vorticity regions respectively. Thick black arrows denote the direction of spanwise vorticity.
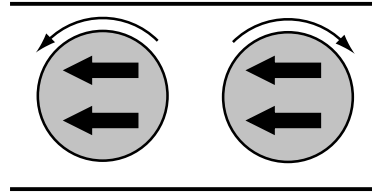
Figure 8b. Sketch of the generation mechanism of zero-mean-absolute-vorticity region for rotating plane-Couette-type flow. Gray and white regions are positive and negative local-absolute-vorticity regions respectively. Thick black arrows denote the direction of spanwise vorticity.

4.   Conclusions

We investigated the creation mechanism of zero-mean-absolute-vorticity state for the rotating plane-Poiseuille- and plane-Couette-type flows. It was found that zero-mean-absolute-vorticity state is created by the action of longitudinal vortical structures for both cases, although the roles of them are different between the two cases.

References

Bech, K. H. & Andersson, H. I. 1997Turbulent plane Couette flow subject to strong system rotation. *J. Fluid Mech.* **347**, 289–314.

BRADSHAW, P. 1969 The analogy between streamline curvature and buoyancy in turbulent shear flow. *J. Fluid Mech.* **36**, 177–191.

JEONG, J. & HUSSAIN, F. 1995 On the identification of a vortex. *J. Fluid Mech.* **285**, 69–94.

Johnston, J. P., Halleen, R. M. & Lezius, D. K. 1972 Effects of spanwise rotation on the structure of two-dimensional fully developed turbulent channel flow. *J. Fluid Mech.* **56**, 533–557.

Kitoh, O. 1999 private communication.

Kristoffersen, R. & Andersson, H. I. 1993 Direct simulations of low-Reynolds number turbulent flow in a rotating channel. J. Fluid Mech. **256**, 163–197.

Lamballais, E., Métais, O. & Lesieur, M. 1998 Spectral-dynamic model for large-eddy simulations of turbulent rotating channel flow. *Theoret. Comput. Fluid Dyn.* **12**, 149–177.

Métais, O., Flores, C., Yanase, S., Riley, J. J. & Lesieur, M. 1995 Rotating free-shear flows. Part 2. Numerical simulations. *J. Fluid Mech.* **293**, 47–80.

Yanase, S., Flores, C., Métais, O. & Riley, J. J. 1993 Rotating free-shear flows. I. Linear stability analysis. *Phys. Fluids* A **5**, 2725–2737.

Yanase, S. & Kaga, Y. 2004 Zero-mean-absolute-vorticity state and vortical structures in rotating channel flow. *J. Phys. Soc. Jpn.* **73**, 1419–1422.

Part F   Instability and transition

INSTABILITY OF LOW-SPEED STREAKS LEADING TO WALL TURBULENCE

Masahito Asai, Yasufumi Konishi
Department of Arospace Engineering, Tokyo Metropolitan Institute of Technology,
Asahigaoka 6-6, Hino, Tokyo 191-0065 Japan
masai@cc.tmit.ac.jp, konishi@krasast8.tmit.ac.jp

Abstract   Nonlinear development of streak instability modes is examined up to the turbulent stage experimentally through artificially producing spanwise-periodic low-speed streaks in a laminar boundary layer. The experiment is focused on the subharmonic sinuous mode of instability. The sinusoidal motion of low-speed streaks caused by the streak instability is maintained three or four wavelengths downstream beyond the nonlinear saturation stage of instability, and subsequently breaks down. After the breakdown, near-wall low-speed streaks with lateral spacing of 100 wall units newly develop, and the mean velocity profile starts to exhibit the log-law. It is also found that the interaction between the quasi-streamwise vortices developing along the neighboring streaks causes large-scale arch-like vortices to develop in the region away from the wall.

Keywords: Wall turbulence, low-speed streaks, streak instability, streamwise vortices

1.   Introduction

With an insight that turbulence is caused and then sustained by a sequence of flow instabilities, we have been working on the transition to wall turbulence. In wall-bounded shear flows, transition depends on disturbance environments and therefore has various paths to wall turbulence even for the same flow geometry. In any transition path, however, prerequisite for the onset of wall turbulence is development of low-speed streaks near the wall. Under low background turbulence, low-speed streaks appear at the later stage after the secondary high-frequency instability. With increasing background turbulence, low-speed streaks appear at the initial stage of transition. When the low-speed streaks are intensified, they undergo oscillatory motions leading to subsequent streak breakdown into turbulent spots or patches (Brandt & Henningson 2002). The oscillatory motion of streaks is due to the so-called streak instability, instability of inflectional velocity profiles across each low-speed streak. The present study concerns the instability and transition of low-speed streaks, which are also

closely related to the regeneration mechanism of coherent near-wall vortices in wall turbulence.

To examine how the streak instability leads to the onset of wall turbulence in detail, it is important to realize laminar low-speed streaks initially as well as to introduce well-controlled artificial disturbances, as has been done in our previous studies (Asai *et al.* 2002, Konishi & Asai 2004). In the present experimental study on the evolution of streak instability, spanwise-periodic low-speed streaks are generated in a laminar boundary layer by using small pieces of screen set normal to the boundary-layer plate with an equal interval in the spanwise direction. In our previous stability experiment (Konishi & Asai 2004), the linear instabilities to the fundamental and subharmonic sinuous modes were examined in detail for the periodic low-speed streaks of various spanwise intervals and the subharmonic sinuous modes were found to be more amplified than the fundamental sinuous modes unless the streak spacing is much larger than the streak width. So, in the present study on the nonlinear development of the streak instability, we focus on the development of the most amplified subharmonic sinuous mode.

2.   Experimental setup and procedure

The whole experiment is conducted in a low turbulence wind tunnel of open jet type. The wind tunnel has three damping screens spanning the diffuser and five damping screens and a honeycomb in the settling chamber of 1200×1200 mm in cross section. The area ratio of the contraction to the test section of 400×400 mm is 9. A boundary-layer plate, which is 10 mm thick and 1100 mm long, is set parallel to the oncoming uniform flow in the test section. The free-stream velocity U_∞ is fixed at 4 m/s throughout the experiment. The free-stream turbulence is less than 0.1% of U_∞. The periodic low-speed streaks are produced in the boundary layer by using small 40-mesh screens (wire-gauzes) set normal to the boundary-layer plate at a location 500mm downstream of the leading edge. Without the screens, Blasius boundary layer develops with the displacement thickness of about 2.5mm at the locaion 500mm downstream of the leading edge. The screens whose width and height are 6mm and 3mm respectively are set with an equal interval of 15mm in the spanwise direction. In order to excite the streak instability, well-controlled external disturbances are introduced into the laminar low-speed streaks by time-periodic suction and blowing through small holes. We here focus on the sinuous mode of instability. In order to excite a sinuous instability mode, holes of 2mm in diameter are drilled at locations at both edges of each screen, 13.5mm downstream of the screens, and are connected separately to two loudspeakers by vinyl hoses. The two loudspeakers are driven with sine-wave signals which are 180 deg out of phase. A constant-temperature hot-wire anemometer is used to measure time-

mean and fluctuation velocities in the streamwise direction, U and u. Flow visualization is done by means of smoke-wire technique. As for the coordinate system, x is the streamwise distance measured from the leading edge, y the normal-to-wall distance, and z the spanwise distance. The x-position of the screens, $x = 500$mm, is denoted by x_0.

3.   Results and discussion

First let us show the laminar low-speed streaks artificially generated by using the screens. Figure 1 illustrates the flow field downstream of the screens in terms of the mean velocity U/U_∞ in the cross-section at $x - x_0 = 60$mm. We see the development of the regularly aligned streaky structure with the spanwise spacing $\lambda = 15$mm, in the region below $y = 4$mm. The distinct low-speed streaks extend far downstream beyond $x - x_0 = 400$mm though the velocity defect across each low-speed streak fills up gradually with x. The low-speed streaks remain laminar in the whole observation region up to $x - x_0 = 400$mm owing to the low background (wind tunnel) turbulence. Spanwise-periodic low-speed streaks are unstable to fundamental and/or subharmonic disturbances whose dominant spanwise wavelengths are the same as the streak spacing and twice the streak spacing respectively. In our previous experiment (Konishi & Asai 2004), the linear instability to fundamental and subharmonic sinuous modes was examined for various streak intervals in detail and subharmonic modes were found to be more amplified than fundamental modes for the present streak geometry. Note that the amplification of fundamental modes becomes weak with decreasing the ratio of the streak spacing to the streak width. So, we here focus on the evolution of the most amplified subharmonic sinuous mode.

Figures 2 and 3 show smoke-wire visualization pictures of the instability process. The streak instability attains a nonlinear saturation around $x - x_0 = 120$mm. Up to the nonlinear saturation stage of instability where a train of quasi-streamwise vortices of alternate sign of vorticity (Jeong *et al.* 1997) develops, the development of streak instability along each low-speed streak is similar to that observed in a singe low-speed streak (Asai *et al.* 2002), showing that interactions between the neighboring streaks are not strong in the early stage of the transition for the subharmonic mode. After the saturation stage, the low-speed streaks suffer from a large spanwise oscillation in each cycle and the neighboring quasi-streamwise vortices (inclined both in the spanwise and normal-to-wall directions) interact with each other, giving rise to strong blow-up motion which causes a large-scale arch-like structure to develop in the outer region. The sinusoidal motion of low-speed streaks continues at least three streamwise wavelengths downstream beyond the nonlinear satura-tion stage. Subsequently the lifted-up streamwise vortices break down into irregular smaller-scale vortices. Figure 4 illustrates the disturbance develop-
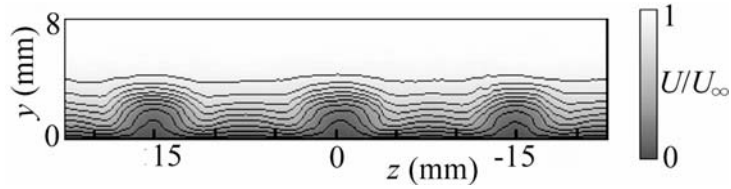
238

Figure 1. Iso-velocity contours in $y - z$ plane at $x - x_0$=60mm.
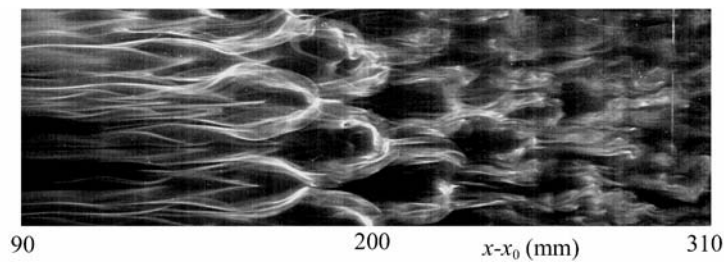

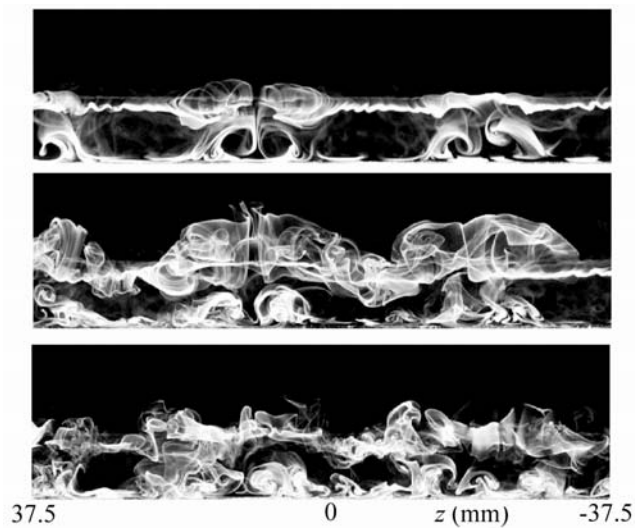*Figure 2.* Flow visualization of development of subharmonic mode: Smoke-wire height is 1.5mm.

Figure 3. Cross-sectional view of smoke-wire visualization. $x - x_0 = 160$mm, 210mm, 270mm. Smoke-wire is located 30mm upstream of the observation location.

ment in terms of r. m. s. intensity of velocity fluctuations. The breakdown stage around $x - x_0 = 200$mm corresponds to the region where the disturbances become weak. After the breakdown, near-wall low-speed streaks newly develop
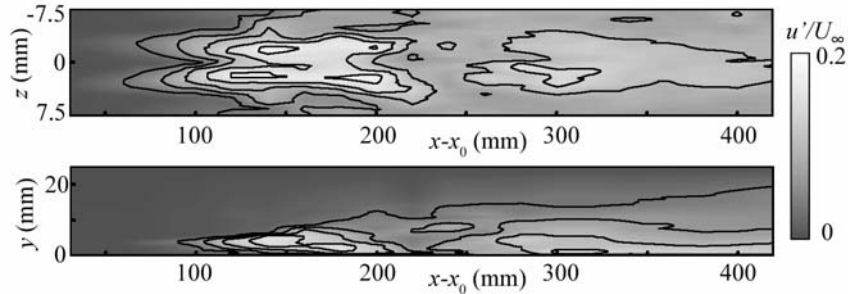
Figure 4. R.m.s. value of velocity fluctuations. Upper, $x - z$ plane at y=3mm. Lower, $x - y$ plane at z=0.
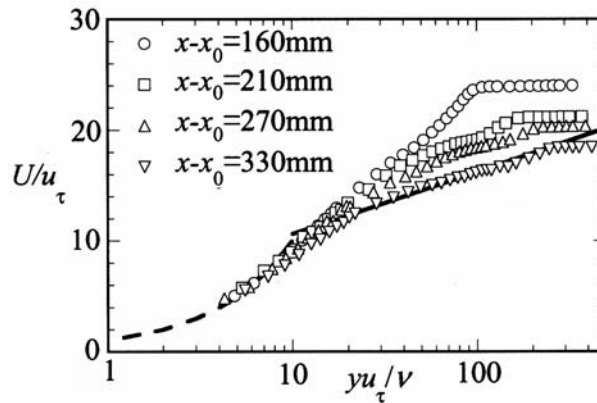
Figure 5. Mean velocity distributions (averaged over -7.5mm$\leq z \leq$7.5mm) at $x - x_0$=160mm, 210mm , 270mm, 330mm.

downstream, that is, a regeneration of low-speed streaks occurs, as demonstrated by Jiménez & Pinelli (1999) and Kawahara & Kida (2001) through numerical simulation. Importantly, the newly-developed low-speed streaks have lateral spacing of 100 wall units, similar to the value in wall turbulence. The time-mean velocity profile (averaged -7.5mm$\leq z \leq$7.5mm) exhibits the log-law at that stage as illustrated in figure 5.

4. Summary

Nonlinear development of subharmonic streak instability mode has been investigated experimentally for spanwise periodic low-speed streaks. The breakdown and subsequent regeneration stages of streaky structure have been demonstrated through exciting well-controlled disturbances. The lateral spacing of

primary, artificially-generated streaks is much larger than that observed in wall turbulence, but low-speed streaks newly-developed after the breakdown of the primary streaks have that of wall turbulence. At that stage, the time-mean velocity distribution exhibits the log-law. It has also been found that the growth of subharmonic modes cause large-scale arch-like vortices to develop in the region away from the wall through the interaction between the quasi-streamwise vortices developing along the neighboring streaks.

References

ASAI, M., MINAGAWA, M. & NISHIOKA, M. 2002 The instability and breakdown of a near-wall low-speed streak *J. Fluid Mech.* **455**, 289–314.

BRANDT, L. & HENNINGSON, D.S. 2002 Transition of streamwise streaks in zero-pressure-gradient boundary layers *J. Fluid Mech.* **472**, 229–261.

JEONG, J, HUSSAIN, F, SCHOPPA W. & KIM, J. 1997 Coherent structures near the wall in a turbulent channel flow *J. Fluid Mech.* **332**, 185–214.

JIMÉNEZ, J. & PINELLI, A. 1999 The autonomous cycle of near-wall turbulence *J. Fluid Mech.* **389**, 335–359.

KAWAHARA, G. & KIDA, S. 2001 Periodic motion embedded in plane Couette turbulence: regeneration cycle and burst *J. Fluid Mech.* **449**, 291–300.

KONISHI, Y. & ASAI, M. 2004 Experimental investigation of the instability of spanwise-periodic low-speed streaks *Fluid Dyn. Res.* **34**, 299–315.

THE TURBULENT ENERGY CASCADE BUILT BY A VORTEX BURST

Yannis Cuypers, Philippe Petitjeans
Laboratoire de Physique et de Mecanique des Milieux Heterogenes
Ecole Superieure de Physique et de Chimie Industrielles, 10 rue Vauquelin
75005 Paris - France
cuypers@pmmh.espci.fr phil@pmmh.espci.fr

Agnes Maurel
Laboratoire Ondes et Acoustique
Ecole Superieure de Physique et de Chimie Industrielles, 10 rue Vauquelin
75005 Paris - France
agnes.maurel@espc.fr

Abstract   We present an experiment where a stretched vortex is experiencing quasi-periodical turbulent bursts inside a laminar environment. The flow is characterized in the spectral and spatial domain using hot film and Particle Image Velocimetry Measurements. Some comparisons with the Lundgren vortex energy cascade mechanism are proposed.

Keywords: Stretched vortex, turbulent cascade, vortex burst, Lundgren vortex

1.   Introduction

We present an experiment where a stretched vortex is experiencing quasi-periodical turbulent bursts inside a laminar environment. Hot film and Particle Image Velocimetry (PIV) measurements show that the turbulent bursts are responsible for the build-up of a Kolmogorov $k^{-5/3}$ energy spectrum over one decade (Cuypers *et al.* 2003, 2004). The main particularity of that flow is that the turbulence generated is resulting from a single coherent structure evolution. The build-up of the experimental turbulent spectrum with time is investigated. The results are compared and interpreted with the Lundgren stretched spiral vortex model (Lundgren 1982) which exhibits an energy cascade mechanism resulting from the evolution of vorticity under the influence of two ingredients: the stretching along the vortex axis and the structure's own differential rotation.
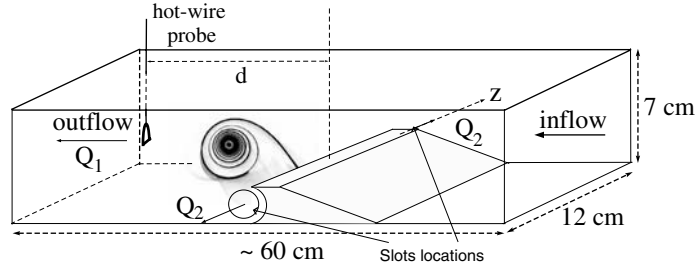
Figure 1. Experimental setup

2. Experimental set up and phenomenological description of the flow

A stretched vortex is generated in a low velocity hydrodynamic channel. A small step added to a laminar boundary layer profile in the bottom wall produces the initial vorticity that is strongly enhanced by the stretching produced by sucking the flow through slots on each lateral wall (Fig.1). Varying the experimental parameters, *i-e* the suction flow-rate Q_2, and the downstream flow-rate Q_1, makes two regimes occur: in the first one the vortex is stable, in the second one the vortex is experiencing periodical bursts. The flow is characterized by the following experimental values: $R = 3$ cm (lateral extension of the burst), $Re = 4000$, with $Re = \Gamma/\nu$ and Γ the vortex circulation for $r = R$). A coarse estimation of the stretching $a = \partial U_z/\partial z$ is given by $a = 1 - 10 \, \mathrm{s}^{-1}$.

We focus on the second regime, where the velocity field of the flow is measured via synchronized hot film velocity measurements and PIV measurements. The PIV measurements are performed in a cross section of the vortex at the middle of the channel (($z = 0$) plane) (Fig.2). Our PIV system is composed of a high resolution camera (1280×1024 pixels) capturing images at a frequency of 4 Hz and a double pulsed Nd:Yag laser delivering 12 mJ at each pulse. We use two measurement areas, 9 cm $\times$ 6.8 cm, and 5 cm $\times$ 4 cm. The interrogation window W chosen is 32×32 pixels [2]. The spatial resolution obtained is 86×64 vectors.

The PIV measurement is synchronized with a hot film measurement. The beginning of the hot film acquisition is triggered by the first PIV measurement and is continuous afterwards. The hot film probe is situated in the middle of the channel and is set parallel to the z axis so that it measures: $U = \sqrt{U_x^2 + U_y^2}$ (Fig.1). U can also be expressed using cylindrical coordinates (r, θ, z) in the
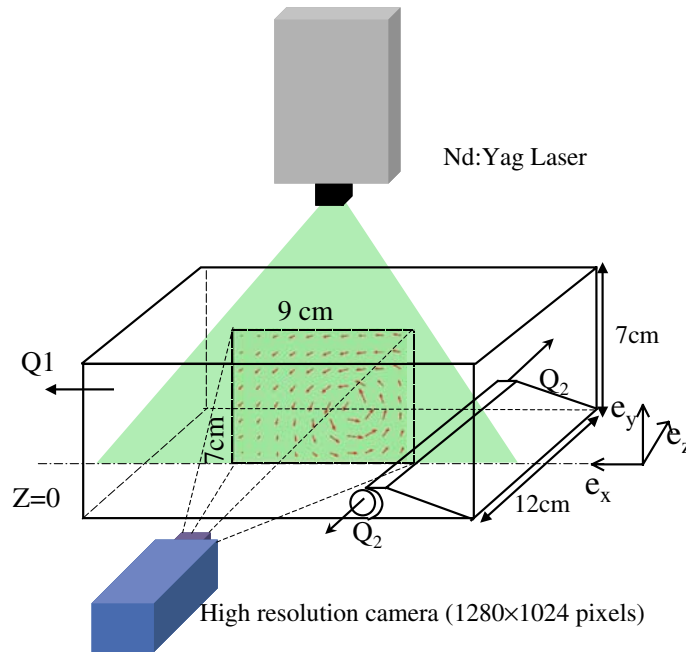
Figure 2. Experimental setup for PIV measurements

reference frame of the vortex core as $U = \sqrt{U_r^2 + U_\theta^2}$, where U_r is the radial velocity and U_θ is the azimuthal velocity.

Figure 3 shows the synchronized hot film and PIV measurements corresponding to a typical cycle of the flow. The vorticity field characterizing the small-scale structure of the flow is shown in background of the PIV velocity fields for a 9 cm × 6.8 cm window. The flow is also illustrated using two visualizations, a laser induced fluorescence visualisation of a cross section of the flow in the $(z = 0)$ plane, and a top view visualization using dye injection.

A typical flow cycle appears to be composed of two stages: a laminar stage and a turbulent stage. The laminar stage (Fig.3 a, b) simply corresponds to the advection of the vortex core in the $(z = 0)$ plane under the influence of the flow. During this stage, the vortex brings a stronger and stronger contribution U_θ to the velocity U recorded by the probe, which therefore grows continuously.

The second stage (Fig.3 c, d) shows rapid erratic velocity fluctuations corresponding to the passage of the turbulent spot on the probe position. On Fig. 3 c, one can observe the beginning of a turbulent part on the hot film signal. As it appears on the PIV measurement, the beginning of this turbulent part corresponds to a burst structure composed of a central vortex core surrounded
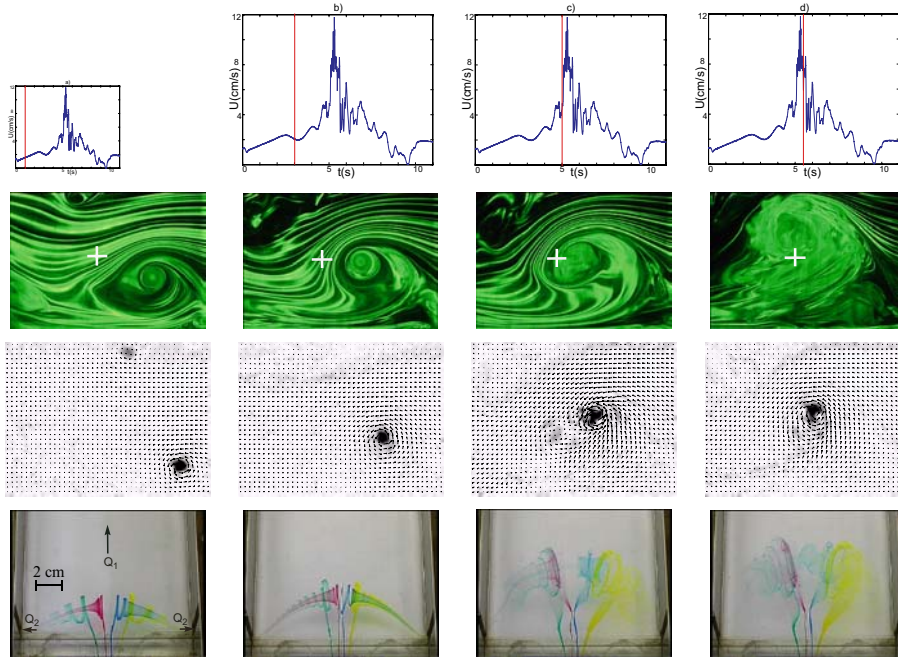
Figure 3. Characterization of one flow cycle, Hot film measurement (1st line), Laser induced fluorescence cross section visualization (2nd line), PIV measurement (3rd line) top view visualization (4th line). (a) $t = 1$ s, (b) $t = 3$ s, (c) $t = 5$ s, (d) $t = 5.5$ s. The hot film position is pictured as a white cross on the visualization

with compact vorticity structures, that are qualified in the following as vorticity patches. At later times (Fig. 3 d), the patches structures have been sheared and have merged in a vortex layer structure. The general evolution described here is reproducible from one turbulent spot to another. Note for instance the good agreement with the visualizations obtained from a different flow cycle.

3. Results

3.1 Hot film data processing

A typical hot film velocity signal shows the quasi-periodical character of the bursts (Fig.4). Each cycle is composed of two parts: a laminar part, for which the vortex is still coherent, showing a smooth increase of the velocity, and a turbulent part associated to the vortex burst, showing rapid velocity fluctuations.

This velocity signal is decomposed between a mean velocity $U_{mean}(t)$ (obtained through cycle averaging) and velocity fluctuations $u(t)$. Using an appropriate rescaling of the hot film data and a local Taylor hypothesis based on the

mean velocity to obtain spatial scales, we compute the energy spectrum $E(k)$ of the turbulent parts averaged over the N bursts (N=200). A neat Kolmogorov $k^{-5/3}$ fall-off is obtained between $k_m = 0.2$ cm^{-1} and $k_M = 2$ cm $^{-1}$ (Fig.6). In the Lundgren model, the inertial range can be estimated between $k_m = 1/R$ and $k_M = \sqrt{a/\nu}$. With our experimental values one gets $k_m \simeq 0.3$ cm^{-1} and 10 cm$^{-1} \leq k_M \leq 34$ cm^{-1} that reasonably compare with the experimental inertial range.
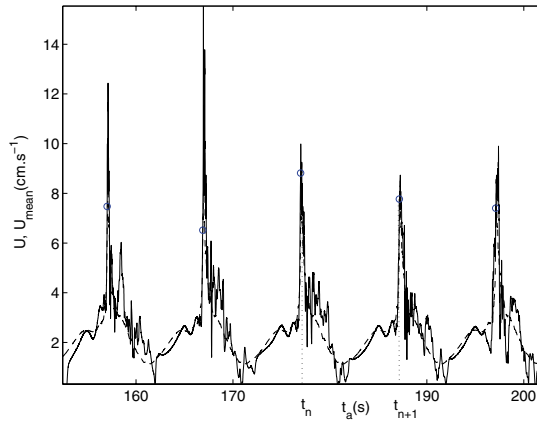
Figure 4.   Temporal recording $U(t_a)$, t_a denotes absolute time; $\circ$ indicates the times t_n of the beginning of the turbulent parts on each cycle; $(t = t_a - t_n; \ t < 5s)$. The mean velocity U_{mean} is overprinted in dashed line

One remarkable property of the Lundgren model is that the time averaging over the lifetime of the vortex always results in the $k^{-5/3}$ spectrum, independently of the spiral structure considered. Indeed instantaneously a spiral vortex gives a k^{-p} energy spectrum, where p is dependent on the flow field characteristics.

To better understand the energy cascade build-up and to go further in the comparison with the Lundgren model, we focus on the temporal evolution of the energy spectrum during the vortex burst. We define the cumulative spectrum $E^c(k, t)$ as the spectrum averaged over the N bursts and computed between $t = 0$ and t, where $t = 0$ denotes the onset of the turbulent parts for each burst. The figure 5a shows the evolution of the cumulative spectrum slope p_c (computed over the inertial range $[k_m; k_M]$) with t. p_c is found to decrease from a value close to -1 and reaches $-5/3$ for $t = T_v = 1.5$ s. The cumulative spectrum is expected to give the averaged spectral contribution of the vortex burst between $t = 0$ s and t. Therefore, we can conclude from this representation that there is a temporal evolution in the spectrum and that averaging over $[0, T_v]$ leads to the $k^{-5/3}$ behavior. T_v can be compared with

the lifetime t_c of a Lundgren vortex which is equal to the diffusion time of the spiral arms. The estimation of this time with our experimental values gives 0.5 s $< t_c < 2.5$ s, in good agreement with T_v.

In order to characterize the evolution in the spectra slopes, we compute the quasi-instantaneous spectra $e_{\Delta t}(k, t)$ over small windows $[t, t + \Delta t]$, ($\Delta t \ll T_v$) within the turbulent parts. The temporal window width Δt is chosen in order to keep a constant $\Delta r = U_{mean}(t)\Delta t$. However, since in this procedure a small Δt implies a small Δr (and therefore a less resolved spectrum), a balance has to be chosen between the precision on time t and the spectral resolution. We are interested in studying the behavior of the instantaneous spectra in the inertial range $[k_m; k_M]$ (fixed by the behavior of $E(k)$). When decreasing Δr, the first resolved k value (except $k = 0$) is given by $1/\Delta r$ and can thus overtake k_m. To give a consistent representation of the spectra, we use the following criterion : Δr (and thus Δt) is chosen in such a way that at least 80% of the inertial range is kept. The spectra $e_{\Delta t}(k, t)$ are expected to give a quasi-instantaneous picture of the vortex bust energy distribution among scales at different times. We find that the slope of the spectra is time dependent and varies between a value close to -1 at the beginning of the burst to a value close to -2 at the end of the burst (Fig.5b).
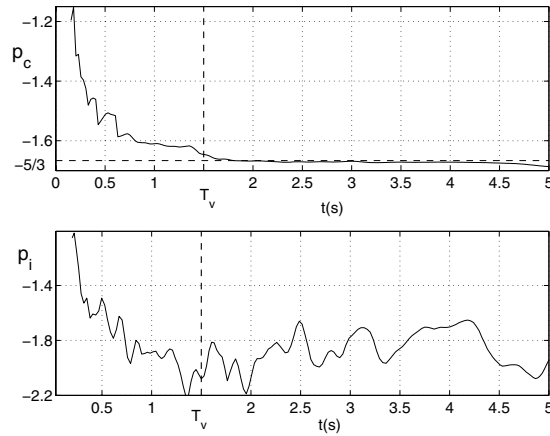

Figure 5.   (a) Variation of the cumulative spectrum slope p_c versus t. (b) Variation of the quasi-instantaneous spectrum-slope p_i versus t.

3.2   PIV data processing

In order to perform a quantitative statistical exploitation of the PIV velocity fields, we have acquired a large amount ($\simeq 4000$) of PIV measurements. The measurement area is 5 cm $\times 4$ cm, resulting in a spatial resolution $\delta r = 0.06$ cm
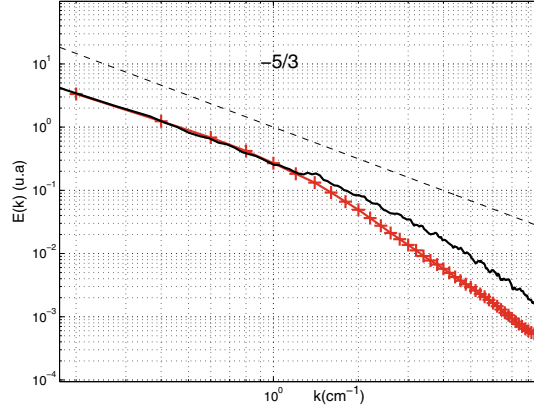
Figure 6. Energy spectrum $E(k)$; (-) computed from hot film measurements; (+) computed from PIV measurements

which is *a priori* sufficient to capture small scales of the inertial range. Owing to the synchronized acquisition of the PIV measurements and hot film measurements, times of PIV acquisition have been rescaled with the burst period. We have then computed the energy spectrum $E(k)$ from 600 PIV velocity fields acquired during the time interval $[0, T_v]$. A good agreement is found between the PIV spectrum and the hot-film spectrum over the scales of the inertial range (Fig.6). For wavenumbers k in the dissipative range, a discrepancy between the two spectra is observed. The steeper decay of the PIV spectrum results from truncation errors introduced by the computational method used, which is based on the vorticity field derived from the velocity field. This measurement confirms both the $k^{-5/3}$ behavior and the ability of PIV measurements to characterize the burst structure.

4.   Prospects

In the Lundgren model, the initial vorticity is a free parameter. Different choices for this parameter may lead to a different evolution in the instantaneous spectrum, although averaging over time should always result in the $k^{-5/3}$ spectrum. Pullin *et al.* (1994) have performed computations for a particular solution of the Lundgren model as a vorticity sheet in the process of roll-up. Their computations lead to a transition from -2 to -1 in the instantaneous spectra inverted compared to the experimental one. On the ground of our PIV measurements, we are actually computing a particular solution of the Lundgren vortex with vorticity patches as the initial condition. We expect that this condition closer to the experiment will allow a transition from -1 to -2.

248

References

CUYPERS, Y., MAUREL, A. AND PETITJEANS, P. 2003 Vortex burst as a source of turbulence *Phys. Rev. Lett.* **91**, 194502.

CUYPERS, Y., MAUREL, A. AND PETITJEANS, P. 2004 Comparison between an experimental turbulent vortex and the Lundgren vortex *J. of Turb.* **5**, 30.

LUNDGREN T S 1982 Strained spiral vortex model for turbulent fine structures *Phys. Fluids* **25**, 2193-2203.

PULLIN, D. I., BUNTINE, J. D. AND SAFFMAN, P. G. 1994 On the spectrum of a stretched spiral vortex *Phys. Fluids* **6**, 3010-3027.

MIXING TRANSITION IN SUPERSONIC STREAMWISE VORTICES

Michio Nishioka, Shoji Sakaue, Kazuya Komada, Hiroyuki Sakoshi, Ikuhiro Furukawa

Department of Aerospace Engineering, Graduate School of Engineering, Osaka Prefecture University, Gakuencho, Sakai, Osaka 599-8531 Japan

nishioka@aero.osakafu-u.ac.jp

Abstract   The present paper describes our recent experimental studies on the supersonic mixing and combustion enhancement using streamwise vortices in spanwise-row configuration. Firing tests verify streamwise vortices of $\Gamma/\nu = 3 \times 10^4$ to be powerful for supersonic combustion enhancement. Cold-flow hot-wire measurements show that Kolmogorov's $-5/3$ power law region appears in the spectrum of ρu-fluctuations in the vortices for Γ/ν above about 10^4. This is not inconsistent with the minimum Reynolds number for the mixing transition proposed by Dimotakis (2000).

Keywords: Mixing transition, Kolmogorov's $-5/3$ power law, supersonic mixing and combustion, turbulence control

1.   Introduction

The propulsion for airbreathing hypersonic flight relies on the so-called supersonic combustion ramjet (scramjet) engine under development. The reason for the supersonic combustion is to avoid the possible large total pressure loss and high static temperature rise that would be caused by the deceleration of hypersonic flow to subsonic. For typical operating conditions of scramjet, the time scale for complete combustion of the fuel hydrogen and the air oxygen will be on the order of (or less than) 1ms so that the problem of providing rapid mixing of molecular level is thus quintessential for the combustor design of scramjet (Ferri 1973, Gutmark *et al.* 1995). To achieve the necessary mixing enhancement by means of turbulence control is a real challenge. This is because the compressibility can strongly suppress vortical motions at supersonic speeds. In compressible mixing layers, for instance, the growth rate of the thickness decreases considerably with increasing the convective Mach number M_c (Bogdanoff 1982, Papamoschou & Roshko 1988). It is well known that low-speed mixing layers are governed by energetic vortical motions called Brown-Roshko

vortices. Such vortical activities are highly suppressed in supersonic mixing layers for M_c beyond 0.6 as demonstrated by Papamoschou & Roshko (1988).

The fuel injector for supersonic combustion should be capable of generating such vortical motions that cause the fuel-air interface area to increase rapidly and enhance the micro mixing of molecular level, hence leading to efficient combustion. For such supersonic mixing enhancement the use of large-scale streamwise vortices seems to be the most advantageous (Nishioka 1990, Gutmark *et al.* 1995, Nishioka *et al.* 2002). We may expect that streamwise vortices are rather "insensitive" to the compressibility effect. This is because their large-scale motion is perpendicular to that of the supersonic mainstream fluid, which is to be entrained into the vortical region. Indeed, for the case of a single streamwise vortex embedded in a Mach 2.4 uniform flow, our stability analyses for various vortices with vorticity distributions of hollow-type indicate that streamwise vortices are almost free from the compressibility effect unless the circumferential velocity component exceeds about 0.6 in terms of Mach number (Nishioka *et al.* 2002). Imagine that streamwise vortices containing the fuel in their core regions break down into small-scale turbulent eddies. No doubt, this increases the fuel-air interface area rapidly and enhances the micro mixing. Therefore it is important to know the flow condition for the supersonic streamwise vortices to undergo the mixing transition in the sense of Dimotakis (2000) (see Section 3). However, the condition for the mixing transition has not been clarified for the present supersonic case in spite of a number of studies made on the supersonic mixing enhancement using streamwise vortices.

In the present paper we first briefly review our studies on the supersonic mixing and combustion enhancement. Next we describe our recent experiments made to examine the mixing capability of a pair of counter-rotating streamwise vortices introduced into a turbulent boundary layer. Our main interests are to measure the streamwise mass-flux fluctuation $(\rho u)'$ by hot-wire and to examine the turbulent activities within the streamwise vortices and their resulting streamwise growth. With all these results we have tried to clarify the mixing transition in our supersonic streamwise vortices.

2. Supersonic mixing and combustion enhancement using streamwise vortices

As emphasized in the introduction the use of streamwise vortices seems to be the most advantageous for supersonic mixing enhancement. Since the first demonstration by Swithenbank & Chigier (1968) many studies have been made through trying various ways of generating streamwise vortices as reviewed in detail (see Gutmark *et al.* 1995). Among those so far evaluated through firing tests the so-called wall-mounted swept ramp injector developed by Northam and others (Northam *et al.* 1989, Northam *et al.* 1991, Drummond *et al.* 1989,

Stouffer *et al.* 1994) was once believed to be the most promising in USA. Even for the wall-mounted swept ramp injector, however, the combustion efficiency is not sufficient according to Stouffer, Vandsburger & Northam (1994). It is thus clear that further studies are needed to explore and develop more effective use of streamwise vortices for enhancing the supersonic mixing and combustion.
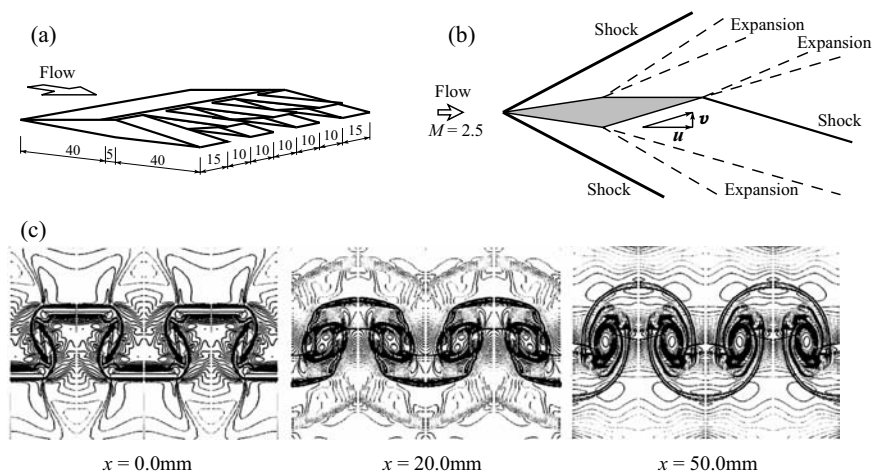

Figure 1. Streamwise-vortex generator called Alternating Wedge (AW) strut, illustrated by typical geometry in (a), assumed 2D inviscid flow in (b) and results (density contours in the vortex formatin region) of direct numerical simulation in (c).

We have been working on the supersonic mixing and combustion enhancement using streamwise vortices. In our studies streamwise vortices are introduced into the otherwise uniform freestream as well as the near-wall flow like the swept ramp injector. Our basic idea for generating streamwise vortices in supersonic air stream (Nishioka 1990, Nishioka & Sunami 1995) is illustrated in Fig. 1 (a) and (b) showing a double-wedge shaped strut. The front half of the strut is of a two-dimensional wedge. The rear half is characterized by spanwise alternating upward and downward expansion-ramps, with each opposite surface parallel to the incoming freestream. This type of strut is called the "Alternating Wedge (AW) strut". The important dimensions are the strut thickness h, the spanwise width of expansion-ramps and the ramp angle θ. The idea for streamwise vortex generation by the AW strut is as follows. The shock and expansion wave pattern around a cross section containing the upward ramp is illustrated in Fig. 1 (b) by assuming 2D-inviscid flow. When two streams along the neighboring upward and downward ramps merge at the their interface, there appears a slip in the vertical velocity direction, with its magnitude of $2v$, see Fig. 1 (b). This introduces the streamwise vorticity necessary for generating streamwise
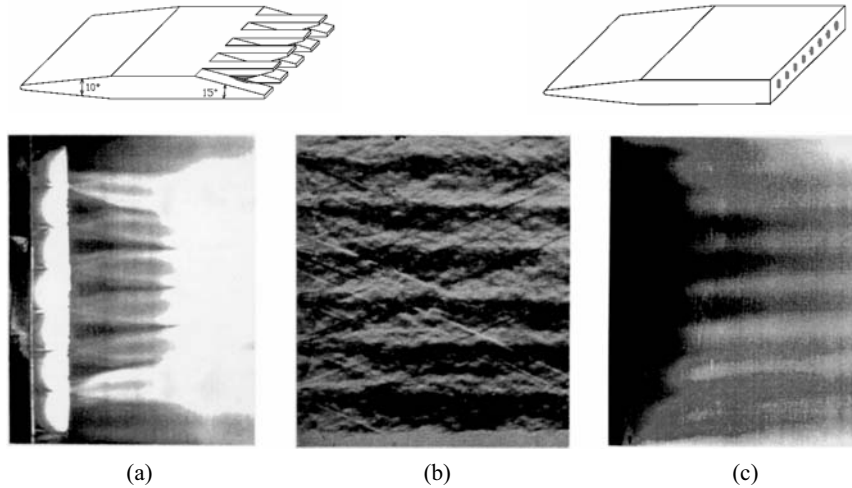
Figure 2. Supersonic combustions with and without the mixing enhancement due to stream-wise vortices introduced by AW strut. (a) firing test of CNR11-R15(direct photo), (b) cold flow (schlieren photo), (c) firing test of multiple orifice strut (Sunami et al. 2002).

vortices in the wake. A measure of the circulation Γ for the streamwise vortex is thus written as $2vh$.

Fig. 1 (c) (Sunami *et al.* 1998, Sunami *et al.* 2002) shows results (density contour maps) of our numerical simulation to illustrate the formation of streamwise vortices in spanwise-row configuration immediately behind CNR10-R11 strut sketched on the top. As for the name of AW strut, CNR10-11, CNR means "AW strut for generating counter rotating streamwise vortices", the figure following CNR, 10 means that the spanwise width of expansion-ramps is 10mm, and the last label R11 means that the ramp angle is 11 degrees. We found (1) that in supersonic flows streamwise vortices can be generated by our AW strut quite easily and almost without additional losses in total pressure such as those due to shock waves, (2) that their breakdown into smaller scale, which is essential for mixing enhancement, can be controlled by their geometry in spanwise row configurations and by various combinations of their scales, intensity of circulation and rotational directions (Sunami & Nishioka 1997, Sunami *et al.* 2001), and (3) that the hydrogen fuel can be injected into their core region. At a freestream Mach number 2.5 firing tests are carried out to realize and confirm the supersonic combustion as demonstrated by in Fig. 2 (a), which shows top-view direct photo indicating the formation of streamwise vortices and their capability of flameholding. Indeed we see intensive supersonic combustion in Fig. 2 (a). Fig. 2 (b) illustrates the formation of streamwise vortices in cold flow. For comparison, firing tests are also made for the case of a generic fuel
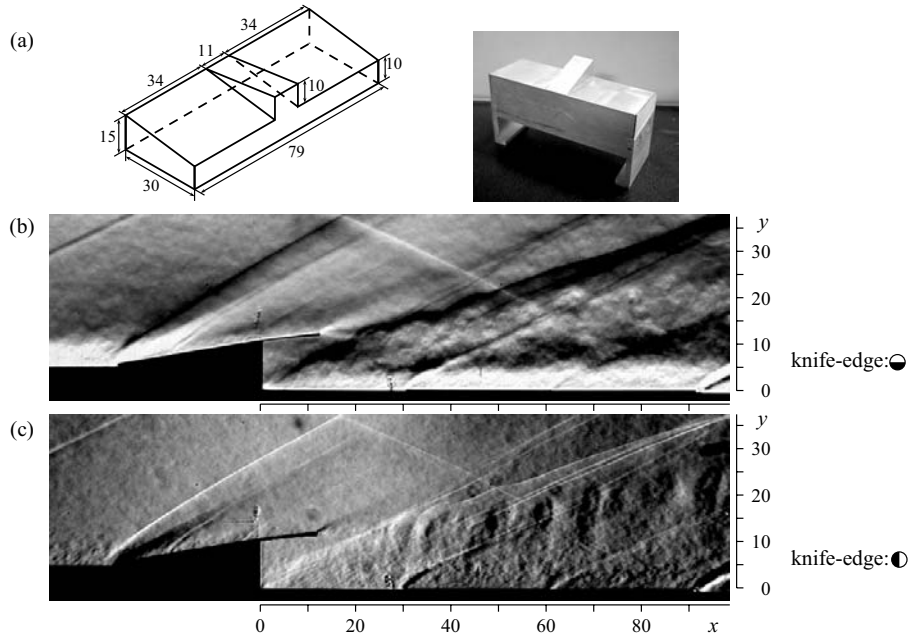
Figure 3. Wall-mounted device generating a pair of couter-rotating streamwise vortices (see (a)). Their streamwise development is illustrated by schlieren photos in (b) and (c).

injection strut (without generating streamwise vortices), see Fig. 2 (c). The results show the effectiveness of the present streamwise vortices for supersonic mixing and combustion enhancement.

3. Mixing transition in supersonic streamwise vortices

We have demonstrated that the mixing enhancement due to streamwise vortices is really powerful. The streamwise vortices in spanwise-row configuration are very effective in enhancing the supersonic combustion. The intensive combustion shown in Fig. 2 (a) is a firm evidence for the appearance of active small-scale eddies. For their appearance we have to know the flow condition, if any. What is most important in this connection is the mixing transition proposed by Dimotakis as noted in the introduction. Small-scale turbulence activities should manifest themselves in their power spectra. Hot-wire measurements have been made across the streamwise vortices using a constant voltage hot-wire anemometer (see Sarma 1993 for the operating principle). It is noted that in supersonic flows a hot-wire measures the streamwise mass-flux and its fluctuations.
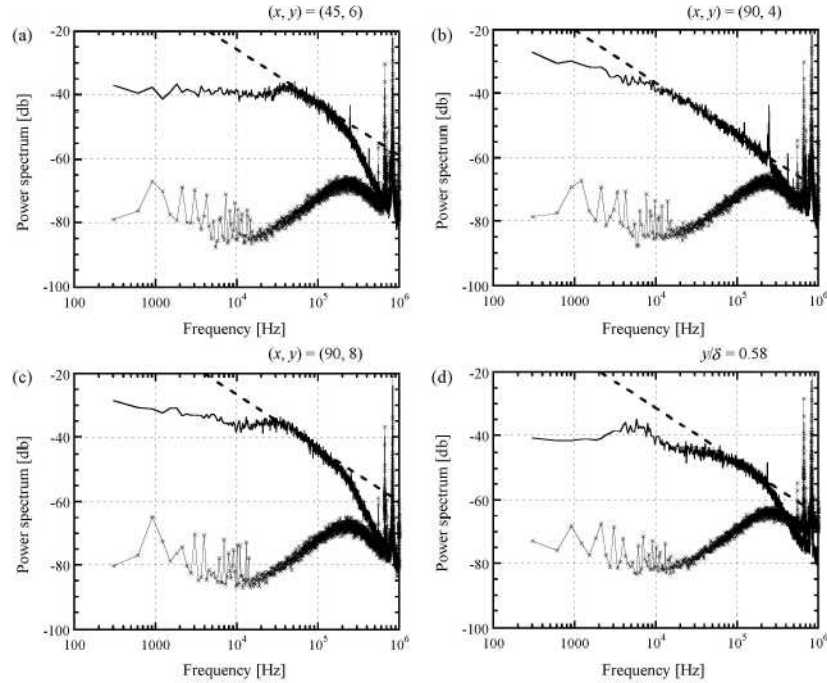
Figure 4. Mass-flux fluctuations in streamwise vortices (see (a) to (c)) and turbulent boundary layer (see (d)) at $M = 2.4$, illustrated by their power spectra. Solid lines indicate the power spectra of ρu-fluctuations, lines with corsses the electric noise, and broken lines the $-5/3$ power law. (a) $(x, y) = (45, 6)$, (b) $(x, y) = (90, 4)$, (c) $(x, y) = (90, 8)$, (d) $y/\delta = 0.58$.

Here we first describe experiments made to see the mixing capability of a pair of counter-rotating streamwise vortices introduced into a near-wall region otherwise occupied by turbulent boundary layer. Our device generating the vortex pair consists of one compression ramp and two neighboring expansion ramps as shown in Fig. 3 (a). The device is installed on the wall of a supersonic wind tunnel of Mach 2.4. Schlieren photos in Fig. 3 (b) and (c) show the generated counter-rotating vortex pair, which moves upwards from the wall by their mutual induced velocity. In these photos we see a thin plate glued on the upper surface of the compression ramp extending downstream by about 10mm. This extension helps maintain the pressure immediately behind the base of the device at a low value to generate strong vortices. During the vortex formation the tunnel wall turbulent boundary layer (6mm in thickness) is partly engulfed into the vortex pair. It is found from a number of schlieren visualization photos that the downstream growth of the vortex pair in height is quite large, indeed, being as large as the growth rate of low-speed mixing layers governed by Brown-Roshko vortices. Hot-wire measurements of mass-flux fluctuations made across the

vortex at various downstream stations indicate that the fluctuation rms intensity is quite large, attaining 20% of the freestream mean value. Results of the corresponding FFT spectrum analyses are given in Fig. 4, which compares streamwise mass-flux ρu-fluctuations in the streamwise vortices and the tunnel-wall turbulent boundary layer. The electric noise spectrum indicates that our hot-wire response is flat at least up to about 300 kHz. Discrete noise components above 600 kHz are due to broadcast radio waves. We see high-frequency ρu-fluctuations even beyond 500 kHz, which is beyond the flat response of hot-wire. The power spectrum partly follows Kolmogorov's $-5/3$ power law, indicating that the streamwise vortex pair generates small-scale turbulent eddies of high mixing power. Similar results are obtained for the case that the same vortex pairs sit side by side in the spanwise direction to form a spanwise row configuration. The circulation of these vortices Γ and the vortex Reynolds number Γ/ν are estimated to be $0.98\mathrm{m}^2/\mathrm{s}$ and 1.8×10^4 respectively. We have carried out similar hot-wire measurements at $M = 1.85$ for the case where $\Gamma = 0.27\mathrm{m}^2/\mathrm{s}$ and $\Gamma/\nu = 0.77 \times 10^4$. In this case there appears almost no Kolmogorov's $-5/3$ power law region in the spectrum of ρu-fluctuations.

Next we describe experiments for the case of streamwise vortices (of $\Gamma = 4.8\mathrm{m}^2/\mathrm{s}$, $\Gamma/\nu = 9.2 \times 10^4$) introduced into the otherwise uniform freestream at $M = 2.4$, in a spanwise row configuration. Fig. 5 (a) shows two kinds of AW struts. One is the same model as used in the firing test. The other is a modified strut with 2-dimensional cavity embedded within the upper and lower strut walls. Supersonic flow over a cavity may undergo strong oscillations. It is thus interesting to see whether or not the streamwise vortices can be excited by disturbances due to the supersonic cavity-flow oscillations. It is important to examine whether or not such turbulence control can excite more energetic fluctuations in the $-5/3$ power law frequency range. By comparing turbulence activities visualized by schlieren photos (in Fig. 5 (b) and (c)) and also by comparing power spectra (in Fig. 6) of ρu-fluctuations within the streamwise vortices, between the two cases with and without cavity-excited high-frequency disturbances (of about 46 kHz), we find that the present turbulence control is quite effective in generating energetic fluctuations in the $-5/3$ power law frequency range.

According to Dimotakis (2000) fully-developed turbulence requires a minimum Reynolds number. Typically, the transition to fully-developed turbulence can be identified as leading to an enhanced-mixing turbulent-flow state characterized by the appearance of Kolmogorov's $-5/3$ power law in the fluctuation power spectrum. He called the transition to fully-developed turbulence the mixing transition and proposed the minimum Reynolds number (defined as Γ/ν for streamwise vortices) to be $1 \sim 2 \times 10^4$ for low-speed jets and mixing layers. The present results described so far for supersonic streamwise vortices are not inconsistent with those low-speed results. It should be added that firing tests
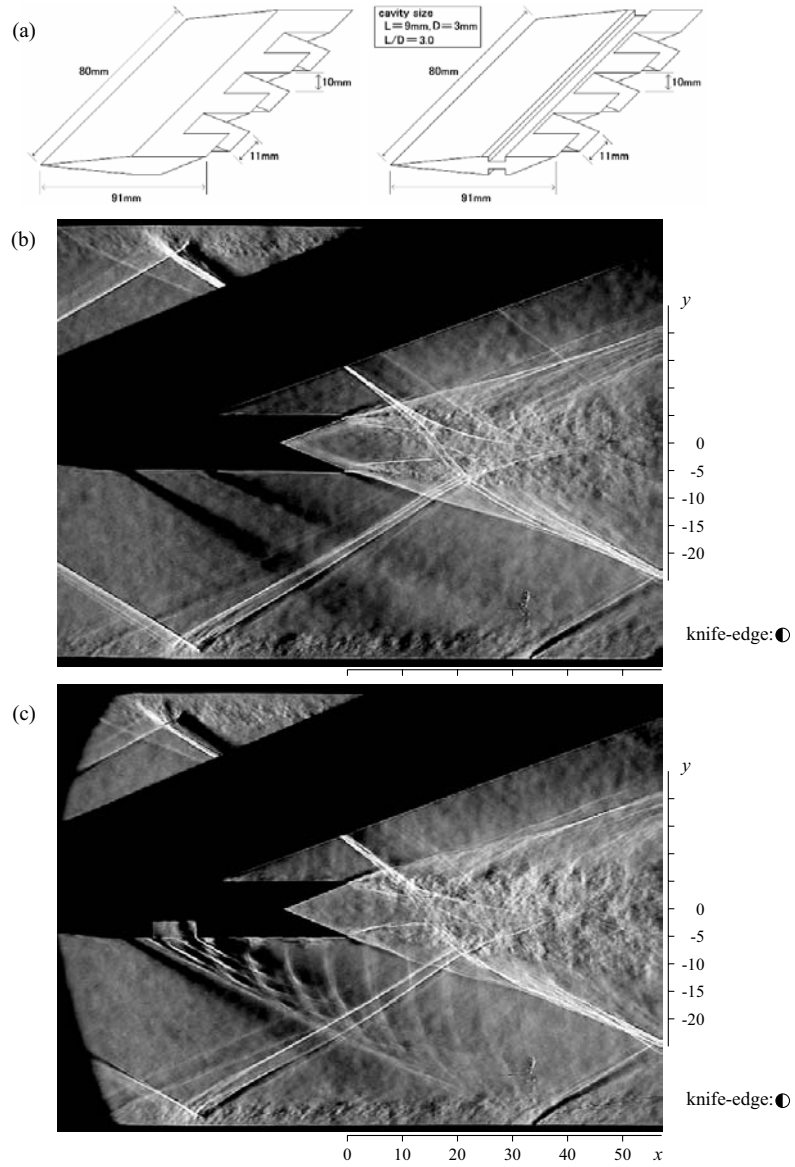
Figure 5. Turbulence activities in streamwise vortices (introduced into otherwise uniform freestream at $M = 2.4$. Compare schlieren photos (b) and (c) taken behind AW struts without and with cavity as shown in (a).

verifies streamwise vortices of $\Gamma/\nu = 3 \times 10^4$ to be powerful for supersonic mixing and combustion enhancement.
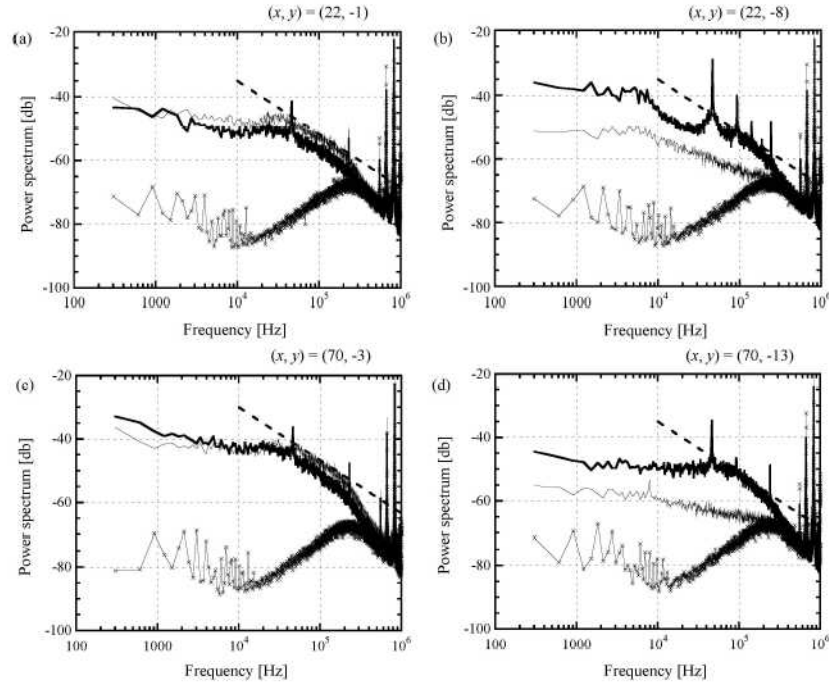
Figure 6. Turbulence activities in streamwise vorticies (introduced into otherwise uniform freestream at $M = 2.4$. Compare power spectra in (a) to (d) obtained behind AW struts without and with cavity as shown in Fig5.(a). Thick and thin lines indicate the cases of with and without cavity excited disturbances, lines with crosses the electric noise, and broken lines the $-5/3$ power law. (a) $(x,y) = (22,-1)$, (b) $(x,y) = (22,-8)$, (c) $(x,y) = (70,-3)$, (d) $(x,y) = (70,-13)$.

4. Summary

We have described our recent studies on the supersonic mixing and combustion enhancement. Streamwise vortices in spanwise-row configuration generated by the AW fuel injector strut are very effective in enhancing the supersonic mixing and combustion. Typically, the transition to fully developed turbulence can be identified as leading to an enhanced-mixing turbulent-flow state characterized by the appearance of Kolmogorov's $-5/3$ power law in the spectrum of ρu-fluctuations. Dimotakis (2000) proposed the minimum Reynolds number (defined as Γ/ν for streamwise vortices) for the mixing transition to be $1 \sim 2 \times 10^4$ for low speed jet and mixing layers. The present supersonic results are not inconsistent with those low-speed results. Firing tests verifies streamwise vortices of $\Gamma/\nu = 3 \times 10^4$ to be powerful for supersonic mixing and combustion enhancement.

258

Acknowledgments

References

BOGDANOFF, D. W. 1982 Compressibility Effects in Turbulent Shear Layers. *AIAA J.* **21** 926–927.

DIMOTAKIS, P. E. 2000 The Mixing Transition in Turbulent Flows. *J. Fluid Mech.* **409** 69–98.

DRUMMOND, J. P., CARPENTER, M. H., RIGGINS, D. W. & ADAMS, M. S. 1989 Mixing Enhancement in a Supersonic Combustor. AIAA Paper 89–2794.

FERRI, A. 1973 Mixing-Controlled Supersonic Combustion. *Ann. Rev. Fluid Mech.* **5**, 301–338.

GUTMARK, E. J., SCHADOW K. C. & YU, K. H. 1995 Mixing Enhancement in Supersonic Free Shear Flows. *Ann. Rev.Fluid Mech.* **27** 375–417.

NISHIOKA, M. 1990 Control of Supersonic Mixing, NAL SP-**12** 39–42.

NISHIOKA, M., HIEJIMA, T., SUNAMI, T. & SAKAUE S. 2002 Streamwise Vortices as a Powerful Means for Supersonic Mixing Enhancement. *Proc. Int. Symp. On Dynamics and Statics of Coherent Structures in Turbulence: Roles of Elementary Vortices* (ed. S. Kida) 217–228.

NISHIOKA, M. & SUNAMI, T. 1995 Some Thoughts and Experiments on the Supersonic Mixing Enhancement. *J. Japan Society of Fluid Mech.* **14** 377–389.

NORTHAM, G. B., CAPRIOTTI, D. P., BYINGTON, C. S. & GREENBERG, I. 1991 Mach 2 and Mach 3 Mixing and Combustion in Scramjets. AIAA Paper 91–2394.

NORTHAM, G. B., GREENBERG, I. & BYINGTON, C. S. 1989 Evaluation of Parallel Injector Configurations for Supersonic Combustion. AIAA Paper 89–2525.

PAPAMOSCHOU, D. & ROSHKO, A. 1988 The Compressible Turbulent Shear Layer Experimental Study. *J. Fluid Mech.* **197** 453–477.

SARMA, G. R. 1993 Analysis of Constant Voltage Anemometer Circuit IEEE, 0-7803-1229-5/93, 731–736.

STOUFFER, S. D., VANDSBURGER, U. & NORTHAM, G. B. 1994 Comparison of Wall Mixing Concepts for Scramjet Combustors. AIAA Paper 94-0587.

SUNAMI, T., MICHAEL, N. W. & NISHIOKA, M. 1998 Supersonic Mixing and Combustion Control Using Streamwise Vortices. AIAA Paper 98–3217.

SUNAMI, T., MICHAEL, N. W., NISHIOKA,M., MURAKAMI, A. & KUDOU, K. 2002 Experiment of Supersonic Mixing and Combustion Enhancement Using Alternating-Wedge Strut: Part 1– Effects of Supersonic Streamwise Vorices in a Scramjet Combustor, *J. Japan Society for Aeronautical and Aerospace Sciences* **50** 135–141.

SUNAMI, T. & NISHIOKA, M. 1997 Breakdown Processes of Supersonic Streamwise Vortices in Spanwise-Row Configurations. *J. Japan Society of Fluid Mech.* **16** 415–424.

SUNAMI, T., TOKUNAGA, H. & NISHIOKA, M. 2001 Supersonic Mixing Enhancement Using Interaction between Supersonic Streamwise Vortices in Double Spanwise-Row Configurations. *J. Japan Society of Fluid Mech.* **20** 316–324.

SWITHENBANK J. & CHIGIER, N. A. 1968 Vortex Mixing for Supersonic Combustion. *12th International Symp. on Combustion* 1153–1162.

EVOLUTION OF VORTEX STRUCTURES IN A MODEL OF THE TURBULENT TRAILING VORTEX

J. M. Faddy, D. I. Pullin

Graduate Aeronautical Laboratories, California Institute of Technology 105-50,
1200 E. California Blvd, Pasadena, CA 91125, USA

faddy@caltech.edu, dale@galcit.caltech.edu

Abstract   We present results obtained from a direct numerical simulation for a model of incompressible trailing vortices consisting of an array of counter-rotating vortices and a superposed axial velocity in a doubly-periodic domain, infinite in the vertical direction. The Reynolds number based on vortex circulation is 1000. It is found that for sufficiently strong axial flow, helical instability modes develop on each vortex. This leads to a decrease in the magnitude of the axial flow and subsequent relaminarization of each vortex. At later times, modes corresponding to the more slowly growing co-operative instability become dominant. These produce their own helical structures followed by the rapid growth of small scales, then vorticity cancellation and decay of the vortex array. In the presence of strong axial flow the helical structure persists and the vortices appear more resistant to the breakdown phenomena than for arrays with no axial flow.

Keywords: Trailing vortices, axial flow, M&M Vortex

1.   Introduction

A detailed knowledge of the interactions between vortices is of great interest both from a fundamental standpoint concerning coherent structures in turbulent flows as well as from the more practical problem of the wake shed from a lifting body; the counter rotating pair that results from the latter having been observed to persist tens of miles downstream of large aircraft (Spalart 1998). The q-vortex (Batchelor vortex), defined by a vorticity distribution that decays exponentially with the square of the radius, is typically chosen as an abstraction of an isolated trailing vortex. While this vortex is Rayleigh stable, the presence of axial velocity proportional to the vorticity renders the flow linearly unstable for sufficiently strong axial motion (Leibovich & Stewartson 1983). It is also well known that the strain field produced on one vortex by the other member of a counter-rotating pair leaves the system susceptible to the long wave length Crow

instability (Crow 1970) as well as short wavelength Widnall modes (Widnall 1974); these instabilities fall under the more general class of elliptic instabilities being a result of two-dimensional flows with elliptic streamlines being unstable to three-dimensional disturbances (Pierrehumbert 1986, Bayly 1986). Presently we discuss results obtained from direct numerical simulation (DNS) of a vortex array that exhibits all of these instability modes. We use an initial condition comprising an array of counter-rotating vortices with superposed axial flow that is an exact weak solution to the incompressible Euler equations.

2. Geometry and initial condition

In Cartesian (x_1, x_2, x_3) co-ordinates we consider DNS of the incompressible Navier-Stokes equations on a domain that is periodic in both the x_1 and x_2 directions and is unbounded in x_3. Numerically, this is achieved by using a Cain's mapping (Cain *et al.* 1984) to stretch onto a computational domain that is periodic in all directions. The vortex axis is chosen along x_1. As (unperturbed) initial condition we utilize the counter-rotating M&M vortex array (Mallier & Maslowe 1993), the vorticity concentration being governed by a parameter C. An axial flow that is proportional to the axial vorticity is chosen resulting in an initial condition that satisfies the steady two-dimensional, three velocity component Euler equations,

$$u_1(x_2, x_3) = \frac{1.56\, u_{3max}}{q_0} \left| \frac{\omega_1(x_2, x_3)}{\omega_1(0,0)} \right|, \tag{1}$$

$$u_2(x_2, x_3) = \frac{C^2 \sinh(Cx_3)\cos(x_2)}{\cosh^2(Cx_3) - C^2\cos^2(x_2)}, \tag{2}$$

$$u_3(x_2, x_3) = -\frac{C \cosh(Cx_3)\sin(x_2)}{\cosh^2(Cx_3) - C^2\cos^2(x_2)}. \tag{3}$$

At any time $t > 0$ the flow then corresponds to an x_2-periodic array of vortex pairs. A parameter q_0 defines the relative strength of the swirl velocity to the axial flow inside a member of the array,

$$q_0 = 1.56\, \frac{u_{3max}}{u_d}, \tag{4}$$

u_d being the difference between the free stream axial velocity (zero presently) and its peak value. The prefactor on the right-hand side of (4) is chosen to produce values of q_0, using the present initial condition, that match those characteristic of the Batchelor vortex. We define a Reynolds number $Re_\Gamma = \Gamma/2\pi\nu$, where ν is the kinematic viscosity and use $C = 0.9$ to define an initial condition with compact vortices.

3.   Direct numerical simulation results

DNS were performed at Re_Γ=1000 for $q_0 = 1$ and $q_0 = \infty$, the latter corresponding to zero initial axial flow. Each vortex in the array (the half domain) is resolved with $64 \times 64 \times 128$ points, the initial core being described by 24 points in the diameter. The axial extent of the domain was chosen to contain one wavelength of the most unstable Crow mode and the time step was chosen to correspond to an initial CFL number of 0.1. The base flow was perturbed initially by divergence-free white noise modulated by an exponential decay in the x_3 direction. As flow diagnostics we define $\langle \epsilon \rangle$, the dissipation integrated over a domain corresponding to a pair of opposite-signed vortices, and $\overline{\Gamma}$, the circulation around one vortex averaged in the x_1 direction. For flow visualization we consider the second invariant of the velocity gradient tensor $Q = -\frac{1}{2} \left(S_{ij}S_{ji} + \Omega_{ij}\Omega_{ji} \right)$ where S_{ij} and Ω_{ij} are the symmetric and antisymmetric parts of the velocity gradient tensor respectively. Positive values of Q are representative of regions in which rotation dominates strain magnitude, hence providing a means to identify vortical structures (Hunt *et al.* 1988, Chong *et al.* 1990).

3.1   Early development

Figure 1 shows visualization of the resulting flow development through iso-surfaces of $Q = 1$, shaded with local dissipation. It is found that the large growth rates associated with susceptibility of the rotational flow to non-axisymmetric instabilities in the presence of axial motion causes each vortex in the linear array to first develop helical structures. This can be seen in figure 2a as a small increase in $\langle \epsilon \rangle$ at around $t = 10$. During this phase, the energy of the axial flow is extracted through turbulence within the core, the perturbations generated presumably being transported outward toward regions of local stability. This behavior has been observed for the isolated Batchelor vortex (Jacquin & Pantano 2002). In these regions, the perturbations do not modify the mainly tangential flow, and so the axial velocity reduces whilst the angular momentum is maintained. Figure 2b shows this, and also the evolution of q towards values that are stable in the linear sense. Ultimately, the core stabilizes with respect to the helical modes and the vortex relaminarizes before the co-operative modes have shown appreciable growth.

3.2   Co-operative instabilities

At later times the more slowly growing co-operative elliptic instabilities (the x_2 periodic analog of the Crow and Widnall modes, referred to as CM and WM henceforth) become apparent as indicated by a large-scale bending of the vortices toward their neighbors, and by short wavelength kinks on each structure
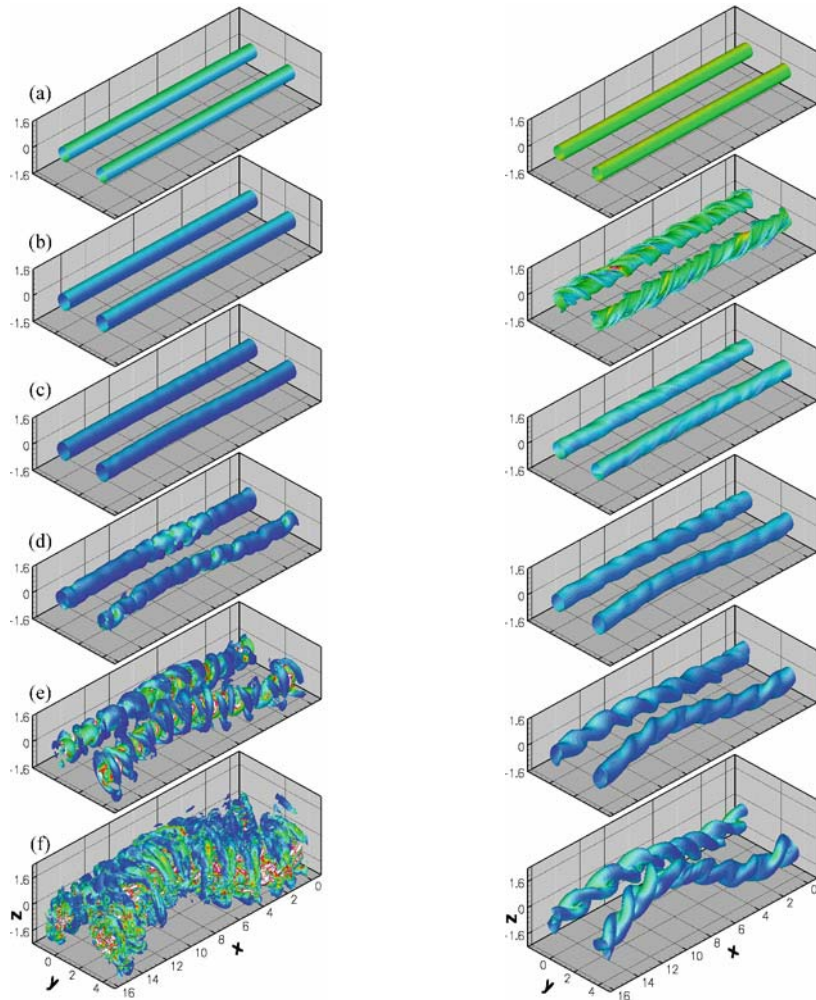
Figure 1. Isosurfaces with $Q = 1$ shaded by dissipation. $Re_\Gamma = 1000$, $C = 0.9$. Left, $q_0 = \infty$. Right $q_0 = 1$. Evolution is from top to bottom and shown at non-dimensional times (a) 0, (b) 12, (c) 21, (d) 32, (e) 40, (f) 45. One vortex pair in the array is shown. $(x, y, z) \equiv (x_1, x_2, x_3)$

respectively. In figure 1e, which corresponds to $t = 40$, a striking difference between the two flows has become apparent. In the absence of axial velocity, the WM has distorted each vortex to the extent where separate tubular structures can be seen surrounding a highly dissipative core region. The next snapshot captured in figure 1f shows that, analogously to the vortex pair experiments
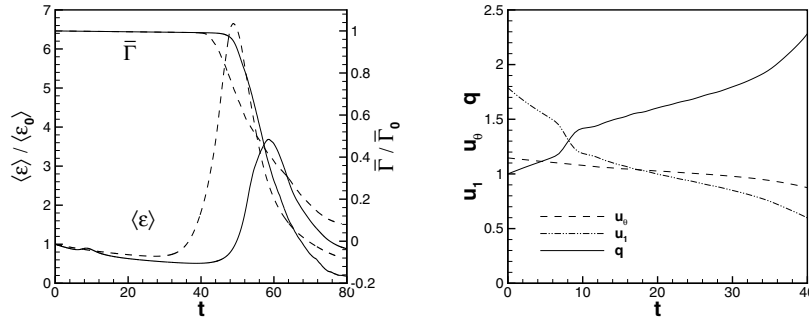
Figure 2a.   Evolution of $\langle \epsilon \rangle$ and $\overline{\Gamma}$. $q_0 = 1$ (solid line), $q_0 = \infty$ (dashed line).

Figure 2b.   Evolution of axial and swirl velocities and q for $q_0=1$.

of Leweke & Williamson (1998), the fluid in these structures is drawn closer to the neighboring vortices where it is quickly wrapped around by the mean circulation. This effect is magnified in regions where the CM pulls pairs of vortices closer together, increasing the local strain and hence the WM growth rate. Ultimately this exchange of vorticity between counter-rotating pairs results in a rapid decrease in circulation and explosive growth in dissipation. In contrast, the helical structure that results from the axial velocity is observed to persist and whilst the WM is still present, the flow appears to be more resistant to the aforementioned phenomenon. This is seen from the volume averaged quantities in figure 2a where the onset of both the sharp decrease in circulation and growth in dissipation is delayed for $q_0 = 1$. Finally, the dissipation peaks in both cases before undergoing a rapid reduction. This maximum is significantly higher for the $q_0 = \infty$ case, providing further evidence of the increased mixing that occurs in the absence of axial flow. As pointed out by Leweke & Williamson (1998), the final state is different from the organized array of vortex rings that would result from the reconnection of the primary structures if only the CM were present.

References

BAYLY, B. J. 1986 3-dimensional instability of elliptic flow. *Phys. Rev. Lett* **57(17)**, 2160–2163.

CAIN, A. B. & FERZIGER, J. H. & REYNOLDS, W. C. 1984 Discrete orthogonal function expansions for non-uniform grids using the fast fourier transform. *J. Comp. Phys* **56**, 272–286.

CHONG, M.S., PERRY, A. E. & CANTWELL, B. J. 1990 A general classification of 3-dimensional flow fields. *Phys. Fluids. A* **2(5)**, 765–777.

CROW, S. C. 1970 Stability theory for a pair of trailing vortices. *AIAA Journal* **8(12)**, 2172–2179.

264

HUNT, J. C. R., WRAY, A. A. & MOIN, P. 1988 Eddies, stream, and convergence zones in turbulent flows. *CTR report.* **CTR-S88**, 193.

JACQUIN, L. & PANTANO, C. 2002 On the persistence of trailing vortices. *J. Fluid Mech* **471**, 159–168.

LEIBOVICH, S. & STEWARTSON, K. 1983 A sufficient condition for the instability of columnar vortices. *J. Fluid Mech.* **126**, 335–356.

LEWEKE, T. & WILLIAMSON, C. H. K. 1998 Cooperative elliptic instability of a vortex pair. *J. Fluid Mech* **360**, 85–119.

MALLIER, R. & MASLOWE, S. A. 1993 A row of counter-rotating vortices. *Phys. Fluids* **5(4)**, 1074–1075.

PIERREHUMBERT, R. T. 1986 Universal short-wave instability of two-dimensional eddies in an inviscid fluid. *Phys. Rev. Lett* **57(17)**, 2157–2159.

SPALART, P. R. 1998 Airplane Trailing Vortices. *Annual Review of Fluid Mechanics* **30**, 107–138.

WIDNALL, S. E. 1974 The instability of short waves on a vortex ring. *J. Fluid Mech* **66**, 33.

HELICAL MODES IN SWIRLING JETS

Jean-Marc Chomaz
Laboratoire d'Hydrodynamique, LadHyX, Ecole Polytechnique-CNRS
F-91128 Palaiseau Cedex, France
chomaz@ladhyx.polytechnique.fr

Francois Gallaire
Laboratoire J.-A. Dieudonné, Université de Nice-Sophia Antipolis, Parc Valrose,
F-06128 Nice Cedex 02, France
gallaire@math.unice.fr

Abstract   The spiral form of vortex breakdown observed in the numerical simulations of Ruith *et al.* (2003) is interpreted as the consequence of the development of a so-called nonlinear global mode originating in the convective/absolute transition of the instability in the lee of the vortex breakdown bubble. This local theory gives an excellent prediction of the precession frequency measured in the three-dimensional DNS.

Keywords: Vortices, centrifugal instability, helical modes

Besides the striking phenomenon of vortex breakdown resulting in a strong deceleration along the jet axis, swirling jets are known to experiment a wide range of helical instabilities, breaking their axisymmetry. The relevant parameter in these studies is the swirl S which measures the ratio of the azimuthal velocity with respect to the axial velocity. These modes of instability are classiÞed according to their azimuthal wavenumber m. The present paper is dedicated to the inßuence of the spatio-temporal development of helical instabilities in the mode selection in swirling jets both in the pre- ($S < S_c$) and post-breakdown ($S > S_c$) regime. An interpretation of the double-helix structure observed for swirl ratios less than S_c by Billant *et al.* (1998) is proposed, based on the local absolutely unstable nature of the swirling jet with regard to the $m = -2$ mode at nozzle exit. Secondly, the spiral form of vortex breakdown observed in the numerical simulations of Ruith *et al.* (2003) is interpreted as the consequence of the development of a so-called nonlinear global mode originating in the con-

vective/absolute transition of the instability in the lee of the vortex breakdown bubble.

1.   Helical structures at the pre-breakdown stage

The goal of this first part is to identify the selection mechanism responsible for the appearance of a double-helix structure in the pre-breakdown stage of swirling jets, such as those of Escudier (1988), or Billant *et al.* (1998). In order to represent satisfactorily the nozzle velocity distributions measured in the latter swirling jet experiment, our basic flow is obtained by combination of classical azimuthal velocity profiles of shielded vortices with classical axial velocity profiles of jets. For the azimuthal velocity U_θ, the three parameters α, r_c and q non-dimensional family of profiles introduced by Carton and McWilliams (1989)

$$U_\theta(r) = qr \, \mathrm{e}^{(-r/r_c)^\alpha} \tag{1}$$

is an excellent approximation of the measured profiles as seen in figure 1. As far as the axial velocity U_z is concerned, the one parameter N non-dimensional family of profiles introduced by Monkewitz (1988)

$$U_z(r) = \frac{1}{1 + (\mathrm{e}^{r^2 \log(2)} - 1)^N} \tag{2}$$

is seen (figure 1 b) to yield a good approximation of the measured profiles if one is willing to neglect the influence of the axial velocity overshoot. This satisfying approximation is further discussed in Gallaire and Chomaz (2003). In the above expressions, the parameters α, r_c and N are determined once and for all in order to fit the measurements. Only the swirl ratio q, defined here as the slope at the origin of the azimuthal velocity is varied throughout the study. Expression (2) fixes the velocity and length scales to be the axial velocity U_c on the jet axis and the jet radius R, which enable us to define a Reynolds number $Re = U_c R/\nu$ as well as another form of the swirl number $S = U_\theta(R/2)/U_c$. As in classical viscous stability analysis, the basic flow (1) and (2), which constitutes an exact stationary solution of the Euler equations in unbounded space, is assumed to be steady and uniform in the axial direction. Formally, this may be achieved by adding a body force that exactly compensates for the viscous diffusion of the basic flow.

Temporal and absolute/convective instability properties are directly retrieved from numerical simulations of the linear impulse response in a box $1440 \times 196 \times 196$ following the method introduced by Delbende *et al.* (1998) at a Reynolds number $Re \sim 670$ for different swirl parameter settings. The temporal growthrates are computed from the evolution of the energy of each Fourier axial and azimuthal component whereas the absolute growthrate is deduced from the space-time-evolution of the energy spreading from the initial local-
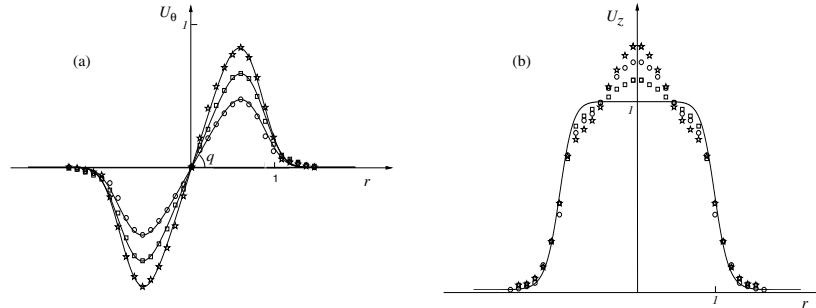
Figure 1. Azimuthal (a) and axial (b) velocity proÞles corresponding to expressions (1) and (2). Symbols refer to experimental data of Billant et al. (1998) at $Re = 666$ and $S = 0.68$ ($\square$), $S = 0.92$ (o), $S = 1.08$ ($\star$).

ized perturbation. Figure 2 demonstrates that a large range of negative helical modes, winding with the underlying rotating basic ßow, are destabilized as the swirl is increased, in close agreement with the asymptotic stability predictions of Leibovich and Stewartson (1983). At $Re \sim 670$, the most unstable mode is $m = -5$, but it should be noted that this selection is due to the damping effect of viscosity. At $Re \sim 1300$ for instance the most unstable mode is $m = -8$ (Gallaire and Chomaz 2003): the temporal study therefore fails to yield a sharp selection principle.

Turning to the spatio-temporal study, Þgure 3 shows that, when the swirl is increased from zero, the swirling jet is determined to Þrst become absolutely unstable to the $m = -2$ mode, winding with the underlying base ßow, above a swirl threshold of $q^{C/A} \sim 1.12$. This transition from convective to absolute instability is proposed as a selection mechanism accounting for the experimental observation of a double-helix, which is interpreted as a global mode triggered by a front located at the nozzle exit where the $m = -2$ mode is absolutely unstable. The theoretical predictions in terms of swirl onset, frequency and wavenumber compare satisfactorily with the experimental observations of Billant *et al.* (1998).

2. Spiral form of vortex breakdown

The widespread phenomenon of vortex breakdown affecting swirling jets is both observed in its axisymmetric form (the bubble) or in its spiral form, as soon as the swirl parameter S is large enough. These synchronized helical vortex breakdown states (see Escudier 1988 for a review) are characterized by small azimuthal wavenumbers ($m = 1$ or $m = 2$), they rotate in time in the same direction as the swirling base ßow but wind in space in the opposite direction.
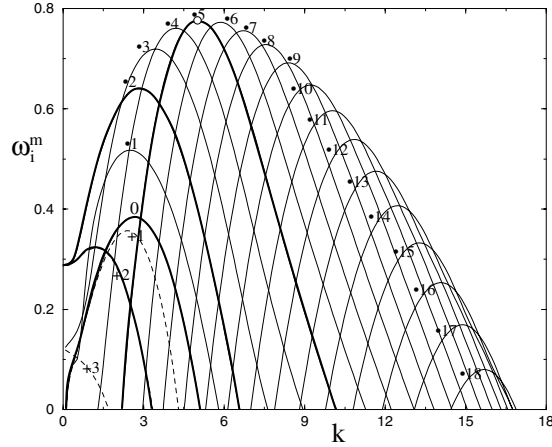
Figure 2. Temporal stability curves for $q = 1.2$ and $Re \sim 670$. The growth-rate ω_i^m is depicted as a function of the axial wavenumber k for different azimuthal wavenumbers $-18 < m < 3$.
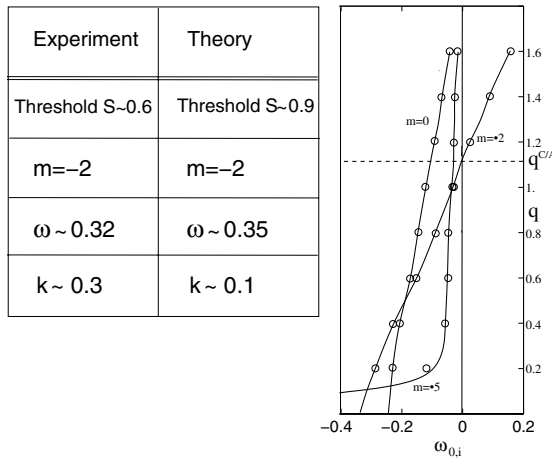

Experiment	Theory
Threshold S~0.6	Threshold S~0.9
m=−2	m=−2
ω ~ 0.32	ω ~ 0.35
k ~ 0.3	k ~ 0.1

Figure 3. Spatio-temporal stability properties. The absolute growth-rate $\omega_{0,i}^m(q)$ as a function of the swirl q for modes $m = 0, m = -2$ and $m = -5$ and comparison between the experimental measurements at onset of the double-helix and the present theory. All other azimuthal modes are convectively unstable, i.e. $\omega_{0,i} \leq 0$.

According to the initial suggestion of Maxworthy (private communication), Delbende *et al.* (1998), and to the first qualitative comparisons with the Batchelor vortex of Yin *et al.* (2000) and Ruith *et al.* (2003), the spiral vortex breakdown is supposed to result form the development of a global mode trig-
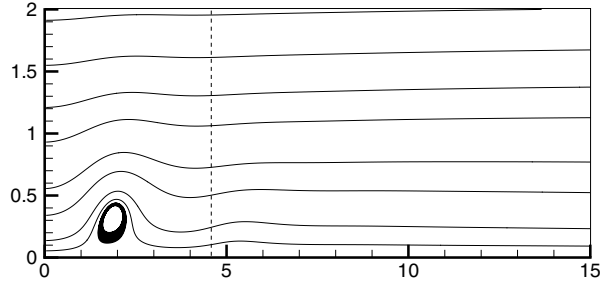
Figure 4. Meridional cut of the streamlines associated to the base ßow obtained numerically by imposing the axisymmetry of the ßow; $S = 1.095$, $Re = 200$ (Ruith et al. 2003).

gered by the absolutely unstable nature of the $m = 1$ mode in the lee of the breakdown bubble.

Our purpose is to validate this hypothesis by using as a base ßow the velocity proÞles obtained in the numerical simulations of Ruith *et al.* (2003) by enforcing the axisymmetry (see Þgure 4). As seen in Þgure 4, vortex breakdown is observed at the swirl number $S = 1.095$, characterized by the typical recirculation zone. At each axial station z along the streamwise axis, the ßow is assumed to be weakly non-parallel and the stability study is conducted on a parallel ßow basis with the base ßow measured locally at the station z. The weakly non-parallel but strongly nonlinear theory of Pier *et al.* (2001) suggests that, if there exists a station $z_{C/A}$ where the imaginary part of the absolute frequency ω_0 vanishes and where the ßow changes from convective ($\omega_{0,i}(z) < 0$ for $z < z_{C/A}$) into absolute ($\omega_{0,i}(z)0$ for $z_{C/A} < z$), then a nonlinear global mode might be triggered with a front located in $z_{C/A}$. This global mode inherits the real absolute frequency at this point $\omega_0(z_{C/A})$.

For the same parameter setting as in Þgure 4 but by relaxing the axisymmetry assumption, Þgure 5 represents the instantaneous emission lines at $t = 1850$ obtained in the DNS with an initial random noise imposed on the base ßow (Þgure 4) at $t = 0$. The ßow settles to a limit cycle oscillating at a well determined frequency ω_G^{NL}.

The stability analysis is conducted by numerical means by the method outlined in Delbende *et al.* (1998) in a box $1440 \times 196 \times 196$. The results are depicted in Þgure 6. Two absolutely unstable regions can be distinguished in shaded. A Þrst region located in the recirculation bubble between $z_{C/A}^1 = 1.1$ and $z_{A/C}^1 = 3.3$ and a second region in the lee of the bubble for $z \geq z_{C/A}^2 = 4.7$.

The value of the global frequency ω_G^{NL} measured in the DNS is shown in Þgure 6 by a horizontal heavy line. The agreement between the measured frequency ω_G^{NL} and $\omega_{0,r,2}^{C/A}$ is excellent, whereas it is less satisfactory with $\omega_{0,r,1}^{C/A}$.
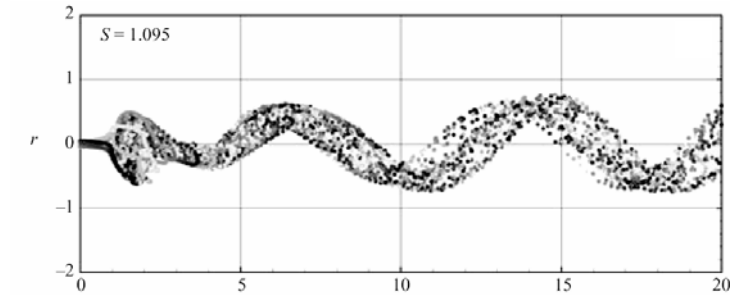
Figure 5. Instantaneous emission lines at $t = 1850$ associated to the three-dimensional flow obtained by DNS at $S = 1.095$ and $Re = 200$ (Ruith et al. 2003).
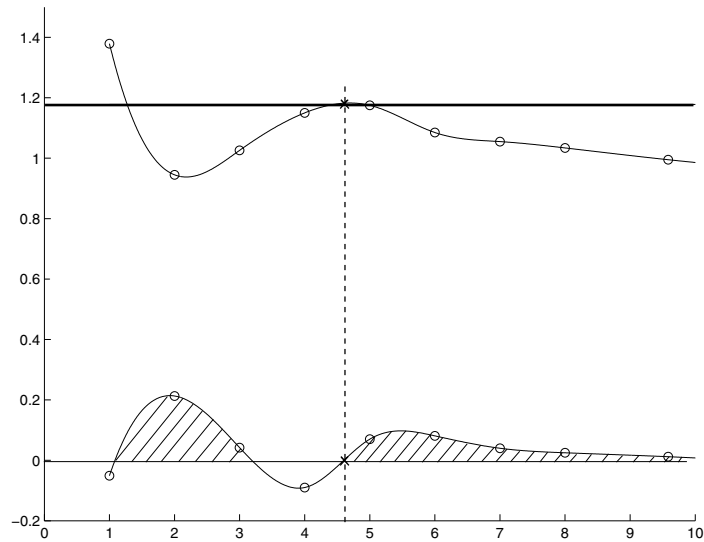

Figure 6. Streamwise evolution of the real $\omega_{0,r}$ and imaginary part $\omega_{0,i}$ of the local absolute frequency as a function of the streamwise coordinate z.

This suggests that the second region is responsible for the global instability and that the transition point $z^2_{C/A}$ plays the role of a wavemaker. The validity of the interpretation of the self-sustained oscillator in term of a nonlinear global mode with a front located at the transition point $z^2_{C/A}$ is further confirmed by the analysis of the streamwise amplitude distribution and wavenumber variation extracted from the DNS.

Acknowledgments

The authors would like to thank M. Ruith, E. Meiburg and P. Huerre for their contributions to the present paper.

References

BILLANT P. , CHOMAZ J.-M. & HUERRE P. 1998 Experimental study of vortex breakdown in swirling jets. *J. Fluid Mech.* **376**, 183Ð219.

CARTON, X.J. & MCWILLIAMS, J.C. 1989 Barotropic and baroclinic instabilities of ax-isymmetric vortices in a quasi-geostrophic model. In *Mesoscale/Synoptic Coherent Structures in Geophysical Turbulence* (ed. J. C. J. Nihoul & B. M. Jamart), pp. 225Ð244. Elsevier.

DELBENDE, I., CHOMAZ, J.-M. & HUERRE P. 1998 Absolute/convective instabilities in the Batchelor vortex: a numerical study of the linear impulse response. *J. Fluid Mech.* **355**, 229Ð254.

ESCUDIER, M. P. 1988 Vortex breakdown : Observations and explanations. *Prog. in Aerospace Sci.* **25**, 189Ð229.

GALLAIRE, F., & CHOMAZ, J.-M. 2003 Mode selection in swirling jets : an experimentally based instability analysis. *J. Fluid Mech.* **494**, 223Ð253.

LEIBOVICH, S. & STEWARTSON, K. 1983 A SufÞcient condition for the instability of colum-nar vortices.

J. Fluid Mech. **126**, 335Ð356.

MONKEWITZ, P.A. 1988 The absolute and convective nature of instability in two-dimensional wakes at Low Reynolds numbers. *Phys. Fluids* **31**, 999Ð1006.

PIER, B., HUERRE, P. & CHOMAZ, J.-M. 2001 Bifurcation to fully nonlinear synchronized structures in slowly varying media. *Physica D.* **148**, 49Ð96.

RUITH, M., CHEN, P., MEIBURG, E. & MAXWORTHY, T. 2003 Three-dimensional vortex breakdown in swirling jets and wakes: direct numerical simulation. *J. Fluid Mech.* **486**, 331Ð378.

YIN, X.Y., SUN, D.J., WEI, M.J. & WU J.Z. 2000 Absolute and convective instability character of slender viscous vortices. *Phys. Fluids.* **12**, 1062Ð1072.

Part G   Dynamics of thin vortices

MOTION OF THREE-DIMENSIONAL VORTEX FILAMENT AND PARTICLE TRANSPORT

Yoshi Kimura
Graduate School of Mathematics, Nagoya University,
Furo-cho, Chikusa-ku, Nagoya 464-8602 Japan
kimura@math.nagoya-u.ac.jp

Abstract   Motions of fluid particles advected by a 3D vortex filament are studied. As extensions of a circular vortex ring, which provides a basis of fluid transport by vortex, two types of motions, elliptic vortex ring and vortex soliton are considered. For an elliptic vortex ring, it is verified that the local induction equation (LIE) describes its motion properly if the aspect ratio is close to 1. Using the solution of LIE, particle motions are simulated for two different induction constants corresponding to a thin and a fat vortex for the circular vortex ring case, respectively. Intrinsic difficulty for calculating the finite transported volume by an elliptic vortex ring is suggested. For a vortex soliton, it is demonstrated that particle motions are confined in a torus near the kink of a soliton for a wide range of parameters that characterize the shape and the strength of the vortex soliton.

Keywords: 3D vortex filament, elliptic vortex ring, vortex soliton, particle transport

1.   Introduction

Transport of fluid particles by an isolated vortex has been a fundamental problem which, particularly if a vortex moves steadily, provides a direct example of long-surviving advection of materials from a turbulent region where a vortex is excited to a laminar region in fluids. The main objective of this paper is to demonstrate such transport by 3D motions of a vortex filament.

The best example of such transport is the case of a circular vortex ring. In this axisymmetric situation, fluid particles are trapped inside a region near the vortex core, and the volume of the region is determined as a function of the parameter σ/L, where σ is the core radius and L is the curvature radius of the vortex ring (Batchelor 1967, Saffman 1992). If this idealistic situation is modified either to time-dependent or to extended 3D flow field, we may have different pictures of transport of particles according to the features of the vortex motion. In this paper, we shall present two such examples of particle transport: one is by an elliptic vortex ring, and the other is by a vortex soliton. The former

provides an example of an unsteady vortex motion by adding a time periodic perturbation to a circular vortex ring, while the latter provides an extended 3D but steady vortex flow in a certain reference frame.

2. Particle transport by an elliptic vortex ring

As a direct modification of the circular vortex ring problem to an unsteady motion, we consider particle transport by an elliptic vortex ring. We have verified numerically that, as long as the ellipticity is small, the motion of an elliptic vortex ring is periodic in time which is well-described by the LIE,

$$\frac{\partial \mathbf{X}}{\partial t} = \frac{\Gamma}{4\pi} \log \left(\frac{L}{\sigma} \right) \left[\frac{\partial \mathbf{X}}{\partial s} \times \frac{\partial^2 \mathbf{X}}{\partial s^2} \right],\tag{1}$$

where $\mathbf{X}(s,t) = (x(s,t), y(s,t), z(s,t))$ is the position of the vortex segment parametrized by the arc-length s, at time t, and Γ is the circulation of the vortex ring. If we assume that the prefactor, $\frac{\Gamma}{4\pi} \log \left(\frac{L}{\sigma} \right)$, is a constant, G called the self-induction constant, the above equation can be written as

$$\mathbf{v}(s) = G\kappa(s)\mathbf{b}(s),\tag{2}$$

where $\mathbf{v}$, κ, and $\mathbf{b}$ are velocity, curvature and the binormal unit vector of the vortex segment parametrized by s. The usage of LIE for the motion of an elliptic vortex ring was first proposed by Arms and Hama (1965). Later it was argued by Dhanak and de Bernardinis (1981) that the LIE is an approximation which neglects such vortex instability as Crow instability or elliptic instability on the core. Figure 1 shows a snapshot of an elliptic vortex ring moving upward. (The initial aspect ratio $a/b = 1.5$, and the thickness of the core is exaggerated.) The curve on each plane is a projection on to the plane. Similar figures were obtained also experimentally (Oshima *et al.* 1988).

It is well-known that the LIE is equivalent with the nonlinear Schrödinger equation (NLS)

$$\mathrm{i}\frac{\partial \phi}{\partial t} + \frac{\partial^2 \phi}{\partial s^2} + \frac{1}{2}|\phi|^2 \phi = 0,\tag{3}$$

where

$$\phi(s,t) = \kappa(s,t) \exp \left[\mathrm{i} \int^s \tau(s',t)\mathrm{d}s' \right],\tag{4}$$

and the time has been rescaled by means of G. The time periodic motion of an elliptic vortex ring implies that the corresponding NLS solution is also a space and time periodic solution. But because of the phase information in (4), not all periodic NLS solutions can apply to closed vortex filament solutions. We shall report this point elsewhere.
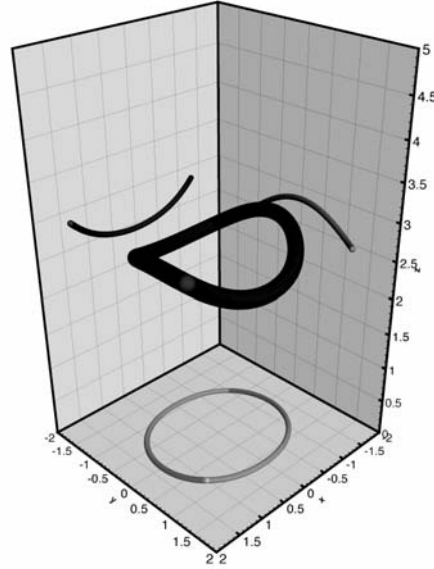
Figure 1. A snapshot of an elliptic vortex ring moving upward. The curve on each plane is a projection of the plane.

For the motion of particles, the Biot-Savart integral,

$$\frac{d\mathbf{r}}{dt} = \frac{1}{4\pi} \int_{-\infty}^{\infty} \frac{\mathbf{X}'(s,t) \times (\mathbf{r} - \mathbf{X}(s,t))}{|\mathbf{r} - \mathbf{X}(s,t)|^3} ds \tag{5}$$

is used to calculate the induced velocity at the position of a particle $\mathbf{r}(t)$. For simplicity, we set the circulation $\Gamma = 1$, which means that a relation $\log\left(\frac{L}{\sigma}\right) = 4\pi G$ is imposed for the thickness (i.e. the ratio between the long and short length scales) of the core.

Figures 2a and 2b are plots of particles carried by an elliptic vortex ring in a reference frame which moves with the center of mass. At $t = 0$, the particles are placed in a plane adjacent to the vortex ring. Figure 2a is the case with $G = 1$ (thin vortex) and Figure 2b is with $G = 0.25$ (fat vortex). For both cases, some particles rotate around the vortex core and move with the unsteady vortex ring. One thing we should point out is that the translational speed of a thin vortex is fast, and that is why smaller number of particles can catch up with the vortex ring while rotating around the core.

As a fundamental transport property, the fluid volume carried by a vortex ring is of interest. This quantity could be approximately measured by the number of particles trapped by the vortex ring. Unfortunately, however, even if the analytical solution for the motion of an elliptic vortex ring is given, it may be
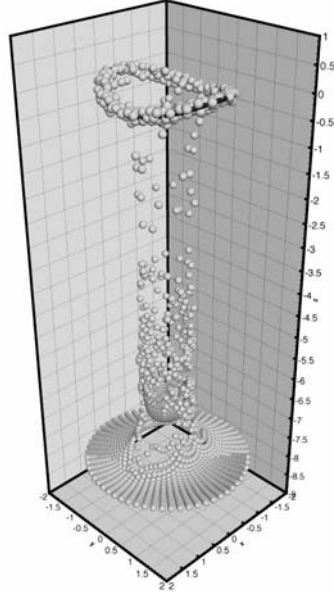
Figure 2a.   Particles driven by an elliptic vortex ring. $G = 1$ (thin vortex)
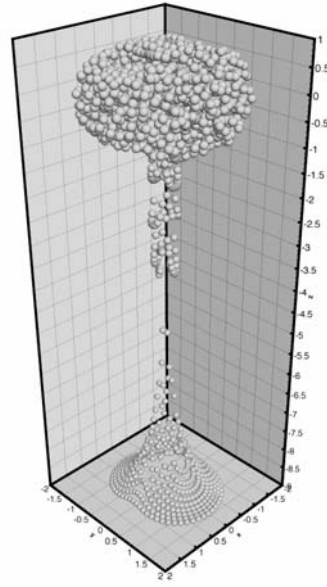
Figure 2b.   Particles driven by an elliptic vortex ring. $G = 0.25$ (fat vortex)

difficult to calculate the definite amount of the volume. The situation can be understood by appeal to an analogy with the corresponding 2D problem of a perturbed vortex pair (Rom-Kedar *et al.* 1990). In this situation, the unstable manifold of a vortex pair (i.e. the boundary of the pair) is dramatically deformed by time periodic sinusoidal perturbations to produce many lobes outside. In Figs. 2a and 2b, scattered particles are observed in the wake of the vortex ring. Those particles may indicate the existence of such lobes in this perturbed vortex ring problem also.

3.   Particle transport by a vortex soliton

The interplay between LIE and NLS was first made clear in the discussion of vortex soliton by Hasimoto (1972). The vortex soliton is one of few steady solutions for a vortex filament under LIE, and it belongs to a class of traveling solutions of NLS (Kida 1981). In the original observation of vortex soliton in a rotating tank experiment by Hopfinger *et. al.* (1981), a transport mechanism of physical quantities such as mass and energy was already suggested. Following the experimental result, it was shown analytically that impulse and angular momentum are transported by a vortex soliton (Kimura 1989), but to investigate

the transport of mass, we need to scrutinize the flow field and track particles around vortex solitons.

Making use of the fact that the motion of a vortex soliton is decomposed into rotation and translation of a fixed shape, we can introduce a moving reference frame in which the vortex soliton is fixed. The equation for the motion of a fluid particle at $\mathbf{r}(t)$ in such a moving frame is

$$\frac{d\mathbf{r}}{dt} = \frac{1}{4\pi} \int_{-\infty}^{\infty} \frac{\mathbf{x}'(s) \times (\mathbf{r} - \mathbf{x}(s))}{|\mathbf{r} - \mathbf{x}(s)|^3} ds + (\nu^2 + \tau^2)G \begin{pmatrix} y \\ -x \\ 0 \end{pmatrix} - 2\tau G \begin{pmatrix} 0 \\ 0 \\ 1 \end{pmatrix},$$

(6)

where $\mathbf{x}(s)$ is the position of the vortex filament parametrized by the arc length s, and ν and τ are half-maximum curvature and torsion, respectively. In our previous paper (Kimura & Koikari 2004), we corroborated the transport of particles by vortex solitons with a wide range of three parameters (ν, τ, G) which characterize the shape and strength of the soliton. Also the following things were reported:

(i) Some particles are confined in a torus region which makes a knot with the loop part of the vortex soliton (Figure 3) The Poincaré section shows a similar structure with the KAM torus for non-integrable Hamiltonian systems.

(ii) The volume of the torus is calculated as a function of the parameters, (ν, τ, G). An optimized shape of the soliton is determined for the maximum rate of transport.

(iii) To explain the essential mechanism of the torus formation, the following ODE system, *the chopsticks model*, is proposed:

$$\frac{d}{dt} \begin{pmatrix} x \\ y \\ z \end{pmatrix} = \frac{1}{2\pi} \frac{1}{|\mathbf{t}_A \times (\mathbf{x} - \mathbf{a}_A)|^2} \begin{pmatrix} \sin\phi \sin\theta\, z - \cos\theta\,(y + y_0) \\ \cos\theta\,(x - x_0) - \cos\phi \sin\theta\, z \\ \cos\phi \sin\theta\,(y + y_0) - \sin\phi \sin\theta\,(x - x_0) \end{pmatrix}$$
$$+ \frac{1}{2\pi} \frac{1}{|\mathbf{t}_B \times (\mathbf{x} - \mathbf{a}_B)|^2} \begin{pmatrix} \sin\phi \sin\theta\, z - \cos\theta\,(y - y_0) \\ \cos\theta\,(x - x_0) + \cos\phi \sin\theta\, z \\ -\cos\phi \sin\theta\,(y - y_0) - \sin\phi \sin\theta\,(x - x_0) \end{pmatrix}$$
$$+ (\nu^2 + \tau^2)G \begin{pmatrix} y \\ -x \\ 0 \end{pmatrix} - 2\tau G \begin{pmatrix} 0 \\ 0 \\ 1 \end{pmatrix},$$

(7)

where ϕ and θ are usual azimuthal and polar angles for tangent vectors,
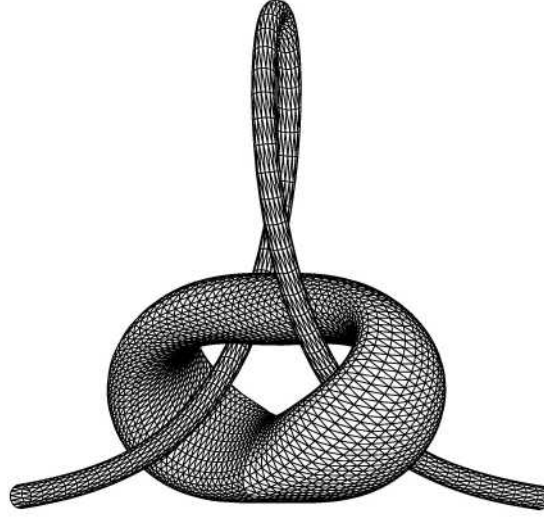
Figure 3. Perspective view of a torus formed by a single trajectory near the loop part of a vortex soliton for $(\nu, \tau) = (1.924, 0.3827)$ and $G = 0.1832$.

respectively (i.e. $\theta = 0$: z-axis, $\theta = \pi/2, \phi = 0$: x-axis), and

$$
\begin{aligned}
|\mathbf{t}_A \times (\mathbf{x} - \mathbf{a}_A)|^2 = {} & (\cos^2 \theta + \sin^2 \phi \sin^2 \theta)\,(x - x_0)^2 \\
& + (\cos^2 \theta + \cos^2 \phi \sin^2 \theta)\,(y + y_0)^2 + \sin^2 \theta\, z^2 \\
& - 2 \sin \theta \cos \theta \sin \phi\, z\,(y + y_0) - 2 \sin \theta \cos \theta \cos \phi\,(x - x_0)\,z \\
& - 2 \sin \phi \cos \phi \sin^2 \theta\,(x - x_0)(y + y_0)
\end{aligned}
$$

and

$$
\begin{aligned}
|\mathbf{t}_B \times (\mathbf{x} - \mathbf{a}_B)|^2 = {} & (\cos^2 \theta + \sin^2 \phi \sin^2 \theta)\,(x - x_0)^2 \\
& + (\cos^2 \theta + \cos^2 \phi \sin^2 \theta)\,(y - y_0)^2 + \sin^2 \theta\, z^2 \\
& - 2 \sin \theta \cos \theta \sin \phi\, z\,(y - y_0) + 2 \sin \theta \cos \theta \cos \phi\,(x - x_0)\,z \\
& + 2 \sin \phi \cos \phi \sin^2 \theta\,(x - x_0)(y - y_0)\,.
\end{aligned}
$$

This model just replaces the original soliton with two straight line vortices (with infinite length) tangent to the two strongest interaction points while keeping the background rotational and translational terms. Interestingly enough, this model still produces a similar torus around the sticks. Figure 4 shows the Poincaré section and the perspective view of the torus produced by the chopsticks model. Although the upper part of the torus is exaggerated because of the absence of the loop of the soliton, the torus

keeps the same topology with the original soliton. Also the Poincaré section looks more regular but still holds the hyperbolic strucuture inside.
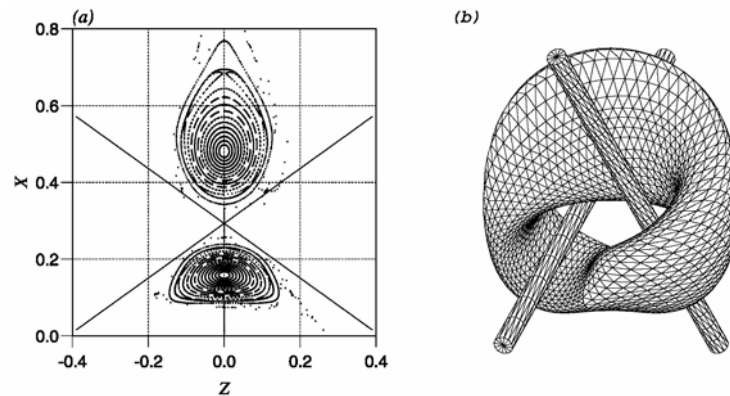

Figure 4. Poincaré section (a) and perspective view (b) of a torus produced by the chopsticks model.

4. Summary

We have demonstrated that a perturbed or an extended circular vortex ring system (such as elliptic vortex ring and vortex soliton) can transport particles. An elliptic vortex ring provides unsteady but periodic perturbation to a circular vortex ring, whose motion can be approximated well by LIE (particularly for ellipses close to a circle.) A possible intrinsic difficulty for calculating a definite value of the transported volume was discussed by referring to the corresponding 2D problem as an example. In contrast with the obscureness for the boundary of the trapped region for an elliptic vortex ring, the torus for a vortex soliton has a rather sharp boundary, and we could compute the transported volume for various parameter values. To explain the torus formation we proposed the chopsticks model. It seems that the configuration of two vortex sticks in 3D space is essential for producing the torus.

The author is grateful of the discussion with Professor Harvey Segur. The second part of this paper is a collaboration with Dr. Souji Koikari.

This paper is dedicated to the late Professor Isao Imai.

References

ARMS, R. J. & HAMA, F. R. 1965 Localized induction concept on a curved vortex and motion of an elliptic vortex ring, *Phys. Fluids* **8** 553–559.

282

BATCHELOR, G. K. 1967 *An introduction to Fluid Dynamics*. (Cambridge University Press)

DHANAK, M. R. & DE BERNARDINIS, B. 1981 The evolution of an elliptic vortex ring, *J. Fluid Mech.* **109**, 189–216.

HASIMOTO, H. 1972 A soliton on a vortex filament, *J. Fluid Mech.* **51** 477–485.

HOPFINGER, E. J., BROWAND, F. & GAGNE, Y. Turbulence and waves in a rotating tank, *J. Fluid Mech.* **125** 505-534.

KIDA, S. 1981 A vortex filament moving without changes of form, *J. Fluid Mech.* **112** 397–409.

KIMURA, Y. 1989 Transport properties of waves on a vortex filament *Physica* **D37** 485–489.

KIMURA, Y. & KOIKARI, S. 2004 Particle transport by a vortex soliton, *J. Fluid Mech.* **510**, 201–218.

NEWTON, P. K. 2000 *The N-Vortex Probem, Analytical Techniques* (Springer)

OSHIMA, Y. IZUTSU, N., OSHIMA, K. & HUSSAIN, A. K. M. F. 1988 Bifurcation of an elliptic vortex ring, *Flluid Dynamics Research* **3** 133–139.

ROM-KEDAR, V., LEONARD, A. & WIGGINS, S. 1990 An analytical study of transport, mixing and chaos in an unsteady vortical flow, *J. Fluid Mech.* **214**, 347–394.

SAFFMAN, P. G. 1992 *Vortex Dynamics*. (Cambridge University Press)

LINEAR AND NONLINEAR INSTABILITY OF A VORTEX RING

Yasuhide Fukumoto
Graduate School of Mathematics and Space Environment Research Center, Kyushu University
33, Fukuoka 812–8581, Japan
yasuhide@math.kyushu-u.ac.jp

Yuji Hattori
Faculty of Engineering, Kyushu Institute of Technology,
Kitakyushu 804-8550, Japan
hattori@mns.kyutech.ac.jp

Abstract   A new linear instability mechanism of curvature origin is established for a vortex ring. The curvature effect reduces O(2) × SO(2) symmetry of a circular-cylindrical tube to O(2), and fuels a pair of Kelvin waves whose azimuthal wavenumbers on the core are separated by one. For Kelvin's vortex ring, the growth rate and eigenfunctions are written out in closed form. In the inviscid case, the curvature effect dominates over the elliptically straining effect, but the former suffers from enhanced viscous damping. There are numerous excitable modes. As a first step toward an understanding of the route to a matured stage, we derive equations for weakly nonlinear evolution of amplitudes of the curvature instability. Our direct numerical simulation successfully captures the elliptical instability.

1.   Introduction

Vortex rings are ubiquitous coherent structures, featured by vortex-tube curvature, in practical flows and in nature. They commonly entail wavy distortions, sometimes resulting in disruption, and their three-dimensional instability has attracted continuous attention (Maxworthy 1977; Naitoh *et al.* 2002). It prevails that the Moore-Saffman-Tsai-Widnall instability (the MSTW instability) is responsible for instability (Widnall *et al.* 1974; Moore & Saffman 1975; Tsai & Widnall 1976; Widnall & Tsai 1977). Its source is the local straining field

that deforms the circular core into an ellipse. Recently we have found a new linear instability mode driven by the effect of curvature (Hattori & Fukumoto 2003; Fukumoto & Hattori 2005).

When viewed locally, a thin vortex ring is regarded as a straight tube. Owing to SO(2)×O(2) symmetry, a circular-cylindrical vortex is spectrally stable and supports an infinite family of three-dimensional oscillations, the Kelvin waves. In the asymptotic expansions of the Navier-Stokes equations for a vortex ring in powers of a small parameter ϵ, the ratio of core- to ring-radii, the curvature effect is embodied as a local dipole field, in proportion to $\cos\theta$ and $\sin\theta$, of $O(\epsilon)$, in terms of the local moving polar coordinates (r, θ) in the meridional plane (Fukumoto & Moffatt 2000). This precedes the quadrupole field of $O(\epsilon^2)$ associated with the elliptical deformation of the core. The dipole field breaks circular (SO(2)-) symmetry of the core and can mediate a parametric resonance between a pair of waves whose azimuthal wavenumbers differ by one.

We exemplify this by an analytically tractable model (Fukumoto & Hattori 2005). Kelvin's vortex ring is an asymptotic solution of the Euler equations which starts at $O(\epsilon^0)$, with a circular vortex of uniform vorticity, that is, the Rankine vortex. Remarkably this model admits a closed-form solution of the linearized Euler equations for disturbances, solely in terms of the Bessel and the modified Bessel functions. We reveal, by an asymptotic analysis, that the most unstable mode occurs in the short-wave limit with radial and azimuthal wavenumbers being of the same magnitude. The limiting value $165/256\epsilon$ of growth rate coincides with the value obtained by the geometric optics method (Hattori & Fukumoto 2003).

This $O(\epsilon)$ instability mode outweighs, in the entire range of ϵ ($0 < \epsilon < 1$), the MSTW instability of $O(\epsilon^2)$. However the viscosity acts to damp preferentially the $O(\epsilon)$ instability, and hence the $O(\epsilon^2)$ mode may take over $O(\epsilon)$ one. After a formulation in §2, a concise description of the $O(\epsilon)$ linear instability is given in §3.

At a large Reynolds number, a great number of resonance modes, of various origins, are excitable. Nonlinear mode interactions hold the key to mode selection and eventual breakdown as demonstrated by numerical simulations (Shariff *et al.* 1994). We address nonlinear evolution of unstable Kelvin modes in two ways. In §4, weakly nonlinear evolution equations of amplitudes of an unstable mode on Kelvin's vortex ring are derived, to cubic order in amplitude, in the form compatible with the Hamiltonian normal form (Knobloch *et al.* 1994). We rely on the inner-product formulation (Moore & Saffman 1975) and on the method of multiple time scales (Sipp 2000).

Further in §5, using the pseudo-spectral method, a direct numerical simulation of the Navier-Stokes equations is conducted for evolution of three-dimensional waves on a Gaussian core at high Reynolds numbers. The targeted question is the competition between the $O(\epsilon)$ and the $O(\epsilon^2)$ effects.

2. Formulation

Kelvin's vortex ring is a thin axisymmetric vortex ring, in an incompressible inviscid fluid, with vorticity proportional to the distance from the axis of symmetry, which propagates steadily in the direction of axis of symmetry. The assumption is made that the ratio ϵ of the core radius σ to the ring radius R is very small:

$$\epsilon = \sigma/R \ll 1. \tag{1}$$

Introduce toroidal coordinates (r, θ, s) co-moving with the ring, linked with the global Cartesian coordinates (x, y, z), with the x-axis lying on the symmetric axis, in such a way as

$$x = r\cos\theta, \quad y = (R + r\sin\theta)\cos(s/R), \quad z = (R + r\sin\theta)\sin(s/R). \tag{2}$$

In the meridional plane $s = 0$, the origin $r = 0$ is maintained at the center of the circular core and the angle θ is measured from the direction parallel to the x-axis. The center circle penetrating inside the toroidal ring is parameterized by the arclength s.

We denote the circulation carried by the ring by Γ and normalize the radial coordinate r by the core radius σ, the velocity by the maximum azimuthal velocity $\Gamma/2\pi\sigma$, the time t by $2\pi\sigma^2/\Gamma$. Let the r and θ components of velocity field be U and V inside the core ($r < 1$). The velocity potential for the exterior irrotational flow ($r > 1$) is denoted by Φ. The basic flow is expanded in powers of ϵ to first order as

$$\boldsymbol{U} = \boldsymbol{U}_0 + \epsilon\boldsymbol{U}_1 + \cdots, \tag{3}$$

whose components, along with the velocity potential for the external flow, are

$$U_0 = 0, \quad V_0 = r, \quad \Phi_0 = \theta, \tag{4}$$

$$U_1 = \frac{5}{8}(1 - r^2)\cos\theta, \quad V_1 = \left(-\frac{5}{8} + \frac{7}{8}r^2\right)\sin\theta,$$
$$\Phi_1 = \left(\frac{1}{8}r - \frac{3}{8r} - \frac{1}{2}r\log r\right)\cos\theta. \tag{5}$$

Circular form of core boundary ($r = 1$) remains intact. Elliptical deformation comes into play at $O(\epsilon^2)$.

The $O(\epsilon)$-field $\boldsymbol{U}_1$ pertains to a dipole field and may be taken as a product of the curvature effect; vortex lines of a steady vortex ring are stretched on the convex side and are contracted on the concave side of the torus. As a consequence, the vorticity is enhanced on the convex side and is weakened on the concave side, producing effectively an anti-parallel vortex pair (Fukumoto & Moffatt 2000).

Superposed on (3) is the following form of the disturbance field (Sipp 2000):

$$\boldsymbol{u} = \alpha\boldsymbol{u}_{01} + \alpha^2\boldsymbol{u}_{02} + \alpha^3\boldsymbol{u}_{03} + \cdots + \epsilon\alpha\boldsymbol{u}_{11} + \epsilon\alpha^2\boldsymbol{u}_{12} + \cdots, \qquad (6)$$

and we inquire into its evolution. The power in α indexes the order of nonlinearity.

Relevant to linear stability are $\alpha\boldsymbol{u}_{01}$ and $\epsilon\alpha\boldsymbol{u}_{11}$. The following section presents an outline of the linear stability result (Fukumoto & Hattori 2005).

3.   Linear instability of $O(\epsilon)$

The global linear stability problem was formulated by Widnall & Tsai (1977), though they skipped analysis of the $O(\epsilon\alpha)$ field. Allowance is made for weak viscous dissipation (*cf.* Eloy & Le Dizes 2001).

3.1   Solution ansatz

The $O(\alpha)$ field is the Kelvin wave. We send a pair of Kelvin waves with azimuthal wavenumbers m and $m+1$, which are capable of being in resonance via the dipole field (5),

$$\begin{aligned}
\boldsymbol{u}_{01} &= \left\{ A_+\boldsymbol{u}_{A_+}(r)e^{\mathrm{i}m\theta} + B_+\boldsymbol{u}_{B_+}(r)e^{\mathrm{i}(m+1)\theta} \right\} e^{\mathrm{i}(ks-\omega t)} \\
&\quad + \left\{ A_-\boldsymbol{u}_{A_-}(r)e^{\mathrm{i}m\theta} + B_-\boldsymbol{u}_{B_-}(r)e^{\mathrm{i}(m+1)\theta} \right\} e^{\mathrm{i}(-ks-\omega t)} + \text{c.c.}, \qquad (7)
\end{aligned}$$

where c.c. stands for complex conjugate. The presence of the field of wavenumber $-k$ signifies the reflection symmetry in the toroidal (s-) direction. The normalized wavenumber k and the frequency ω are expanded as $k = k_0 + \epsilon k_1 + \cdots$, and $\omega = \omega_0 + \epsilon\omega_1 + \cdots$.

To have an idea, we write the r-component of the Navier-Stokes equations as

$$\begin{aligned}
-\mathrm{i}\omega_0 u_{11} &+ \frac{\partial u_{11}}{\partial\theta} - 2v_{11} + \frac{\partial\pi_{11}}{\partial r} \\
&= \left(i\omega_1 - \frac{\partial U_1}{\partial r} \right) u_{01} - U_1\frac{\partial u_{01}}{\partial r} - \frac{V_1}{r}\frac{\partial u_{01}}{\partial\theta} - \left(\frac{1}{r}\frac{\partial U_1}{\partial\theta} - \frac{2V_1}{r} \right) v_{01} \\
&\quad + \tilde{\nu}\left\{ \left(\frac{\partial^2}{\partial r^2} + \frac{1}{r}\frac{\partial}{\partial r} + \frac{1}{r^2}\frac{\partial^2}{\partial\theta^2} - k_0^2 - \frac{1}{r^2} \right) u_{01} - \frac{2}{r^2}\frac{\partial v_{01}}{\partial\theta} \right\}, \qquad (8)
\end{aligned}$$

where π_{11} is the disturbance pressure and $\tilde{\nu} = 2\pi\nu/(\Gamma\epsilon)$ is the normalized viscosity, being supposed of $O(\epsilon^0)$. Thence, the $O(\alpha\epsilon)$ field takes the following

angular dependence:

$$
\begin{aligned}
\boldsymbol{u}_{11} = \Big\{ &B_+ \big[\boldsymbol{s}_{B_+}(r)e^{\mathrm{i}m\theta} + \boldsymbol{u}_{11}^{(m+2)}(r)e^{\mathrm{i}(m+2)\theta} \big] \\
&+ A_+ \big[\boldsymbol{s}_{A_+}(r)e^{\mathrm{i}(m+1)\theta} + \boldsymbol{u}_{11}^{(m-1)}(r)e^{\mathrm{i}(m-1)\theta} \big] \Big\} \, e^{\mathrm{i}(ks-\omega t)} \\
&+ \big[e^{\mathrm{i}(-ks-\omega t)} \text{ terms} \big] + \text{c.c.}
\end{aligned}
\tag{9}
$$

Emergence of the same wavenumber pair $(m, m+1)$ with (7) indicates possibility of parametric resonance.

3.2 Growth rate and short-wavelength asymptotics

The Navier-Stokes equations for $\boldsymbol{s}_{B_+}(r)$ collapse to a single second-order ordinary differential equation for the disturbance pressure. This equation can be integrated with use of the Bessel functions of first kind, and thereafter the velocity field $\boldsymbol{s}_{B_+}(r)$ are deduced in closed form. The exterior velocity potential is constructed in terms of the modified Bessel functions of second kind. The boundary conditions at $O(\epsilon\alpha)$ bring in the condition on $\boldsymbol{u}_{01}$ for $\boldsymbol{s}_{B_+}(r)$ to be soluble. The same procedure is repeated for $\boldsymbol{s}_{A_+}(r)$. The requirement for simultaneous existence of non-vanishing A_+ and B_+ gives rise to the correction ω_1 to the frequency. If ω_1 is an imaginary number, parametric resonance is invited and the magnitude of the imaginary part provides the growth rate σ_1.

For resonance, it suffices to evaluate σ_1 at the intersection points of the dispersion curves of m and $m+1$ modes. In the absence of viscosity, the local maximum growth rate $\sigma_{1\mathrm{max}}$, that is attained in the midway ($k_1 = 0$) of each unstable wavenumber band, is provided by

$$
\begin{aligned}
\sigma_{1\mathrm{max}}^2 = \\
-\frac{(\omega_0 - m)^3(\omega_0 - m - 1)^3(\omega_0 - m + 1)(\omega_0 - m + 2)(\omega_0 - m - 2)(\omega_0 - m - 3)h^2}{1024 k_0^4 (2\omega_0 - 2m - 1)^4 f^{(1)} f^{(2)}} ,
\end{aligned}
\tag{10}
$$

where $f^{(1)}$ is defined, using the notation $K_m = K_m(k_0)$ for the modified Bessel function, by

$$
\begin{aligned}
f^{(1)} = &m\big[\omega_0^3 - (3m+4)\omega_0^2 + 3m^2\omega_0 - m(m^2 - 4m - 8)\big] + 2k_0^2(\omega_0 - m)^2 \\
&+ 4\big[(m+1)\omega_0^2 - 2m^2\omega_0 + m(m^2 - m - 4)\big]\frac{k_0 K_{m+1}}{K_m} \\
&- 2(\omega_0 - m + 2)(\omega_0 - m - 2)\frac{k_0^2 K_{m+1}^2}{K_m^2} ,
\end{aligned}
\tag{11}
$$

and similarly for $f^{(2)}$ and h.

We have evaluated $\sigma_{1\max}$ at many of intersection points (k_0, ω_0) of the dispersion curves. It is probable that resonance occurs at every intersection points of upgoing branch of m wave and downgoing branches of $m+1$ and that other intersection points exhibit no loss of stability. This fact is accounted for by the signature of wave energy. The energy of upgoing braches (cograde mode) is positive and that of downgoing branches (retrograde modes) is negative (Fukumoto 2003). The above result is consistent with the necessary condition for loss of stability that signatures of the energy of degenerate modes be opposite (MacKay 1986). Given a combination $(m, m+1)$, relatively large growth rate $\sigma_{1\max}$ is maintained at the sequence of intersection points with $\omega_0 \approx m + 1/2$ as is read off from (10). Among them, the largest growth rate is taken at the intersection point of the smallest wavenumber. Table 1 lists the values of $\sigma_{1\max}$, along with of (k_0, ω_0) of the first intersection points, for small m. The tendency is clear that the largest growth rate of $(m, m+1)$ resonance increases with m.

Table 1. The most unstable modes for a given $(m, m+1)$

$(m, m+1)$	k_0	ω_0	$\sigma_{1\max}$
$(0, 1)$	0.81348683	0.59708954	0.054341234
$(1, 2)$	1.17352897	1.56470856	0.152116646
$(2, 3)$	1.50383466	2.54945870	0.214606641
$(3, 4)$	1.82101796	3.54021094	0.259041769
$(4, 5)$	2.13006949	4.53394704	0.292771395
$(5, 6)$	2.43339746	5.52940916	0.319520462

The most unstable mode occurs in the short-wave limit with radial and azimuthal wavenumbers being of the same magnitude, and the asymptotics of $\sigma_{1\max}$ is manipulated as

$$\sigma_{1\max} \approx 0.64453125 - 1.548698742/m^{2/3} \, .$$

The limit $165/256$ (≈ 0.64453125) agrees with the result of the WKB method (Hattori & Fukumoto 2003).

The value $\epsilon\sigma_{1\max}$ is compared with the growth rate of $O(\epsilon^2)$ (Widnall & Tsai 1977). The $O(\epsilon)$ instability mode surpasses that of $O(\epsilon^2)$. However care should be exercised. Unlike the latter, the dominant unstable eigenmodes of $O(\epsilon)$ have short wavelengths in all radial, azimuthal and toroidal directions and is therefore liable to substantial viscous damping.

3.3 Viscous selection

When viscosity is small, a rather systematic treatment, though incomplete, is feasible for our inviscid basic flow (3), namely integrating (8) and other components of the Navier-Stokes equations with the inviscid boundary conditions
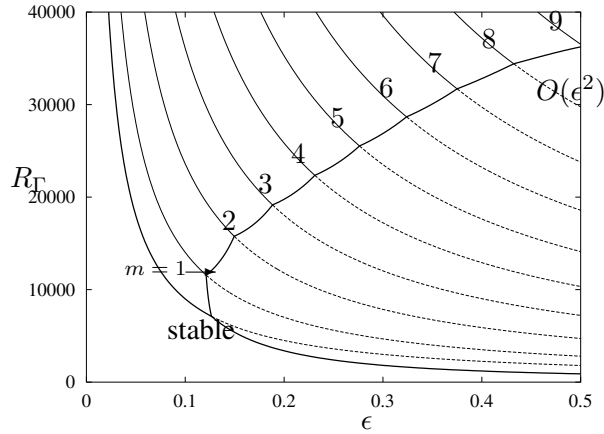
Figure 1. Regions dominated by one of $(m, m+1)$ modes of the $O(\epsilon)$ effect, with m indicated. The left thick line is the critical curve for the $O(\epsilon)$ mode. The right thick line is the critical one, the right-hand side of which is superseded by the $O(\epsilon^2)$ effect.

(Eloy & Le Dizes 2001). A similar analysis is conducted for the $O(\epsilon^2)$ effect. At a high Reynolds number $R_\Gamma = \Gamma/\nu$, the dominant unstable mode of $O(\epsilon^2)$ would be the first stationary helical-helical wave resonance.

We draw, in Fig. 1, border curves in the parameter space (ϵ, R_Γ) dividing the regions according to dominant modes. The solid lines are concerned with the $O(\epsilon)$ instability modes. The left thick line is the cut-off curve $R_\Gamma \approx 899.90244/\epsilon$, below which all modes are damped. At $(\epsilon, R_\Gamma) \approx (0.1265, 7115)$, this gives way to the cut-off curve of the $O(\epsilon^2)$ (the lower thick line). The band bounded by the thick line and adjacent line is the region where the $(1, 2)$ mode is dominant, and is then followed by the dominant region of the $(2, 3)$ mode in increasing order in R_Γ. The right thick line with R_Γ increasing with ϵ, except at smaller ϵ, is the critical line, in the right region of which the $O(\epsilon^2)$ effect surpasses the $O(\epsilon)$ effect. For $R_\Gamma < 10000$, the range of ϵ dominated by the $O(\epsilon)$ effect is not wide, but it expands with R_Γ for $R_\Gamma > 10000$.

4. Weakly nonlinear analysis

4.1 Amplitude equation

Here we briefly summarize the weakly nonlinear analysis of the curvature instability and derive amplitude equations.

By substituting the velocity field expressed as (6), we obtain a linear ordinary differential equation at each order. The matching conditions at the core boundary should be expanded and expressed at $r = 1$. The resulting equations

become more and more complicated at higher orders. To avoid this, we place a slip wall at $r = 1$ that surrounds the vortex-ring core so that the conditions reduce to $u_{ij} = 0$ at $r = 1$. This simplification does not change the nature of linear instability significantly. In particular, the results in the short wavenumber limit are unchanged. Of course, this does not exclude the possibility that nonlinear properties do change; the effects of matching conditions remain to be checked. Note also that the form of the amplitude equation is unchanged by this simplification.

At $O(\alpha^2)$, all the relevant equations are non-degenerate. They have forcing terms due to nonlinear interaction of $O(\alpha)$ waves. Hence $\boldsymbol{u}_{02}$ is a sum of terms like $A_+ B_+ \boldsymbol{r}_{A_+ B_+} e^{i[(2m+1)\theta + 2ks - 2\omega t]}$.

At $O(\alpha^3)$, we have to deal with the equations for the modes that have the same azimuthal and toroidal wavenumbers and frequencies with the Kelvin modes in (7) since they have forcing terms due to nonlinear interaction of $O(\alpha)$ and $O(\alpha^2)$ waves. They are degenerate. Hence compatibility conditions should be imposed; the amplitudes of the Kelvin waves $A_\pm$ and $B_\pm$ vary with time scale $O(\alpha^2)$ to meet these conditions. Thus the curvature instability and the nonlinear effects compete when $O(\epsilon) = O(\alpha^2)$.

We should also take account of mean flow correction which arises at $O(\epsilon \alpha^2)$. This is because the waves draw energy from the mean flow so that it is modified at $O(\alpha^2)$.

The resulting amplitude equations are written as

$$\frac{\mathrm{d}A_\pm}{\mathrm{d}t} = aB_\pm$$
$$+ \mathrm{i} \left(c_1 \left|A_\pm\right|^2 + c_2 \left|B_\pm\right|^2 + c_3 \left|A_\mp\right|^2 + c_4 \left|B_\mp\right|^2 + d_1 C_\pm + d_2 C_\mp \right) A_\pm, \tag{12}$$

$$\frac{\mathrm{d}B_\pm}{\mathrm{d}t} = bA_\pm$$
$$+ \mathrm{i} \left(c_5 \left|A_\pm\right|^2 + c_6 \left|B_\pm\right|^2 + c_7 \left|A_\mp\right|^2 + c_8 \left|B_\mp\right|^2 + d_3 C_\pm + d_4 C_\mp \right) B_\pm, \tag{13}$$

$$\frac{\mathrm{d}C_\pm}{\mathrm{d}t} = A_\pm \overline{B_\pm} + \overline{A_\pm} B_\pm, \tag{14}$$

where $C_\pm$ is the amplitude of mean flow correction.

The coefficients in the above equations can be evaluated using the inner product. For example, c_1 is given by

$$\mathrm{i} c_1 = \frac{\left\langle \boldsymbol{u}_{A_+} | \mathcal{S}_{|A_+|^2 A_+} \right\rangle}{\left\langle \boldsymbol{u}_{A_+} | \mathcal{L} \boldsymbol{u}_{A_+} \right\rangle},$$

where $\mathcal{S}_{|A_+|^2 A_+}$ is the forcing term which arises at $O(\alpha^3)$ for the mode $e^{i(m\theta + ks - \omega t)}$ and $\mathcal{L}$ is a simple linear operator projecting to space of the adjoint eigenmode.

4.2 Example

The coefficients of the amplitude equations can be evaluated numerically. The Euler equations at each order are discretized by Chebyshev collocation method. Then the resulting linear equations are solved using the singular-value decomposition.
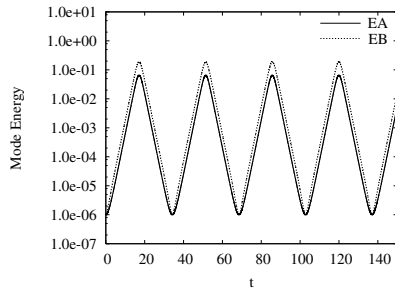

Figure 2a. Evolution of mode energy.
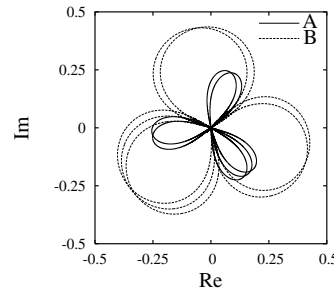
Figure 2b. Orbits of mode amplitudes A and B in complex plane.

For simplicity we consider the case $A_- = B_- = C_- = 0$. An example is shown in Fig. 2. The chosen modes are $m = 5$, $(k, \omega) \approx (2.42077, 5.50853)$. The linear growth rate is $\sigma_1 \approx 0.375$ which is a little larger than the corresponding value of the actual vortex ring 0.319520462 in Table 1. In Fig. 2a, the time evolution of the mode energy is shown to be almost periodic. In one period, starting from small values, mode energy first grows exponentially because of the curvature instability; it reaches the maximum and then decays exponentially. The orbits of A_+ and B_+ in the complex plane are shown in Fig. 2b. The exponential growth and decay correspond to anti- and in-phases of A and B. The nonlinear terms in (12)-(14) control the phase difference between the two modes.

5. Direct numerical simulation

Direct numerical simulation is carried out to study fully nonlinear behavior of unstable motion of the vortex rings. The three-dimensional incompressible Navier-Stokes equations are solved by the pseudo-spectral method assuming periodic boundary conditions. The initial vorticity field is set to be Gaussian distribution; Kelvin's vortex ring is difficult to deal with numerically since

its vorticity distribution is discontinuous at the core boundary. The Reynolds number based on the circulation is $R_\Gamma = 10^4$. The number of Fourier modes is 128^3.

The initial disturbance is set to pairs of Kelvin waves which correspond to the curvature or Widnall instabilities. Since it is not easy to obtain Kelvin waves on Gaussian vortex rings, Kelvin waves on the Rankine vortex are used with appropriate scale transformation. For the actual vortex ring, periodicity in s implies that k/ϵ should be an integer n, which is the number of waves along the core axis of the vortex ring. Two pairs are chosen for the curvature instability: (i) $(m, m+1) = (1, 2)$, $n = 5$; (ii) $(m, m+1) = (2, 3)$, $n = 6$. For the Widnall instability, one pair of bending waves is chosen: $n = 9$. All these cases have the smallest wavenumber among principal pairs for fixed m.

Figure 3b. Time evolution of energy of disturbance. Widnall instability.
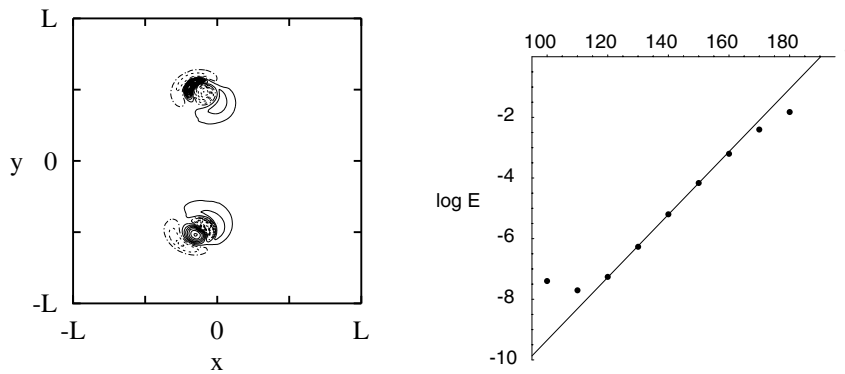
Figure 3a. Contours of vorticity of disturbance. Widnall instability.

The results for the case corresponding to the Widnall instability are shown in Fig. 3. The disturbance vorticity on a cross-section is shown by contours in Fig. 3a. Here the disturbance vorticity is the difference between the disturbed and undisturbed vortex rings. The vorticity distribution looks like that of the *elliptic instability* (Waleffe 1990). Time evolution of disturbance energy is shown in Fig. 3b. Exponential growth is observed for $120 < t < 170$.

We have been as yet unable to detect the curvature instability. There are two possible reasons for this. One is that waves on Gaussian vortex rings decay due to the presence of critical layers, which themselves are subtle problems to be explored. The other is that the Reynolds number is not sufficiently large for the instability to overcome the viscous effect as suggested from the viscous selection studied for Kelvin's vortex ring in §3.3.

6. Summary

There are an abundance of instability modes even on a single vortex ring (see, for example, Maxworthy 1977; Naitoh *et al.* 2002). The MSTW instability is no doubt realizable as shown by direct numerical simulations by Shariff *et al.* (1994) and in the preceding section (§5). This paper has clarified that a vortex ring has richer sources for instability than an elliptically strained vortex tube. A parametric resonance of curvature origin is peculiar to the vortex ring, and is waiting for experimental and numerical support for its realizability. To be realistic, a Gaussian core could be a sensible model. Only local stability analysis has been carried through (Hattori & Fukumoto 2003), and a global stability analysis is demanded. This core accommodates not only discrete but also continuous spectra, and thus the problem is very complicated.

We have proceeded to a weakly nonlinear stage, and, as a preliminary study, have derived amplitude equations of a single resonance mode confined in a rigid circular cylinder with frictionless boundary. A secondary instability of Kelvin waves may show up and smears out the primary mode, possibly as a result of nonlinear interactions of several modes. Hamiltonian normal forms can be extended to include a number of excited modes. The normal forms provide not only a justification to the singular-perturbation analysis but also a perspective on complicated nonlinear interactions. Currently we make an effort to compute the coefficients of the amplitude equations. Hopefully this scheme will provide a scenario of how such a large amount of energy as to disrupt a ring is transferred from the basic flow into small-scale disturbances.

Acknowledgments

References

ELOY, C. & LE DIZÈS, S. 2001 Stability of the Rankine vortex in a multipolar strain field. *Phys. Fluids* **13**, 660–676.

FUKUMOTO, Y. 2003 The three-dimensional instability of a strained vortex tube revisited. *J. Fluid Mech.* **493**, 287 – 318.

FUKUMOTO, Y. & HATTORI, Y. 2005 Curvature instability of a vortex ring. *J. Fluid Mech.* **526**, 77–115.

FUKUMOTO, Y. & MOFFATT, H. K. 2000 Motion and expansion of a viscous vortex ring. Part 1. A higher-order asymptotic formula for the velocity. *J. Fluid Mech.* **417**, 1 – 45.

HATTORI, Y. & FUKUMOTO, Y. 2003 Short-wavelength stability analysis of thin vortex rings. *Phys. Fluids* **15**, 3151 – 3163.

KNOBLOCH, E., MAHALOV, A. & MARSDEN, J. E. 1994 Normal forms for three-dimensional parametric instabilities in ideal hydrodynamics, *Physica D* **73**, 49–81.

MACKAY, R. S. 1986 Stability of equilibria of Hamiltonian system. In *Nonlinear Phenomena and Chaos* (ed. S. Sarkar), pp. 254–270. Adam Hilger, Bristol.

MAXWORTHY, T. 1977 Some experimental studies of vortex rings. *J. Fluid Mech.* **81**, 465–495.

MOORE, D. W. & SAFFMAN, P. G. 1975 The instability of a straight vortex filament in a strain field. *Proc. R. Soc. Lond. A* **346**, 413 – 425.

NAITOH, T., FUKUDA, N., GOTOH, T., YAMADA, H. & NAKAJIMA, K. 2002 Experimental study of axial flow in a vortex ring. *Phys. Fluids* **14**, 143–149.

SHARIFF, K., VERZICCO, R. & ORLANDI, P. 1994 A numerical study of three-dimensional vortex ring instabilities: viscous corrections and early nonlinear stage. *J. Fluid Mech.* **279**, 351–375.

SIPP, D. 2000 Weakly nonlinear saturation of short-wave instabilities in a strained Lamb-Oseen vortex. *Phys. Fluids* **12**, 1715-1729.

TSAI, C.-Y. & WIDNALL, S. E. 1976 The stability of short waves on a straight vortex filament in a weak externally imposed strain field. *J. Fluid Mech.* **73**, 721–733.

WALEFFE, F. 1990 On the three-dimensional instability of strained vortices *Phys. Fluids A* **2**, 76–80.

WIDNALL, S. E., BLISS, D. B. & TSAI, C.-Y. 1974 The instability of short waves on a vortex ring. *J. Fluid Mech.* **66**, 35–47.

WIDNALL, S. E. & TSAI, C.-Y. 1977 The instability of the thin vortex ring of constant vorticity. *Phil. Trans. R. Soc. Lond. A* **287**, 273–305.

MOTION OF UNSTABLE POLYGONAL RING OF VORTEX POINTS ON SPHERE WITH POLE VORTICES

Takashi Sakajo

Department of Mathematics, Hokkaido University,
Kita 10 Nishi 8, Kita-ku, Sapporo 060-0810 Japan

sakajo@math.sci.hokudai.ac.jp

Abstract   We consider the motion of N identical vortex points on a sphere with two vortex points fixed at the both poles. The vortex points are spaced equally along a line of latitude, which is called the polygonal ring of vortex points or *the N-ring*. Starting with the linear stability analysis, we investigate the unstable motion of the perturbed N-ring; We give a brief summary in terms of the transition of unstable periodic motions for even N-ring studied in a preceding paper (Sakajo 2004). Then we study an unstable non-trivial recurrent motion of a 3-ring as an example of complex dynamics of odd N-rings.

Keywords: Vortex points, flows on sphere, pole vortex, N-ring

1.   Introduction

We consider the motion of incompressible and inviscid fluids on a sphere to understand basic dynamical process observed in many atmospheric phenomena on Earth. In particular, local regions where vorticity is extremely dense are of importance, since they dominate global dynamics of the flow. One of the examples of such singular vorticity regions is a vortex point in which vorticity concentrates in a point. In the present article, we focus on the motion of a polygonal ring consisting of N identical vortex points that are equally spaced at a line of latitude, which is called "N-ring". Furthermore, in order to incorporate the effect of rotation of the sphere in the problem, we introduce two vortex points fixed at the both poles.

Let (Θ_m, Ψ_m) denote the position of the mth vortex point in the spherical coordinates. The strengths of the vortex points are identical with each other, say $\Gamma = 2\pi/N$. Then, the motion of the N-vortex points is described by the

Hamiltonian dynamical system (Newton 2001), whose Hamiltonian is given by

$$H = -\frac{\Gamma^2}{4\pi} \sum_{j<m}^{N} \log(1 - \cos\gamma_{mj}) - \frac{\Gamma_n\Gamma}{4\pi} \sum_{m=1}^{N} \log(1 - \cos\Theta_m)$$

$$- \frac{\Gamma_s\Gamma}{4\pi} \sum_{m=1}^{N} \log(1 + \cos\Theta_m), \tag{1}$$

in which Γ_n and Γ_s represent the strengths of the north and the south pole vortices respectively, γ_{mj} represents the central angle between the mth and the jth vortex points, and $\cos\gamma_{mj} = \cos\Theta_m\cos\Theta_j + \sin\Theta_m\sin\Theta_j\cos(\Psi_m - \Psi_j)$. With certain canonical variables, the equations of motion of the N-vortex points are derived from the Hamiltonian as

$$\dot{\Theta}_m = -\frac{\Gamma}{4\pi} \sum_{j\neq m}^{N} \frac{\sin\Theta_j\sin(\Psi_m - \Psi_j)}{1 - \cos\gamma_{mj}}, \tag{2}$$

$$\sin\Theta_m\dot{\Psi}_m = -\frac{\Gamma}{4\pi} \sum_{j\neq m}^{N} \frac{\cos\Theta_m\sin\Theta_j\cos(\Psi_m - \Psi_j) - \sin\Theta_m\cos\Theta_j}{1 - \cos\gamma_{mj}}$$

$$+ \frac{\Gamma_n}{4\pi}\frac{\sin\Theta_m}{1 - \cos\Theta_m} - \frac{\Gamma_s}{4\pi}\frac{\sin\Theta_m}{1 + \cos\Theta_m}, \qquad m = 1, 2, \cdots, N. \tag{3}$$

Note that the summation $\sum_{i=0}^{N}\cos\Theta_i$ is invariant due to (2). Our goal is to understand the motion of the perturbed N-ring in the presence of the pole vortices. This paper consists of five sections. In §2 and §3, we review some results in terms of linear stability analysis and the motion of even N-ring studied in a preceding paper (Sakajo 2004). Then we investigate numerically an unstable motion of a perturbed 3-ring in §4. The last section gives a brief summary of the paper.

2.　Linear stability analysis for the N-ring

We consider the linear stability of the following perturbed N-ring at the line of latitude θ_0:

$$\Theta_m(t) = \theta_0 + \epsilon\theta_m(t), \quad \Psi_m(t) = \frac{2\pi m}{N} + \epsilon\varphi_m(t),$$

$$\epsilon \ll 1, \quad m = 1, 2, \cdots, N.$$

While the linear stability analysis of the N-ring without the pole vortices were done by Boatto and Cabral (2003), all the eigenvalues and the eigenvectors of the linearized equations for (θ_m, φ_m) with pole vortices are given explicitly

in Sakajo (2004). Here, we review the results just in terms of the eigenvalues following the latter paper. Let $\lambda_p^{\pm}$ denote the eigenvalues, then we have

$$\lambda_p^{\pm} = \pm \frac{1}{2N \sin^2 \theta_0} \sqrt{(pN - p^2)^2 + C_N (pN - p^2)}, \quad p = 0, 1, \cdots, N - 1,$$

(4)

in which

$$C_N = (1 - N)(1 + \cos^2 \theta_0) - \frac{(\Gamma_n - \Gamma_s)}{\pi} N \cos \theta_0 - \frac{(\Gamma_n + \Gamma_s)}{2\pi} N(1 + \cos^2 \theta_0).$$

It indicates that when $N = 2M$, we have $\lambda_0^{\pm} = 0$, $\lambda_p^{\pm}$ for $p = 1, \cdots, M - 1$ are double, and $\lambda_M^{\pm}$ are simple. On the other hand, when $N = 2M + 1$, $\lambda_0^{\pm} = 0$ and $\lambda_p^{\pm}$ for $p = 1, \cdots, M$ are double. Moreover, they satisfy the order $\left(\lambda_1^{\pm}\right)^2 < \left(\lambda_2^{\pm}\right)^2 < \cdots < \left(\lambda_M^{\pm}\right)^2$. Hence, if $\left(\lambda_M^{\pm}\right)^2 < 0$, then all the eigenvalues are pure imaginary and the N-ring is neutrally stable, which means that the stability of the N-ring is determined by that of the largest eigenvalues $\lambda_M^{\pm}$.

3. Four periodic orbits for even N-ring

In this case, we can reduce the equations (2) and (3) to an integrable system in the following steps. First, we reduce them to the equations for (Θ_1, Ψ_1) and (Θ_2, Ψ_2) by imposing the pairing symmetry; $\Theta_{2m-1} = \Theta_1$, $\Theta_{2m} = \Theta_2$, $\Psi_{2m-1} = \Psi_1$, and $\Psi_{2m} = \Psi_2$ for $m = 1, \cdots, M$. Next, recalling that $\cos \Theta_1 + \cos \Theta_2$ is invariant in time, we further reduce the equations to those for the two variables $(\Theta_1, \Phi \equiv \Psi_1 - \Psi_2)$, which is integrable. As a matter of fact, the unstable and the stable manifolds of the largest eigenvalues $\lambda_M^{\pm}$ are embedded in the reduced phase space. Accordingly, it is sufficient to give contour plots for the reduced Hamiltonian (1) to see the global dynamics of the perturbed N-ring. As a result, either of four periodic solutions; *linearly periodic*, *nonlinearly periodic*, *swing-by* and *revolving*, appears in even N-rings depending on the strength of the pole vortices and the initial perturbation. Figure 1 shows an example of the periodic orbits for a 4-ring at the equator. In addition, we can also show that the stability of the periodic orbits is determined by the second largest eigenvalue λ_{M-1}^+, since its unstable manifold is transverse to the reduced phase space. See Sakajo (2004) for the detailed analysis.

4. Recurrent motion of a perturbed 3-ring at the equator

When the number of the vortex points is odd, the largest eigenvalues $\lambda_M^{\pm}$ that determine the stability of the N-ring are double. Hence, when the N-ring becomes unstable, its motion could be complicated in general. Thus we specifically consider an unstable motion of a 3-ring at the equator with the identical
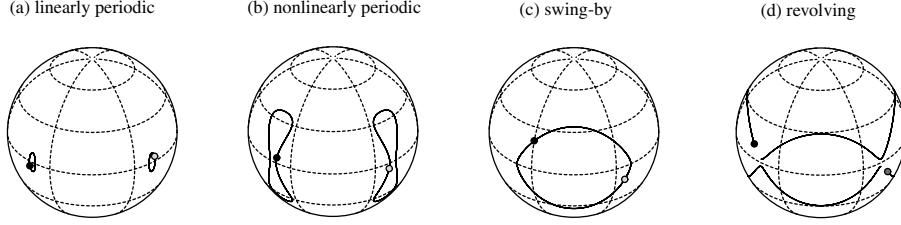
Figure 1. Periodic orbits for the perturbed 4-ring at the equator. (a) $\Gamma_n = \Gamma_s = 0.4\pi$, (b) $\Gamma_n = \Gamma_s = 0.1\pi$, (c) and (d) $\Gamma_n = \Gamma_s = -0.1\pi$. As $\Gamma_n + \Gamma_s$ decreases, the realizable periodic orbits change like (a) → (b) → either (c) or (d).

pole vortices as a simple example. The linear stability analysis shows that the 3-ring is linearly unstable if $\Gamma_n + \Gamma_s < 0$, and the two eigenvectors corresponding to the largest eigenvalues $\lambda_1^\pm$ are given by

$$\psi_1^\pm = \left(\frac{\sqrt{3}}{3}, -\frac{\sqrt{3}}{6}, -\frac{\sqrt{3}}{6}, \pm\sqrt{\frac{-(\Gamma_n + \Gamma_s)}{4\pi}}, \mp\sqrt{\frac{-(\Gamma_n + \Gamma_s)}{4\pi}}, \mp\sqrt{\frac{-(\Gamma_n + \Gamma_s)}{4\pi}} \right),$$

$$\phi_1^\pm = \left(0, \frac{1}{2}, -\frac{1}{2}, 0, \pm\frac{1}{2}\sqrt{\frac{-3(\Gamma_n + \Gamma_s)}{4\pi}}, \mp\frac{1}{2}\sqrt{\frac{-3(\Gamma_n + \Gamma_s)}{4\pi}} \right).$$

Note that the eigenvectors $\psi_1^\pm$ and $\phi_1^\pm$ have the symmetry $\dot{\Theta}_1 = -\dot{\Theta}_2 = -\dot{\Theta}_3, \dot{\Psi}_1 = -\dot{\Psi}_2 = -\dot{\Psi}_3$ and $\dot{\Theta}_1 = 0, \dot{\Theta}_2 = -\dot{\Theta}_3, \dot{\Psi}_1 = 0, \dot{\Psi}_2 = -\dot{\Psi}_3$ respectively.

Figure 2(a) shows evolutions of $\cos\Theta_i$ ($i = 1, 2, 3$) from $t = 0$ to 500. The initial condition is given by $(\Theta_1, \Theta_2, \Theta_3, \Psi_1, \Psi_2, \Psi_3) = \left(\frac{\pi}{2}, \frac{\pi}{2}, \frac{\pi}{2}, 0, \frac{2\pi}{3}, \frac{4\pi}{3} \right) + \epsilon(\lambda\psi_1^+ + (1-\lambda)\phi_1^+)$ with $\epsilon = 1.0 \times 10^{-4}$ and $\lambda = 1$. They look complicated, but in fact the evolution consists of four patterns of orbits. To see it clearly, we project the evolutions on the phase space of $(\cos\Theta_2, \cos\Theta_3)$ in Figure 2(b). The phase space equivalently shows the motion of the three variables, since $\cos\Theta_1$ is determined by the invariant $\sum_{i=1}^{3}\cos\Theta_i = 0$ automatically. The 3-ring corresponds to the origin in the phase space. The diagonal dotted line represents the restricted subspace, say Q; $\cos\Theta_1 = 0$ and $\cos\Theta_2 + \cos\Theta_3 = 0$, i.e. $\Theta_1 = \frac{\pi}{2}$ and $\Theta_2 = -\Theta_3$. First, the orbit departs in the direction normal to the subspace, and returns the neighborhood of the origin after passing by the vicinity of the orbit labeled 'A'. Then it goes along the orbit labeled 'B' embedded in Q, and returns the neighborhood of the origin again. In a similar way, the evolution traces the orbits 'C' and 'D' alternatively afterwords.

The recurrent repetition of the four patterns is due to the periodic structure of the heteroclinic orbits of the 3-ring embedded in the whole phase
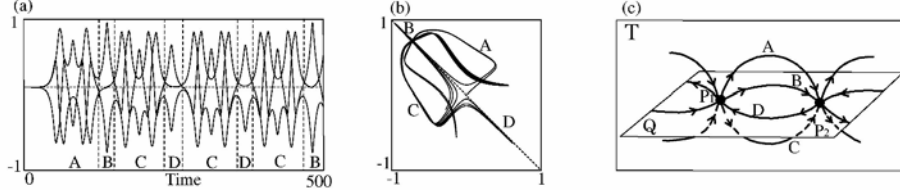
Figure 2. (a) Long time evolution of $\cos \Theta_i$ ($i = 1, 2, 3$) for a perturbed 3-ring at the equator when $\Gamma_n = \Gamma_s = -0.2\pi$. (b) The evolution projected on $(\cos \Theta_2, \cos \Theta_3)$ plane. (c) Topological structure of the heteroclinic orbits of the 3-ring in the phase space $\mathbb{T}$. The two points P_1 and P_2 correspond to the 3-ring configuration and the planar subspace represents Q; $\Theta_1 = \frac{\pi}{2}$ and $\Theta_2 = -\Theta_3$, corresponds to the dotted line in (b).

space $\mathbb{T} = [0, \pi]^3 \times (\mathbb{R}/2\pi\mathbb{Z})^3$. See Fig. 2(c) for the schematic reference. Let us recall that the 3-ring configuration corresponds to the two points in $\mathbb{T}$, P_1:$(\frac{\pi}{2}, \frac{\pi}{2}, \frac{\pi}{2}, 0, \frac{2\pi}{3}, \frac{4\pi}{3})$ and P_2:$(\frac{\pi}{2}, \frac{\pi}{2}, \frac{\pi}{2}, 0, \frac{4\pi}{3}, \frac{2\pi}{3})$. These two points are connected by four heteroclinic orbits, 'A', 'B', 'C' and 'D'. When we compare the symmetry of the two eigenvectors with the evolutions of $\cos \Theta_i$ in Fig. 2(a) at the very moment when they deviate from the 3-ring configuration, the orbits 'A' and 'C' correspond to the heteroclinic orbits whose tangent vectors are $\psi_1^{\pm}$, while the heteroclinic orbits 'B' and 'D' embedded in Q have the tangent vector $\phi_1^{\pm}$. The evolution of the perturbed 3-ring traces the structure passing near the 3-ring recurrently.

Figure 3(a) shows long-time evolutions of a perturbed 3-ring for $\Gamma_n = \Gamma_s = -0.4\pi$ and $\lambda = 1$. The evolution follows the periodic structure of the heteroclinic orbits similarly. Figure 3(b) shows the evolution of the 3-ring for another initial perturbation, i.e. $\Gamma_n = \Gamma_s = -0.2\pi$ and $\lambda = 0.5$. The perturbed 3-ring still traces the structure again, though their shapes are different from the previous cases. It suggests that the structure of the heteroclinic orbits exists as long as the 3-ring is located at the equator and the pole vortices are identical. However, it is structurally unstable. Indeed, the orbit of the 3-ring for $\Gamma_n = -0.2\pi$ and $\Gamma_s = -0.15\pi$ and $\lambda = 1$ in Fig. 3(c) shows that it deviates from the structure and evolves disorderly as time proceeds.

5. Summary

We have investigated the unstable motion of the N-ring of the vortex points on the sphere in the presence of the pole vortices. The unstable motion of even N-ring is generally classified into four typical periodic orbits and the transition among these periodic orbits is observed as the strength of pole vortices changes. On the other hand, a 3-ring at the equator with identical pole vortices traces the vicinity of the periodic structure of the heteroclinic orbits connecting between the 3-rings. However, since the structure is non-generic, further analysis is
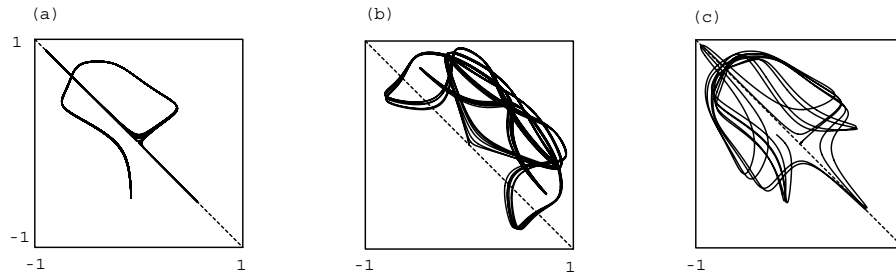
Figure 3. The evolutions of a perturbed 3-ring at the equator plotted in the projected phase space $(\cos\Theta_2, \cos\Theta_3)$ for (a) $\Gamma_n = \Gamma_s = -0.4\pi$, $\lambda = 1$, (b) $\Gamma_n = \Gamma_s = -0.2\pi$, $\lambda = 0.5$, and (c) $\Gamma_n = -0.2\pi, \Gamma_s = -0.15\pi, \lambda = 1$.

required in order to deal with the unstable motion of odd N-rings in general. The present study implies that in the fluid motion of the polygonal ring of the coherent vortex structures on the sphere, the pole vortices and the number of the vortex structures affect not only the linear stability, but also their nonlinear unstable long-time evolution substantially.

References

BOATTO, S. AND CABRAL, H.E. 2003 Nonlinear stability of a latitudinal ring of point vortices on a nonrotating sphere, *SIAM J. Appl. Math.* **64**, 216–230.

SAKAJO, T 2004 Transition of global dynamics of a polygonal vortex ring on a sphere with pole vortices. *Physica D* **196**, 243 – 264.

NEWTON, P.K. 2001 The N-vortex problem, Analytical techniques *(Springer-Verlag, New York).*

Part H   Finite-time singularity

INVARIANTS, DIFFUSION AND TOPOLOGICAL CHANGE IN INCOMPRESSIBLE NAVIER-STOKES EQUATIONS

Peter Constantin
Department of Mathematics, The University of Chicago, Chicago, Il 60637, U.S.A
const@math.uchicago.edu

Koji Ohkitani
Research Institute for Mathematical Sciences, Kyoto University, Kyoto 606-8502, Japan
ohkitani@kurims.kyoto-u.ac.jp

Abstract   We discuss the effect that the presence of a small viscosity has on the evolution of fields that are transported unchanged in the absence of viscosity. We employ a diffusive Lagrangian formulation and show that the Cauchy invariant, the helicity density, the Jacobian determinant, and the virtual velocity obey parabolic equations that are well-behaved as long as the diffusive transformations are invertible. We call such quantities *diffusive Lagrangian*. We show by numerical calculations that the loss of invertibility of the diffusive transformation can occur, and that the time scale on which it does can be short even when the viscosity is small. We present quantitative evidence relating the loss of invertibility to the physical phenomenon of vortex reconnection.

1.   Introduction

The Euler equations of incompressible fluid mechanics are

$$D_t u + \nabla p = 0 \tag{1}$$

with $\nabla \cdot u = 0$. The velocity $u = u(x,t) = (u_1, u_2, u_3)$ is a function of $x \in \mathbf{R}^3$ and $t \in \mathbf{R}$. The material derivative associated to the velocity u is $D_t = D_t(u, \nabla) = \partial_t + u \cdot \nabla$. The Lagrangian particle maps are

$$a \mapsto X(a,t), \quad X(a,0) = a.$$

For fixed a, the trajectories of u obey

$$\frac{dX}{dt} = u(X, t).$$

The incompressibility condition implies

$$det\,(\nabla_a X) = 1.$$

The Euler equations can be described (Arnold & Khesin 1998) formally as Euler-Lagrange equations resulting from the stationarity of the action

$$\int_a^b \int |u(x, t)|^2 \, dx dt$$

with $u(x, t) = \frac{\partial X}{\partial t}(A(x, t), t)$, with fixed end values at $t = a, b$ and $A(x, t) = X^{-1}(x, t)$. The incompressible Euler equations are a canonical Hamiltonian system in infinite dimensions in variables now known as Clebsch variables (Clebsch 1858; Lamb 1932; Zakharov &Kuznetsov 1970). Clebsch variables are a pair of scalars θ, φ which are constant on particle paths,

$$D_t \varphi = D_t \theta = 0$$

and also determine the velocity via

$$u^i(x, t) = \theta(x, t) \frac{\partial \varphi(x, t)}{\partial x_i} - \frac{\partial n(x, t)}{\partial x_i}.$$

The function $n(x, t)$ is required in order to keep incompressibility, $\nabla \cdot u = 0$ and is computed using a Poisson equation. Not all solutions of the Euler equations can be represented using just one pair of Clebsch variables.

The incompressible Euler equations can be written as an active scalar system (Constantin 2001a)

$$\begin{cases} D_t A = 0, \\ D_t v = 0, \\ u = W[A, v]. \end{cases} \tag{2}$$

The variable A represents the inverse of the Lagrangian map (the "back-to-labels" map), v is the virtual velocity, conserved along particle paths, and $W[A, v]$ is the Weber formula (Weber 1868). Active scalars (Constantin 1994) are solutions of passive scalar equations $D_t \theta = 0$ which determine the velocity through a time independent, possibly non-local equation of state $u = U[\theta]$. Knowledge of the values of the active scalars at an instance of time is sufficient to determine the time derivatives of the active scalar at that instance in time. The Clebsch variables are a pair of active scalars. The Euler equations can be represented with many active scalars. The Weber formula (Weber 1868) is

$$u^i(x, t) = \left(v^j(x, t)\right) \frac{\partial A^j(x, t)}{\partial x_i} - \frac{\partial n(x, t)}{\partial x_i}.$$

The vector v is the virtual velocity. Because it obeys $D_t v = 0$, it follows that

$$v = u_{(0)}(A),$$

where $v_{|t=0} = u_{(0)}$. The Weber formula, together with boundary conditions and the divergence-free requirement, is written symbolically as

$$u = W[A, v] = \mathbf{P}\left\{(\nabla A)^T v\right\}, \tag{3}$$

where $\mathbf{P}$ is the corresponding projector on divergence-free functions. The circulation is the loop integral

$$C_\gamma = \oint_\gamma u \cdot dx$$

and the conservation of circulation is the statement that

$$\frac{d}{dt} C_{\gamma(t)} = 0$$

for all loops carried by the flow. This follows from the Weber formula because

$$u^j(X(a,t)) \frac{\partial X^j}{\partial a_i} = u^i_{(0)}(a) - \frac{\partial \tilde{n}(a,t)}{\partial a_i},$$

and the right-hand side is the sum of a time independent function of labels and a label gradient. Vice versa, one can show that the above formula follows from the conservation of circulation. The Weber formula is thus equivalent to the conservation of circulation.

Differentiating the Weber formula and taking the antisymmetric part, one obtains the Cauchy formula

$$\omega_i = \frac{1}{2}\epsilon_{ijk}\left(Det\left[\frac{\partial A}{\partial x_j}; \frac{\partial A}{\partial x_k}; \omega_{(0)}(A)\right]\right).$$

The function $\omega = \nabla \times u$ is the vorticity, $\omega_{(0)}$ is the vorticity at some fixed time, $t = 0$. By linear algebra, this is equivalent with the familiar form in Lagrangian coordinates, $\omega(X(a,t),t) = \frac{\partial X}{\partial a}\omega_{(0)}(a)$ for smooth Euler flows because A is invertible and $det(\nabla_a X) = 1$. But the form above, that is $\omega = (det(\nabla A))(\nabla A)^{-1}\omega_{(0)}$ in Eulerian coordinates is the one that can be generalized to Navier-Stokes flows.

We write symbolically the Cauchy formula as

$$\omega = \mathcal{C}[\nabla A, \zeta] \tag{4}$$

with ζ the Cauchy invariant

$$\zeta(x,t) = \omega_{(0)} \circ A$$

and $\circ A$ denotes composition with A. Thus, the active scalar system

$$
\begin{cases}
\quad\quad\quad D_t A = 0, \\
\quad\quad\quad D_t \zeta = 0, \\
u = \nabla \times (-\Delta)^{-1} \left(\mathcal{C}[\nabla A, \zeta] \right)
\end{cases}
\tag{5}
$$

is an equivalent formulation of the Euler equations, in terms of the Cauchy invariant ζ. The Cauchy invariant, which is the Lagrangian curl of the virtual velocity,

$$
\nabla^A \times v = \zeta,
$$

is conserved along particle trajectories, $(\partial_t + u \cdot \nabla)\zeta = 0$. The role of conserved quantities in nonlinear evolution equations cannot be over-estimated. In the case of the Euler equations, besides the circulation conservation, virtual velocity and Cauchy invariant, the total helicity (Moffatt 1969) and the total kinetic energy are also conserved by sufficiently smooth flows.

The total kinetic energy is proportional to the L^2 norm of velocity. The Onsager conjecture (Onsager 1949, Eyink 1994) states that conservation of energy occurs if and only if the solutions are smoother than the velocities supporting the Kolmogorov theory (roughly speaking, Holder continuous of exponent $1/3$). The "if" part was proved (Constantin, E & Titi 2004).

The total helicity is the integral $\int (u \cdot \omega) dx$, where $\omega = \nabla \times u$ is the vorticity. Its integrand $u \cdot \omega$ is not conserved along particle paths. The variable $w = (\nabla A)^T v$ has the same curl as u, $\nabla \times w = \omega$ and the quantity $\int (w \cdot \omega) dx$ equals the total helicity. The modified helicity density $w \cdot \omega$ is conserved along particle paths; in fact it equals pointwise the scalar product $v \cdot \zeta$ of two conserved quatities. For any vortex tube — a region whose boundary is formed with vortex lines — the integrals of $w \cdot \omega$ and $u \cdot \omega$ on the vortex tube are identical. A closed formulation of the Euler equations in terms of w has been used for numerical calculations and for a Hamiltonian formalism (Buttke 1993, Buttke &Chorin 1993, Chorin 1994, Kuzmin 1983, Oseledets 1989, Roberts 1972; an earlier Hamiltonian formalism used Clebsch variables (Clebsch 1858; Zakharov &Kuznetsov 1970)).

To summarize: in the case of smooth ideal fluids the virtual velocity v, the Cauchy invariant ζ, the modified helicity density $w \cdot \omega$, the determinant $det(\nabla A)$ are transported frozen in the flow. Thus, after recording their values at some instance of time, they are computed just by using composition with the map A. For instance: $v(x,t) = u_{(0)}(A(x,t))$, where $u_{(0)}$ is the velocity at time $t = 0$ and $\zeta(x,t) = \omega_{(0)}(A(x,t))$, where $\omega_{(0)}$ is the vorticity at time $t = 0$.

What is the fate of these quantities in slightly viscous flows?

2. Diffusive lagrangian formulation of the navier-stokes equations

The Navier-Stokes equations are

$$D_\nu u + \nabla p = 0, \tag{6}$$

together with the incompressibility condition $\nabla \cdot u = 0$. The operator D_ν

$$D_\nu = D_\nu(u, \nabla) = \partial_t + u \cdot \nabla - \nu \Delta \tag{7}$$

describes advection with velocity u and diffusion with kinematic viscosity $\nu > 0$. When $\nu = 0$, we recover formally the Euler equations (1), and $D_{\nu|\nu=0} = D_t$.

A diffusive Lagrangian description of viscous fluids (Constantin 2001b, Constantin 2003) represents the fluid in terms of near identity transformations A and virtual velocities v. The equation corresponding to (2) is

$$\left\{ \begin{array}{c} D_\nu A = 0, \\ D_\nu v = 2\nu C \nabla v, \\ u = W[A, v]. \end{array} \right. \tag{8}$$

The relation $u = W[A, v]$ is the Weber formula (3), same as in the case of $\nu = 0$. The right-hand side of (8) is given terms of the connection coefficients

$$C_{k;i}^m = \left((\nabla A)^{-1} \right)_{ji} \left(\partial_j \partial_k A^m \right).$$

The detailed form of virtual velocity equation in (8) is

$$D_\nu v_i = 2\nu C_{k;i}^m \partial_k v_m.$$

The connection coefficients are related to the Christoffel coefficients of the flat Riemannian connection in $\mathbf{R}^3$ computed using the change of variables $a = A(x, t)$:

$$C_{k;i}^m(x, t) = -\Gamma_{ji}^m(A(x, t)) \frac{\partial A^j(x, t)}{\partial x_k}.$$

The equation $D_\nu(u, \nabla) A = 0$ describes advection *and diffusion* of labels. Use of traditional ($D_t A = 0$) Lagrangian variables when $\nu > 0$ would introduce third-order derivatives of A in the viscous evolution of the Cauchy invariant, making the equations unbalanced: the passive characteristics of u are not sufficient to reconstruct the dynamics.

The system (8) is well posed, and the velocity u solves exactly the incompressible Navier-Stokes equations. The diffusion of labels is a consequence of the physically natural idea of adding Brownian motion to the Lagrangian flow. Indeed, if $u(X(a, t), t)$ is known, and if

$$dX(a, t) = u(X(a, t), t)dt + \sqrt{2\nu}dW(t), \ X(a, 0) = a,$$

with $W(t)$ standard independent Brownian motions in each component, and if

$$Prob\{X(a,t) \in dx\} = \rho(x,t;a)dx$$

then the expected value of the back to labels map

$$A(x,t) = \int \rho(x,t;a)a\,da$$

solves

$$D_\nu(u,\nabla)A = 0.$$

We associate to the virtual velocity v the Eulerian-Lagrangian curl of v

$$\zeta = \nabla^A \times v, \tag{9}$$

where $\nabla_i^A = \left((\nabla A)^{-1}\right)_{ji} \partial_j$ is the pull back of the Eulerian gradient. The viscous analogue of the Eulerian-Lagrangian Cauchy invariant active scalar system (5) is

$$\begin{cases} D_\nu A = 0, \\ D_\nu \zeta^q = 2\nu G_p^{qk} \partial_k \zeta^p + \nu T_p^q \zeta^p, \\ u = \nabla \times (-\Delta)^{-1} \left(\mathcal{C}[\nabla A, \zeta]\right). \end{cases} \tag{10}$$

The Cauchy transformation

$$\mathcal{C}[\nabla A, \zeta] = (det(\nabla A))(\nabla A)^{-1}\zeta$$

is the same as the one used in the Euler equations, (4). The specific form of the two terms on the right-hand side of the Cauchy invariant's evolution are

$$G_p^{qk} = \delta_p^q C_{k;m}^m - C_{k;p}^q \tag{11}$$

and

$$T_p^q = \epsilon_{qji}\epsilon_{rmp}C_{k;i}^m C_{k;j}^r. \tag{12}$$

The system (8) is equivalent to the Navier-Stokes system. When $\nu = 0$, the system reduces to (2). The system (10) is equivalent to the Navier-Stokes system, and reduces to (5) when $\nu = 0$.

3.   Group expansion = resetting

The pair (A, v) should be thought of as a chart on a manifold, representing the solution u. The validity of the chart is local. When the chart becomes inconvenient to represent the solution, we change the chart. This may (and will) happen if ∇A becomes non-invertible. Likewise, the pair (A, ζ) formed with the "back-to-labels" map A and the diffusive Cauchy invariant ζ are convenient charts. In order to clarify this statement let us introduce the terminology of

"group expansion" for the procedure of resetting. More precisely, the group expansion for (8) is defined as follows. Given a time interval $[0, T]$ we consider resetting times

$$0 = t_0 < t_1 < \ldots < t_n \ldots \leq T.$$

On each interval $[t_i, t_{i+1}]$, $i = 0, \ldots$ we solve the system (8):

$$\begin{cases} D_\nu(u, \nabla)A = 0, \\ D_\nu(u, \nabla)v = 2\nu C \nabla v, \\ u = \mathbf{P}\left((\nabla A)^T v\right). \end{cases}$$

with resetting values

$$\begin{cases} A(x, t_i) = x, \\ v(x, t_i + 0) = ((\nabla A)^T v)(x, t_i - 0). \end{cases}$$

For mathematical reasons we require the strong resetting criterion that $\nabla \ell = (\nabla A) - \mathbf{I}$ must be smaller than a preassigned value ϵ in an analytic norm: $\exists \lambda$ such that for all $i \geq 1$ and all $t \in [t_i, t_{i+1}]$ one has

$$\int e^{\lambda |k|} \left| \widehat{\ell}(k) \right| dk \leq \epsilon < 1.$$

Here $\ell \equiv A - x$ and $\widehat{\ell}(k)$ is its Fourier Transform. If there exists N such that $T = \sum_{i=0}^{N}(t_{i+1} - t_i)$ then we say that the group expansion *converges* on $[0, T]$. A group expansion of (10) is defined similarly. The resetting conditions are

$$\begin{cases} A(x, t_i) = x, \\ \zeta(x, t_i + 0) = \mathcal{C}[(\nabla A))(x, t_i - 0), \zeta(x, t_i - 0)]. \end{cases}$$

The strong analytic resetting criterion is the same. The first interval of time $[0, t_1)$ is special. The initial value for v is u_0 (the initial datum for the Navier-Stokes solution), and the initial value for ζ is ω_0, the corresponding vorticity. The local time existence is used to guarantee invertibility of the matrix ∇A on $[0, t_1)$ and Gevrey regularity (Foias & Temam 1989) to pass from moderately smooth initial data to Gevrey class regular solutions. Note that the resetting data are such that both u and ω are time continuous. We proved (Constantin 2003) the following result. We take u_0, divergence-free and with square-integrable gradient, and consider $T > 0$, a time interval. We assume that the solution of the Navier-Stokes equations with initial datum u_0 obeys $\sup_{0 \leq t \leq T} \|\omega(\cdot, t)\|_{L^2(dx)} < \infty$. Then there exists $\lambda > 0$ so that, for any $\epsilon > 0$, there exists $\tau > 0$ such that both group expansions converge on $[0, T]$ and the resetting intervals can be chosen to have any length up to τ, $t_{i+1} - t_i \in [0, \tau]$. The velocity u, solution of the Navier-Stokes equation with initial datum u_0, obeys the Weber formula (3). The vorticity $\omega = \nabla \times u$ obeys the Cauchy formula (4).
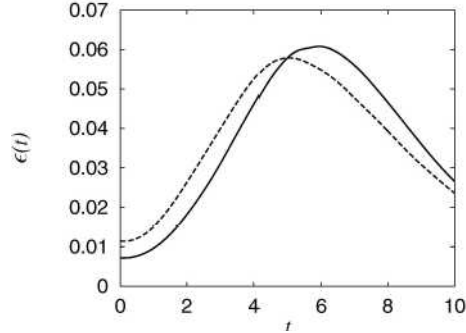
Figure 1. Evoultion of the energy disspation rate $\epsilon(t)$ for $\nu = 2.5 \times 10^{-3}$(solid) and 4×10^{-3}(dashed).

Conversely, if one group expansion converges, then so does the other, using the same resetting times. The Weber and Cauchy formulas apply and reconstruct the solution of the Navier-Stokes equation. The enstrophy is bounded $\sup_{0 \le t \le T} \|\omega(\cdot, t)\|_{L^2(dx)} < \infty$, and the Navier-Stokes solution is smooth.

The quantity λ can be estimated explicitly in terms of the bound of enstrophy, time T, and kinematic viscosity ν. The bound is algebraic: a negative power of the enstrophy, if all other quantities are fixed. The maximal time step τ is proportional to ϵ, with a coefficient of proportionality that depends algebraically on the bound on enstrophy, time T and ν. The converse statement, that if the group expansion converges, then the enstrophy is bounded, follows from the fact that there are finitely many resettings. Indeed, the Cauchy formula and the near identity bound on ∇A imply a doubling condition on the enstrophy on each interval. It is well-known that the condition regarding the boundedness of the enstrophy implies regularity of the Navier-Stokes solution. Our definition of convergent group expansion is very demanding, and it is justified by the fact that once the enstrophy is bounded, one could mathematically demand analytic norms. But the physical resetting criterion is the invertibility of the matrix ∇A. The Euler equations require no resetting as long as the solution is smooth. The Navier-Stokes equations, at least numerically, require numerous and frequent resettings.

4. Vortex reconnection and resetting

We show an example of numerical simulations of decaying Navier-Stokes turbulence developing from a random initial condition with energy spectrum

$$E(k) \propto k^2 \exp(-k^2), \int_0^\infty E(k)dk = 1.$$
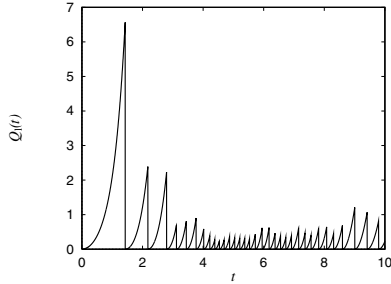
Figure 2.   Evoultion of $Q_\ell(t)$ for $\nu = 2.5 \times 10^{-3}$.
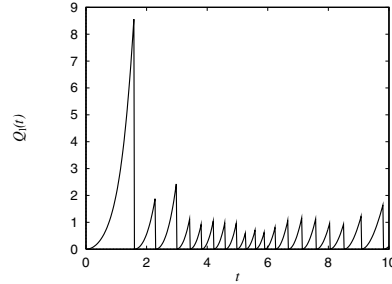
Figure 3.   Evoultion of $Q_\ell(t)$ for $\nu = 4 \times 10^{-3}$.

The computation was done by 2/3-dealiased pseudo-spectral method under periodic boundary conditions, with grid points 256^3 and 512^3. In Figure 1 we plot time evolution of the dissipation rate of total kinetic energy for two different values of viscosity $\nu = 2.5 \times 10^{-3}$ and 4×10^{-3}. They are peaked around $t = 5$. We solve the Navier-Stokes equations (6) and the equations for $\ell \equiv A - x$

$$D_\nu \ell + u = 0 \tag{13}$$

simultaneously. We reset as $\ell = 0$ when $\det(\nabla A) < \epsilon$ somewhere in the flow, where ϵ is a small preassigned number, here taken to be 0.01. Squared L^2 norm of $\nabla \times \ell$ is defined by

$$Q_\ell(t) = \frac{1}{2} \left\langle |\nabla \times \ell|^2 \right\rangle,$$

where the brackets denote a spatial average. We show its evolution for $\nu = 2.5 \times 10^{-3}$ in Figure 2 and for $\nu = 4 \times 10^{-3}$ in Figure 3. In both cases frequent resettings take place when turbulence is developed. It should be noted that the smaller viscosity is, the more frequently the resetting occur. It it well known that in decaying turbulence starting from a smooth initial condition vortex layers are observed in the early stage which change their form into vortex tubes in the later developed stage. In Figures 4 and 5, we compare spatial distributions with relatively small $\det(\nabla A)$ with high vorticity regions at early $t = 1$ and developed $t = 6$ for the case of $\nu = 2.5 \times 10^{-3}$. We see that in the early stage the regions with small $\det(\nabla A)$ have layer-like structure and exist between vortex layers. In the developed stage, regions with small $\det(\nabla A)$ have tube-like structure and exist apparently in closer vicinity of vortex tubes. See Ohkitani & Constantin (2005) for details.

There is a deep connection between these resetting times and vortex reconnection (Ohkitani & Constantin 2003, Ohkitani & Constantin 2005). In the Euler equation, as long as the solution is smooth, the Cauchy invariant obeys

312
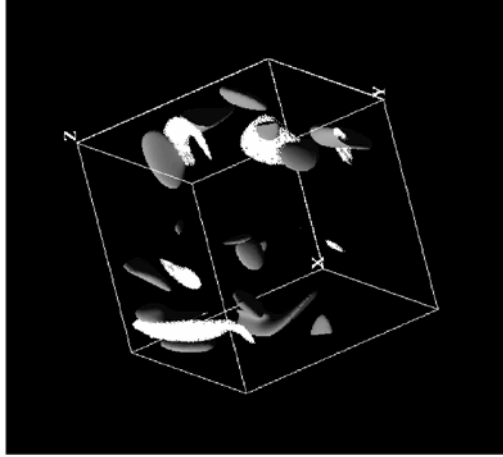
Figure 4. White symbols are placed in regions with $\det(\nabla A) < 1.03 \min_x \det(\nabla A) \approx 0.980$. There are 76556 such points out of 256^3. Isosurfaces of vorticity are shown in grey at $|\boldsymbol{\omega}|^2 = 4 \left\langle |\boldsymbol{\omega}|^2 \right\rangle$.
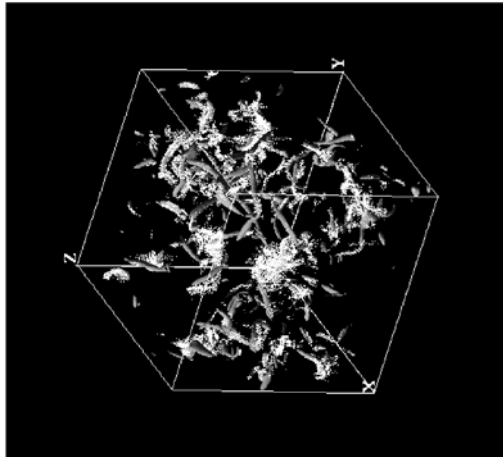

Figure 5. White symbols are placed in regions with $\det(\nabla A) < 1.045 \min_x \det(\nabla A) \approx 0.997$. There are 62838 such points out of 256^3. Isosurfaces of vorticity are shown in grey at $|\boldsymbol{\omega}|^2 = 10 \left\langle |\boldsymbol{\omega}|^2 \right\rangle$.

$\zeta(x,t) = \omega_{(0)}(A(x,t))$ with $\omega_{(0)} = \omega_0$, the initial vorticity. The topology of vortex lines is frozen in time. In the Navier-Stokes system the topology changes. This is the phenomenon of vortex reconnection. There is ample numerical and physical evidence for this phenomenon. In the more complex, but similar case of magneto-hydrodynamics, magnetic reconnection occurs, and has powerful physical implications. Vortex reconnection is a dynamical dissipative process.

The solutions of the Navier-Stokes equations obey a space time average bound (Constantin 2003)

$$\int\limits_0^T \int\limits_{\mathbf{R}^3} |\omega(x,t)| \left| \nabla_x \left(\frac{\omega(x,t)}{|\omega(x,t)|} \right) \right|^2 dx dt \le \frac{1}{2} \nu^{-2} \int\limits_{\mathbf{R}^3} |u_0(x,t)|^2 dx.$$

This bound is consistent with the numerically observed fact that the region of high vorticity is made up of relatively straight vortex filaments (low curvature of vortex lines) separated by distances that vanish with viscosity. The process by which this separation is achieved is vortex reconnection. When vortex lines are locally aligned, a geometric depletion of nonlinearity occurs, and the local production of enstrophy drops. Actually, the Navier-Stokes equations have global smooth solutions if the vorticity direction field $\frac{\omega}{|\omega|}$ is Lipschitz continuous (Constantin & Fefferman 1993) in regions of high vorticity. So, vortex reconnection is a regularizing mechanism.

5.   Invariants = diffusive lagrangian quantities

The reason for the fact that resettings are necessary is that, in the presence of viscosity, there is change in the determinant $det(\nabla A)$. This rate of change is given by

$$D_\nu \left(\log(det(\nabla A)) \right) = \nu \left\{ C^i_{k;s} C^s_{k;i} \right\}. \tag{14}$$

The right-hand side has units of inverse time, and determines the duration of the chart. In ideal fluids the main physical processes are those of folding and stretching. In terms of the back-to-labels, stretching is represented by ∇A and folding by composition with A. So, for instance, the variable $w = (\nabla A)^T v$ is the product of both stretching and folding (because $v = u_0 \circ A$). In the presence of viscosity there is molecular mixing which is enhanced by folding, and the process of folding cannot be separated from that of diffusion. The Cauchy invariant, the virtual velocity, the determinant $det(\nabla A)$ and the modified helicity density, are not invariant anymore: they diffuse.

Using the smooth change of variables $a = A(x,t)$ (at each fixed time t) we compute the Euclidean Riemannian metric by

$$g^{ij}(a,t) = (\partial_k A^i)(\partial_k A^j)(x,t). \tag{15}$$

The equations for the virtual velocity and for the Cauchy invariant can be solved by following the path A, i.e., by seeking

$$\begin{aligned} v(x,t) &= \upsilon(A(x,t),t), \\ \zeta(x,t) &= \xi(A(x,t),t). \end{aligned} \tag{16}$$

The equations for υ and ξ become purely diffusive. Using $D_\nu A = 0$, the operator D_ν becomes

$$D_\nu(f \circ A) = \left((\partial_t - \nu g^{ij}\partial_i\partial_j)f\right) \circ A. \qquad (17)$$

The equation for υ follows from (8):

$$\partial_t \upsilon_i = \nu g^{mn}\partial^2_{mn}\upsilon_i - 2\nu V_i^{mj}\partial_m\upsilon_j \qquad (18)$$

with

$$V_i^{mj} = g^{mk}\Gamma^j_{ik}.$$

The derivatives are with respect to the Cartesian coordinates a. The equation reduces to $\partial_t\upsilon = 0$ when $\nu = 0$, and in that case we recover $\upsilon = u_{(0)}$, the time independent initial velocity. For $\nu > 0$ the system is parabolic and well posed. The equation for ξ follows from (10):

$$\partial_t\xi^q = \nu g^{ij}\partial^2_{ij}\xi^q + 2\nu W_n^{qk}\partial_k\xi^n + \nu T^q_p\xi^p \qquad (19)$$

with

$$\begin{cases} W_n^{qk} = -\delta^q_n g^{kr}\Gamma^p_{rp} + g^{kp}\Gamma^q_{pn}, \\ T^q_p = \epsilon_{qji}\epsilon_{rmp}\Gamma^r_{\alpha j}\Gamma^m_{\beta i}g^{\alpha\beta}. \end{cases}$$

Again, when $\nu = 0$ this reduces to the invariance $\partial_t\xi = 0$. But in the presence of ν this is a parabolic system. Both the Cauchy invariant and the virtual velocity equations start out looking like the heat equation because $g^{mn}(a,0) = \delta^{mn}$ and $\Gamma^i_{jk}(a,0) = 0$. As for the helicity, if we consider the modified density $h = w \cdot \omega$, we have first of all that

$$\int_{T\circ A}(u \cdot \omega)dx = \int_{T\circ A} h dx,$$

and then, because $h = ((\upsilon \cdot \xi) \circ A)det(\nabla A)$, it follows that

$$\int_{T\circ A} h dx = \int_T (\upsilon \cdot \xi)da.$$

Therefore, the modified helicity density is $\upsilon \cdot \zeta$. The product of two diffusive Lagrangian quantities is diffusive Lagrangian, as it is easily verified. Finally, considering

$$g = det(g_{ij}), \qquad (20)$$

where g_{ij} is the inverse of g^{ij} and observing that

$$g(A(x,t)) = (det(\nabla A))^{-2},$$

we deduce that (14) becomes

$$\partial_t(\log(\sqrt{g})) = \nu g^{ij}\partial_i\partial_j\log(\sqrt{g}) - \nu g^{\alpha\beta}\Gamma^m_{\alpha p}\Gamma^p_{\beta m}. \qquad (21)$$

The initial datum is zero. The equation is parabolic, has a maximum principle and is driven by the last term. The form (21) of (14) has the same interpretation: the connection coefficients define an inverse length scale associated to A. The corresponding inverse time scale

$$\nu \left\{ C_{k;s}^i C_{k;i}^s \right\} = \nu \left\{ g^{mn} \Gamma_{ms}^i \Gamma_{ni}^s \right\} \circ A$$

decides the time interval of validity of the chart A.

The metric coefficients g^{ij} determine the Riemannian connection coefficients, as it is well known. But they do not determine their own evolution as they change under the Navier-Stokes equations. (The evolution equation of g^{ij} involves ∇u and ∇A). It is therefore remarkable that the virtual velocity, Cauchy invariant and helicity density and volume element evolve according to equations that do not involve explicitly the velocity, once one computes in a diffusive Lagrangian frame. Thus, in the presence of viscosity, the ideal Lagrangian invariants become *diffusive Lagrangian*, that is they obey *linear* second-order parabolic equations with coefficients determined locally from the Euclidean Riemannian metric induced by the change of variables A. These ideal invariants have the property that, if $I = \phi \circ A$ denotes the invariant, then

$$\frac{\partial \phi(a, t)}{\partial t} = \nu \mathcal{L}[g, \partial_a] \phi(a, t),$$

where $\mathcal{L}$ is a second-order PDE with elliptic principal part and with coefficients computed from $g^{ij}(a, t)$ and its a derivatives, where $g^{ij}(A(x, t), t) = (\partial_k A^i)(\partial_k A^j)$. The operators $\mathcal{L}$ start from the Laplacian, $\mathcal{L}[g, \partial_a]_{|t=0} = \Delta_a$. Formally, when $\nu = 0$, one reverts to invariance, $I = \phi_0(A)$, where ϕ_0 is the initial datum. But, in addition, as long as A is known and invertible, using it as a chart, one can compute the evolution of the invariant, in a well-posed manner, without recourse to information extraneous to the chart.

The metric itself is *not* diffusive Lagrangian. The description in terms of diffusive Lagrangian transformations allows us to quantify the process of vortex reconnection (Ohkitani & Constantin 2003, Ohkitani & Constantin 2005): the change of charts is dictated by the requirement that ∇A be invertible. The loss of invertibility is numerically observed, and documented to occur during the periods of topological change in the vorticity field. (Note that the noninvertibility of ∇A is a clearly defined concept, while viscous vortex reconnection, while clearly visible to the eye, is not a clearly defined concept: for viscous flows the vorticity does not have conserved topology.) We have considered so far calculations with different initial data: one and two pairs of vortex tubes, random initial vorticity and Taylor-Green vortices. There have been several Reynolds numbers computed. So far, the computations are consistent with a conjectured "connection anomaly" which is a statement about the fact that in

the limit of zero viscosity, the reconnection inverse time scale $\nu|C|^2$ is bounded away from zero.

6.   Summary

We have described a diffusive Lagrangian formulation of the Navier-Stokes equations by comparing it with its inviscid counterpart based on Weber formula. We point out theoretically that non-invertibility of diffusive Lagrangian transformations can occur and show that it does occur using numerical simulations. The non-invertibility is related with vortex reconnection. Thus, an alternative description of the Navier-Stokes flows is obtained in terms of near-identity transformations of the diffusive Lagrangian labels and of the virtual velocity.

This formulation has merits in studying reconnection phenomena taking place in turbulence of neutral fluid and in magneto-hydrodynamic turbulence. Also, it offers a method of quantifying anomalous nature of the inviscid limit of the Navier-Stokes equations at zero viscosity limit. Numerical results on these issues will be reported elsewhere.

Acknowledgments

References

Arnold, V. I.& Khesin, B. A. 1998, *Topological methods in Hydrodynamics*, Applied Mathematical Sciences, **125**, Springer-Verlag, New York.

Buttke, T. 1993 Lagrangian numerical methods which preserve the Hamiltonian structure of incompressible fluid flow, in *Vortex flows and related numerical methods*, Beale,J.T.& Cottet, G.H. & Huberson, S.(Eds), NATO ASI Series, Vol. 395, Kluwer, Norwell.

Buttke, T.& Chorin, A. 1993 Turbulence calculations in magnetization variables, Appl. Num. Math. **12**, 47-54.

Chorin, A. 1994 *Vorticity and Turbulence*, Applied Mathematical Sciences **103**, Springer-Verlag.

Chorin, A. 1973 Numerical study of slightly viscous flow, J. Fluid. Mech **57** (1973), 785-796.

Clebsch, A. 1858 Uber die integration der hydrodynamischen Gleichungen, J. Reine Angew. Math. **58**, 1–10.

Constantin, P. 1994 Geometric and analytic studies in turbulence, in *Trends and Perspectives in Appl. Math.*, Sirovich, L. ed., Appl. Math. Sciences **100**, Springer-Verlag.

Constantin, P. 2001 An Eulerian-Lagrangian approach for incompressible fluids: local theory, Journal of the AMS, **14**, 263-278.

Constantin, P. 2001 An Eulerian-Lagrangian approach to the Navier-Stokes equations, Commun. Math. Phys. **216**, 663-686.

Constantin, P. 2003 Near identity transformations for the Navier-Stokes equations, in *Handbook of Mathematical Fluid Dynamics*, Volume 2, Friedlander, S. and Serre, D. Edtrs, Elsevier.

Constantin, P.& E, W.& Titi, E. 1994 Onsager's conjecture on the energy conservation for solutions of Euler's equations, Commun. Math. Phys., **165** 207-209.

Constantin, P.& Fefferman, C. 1993 Direction of vorticity and the problem of global regularity for the Navier-Stokes equations, Indiana Univ. Math. Journal, **42** 775-794.

Eyink, G. 1994 Energy dissipation without viscosity in the ideal hydrodynamics, I. Fourier analysis and local energy transfer, Phys. **D 3-4**, 222-240.

Foias, C.& Temam, R. 1989 Gevrey class regularity for the solutions of the Navier-Stokes equations, J. Funct. Anal. **87**, 359-369.

Kuzmin, G.A. 1983 Ideal incompressible hydrodynamics in terms of momentum density, Phys. Lett. A **96**, 88-90.

H. Lamb, *Hydrodynamics*, Cambridge University Press, Cambridge, 1932.

Moffatt, H.K. 1969 The degree of knottedness of tangled vortex lines, J. Fluid Mech., **35**, 117-129.

Onsager 1949, Statistical Hydrodynamics, Nuovo Cimento **6**(2), 279-287.

Ohkitani, K.& Constantin,P. 2003 Numerical study of the Eulerian-Lagrangian formulation of the Navier-Stokes equations, Phys. Fluids **15-10**, 3251-3254.

Ohkitani, K. & Constantin, P. 2005 Numerical study of the Eulerian-Lagrangian analysis of the Navier-Stokes turbulence, work in preparation.

Oseledets, V.I. 1989 On a new way of writing the Navier-Stokes equation. The Hamiltonian formalism. Commun. Moscow Math. Soc (1988), Russ. Math. Surveys **44**, 210-211.

Roberts, P.H. 1972 A Hamiltonian theory for weakly interacting vortices, Mathematica **19**, 169-179.

Weber, W. 1868 Uber eine Transformation der hydrodynamischen Gleichungen, J. Reine Angew. Math. **68**, 286-292.

Zakharov, V.E. & Kuznetsov, E.A. 1970 Variational principle and canonical variables in magnetohydrodynamics, Doklady Akademii Nauk SSSR **194**, 1288-1289.

EVOLUTION OF COMPLEX SINGULARITIES AND KOLMOGOROV SCALING IN TRUNCATED THREE-DIMENSIONAL EULER FLOWS

Cyril Cichowlas
Laboratoire de Physique Statistique de l'Ecole Normale Supérieure,
associé au CNRS et aux Universités Paris VI et VII, 24 Rue Lhomond, 75231 Paris, France
cichowla@clipper.ens.fr

Fabrice Debbasch
ERGA, CNRS UMR 8112,
4 Place Jussieu,
F-75231 Paris Cedex 05, France
fabrice.debbasch@wanadoo.fr

Marc Brachet
Laboratoire de Physique Statistique de l'Ecole Normale Supérieure,
associé au CNRS et aux Universités Paris VI et VII, 24 Rue Lhomond, 75231 Paris, France
brachet@lps.ens.fr

Abstract   The analyticity strip method is used to trace complex singularities in direct numerical simulations of the Taylor-Green flows, performed with up to 2048^3 collocation points. No indication of finite-time real singularity is found. Simulations are also carried out beyond the time at which the truncated equations cease to approximate the original Euler equations. Kolmogorov-like turbulence is then obtained during an intermediate regime of the spontaneous relaxation of (time-reversible) spectrally-truncated Euler equations towards absolute equilibrium.

Keywords: Incompressible perfect fluid, finite time singularity, absolute equilibrium, Kolmogorov turbulence

1.   Introduction

The purpose of the present contribution is to study the dynamics of spectrally truncated 3-D incompressible Euler flows. Two quite different regimes are investigated.

The first regime is related to the possible existence of a finite-time infinite-vorticity singularity in three-dimensional incompressible Euler flow developing from smooth initial conditions. This is still an open mathematical problem (Frisch *et al.* 2003). One possible approach to the problem is the so-called analyticity strip method (Sulem *et al.* 1983). The basic idea of this method is to trace complex singularities numerically on direct numerical simulations (DNS) of the Euler equation with enough spatial resolution to capture the exponential tails in the Fourier transforms. The logarithmic decrement of the energy spectrum at high-k is twice the width $\delta(t)$ of the analyticity strip of the velocity field and the problem of blowup comes down to checking if $\delta(t)$ vanishes in a finite time. This method has been applied to three-dimensional Euler flows generated by the Taylor & Green (1937) (TG) initial conditions, with resolutions 256_3 (Brachet *et al.* 1983) and 864_3 (Brachet *et al.* 1992). It was observed that, after an early transient period, the width of the analyticity strip of the velocity field decayed exponentially in time. In this contribution we present simulations performed with up to 2048^3 collocation points; no indication of finite-time real singularity is found.

The second regime of the spectrally truncated Euler flow is obtained by carrying out the integration beyond the time at which the truncated equations cease to approximate the original Euler equations. It is well known (Kraichnan 1973; Orazag 1977) that the (spectrally) truncated Euler equations admit statistically stationary exact solutions, the so-called absolute equilibria, with Gaussian distribution f^* and energy spectra $E(k)$ proportional to k^2. The dynamics of spectrally truncated time reversible nonlinear equations has already been studied in the particular cases of 1-D Burgers-Hopf models (Majda & Timofeyev 2000) and 2-D quasi-geostrophic flows (Majda & Abramov 2003). A central point in these studies was the nature of the statistical equilibrium that is achieved at large times (Orazag 1977). Several equilibria are *a priori* possible because both (truncated) 1-D Burgers-Hopf and 2-D quasi-geostrophic flow models admit, besides the energy, a number of additional conserved quantities. The case of spectrally truncated 3-D incompressible Euler flows is of a different nature because (except for helicity that identically vanishes for the flows considered here) there is no known additional conserved quantity (Frisch 1995). The equilibrium is thus unique. In this contribution we present simulations displaying Kolmogorov-like turbulence during an intermediate regime of the spontaneous relaxation toward this equilibrium.

This article is organized as follows: Section 2 is a short review of (standard) basic definitions and numerical algorithms. The singularity problem is addressed in Section 3 and the turbulent regime is presented in Section 4. Finally Section 5 is our conclusion.

2. Definition of the system

The three-dimensional incompressible Euler equations,

$$\partial_t \mathbf{v} + (\mathbf{v} \cdot \nabla)\mathbf{v} = -\nabla p \,, \tag{1}$$

$$\nabla \cdot \mathbf{v} = 0 \,, \tag{2}$$

with (2π-periodic) initial data are solved numerically using standard (Gottlieb & Orszag 1977) pseudo-spectral methods with resolution N. Time marching is done with a second-order leapfrog finite-difference scheme. Fourth-order Runge-Kutta method is used to start the leapfrog and to periodically couple even and odd time steps. The solutions are dealiased by suppressing, at each time step, the modes for which at least one wave-vector component exceeds two-thirds of the maximum wavenumber $N/2$ (thus a 1024^3 run is truncated at $k_{\max} = 341$). Symmetries are used in a standard way (Brachet *et al.* 1983) to reduce memory storage and speed up computations.

The computations are carried out using the (incompressible) Taylor-Green vortex (Taylor & Green 1937) single–mode initial conditions,

$$u^{\mathrm{TG}} = \sin(x)\cos(y)\cos(z) \,, \;\; v^{\mathrm{TG}} = -u^{\mathrm{TG}}(y, -x, z) \,, \;\; w^{\mathrm{TG}} = 0 \,. \tag{3}$$

Series of runs are made by varying the resolution N.

In order to monitor the time-evolution of the flows we periodically extract from the computation the energy spectrum, defined by averaging $\hat{\mathbf{v}}(\mathbf{k}', t)$ (the spatial Fourier transform of the solution to Eq. (1)) on spherical shells of width $\Delta k = 1$,

$$E(k, t) = \frac{1}{2} \sum_{k - \Delta k/2 < |\mathbf{k}'| < k + \Delta k/2} |\hat{\mathbf{v}}(\mathbf{k}', t)|^2. \tag{4}$$

3. Initial dynamics of complex singularities

When the velocity field is analytic, the energy spectrum $E(k, t)$ decays exponentially at large k (with a possible algebraic prefactor). The logarithmic decrement is twice the width $\delta(t)$ of the analyticity strip of the solution continued to complex spatial variables. The basic idea of the analyticity strip method (Sulem *et al.* 1983) is to trace the temporal behavior of $\delta(t)$ in order to obtain evidence for or against blowup.

In order to extract $\delta(t)$ from the numerical integrations a least-square fit is performed on the logarithm of the computed energy spectrum, using the functional form,

$$\mathrm{Log}(E(k, t)) = C - n\mathrm{Log}(k) - 2\delta k \,. \tag{5}$$

E(k)

E(k)
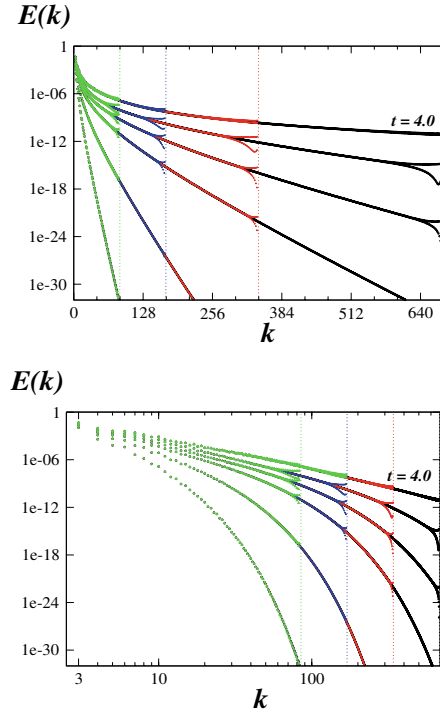
Figure 1.   Energy spectra at $t = (1.3, 1.9, 2.5, 2.9, 3.4, 4.0)$ and resolutions 256^3, 512^3, 1024^3 and 2048^3; the spectral cut-off is indicated, for each resolution, by the vertical dotted-lines. Left: Lin-Log, right: Log-Log.

The error on the fit interval $k_1 \leq k \leq k_2$,

$$\chi^2 = \sum_{k_1 \leq k_i \leq k_2} (\text{Log}(E(k_i, t)) - (C - n\text{Log}(k_i) - 2\delta k_i))^2 \qquad (6)$$

is minimized by solving the equations $\partial\chi^2/\partial C = 0, \partial\chi^2/\partial n = 0$ and $\partial\chi^2/\partial\delta = 0$. Note that these equations are linear in the fit parameters C, n and δ.

Examples of energy spectra to be fitted in such a way are presented on Fig. 1. It is apparent on the figure that resolution-dependent spectral even-odd oscillations are present, at certain times, on the TG energy spectrum. Note that this behavior is produced by the round-off error $\sim 10^{-15}$. For a given precision and resolution, the maximum time up to which the simulation is reliable should be the first instance at which the value of the spectrum at the highest wavenumber becomes comparable to the square of the round-off error. However, these round-off errors only affect the highest wavenumbers of the TG energy spectrum. They are eliminated by averaging the TG spectrum on shells of width $\Delta k = 2$ before performing the fit (Brachet *et al.* 1983).
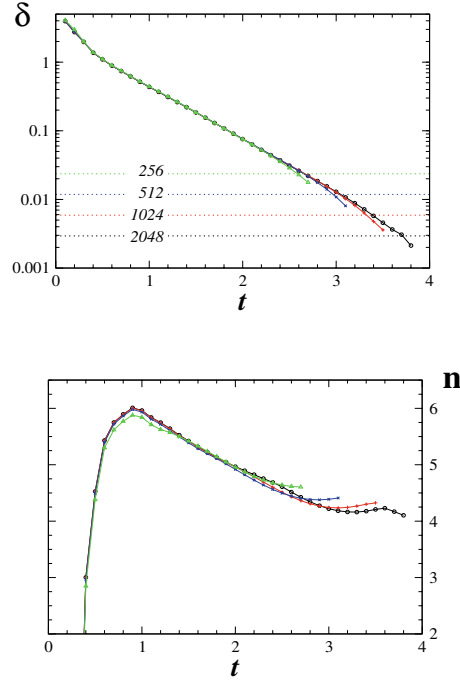
Figure 2. Time evolution of decrement δ (left) and exponent n (right) for TG flow at various resolutions (see Eq. 5). Fits are performed within the intervals $k = 5$ to $\min(k_\mathrm{R}, N/3)$, where $k_\mathrm{R} = \min_{E(k)<10^{-32}}(k)$ marks the beginning of roundoff noise at short times ($t \le 2.6$, see Fig. 1).

The measure of $\delta(t)$ is reliable as long as it remains larger than a few mesh sizes, a condition required for the smallest scales to be accurately resolved and spectral convergence ensured. Thus only the fits giving a value of δ such that $\delta k_\mathrm{max} > 2$ will be considered. Fig. 2 displays the values of δ and n for the flow. It is visible that, after a short transient period, $\delta(t)$ decays like

$$\delta(t) = \delta_0^\mathrm{TG} e^{-t/T_\mathrm{TG}} \tag{7}$$

with a characteristic decay time $T_\mathrm{TG} = 0.56$ and $\delta_0^\mathrm{TG} = 2.70$, up to a time $t = 3.7$ at resolution 2048^3 when it becomes comparable to twice the smallest resolved scale.

4.   Subsequent turbulent behavior

To rephrase the conclusion of the preceding section, for times larger than $t = 3.7$ the solution to the 2048^3 spectrally truncated equations becomes sensitive to the spectral cutoff and therefore stops approximating the solution to the full
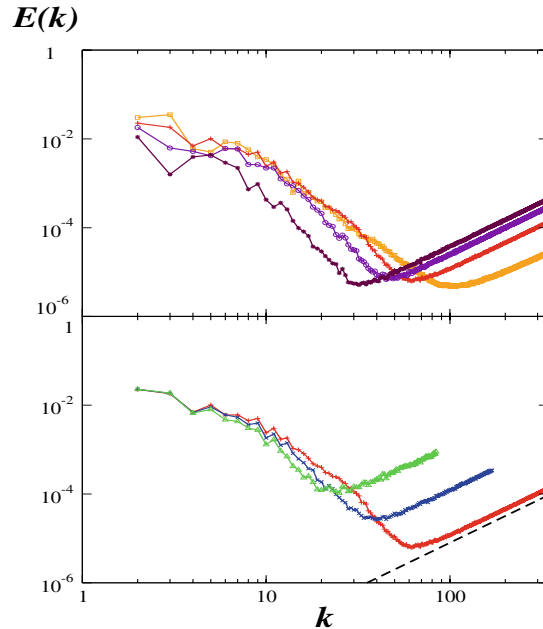
Figure 3. Energy spectra, top: resolution 1024^3 at $t = (6.5, 8, 10, 14)$ ($\diamond,+,\circ,*$); bottom: resolutions 256^3 (triangle $\triangle$), 512^3 (cross $\times$) and 1024^3 (cross $+$) at $t = 8$, the dashed line indicates k^2 scaling.

(untruncated) Euler equations. The numerical integration can nevertheless be continued; however, it is not clear what physical system (if any) the truncated equations represent in this regime.

The first effect of the spectral truncation is to accumulate energy near the cutoff and the spectrum stops being decreasing at high-k. Shortly after this crisis, the high-k spectrum becomes proportional to k^2 and this region then spreads to lower wavenumbers.

As already mentioned in the introduction, it is well known (Kraichnan 1973; Orazag 1977) that the spectrally truncated Euler equations (1), (2) admit statistically stationary exact solutions, the so-called absolute equilibria, with Gaussian distribution and energy spectra proportional to k^2. It thus appears that the truncated 3-D Eulerian dynamics is relaxing toward that equilibrium.

Figure 3 displays the time evolution (top) and resolution dependence (bottom) of the energy spectra at later times. It is apparent that a wavenumber $k_{\min}$ (such that $E(k) \geq E(k_{\min})$) spontaneously appears in the flow. The modes with $k > k_{\min}$ appear to be in absolute equilibrium (see the dashed line at the
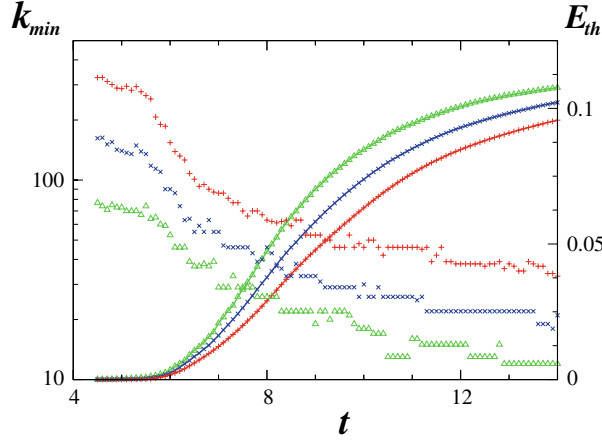
Figure 4. Time evolution of $k_{\min}$ (left vertical axis) and E_{th} (right vertical axis) at resolutions 256^3 (triangle $\triangle$), 512^3 (cross $\times$) and 1024^3 (cross $+$).

bottom of the figure). Defining the thermalized (or dissipated) energy E_{th} by

$$E_{\text{th}}(t) = \sum_{k_{\min} < k} E(k, t) \,, \tag{8}$$

the time evolutions of $k_{\min}$ and E_{th} are presented on Fig. 4. It is apparent on the figure that, for all resolutions, $k_{\min}$ decreases and E_{th} increases with time and that, for all times, $k_{\min}$ increases and E_{th} decreases with the resolution.

A first hint for Kolmogorov behavior is given by the energy dissipation rate,

$$\varepsilon(t) = \frac{\mathrm{d}E_{\text{th}}(t)}{\mathrm{d}t} \,. \tag{9}$$

Indeed, perhaps one of the main quantitative results of this paper is the excellent agreement of the energy dissipation rate shown on Fig. 5 (top) with the corresponding data in the viscous TG flow (see Fig. 7 in Brachet *et al.* (1983) and Fig. 5.12 in Frisch (1995)). Both the time for maximum energy dissipation $t_{\max} \simeq 8$ and the value of the dissipation rate at that time $\epsilon(t_{\max}) \simeq 1.5 \, 10^{-2}$ are in quantitative agreement.

A confirmation for Kolmogorov behavior around $t_{\max}$ is displayed on Fig. 5 (bottom). The value of the inertial-range exponent n, obtained by a low-k least square fit of the $\log$ of the energy spectrum with the function $\text{cte.} - n \log(k)$, is close to $5/3$ (horizontal dashed line) when $t \simeq t_{\max}$. Assuming Kolmogorov scaling $E(k) \sim \varepsilon^{2/3} k^{-5/3}$ in the $k < k_{\min}$ range and absolute equilibrium $E(k) \sim 3k^2 E_{\text{th}}/k_{\max}^3$ in the $k > k_{\min}$ range, one obtains a first estimation k_{m} for the observed wavenumber $k_{\min}$ (Cichowlas *et al.* 2005),
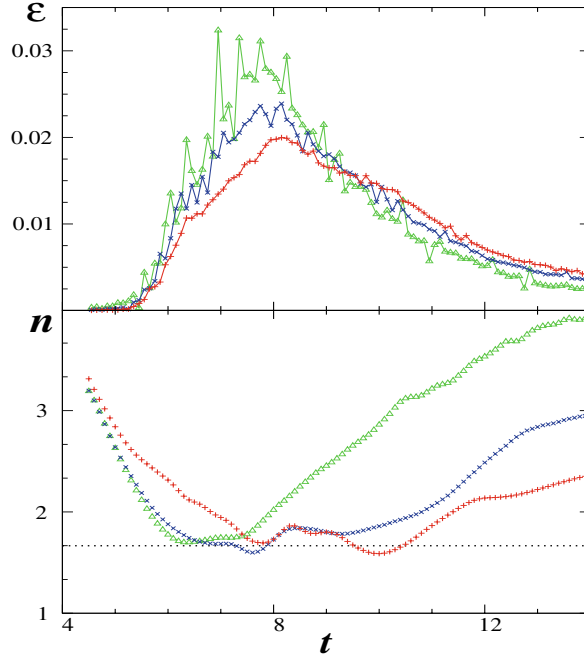
Figure 5. Temporal evolution of, top: energy dissipation ε; bottom: k^{-n} inertial range prefactor n at resolutions 256^3 (triangle $\triangle$), 512^3 (cross $\times$) and 1024^3 (cross $+$).

$$k_{\mathrm{m}} \sim \left(\frac{\varepsilon}{E_{\mathrm{th}}^{3/2}} \right)^{2/11} k_{\mathrm{max}}^{9/11} . \tag{10}$$

The ratio $k_{\min}/k_m$ is displayed on Fig. 6. It is seen to be reasonably constant on the figure.

5. Discussion and conclusion

In summary, complex singularities in DNS (resolutions up to 2048^3) of Taylor Green flow have been traced with the analyticity strip method. Note that the so called Kida-Pelz flow (Kida 1985; Pelz 2001) has also been investigated in this way by Cichowlas & Brachet (2005) using a generalized energy spectra fit procedure needed to take into account oscillations caused by interferences between complex singularities. Using resolutions up to 2048^3, exponential-in-time decay of δ was also found for this flow.
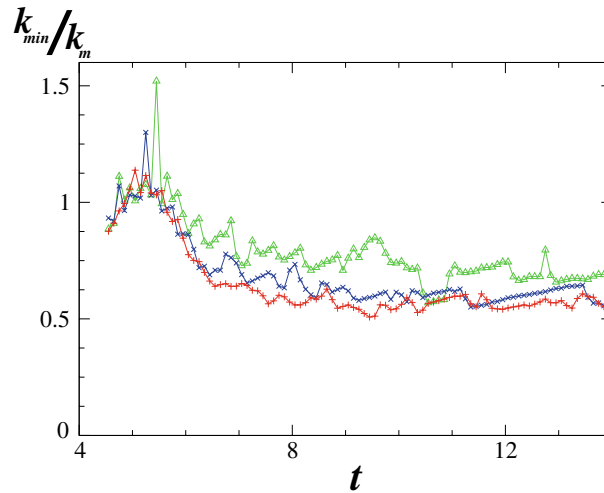
Figure 6. Time evolution of the ratio $k_{\min}/k_m$ at resolutions 256^3 (triangle Δ), 512^3 (cross $\times$) and 1024^3 (cross $+$).

Considering the truncated equations as a dynamical system in its own right, even when its solutions do not approximate solutions to the original Euler equations, we have observed the emergence of Kolmogorov-like turbulence during an intermediate regime of the spontaneous relaxation towards absolute equilibrium. Scaling laws have also been obtained for the dissipative effects that spontaneously appear in this time-reversible system. Let us finally remark that the temporal fluctuations around the equilibria are related to the equilibrium correlation functions by a fluctuation dissipation theorem. This point was used by Cichowlas *et al.* (2004), together with Monte-Carlo simulations, to estimate the magnitude of the dissipative effects.

Acknowledgments

References

BRACHET, M.E., MEIRON, D.I., ORSZAG, S.A., NICKEL, B.G., MORF, R.H. & FRISCH, U. 1983 Small-scale structure of the Taylor–Green vortex *J. Fluid Mech.* **130**, 411-452.

328

BRACHET, M.E., MENEGUZZI, M., VINCENT, A.,POLITANO, H. & SULEM, P.L. Numerical evidence of smooth self-similar dynamics for three-dimensional ideal flows *Phys. of Fluids A* **4**, 2845-2854.

CICHOWLAS, C., BONAITI, P., DEBBASCH, F. & BRACHET, M.E. 2004 Kolmogorov Scaling in Truncated 3-D Euler Flows *http://arxiv.org/abs/nlin.CD/0410064*

CICHOWLAS, C., BONAITI, P., DEBBASCH, F. & BRACHET, M.E. 2005 Kolmogorov scaling and thermal relaxation in spectrally-truncated incompressible Euler equations (in preparation).

CICHOWLAS, C. & BRACHET, M.E. 2005 Evolution of complex singularities in Kida-Pelz and Taylor-Green inviscid flows *Fluid Dyn. Res.* **36**, 239-248.

FRISCH, U. 1995 Turbulence, the legacy of A. N. Kolmogorov *Cambridge Univ. Press, Cambridge*.

FRISCH, U., MATSUMOTO, T. & BEC, J. 2003 Singularities of Euler flow? Not out of the blue! *J. Stat. Phys.* **113**, 761-781.

GOTTLIEB, D. & ORSZAG, S.A. 1977 Numerical analysis of spectral methods *SIAM*.

KIDA, S. 1985 Three-dimensional periodic flows with high symmetry *J. Phys. Soc. Japan* **54**, 2132-2136.

KRAICHNAN, R.H. 1973 Helical turbulence and absolute equilibrium *J. Fluid Mech.* **59**, 745-752.

MAJDA, A.J. & ABRAMOV, R. 2003 Statistically relevant conserved quantities for truncated quasi-geostrophic flow *Proc. Natl. Acad. Sci.* **100**, 3841–3846.

MAJDA, A.J. & TIMOFEYEV, I. 2000 Remarkable statistical behavior for truncated Burgers-Hopf dynamics *Proc. Natl. Acad. Sci.* **97**, 12413–12417.

ORSZAG, S.A. 1977 Statistical theory of turbulence in *Les Houches 1973: Fluid dynamics, R. Balian & J.L. Peube eds. Gordon and Breach, New York*.

PELZ, R.B. 2001 Symmetry and the hydrodynamic blowup problem *J.Fluid Mech.* **444**, 343-382.

SULEM, C., SULEM, P.L. & FRISCH, H. 1983 Tracing complex singularities with spectral methods *J. Comp.Phys.* **50**, 138-161.

TAYLOR, G. I. & GREEN, A. E. 1937 Mechanism of the production of small eddies from large ones *Proc. Roy. Soc. Lond. A* **158**, 499–521.

HELICITY GENERATION IN THREE-DIMENSIONAL EULER AND TURBULENCE

Robert M. Kerr
School of Engineering,
University of Warwick,
Coventry CV4 7AL, United Kingdom
Robert.Kerr@warwick.ac.uk

Abstract   Helicity produced by nearly singular vortex interactions is shown to play a role in the ensuing development of turbulence. This might provide a link between turbulence and the dynamics of the three-dimensional Euler equations, where numerical evidence has suggested that there might be a singularity. Interactions between regions of oppositely signed helicity in both physical and Fourier space are shown to be associated with the transfer of energy to small scales and the formation of vortex tubes, both being properties of fully developed turbulence.

Keywords: Turbulence, PDEs

1.   Introduction

The focus in this contribution will be vortex lines that originate from within the regions of the most intense vorticity, leave it, then spiral outwards. Spiraling vortex lines are helical such that the helicity density, the scalar product of the velocity and vorticity vectors $H(x) = \boldsymbol{u} \cdot \boldsymbol{\omega}$, would have a distinct sign, either positive or negative, depending upon the sense of twist in the spiral. The inviscid dynamics would be governed by the inviscid helicity evolution equation,

$$\frac{\partial(\boldsymbol{u} \cdot \boldsymbol{\omega})}{\partial t} + (\boldsymbol{u} \cdot \boldsymbol{\nabla})(\boldsymbol{u} \cdot \boldsymbol{\omega}) = \boldsymbol{\nabla} \cdot \left[\boldsymbol{\omega}(\tfrac{1}{2}u^2 - p) \right]. \tag{1}$$

In addition to the Lagrangian transport on the left-hand side, there is transport of helicity density along vortex lines on the right-hand side. The helicity density can increase locally due to this transport.

When integrated over space (V) these equations conserve helicity,

$$\frac{\mathrm{d}H}{\mathrm{d}t} = \frac{\mathrm{d}}{\mathrm{d}t} \int \boldsymbol{u} \cdot \boldsymbol{\omega} \mathrm{d}V = 0 \,, \tag{2}$$

a second quadratic conservation property of the 3D incompressible Euler equations in addition to the kinetic energy $KE = \int \tfrac{1}{2}u^2 \mathrm{d}V$. Therefore, any local

Figure 1. Three views of vortex lines leaving the region of a nearly singular Euler interaction. The region of most intense vorticity is enclosed by the isosurfaces. The diagram below shows how vortex lines around each of the four quadrants would wrap up as helicity of opposite sign is expelled from either side of this interaction. Dark lines indicate $H > 0$ and light lines indicate $H < 0$.
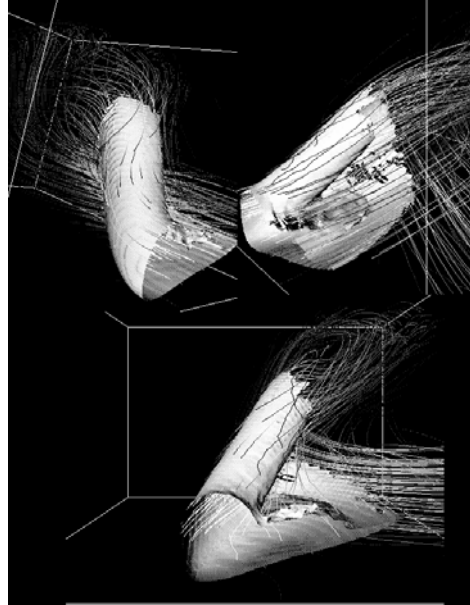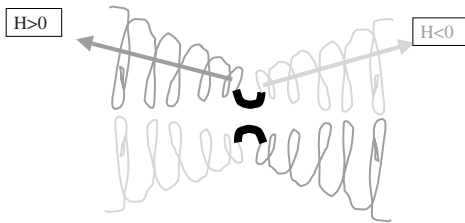
increase in helicity of one sign (say positive) must be balanced by an equal increase in helicity of the opposite (say negative) sign. These positive and negative changes must occur along connected vortex lines.

The primary mathematical condition for whether there is a singularity of the 3D incompressible, Euler equations is that the time integral of the maximum of the vorticity controls any singularity of 3D Euler (Beale *et al.* 1984),

$$\lim_{t \to T} \int_0^t \|\boldsymbol{\omega}\|_\infty \, \mathrm{d}s \to \infty. \tag{3}$$

Here $\|\boldsymbol{\omega}\|_\infty$ is the L_∞ norm of vorticity, or the peak value of magnitude of vorticity over all space. Kerr (1993) and Grauer *et al.* (1998) have obtained numerical evidence that $\|\boldsymbol{\omega}\|_\infty \approx 19/(T - t)$, where the possible singular time is T, which is consistent with this test.

Another mathematical property associated with swirl that can be derived from the time integral constraint is that infinite vortex line length must be generated (Majda and Constantin, private communication), a result that has been used in a new mathematical proof (Deng *et al.* 2005). This can be accommodated only if the vortex line length goes to infinity or if it becomes tightly curled or helical. Evidence will be presented here that infinitely long vortex line length in a nearly singular interaction is accommodated by being curled up. Then by transferring these ideas to a more general flow, it will be suggested that these helical regions could play a crucial role in the generation of turbulence following viscous reconnection.

2.   **Helicity generation in Euler**

Figure 1 shows three views of how vorticity leaves the region of most intense vorticity for two interacting anti-parallel Euler vortices just before viscosity from the Navier-Stokes equations would initiate vortex reconnection. Only half of one of the anti-parallel vortices is shown. A similar figure appeared on the cover of the January 1996 issue of Nonlinearity (Kerr 1996).

The diagram in the lower left of Fig. 1 illustrates how helicity density is forced out during such an interaction. The nearly singular interaction is indicated by the black lines. As their interaction becomes more intense, helical vortex lines are forced out in opposite directions with oppositely signed helicity, as indicated by the different brightness to the vortex lines extending from the central non-helical region. As helicity density accumulates in each quadrant, the magnitude of its integral grows as

$$H_q \to 0.25\sqrt{E\Omega} = C\sqrt{E}\sqrt{-\log(T-t)}, \tag{4}$$

where T is the singular time that is suggested by the anti-parallel Euler calculations (Kerr 1993), C is a undetermined coefficient and $\Omega = \int \omega^2 \mathrm{d}V$ is the enstrophy. This growth in H_q is the order of the maximum value allowed by the constant energy and growing enstrophy and implies that the vortex lines are very helical and Beltramized.

An increase in enstrophy consistent with logarithmic growth was observed in Kerr (1993), but the stronger evidence is the empirical observation there that the enstrophy production in Euler obeys

$$\Omega_{pr} = \frac{\mathrm{d}\Omega}{\mathrm{d}t} = \int \omega_i e_{ij} \omega_j \mathrm{d}V \sim \frac{1}{T-t}, \quad \text{where} \quad e_{ij} = \frac{1}{2}\left(\frac{\partial u_i}{\partial x_j} + \frac{\partial u_j}{\partial x_i}\right) \tag{5}$$

in addition to $\|\boldsymbol{\omega}\|_\infty$ obeying $1/(T-t)$. That is

$$\Omega \sim \int \frac{1}{T-t}\mathrm{d}t \sim -\log(T-t). \tag{6}$$

The scenario for helicity generation just given applies only before viscosity becomes important. Because the anti-parallel vortex interaction generates its own small scales, eventually small-scale viscous dissipation will take over and the anti-parallel vortex lines in the center (black) will be annihilated. This leads to vortex reconnection but not to any significant dissipation of either the kinetic energy or helicity. Only later after finite helicity dissipation by reconnection would there be changes in topology such as occurs in the linking and unlinking of vortex rings.

3. Helicity for random initial conditions

The anti-parallel initial condition is artificial and contrived to give the maximum growth in the peak vorticity in the shortest time. This is useful for investigating the question of whether there is a singularity of the inviscid, incompressible Euler equations, but might not be relevant to the role of vorticity growth and reconnection for turbulence in general. Even when the symmetries are relaxed and there are only a few vortex tubes in arbitrary configurations, the calculations never seem to reach a convincing $-5/3$ regime and turbulence. However, calculations starting with a few Fourier modes have for many years been able to reach a convincing $-5/3$ regime and a turbulent state (Brachet *et al.* 1983). Can the paradigm of the interaction of a few vortex tubes be applied to an initial condition with just a few Fourier modes?

Vortex tubes do not appear to be a good description of the state that evolves from a few Fourier modes. It has long been known that vortex sheets dominate these flows and it was recently shown that their interaction and reconnection is from an orthogonal configuration that is inherently helical and dissipative (Holm & Kerr 2002). Helical vortex tubes form due to reconnection and dissipation, instead of leading to reconnection and dissipation. Only after the helical tubes form does a $-5/3$ spectrum form.

To understand this better, more analysis of a flow generated by a few randomly chosen Fourier modes is presented. The decay of kinetic energy, growth of $\|\boldsymbol{\omega}\|_\infty$, and the variation in time of helicity in Fig. 2 set the timescales. The first signs of dissipation are changes in helicity starting about $t = 0.3$, but the most interesting period is around $t = 0.5$ when the sign of $\mathrm{d}H/\mathrm{d}t$ reverses and $\|\boldsymbol{\omega}\|_\infty$ reaches its largest value. The first strong interactions between vortices are just before this time. Figure 3 shows two times in this period when all of the intense vorticity is in vortex sheets and those sheets are interacting strongly. Only $1/4^3$ of the entire domain is shown, centered upon the position of $\|\boldsymbol{\omega}\|_\infty$, the maximum of vorticity over the entire domain. The most significant interaction is between two overlying, curled up sheets in the center. At $t = 0.41$ these
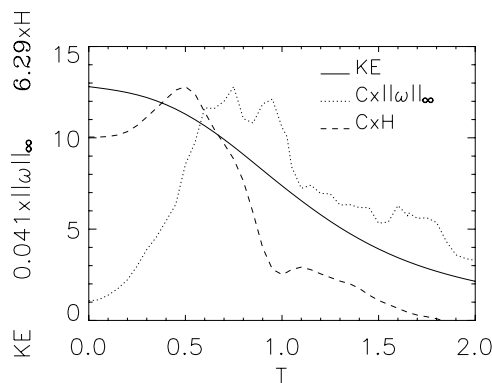
Figure 2. Time dependence of kinetic energy KE, $\|\omega\|_\infty$, and integral helicity H for a 256^3 direct numerical simulation initialized with a few Fourier modes. The time scale is set by the first peak in $\|\omega\|_\infty$ around $t = 0.5$. The constants used for scaling are indicated on the left.
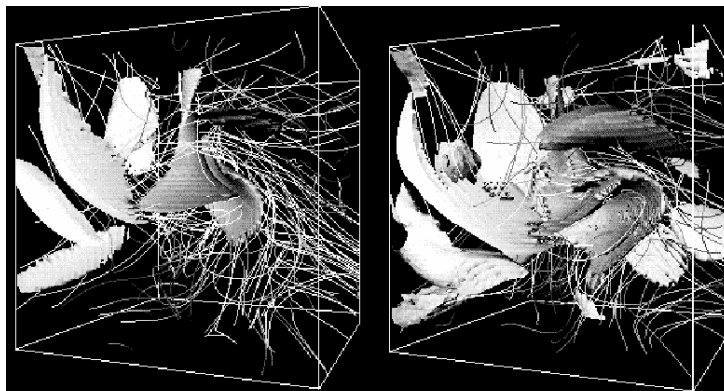
Figure 3. Times $t = 0.41$ (left) and $t = 0.45$ (right) for a calculation initialised with a few Fourier modes. The interacting vortex sheets at $t = 0.41$ are in the center, which seem to curl around reach other into a very localised anti-parallel configuration at $t = 0.45$.

are distinct sheets, possibly with anti-parallel vorticity. By $t = 0.45$ they appear to have merged into one structure while another sheet-like region is hovering overhead. If a singularity is necessary for dissipation to begin, this interaction is the best candidate from this flow. However, whether this description is accurate will require higher-resolution simulations of this or a similar initial condition. Fig. 4 shows the helicity structures that appear. The interacting structures at $t = 0.45$ are now in the upper right of Fig. 4(a) at $t = 0.5$, which shows the whole length of the vortex tube that is forming. From this, the orthogonal vortex tubes in Fig. 4(c) at $t = 0.7$ develop as the interaction works its way down, annihilates, and dissipates the dominant light hashed structure in Fig. 4(a).

The product of the inviscid helicity generation is best illustrated in Fig. 4(b), which focuses upon the structure in the upper right in Fig. 4(a). The arrangement of helicity is not clearly associated with the vortex structures, but after viewing this state from several angles, it can be concluded that there is positive and negative helicity density along the different ends of the two interacting vortex structures, consistent with the statement that helicity flux occurs along vortex lines in such a way as to create regions of oppositely signed helicity density. That is, the light hashes (negative $H(x)$) at the top and dark hashes (positive $H(x)$) on the bottom are along one structure, and the light hashes on the right and dark hashes in the middle and on the left are along the other structure.

The end product is two orthogonal vortex tubes with oppositely signed helicity at $t = 0.7$. This is an inherently dissipative interaction. Sheets of dissipation between vortices were first identified in a simulation by Kerr (1985). Moffatt (1985) proposed that there could be sheets of dissipation separating regions of maximally positive and negative helicity. The new results tie those ideas

together. Orthogonal vortex tubes without dissipation (Boratav *et al.* 1992) must have the same sign of helicity.

4.   Helicity spectra

Why would regions of oppositely signed helicity be related to dissipation? Usually helicity is thought to suppress nonlinearity and dissipation, but this is when one sign of helicity dominates, not for when both signs appear. Fig. 5 shows the helicity co-spectrum $H(k) = \int \Delta k \, \boldsymbol{u}(k) \cdot \boldsymbol{\omega}(k) \mathrm{d}\Omega$, where Δk represents a shell of wavenumbers k' for $k - \frac{1}{2} < k' < k + \frac{1}{2}$. The nonlinear helicity transfer spectrum is

$$H_{tr}(k) = \int \Delta k \, \mathbf{N}(\mathbf{k}) \cdot \boldsymbol{\omega}(\mathbf{k}) \mathrm{d}\boldsymbol{\Omega}, \tag{7}$$

where $\mathbf{N}(\mathbf{k})$ is the Fourier transform of the physical space nonlinear term $-(\boldsymbol{u} \cdot \nabla)\boldsymbol{u} - \nabla p$ in the Navier-Stokes equation. Between $t = 0.4$ and 0.5, $H(k)$ is rapidly oscillating between wavenumber shells. At any given time, these oscillations are more pronounced in the transfer spectrum $H_{tr}(k)$ than in the helicity co-spectrum. $H_{tr}(k)$ also shows signs that its positive and negative peaks are moving to higher wavenumbers, perhaps associated with an energy cascade. Strong oscillations in the helicity would not be consistent with anti-parallel vortices, where due to symmetries the total helicity would be zero as shown in the diagram in Fig. 1. This does not rule out the possibility that at sufficiently high Reynolds number and sufficiently small scales that the interaction (possible near $t = 0.42$) could become anti-parallel. But it does seem to rule out an anti-parallel interaction appearing at the scales resolved in this calculation.

Since helicity is conserved, if helicity grows positively in one shell, it must grow negatively in an adjacent shell. The result is the oscillating co-spectrum observed. Previously this had only been seen in a simulation initialized with a contrived set of Fourier modes designed to produce helicity and for which no physical space graphics were done. In this case we can also see the physical space structure, which is likewise associated with the appearance of positive and negative helicity regions. Comparing the physical space and spectral space structures, a partial explanation of the time dependence of the integral helicity in Fig. 2 can be given.

At $t = 0.3$, the highest wavenumber oscillation is centered around $k = 6$ and is negative. This is the first peak to be dissipated, leaving behind positive helicity. This spectral dissipation is probably associated with the annihilation process between light hashed (negative) helical regions that is still going on at $t = 0.5$ in the upper right of Fig. 4(b). As time increases, the spectral peaks move gradually to higher wavenumbers, so that after the negative peak has largely dissipated, a strong moderate wavenumber positive peak follows.
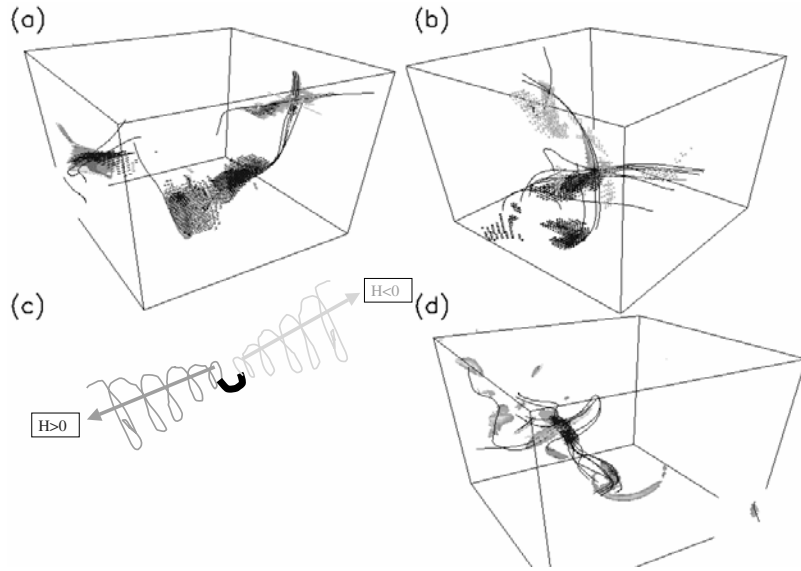
Figure 4. (a) **t=0.5** Isosurfaces of vorticity in as opaque surfaces for $1/2^3$ of the domain with sample vortex lines. High positive and negative helicity are indicated by dark hashes for $H > 0$ and light hashes for $H < 0$. The box is such that $\|\boldsymbol{\omega}\|_\infty$ for $t = 0.5$ and 0.7 will both be contained within it. $\|\boldsymbol{\omega}\|_\infty$ at $t = 0.5$ is within the cross at upper right. (b) **t=0.5** $1/4^3$ of the domain focussing upon the structure from the upper right in (a). (c) Diagram of how helicity density is produced by transport along vortex lines. In general there is creation of $H > 0$ (darker hashes) to the lower left and $H < 0$ (lighter hashes) in the upper right in frames (a) and (b). (d) **t=0.7** The position of the $\|\boldsymbol{\omega}\|_\infty$ at $t = 0.5$ was in the upper left corner and has now dissipated. The transverse structure that was a sheet at $t = 0.5$ has now rolled up into the light gray ($H < 0$) tube behind the dark gray ($H > 0$) tube.

From this time on, dissipation of positive helicity dominates and the positive peak of H in Fig. 2 decays.

There is a similarity between the observed spectral structure and shell models that have been related to the nonlinear terms of the Navier-Stokes equations (Biferale & Kerr 1995). In particular, the 3D version of the GOY (Gledzer-Ohkitani-Yamada) shell model has a helicity-like property that alternates between adjacent shells. However, despite the similarities in the important terms, there appear to be major differences between the GOY model and the Navier-Stokes equations in their energy cascade mechanisms. In GOY, the turbulent statistics are the result of long-time averages and the role of 'helicity' is to sporadically block the cascade. The important helicity mechanism in this DNS calculation appears to be a single pulse of helicity that moves to high wavenumbers, is not blocked, and is a pre-cursor to the true energy cascade, which forms
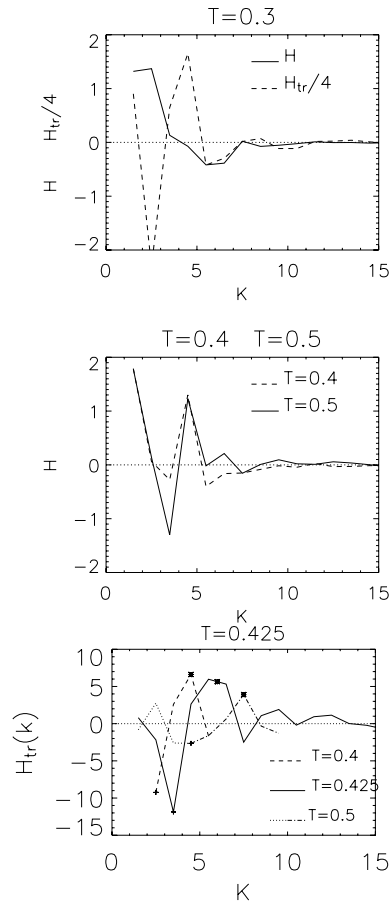
Figure 5. Helicity spectra $H(k)$ at $t = 0.3$, 0.4 and 0.5 and a helicity transfer spectrum $H_{tr}(k)$ at $t = 0.3$. Most of the change in the helicity spectrum occurs between $t = 0.3$ and 0.4, the period during which in physical space regions of negative and positive helicity density emerge, as shown in Fig. 4. Note the relationship between the oscillations in $H(k)$ at $t = 0.5$ and the oscillations in $H_{tr}(k)$ at $t = 0.3$. The high negative and positive transfer rates at $t = 0.3$ result in the changes seen in the helicity spectrum at $t = 0.4$. in positive helicity in Fig. 2 for $t < 0.5$. In the bottom frame, the full transfer spectrum $H_{tr}(k)$ at $t = 0.425$ is shown along with segments of the $t = 0.3$ and 0.5 transfer spectra to show how the spectrum appears to move to higher wavenumbers as time progresses. The peak positives are marked with $\star$'s and the peak negatives are marked with $+$'s. The change from a rise in positive helicity for $t < 0.5$ in Fig. 2 to a fall in positive helicity for $t > 0.5$ can be understood as follows: The negative peak in helicity at $t = 0.4$ and $k \approx 6$ is responsible for the rise. And as the negative transfer for $t \leq 0.4$ is replaced by a positive transfer around $t = 0.425$, this leads to the positive peak in helicity at $t = 0.5$ and $k \approx 6$ in the middle frame and a fall in positive helicity.

not long after $t = 0.7$. Of more significance is that in a helical decomposition of interactions in Fourier space (Waleffe 1993), it has been shown that the term with the largest energy transfer coefficient comes from terms similar to models like the GOY model, with alternating helicity bands contributing.

5.   Summary

This paper shows that while regions of like-sign helicity suppress nonlinearity, interacting regions of oppositely signed helicity might enhance nonlinearity and the cascade. The origin of the helicity could come from inviscid vortex interactions which create local regions of strong helicity even while conserving helicity globally. This happens in both Fourier and physical space. The

interacting transverse, helical vortex tubes at $t = 0.7$ in Fig. 4(d) might be the physical space manifestation of this.

Acknowledgments

References

BEALE, J.T., KATO, T., & MAJDA, A. 1984 Remarks on the breakdown of smooth solutions of the 3-D Euler equations, *Commun. Math. Phys.* **94**, 61-66.

BIFERALE, L. & KERR, R.M. 1995 On the role of inviscid invariants in shell models of turbulence, *Phys. Rev E* **52**, 6113–6122.

BORATAV, O.N., PELZ, R.B., & ZABUSKY, N.J. 1993 Reconnection in orthogonally interacting vortex tubes: Direct numerical simulations and quantifications., *Phys. Fluids A* **5**, 581–605.

BRACHET, M. E., MEIRON, D. I., ORSZAG, S.A., NICKEL, B.G., MORF, R.H., & FRISCH, U. 1983 Small-scale structure of the Taylor-Green vortex., *J. Fluid Mech.* **130**, 411–452.

DENG, J., HOU, T. Y., & YU, X. 2005 Geometric properties and non-blowup of 3-D incompressible Euler flow, *Comm. in PDE* **30**, 225–243.

GRAUER, R., MARLIANI, C., & GERMASCHEWSKI, K. 1998 Adaptive mesh refinement for singular solutions of the incompressible Euler equations., *Phys. Rev. Lett.* **80**, 4177–4180.

HOLM, D.D. & KERR, R.M. 2002 Transient vortex events in the initial value problem for turbulence., *Phys. Rev. Lett.* **88**, 244501.

KERR, R.M. 1985 Higher order derivative correlations and the alignment of small–scale structures in isotropic numerical turbulence, *J. Fluid Mech* **153**, 31-58.

KERR, R.M. 1993 Evidence for a singularity of the three-dimensional incompressible Euler equations., *Phys. Fluids A* **5**, 1725–1746.

KERR, R.M. 1996 Cover illustration: vortex structure of Euler collapse., *Nonlinearity* **9**, 271–272.

MOFFATT, H.K. 1985 Magnetostatic equilibria and analogous Euler flows of arbitrarily complex topology. Part 1, fundamentals, *J. Fluid Mech.* **159**, 359–378.

WALEFFE, F. 1993 Inertial transfers in the helical decomposition, *Phys. Fluids A* **5**, 677–685.

Part I   Superfluid turbulence

SUPERFLUID TURBULENCE AND DYNAMICS OF QUANTIZED VORTICES

Makoto Tsubota
Department of Physics,
Graduate School of Science, Osaka City University,
Sugimoto 3-3-138, Sumiyoshi-ku, Osaka 558-8585 Japan
tsubota@sci.osaka-cu.ac.jp

Abstract   Superfluid turbulence has been one of the most important problems of superfluid hydrodynamics, in which quantized vortices play a significant role. The recent research on superfluid turbulence enters a new stage rather different from the old ones chiefly devoted to thermal counterflow. After describing the current motivation on these topics, we discuss our research which studies the energy spectrum both by the vortex filament model and the Gross-Pitaevskii model. Both energy spectra are consistent with the Kolmogorov law, which shows a close similarity between superfluid (quantum) and classical turbulence.

Keywords: Superfluid helium, superfluid turbulence, quantized vortices, two-fluid model

1.   Introduction

Below the λ temperature T_λ at about 2.2K, liquid helium enters the superfluid state called helium II (Donnelly 1991). This superfluid transition is microscopically caused by Bose-Einstein condensation of helium atoms which is a typical quantum phenomenon in a system consisting of Bose particles. Helium II behaves like an irrotational ideal fluid, and its characteristic phenomena can be explained well by a two-fluid model. The two-fluid model states that helium II is a mixture of inviscid superfluid and viscous normal fluid with total density $\rho = \rho_s + \rho_n$, where ρ_s and ρ_n are the densities of the superfluid and the normal fluid. Their mixing ratio depends on temperature. Above T_λ, the whole fluid joins the normal fluid, while as the temperature is reduced below T_λ, ρ_s increases and ρ_n decreases, and the whole fluid becomes superfluid about below 1K. The superfluid corresponds to the Bose-Einstein condensate (BEC) and the normal fluid has all of the thermal excitations of the system.

Most early experimental studies focused on thermal counterflow. When helium II is confined in a channel closed at one end with a heater, superfluid

enters from the other open end and flows toward the heater. On reaching the heater, normal fluid is created, which then flows back toward the open end. This situation is called thermal counterflow. It is laminar at low relative velocities, but when the relative velocity exceeds some critical velocity, the superflow becomes turbulent and has dissipation. The concept of superfluid turbulence was introduced by Feynman who proposed that the superfluid turbulent state consists of a disordered set of quantized vortices (Feynman 1955) that is called a vortex tangle, which dissipates via mutual friction between the vortex cores and the normal flow. This picture was confirmed experimentally by Hall and Vinen (Hall and Vinen 1956a, 1956b, Vinen 1957a, 1957b, 1957c).

Although our understanding of superfluid turbulence and vortex dynamics has made significant gains since the early studies (Barenghi *et al.* 2001), the recent interest has shifted to the nature of superfluid turbulence (Vinen and Niemela 2002), apart from the case of counterflow. After describing the properties of quantized vortices and the current motivations on this field, we discuss our recent activity on the theoretical and numerical study of dynamics of quantized vortices. The motivation comes from how superfluid turbulence relates to classical turbulence. Superfluid turbulence is shown to have an energy spectrum consistent with the Kolmogorov law (Araki *et al.* 2002, Nore *et al.* 1997) by the vortex filament model and the Gross-Pitaevskii model, respectively.

2. Quantized vortices

2.1 What is a quantized vortex?

Below a critical temperature in an ideal Bose gas, a finite fraction of the particles occupies the same single-particle ground state and forms a BEC. When the particles have mutual interaction, single-particle states are no longer meaningful. However a condensate wave function $\Psi(\boldsymbol{r}, t)$ is still defined as the ensemble average of the quantum amplitude for removing a particle at position $\boldsymbol{r}$ from the condensate. Then the dynamics of $\Psi(\boldsymbol{r}, t)$ is described by the Gross-Pitaevskii (GP) equation (Donnelly 1991)

$$\mathrm{i}\hbar \frac{\partial \Psi(\boldsymbol{r}, t)}{\partial t} = \left(-\frac{\hbar^2}{2m} \nabla^2 + g|\Psi(\boldsymbol{r}, t)|^2 - \mu \right) \Psi(\boldsymbol{r}, t). \tag{1}$$

Here $g = 4\pi\hbar^2 m/a$ represents the strength of interaction characterized by the s-wave scattering length a, m the mass of each particle, and μ the chemical potential. Writing $\Psi = |\Psi| \exp(\mathrm{i}\theta)$, the squared amplitude $|\Psi|^2$ is the condensate density and the gradient of the phase θ gives the superfluid velocity $\boldsymbol{v}_s = (\hbar/m)\nabla\theta$, which is a frictionless flow of the condensate. Hence the vorticity $\mathrm{rot}\boldsymbol{v}$ vanishes everywhere in a single-connected region of the fluid; any rotational flow is carried only by a quantized vortex. In the core $\Psi(\boldsymbol{r}, t)$ vanishes, and the circulation of $\boldsymbol{v}_s$ along a closed path $\mathcal{C}$ around the core is

quantized as

$$\oint_{\mathcal{C}} \mathrm{d}\boldsymbol{s} \cdot \boldsymbol{v}_s = \frac{\hbar}{m} \oint_{\mathcal{C}} \mathrm{d}\boldsymbol{s} \cdot \nabla\theta = n\kappa \quad (n = 0, \pm 1, \pm 2, \cdots), \qquad (2)$$

with the quantum of circulation $\kappa = h/m$. Such a vortex with the quantized circulation is called a quantized vortex.

A quantized vortex is a topological defect characteristic of a Bose-Einstein condensate, being different from a vortex in a classical viscous fluid. First, the circulation is quantized, which is contrary to the classical vortex that can have any value of circulation. Second, a quantized vortex is a vortex of inviscid superflow. Thus, it cannot decay by the viscous diffusion of vorticity that occurs in a classical fluid. A quantized vortex can decay by shortening the length of the core through mutual friction with the normal fluid, by breaking into smaller and smaller vortex loops through reconnections and finally changing to some elementary excitations, or by transferring energy to smaller length scales through a Kelvin wave cascade (Vinen *et al.* 2003) followed by acoustic emission (Vinen 2000). Third, the core of a quantized vortex is very thin, being the order of the coherence length defined by $\xi = \hbar/(\sqrt{2mg}|\Psi|)$, which is only a few angstroms in helium II. Because the vortex core is very thin and does not decay by diffusion, it is always possible to identify the position of a quantized vortex in the fluid. These properties make a quantized vortex more stable and definite than a classical vortex, which allows us to consider a quantized vortex as an *elementary vortex* in superfluid turbulence.

2.2 Formulation of the dynamics of quantized vortices

Since the early studies on superfluid turbulence, lots of experimental works have been devoted chiefly to thermal counterflow, revealing many important properties (Tough 1982). However,the nonlinear and nonlocal dynamics of vortices delayed progress in further microscopic understanding of the vortex tangle. It was Schwarz who overcame these difficulties (Schwarz 1985, 1988). His most important contribution was to develop the direct numerical simulation of vortex dynamics connected with dynamical scaling analysis, thus enabled us to calculate such physical quantities as the vortex line density, various anisotropic parameters, and the mutual friction force. The observable quantities obtained with Schwarz's theory agreed well with the experimental results of the steady state of the vortex tangle. This research field pioneered by Schwarz has generated many new areas of study in vortex dynamics (Barenghi *et al.* 2001).

Now we have two kinds of formulation of the dynamics of quantized vortices. One is the vortex filament model and the other is the analysis of the GP equation. This subsection reviews briefly these two methods.

As described in the last subsection, a quantized vortex has the quantized circulation. The vortex core is extremely thin, being the order of atomic size in

helium II, much smaller than any other characteristic scale in the vortex motion. These properties allow us to represent a quantized vortex as a vortex filament. In a classical fluid dynamics (Saffman 1992) the vortex filament model is more or less a toy model, while it is *realistic* for a quantized vortex in superfluid helium. The vortex filament model for a quantized vortex was pioneered and developed by Schwarz (1985, 1988).

The vortex filament formulation represents a quantized vortex as a filament passing through the fluid and having a definite direction corresponding to its vorticity. Except for the thin core region, the superflow velocity field has a classically well-defined meaning and can be described by ideal fluid dynamics. The velocity at a point $\boldsymbol{r}$ due to a filament is given by the Biot-Savart expression

$$\boldsymbol{v}_s(\boldsymbol{r}) = \frac{\kappa}{4\pi} \int_{\mathcal{L}} \frac{(\boldsymbol{s}_1 - \boldsymbol{r}) \times \mathrm{d}\boldsymbol{s}_1}{|\boldsymbol{s}_1 - \boldsymbol{r}|^3}, \tag{3}$$

where κ is the quantum of circulation. The filament is represented by a parametric form $\boldsymbol{s} = \boldsymbol{s}(\xi, t)$ with a one-dimensional coordinate ξ along the filament. The vector $\boldsymbol{s}_1$ refers to a point on the filament and the integration is taken along the filament $\mathcal{L}$. Helmholtz's theorem for a perfect fluid states that the vortex moves with the superfluid velocity. Attempting to calculate the velocity $\boldsymbol{v}_s$ at a point $\boldsymbol{r} = \boldsymbol{s}$ on the filament makes the integral diverge as $\boldsymbol{s}_1 \to \boldsymbol{s}$. To avoid this divergence, we separate the velocity $\dot{\boldsymbol{s}}$ of the filament at the point $\boldsymbol{s}$ into two components (Schwarz 1985):

$$\dot{\boldsymbol{s}} = \frac{\kappa}{4\pi}(\boldsymbol{s}' \times \boldsymbol{s}'') \ln\left(\frac{2(\ell_+\ell_-)^{1/2}}{e^{1/4}a_0}\right) + \frac{\kappa}{4\pi} \int_{\mathcal{L}}' \frac{(\boldsymbol{s}_1 - \boldsymbol{r}) \times \mathrm{d}\boldsymbol{s}_1}{|\boldsymbol{s}_1 - \boldsymbol{r}|^3}. \tag{4}$$

The first term is the localized induction field arising from a curved line element acting on itself, and ℓ_+ and ℓ_- are the lengths of the two adjacent line elements, after discretization, that hold the point $\boldsymbol{s}$ between them. The prime denotes differentiation with respect to the arc length ξ. The mutually perpendicular vectors $\boldsymbol{s}'$, $\boldsymbol{s}''$ and $\boldsymbol{s}' \times \boldsymbol{s}''$ point along the tangent, the normal and the binormal at the point $\boldsymbol{s}$, respectively, and their magnitudes are 1, R^{-1} and R^{-1} with the local radius R of curvature. The parameter a_0 is a cutoff parameter equal to the core radius. Thus, the first term represents the tendency for the point at $\boldsymbol{s}$ to move in the binormal direction with a velocity inversely proportional to R. The second term represents the nonlocal field obtained by integrating the integral of Eq. (3) for the range excluding the segments ℓ_+ and ℓ_- along the rest of the filament.

The approximation that neglects the nonlocal terms and replaces Eq. (4) by $\dot{\boldsymbol{s}} = \beta \boldsymbol{s}' \times \boldsymbol{s}''$ is called the localized induction approximation (LIA). Here the coefficient β is defined by $\beta = (\kappa/4\pi) \ln(c\langle R \rangle / a_0)$, where c is a constant of order 1 and $(\ell_+\ell_-)^{1/2}$ is replaced by the mean radius of curvature $\langle R \rangle$ along the

length of the filament. Most of Schwarz's numerical studies on vortex tangles used the LIA because this approximation can greatly reduce computation times. Although the method is effective for the analysis of dense tangles (due to cancellations between nonlocal contributions), it does not include the intervortex interaction properly. Because our present problems need to take much account of the interaction, our numerical simulations are done not by the LIA but by the fully Biot-Savart law of Eq. (4) .

A better understanding of vortices in a real system results when one includes the boundaries in the analyses. For this, the boundary-induced velocity field $\boldsymbol{v}_{s,b}$ is added to $\boldsymbol{v}_s$ so that the superflow can satisfy the boundary condition of an inviscid flow. If the boundaries are specular plane surfaces, $\boldsymbol{v}_{s,b}$ is just the field due to an image vortex made by reflecting the vortex into the plane and reversing its sign of vorticity. To allow for another applied field, we include $\boldsymbol{v}_{s,a}$. Hence, the total velocity $\dot{\boldsymbol{s}}_0$ of the vortex filament without dissipation is

$$\dot{\boldsymbol{s}}_0 = \frac{\kappa}{4\pi}(\boldsymbol{s}' \times \boldsymbol{s}'') \ln\left(\frac{2(\ell_+\ell_-)^{1/2}}{e^{1/4}a_0}\right) + \frac{\kappa}{4\pi}\int_{\mathcal{L}}' \frac{(\boldsymbol{s}_1 - \boldsymbol{r}) \times \mathrm{d}\boldsymbol{s}_1}{|\boldsymbol{s}_1 - \boldsymbol{r}|^3}$$
$$+ \boldsymbol{v}_{s,b}(\boldsymbol{s}) + \boldsymbol{v}_{s,a}(\boldsymbol{s}). \tag{5}$$

At finite temperatures it is necessary to consider the mutual friction between the vortex core and the normal flow $\boldsymbol{v}_n$. Including this term, the velocity of $\boldsymbol{s}$ is given by

$$\dot{\boldsymbol{s}} = \dot{\boldsymbol{s}}_0 + \alpha\boldsymbol{s}' \times (\boldsymbol{v}_n - \dot{\boldsymbol{s}}_0) - \alpha'\boldsymbol{s}' \times [\boldsymbol{s}' \times (\boldsymbol{v}_n - \dot{\boldsymbol{s}}_0)], \tag{6}$$

where α and α' are the temperature-dependent friction coefficients, and $\dot{\boldsymbol{s}}_0$ is calculated from Eq.(5).

The method of the numerical simulation based on this model is described in detail in Schwarz (1985, 1988) and Tsubota *et al.* (2000). A vortex filament is represented by a single string of points with a distance $\Delta\xi$. The vortex configuration at a given time determines the velocity field in the fluid, thus moving the vortex filaments according to Eqs. (5) and (6). Both local and nonlocal terms are represented by means of line elements connecting two adjacent points. As the vortex configuration develops and, particularly, when two vortices approach each other, the distance between neighboring points can change. Then it is necessary to add or remove points properly to retain sufficient local resolution. Through the cascade process, a long vortex can break up through many reconnections, eventually becoming a vortex that is smaller than the space resolution $\Delta\xi$. The simulations cannot follow the dynamics below this resolution, so these vortices are eliminated numerically.

It is important to properly include vortex reconnection when simulating vortex dynamics. A numerical study of a classical fluid showed that the close interaction of two vortices leads to their reconnection, chiefly because of the

viscous diffusion of the vorticity (Boratav *et al.* 1992). Schwarz assumed that two vortex filaments reconnect when they get close within a critical distance, and showed that the statistical quantities such as vortex line density were not sensitive to how to make reconnections. Even after the Schwarz's works, it was still unclear whether quantized vortices can actually reconnect or not. However, Koplik and Levine solved directly the GP equation to show the two close quantized vortices reconnected even in an inviscid superfluid (Koplik and Levine 1993). More recent simulations showed that reconnections were accompanied by acoustic emissions (Leadbeater *et al.* 2001, Ogawa *et al.* 2002).

The analysis of the GP equation, which is another method, can explain well not only the vortex dynamics but also the phenomena concerned with vortex cores such as reconnection and nucleation. However, strictly speaking, the GP equation is not applicable to helium II because it does not have such short-wavelength excitations as rotons which are actually present in this system. The GP equation is well applicable rather to BEC of a dilute atomic Bose gas (Tsubota *et al.* 2002).

2.3   Recent studies on superfluid turbulence

Although our understanding of superfluid turbulence and vortex dynamics has improved, the relation between superfluid turbulence and classical turbulence remains a major unsolved problem (Vinen 2000, Vinen and Niemela 2002). Recent experimental research on superfluid turbulence apart from thermal counterflow has found support for the Kolmogorov law that is one of the most important statistical law in fully developed turbulence. Maurer and Tabeling measured local pressure fluctuations in helium flows driven by two counter-rotating disks in a range of temperature between 1.4 and 2.3 K and obtained the Kolmogorov spectrum above and below T_λ (Maurer and Tabeling 1998). A group at the University of Oregon reported in a series of papers (Smith *et al.* 1993, Stalp *et al.* 1999, Skrbek and Stalp 2000) the attenuation of second sound behind a grid that moved steadily through helium II at temperatures above 1 K. Among these works, Stalp *et al.* measured the decay of grid turbulence in helium II and showed that the experimental results were consistent with a classical model of energy spectrum that included the Kolmogorov law. Then, Vinen analyzed the similarity between superfluid turbulence and classical turbulence (Vinen 2000) and showed the importance of length scales for understanding the energy of the velocity field. For example, although superfluid turbulence is made of a tangle of quantized vortices, the situation depends on whether the length scale is larger or smaller than the vortex line spacing ℓ. Furthermore, at relatively high temperatures, the normal fluid and the superfluid are coupled by mutual friction at all relevant scales larger than ℓ, and hence the system follows the Kolmogorov law at these scales. This theory was shown to be consistent

with the previous experimental results by Stalp *et al.*, thus forming a consistent picture of superfluid turbulence with an appreciable component of normal fluid.

Then appears a very important question; how is the energy spectrum of superfluid turbulence at very low temperatures where the normal fluid component is negligible? This is significant in the following reasons. First, superflow at such low temperatures guarantees that any dissipation could work only at some very small scales. This means the presence of a definite inertial range in which the energy is transferred from larger to smaller scales by the Richardson cascade process. The resulting small vortices whose size becomes close to the coherence length would be unable to keep its vortex nature to change into some elementary excitations, or dissipate by acoustic emission (Vinen 2000), but the inertial range should be independent of such dissipative mechanisms. Second, superfluid turbulence is made of a tangle of quantized vortices. The inertial range of a classical fluid is believed to be sustained by the Richardson cascade, while the identification of each vortex in turbulence is rather obscure. On the other hand, quantized vortices are definite and stable as described before, so that the physical picture of the inertial range and the Richardson cascade could be clearer than that in a classical turbulence. Therefore superfluid turbulence without the normal fluid component may give a typical and simple prototype of turbulence.

There are no experimental studies of the energy spectrum of superfluid turbulence at very low temperatures. Nevertheless, the two numerical works on this topic indicate that the Kolmogorov law also applies to superfluid turbulence at very low temperatures. Starting from a flow that mimicks a Taylor-Green vortex, Nore *et al.* (1997) studied the decaying turbulence by using the GP equation. The energy spectrum showed a transient Kolmogorov form over a range of wave numbers less than ℓ^{-1}, but the acoustic emission is closely connected with the vortex dynamics and the situation is complicated. Our group studied the energy spectrum under the vortex filament formulation and found that the Kolmogorov law should apply to superfluids at very low temperatures (Araki *et al.* 2002). Furthermore we investigated the energy spectrum also by the GP equation very recently.

3. Energy spectrum of superfluid turbulence

3.1 Vortex filament model

To understand whether or not superfluid turbulence realizes the Kolmogorov spectrum at very low temperatures, we calculate the energy spectrum. The energy spectrum is originally calculated by the Fourier transform of the fluid velocity $v(r)$. The superfluid velocity $v_s(r)$ is determined by the configuration of quantized vortices in our vortex filament model. Therefore, we can calculate the energy spectrum directly from the configuration of vortices. This is a big

advantage of this formulation because it makes the numerical calculation of the spectrum less time-consuming than the method via $\boldsymbol{v}(\boldsymbol{r})$. Using the Fourier transform $\widetilde{\boldsymbol{v}}_s(\boldsymbol{k}) = (2\pi)^{-3} \int \mathrm{d}\boldsymbol{r}\boldsymbol{v}_s(\boldsymbol{r})\exp(-\mathrm{i}\boldsymbol{k}\cdot\boldsymbol{r})$ and Parseval's theorem $\int \mathrm{d}\boldsymbol{k}|\widetilde{\boldsymbol{v}}_s(\boldsymbol{k})|^2 = (2\pi)^{-3}\int \mathrm{d}\boldsymbol{r}|\boldsymbol{v}_s(\boldsymbol{r})|^2$, the kinetic energy of the superfluid velocity per unit mass is expressed as

$$E = \frac{1}{2}\int \mathrm{d}\boldsymbol{r}|\boldsymbol{v}_s(\boldsymbol{r})|^2 = \frac{(2\pi)^3}{2}\int \mathrm{d}\boldsymbol{k}|\widetilde{\boldsymbol{v}}_s(\boldsymbol{k})|^2. \tag{7}$$

The vorticity $\boldsymbol{\omega}(\boldsymbol{r}) = \mathrm{rot}\boldsymbol{v}_s(\boldsymbol{r})$ is represented in Fourier space as $\widetilde{\boldsymbol{v}}_s(\boldsymbol{k}) = \mathrm{i}\boldsymbol{k}\times\widetilde{\boldsymbol{\omega}}(\boldsymbol{k})/|\boldsymbol{k}|^2$, so that we have $E = \left((2\pi)^3/2\right)\int \mathrm{d}\boldsymbol{k}|\widetilde{\boldsymbol{\omega}}(\boldsymbol{k})|^2/|\boldsymbol{k}|^2$. The vorticity $\boldsymbol{\omega}(\boldsymbol{r}) = \kappa \int \mathrm{d}\xi \boldsymbol{s}'(\xi)\delta(\boldsymbol{s}(\xi)-\boldsymbol{r})$ in the vortex filament formulation is rewritten as $\widetilde{\boldsymbol{\omega}}(\boldsymbol{k}) = \left(\kappa/(2\pi)^2\right)\int \mathrm{d}\xi \boldsymbol{s}'(\xi)\exp(-\mathrm{i}\boldsymbol{s}(\xi)\cdot\boldsymbol{k})$. Using the definition of the energy spectrum $E(k)$ from $E = \int_0^\infty \mathrm{d}k E(k)$, these relations yield

$$E(k) = \frac{\kappa^2}{2(2\pi)^3}\int \frac{\mathrm{d}\Omega_k}{|\boldsymbol{k}|^2}\int\int \mathrm{d}\xi_1\mathrm{d}\xi_2 \boldsymbol{s}'(\xi_1)\cdot\boldsymbol{s}'(\xi_2)\exp(-\mathrm{i}\boldsymbol{k}\cdot(\boldsymbol{s}(\xi_1)-\boldsymbol{s}(\xi_2))), \tag{8}$$

where $\mathrm{d}\Omega_k = k^2\sin\theta_k \mathrm{d}\theta_k \mathrm{d}\phi_k$ is the surface element in spherical coordinates. This formula connects the energy spectrum directly with the vortex configuration.

Starting from the Taylor-Green vortex in a 1cm-sized cube and following the vortex motion without the mutual friction, we obtained a roughly homogeneous and isotropic vortex tangle (Araki *et al.* 2002). This is a decaying turbulence, being dissipated by a cutoff of the smallest vortices whose size is comparable to the space resolution $\Delta\xi = 1.83 \times 10^{-2}$ cm. At first, the energy spectrum has a large peak at the largest scale where the energy is concentrated, but the spectrum changes as the vortices become homogeneous and isotropic. The time dependence of the energy dissipation rate ϵ shows that $\mathrm{d}\epsilon/\mathrm{d}t$ becomes small after about 70 sec and artifacts of the initial state disappear. Similarly, the isotropic parameters introduced by Schwarz (1988) indicate a nearly isotropic vortex tangle after 70 sec. Figure 1 shows that the energy spectrum of the vortex tangle at 70 sec agrees quantitatively with the Kolmogorov spectrum in small k region. The dissipative mechanism due to the cutoff works only at the largest wave number $k \sim 2\pi/\Delta\xi = 343\,\mathrm{cm}^{-1}$. Note, however, that the energy spectrum at small k region is affected by the dissipation rate. By monitoring the development of the vortex size distribution, such decay of a tangle is found to be sustained by the Richardson cascade process (Tsubota *et al.* 2000). These results support the classical picture of the inertial range in superfluid turbulence at very low temperatures.

The power of the spectrum changes from $-5/3$ to -1 at about $k \sim 2\pi/\ell$. The k^{-1} spectrum comes from the contribution of the velocity near each single vortex. Our simulation of this k^{-1} regime (Vinen *et al.* 2003) indicates that the
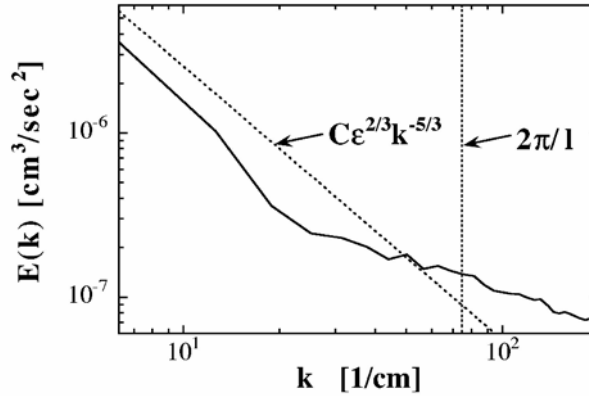
Figure 1. Comparison of the energy spectrum (solid line) numerically obtained at a late stage with the Kolmogorov law (dotted line) with $C = 1$ and $\epsilon = 1.287 \times 10^{-6}$ cm^2/sec^3 (Araki, Tsubota and Nemirovskii, Phys. Rev. Lett. 89, 145301-3, 2002, reproduced with permission. Copyright (2002) by the American Physical Society).

energy cascade is due to the Kelvin wave cascade process. The simulations of Vinen et al. showed that when there is continuous excitation of small k Kelvin waves along a single vortex and if a sink removes the energy at large wave numbers, then the nonlinear coupling between different modes leads to a net flow of energy from small to large wave numbers. This results in a simple steady spectrum of Kelvin waves that is insensitive to the strength and frequency of the excited drive.

A specific picture of vortex tangles at very low temperatures has emerged from these studies. In the low k regime, the vortex tangle has the inertial range in which the Kolmogorov spectrum is realized and the Richardson cascade process describes the energy flow to larger wave numbers; in this regime, superfluid turbulence mimics classical turbulence. In the regime with $k \geq 2\pi/\ell$, the Kelvin wave cascade process is relevant to the transfer of energy to the high wave numbers above which some other mechanism dissipates the energy; this cascade process may be obscure in classical turbulence because the wave number becomes comparable to the Kolmogorov wave number, but it is clearly seen in superfluid turbulence at very low temperatures.

3.2   The GP equation

Very recently we have investigated superfluid turbulence of the GP equation by introducing the dissipation term which works only in scales smaller than the healing length ξ. This dissipation removes sound waves with short wavelength.

Hence, there is no return of the energy from sound waves to vortices, which enables us to study the Kolmogorov law more clearly than the usual GP model,

$$i\frac{\partial}{\partial t}\Phi(\boldsymbol{r}, t) = [-\nabla^2 - \mu + g|\Phi(\boldsymbol{r}, t)|^2]\Phi(\boldsymbol{r}, t). \tag{9}$$

Here μ is the chemical potential and g is a coupling constant. The vortex core size is given by $\xi = 1/\sqrt{g\rho}$.

To solve the GP equation numerically with high accuracy, we use Fourier spectral method in space with the periodic boundary condition in a box with spatial resolutions of 256^3 grids, which makes us solve the Fourier transformed GP equation,

$$i\frac{\partial}{\partial t}\widetilde{\Phi}(\boldsymbol{k}, t) = [k^2 - \mu]\widetilde{\Phi}(\boldsymbol{k}, t)$$
$$+ \frac{g}{V^2}\sum_{\boldsymbol{k}_1, \boldsymbol{k}_2} \widetilde{\Phi}(\boldsymbol{k}_1, t)\widetilde{\Phi}^*(\boldsymbol{k}_2, t) \times \widetilde{\Phi}(\boldsymbol{k} - \boldsymbol{k}_1 + \boldsymbol{k}_2, t). \tag{10}$$

Here V is the volume of the system and $\widetilde{\Phi}(\boldsymbol{k}, t)$ is the spatial Fourier component of $\Phi(\boldsymbol{r}, t)$ with the wave number $\boldsymbol{k}$. We consider the system of $g = 1$. We choose the spatial resolution $\Delta x = 0.125$ and $V = 32^3$ i.e., $\Delta k = 2\pi/32$ where the scale of length is normalized by ξ. The time resolution is $\Delta t = 1 \times 10^{-4}$.

To obtain a turbulent state, we start from an initial configuration where the condensate density ρ_0 is uniform and the phase $\phi_0(\boldsymbol{r})$ has a random spatial distribution. The initial velocity $\boldsymbol{v}(\boldsymbol{r}, t = 0) = 2\nabla\phi_0(\boldsymbol{r})$ is random and produces soon homogeneous and isotropic turbulence with many quantized vortex loops.

Now we introduce a dissipation term in Eq. (10) in order to remove the sound waves whose wavelength is shorter than the healing length; this procedure makes our work completely different from that of Nore *et al.*(1997). The imaginary unit i in the left-hand side of Eq. (10) is replaced by $(i - \gamma(k))$, where $\gamma(k) = \gamma_0\theta(k - 2\pi/\xi)$ with the step function $\theta(x)$. The effect of this dissipation is shown in Fig. 2. We define the total energy

$$E = \frac{1}{\int d\boldsymbol{r}\rho}\int d\boldsymbol{r}\,\Phi^*[-\nabla^2 + \frac{g}{2}|\Phi|^2]\Phi, \tag{11}$$

the kinetic energy

$$E_{kin} = \frac{1}{\int d\boldsymbol{r}\rho}\int d\boldsymbol{r}\,[(|\Phi|\nabla\phi)]^2 \tag{12}$$

and divide E_{kin} to the compressible part $E_{kin}^c = \int d\boldsymbol{r}\,[(|\Phi|\nabla\phi)^c]^2/\int d\boldsymbol{r}\,\rho$ due to sound waves and the incompressible part $E_{kin}^i = \int d\boldsymbol{r}\,[(|\Phi|\nabla\phi)^i]^2/\int d\boldsymbol{r}\,\rho$ by vortices, where $\text{rot}(|\Phi|\nabla\phi)^c = 0$ and $\text{div}(|\Phi|\nabla\phi)^i = 0$ (Nore *et al.* 1997, Ogawa *et al.* 2002). Figure 2 shows the time development of E, E_{kin}, E_{kin}^c and E_{kin}^i in the case of (a) $\gamma_0 = 0$ and (b) 1.
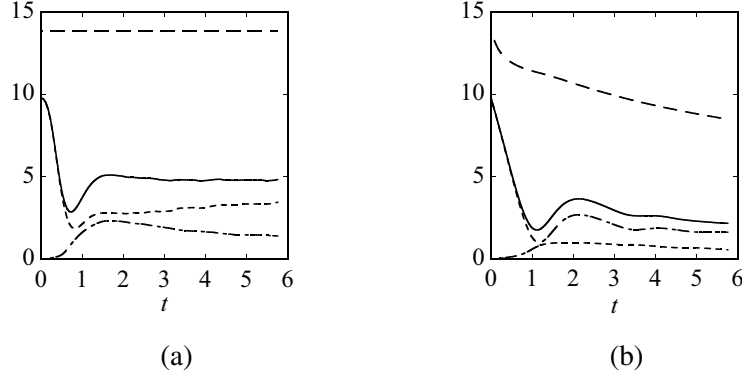
Figure 2. Development of E (long-dashed line), E_{kin} (thick solid line), E^c_{kin} (short-dashed line) and E^i_{kin} (dashed-and-dotted line) with (a) $\gamma_0 = 0$ and (b) 1.

Without dissipation (Fig. 2(a)), the compressible kinetic energy E^c_{kin} is increased with the acoustic emission. Introduction of dissipation (Fig. 2(b)) suppresses E^c_{kin} to make E^i_{kin} more dominant. This dissipation term works only at small scales and gives us the inertial range $\Delta k < k < 2\pi/\xi$ in which the energy is not dissipated.

Then the spectrum of the incompressible kinetic energy $E^i_{kin}(k)$ defined as $E^i_{kin} = \int dk E^i_{kin}(k)$ is expected to take the Kolmogorov form. After a transient period, the spectrum approaches the Kolmogorov power-law. By assuming that the spectrum $E^i_{kin}(k)$ is proportional to $k^{-\eta}$ in the inertial range $\Delta k < k < 2\pi/\xi$, we determine the exponent η, whose time development is shown in Fig. 3 (a). Our superfluid turbulence certainly satisfies the Kolmogorov law $E^i_{kin}(k) \propto k^{-5/3}$ from $t \simeq 4$ to 10. For a quantitative comparison with the Kolmogorov law, we calculate the energy dissipation rate $\epsilon = dE^i_{kin}/dt$. Figure 3 (b) shows that ϵ, therefore the spectrum $\epsilon^{2/3}k^{-\eta}$, is almost invariant in the period $4 \leq t \leq 10$. Eliminating sound waves by the dissipation term $\gamma(k)$ is essential to realize the Kolmogorov law. When $\gamma_0 = 0$, η shows the Kolmogorov power only in the shorter period $4 \leq t \leq 7$; sound waves disturb the inertial range.

The time development of the spatial distribution of vortices is shown in Fig. 4 (a)-(e). It is clear in Fig. 4 (c)-(e) that vortices are making a fully developed turbulence. In Fig. 4 (f), we plot the energy spectrum $E^i_{kin}(k)$ and $E^c_{kin}(k)$ at $t = 5.8$ obtained by taking an ensemble average over 20 different initial states.

The energy spectrum agrees quantitatively with the Kolmogorov law, so that we can find that the incompressible kinetic energy of superfluid turbulence without the effect of compressible sound waves satisfies the Kolmogorov law.

(a)   (b)
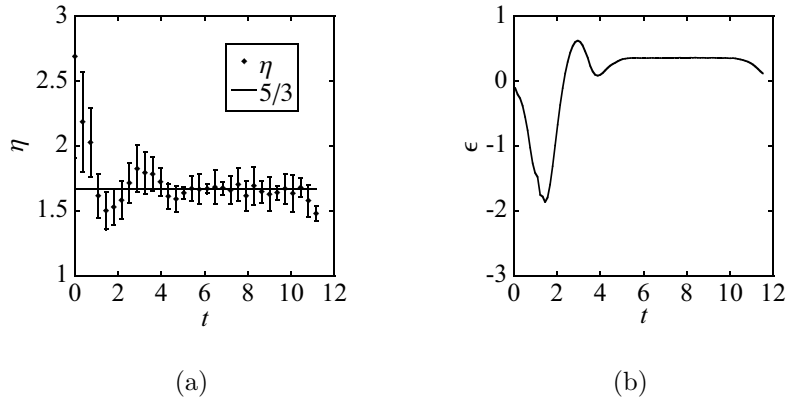
Figure 3.   Time-development of (a) the exponent η of the spectrum and (b) the dissipation rate ϵ. $\gamma_0 = 1$.

(a)   (b)   (c)

(d)   (e)   (f)
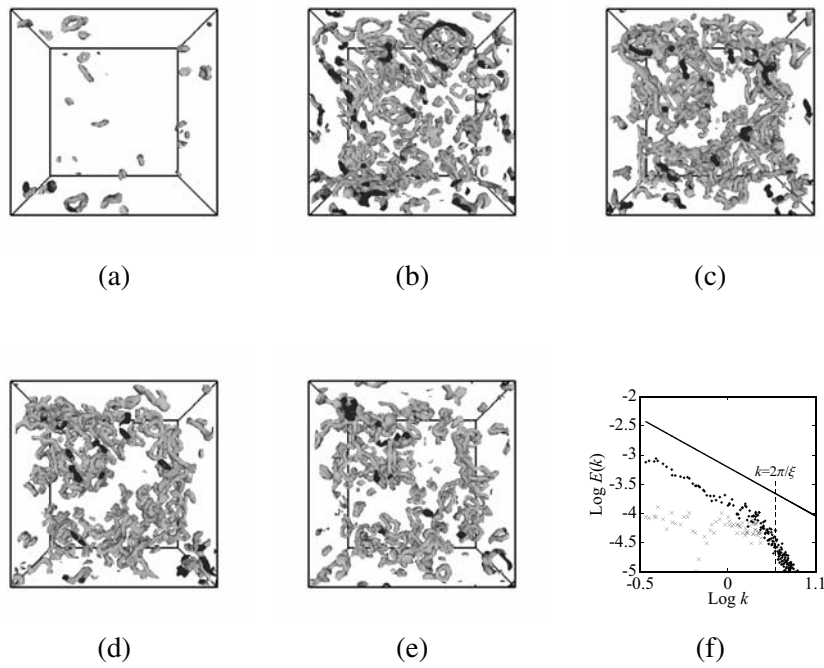
Figure 4.   Isosurface plot of 98% of maximum vorticity $|\mathrm{rot}\boldsymbol{v}(\boldsymbol{r},t)|$ (a)-(e) for $t = 0.5, 2, 4,$ 6 and 8, and (f) the energy spectrum $E_{kin}^i(k)$ at $t = 5.8$. In (f), the energy spectrum of E_{kin}^i (closed circle) and E_{kin}^c (cross) was obtained by taking an ensemble average over 20 different initial states, and the solid line refers to the Kolmogorov law with $C = 1$.

4.   Summary

The recent research activity of superfluld turbulence is entering a new stage rather different from the old ones. After describing the current motivation, we showed our research which studied the energy spectrum both by the vortex filament model and the GP model; the both energy spectra are consistent with the Kolmogorov law. These studies show close similarity between superfluid and classical turbulence, leading to the significant interdisciplinary research.

I am grateful for research collaboration with S. K. Nemirovskii, W. F. Vinen, T. Araki, M. Kobayashi and A. Mitani.

References

ARAKI, T., TSUBOTA, M. & NEMIROVSKII, S.K. 2002 Energy Spectrum of Superfluid Turbulence with No Normal-Fluid Component. *Phys. Rev. Lett.* **89**, 145301(1–4).

BARENGHI, C.F., DONNELLY, R.J. & VINEN, W.F. (EDS.) 2001 *Quantized Vortex Dynamics and Superfluid Turbulence*, Springer.

BORATAV, O.N., PELZ, R.B. & ZABUSKY, N.J. 1992 Reconnection in Orthogonally Interacting Vortex Tubes: Direct Numerical Simulations and Quantifications. *Phys. Fluids A* **4**, 581–605.

DONNELLY, R.J. 1991 *Quntized Vortices in Helium II*, Cambridge University Press.

FEYNMAN, R.P. 1955 Application of quantum mechanics to liquid helium. In *Progress in Low Temperature Physics Vol. 1* (ed. C.J. Gorter), pp. 17–53. North-Holland.

HALL, H.E. & VINEN, W. F. 1956a The rotation of liquid helium II I. Experiments on the propagation of second sound in uniformly rotating helium II. *Proc. Roy. Soc. A* **238**, 204–214.

HALL, H.E. & VINEN, W. F. 1956b The rotation of liquid helium II II. The theory of mutual friction in uniformly rotating helium II. *Proc. Roy. Soc. A* **238**, 215–234.

KOPLIK, J., & LEVINE, H. 1993 Vortex Reconnection in Superfluid Helium. *Phys. Rev. Lett.* **71**, 1375–1378.

LEADBEATER, M., WINIECKI, T., SAMUELS, D.C., BARENGHI, C.F., & ADAMS, C.S. 2001 Sound Emission due to Superfluid Vortex Reconnection. *Phys. Rev. Lett.* **86**, 1410–1413.

MAURER, J. & TABELING, P. 1998 Local Investigation of Superfluid Turbulence. *Europhys. Lett.* **43**, 29–34.

NORE, C., ABID, M. & BRACHET, M.E. 1997 Decaying Kolmogorov Trubulence in a Model of Superflow. *Phys. Fluids* **9**, 2644–2669.

OGAWA, S., TSUBOTA, M. & HATTORI, Y. 2002 Study of Reconnection and Acoustic Emission of Quantized Vortices in Superfluid by hte Numerical Analysis of the Gross-Pitaevskii Equation. *J. Phys. Soc. Jpn.* **71**, 813–821.

SAFFMAN, P.G. 1992 *Vortex Dynamics*, Cambridge University Press.

SCHWARZ, K.W. 1985 Three-dimensional Vortex Dynamics in Superfluid ^{4}He: Line-line and line-boundary interactions. *Phys. Rev. B* **31**, 5782–5804.

SCHWARZ, K.W. 1988 Three-dimensional Vortex Dynamics in Superfluid ^{4}He: Homogeneous Superfluid Turbulence. *Phys. Rev. B* **38**, 2398–2417.

SKRBEK, L. & STALP, S.R. 2000 On the Decay of Homogeneous Isotropic Turbulence. *Phys. Fluids* **12**, 1997–2019.

SMITH, M.R., DONNELLY, R.J., GOLDENFELD, N., & VINEN, W.F. 1993 Decay of Vorticity in Homogeneous Turbulence. *Phys. Rev. Lett.* **71**, 2583–2586.

354

STALP, R.P., SKRBEK, L. & DONNELLY, R.J. 1999 Decay of Grid Turbulence in a Finite Channel. *Phys. Rev. Lett.* **82**, 4831–4834.

TOUGH, J.T. 1982 Superfluid Turbulence. In *Progress in Low Temperature Physics Vol. 8* (ed. D.F. Brewer), pp. 133–219. North-Holland.

TSUBOTA, M., ARAKI, T. & NEMIROVSKII, S.K. 2000 Dynamics of vortex tangle without mutual friction in superfluid ^{4}He. *Phys. Rev. B* **62**, 11751–11762.

TSUBOTA, M., KASAMATSU, K. & UEDA, M. 2002 Vortex Lattice Formation in a Rotating Bose-Einstein Condansate. *Phys. Rev. A* **65**, 023603(1–4).

VINEN, W. F. 1957a Mutual friction in a heat current in liquid helium II I. Experiments on steady heat currents. *Proc. Roy. Soc. A* **240**, 114–127.

VINEN, W. F. 1957b Mutual friction in a heat current in liquid helium II II. Experiments on transient effects. *Proc. Roy. Soc. A* **240**, 128–143.

VINEN, W. F. 1957c Mutual friction in a heat current in liquid helium II III. Theory of the mutual friction. *Proc. Roy. Soc. A* **242**, 493–515.

VINEN, W.F. & NIEMELA, J.J. 2002 Quantum Turbulence. *J. Low Temp. Phys.* **128**, 167–232.

VINEN, W.F. 2000 Classical Character of Turbuelnce in a Quantum Liquid. *Phys. Rev. B* **61**, 1410–1420.

VINEN, W.F., TSUBOTA, M. & MITANI, A. 2003 Kelvin-wave Cascade on a Vortex in Superfluid 4He at a Very Low Temperatures. *Phys. Rev. Lett.* **91**, 135301(1–4).

DECAY OF QUANTUM TURBULENCE BY KELVIN WAVE CASCADE

Akira Mitani, Makoto Tsubota
Department of Physics, Osaka City University
Sugimoto 3-3-138, Sumiyoshi-ku, Osaka 558-8585, Japan
amitani@sci.osaka-cu.ac.jp, tsubota@sci.osaka-cu.ac.jp

W. F. Vinen
School of Physics and Astronomy, University of Birmingham,
Birmingham B15 2TT, United Kingdom
w.f.vinen@bham.ac.uk

Abstract   A study by computer simulation is reported of the behavior of a quantized vortex line at a very low temperature when there is continuous excitation of Kelvin waves with a low wave number. The energy of Kelvin wave is dissipated only at very high wave numbers. It was shown in previous report (Vinen *et al.* 2003) that nonlinear coupling leads to a net flow of energy to higher wave numbers and to the development of a simple spectrum of Kelvin waves. These results are likely to be relevant to the decay of turbulence in superfluid ^{4}He at very low temperatures. To identify the wave number dependence of this spectrum more precisely, we improve the excitation and dissipation method. In this method, the operations of both excitation and dissipation are done in the Fourier space as contrasted with the previous method, whose operations were performed in the real space. The present results are consistent with our previous results not only on the wave number dependence but also on the absolute value. This means the spectrum that we have got is robust one.

Keywords: Quantum turbulence, Kelvin wave

1.   Introduction

Superfluid ^{4}He (helium II) behaves like an irrotational ideal fluid, whose characteristic phenomena can be explained well by the Landau two-fluid model. In this model, the system is described as consisting of two inter-penetrating fractions, the frictionless (superfluid) and viscous (normal) components. A quantized vortices can be formed in superfluid ^{4}He as topological defects that arise from the order parameter in Bose-Einstein condensates. Feynman intro-

duced the concept of superfluid turbulence that consists of a disordered set of quantized vortices, called a vortex tangle. Subsequently, numerous elegant experiments and theories have established the basic properties of this quantum turbulence (Donnelly 1991). It is also well known that mutual friction, which is exerted on a vortex when it moves relative to the normal fluid, is responsible for the decay of quantum turbulence. However, a recent experiment has shown that the quantum turbulence in superfluid ^{4}He decays even at mK temperatures where the normal fluid is so negligible that the mutual friction does not work (Davis, *et al.* 2000). The origin of this decay has remained a mystery. Motivated by this experiment, we study numerically the behavior of a quantized vortex line at a very low temperature.

2. Kelvin wave cascade and decay of quantum turbulence

Quantized vortices can support a transverse and circularly polarized wave motion (a Kelvin wave), with the approximate dispersion relation

$$\omega \approx \frac{\kappa k^2}{4\pi} \left[\log \left(\frac{1}{ka} \right) + c \right] \tag{1}$$

for a rectilinear vortex, where κ is the quantum of circulation, a is the vortex core parameter, and $c \approx 1$. Kelvin waves in uniformly rotating superfluid ^{4}He were first observed experimentally by Hall (1958), and a number of interesting experimental and theoretical studies have been published subsequently; see, for example, the sutudy of nonlinear effects, leading to soliton behavior (Hasimoto 1972) and to an associated side band instability (Samuels & Donnelly 1990).

At temperatures where there is a significant fraction of normal fluid, Kelvin waves in superfluid ^{4}He are damped by mutual friction. This study is concerned with the expected behavior of Kelvin waves at very low temperatures, when damping due to mutual friction can be neglected. Under these conditions Kelvin waves can be damped only by radiation of phonons, but the damping is expected to be extremely small unless the frequency is very large (Vinen 2001). Kelvin waves of lower frequency are essentially undamped. In these circumstances Kelvin waves with low wave numbers can lose energy only by nonlinear coupling to waves of different wave numbers.

We are led therefore to consider the following situation. In quantum turbulence, it is known that the quantized vortices frequently undergo topology-changing reconnections when two vortices in the vortex tangle become close each other. These continual reconnections excite kinks on the vortices, which consist of relatively low wave number Kelvin modes. Nonlinear effects give rise to a transfer of energy to other modes, particularly at higher wave numbers. This process will presumably continue until modes are excited that have a frequency sufficiently high for effective phonon radiation. As a result, the quantum turbulence can decay without mutual friction. It was shown that non-

linear coupling leads to a net flow of energy to higher wave numbers and that there is a steady state, in which energy is injected at a low wave number and dissipated at high wave numbers and there is some well-defined and simple spectrum of Kelvin wave (Vinen *et al.* 2003). To identify the wave number dependence of this spectrum more precisely, we improved the excitation and dissipation method. In this method, the operations of both excitation and dissipation are done in the Fourier space as contrasted with the previous method, whose operations were done in the real space. The present purpose is to get more precise wave number dependence with this new method and to compare the result with our previous one, by means largely of computer simulations.

3. Numerical method

We consider a model system in which the helium is contained in the space between two parallel sheets, separated by distance $l_B = 1$cm, with a single, initially rectilinear, vortex stretched perpendicularly between the two sheets. Kelvin waves can be excited on this vortex. Periodic boundary conditions are applied at each end. Thus the allowed wave numbers of the Kelvin wave are given by

$$k = \frac{2\pi n}{l_B}, \tag{2}$$

where n is an integer (>0).

The dynamical simulations of the vortex are based on the vortex filament model, being similar to those described by Schwartz and used in more recent work by one of the authors (Schwarz 1985, Tsubota *et al.* 2000). The undisplaced vortex lies along the z-axis. The numerical simulation is based on the full Biot-Savart law and therefore both local and non-local contribution are taken into account. Both excitation of Kelvin wave at a low wave number and dissipation at the high wave numbers are operated in Fourier space. The concrete procedure is the following. At every time period $\tau(s)$, the Fourier component $\bar{\zeta}_k$ of the Kelvin wave is renewed to $\bar{\zeta}_k + V_{\mathrm{ex}}$ at $k = k_{\mathrm{ex}}$, and to 0 at all wave numbers larger than k_{dis}. Then, the motion of the vortex is simulated using full Biot-Savart law.

4. Results

Figure 1 shows the tempoal evolution of the line length after the application of an operation with $V_{\mathrm{ex}} = 7.81 \times 10^{-4}$cm, $k_{\mathrm{ex}} = 10\pi(\mathrm{cm}^{-1})$, $k_{\mathrm{dis}} = 246\pi(\mathrm{cm}^{-1})$, $\tau = 10(\mathrm{s})$. The almost flat line over $3.4 \times 10^4 < t < 5 \times 10^4$ suggests the existence of a steady state. As we turned off only excitation (dissipation is still effective) at $t = 5 \times 10^4(\mathrm{s})$, the line length suddenly decreases. This implies that the energy of Kelvin wave injected at a low wave number
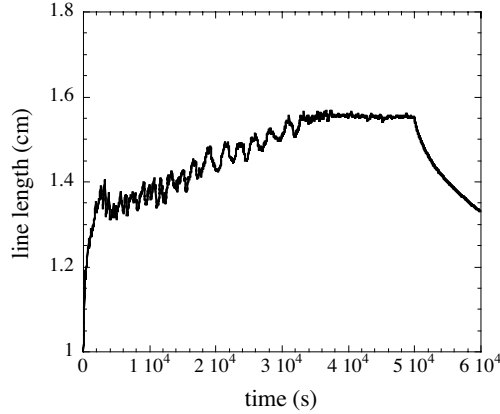
Figure 1. The development in time of the total length of the vortex line. The excitation is turned off at $t = 5 \times 10^4 (s)$.

escapes at high wave numbers, hence there is a net flow of energy to higher wave numbers caused by nonlinear coupling of vortex dynamics.

We express our more detailed results in terms of the root mean square amplitudes $\bar{\zeta}_k(t) = \langle \zeta_k^* \zeta_k \rangle^{1/2}$ of the Fourier components of the displacement of the vortex. Figure 2 shows how these amplitudes develop in time. Initially only the mode that resonates with the drive is excited. As time passes, nonlinear interactions lead to the excitation of all other modes. Eventually the spectrum reaches a steady state, shown by the solid line. For large values of k, the steady state is observed to have, to a good approximation, a spectrum of the simple form (Vinen *et al.* 2003)

$$\bar{\zeta}_k^2 \propto k^{-3}. \tag{3}$$

Figure 3 shows the comparison of our new and old results. They are consistent not only on the wave number dependence but also on the absolute value, especially at large values of k. This result suggests that the simple spectrum power-law (3) is concerned with the robust property of Kelvin wave cascade in the steady state. However, some recent analytical and numerical studies have reported slightly different power-law behavior ($\bar{\zeta}_k^2 \propto k^{-17/5} = k^{-3.4}$) in quasi-steady state (Kozik *et al.* 2004). We are trying to identify much more accurate power-law behavior to settle the controversy between ours and other recent results.
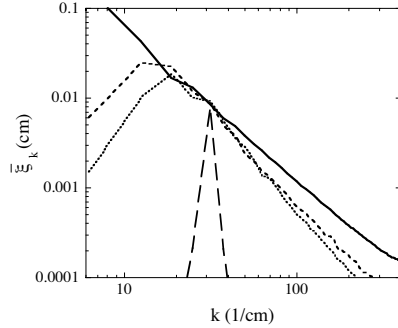
Figure 2. The time development of $\bar{\zeta}_k$. The long-dashed line, dotted line, short-dashed line, and the solid line refer to averages over 0-200, 400-600, 800-1000, 40000-40200 s, respectively. The solid line relates to the steady state.
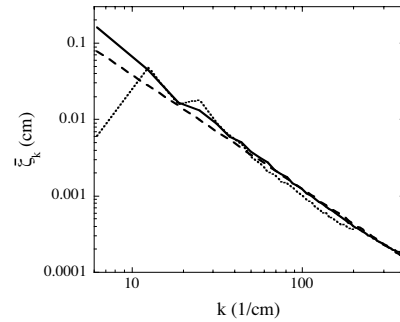
Figure 3. Steady-state values of $\bar{\zeta}_k$ for two different methods of excitation and damping. The dotted line is obtained by real space method, whereas the solid line by the wave number space method. The long-dashed line has the form of Eq.(3).

5. Summary

We have reported the results of numerical simulations of the behavior of Kelvin waves on a rectilinear quantized vortex of finite length in superfluid ^{4}He at a temperature so low that the waves suffer no attenuation arising from mutual friction with the normal fluid, the only attenuation arising from phonon radiation at a very high wave number. A low wave number wave is excited periodically. The amplitude of the driven mode increases until nonlinear coupling leads to a transfer of energy to all other modes. A steady state is established, described by a simple spectrum, whose wave number dependence is written as $\bar{\zeta}_k^2 \propto k^{-3}$ same as our previous result.

References

Davis, S.L, Hendry, P.C. & McClintock, P.V.E. 2000 Decay of quantized vorticity in superfluid ^{4}He at mK temperatures. *Physica B* **280**, 43.

Donnelly, R.J. 1991 *Quantized Vortices in Helium II* (Cambridge University Press).

Hall, H. E.1958 An Experimental and Theoretical Study of Torsional Oscillations in Uniformly Rotating Liquid Helium II. , *Proc. R. Soc. London, Ser. A* **245**, 546.

Hasimoto, H. 1972 A soliton on a vortex filament. *J. Fluid Mech.* **51** 477.

Kozik, E. V. & Svistunov, B. 2004 Kelvin-Wave Cascade and Decay of superfluid Turbulence. *Phys. Rev. Lett.* **92**, 035301, and Scale Separation Scheme for Simulating Superfluid Turbulence: Kelvin-Wave Cascade. *cond-mat*/0408241.

Samuels, D.C., & Donnelly, R.J. 1990 Sideband Instability and Recurrence of Kelvin Waves on Vortex Cores. *Phys. Rev. Lett.* **64**, 1385.

Schwarz, K. W. 1985 Three-dimensional vortex dynamics in superfluid [4]He: Line-line and line-boundary interactions *Phys. Rev. B* **61**, 1410.

Tsubota, M., Araki, T. & Nemirovskii, S.K. 2000 Dynamics of vortex tangle without mutual friction in superfluid [4]He. *Phys. Rev. B* **62**, 11751.

Vinen, W.F. 2001 Classical Character of Turbulence in a Quantum Liquid. *Phys. Rev. B* **61**, 1410.

Vinen, W.F., Tsubota, M. & Mitani, A. 2003 Kelvin-Wave Cascade on a Vortex in Superfluid [4]He at a Very Low Temperature. *Phys. Rev. Lett.* **91**, 135301.

FLOW PHASE DIAGRAM FOR THE HELIUM SUPERFLUIDS

Ladislav Skrbek
Joint Low Temperature Laboratory, Institute of Physics ASCR and Faculty of Mathematics and Physics, Charles University,
V Holesovickach 2, 180 00 Prague, Czech Republic
skrbek@fzu.cz

Abstract   The flow phase diagram predicted by Volovik (2003) is discussed based on available experimental data for He II and ^{3}He-B superfluids. The effective temperature-dependent but scale-independent Reynolds number $Re_{eff} = 1/q \equiv (1-\alpha')/\alpha$, where α and α' are the mutual friction parameters, and the superfluid Reynolds number characterizing the circulation of the superfluid component in units of the circulation quantum are used as the dynamic parameters.

Keywords: Superfluid, helium, quantum turbulence, mutual friction

1.   Introduction

The flow of quantum liquids such as He II or ^{3}He-B can be described in the framework of the two fluid model (see, e.g., Tough 1982), assuming the quantum liquid as consisting of two interpenetrating fluids — the inviscid superfluid and the viscous normal fluid. Circulation in the superfluid component is quantized in units of κ (0.997×10^{-3} cm^2/s for He II and 0.662×10^{-3} cm^2/s for ^{3}He-B); we assume singly quantized vortices. We consider flows that can be approximated as isothermal. Quantized vortices couple the normal fluid and the superfluid velocity fields by mutual friction (Vinen 1957).

2.   Hydrodynamic continuous approach to superfluid turbulence

Following the approach of Volovik (2003, 2004), let us assume that the quantized vortices in the flow are arranged in such a way that the coarse-grained hydrodynamic equation,

$$\frac{\partial \mathbf{v}}{\partial t} + \boldsymbol{\nabla}\mu = \mathbf{v} \times \boldsymbol{\omega} + q\hat{\boldsymbol{\omega}} \times (\boldsymbol{\omega} \times \mathbf{v}), \tag{1}$$

361

obtained from the Euler equation after averaging over vortex lines (see Sonin 1987), provides a sufficiently accurate description of the superflow velocity field **v**. It is written in the frame of reference of the normal fluid — such a possibility arises for ^{3}He-B, whose highly viscous normal component is effectively clamped by the walls in a laboratory size container and possibly also in He II at fairly low temperatures $\simeq 1$ K and below (Donnelly & Barenghi 1998). Here $q = \alpha/(1 - \alpha')$, where α and α' are the dimensionless mutual friction parameters, μ denotes the chemical potential, $\boldsymbol{\omega} = \nabla \times \mathbf{v}$ is the coarse-grained vorticity and $\hat{\boldsymbol{\omega}}$ is a unit vector in the direction of $\boldsymbol{\omega}$. The analysis of the fluid dynamical problem based on this equation has been performed in Volovik (2003, 2004), and L'vov *et al.* (2004). As it was first emphasized in Finne (2003), Eq. (1) has a very remarkable property which makes it distinct from the ordinary Navier-Stokes equation where the relative importance of the inertial and dissipative terms is given by the Reynolds number, which in turn depends on the geometry of the particular flow under study. Here the role of the effective Reynolds number is played by the parameter $Re_{eff} = q^{-1} = (1 - \alpha')/\alpha$ that depends on temperature via the dimensionless mutual friction parameters α and α', but not on geometry.

A wide range of q values is easily experimentally achievable; with q increasing with temperature in both He II (Donnelly & Barenghi 1998) and ^{3}He-B (Bevan *et al.* 1997). Like the usual Navier-Stokes equation, Eq. (1) has both laminar ($q \gg 1$) and turbulent ($q \ll 1$) solutions. It was claimed, however, that the 3D energy spectrum is of usual (possibly logarithmically corrected) Kolmogorov form $E(k) \cong \varepsilon^{2/3} k^{-5/3}$ (Volovik 2003, 2004). Vinen (2004) recently developed a different approach, based on physical arguments concerning the turnover and decay times of eddies of various sizes, confirmed by numerical solutions of a second-order diffusion equation that describes flow of turbulent energy in k-space. Owing to the action of mutual friction, there is strong damping of large eddies, with the result that at low wave numbers the energy spectrum falls much more rapidly (approaching k^{-3}) than the Kolmogorov spectrum. However, the damping remains weak for small eddies, so that the Kolmogorov spectrum is recovered for large k, beyond a certain critical wave number. Vinen also correctly points out that this feature is inherently contained in Eq. (1). The most recent theoretical discussion of this issue by L'vov *et al.* (2004), based on the analytical solution of the first-order k-space diffusion equation, confirms the crucial role of mutual friction force on a large scale. Although this interesting problem of superfluid turbulence in the presence of a stationary normal fluid is most likely not yet fully settled, we believe that the main features of such a turbulent superflow have been firmly established.

3. Continuous versus quantum description of superfluid turbulence

The continuous approach for considering superfluid turbulence based on Eq. (1) would be fully applicable in the limit $\kappa \to 0$. As pointed out in Volovik (2003, 2004), at finite κ one has to ensure that at all scales, including the smallest scale r_0, the "granularity" due to individual vortices does not become important, so that the circulation $v_{r0}r_0 \gg \kappa$.

In order to apply an analysis based on Eq. (1) to superflow, we must bear in mind that this coarse-grained equation sufficiently accurately describes the superfluid velocity field on the scale over which the averaging is done. This approach cannot therefore include initial conditions similar to those commonly believed to apply in counterflow turbulence in He II if only a single scale is assumed. Such a distribution of vortices is described by the phenomenological Vinen equation (Vinen 1957). It is well known and in agreement with local induction approximation simulations (Schwarz 1988) that there is a critical self-sustaining counterflow velocity, above which the turbulence is in dynamical equilibrium and, at least approximately, homogeneous.

Now let us increase the counterflow velocity U_{cf}, assuming that the normal fluid velocity profile remains flat, and continue the discussion in the reference frame where the normal fluid is at rest. It is an established experimental fact that another transition from turbulent state I to turbulent state II occurs, with distinctly different features, in accord with Tough's classification scheme (Tough 1982). It has been a long lasting challenge to explain the nature of this transition. We believe that the answer might be hidden in Volovik's analysis. He suggests the existence of the flow phase diagram (Volovik 2003, 2004, see also L'vov *et al.* (2004), where this result is confirmed) that contains a crossover between what he calls the Kolmogorov and Vinen states of superfluid turbulence when $Re_s q^2 \simeq 1$.

4. Experimental data supporting the existence of the flow phase diagram

There are many experimental data that can be used in order to probe the existence of the phase diagram suggested by Volovik as we show in Fig. 1. The recent experiment of Finne *et al.* (2003) provides evidence for a velocity independent transition from a laminar to a turbulent flow regime in rotating ^{3}He-B, where values of q of order unity are experimentally easily accessible.

In He II these large values of q occur very close to the lambda point, where, to our knowledge, no reliable measurements exist that can be considered in the frame of reference of the normal fluid. On the other hand, there is ample experimental data on counterflow He II turbulence at lower temperatures. However, the data on the transition into superfluid state I (Vinen state) in tubes and capil-
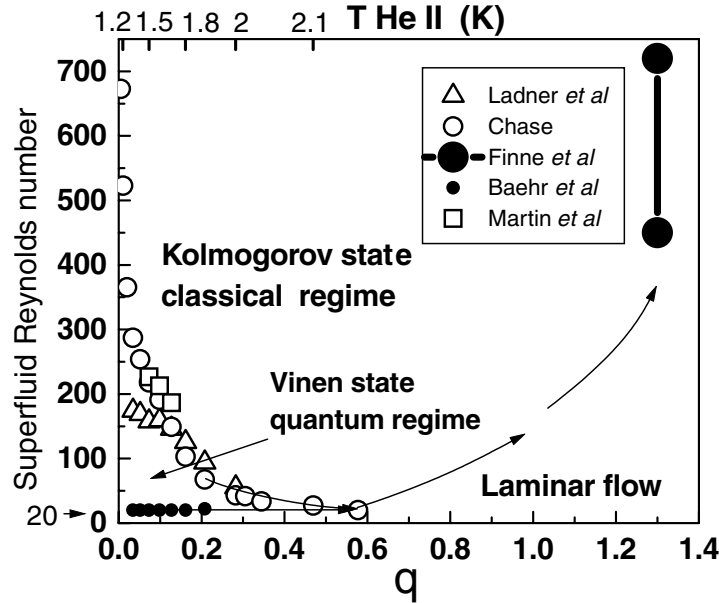
Figure 1. The observed flow phase diagram of He II and ^{3}He -B superfluids in the unique frame of reference where the normal fluid is at rest. The abscissa, q, represents the inverse of the Reynolds number for superflow (for convenience the corresponding temperature in He II is indicated on the upper axis), while the ordinate, Re_s, represents the strength of circulation at the outer scale of the flow in units of κ. The two big connected filled points mark approximately the region where the velocity-independent onset of superfluid turbulence has been observed by various methods of vortex loop injection into rotating ^{3}He-B in the vortex-free Landau state (for $\Delta T \approx 0.05\ T_c$ around 0.6 T/T_c at 29 bar, see Fig. 3 in Finne et al. 2003). The small filled circles represent the onset of turbulent state I in pure superflow of He II when the motion of the normal fluid was inhibited by superleaks (Baehr et al. 1983); the crosses (Ladner et al. 1976), open squares (Martin & Tough 1983) and open circles (Chase 1962) mark the transition from state I into state II for counterflowing He II.

laries of various sizes cannot be reliably used here, as it is believed that below this threshold the viscous normal fluid possesses a velocity profile similar to ordinary viscous flow in a pipe. A unique frame of reference is not, therefore, provided by the normal fluid. However, Baehr *et al.* (1983) studied the transition from dissipationless superflow to homogeneous superfluid turbulence, when both ends of the pipe were blocked by superleaks and the normal fluid inside the pipe thus remains stationary (at least on average), thereby providing this unique frame of reference. These data, spanning the temperature range 1.3 K $< T <$ 1.9 K, mark the transition from laminar flow into the Vinen state (state I) shown in Fig. 1.

That the existence of the normal fluid reference frame is important can be demonstrated using a different set of data of Baehr and Tough (1984) obtained for flows where at a fixed temperature the normal and superfluid velocities can be varied independently. If the normal fluid flow profile were flat, one would expect that the critical counterflow velocity for transition into turbulent state I, simply as a consequence of the Galilean invariance, stays unchanged. This does not happen, as the observed critical counterflow velocity increases with the imposed averaged normal fluid velocity, supposedly due to the fact that its flow profile is not flat.

Various counterflow experiments clearly display the transition from state I (Vinen) into state II (Kolmogorov) — the signature is pronounced on temperature and pressure difference versus heat input dependencies. We use here the data of Tough's group (Ladner *et al.* 1976 – Table I, and Martin & Tough 1983), assuming that in state I the normal fluid profile is flat, again providing the unique frame of reference with the normal fluid at rest. Let us point out that this transition into a different flow regime is accompanied with a pronounced increase of fluctuations (Lorenson *et al.* 1985), characteristic of phase transitions. The data of Ladner *et al.* (1976) also clearly show that on increasing the temperature the difference in counterflow velocity between state I and II transitions decreases until around 2 K they become indistinguishable.

The crossover to superfluid turbulence state II has been observed in channels of circular and square crossection, but not in narrow channels of high aspect ratio rectangular crossection (Henberger & Tough 1981). Naturally, the transition cannot take place if the size of the sample intervenes. If some dimension of the channel is too small, its physical size limits the size of eddies.

As another set of experimental data marking the state I-state II transition we have used the thermal conduction measurements of He II in tubes of various diameters of Chase (1962). We have scanned the available experimental data and found that they collapse onto a single curve if Reynolds number scaling is applied. The open circles in Fig. 1 correspond to the onset of state II.

We emphasize that the procedure used to acquire the data points shown in the flow diagram is probably not very accurate for several reasons, such as different temperature scales or uncertainty in values of q, and more work is needed to map it out accurately. We believe, however, that the essential physics is displayed clearly and that Fig. 1 supports the ideas underlying the physical problem of superfluid turbulence.

Acknowledgements

366

References

BAEHR, M.L., OPATOWSKY, L.B. & J.T. TOUGH 1983 Transition from dissipationless superflow to homogeneous superfluid turbulence. *Phys. Rev. Lett.* **51**, 2295–2298.

BAEHR, M.L. & J.T. TOUGH 1984 Critical velocity in two-fluid flow of He II. *Phys. Rev. Lett.* **53**, 1669–1672.

BEVAN, T.D.C., MANNINEN, A.J., COOK, J.B., ALLES, H., HOOK, J.R. & HALL, H.E. 1997 Vortex mutual friction in superfluid ^{3}He. *J. Low Temp. Phys.* **109**, 423–460.

CHASE, C.E. 1962 Thermal conduction in Helium II. Temperature dependence. *Phys. Rev.* **127**, 361–370; Effects of channel geometry. *Phys. Rev.* **131**, 1898–1903.

DONNELLY, R.J. & BARENGHI, C.F. 1998 The observed properties of liquid helium at the saturated vapor pressure. *J. Phys. Chem. Data* **27** 1217–1274.

FINNE, A.P., ARAKI, T., BLAAUWGEERS, R., ELTSOV, V.B., KOPNIN, N.B., KRUSIUS, M., SKRBEK, L., TSUBOTA, M & VOLOVIK, G.E 2003 An intrinsic velocity-independent criterion for superfluid turbulence. *Nature* **424**,1022–1025.

HENBERGER, J.D. & TOUGH J.T. 1981 C.P. Geometric effects on superfluid turbulence: Rectangular, square, and circular tubes compared. *Phys. Rev. B* **23**, 413–414.

LADNER, D.R., CHILDERS, R.K. & TOUGH, J.T. 1976 Helium II thermal counterflow at large heat currents. *Phys. Rev. B* **13**, 2918–2923.

LORENSON, C.P., GRISWOLD, D., NAYAK, V.U. & TOUGH J.T. 1985 Dynamic features of superfluid turbulence near the second critical heat current. *Phys. Rev. Lett.* **55**, 1494-1497.

L'VOV, V.S., NAZARENKO, S.V. & VOLOVIK, G.E. 2004 Energy spectra of developed superfluid turbulence. *Pis'ma v ZHETF* **80**, 546–550.

MARTIN, K.P. & TOUGH J.T 1983 Evolution of superfluid turbulence in thermal counterflow. *Phys. Rev. B* **27**, 2788–2799.

SCHWARZ, K.W. 1988 Three-dimensional vortex dynamics in superfluid ^{4}He: Homogeneous superfluid turbulence. *Phys. Rev. B* **38**, 2398–2417.

SONIN, E.B. 1987 Vortex oscillations and hydrodynamics of rotating superfluids *Rev. Mod. Phys.* **59**, 87–155.

TOUGH, J.T. 1982 Superfluid turbulence. In *Prog. in Low Temp. Phys.* (ed. D.F. Brewer) Vol.VIII, North-Holland, Amsterdam pp. 133–218.

VINEN, W.F. 1957 Mutual friction in a heat current in liquid helium II. *Proc. Roy. Soc. A* **240** 114–127, 128–143; **242** 493–515; **243** 400–413.

VINEN, W.F. 2004 The theory of quantum grid turbulence in superfluid ^{3}He-B. submitted to *Phys. Rev. B*.

VOLOVIK, G.E. 2003 Classical and quantum regimes of superfluid turbulence. *JETP Letters* **78**, 553–557.

VOLOVIK, G.E. 2004 On developed superfluid turbulence. *J. Low Temp. Phys.* **136**, 309–328.

List of Participants

Abe, Hiroyuki
Japan Aerospace Exploration Agency
Japan
habe@chofu.jaxa.jp

Arimitsu, Toshihico
Graduate School Pure & Appl. Sci.
University of Tsukuba
Japan
arimitsu@cm.ph.tsukuba.ac.jp

Bajer, Konrad
Institute of Geophysics
Warsaw University
Poland
kbajer@fuw.edu.pl

Brasseur, James G.
Dept. Mechanical Engineering
Pennsylvania State University
USA
brasseur@psu.edu

Chakraborty, Pinaki
Dept. Theor. & Appl. Mech.
Univ. Illinois at Urbana-Champaign
USA
chakrabo@uiuc.edu

Chong, Min Seong
Dept. Mech. & Manufacturing Eng.
University of Melbourne
Australia
min@unimelb.edu.au

Arimitsu, Naoko
Graduate School of EIS
Yokohama National University
Japan
arimitsu@ynu.ac.jp

Asai, Masahito
Dept. Aerospace Engineering
Tokyo Metro. Inst. Tech.
Japan
masai@cc.tmit.ac.jp

Brachet, Marc-Etienne
Laboratoire de Physique Statistique
Ecole Normale Superieure
France
marc_brachet@noos.fr

Brethouwer, Geert
Japan Aerospace Exploration Agency
Japan
geert@chofu.jaxa.jp

Chomaz, Jean-Marc
Laboratoire d'Hydrodynamique
CNRS-Ecole Polytechnique
France
chomaz@ladhyx.polytechnique.fr

Constantin, Peter
Dept. Mathematics
University of Chicago
USA
const@cs.uchicago.edu

Donnelly, Russell J.
University of Oregon
USA
russ@vortex.uoregon.edu

Dritschel, David
Dept. Applied Mathematics
University of St Andrews
UK
dgd@mcs.st-and.ac.uk

Frisch, Uriel
Laboratoire Cassiopee
Observatoire de la Cote d'Azur
France
uriel@obs-nice.fr

Fukuda, Kota
Dept. Mechanical Engineering
Yokohama National University
Japan
d02sb104@ynu.ac.jp

Fukumoto, Yasuhide
Graduate School of Mathematics
Kyushu University
Japan
yasuhide@math.kyushu-u.ac.jp

Fukunishi, Yu
Dept. Mechanical Engineering
Tohoku University
Japan
fushi@fluid.mech.tohoku.ac.jp

Funakoshi, Mitsuaki
Graduate School of Informatics
Kyoto University
Japan
mitsu@i.kyoto-u.ac.jp

Goto, Susumu
Dept. Mech. Eng. & Sci.
Kyoto University
Japan
goto@mech.kyoto-u.ac.jp

Gotoh, Toshiyuki
Graduate School of Engineering
Nagoya Institute of Technology
Japan
gotoh@system.nitech.ac.jp

Hanazaki, Hideshi
Dept. Mech. Eng. & Sci.
Kyoto University
Japan
hanazaki@mech.kyoto-u.ac.jp

Hanninen, Risto M.
Dept. Physics
Osaka City University
Japan
rhannine@sci.osaka-cu.ac.jp

Hirata, Katsuya
Dept. Mechanical Engineering
Doshisha University
Japan
khirata@doshisha.ac.jp

Horiuti, Kiyosi
Dept. Mechano-Aerospace Eng.
Tokyo Institute of Technology
Japan
khoriuti@mes.titech.ac.jp

Hussain, Fazle
Dept. Mechanical Engineering
University of Houston
USA
fhussain@uh.edu

Ishioka, Keiichi
Dept. Geophysics
Kyoto University
Japan
ishioka@gfd-dennou.org

Ito, Yasumasa
Dept. Mech. Eng. & Sci.
Kyoto University
Japan *ito@mech.kyoto-u.ac.jp*

Izawa, Seiichiro
Dept. Mechanical Engineering
Tohoku University
Japan
izawa@fluid.mech.tohoku.ac.jp

Jiménez, Javier
School of Aeronautics
Spain
jimenez@torroja.dmt.upm.es

Kawahara, Genta
Dept. Aeronautics & Astronautics
Kyoto University
Japan
gkawahara@kuaero.kyoto-u.ac.jp

Kida, Shigeo
Dept. Mech. Eng. & Sci.
Kyoto University
Japan
kida@mech.kyoto-u.ac.jp

Kin, Eiko
Dept. Mathematics
Kyoto University
Japan
kin@math.kyoto-u.ac.jp

Itano, Tomoaki
Dept. Aeronautics & Astronautics
Kyoto University
Japan
itano@kuaero.kyoto-u.ac.jp

Iwayama, Takahiro
Graduate School of Sci. & Tech.
Kobe University
Japan
iwayama@kobe-u.ac.jp

Izshizawa, Toshiaki
Dept. Astronomy
Kyoto University
Japan
ishizawa@kusastro.kyoto-u.ac.jp

Kaga, Yoshito
Grad. Sch. Natural Sci. & Tech.
Okayama University
Japan
kaga@et2001.mech.okayama-u.ac.jp

Kerr, Robert M.
School of Engineering
University of Warwick
UK
robert.kerr@warwick.ac.uk

Kimura, Yoshi
Graduate School of Mathematics
Nagoya University
Japan
kimura@math.nagoya-u.ac.jp

Kitamura, Yuji
Dept. Geophysics
Kyoto University
Japan
kitamura@kugi.kyoto-u.ac.jp

Komori, Satoru
Dept. Mech. Eng. & Sci.
Kyoto University
Japan
komori@mech.kyoto-u.ac.jp

Kuwahara, Haruka
Dept. Mech. Sci.& Eng.
Nagoya University
Japan
haruka@sps.mech.nagoya-u.ac.jp

Mashiko, Takashi
Dept. Physics
University of Tokyo
Japan
mash@daisy.phys.s.u-tokyo.ac.jp

Matsumoto, Takeshi
Dept. Physics
Kyoto University
Japan
takeshi@kyoryu.scphys.kyoto-u.ac.jp

Matsuo, Yuichi
Japan Aerospace Exploration Agency
Japan
matsuo.yuichi@jaxa.jp

Mitani, Akira
Dept. Physics
Osaka City University
Japan
amitani@sci.osaka-cu.ac.jp

Miyauchi, Toshio
Dept. Mech. & Aero. Eng.
Tokyo Institute of Technology
Japan
tmiyauch@mes.titech.ac.jp

Miyazaki, Takeshi
Dept. Mech. Eng. & Intel. Sys.
Univ. Electro-Communications
Japan
miyazaki@mce.uec.ac.jp

Mizuno, Yoshinori
Kyoto University
Japan
mizuno@acs.i.kyoto-u.ac.jp

Moffatt, H. Keith
Dept. Appl. Math.& Theor. Phys.
University of Cambridge
UK
h.k.moffatt@damtp.cam.ac.uk

Moisy, Frederic
Laboratoire Fluides, Automatique
et Systemes Thermiques
France
moisy@fast.u-psud.fr

Mouri, Hideaki
Meteorological Research Institute
Japan
hmouri@mri-jma.go.jp

Nagata, Kouji
Dept. Mech. Eng. & Sci.
Kyoto University
Japan
nagata@mech.kyoto-u.ac.jp

Nagata, Masato
Dept. Aeronautics & Astronautics
Kyoto University
Japan
nagata@kuaero.kyoto-u.ac.jp

Nemirovskii, Sergey K.
Institute for Thermophysics
Russia
nemir@itp.nsc.ru

Nishioka, Michio
Dept. Aerospace Engineering
Osaka Prefecture University
Japan
nishioka@aero.osakafu-u.ac.jp

Ogasawara, Takeshi
Dept. Physics
Kyoto University
Japan
ogasawara@kyoryu.scphys.kyoto-u.ac.jp

Ohkitani, Koji
Res. Inst. Math. Sci.
Kyoto University
Japan
ohkitani@kurims.kyoto-u.ac.jp

Orlandi, Paolo
Dept. Mechanics & Aeronautics
University of Rome "La Sapienza"
Italy
orlandi@kolmogorov.ing.uniroma1.it

Otheguy, Pantxika
Laboratoire d'Hydrodynamique
CNRS-Ecole Polytechnique
France
pantxika.otheguy@ladhyx.polytechnique.fr

Petitjeans, Philippe
Ecole Superieure de Physique
et de Chimie Industrielles
France
phil@pmmh.espci.fr

Pullin, Dale I.
Graduate Aeronautical Laboratories
California Institute of Technology
USA
dale@galcit.caltech.edu

Ricca, Renzo L.
Dept. Mathematics & Applications
University of Milano-Bicocca
Italy
ricca@matapp.unimib.it

Rubinstein, Robert
NASA Langley Research Center
USA
r.rubinstein@larc.nasa.gov

Ruppert-Felsot, Jori E.
Center for Nonlinear Dynamics
University of Texas at Austin
USA
jori@chaos.ph.utexas.edu

Sakai, Yasuhiko
Dept. Mech. Sci. & Eng.
Nagoya University
Japan
ysakai@mech.nagoya-u.ac.jp

Sakajo, Takashi
Dept. Mathematics
Hokkaido University
Japan
sakajo@math.sci.hokudai.ac.jp

Sakakibara, Jun
University of Tsukuba
Japan
sakakibara@loz.tsukuba.ac.jp

Sasaki, Yoshi K.
School of Meteorology
The University of Oklahoma
USA
sasaki@ou.edu

Shimomura, Yutaka
Dept. Physics
Keio University
Japan
yutaka@phys-h.keio.ac.jp

Takahashi, Naoya
Dept. Mech. Eng. & Intel. Sys.
Univ. Electro-Communications
Japan
naoya@mce.uec.ac.jp

Toh, Sadayoshi
Dept. Physics
Kyoto University
Japan
toh@kyoryu.scphys.kyoto-u.ac.jp

Tsubota, Makoto
Dept. Physics
Osaka City University
Japan
tsubota@sci.osaka-cu.ac.jp

Ueno, Kazuyuki
Dept. Aerospace Engineering
Tohoku University
Japan
ueno@cfd.mech.tohoku.ac.jp

Vassilicos, J. Christos
Dept. Aeronautics
Imperial College London
UK
j.c.vassilicos@imperial.ac.uk

Sharon, Eran
The Racah Institute of Physics
The Hebrew University of Jerusalem
Israel
erans@vms.huji.ac.il

Skrbek, Ladislav
Inst. Phys. ASCR & Charles Univ.
Joint Low Temperature Laboratory
Czech Republic
skrbek@fzu.cz

Tatsumi, Tomomasa
Kyoto University
Japan
tatsumi@skyblue.ocn.ne.jp

Toyoda, Kuniaki
Hokkaido Institute of Technology
Japan
toyoda@bit.ac.jp

Tsuji, Yoshiyuki
Dept. Energy Eng. & Sci.
Nagoya University
Japan
c42406a@nucc.cc.nagoya-u.ac.jp

van Veen, Lennaert
Dept. Mech. Eng. & Sci.
Kyoto University
Japan
veen@mech.kyoto-u.ac.jp

Vinen, William F.
School of Physics & Astronomy
University of Birmingham
UK
w.f.vinen@bham.ac.uk

Watanabe, Takeshi
Dept. Mech. Eng. Appl. Phys. Prog.
Nagoya Institute of Technology
Japan
watanabe@nitech.ac.jp

Xiong, Ao-kui
Dept. Mechanical Engineering
Tohoku University
Japan
xiong@fluid.mech.tohoku.ac.jp

Yoden, Shigeo
Dept. Geophysics
Kyoto University
Japan
yoden@kugi.kyoto-u.ac.jp

Wells, John
Ritsumeikan University
Japan
jwells@se.ritumei.ac.jp

Yamada, Michio
Res. Inst. for Math. Sci.
Kyoto University
Japan
yamada@kurims.kyoto-u.ac.jp

Mechanics

1. M. Lesieur: *Turbulence in Fluids.* 2nd rev. ed., 1990   ISBN 0-7923-0645-7
2. O. Métais and M. Lesieur (eds.): *Turbulence and Coherent Structures.* 1991
                                                                        ISBN 0-7923-0646-5
3. R. Moreau: *Magnetohydrodynamics.* 1990   ISBN 0-7923-0937-5
4. E. Coustols (ed.): *Turbulence Control by Passive Means.* 1990   ISBN 0-7923-1020-9
5. A.A. Borissov (ed.): *Dynamic Structure of Detonation in Gaseous and Dispersed Media.* 1991
                                                                        ISBN 0-7923-1340-2
6. K.-S. Choi (ed.): *Recent Developments in Turbulence Management.* 1991 ISBN 0-7923-1477-8
7. E.P. Evans and B. Coulbeck (eds.): *Pipeline Systems.* 1992   ISBN 0-7923-1668-1
8. B. Nau (ed.): *Fluid Sealing.* 1992   ISBN 0-7923-1669-X
9. T.K.S. Murthy (ed.): *Computational Methods in Hypersonic Aerodynamics.* 1992
                                                                        ISBN 0-7923-1673-8
10. R. King (ed.): *Fluid Mechanics of Mixing.* Modelling, Operations and Experimental Techniques. 1992   ISBN 0-7923-1720-3
11. Z. Han and X. Yin: *Shock Dynamics.* 1993   ISBN 0-7923-1746-7
12. L. Svarovsky and M.T. Thew (eds.): *Hydroclones.* Analysis and Applications. 1992
                                                                        ISBN 0-7923-1876-5
13. A. Lichtarowicz (ed.): *Jet Cutting Technology.* 1992   ISBN 0-7923-1979-6
14. F.T.M. Nieuwstadt (ed.): *Flow Visualization and Image Analysis.* 1993 ISBN 0-7923-1994-X
15. A.J. Saul (ed.): *Floods and Flood Management.* 1992   ISBN 0-7923-2078-6
16. D.E. Ashpis, T.B. Gatski and R. Hirsh (eds.): *Instabilities and Turbulence in Engineering Flows.* 1993   ISBN 0-7923-2161-8
17. R.S. Azad: *The Atmospheric Boundary Layer for Engineers.* 1993   ISBN 0-7923-2187-1
18. F.T.M. Nieuwstadt (ed.): *Advances in Turbulence IV.* 1993   ISBN 0-7923-2282-7
19. K.K. Prasad (ed.): *Further Developments in Turbulence Management.* 1993
                                                                        ISBN 0-7923-2291-6
20. Y.A. Tatarchenko: *Shaped Crystal Growth.* 1993   ISBN 0-7923-2419-6
21. J.P. Bonnet and M.N. Glauser (eds.): *Eddy Structure Identification in Free Turbulent Shear Flows.* 1993   ISBN 0-7923-2449-8
22. R.S. Srivastava: *Interaction of Shock Waves.* 1994   ISBN 0-7923-2920-1
23. J.R. Blake, J.M. Boulton-Stone and N.H. Thomas (eds.): *Bubble Dynamics and Interface Phenomena.* 1994   ISBN 0-7923-3008-0

Mechanics

Mechanics

Mechanics

68. I.D. Abrahams, P.A. Martin and M.J. Simon (eds.): *IUTAM Symposium on Diffraction and Scattering in Fluid Mechanics and Elasticity*. Proceedings of the IUTAM Symposium held in Manchester, (UK, 16-20 July 2000). 2002   ISBN 1-4020-0590-3

69. P. Chassaing, R.A. Antonia, F. Anselmet, L. Joly and S. Sarkar: *Variable Density Fluid Turbulence*. 2002   ISBN 1-4020-0671-3

70. A. Pollard and S. Candel (eds.): *IUTAM Symposium on Turbulent Mixing and Combustion.* Proceedings of the IUTAM Symposium held in Kingston, Ontario, Canada, June 3-6, 2001. 2002   ISBN 1-4020-0747-7

71. K. Bajer and H.K. Moffatt (eds.): *Tubes, Sheets and Singularities in Fluid Dynamics*. 2002
                                                                      ISBN 1-4020-0980-1

72. P.W. Carpenter and T.J. Pedley (eds.): *Flow Past Highly Compliant Boundaries and in Collapsible Tubes*. IUTAM Symposium held at the Univerity of Warwick, Coventry, United Kingdom, 26-30 March 2001. 2003   ISBN 1-4020-1161-X

73. H. Sobieczky (ed.): *IUTAM Symposium Transsonicum IV.* Proceedings of the IUTAM Symposium held in Göttingen, Germany, 2-6 September 2002. 2003   ISBN 1-4020-1608-5

74. A.J. Smits (ed.): *IUTAM Symposium on Reynolds Number Scaling in Turbulent Flow*. Proceedings of the IUTAM Symposium held in Princeton, NJ, U.S.A., September 11-13, 2002. 2003
                                                                      ISBN 1-4020-1775-8

75. H. Benaroya and T. Wei (eds.): *IUTAM Symposium on Integrated Modeling of Fully Coupled Fluid Structure Interactions Using Analysis, Computations and Experiments*. Proceedings of the IUTAM Symposium held in New Jersey, U.S.A., 2-6 June 2003. 2003 ISBN 1-4020-1806-1

76. J.-P. Franc and J.-M. Michel: *Fundamentals of Cavitation*. 2004   ISBN 1-4020-2232-8

77. T. Mullin and R.R. Kerswell (eds.): *IUTAM Symposium on Laminar Turbulent Transition and Finite Amplitude Solutions*. 2005   ISBN 1-4020-4048-2

78. R. Govindarajan (ed.): *Sixth IUTAM Symposium on Laminar-Turbulent Transition*. Proceedings of the Sixth IUTAM Symposium on Laminar-Turbulent Transition, Bangalore, India, 2004. 2006   ISBN 1-4020-3459-8